

**A Progress Report**

**January 1, 1993 to June 30, 1993**

**NASA-UVA LIGHT AEROSPACE ALLOY AND STRUCTURES  
TECHNOLOGY PROGRAM (LA<sup>2</sup>ST)**

**NASA-LaRC Grant NAG-1-745**

**Submitted to:**

**National Aeronautics and Space Administration  
Langley Research Center  
Hampton, Virginia 23665**

**Attention:**

**Mr. Richard J. Siebels  
Grants Officer  
MS 126**

**For Review by:**

**Mr. Dennis L. Dicus  
Grant Monitor  
Metallic Materials Branch, MS 188A**

**Submitted by:**

**Richard P. Gangloff  
Professor**

**Report No. UVA/528266/MS94/113  
July 20, 1993**

**DEPARTMENT OF MATERIALS SCIENCE  
AND ENGINEERING**

N93-31739

Unclas

G3/26 0176694

(NASA-CR-193412) NASA-UVA LIGHT  
AEROSPACE ALLOY AND STRUCTURES  
TECHNOLOGY PROGRAM (LA2ST) Progress  
Report, 1 Jan. - 30 Jun. 1993  
(Virginia Univ.) 441 p

SCHOOL OF

**ENGINEERING**   
**& APPLIED SCIENCE**

University of Virginia  
Thornton Hall  
Charlottesville, VA 22903

**UNIVERSITY OF VIRGINIA**  
**School of Engineering and Applied Science**

The University of Virginia's School of Engineering and Applied Science has an undergraduate enrollment of approximately 1,500 students with a graduate enrollment of approximately 600. There are 160 faculty members, a majority of whom conduct research in addition to teaching.

Research is a vital part of the educational program and interests parallel academic specialties. These range from the classical engineering disciplines of Chemical, Civil, Electrical, and Mechanical and Aerospace to newer, more specialized fields of Applied Mechanics, Biomedical Engineering, Systems Engineering, Materials Science, Nuclear Engineering and Engineering Physics, Applied Mathematics and Computer Science. Within these disciplines there are well equipped laboratories for conducting highly specialized research. All departments offer the doctorate; Biomedical and Materials Science grant only graduate degrees. In addition, courses in the humanities are offered within the School.

The University of Virginia (which includes approximately 2,000 faculty and a total of full-time student enrollment of about 17,000), also offers professional degrees under the schools of Architecture, Law, Medicine, Nursing, Commerce, Business Administration, and Education. In addition, the College of Arts and Sciences houses departments of Mathematics, Physics, Chemistry and others relevant to the engineering research program. The School of Engineering and Applied Science is an integral part of this University community which provides opportunities for interdisciplinary work in pursuit of the basic goals of education, research, and public service.

NASA-UVA LIGHT AEROSPACE ALLOY  
AND STRUCTURES TECHNOLOGY PROGRAM

502205

LA<sup>2</sup>ST

**Program Director:**

Richard P. Gangloff

**Co-principal Investigators:**

John R. Scully  
Glenn E. Stoner  
Earl A. Thornton  
Franklin E. Wawner, Jr.  
John A. Wert

**NASA-LaRC Grant Monitor:**

Dennis L. Dicus





## TABLE OF CONTENTS

	<u>Page</u>
Executive Summary	v
Introduction	1
Summary Statistics	7
Grant Publications (Cumulative, Refereed)	15
Completed Projects	19
Administrative Progress	23
Current Projects	25
Research Progress and Plans	29
Project 1    Environmental Fatigue Crack Growth and Cracking Mechanisms in Al-Li-Cu Alloy 2090 D.C. Slavik and R.P. Gangloff	29
Project 2    Elevated Temperature Damage Tolerance of Advanced Ingot Metallurgy Aluminum Alloys M.J. Haynes and R.P. Gangloff	37
Project 3    Cryogenic Temperature Effects on the Deformation and Fracture of Al-Li-Cu-In Alloys J.A. Wagner and R.P. Gangloff	43
Project 4    The Effect of Temperature on the Fracture Toughness of Weldalite™ X2095 C.L. Lach and R.P. Gangloff	47
Project 5    Mechanisms of Localized Corrosion in Alloys 2090 and X2095 F. Douglas Wall and G.E. Stoner	49
Project 6    The Effects of Zinc Additions on Precipitation and SCC in Alloy 8090 R.J. Kilmer and G.E. Stoner	51

## TABLE OF CONTENTS (continued)

	<u>Page</u>
Project 7    Hydrogen Interactions in Aluminum-Lithium Alloy 2090 and Model Alloys S.W. Smith and J.R. Scully	53
Project 8    Metastable Pitting of Al Alloys in Halide Solutions S.T. Pride, J.R. Scully and J.L. Hudson	57
Project 9    Investigation of the Effect of Thermal Exposure on the Mechanical Properties of Ti/SiC Composites D.B. Gundel and F.E. Wawner	63
Project 10   Processing and Superplastic Properties of Weldalite Sheet M. Lyttle and J.A. Wert	67
Project 11   Environmental Effects in Fatigue Life Prediction	71
11A:    Dynamic Strain Effects on Cracking in AA7075-T651 M. Mason and R.P. Gangloff	71
11B:    Environmental Effects on Fatigue Crack Propagation and Closure in Titanium Alloys S.S. Kim and R.P. Gangloff	77
Project 12   Experimental Study of the Nonlinear Viscoplastic Response of High Temperature Structures	81
12A:    Finite Element TVP Analysis	
12B:    Bodner-Partoorn Constitutive Models	
12C:    Thermal-Structural Tests of Panels M.F. Coyle, M.A. Rowley and E.A. Thornton	

TABLE OF CONTENTS (continued)

	<u>Page</u>
Appendix I: Grant Publications (January 1 to June 30, 1993)	83
Appendix II: Grant Presentations (January 1 to June 30, 1993)	85
Appendix III: Grant Progress Reports (January, 1988 to December, 1992)	87
Appendix IV: Agenda of the Fourth Annual NASA-UVa LA <sup>2</sup> ST Grant Review Meeting	89
Distribution List	



# NASA-UVA LIGHT AEROSPACE ALLOY AND STRUCTURES TECHNOLOGY PROGRAM

## EXECUTIVE SUMMARY

The NASA-UVa Light Aerospace Alloy and Structures Technology (LA<sup>2</sup>ST) Program continues a high level of activity, with projects being conducted by graduate students and faculty advisors in the Departments of Materials Science and Engineering, and Mechanical and Aerospace Engineering at the University of Virginia. This work is funded by the NASA-Langley Research Center under Grant NAG-1-745. Here, we report on progress achieved between January 1 and June 30, 1993. These results were presented at the Fourth Annual NASA-UVa LA<sup>2</sup>ST Grant Review Meeting held at the Langley Research Center in July of 1993.

The objective of the LA<sup>2</sup>ST Program is to conduct interdisciplinary graduate student research on the performance of next generation, light weight aerospace alloys, composites and thermal gradient structures in collaboration with NASA-Langley researchers. Specific technical objectives are presented for each research project. We generally aim to produce relevant data and basic understanding of material mechanical response, environmental/corrosion behavior, and microstructure; new monolithic and composite alloys; advanced processing methods; new solid and fluid mechanics analyses; measurement advances; and critically, a pool of educated graduate students for aerospace technologies.

The accomplishments presented in this report are as follows.

- oo Four research areas are actively investigated, including: (1) Mechanical and Environmental Degradation Mechanisms in Advanced Light Metals and Composites, (2) Aerospace Materials Science, (3) Mechanics of Materials and Composites for Light Aerospace Structures, and (4) Thermal Gradient Structures.
- oo Thirteen research projects are being conducted by 8 PhD and 5 MS level graduate students, 6 faculty members, and 1 Research Associate from two departments in the School of Engineering and Applied Science at UVa. Each project is planned and executed in conjunction with a specific branch and technical monitor at NASA-LaRC.
- oo No undergraduates were recruited to conduct research at NASA-LaRC during the

Summer of 1993. Three undergraduates are participating in LA<sup>2</sup>ST research at UVa. The undergraduate program will be emphasized in 1994.

- oo Accomplishments between January and June of 1993 include 5 journal or proceedings publications, 1 NASA progress report, 1 NASA Contractor Report, 9 presentations at national technical meetings, and 5 Dissertations/Theses. Six students graduated during this reporting period, 5 with the PhD and 1 with the Masters of Science Degree. The LA<sup>2</sup>ST totals since 1986 are 68 publications (37 archival journal or book publications), 13 PhD dissertations or MS theses, 77 external technical presentations, 14 NASA progress reports and 2 NASA Contractor Reports. Since 1986, 23 graduate students, including 22 citizens of the United States, have been involved with LA<sup>2</sup>ST research; 14 have received the MS or PhD degree. Four post-doctoral research associates have participated in LA<sup>2</sup>ST research.
  
- oo *Research on environmental fatigue of Al-Li-Cu alloys* has been completed and the student successfully defended his PhD dissertation. Fatigue crack propagation kinetics and microscopic damage modes were characterized for four microstructures of AA2090, cyclically stressed in vacuum and aqueous NaCl. Microstructural effects are generally unimportant, particularly for commercial unrecrystallized plate and sheet, and when considered based on a crack tip strain range parameter. Microscopic crack paths are near-{111} for fatigue in vacuum and near-{521} for NaCl for each microstructure; as quantitatively defined by Electron Back Scattering Pattern analysis. The former is understood based on localized deformation band cracking, while the latter high index cracking plane is inconsistent with the proposed mechanisms for hydrogen environment embrittlement in aluminum alloys. (Project 1)
  
- oo *Research on mechanisms of localized corrosion and environmental fracture in Al-Cu-Li-Mg-Ag alloy X2095 and compositional variations* suggests that the anodic T<sub>1</sub> phase and a Cu-depleted zone may define a pathway for propagation of localized corrosion and may play a strong role in determining the environmentally assisted cracking (EAC) behavior of these alloys. Capillary electrophoresis analysis of solutions taken from Al-Cu-Li alloys exposed to a small volume of NaCl solution indicates the possibility of an alkaline occluded environment with significant lithium concentration being generated within a short amount of time. This information will help to refine the understanding of the electrochemical processes involved in the EAC behavior of advanced aluminum alloys. (Project 5)

- oo ***Research on the effect of zinc additions on the precipitation and stress corrosion cracking behavior of alloy 8090*** demonstrates that low to intermediate (~ 1 w/o) zinc additions to AA 8090 type alloys increase the resistance to fracture induced by alternate immersion-time to failure tests, slow rising load SCC tests, and embrittlement by hydrogen charging. Furthermore, these additions allow the alloy to maintain this resistance over a broader range of heat treatment, especially the intermediate age condition. (Project 6)
  
- oo ***Research on hydrogen interactions with Al-Li-Cu alloy 2090 and model alloys*** has shown that hydrogen significantly affects intergranular fracture processes in underaged 2090 alloys. Thermal desorption spectroscopy has been used to measure trapped hydrogen in these alloys. Correlation of trapping analysis with the mechanical testing and fractography will yield a more complete understanding of HEAC for aluminum-lithium alloys. (Project 7)
  
- oo ***Research on metastable pitting of aluminum alloys*** has identified factors which promote the transition from metastable to stable pitting for pure Al. Lower micropit nucleation frequencies at a given  $\text{Cl}^-$  concentration, applied potential, and selective elimination of micropits with high pit current densities are some of the factors which can contribute to pitting inhibition. This work is enabled by a NASA Graduate Student Researchers Program Fellowship (Under-Represented Minority Focus). (Project 8)
  
- oo ***Research on the cryogenic fracture toughness of Al-Cu-Li + In alloys*** is focusing on a model to describe the progression of fracture in commercial 2090-T81 plate at ambient and cryogenic temperatures. Transgranular shear fracture linking delaminations along grain boundaries crosses numerous grains, regardless of the apparent orientation of the grains. While both  $K_{IC}$  and stable tearing resistance increase with decreasing temperature from 25°C, the largest toughness increase occurs between -150 and -180°C. (Project 3)
  
- oo ***Research on the fracture toughness of Weldalite™*** was not conducted during this reporting period because the graduate student was on leave from NASA-LaRC. (Project 4)

- oo *Research on elevated temperature cracking of advanced I/M aluminum alloys* demonstrates that  $K_{IC}$  (from J- $\Delta a$ ) for AA2519 + Mg, 2519 + Mg/Ag and 2650 are greater than 2618 and RS P/M 8009, all at 25°C. Plane stress growth toughnesses ( $K_C$  at 25°C) of the two variants of 2519 are superior to that of 2024-T3.  $K_{IC}$  for 2519 + Ag is independent of temperature between 25 and 175°C, while that of Mg modified 2519 is maximum at about 100°C before declining at 175°C.  $K_C$  for each 2519 variant initially increases and then falls as temperature increases to 175°C; plane stress toughness decreases less rapidly for the alloy with the Ag addition. Microvoid coalescence is the fracture mechanism for each alloy at all temperatures.

(Project 2)

- oo *Research on the response of Ti-1100/SCS-6 composites to thermal exposure* indicates that defects in the material incurred during initial processing cause significant tensile property degradation following exposure. Fiber-fiber contact and poor matrix-ply bonding permit much greater environmental attack of the matrix than in materials without these defects. Well-consolidated composites retain 80 to 90% (transverse and longitudinal, respectively) of their as-fabricated properties after thermal cycling from 150 to 800°C, 500 times in air.

(Project 9)

- oo *Research on superplastic forming of Weldalite™* has determined the uniaxial superplastic properties of Weldalite™ sheet for longitudinal and transverse specimen orientations. Grain size, microtexture, and boundary misorientation measurements have been performed in an effort to understand microstructural evolution during forming and its effect on the orientation dependence of superplastic flow properties. To help interpret the data, a simulative model has been formulated to show how various deformation mechanisms contribute to microstructural evolution.

(Project 10)

- oo *Research to incorporate environmental effects into fracture mechanics fatigue life prediction codes such as NASA FLAGRO* is progressing in two directions.

++ Linear superposition does not predict environmental fatigue crack propagation in the susceptible orientation (SL) and temper (T651) of AA7075 fully immersed in aqueous NaCl. Measured time-based crack growth rates (plateau  $da/dt$ ) are too low to predict either the observed environmental fatigue crack growth rates or the frequency dependence at fixed  $\Delta K$ . Applied crack tip strain rates do not appear to enhance  $K_{ISCC}$  or  $da/dt$ .



++ Fatigue crack growth rates in Ti-6Al-4V (ELI) increase for aqueous NaCl compared to moist air, and increase with increasing R for both environments, an effect accounted for by crack closure. This trend is generally (but not precisely) modeled by the empirical, closure-modified Newman-Forman equation. Closure levels depend on  $\Delta K$  and R, and are environment sensitive, implying mechanisms other than plasticity. Increasing R does not enhance intrinsic  $da/dN$  for either environment. Complex  $da/dN$  vs  $\Delta K$  relationships for moist air and NaCl are not caused by closure, but are associated with environmental embrittlement.

(Project 11)

- oo *Research on thermoviscoplastic behavior* of high temperature alloy panels demonstrated material and geometric nonlinearities. Experiments with instrumented Hastelloy-X panels provided elastic and inelastic temperature and displacement data for thermal buckling. An experimental program characterized the viscoplastic deformation response of Hastelloy-X and 2618 and 8009 aluminum alloys. Correlation of computational and experimental results for panel buckling has been initiated.

(Project 12)



## INTRODUCTION

### Background

In 1986 the Metallic Materials Branch in the Materials Division of the NASA-Langley Research Center initiated sponsorship of graduate student engineering and scientific research in the Department of Materials Science and Engineering at the University of Virginia<sup>[1]</sup>. This work emphasized the mechanical and corrosion behavior of light aerospace alloys, particularly Al-Li-Cu based compositions, in aggressive aerospace environments<sup>[2-4]</sup>.

In the Fall of 1988, the scope of this program increased to incorporate research at UVa on the development and processing of advanced aerospace materials<sup>[5]</sup>. Additional funding was provided by the Metallic Materials and Mechanics of Materials Branches at NASA-LaRC. In early 1989 the program was further enhanced to include interdisciplinary work on solid mechanics and thermal structures, with funding from several Divisions within the Structures Directorate at NASA-LaRC<sup>[6]</sup>. The Departments of Civil Engineering (Applied Mechanics Program) and of Mechanical and Aerospace Engineering at UVa participated in this expanded program. With this growth, the NASA-UVa Light Aerospace Alloy and Structures Technology Program (or LA<sup>2</sup>ST Program) was formed within the School of Engineering and Applied Science at UVa.

Since 1989, the LA<sup>2</sup>ST program has operated with full participation from about 10 faculty and 15 graduate students, as outlined in the last eight progress reports<sup>[7-14]</sup> and four grant renewal proposals<sup>[15-18]</sup>. Some contraction in the scope of the LA<sup>2</sup>ST Program occurred in 1993, with the elimination of two programs in solid mechanics and thermal structures<sup>[18]</sup>. Three 2-day Grant Review Meetings were held in June of 1990, 1991 and 1992 at the Langley Research Center, with over 25 faculty and graduate students from UVa participating. Since 1990, undergraduate engineering students have been involved in research projects at both NASA-LaRC and UVa.

In October of 1991, Dean E.A. Starke proposed a substantial enhancement to the base LA<sup>2</sup>ST Program<sup>[19,20]</sup>. The objective of this supplement is to involve UVa faculty with engineering scientists from aluminum alloy producers and airframe manufacturers in a broad research program to develop aluminum alloys and composites for elevated temperature High Speed Civil Transport applications. This research began in January of 1992 and the results are separately reported.

### Problem and Needs

Future aerospace structures require high performance light alloys and metal matrix composites with associated processing and fabrication techniques; new structural design methods and concepts with experimental evaluations; component reliability/durability/damage tolerance prediction procedures; and a pool of masters and doctoral level engineers and scientists. Work on advanced materials and structures must be interdisciplinary and integrated. The thermal and chemical effects of aerospace environments on light metals and composites are particularly important to material performance. Nationally, academic efforts in these areas are limited. The NASA-UVa LA<sup>2</sup>ST Program addresses these needs.

### LA<sup>2</sup>ST Program

As detailed in the original proposal<sup>[6]</sup> and affirmed in the most recent renewal<sup>[18]</sup>, faculty from the Departments of Materials Science and Engineering, Mechanical and Aerospace Engineering, and Civil Engineering and Applied Mechanics at UVa are participating in the LA<sup>2</sup>ST research and education program focused on high performance, light weight, aerospace alloys and structures. We aim to develop long term and interdisciplinary collaborations between graduate students, UVa faculty, and NASA-Langley researchers.

Our research efforts are producing basic understanding of materials performance, new monolithic and composite alloys, advanced processing methods, solid and fluid mechanics analyses, and measurement advances. A major product of the LA<sup>2</sup>ST program is graduate students with interdisciplinary education and research experience in materials science, mechanics and mathematics. These advances should enable various NASA technologies.

The scope of the LA<sup>2</sup>ST Program is broad. Four research areas are being investigated, including:

- oo Mechanical and Environmental Degradation Mechanisms in Advanced Light Metals and Composites,
- oo Aerospace Materials Science,
- oo Mechanics of Materials and Composites for Light Aerospace Structures,
- oo Thermal Gradient Structures.

Thirteen research projects are currently ongoing within these four areas and are reported here. These projects currently involve six faculty, one research associate and thirteen graduate students. Over one-half the graduate students are currently at the doctoral level (8 of 13), all are citizens of the United States, one is supported by the NASA Minority Grant Program, and three are cosponsored by the University of Virginia Academic Enhancement Program or private industry. In each case the research provides the basis for the thesis or dissertation requirement of graduate studies at the University of Virginia. Each project is developed in conjunction with a specific LaRC researcher. Research is conducted at either UVa or LaRC, and under the guidance of UVa faculty and NASA staff. Participating students and faculty are closely identified with a NASA-LaRC branch.

#### Organization of Progress Report

This progress report first provides LA<sup>2</sup>ST Program administrative information including statistics on the productivity of faculty and graduate student participants, a history of current and graduated students, refereed or archival publications, and a list of ongoing projects with NASA and UVa advisors.

Thirteen sections summarize the technical accomplishments of each research project, emphasizing the period from January 1 to June 30, 1993. Each program section contains a brief narrative of objective, recent progress, conclusions and immediate milestones; coupled with a set of visual aids presented at the Fourth Annual NASA-UVa LA<sup>2</sup>ST Grant Review Meeting held at NASA-LaRC in July of 1993. The agenda of this meeting is presented in Appendix IV.

Appendices I through III document grant-sponsored publications, conference participation and citations of all LA<sup>2</sup>ST Progress Reports.

#### References

1. R.P. Gangloff, G.E. Stoner and M.R. Louthan, Jr., "Environment Assisted Degradation Mechanisms in Al-Li Alloys", University of Virginia, Proposal No. MS-NASA/LaRC-3545-87, October, 1986.
2. R.P. Gangloff, G.E. Stoner and R.E. Swanson, "Environment Assisted Degradation Mechanisms in Al-Li Alloys", University of Virginia, Report No. UVA/528266/MS88/101, January, 1988.

3. R.P. Gangloff, G.E. Stoner and R.E. Swanson, "Environment Assisted Degradation Mechanisms in Advanced Light Metals", University of Virginia, Report No. UVA/528266/MS88/102, June, 1988.
4. R.P. Gangloff, G.E. Stoner and R.E. Swanson, "Environment Assisted Degradation Mechanisms in Advanced Light Metals", University of Virginia, Report No. UVA/528266/MS89/103, January, 1989.
5. T.H. Courtney, R.P. Gangloff, G.E. Stoner and H.G.F. Wilsdorf, "The NASA-UVa Light Alloy Technology Program", University of Virginia, Proposal No. MS NASA/LaRC-3937-88, March, 1988.
6. R.P. Gangloff, "NASA-UVa Light Aerospace Alloy and Structures Technology Program", University of Virginia, Proposal No. MS NASA/LaRC-4278-89, January, 1989.
7. R.P. Gangloff, "NASA-UVa Light Aerospace Alloy and Structures Technology Program", University of Virginia, Report No. UVA/528266/MS90/104, August, 1989.
8. R.P. Gangloff, "NASA-UVa Light Aerospace Alloy and Structures Technology Program", University of Virginia, Report No. UVA/528266/MS90/105, December, 1989.
9. R.P. Gangloff, "NASA-UVa Light Aerospace Alloy and Structures Technology Program", UVa Report No. UVA/528266/MS90/106, June, 1990.
10. R.P. Gangloff, "NASA-UVa Light Aerospace Alloy and Structures Technology Program", UVa Report No. UVA/528266/MS91/107, January, 1991.
11. R.P. Gangloff, "NASA-UVa Light Aerospace Alloy and Structures Technology Program", UVa Report No. UVA/528266/MS91/108, July, 1991.
12. R.P. Gangloff, "NASA-UVa Light Aerospace Alloy and Structures Technology Program", UVa Report No. UVA/528266/MS92/109, January, 1992.
13. R.P. Gangloff, "NASA-UVa Light Aerospace Alloy and Structures Technology Program", UVa Report No. UVA/528266/MS93/111, July, 1992.
14. R.P. Gangloff, "NASA-UVa Light Aerospace Alloy and Structures Technology Program", UVa Report No. UVA/528266/MSE93/112, March, 1993.
15. R.P. Gangloff, "NASA-UVa Light Aerospace Alloy and Structures Technology Program", University of Virginia, Proposal No. MS-NASA/LaRC-4512-90, November, 1989.

16. R.P. Gangloff, "NASA-UVa Light Aerospace Alloy and Structures Technology Program", University of Virginia, Proposal No. MS-NASA/LaRC-4841-91, September, 1990.
17. R.P. Gangloff, "NASA-UVa Light Aerospace Alloy and Structures Technology Program", University of Virginia, Proposal No. MS-NASA/LaRC-5219-92, October, 1991.
18. R.P. Gangloff, "NASA-UVa Light Aerospace Alloy and Structures Technology Program", University of Virginia, Proposal No. MSE-NASA/LaRC-5691-93, November, 1992.
19. R.P. Gangloff, E.A. Starke, Jr., J.M. Howe and F.E. Wawner, "NASA-UVa Light Aerospace Alloy and Structures Technology Program: Supplement on Aluminum Based Materials for High Speed Aircraft", University of Virginia, Proposal No. MS NASA/LaRC-5215-92, October, 1991.
20. R.P. Gangloff, E.A. Starke, Jr., J.M. Howe and F.E. Wawner, "NASA-UVa Light Aerospace Alloy and Structures Technology Program: Supplement on Aluminum Based Materials for High Speed Aircraft", University of Virginia, Proposal No. MSE NASA/LaRC-5691-93, November, 1992.





## SUMMARY STATISTICS

Table I documents the numbers of students and faculty who participated in the LA<sup>2</sup>ST Program, both during this reporting period and since the program inception in 1986. Academic and research accomplishments are indicated by the degrees awarded, publications and presentations. Specific graduate students and research associates who participated in the LA<sup>2</sup>ST Program are named in Tables II and III, respectively.

*TABLE I: LA<sup>2</sup>ST Program Statistics*

	<u>Current</u> <u>1/1/93 to 6/30/93</u>	<u>Cumulative</u> <u>1986 to 6/30/93</u>
PhD Students--UVa:	7	15
--NASA-LaRC:	1	1
MS Students--UVa:	4	5
--NASA:	1	1
--VPI:	0	1
Undergraduates--UVa:	3	9
--NASA-LaRC:	0	11
Faculty--UVa:	6	11
--VPI:	0	1
Research Associates--UVa:	1	4
PhD Awarded:	5	10
MS Awarded:	1	4

*TABLE I: LA<sup>2</sup>ST Program Statistics (continued)*

	Current <u>1/1/93 to 6/30/93</u>	Cumulative <u>1986 to 6/30/93</u>
Employers--NASA:	1	2
--Federal:	1	3
--University:	1	1
--Industry:	2	4
--Next degree:	0	2
Publications:	5	68
Presentations:	9	77
Dissertations/Theses:	5	13
NASA Reports:	1	15

TABLE II  
GRADUATE STUDENT PARTICIPATION IN THE NASA-UVa LA<sup>2</sup>ST PROGRAM  
June, 1993

<u>POS #</u>	<u>GRADUATE STUDENT EMPLOYER</u>	<u>ENTERED PROGRAM</u>	<u>DEGREE COMPLETED</u>	<u>LANGLEY RESIDENCY</u>	<u>RESEARCH TOPIC</u>	<u>UVa/NASA-LaRC ADVISORS</u>
1.	R. S. Piascik NASA-Langley	6/86	Ph.D. 10/89		Damage Localization Mechanisms in Corrosion Fatigue of Aluminum-Lithium Alloys	R. P. Gangloff D. L. Dicus
2.	J. P. Moran NIST	9/88	Ph.D. 12/89		An Investigation of the Localized Corrosion and Stress Corrosion Cracking Behavior of Alloy 2090	G. E. Stoner W. B. Lisagor
3.	R. G. Buchheit Sandia National Laboratories	6/87	Ph.D. 12/90		Measurements and Mechanisms of Localized Aqueous Corrosion in Aluminum-Lithium Alloys	G. E. Stoner D. L. Dicus
4.	D. B. Gundel Ph.D.-UVa	9/88	M.S. 12/90		Investigation of the Reaction Kinetics Between SiC Fibers and Titanium Matrix Composites	F. E. Wawner W. B. Brewer
5.	F. Rivet (VPI)	9/88	M.S. 12/90		Deformation and Fracture of Aluminum- Lithium Alloys: The Effect of Dissolved Hydrogen	R. E. Swanson (VPI) D. L. Dicus
6.	C. Copper Ph.D.-UVa	4/89	M.S. 12/90		Design of Cryogenic Tanks for Space Vehicles	W. D. Pilkey J. K. Haviland D. R. Rummel M.J. Stuart
7.	J. A. Wagner NASA-Langley	6/87	Ph.D.	PhD Research @ LaRC	Temperature Effects on the Deformation and Fracture of Al-Li-Cu-In Alloys	R. P. Gangloff W. B. Lisagor J. C. Newman
8.	W. C. Porr, Jr. David Taylor Naval Ship R&DC	1/88	Ph.D. 6/92		Elevated Temperature Failure of an Advanced Powder Metallurgy Aluminum Alloy	R. P. Gangloff C. E. Harris

TABLE II (continued)  
GRADUATE STUDENT PARTICIPATION IN THE NASA-UVa LA<sup>2</sup>ST PROGRAM  
(continued)

<u>POS #</u>	<u>GRADUATE STUDENT EMPLOYER</u>	<u>ENTERED PROGRAM</u>	<u>DEGREE COMPLETED</u>	<u>LANGLEY RESIDENCY</u>	<u>RESEARCH TOPIC</u>	<u>UVa/NASA-LaRC ADVISORS</u>
9.	J. B. Parse Consultant	9/88	Ph.D. 6/92		Quantitative Characterization of the Spatial Distribution of Particles in Materials	J. A. Wert D. R. Tenney
10.	D. C. Slavik Knolls Atomic Power Laboratory	9/89	Ph.D. 6/93		Environment Enhanced Fatigue of Advanced Aluminum Alloys and Composites	R. P. Gangloff D. L. Dicus
11.	C. L. Lach NASA-Langley	9/89	M.S.	MS Research @LaRC	Effect of Temperature on the Fracture Toughness of Weldalite <sup>TM</sup> 049	R. P. Gangloff W. B. Lisagor
12.	R. J. Kilmer General Motors	11/89	Ph.D. 9/93		Effect of Zn Additions on the Environmental Stability of Alloy 8090	G. E. Stoner W. B. Lisagor
13.	M. F. Coyle	12/89	Ph.D.		Visoplastic Response of High Temperature Structures	E. A. Thornton J. H. Starnes, Jr.
14.	C. J. Lissenden University of Kentucky; Engineering Mechanics	9/90	Ph.D. 6/93		Inelastic Response of Metal Matrix Composites Under Biaxial Loading	C. T. Herakovich M. J. Pindera W. S. Johnson
15.	C. Cooper AMP Incorporated	1/91	Ph.D. 6/93		Shell Structures Analytical Modeling	W. D. Pilkey J. K. Haviland M. Shuart J. Stroud

TABLE II (continued)  
GRADUATE STUDENT PARTICIPATION IN THE NASA-UVa LA<sup>2</sup>ST PROGRAM  
(continued)

16.	Douglas Wall	4/91	Ph.D.		Measurements and Mechanisms of Localized Corrosion in Al-Li-Cu Alloys	G. E. Stoner D. L. Dicus
17.	S. W. Smith	4/91	Ph.D.		Hydrogen Interactions with Al-Li Alloys	J. R. Scully W. B. Lisagor
18.	D. B. Gundel	4/91	Ph.D.		Effect of Thermal Exposure on the Mechanical Properties of Titanium/SiC Composites	F. E. Wawner W. B. Brewer
19.	K. McCarthy	5/91	M.S. 6/93 (Nonthesis)		Shell Structures Analytical Modeling	W. D. Pilkey M. J. Shuart J. Stroud
20.	M. Lyttle	12/91	M.S.		Superplasticity in Al-Li-Cu Alloys	J. A. Wert T. T. Bales
21.	T. Johnson NASA-LaRC	12/91	Ph.D. 6/93	(NASA Minority Grantee)	Shell Structures Analytical Modeling	W. D. Pilkey M. J. Shuart J. Stroud
22.	S. T. Pride	12/91	Ph.D.	(NASA Minority Grantee)	Metastable Pitting of Al Alloys	J. R. Scully D. L. Dicus
23.	M. A. Rowley	1/92	M.S. 6/93	(UVa AEP Sponsored)	Viscoplasticity of Metals	E. A. Thornton J. H. Starnes, Jr.
24.	M. J. Haynes	9/92	M.S.		Elevated Temperature Fracture of Advanced IM Al Alloys	R. P. Gangloff TBD
25.	M. Mason	9/92	M.S.		Environmental Effects in Fatigue Life Prediction	R. P. Gangloff R. S. Piascik



TABLE III  
Post-Doctoral Research Associate Participation  
in NASA-UVA LA<sup>2</sup>ST Program

<u>Pos</u> <u>#</u>	<u>Res. Assoc.</u>	<u>Tenure</u>	<u>Research</u>	<u>Supervisor</u>
1.	Yang Leng	3/89 to 12/91	Elevated Tempera- ture Deformation and Fracture of PM AL Alloys and Composites	R. P. Gangloff
2.	Farshad Mizadeh	7/89 to 12/91	Deformation of Metal Matrix Composites	C. T. Herakovich and Marek-Jerzy Pindera
3.	A.K.Mukhopadhyay	6/91 to 6/92	Aluminum Alloy Development	E. A. Starke, Jr.
4.	Sang-Shik Kim	12/91 to 12/93	Environmental Fatigue Life Prediction	R. P. Gangloff

17





GRANT PUBLICATIONS: (REFEREED JOURNALS, ARCHIVAL PROCEEDINGS  
AND NASA CONTRACTOR REPORTS)

The following papers are based on research conducted under LA<sup>2</sup>ST Program support, and are published in the referred or archival literature.

37. D. Gundel, P. Taylor and F. Wawner, "The Fabrication of Thin Oxide Coatings on Ceramic Fibers by a Sol-Gel Technique", Journal of Materials Science, in review (1993).
36. W.C. Porr, Jr. and R.P. Gangloff, "Elevated Temperature Fracture of RS/PM Alloy 8009: Part I-Fracture Mechanics Behavior", Metallurgical Transactions A, in review (1993).
35. J.B. Parse and J.A. Wert, "Effects of Deformation Processing on the Oxide Particle Distribution in PM Al Alloy Sheet", Metallurgical Transactions A, in review (1993).
34. R.S. Piascik and R.P. Gangloff, "Environmental Fatigue of an Al-Li-Cu Alloy: Part III - Modeling of Crack Tip Hydrogen Damage", Metallurgical Transactions A, in review (1993).
33. R.G. Buchheit, G.E. Stoner and G.J. Shiflet, "Corrosion Properties of a Rapidly Solidified Al<sub>90</sub>Fe<sub>5</sub>Gd<sub>5</sub> Alloy", J. Electrochem. Soc., in review (1993).
32. D. Gundel and F. Wawner, "The Influence of Fabrication Quality on the Response of Titanium/SiC Fiber Composites to Thermal Exposure", Composites Engineering, in press (1993).
31. E.A. Thornton, "Thermal Buckling of Plates and Shells," Applied Mechanics Reviews, in press, (1993).
30. D.C. Slavik, J.A. Wert and R.P. Gangloff, "Determining Fracture Facet Crystallography Using Electron Back Scatter Patterns and Quantitative Tilt Fractography", Journal of Materials Research, in press, October (1993).
29. E.A. Thornton and J.D. Kolenski, "Viscoplastic Response of Structures with Intense Local Heating", Journal of Aerospace Engineering, in press (1993).
28. R.P. Gangloff and S.S. Kim, "Environment Enhanced Fatigue Crack Propagation in Metals: Inputs to Fracture Mechanics Life Prediction Models", NASA Contractor Report, in press (1993).

27. D.C. Slavik, C.P. Blankenship, Jr., E.A. Starke, Jr. and R.P. Gangloff, "Intrinsic Fatigue Crack Growth Rates for Al-Li-Cu-Mg Alloys in Vacuum", Metallurgical Transactions A, in press, August (1993).
26. R.P. Gangloff, R.S. Piascik, D.L. Dicus and J.C. Newman, "Fatigue Crack Propagation in Aerospace Aluminum Alloys", Journal of Aircraft, in press (1993).
25. R.S. Piascik and R.P. Gangloff, "Environmental Fatigue of an Al-Li-Cu Alloy: Part II - Microscopic Hydrogen Cracking Processes", Metallurgical Transactions A, in press (1993).
24. R.G. Buchheit, J.P. Moran and G.E. Stoner, "The Electrochemical Behavior of the  $T_1$  ( $Al_2CuLi$ ) Intermetallic Compound and Its Role in Localized Corrosion of Al-3Cu-2Li Alloys", Corrosion, in press (1993).
23. E.A. Thornton, M.F. Coyle, and R.N. McLeod, "Experimental Study of Plate Buckling Induced by Spatial Temperature Gradients," Journal of Thermal Stresses, in press (1993).
22. J.B. Parse and J.A. Wert, "A Geometrical Description of Particle Distributions in Materials", Modeling and Simulation in Materials Science and Engineering, Vol. 1, pp. 275-296 (1993).
21. D.C. Slavik and R.P. Gangloff, "Microscopic Processes of Environmental Fatigue Crack Propagation in Al-Li-Cu Alloy 2090", in Fatigue '93, Vol. II, J.-P. Bailon and J.I. Dickson, eds., EMAS, West Midlands, UK, pp. 757-765 (1993).
20. C.J. Lissenden, M-J. Pindera and C.T. Herakovich, "Response of SiC/Ti Tubes Under Biaxial Loading in the Presence of Damage," Damage Mechanics in Composites, D.H. Allen and D.C. Lagoudas, Eds., ASME-AMD-Vol. 150, pp. 73-90 (1992).
19. J.A. Wagner and R.P. Gangloff, "Fracture Toughness of Al-Li-Cu-In Alloys", Scripta Metallurgica et Materialia, Vol. 26, pp. 1779-1784 (1992).
18. J.P. Moran, R.G. Buchheit, Jr., and G.E. Stoner, "Mechanisms of SCC of Alloy 2090 (Al-Li-Cu) - A Comparison of Interpretations from Static and Slow Strain Rate Techniques", Parkins Symposium on Fundamental Aspects of Stress Corrosion Cracking, S.M. Bruemmer, E.I. Meletis, R.H. Jones, W.W. Gerberich, F.P. Ford and R.W. Staehle, eds., TMS-AIME, Warrendale, PA, p. 159 (1992).
17. R.G. Buchheit, Jr., J.P. Moran, F.D. Wall, and G.E. Stoner, "Rapid Anodic Dissolution Based SCC of 2090 (Al-Li-Cu) by Isolated Pit Solutions," Parkins Symposium on Fundamental Aspects of Stress Corrosion Cracking, S.M. Bruemmer, E.I. Meletis, R.H. Jones, W.W. Gerberich, F.P. Ford and R.W. Staehle, eds., TMS-AIME, Warrendale, PA, p. 141 (1992).

16. R.J. Kilmer, T.J. Witters and G.E. Stoner, "Effect of Zn Additions on the Precipitation Events and Implications to Stress Corrosion Cracking Behavior in Al-Li-Cu-Mg-Zn Alloys", Proceedings of the Sixth International Al-Li Conference, M. Peters and P.J. Winkler, eds., DGM Informationsgesellschaft, Verlag, pp. 755-760 (1992).
15. C.T. Herakovich and J.S. Hidde, "Response of Metal Matrix Composites with Imperfect Bonding", Ultramicroscopy, Vol. 40, pp. 215-228 (1992).
14. R.G. Buchheit, Jr., F.D. Wall, G.E. Stoner and J.P. Moran, "Stress Corrosion Cracking of Al-Li-Cu-Zr Alloy 2090 in Aqueous  $\text{Cl}^-$  and Mixed  $\text{Cl}^-/\text{CO}_3^{2-}$  Environments", CORROSION/91, Paper No. 99, NACE, Houston, TX (1991).
13. R.P. Gangloff, D.C. Slavik, R.S. Piascik and R.H. Van Stone, "Direct Current Electrical Potential Measurement of the Growth of Small Fatigue Cracks", in Small Crack Test Methods, ASTM STP 1149, J.M. Larsen and J.E. Allison, eds., ASTM, Philadelphia, PA, pp. 116-168 (1992).
12. R.J. Kilmer and G.E. Stoner, "The Effect of Trace Additions of Zn on the Precipitation Behavior of Alloy 8090 During Artificial Aging", Proceedings, Light Weight Alloys for Aerospace Applications II, E.W. Lee, ed., TMS-AIME, Warrendale, PA, pp. 3-15, 1991.
11. W.C. Porr, Jr., Anthony Reynolds, Yang Leng and R.P. Gangloff, "Elevated Temperature Cracking of RSP Aluminum Alloy 8009: Characterization of the Environmental Effect", Scripta Metallurgica et Materialia, Vol. 25, pp. 2627-2632 (1991).
10. J. Aboudi, J.S. Hidde and C.T. Herakovich, "Thermo-mechanical Response Predictions for Metal Matrix Composites", in Mechanics of Composites at Elevated and Cryogenic Temperatures, S.N. Singhal, W.F. Jones and C.T. Herakovich, eds., ASME AMD, Vol. 118, pp. 1-18 (1991).
9. R.S. Piascik and R.P. Gangloff, "Environmental Fatigue of an Al-Li-Cu Alloy: Part I - Intrinsic Crack Propagation Kinetics in Hydrogenous Environments", Metallurgical Transactions A, Vol. 22A, pp. 2415-2428 (1991).
8. W.C. Porr, Jr., Y. Leng, and R.P. Gangloff, "Elevated Temperature Fracture Toughness of P/M Al-Fe-V-Si", in Low Density, High Temperature Powder Metallurgy Alloys, W.E. Frazier, M.J. Koczak, and P.W. Lee, eds., TMS-AIME, Warrendale, PA, pp. 129-155 (1991).
7. Yang Leng, William C. Porr, Jr. and Richard P. Gangloff, "Time Dependent Crack Growth in P/M Al-Fe-V-Si at Elevated Temperatures", Scripta Metallurgica et Materialia, Vol. 25, pp. 895-900 (1991).

6. R.J. Kilmer and G.E. Stoner, "Effect of Zn Additions on Precipitation During Aging of Alloy 8090", Scripta Metallurgica et Materialia, Vol. 25, pp. 243-248 (1991).
5. D.B. Gundel and F.E. Wawner, "Interfacial Reaction Kinetics of Coated SiC Fibers", Scripta Metallurgica et Materialia, Vol. 25, pp. 437-441 (1991).
4. R.G. Buchheit, Jr., J.P. Moran and G.E. Stoner, "Localized Corrosion Behavior of Alloy 2090-The Role of Microstructural Heterogeneity", Corrosion, Vol. 46, pp. 610-617 (1990).
3. Y. Leng, W.C. Porr, Jr. and R.P. Gangloff, "Tensile Deformation of 2618 and Al-Fe-Si-V Aluminum Alloys at Elevated Temperatures", Scripta Metallurgica et Materialia, Vol. 24, pp. 2163-2168 (1990).
2. R.P. Gangloff, "Corrosion Fatigue Crack Propagation in Metals", in Environment Induced Cracking of Metals, R.P. Gangloff and M.B. Ives, eds., NACE, Houston, TX, pp. 55-109 (1990).
1. R.S. Piascik and R.P. Gangloff, "Aqueous Environment Effects on Intrinsic Corrosion Fatigue Crack Propagation in an Al-Li-Cu Alloy", in Environment Induced Cracking of Metals, R.P. Gangloff and M.B. Ives, eds., NACE, Houston, TX, pp. 233-239 (1990).

COMPLETED PROJECTS: (1986 to present reporting period)

1. **DAMAGE LOCALIZATION MECHANISMS IN CORROSION FATIGUE OF ALUMINUM-LITHIUM ALLOYS**  
Faculty Investigator: R.P. Gangloff  
Graduate Student: Robert S. Piascik  
Degree: PhD  
UVa Department: Materials Science and Engineering (MS&E)  
NASA-LaRC Contact: D. L. Dicus (Metallic Materials)  
Start Date: June, 1986  
Completion Date: November, 1989  
Employment: NASA-Langley Research Center
  
2. **AN INVESTIGATION OF THE LOCALIZED CORROSION AND STRESS CORROSION CRACKING BEHAVIOR OF ALLOY 2090 (Al-Li-Cu)**  
Faculty Investigator: Glenn E. Stoner  
Graduate Student: James P. Moran  
Degree: PhD  
UVa Department: MS&E  
NASA-LaRC Contact: W.B. Lisagor (Metallic Materials)  
Start Date: September, 1988  
Completion Date: December, 1989  
Co-Sponsor: ALCOA  
Employment: ALCOA Laboratories
  
3. **MECHANISMS OF LOCALIZED CORROSION IN AL-LI-CU ALLOY 2090**  
Faculty Investigator: G.E. Stoner  
Graduate Student: R.G. Buchheit  
Degree: PhD  
UVa Department: MS&E  
NASA-LaRC Contact: D.L. Dicus (Metallic Materials)  
Start Date: June, 1987  
Completion Date: December, 1990  
Cosponsor: Alcoa  
Employment: Sandia National Laboratories

4. DEFORMATION AND FRACTURE OF ALUMINUM-LITHIUM ALLOYS: THE EFFECT OF DISSOLVED HYDROGEN  
Faculty Investigator: R.E. Swanson (VPI)  
Graduate Student: Frederic C. Rivet  
Degree: MS  
VPI Department: Materials Engineering  
NASA-LaRC Contact: D.L. Dicus (Metallic Materials)  
Start Date: September, 1988  
Completion Date: December, 1990  
Employment: Not determined
5. INVESTIGATION OF THE REACTION KINETICS BETWEEN SiC FIBERS AND SELECTIVELY ALLOYED TITANIUM MATRIX COMPOSITES AND DETERMINATION OF THEIR MECHANICAL PROPERTIES  
Faculty Investigator: F.E. Wawner  
Graduate Student: Douglas B. Gundel  
Degree: MS  
UVa Department: MS&E  
NASA-LaRC Contact: D.L. Dicus and W.B. Brewer (Metallic Materials)  
Start Date: January, 1989  
Completion Date: December, 1990  
Employment: Graduate School, University of Virginia; PhD candidate on LA<sup>2</sup>ST Program; Department of Materials Science
6. DESIGN OF CRYOGENIC TANKS FOR SPACE VEHICLES  
Faculty Investigators: W.D. Pilkey and J.K. Haviland  
Graduate Student: Charles Copper  
Degree: MS  
UVa Department: Mechanical and Aerospace Engineering (MAE)  
NASA-LaRC Contact: D.R. Rummeler (Structural Mechanics Division), R.C. Davis and M.J. Shuart (Aircraft Structures)  
Start Date: April, 1989  
Completion Date: December, 1990  
Employment: Graduate School, University of Virginia; PhD candidate on NASA-Headquarters sponsored program; Department of Mechanical and Aerospace Engineering

7. ELEVATED TEMPERATURE FRACTURE OF AN ADVANCED RAPIDLY SOLIDIFIED, POWDER METALLURGY ALUMINUM ALLOY  
Faculty Investigator: R.P. Gangloff  
Graduate Student: William C. Porr, Jr.  
Degree: PhD  
UVa Department: MS&E  
NASA-LaRC Contact: C.E. Harris (Mechanics of Materials)  
Start Date: January, 1988  
Completion Date: June, 1992  
Employment: David Taylor Naval Ship R&D Center
8. QUANTITATIVE CHARACTERIZATION OF THE SPATIAL DISTRIBUTION OF PARTICLES IN MATERIALS: APPLICATION TO MATERIALS PROCESSING  
Faculty Investigator: John A. Wert  
Graduate Student: Joseph Parse  
Degree: PhD  
UVa Department: MS&E  
NASA-LaRC Contact: D.R. Tenney (Materials Division)  
Start Date: September, 1988  
Completion Date: June, 1992  
Employment: Private Consultant
9. ENVIRONMENTAL FATIGUE CRACK GROWTH AND CRACKING MECHANISMS IN Al-Li-Cu Alloy 2090  
Faculty Investigator: R.P. Gangloff  
Graduate Student: Donald C. Slavik  
Degree: PhD  
UVa Department: MS&E  
NASA-LaRC Contact: D.L. Dicus (Metallic Materials)  
Start Date: September, 1989  
Completion Date: June, 1993  
Employment: Knolls Atomic Power Laboratory
10. INELASTIC DEFORMATION OF METAL MATRIX COMPOSITES UNDER BIAXIAL LOADING  
Faculty Investigators: Carl T. Herakovich and Marek-Jerzy Pindera  
Graduate Student: Mr. Clifford J. Lissenden  
Degree: PhD  
UVa Department: Civil Engineering and the Applied Mechanics Program  
NASA-LaRC Contact: W.S. Johnson (Mechanics of Materials)  
Start Date: September, 1990  
Completion Date: June, 1993  
Employment: University of Kentucky, Department of Engineering Mechanics

11. EFFECT OF TEMPERATURE ON THE RESPONSE OF METALLIC SHELL STRUCTURES

Faculty Investigators: W.D. Pilkey and J.K. Haviland

Graduate Student: Karen McCarthy; MS candidate

Degree: MS (non-thesis)

Graduate Student: Theodore Johnson (NASA Minority Grantee)

Degree: PhD

Employment: NASA-LaRC

Graduate Student: Charles Copper

Degree: PhD

Employment: AMP Incorporated

UVa Department: MAE

NASA-LaRC Contact: Drs. M.J. Shuart and Jeffrey Stroud (Aircraft Structures)

Start Date: April, 1991

Completion Date: May, 1993

12. EFFECTS OF Zn ADDITIONS ON THE PRECIPITATION AND STRESS CORROSION CRACKING BEHAVIOR OF ALLOY 8090

Faculty Investigator: Glenn E. Stoner

Graduate Student: Raymond J. Kilmer

Degree: PhD

Department: MS&E

NASA-LaRC Contact: W.B. Lisagor (Metallic Materials)

Start Date: September, 1989

Completion Date: September, 1993

Cosponsor: Alcoa

Employment: General Motors



## ADMINISTRATIVE PROGRESS

### Faculty Participation

Professors Herakovich, Pindera, Pilkey and Haviland were not supported during this reporting period, as outlined in the 1992 renewal proposal<sup>[2]</sup>.

### Brochure

The brochure prepared in March of 1991 was employed to advertise the LA<sup>2</sup>ST program during this reporting period. Copies were nationally distributed to stimulate graduate and undergraduate recruitment.

### Graduate Student Recruitment

The LA<sup>2</sup>ST Program has encountered no problems in recruiting the best graduate students entering the participating Departments at UVa, and in sufficient numbers to achieve our education and research objectives. There was no recruitment activity during this reporting period.

### Undergraduate Research Participation

In April of 1990, the LA<sup>2</sup>ST Program was increased in scope to include undergraduate engineering students<sup>[3]</sup>. Four students worked at NASA-LaRC during the Summer of 1990, none were recruited for the 1991 program, and seven were successfully recruited to work at NASA-LaRC during the Summer of 1993. Each student was, at the time, a rising senior in an engineering or science major closely related to aerospace materials and mechanics. Represented universities have included Harvard, Georgia Institute of Technology, Virginia Polytechnic Institute, Duke, the University of Missouri, California Polytechnical Institute, and North Carolina State University.

Professor Glenn E. Stoner assumed responsibility for the 1993 Summer Undergraduate Program. No qualified applicants were identified for 1993 Summer employment at NASA-LaRC. The budgeted funds will not be billed to NASA and can be carried-over to support the 1994 program.

Three undergraduate students were recruited during this reporting period to work at UVa with Professor Gangloff. These students are being partially supported by the UVa Academic Enhancement Program.

### Complementary Programs at UVa

The School of Engineering and Applied Science at UVa has targeted light materials and thermal structures research for aerospace applications as an important area for broad

growth. The LA<sup>2</sup>ST Program is an element of this thrust. Several additional programs are of benefit to LA<sup>2</sup>ST work.

In 1988, the Board of Visitors at UVa awarded SEAS an Academic Enhancement Program Grant in the area of Light Thermal Structures. University funds have been used to seed the establishment of a world-class center of excellence which incorporates several SEAS Departments. This program is lead by Professor Thornton and directly benefits NASA.

The Light Metals Center has existed within the Department of Materials Science and Engineering at UVa for the past ten years under the leadership of Professor H.G.F. Wilsdorf, and after his retirement, under leadership of Dean Starke. A Virginia Center for Innovative Technology Development Center in Electrochemical Science and Engineering was established in 1988 with Professor G.E. Stoner as Director. Professors Pilkey, Thornton and Gangloff recently completed NASA-Headquarters sponsored research to examine "Advanced Concepts for Metallic Cryo-thermal Space Structures"<sup>[4,5]</sup>.

#### References

1. R.P. Gangloff, E.A. Starke, Jr., J.M. Howe and F.E. Wawner, "NASA-UVa Light Aerospace Alloy and Structures Technology Program: Supplement on Aluminum Based Materials for High Speed Aircraft", University of Virginia, Proposal No. MS NASA/LaRC-5215-92, October, 1991.
2. R.P. Gangloff, "NASA-UVa Light Aerospace Alloy and Structures Technology Program", University of Virginia, Proposal No. MSE-NASA/LaRC-5691-93, November, 1992.
3. R.P. Gangloff, "NASA-UVa Light Aerospace Alloy and Structures Technology Program: A Supplementary Proposal", University of Virginia, Proposal No. MS NASA/LaRC-4677-90, April, 1990.
4. W.P. Pilkey, "Advanced Concepts for Metallic Cryo-thermal Space Structures", University of Virginia Proposal No. MAE-NASA/HQ-4462-90, August, 1989.
5. W.P. Pilkey, "Advanced Concepts for Metallic Cryo-thermal Space Structures", University of Virginia Report No. UVA/528345/MAE91/101, February, 1991.

## CURRENT PROJECTS

### **MECHANICAL AND ENVIRONMENTAL DEGRADATION MECHANISMS IN ADVANCED LIGHT METALS AND COMPOSITES**

1. ENVIRONMENTAL FATIGUE CRACK GROWTH AND CRACKING  
MECHANISMS IN Al-Li-Cu Alloy 2090  
Faculty Investigator: R.P. Gangloff  
Graduate Student: Donald Slavik; PhD Candidate  
UVa Department: Materials Science and Engineering (MS&E)  
NASA-LaRC Contact: D.L. Dicus (Metallic Materials)  
Start Date: September, 1989  
Anticipated Completion Date: June, 1993  
Project #1
  
2. ELEVATED TEMPERATURE DAMAGE TOLERANCE OF ADVANCED INGOT  
METALLURGY WROUGHT ALUMINUM ALLOYS  
Faculty Investigator: R.P. Gangloff  
Graduate Student: Michael J. Haynes  
UVa Department: MS&E  
NASA-LaRC Contact: To be determined (Metallic Materials)  
Start Date: September, 1992  
Completion Date: December, 1994  
Project #2
  
3. CRYOGENIC TEMPERATURE EFFECTS ON THE DEFORMATION AND  
FRACTURE OF Al-Li-Cu and Al-Li-Cu-In ALLOYS  
Faculty Investigator: R.P. Gangloff  
Graduate Student: John A. Wagner; PhD candidate and NASA-LaRC  
employee  
UVa Department: MS&E  
NASA-LaRC Contacts: W.B. Lisagor (Metallic Materials) and J.C. Newman  
(Mechanics of Materials)  
Start Date: June, 1987  
Anticipated Completion Date: December, 1993  
Project #3

4. THE EFFECT OF CRYOGENIC TEMPERATURE ON THE FRACTURE TOUGHNESS OF WELDALITE™ X2095  
Faculty Investigator: R.P. Gangloff  
Graduate Student: Cynthia L. Lach; MS candidate and NASA-LaRC employee  
UVa Department: MS&E  
NASA-LaRC Contacts: W.B. Lisagor (Metallic Materials)  
Start Date: August, 1990  
Anticipated Completion Date: May, 1994  
Project #4
5. MECHANISMS OF LOCALIZED CORROSION IN 2090 AND X2095  
Faculty Investigator: G.E. Stoner  
Graduate Student: Douglas Wall; PhD candidate  
UVa Department: MS&E  
NASA-LaRC Contact: M.S. Domack (Metallic Materials)  
Start Date: April, 1991  
Completion Date: May, 1994  
Cosponsor: Reynolds Metals Company  
Technical Contact: A. Cho  
Project #5
6. EFFECTS OF Zn ADDITIONS ON THE PRECIPITATION AND STRESS CORROSION CRACKING BEHAVIOR OF ALLOY 8090  
Faculty Investigator: Glenn E. Stoner  
Graduate Student: Raymond J. Kilmer; PhD candidate  
Department: MS&E  
NASA-LaRC Contact: W.B. Lisagor (Metallic Materials)  
Start Date: September, 1989  
Anticipated Completion Date: June, 1993  
Cosponsor: Alcoa  
Project #6
7. HYDROGEN INTERACTIONS IN ALUMINUM-LITHIUM ALLOY 2090 AND SELECTED MODEL ALLOYS  
Faculty Investigator: John R. Scully  
Graduate Student: Stephen W. Smith; PhD Candidate  
Department: MS&E  
NASA-LaRC Contact: W.B. Lisagor and D.L. Dicus (Metallic Materials)  
Start Date: April, 1991  
Anticipated Completion Date: To be determined  
Cosponsor: Virginia CIT  
Project #7

8. METASTABLE PITTING OF Al ALLOYS IN HALIDE SOLUTIONS

Faculty Investigators: John R. Scully and J.L. Hudson  
Graduate Student: Sheldon T. Pride; PhD Candidate  
Department: Chemical Engineering  
NASA-LaRC Contact: D.L. Dicus (Metallic Materials)  
Start Date: September, 1991  
Anticipated Completion Date: To be determined  
Cosponsor: NASA Graduate Student Researchers Program;  
Under Represented Minority Emphasis  
Project #8

AEROSPACE MATERIALS SCIENCE

9. INVESTIGATION OF THE EFFECT OF THERMAL TREATMENT ON THE MECHANICAL PROPERTIES OF Ti-1100/SCS-6 COMPOSITES

Faculty Investigator: F.E. Wawner  
Graduate Student: Douglas B. Gundel; PhD candidate  
UVa Department: MS&E  
NASA-LaRC Contact: D.L. Dicus and W.B. Brewer (Metallic Materials)  
Start Date: April, 1991  
Anticipated Completion Date: June, 1993  
Project #9

10. PROCESSING AND SUPERPLASTIC PROPERTIES OF WELDALITE™ SHEET

Faculty Investigator: John A. Wert  
Graduate Student: Mark Lyttle; MS Candidate  
UVa Department: MS&E  
NASA-LaRC Contact: T.T. Bales (Metallic Materials)  
Start Date: September, 1991  
Anticipated Completion Date: September, 1993  
Project #10

## **MECHANICS OF MATERIALS FOR LIGHT AEROSPACE STRUCTURES**

### **11. ENVIRONMENTAL EFFECTS IN FATIGUE LIFE PREDICTION: MODELING CRACK PROPAGATION IN LIGHT AEROSPACE ALLOYS**

Faculty Investigator: R.P. Gangloff  
Graduate Student: Mark Mason; MS Candidate  
Post Doctoral Research Associate: Dr. Sang-Shik Kim  
UVa Department: MS&E  
NASA-LaRC Contact: R.S. Piascik (Mechanics of Materials)  
Start Date: January, 1992  
Anticipated Completion Date: December, 1994  
Project #11

## **THERMAL GRADIENT STRUCTURES**

### **12. EXPERIMENTAL STUDY OF THE NONLINEAR VISCOPLASTIC RESPONSE OF HIGH TEMPERATURE STRUCTURES**

Faculty Investigator: Earl A. Thornton  
Graduate Student: Marshall F. Coyle; PhD candidate  
Graduate Student: Mark A. Rowley; MS candidate  
UVa Department: Mechanical and Aerospace Engineering  
NASA-LaRC Contact: James H. Starnes, Jr. (Aircraft Structures)  
Start Date: January, 1990  
Anticipated Completion Date: To be determined  
Cosponsor: UVa Academic Enhancement Program  
Project #12

## RESEARCH PROGRESS AND PLANS (January 1 to June 30, 1993)

Research progress, recorded during the period from January 1, 1993 to June 30, 1993, is summarized for each project in the following sections. The standard format includes the program objective, recent progress, conclusions, and immediate milestones; coupled with a set of visual aids presented at the Fourth Annual NASA-UVa LA<sup>2</sup>ST Grant Review Meeting held at NASA-LaRC in July of 1993. The agenda of this meeting is presented in Appendix IV.

### Project #1     **Environmental Fatigue Crack Growth and Cracking Mechanisms in Al-Li-Cu Alloy 2090**

Donald C. Slavik and Richard P. Gangloff

#### Objective

The objectives of this PhD research are to: (a) characterize the effect of microstructure on environmental fatigue crack propagation (FCP), and (b) quantitatively define the microscopic damage mechanisms involved in vacuum and hydrogen-environmental FCP; in each case for Al-Li-Cu alloys.

Specific objectives are to: a) vary the microstructure of commercially produced AA2090 and determine how this influences intrinsic  $da/dN$  and  $da/dN-\Delta K$  transition behavior in inert and aggressive environments, b) implement diffraction techniques capable of identifying grain misorientations and precise fatigue crack facet crystallography in unrecrystallized and recrystallized AA2090 microstructures, c) use grain microtexture, facet crystallography, and slip system predictions to identify fatigue damage modes, d) correlate microscopic crack paths and microstructural features with intrinsic  $da/dN$ , and e) establish the applicability of current  $da/dN-\Delta K$  models and limiting uncertainties for planar slip Al-Li alloys.

#### Technical Approach

Intrinsic  $da/dN$  behavior is characterized with high mean stress constant  $K_{max}$  fracture mechanics experiments developed under a previous NASA-LA<sup>2</sup>ST program. The influence of environment on FCP rates is established with experiments in an ultrahigh vacuum and in

a deaerated, aqueous 1 wt% NaCl solution at a constant electrode potential.

The influence of grain and subgrain size on AA2090 FCP rates is determined with commercially available unrecrystallized microstructures (fine and coarse subgrains), and with recrystallized microstructures (fine and coarse grains) which are produced with thermo-mechanical processing techniques. Grain sizes are measured with optical metallography, while precipitates and subgrains are imaged with the TEM. Tensile properties, pitting potentials, and global textures are measured from smooth bar tensile tests, electrochemical polarization experiments, and x-ray diffraction techniques, respectively.

Microscopic fracture modes are qualitatively determined with SEM fractography. Grain and subgrain misorientations are directly measured with EBSPs, and fracture facet crystallography is identified with EBSPs coupled with tilt fractography measurements for both unrecrystallized and recrystallized microstructures. Likely microscopic damage modes, based on qualitative SEM fractography and quantitative fatigue fracture crystallography, are identified to explain observed intrinsic FCP rate trends and needs for quantitative  $da/dN-\Delta K$  models.

### Current Status

Mr. Slavik successfully defended his PhD Dissertation in June of 1993 and has reported to work at the Knolls Atomic Power Laboratory in Schenectady, New York. This project is completed.

### Recent Progress

The results of this research are summarized by the Conclusions from Mr. Slavik's dissertation, as follows.

#### **Vacuum Fatigue Cracking**

oo When compared on a  $\Delta K$  or a  $\Delta K/E$  basis,  $da/dN$  in vacuum is enhanced up to 2.4-fold for unrecrystallized sheet, 1.3-fold for the recrystallized fine grain sheet, and 4.3-fold for recrystallized coarse grain sheet, all compared to unrecrystallized AA2090 plate. A single power law represented  $da/dN-\Delta K$  behavior for the AA2090 microstructures with a Paris exponent which varies from 5.2 to 6.0.

oo Facetted cracking modes and tortuous cracking profiles form for vacuum fatigue crack propagation of AA2090 independent of texture,  $\Delta K$ , or grain and subgrain structure.



- o Fracture facet crystallography is quantitatively determined for AA2090 with electron back scatter pattern analysis, coupled with tilt fractography measurements. Facets are not parallel to  $\{100\}$  or  $\{110\}$  due to an alternate slip fracture mechanism, and are not identically crystallographic along single  $\{111\}$  slip planes. Facets are instead typically near- $\{111\}$ , consistent with fracture through deformation bands which are complex dislocation structures and which are not macroscopically  $\{111\}$ .

- oo Strong crystallographic texture and subgrain structure are not prerequisites for deformation band cracking in AA2090. Tortuous near- $\{111\}$  cracking profiles are formed for unrecrystallized (brass-type) and recrystallized (random grains) microstructures.

- oo Predicted resolved shear stresses at the crack tip are high on multiple slip systems for both textured and random grains orientations in AA2090, resulting in multiple near- $\{111\}$  fracture facets within single grains. Facets predominately form on planes with a high resolved shear stress, but geometrically necessary near- $\{111\}$  facets also develop to link the dominant facets into a single crack profile.

- oo A crack tip strain range parameter ( $\Delta K^2/E\sigma_{ys}$ ) uniquely correlates  $da/dN$  within a 2-fold variation for the four AA2090 microstructures. Texture, subgrain size, and grain size do not dramatically influence  $da/dN$  in inert environments when compared on the crack tip strain range basis. This result implies that fatigue damage accumulation within deformation bands is similar for unrecrystallized and recrystallized AA2090 microstructures with varying slip lengths.

- oo Discontinuous crack jump distances ( $\Delta a$ ) and a crack tip failure criterion ( $\Delta N$ ) are needed to model intrinsic  $da/dN$ - $\Delta K$  behavior. Relationships between the crack tip strain range,  $\Delta a$ ,  $\Delta N$ , and  $\Delta K$  have not been experimentally identified for a wide range of materials and microstructures, but are needed to develop realistically predictive  $da/dN$ - $\Delta K$  models.

### **Aqueous NaCl Fatigue Cracking**

- oo In comparison to inert environment fatigue cracking, aqueous NaCl accelerates  $da/dN$  at all  $\Delta K$  and promotes multiple  $da/dN$ - $\Delta K$  power law transitions for each AA2090 microstructure. When compared either on a  $\Delta K$  or a crack tip strain range basis, FCP rates are similar for UR sheet, UR plate, and RF sheet, while  $da/dN$  is reduced for RC sheet, particularly at low  $\Delta K$  and  $\Delta \epsilon$ .

- oo Aqueous NaCl fatigue fracture modes for AA2090 are  $\Delta K$  dependent. Deformation

band cracking, thin fracture facets, and intersubgranular cracking modes form for the different AA2090 microstructures at intermediate and high  $\Delta K$ . At low  $\Delta K$ , fracture is predominately transgranular, but is markedly different than the faceted fracture surface that is produced in vacuum. Repetitive saw-tooth cracking profiles are typical of fatigue crack propagation in highly textured UR plate in aqueous NaCl. Facet orientations are more varied for the randomly oriented grains in the recrystallized microstructures, but are otherwise similar to the unrecrystallized cases.

- oo Transgranular fracture facets at low  $\Delta K$  cluster around a  $\{521\}$  cracking plane for AA2090 in aqueous NaCl. Half of the facets analyzed are within  $5^\circ$ , and 8 of 9 facets grouped within  $10^\circ$  of  $\{521\}$  for unrecrystallized plate. The facets are crystallographically more varied for recrystallized sheet, yet 50% of the facets are within  $10^\circ$  of  $\{521\}$ .

- oo The  $\{521\}$  cracking plane is inconsistent with: a)  $T_1$  or crystallographic dissolution and ligament rupture, b) hydrogen trapping at matrix  $T_1$  interfaces and decohesion, c) hydrogen enhanced localized plasticity and near- $\{111\}$  deformation band decohesion, or d) brittle hydrogen induced  $\{100\}/\{110\}$  cracking. Fracture on a  $\{100\}$  plane was rarely observed, even when favorably oriented normal to the applied loading axis.

- oo Paris law  $da/dN$ - $\Delta K$  transition behavior does not simply correlate with either unique  $\Delta K$  dependent damage modes or microstructural influences on slip. Neither  $\Delta K$  nor  $\Delta \epsilon$  correlated the FCP rates of the recrystallized coarse grain sheet compared to the other AA2090 microstructures, particularly at low  $\Delta K$ .

- oo A semi-quantitative corrosion fatigue model does not predict the  $da/dN$ - $\Delta K$  trends for the recrystallized coarse grain sheet compared to the other AA2090 microstructures, possibly because: a) model constants are microstructure sensitive, b) improved  $\Delta a$  and  $\Delta N$  relationships are needed, and c) a failure criterion which includes the process zone hydrogen concentration, crack tip strain range, normal stress, and microstructure is not well understood.

- oo  $LiAlH_4$  formation and cracking may explain observed  $\{521\}$  fracture planes and  $da/dN$  trends for AA2090. Crack tip process zone dilatation may be a critical feature influencing  $LiAlH_4$  nucleation, growth, and fracture. Hydrides are not observed in the current study, and published crystallographic relationships are inaccurate. Such information is needed to determine if  $LiAlH_4$  is a viable environmental fatigue fracture mechanism for Al-Li-Cu alloys.

## Presentation Viewgraphs

1. Title
2. Fatigue crack growth rate data for Vintage III, unrecrystallized, peak-aged sheet of AA 2090; as functions of applied stress intensity range at constant high  $K_{MAX}$  and of environment. Note the single power-law behavior for the vacuum case compared to the more complex response for moist air and aqueous chloride. Excellent agreement is observed for  $da/dN$  from constant  $\Delta K$  experiments (filled circles) and from a continuously decreasing  $\Delta K$  experiment (open circles) in NaCl.
3. A summary of the elements of the technical approach.
4. Four microstructures of AA2090 were produced at UVa by specialized thermal-mechanical processing. Grain sizes and shapes determined with optical metallography are shown for: a) UR sheet (3.2 mm thickness) purchased in the T3 condition from Alcoa (Vintage III) and aged for 18 hrs at 155°C at UVa; b) UR plate (19 mm thickness) purchased as T81 (aged for 18 hours at 160°C) from Alcoa (Vintage III), c) RF sheet produced from UR plate at UVa by overaging, hot rolling, fast-rate solution treating, stretching and aging at 155°C for 18 hours; and d) RC sheet produced from UR plate at UVa by overaging, hot rolling, slow-rate solution treating, stretching and aging at 155°C for 18 hours. The recrystallized microstructures were electrochemically etched and viewed with polarized light.
5. The FCP response of UR sheet and UR plate AA2090 in vacuum and aqueous NaCl.
6. Least squares trend lines representing the intrinsic  $da/dN$  versus  $\Delta K$  behavior of each of the four microstructures of AA2090. FCP is essentially described by a single power law, with the maximum variability in  $da/dN$  shown in Figure 5 for UR Sheet. When correlated in terms of crack tip strain range (proportional to  $\Delta K^2/\sigma_{ys}E$ ), there is no resolvable microstructural effect on vacuum FCP kinetics.
7. Fatigue crack growth in vacuum proceeds by a faceted microscopic process for each of the four microstructures. Here, results for UR plate AA2090 are consistent with the literature claim of  $\{111\}$ -type slip band cracking. This literature is based on an inconclusive X-ray texture analysis, combined with the facet angles of near 60° seen on two-dimensional metallographic sections. Etch pitting of fatigue crack surface facets provides more conclusive results, albeit without providing precise orientation measurements.
8. A method, based on Electron Back-Scattering Pattern (EBSP) analysis coupled with quantitative tilt fractography, was developed to precisely measure the crystallographic orientations of fatigue crack surface facets. Here, the relationship between the crack surface, for tilt analysis of the facet pole, and a metallographically polished plane, for grain orientation measurement, is illustrated.
9. Typical AA2090 EBSPs and zone axis locations for: a) RC sheet, and b) UR plate.

10. SEM fractographs of a AA2090 facet with varying tilts around the T-axis (tilt angles are marked on the micrographs).
11. An SEM image of a metallographically prepared T-plane intersecting a vacuum fatigue crack surface in UR plate AA2090, coupled with a stereographic projection summarizing tilt fractography and EBSP analyses for the indicated grain. Note that EBSP yields a grain orientation consistent with the expected Brass texture. Poles for the three facets marked with "X" in the SEM image are plotted on the projection. Facet poles and  $\{111\}$  poles are nearly coincident. The operation of multiple slip systems, and possible slip band cracks, is confirmed by calculations of critical resolved shear stresses on slip planes within the crack tip field.
12. Fracture facet crystallography summarized on a stereographic triangle showing predominately near- $\{111\}$  cracking in vacuum for AA2090 independent of texture and subgrain structure in both UR plate and RC sheet. For these cases, 38 facets were characterized; 77% (for RC sheet) and 84% (for UR plate) of the facet poles were within  $10^\circ$  of a  $\{111\}$  pole.
13. Fatigue crack facets in the AA2090/vacuum system may not be precisely parallel to  $\{111\}$  because of the complexity of slip deformation bands, particularly within the highly strained crack tip field.
14. Conclusions of the experiments and analyses on the four microstructures of AA2090 in vacuum.
15. Least squares trend lines representing intrinsic  $da/dN$  versus  $\Delta K$  behavior of each of the four microstructures of AA2090, cyclically loaded in aqueous NaCl at fixed electrode potential of  $-840 \text{ mV}_{\text{sce}}$ . In contrast to vacuum behavior, FCP is described by multiple power-laws, with specific transition stress intensity ranges ( $\Delta K_{\text{TRANSITION}}$ ). When correlated in terms of crack tip strain range (proportional to  $\Delta K^2/\sigma_{ys}E$ ), there is no resolvable microstructural effect on FCP kinetics for three of the four cases. The lowest strength case, RC AA2090 sheet, exhibits improved resistance to environmental FCP.
16. Yoder and coworkers argue that a  $da/dN$ - $\Delta K$  power law transition occurs when the cyclic plastic zone diameter equals the distance between microstructural barriers to slip. Specific  $\Delta K_{\text{TRANSITION}}$  values are tabulated for the four microstructures of AA2090. Neither vacuum nor NaCl FCP kinetics data support these predictions, and a specific damage mechanism was not proposed.
17. Piascik and Gangloff developed a semi-quantitative explanation for hydrogen environment-specific growth rate transitions. Such complex  $da/dN$ - $\Delta K$  behavior is controlled by the parallel operation of multiple environment sensitive cracking modes that occur in varying proportion and at varying rates, both depending on  $\Delta K$ . For AA2090, they hypothesized that the lowest  $\Delta K_{\text{TRANSITION}}$  is due to the cyclic plastic zone just enveloping the smallest subgrains for any environment that produces atomic hydrogen.

18. The current experiments were designed to eliminate subgrains, and thus to test this hypothesis.
19. There is a strong decrease in  $da/dN$ , at any near-threshold crack tip plastic strain range, with the elimination of subgrains for FCP in the AA2090/NaCl system. While the extent of the transition behavior is reduced, a low- $\Delta K$  power law change is none-the-less observed for RC sheet of AA2090. Additionally for UR sheet, the microscopic fatigue crack path does not change at the power law transition. The current results do not strongly support earlier work on Vintage II UR plate of AA2090.
20. Environment affects a strong transition in the microscopic fatigue crack path for each of the four microstructures of AA2090. Here, the results for UR plate show such a change in the near- $\{111\}$  cracking mode typical of vacuum FCP.
21. An SEM image of a metallographically prepared T-plane intersecting an NaCl vacuum fatigue crack surface in UR plate AA2090, coupled with a stereographic triangle summarizing tilt fractography and EBSD analyses for 8 separate grains. In all cases EBSD yielded a grain orientation consistent with the expected Brass texture. While environmental fatigue facets were highly repetitive and apparently crystallographically oriented, facet surfaces were not parallel to a low index plane. Facets were never observed to be parallel to  $\{100\}$ ,  $\{110\}$  or  $\{111\}$  planes; rather, the average facet was near- $\{521\}$ .
22. Results for RC sheet AA2090 in NaCl were essentially similar to the behavior of UR plate. Environmental fatigue facets were more varied in orientation; low index cracks were observed for two cases and only one-half of the facet poles were near- $\{521\}$ . Specifically for both microstructures, 18 facets were characterized; 50% (for RC sheet) and 87% (for UR plate) of the facet poles were within  $10^\circ$  of  $\{521\}$ .
23. The near- $\{521\}$  facet orientation for the two microstructures of AA2090; and more particularly the lack of clearly defined  $\{100\}$ ,  $\{110\}$  or  $\{111\}$  facets; enables us to preclude several hypothesized mechanisms for environmental FCP in Al-Li-Cu alloys.
24. A hydride ( $\text{LiAlH}_4$ ) cracking mechanism may be consistent with the observed environmental fatigue crack surface facets. Two problems are, however, identified. (1) We did not observe hydrides in either environmental fatigue, hydrogen precharged or slow strain rate specimens of AA2090. Only one group has reported this phase. (2) The reported hydride habit plane and preferred orientation are apparently incorrect.
25. Conclusions of the experiments and analyses on the four microstructures of AA2090 in NaCl.

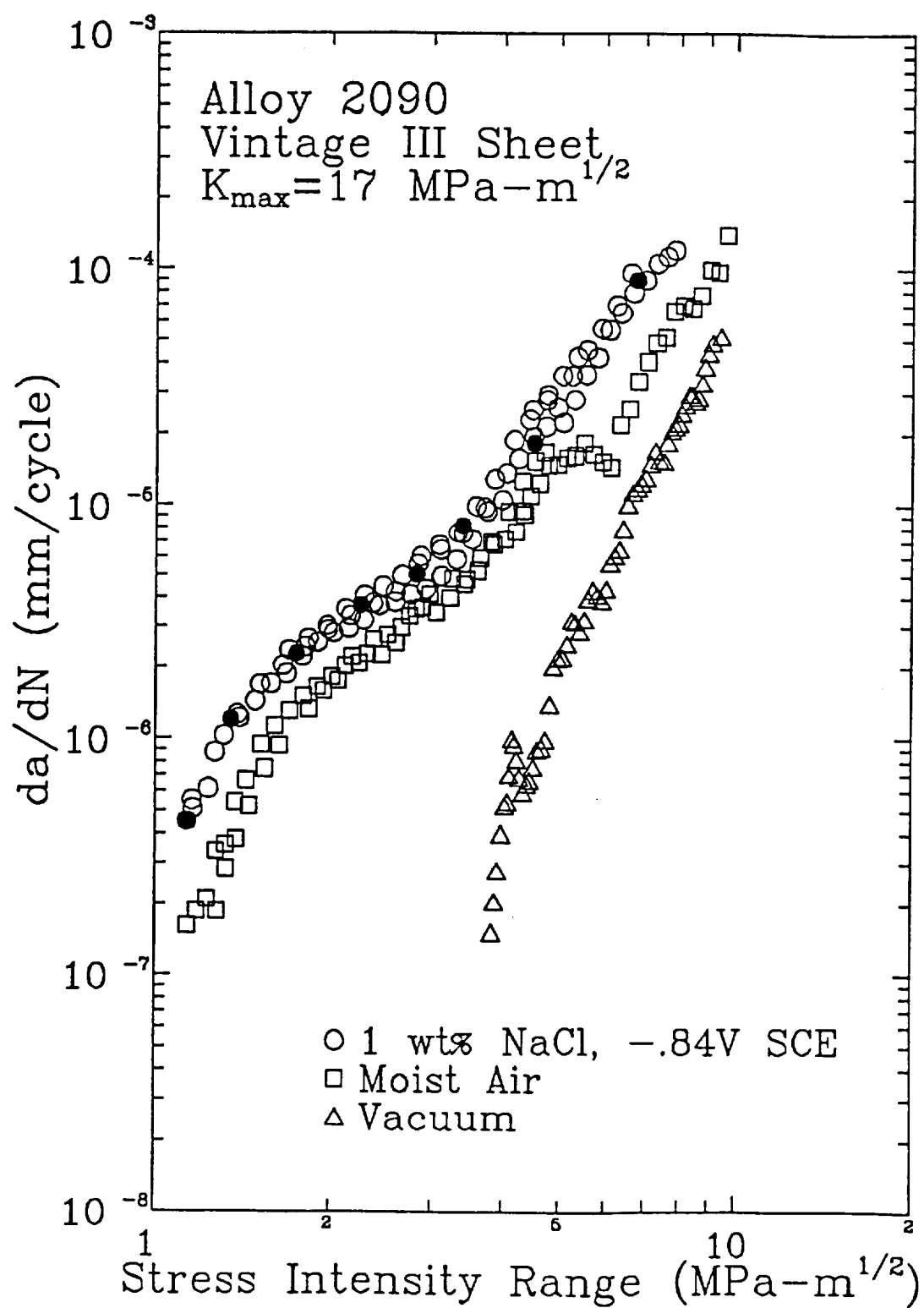


# **Environmental Fatigue Crack Growth Rates and Cracking Mechanisms for AA2090**

**D.C. Slavik and R.P. Gangloff  
University of Virginia**

**Supported by NASA Langley Research Center  
D.L. Dicus, Project Monitor  
Metallic Materials Branch**

INTENTIONALLY BLANK





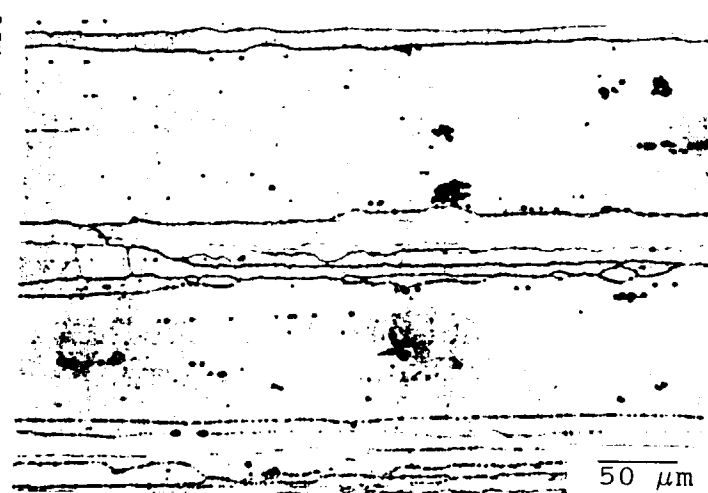
# **Procedure**

- o Change peak aged AA2090 microstructure**
  - thermomechanical processing**
- o Measure intrinsic environmental  $da/dN$** 
  - 5  $\mu$ Pa ultrahigh vacuum**
  - 1 wt% NaCl solution at  $-840\text{mV}_{\text{SCE}}$**
- o Quantitatively probe local fracture processes**
  - electron back scatter patterns (EBSPs)**
  - quantitative tilt fractography**
- o Predict local slip conditions**
  - measured grain microtextures**
  - crack tip stress state**
- o Critically evaluate proposed crack growth rate concepts**
  - microscopic damage mechanisms**
  - microstructure and  $da/dN$  relationships**

## AA2090 Microstructures (L-Plane)



Unrecrystallized Sheet



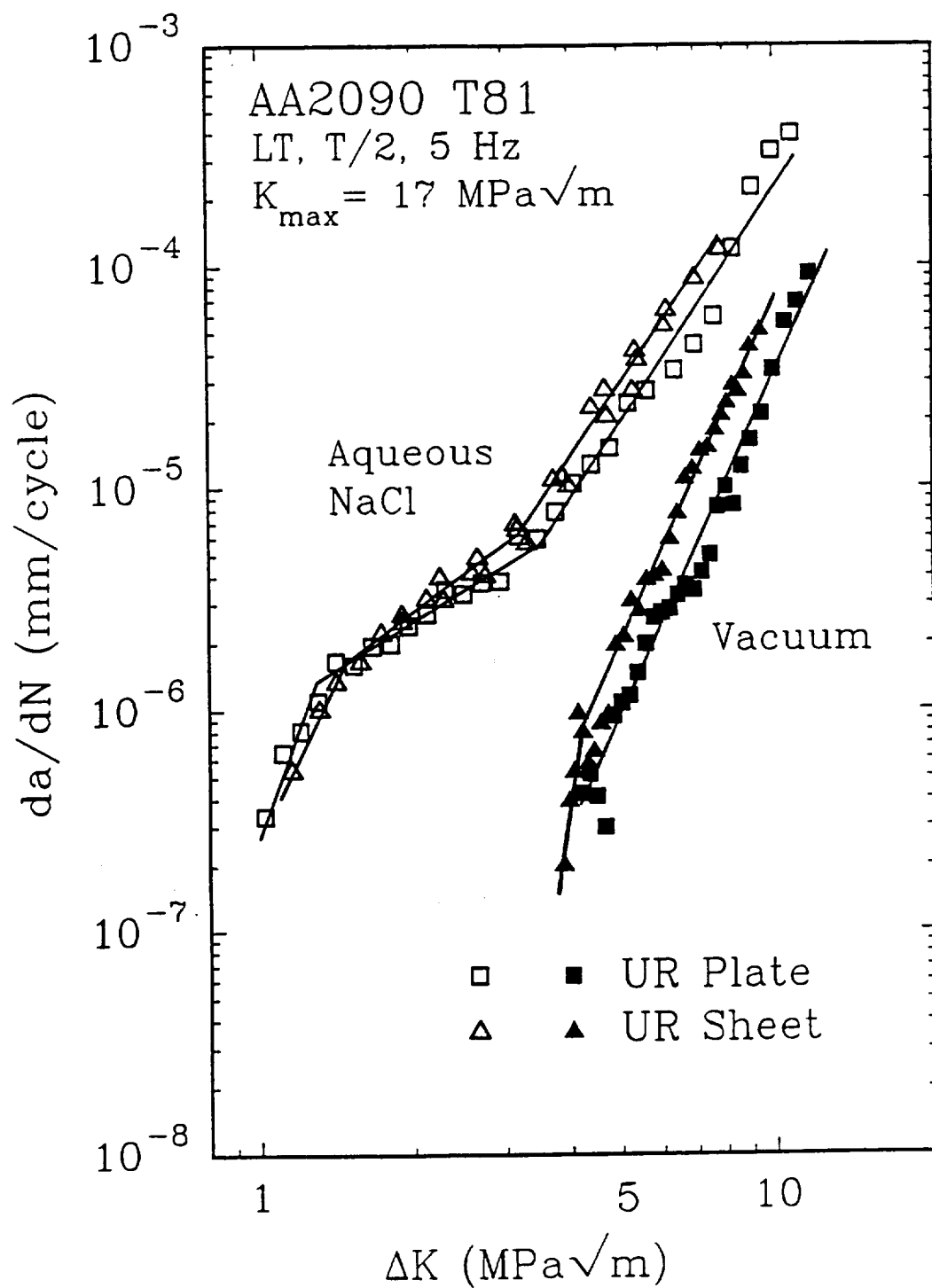
Unrecrystallized Plate



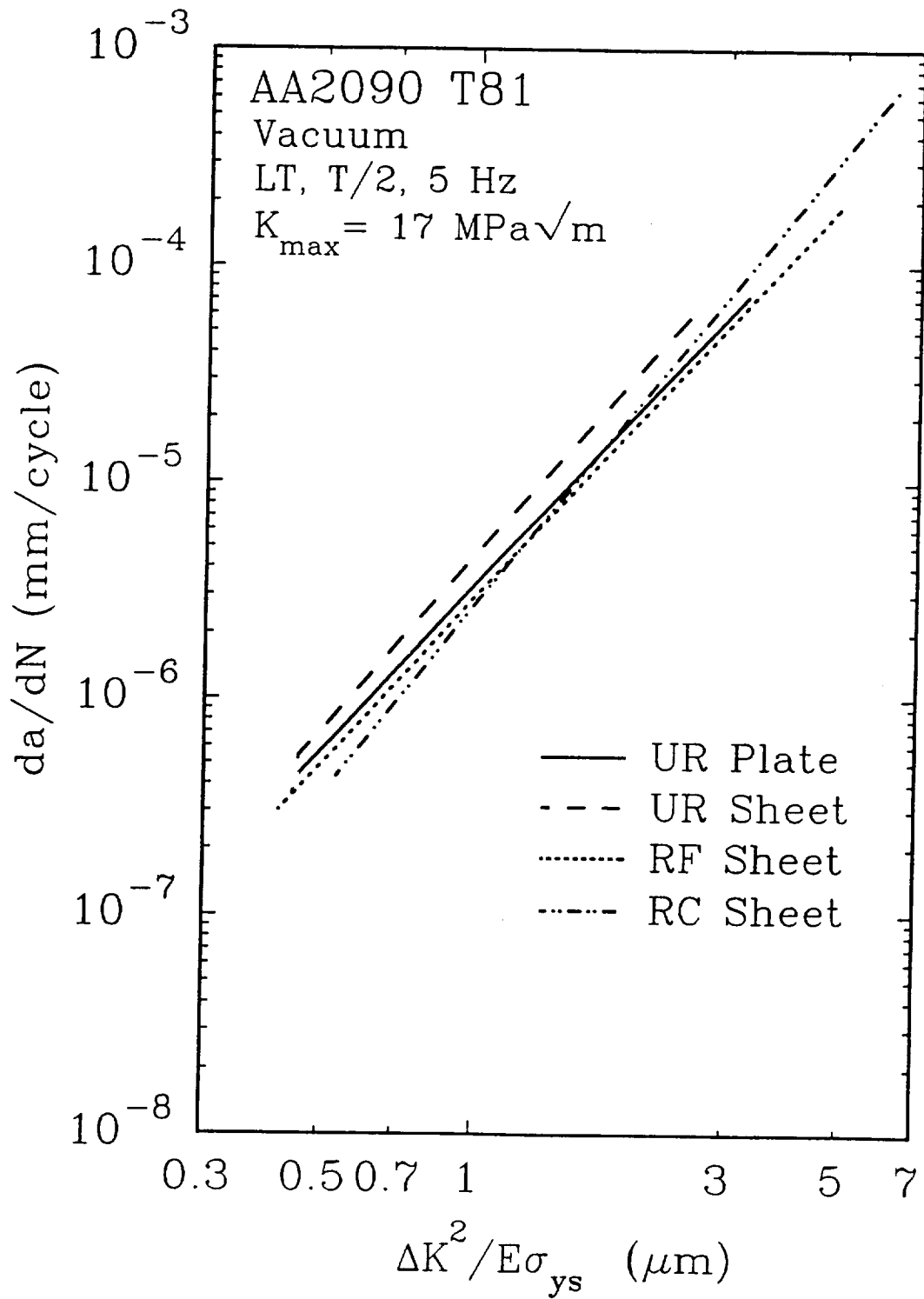
Recrystallized Sheet

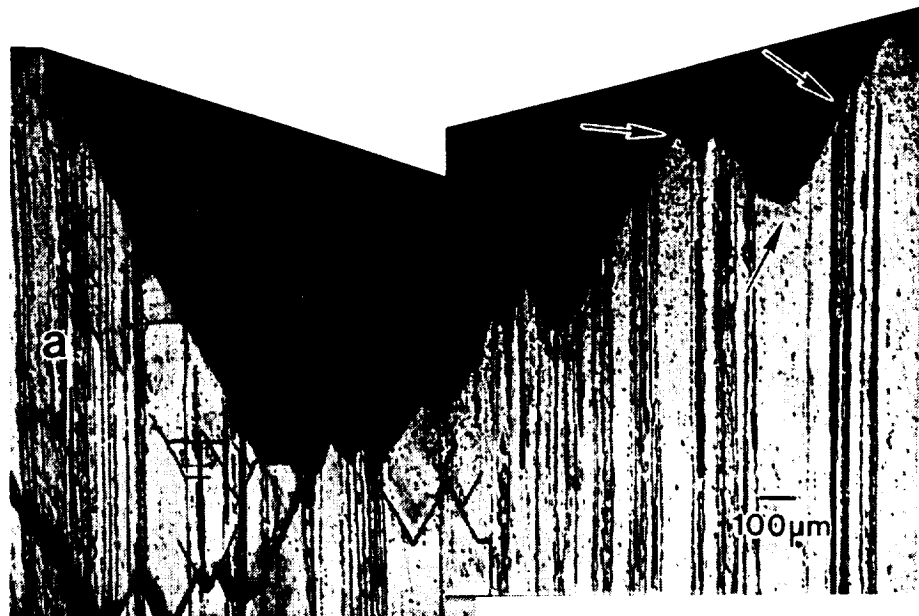


Recrystallized Sheet



$da/dN$ - $\Delta K$  for unrecrystallized AA2090 at constant  $K_{\max} = 17 \text{ MPa}\sqrt{\text{m}}$  in aqueous 1 wt% NaCl at a fixed electrode potential of  $-0.840 \text{ V}_{\text{SCE}}$

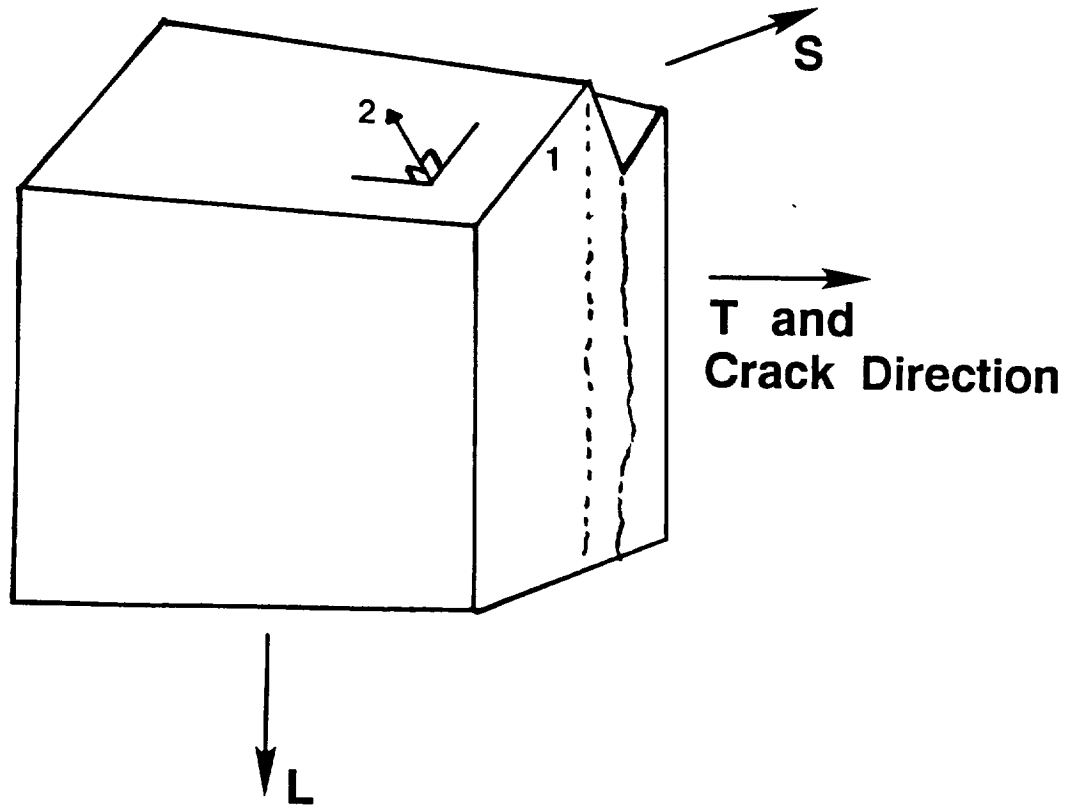




Etched T-plane sections for UR plate showing tortuous vacuum cracking profiles for: a) 0° sample tilt (optical microscopy), and b) a 30° sample tilt from the T-plane toward the fracture surface (SEM fractography)

# Fatigue Crack Growth Specimens

## LT Orientation

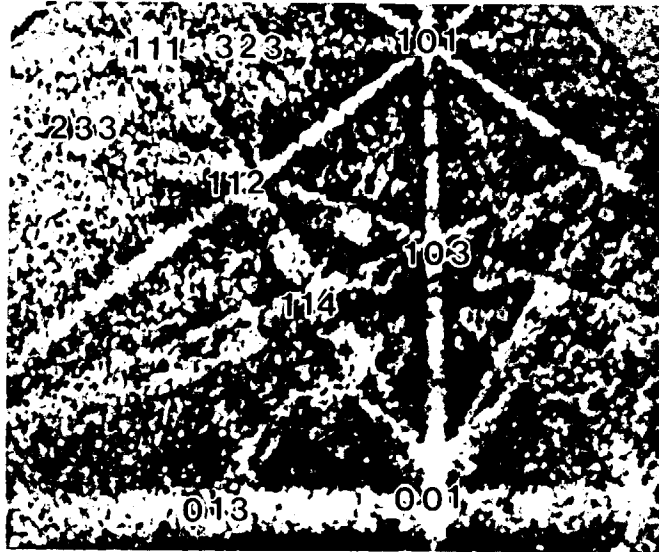


### Facet Crystallographic Analysis

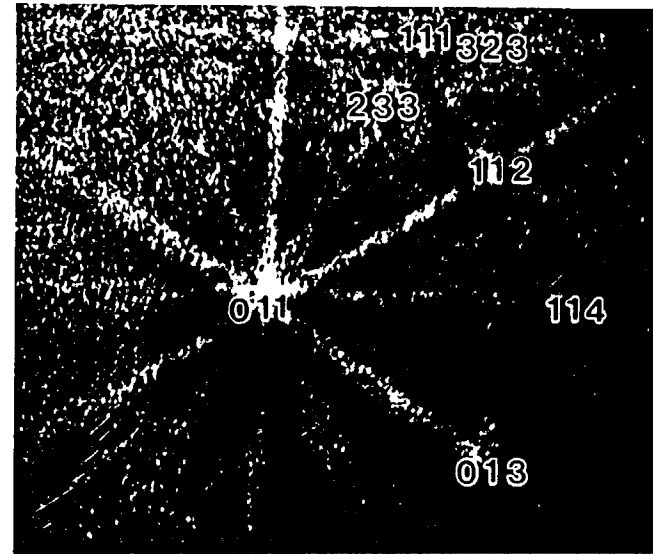
- 1 Grain orientation with EBSPs off polished T-plane
- 2 Facet pole from quantitative tilt fractography

# AA2090 Electron Back Scatter Patterns

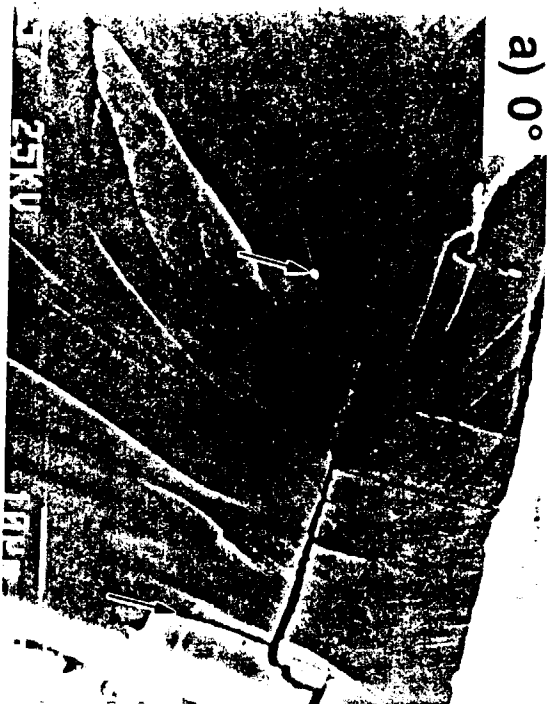
## Recrystallized



## Unrecrystallized



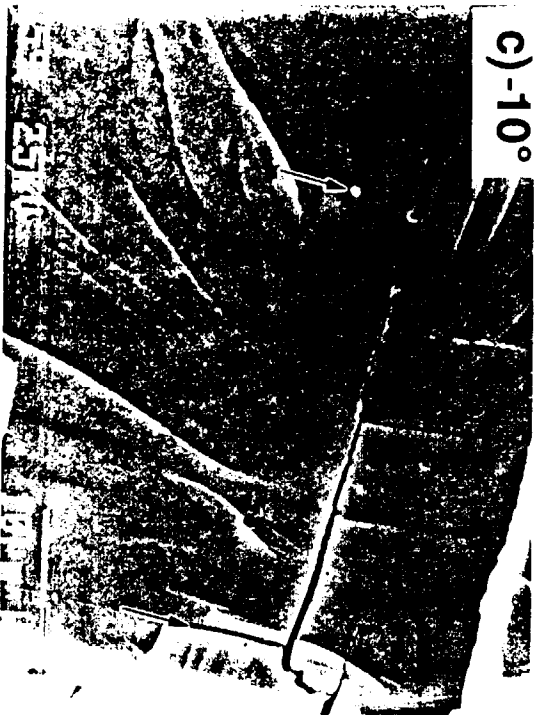
a)  $0^\circ$



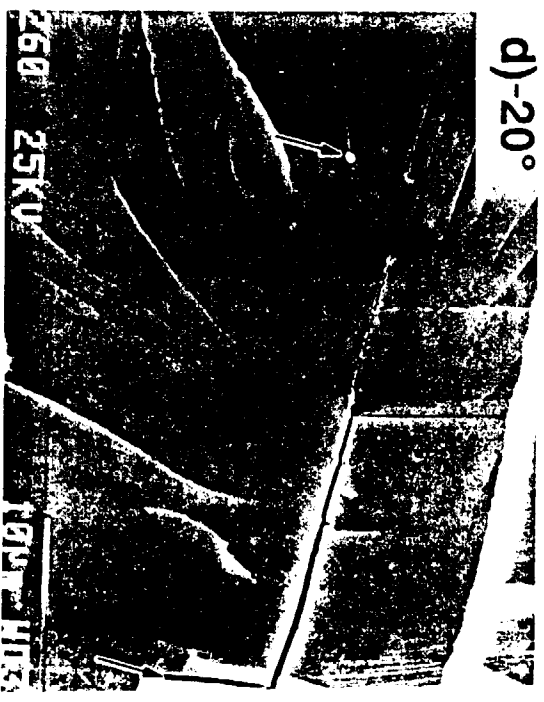
b)  $-5^\circ$



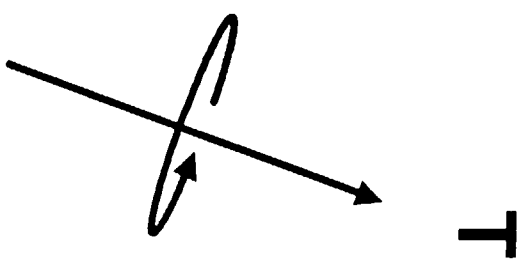
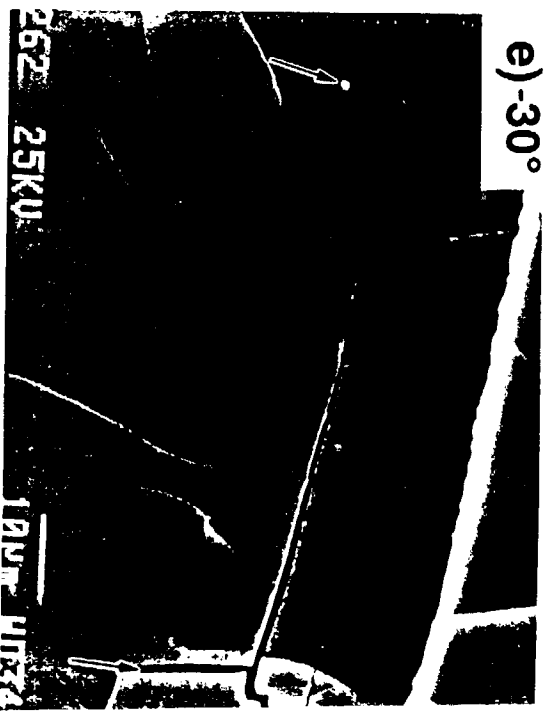
c)  $-10^\circ$



d)  $-20^\circ$



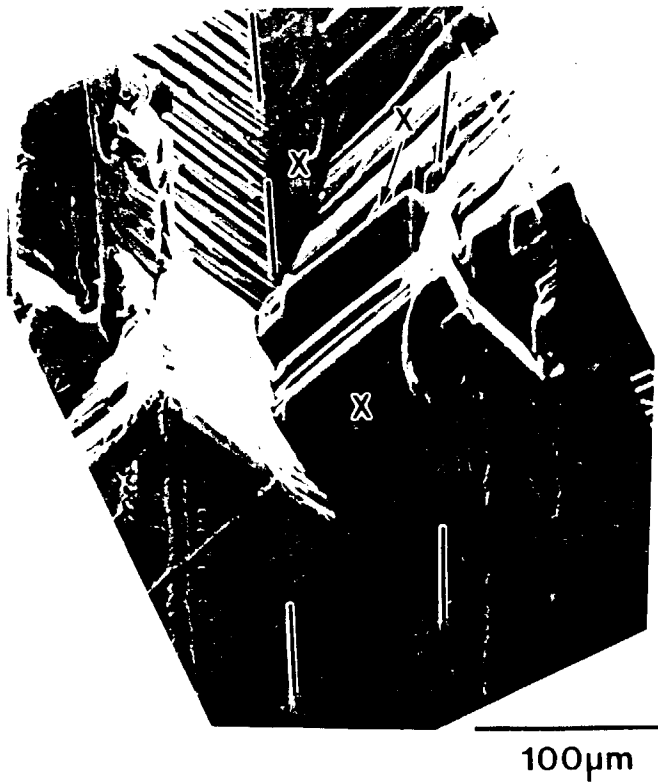
e)  $-30^\circ$



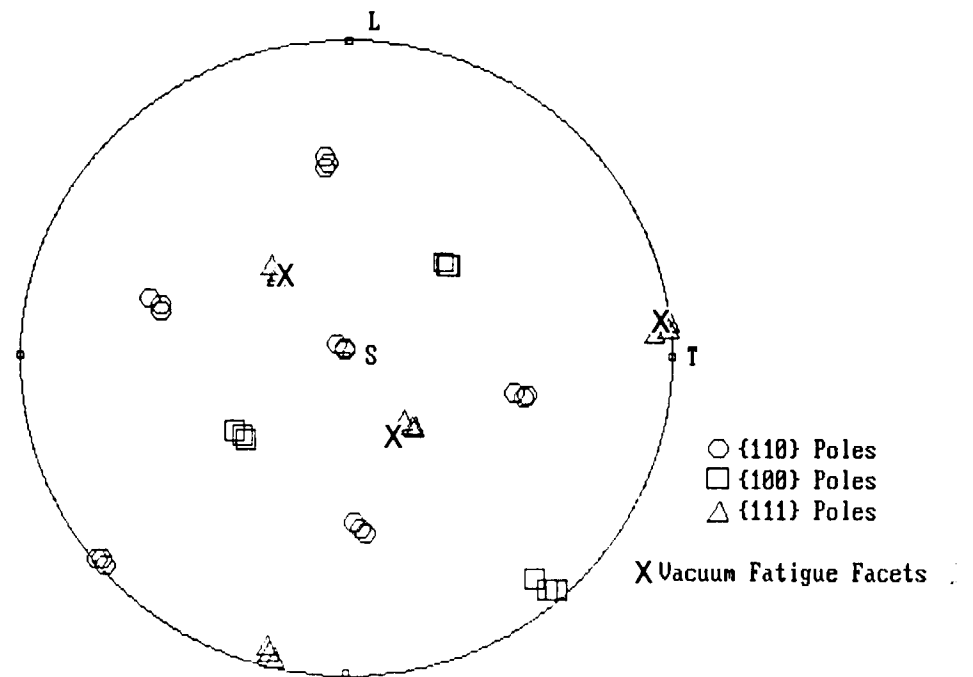


# Unrecrystallized Plate Vacuum Cracking

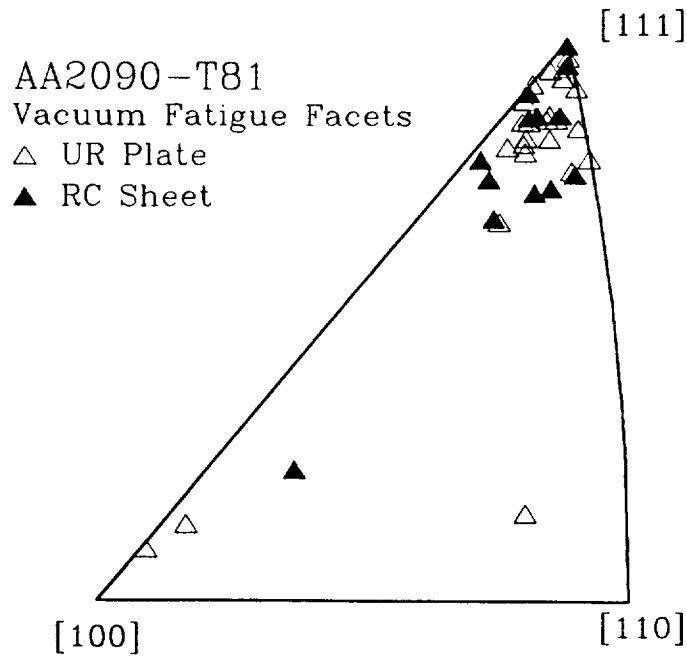
## Tilt Fractography



## Facet Crystallography



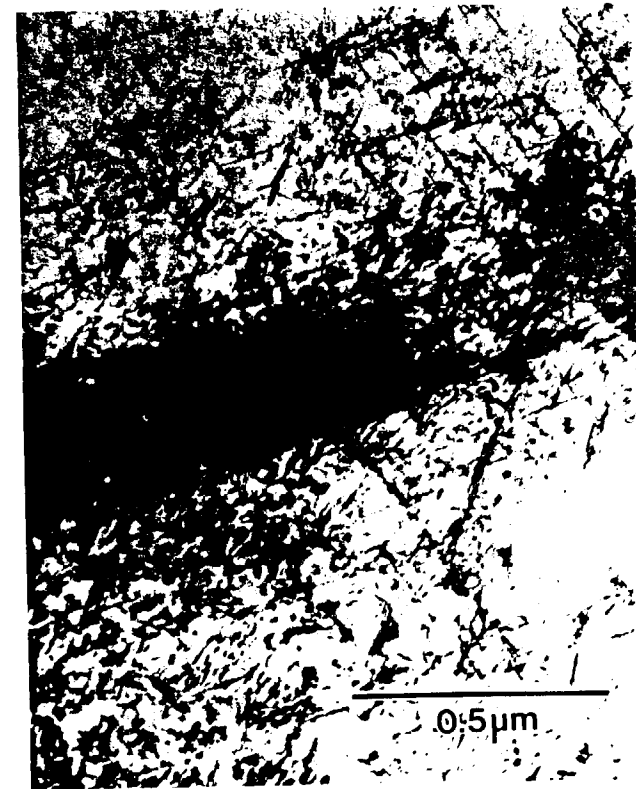
# Vacuum Facet Crystallography Summary



- o Facets generally near  $\{111\}$
- o But not identically crystallographic along  $\{111\}$

# AA2090 Vacuum Cracking Mechanism

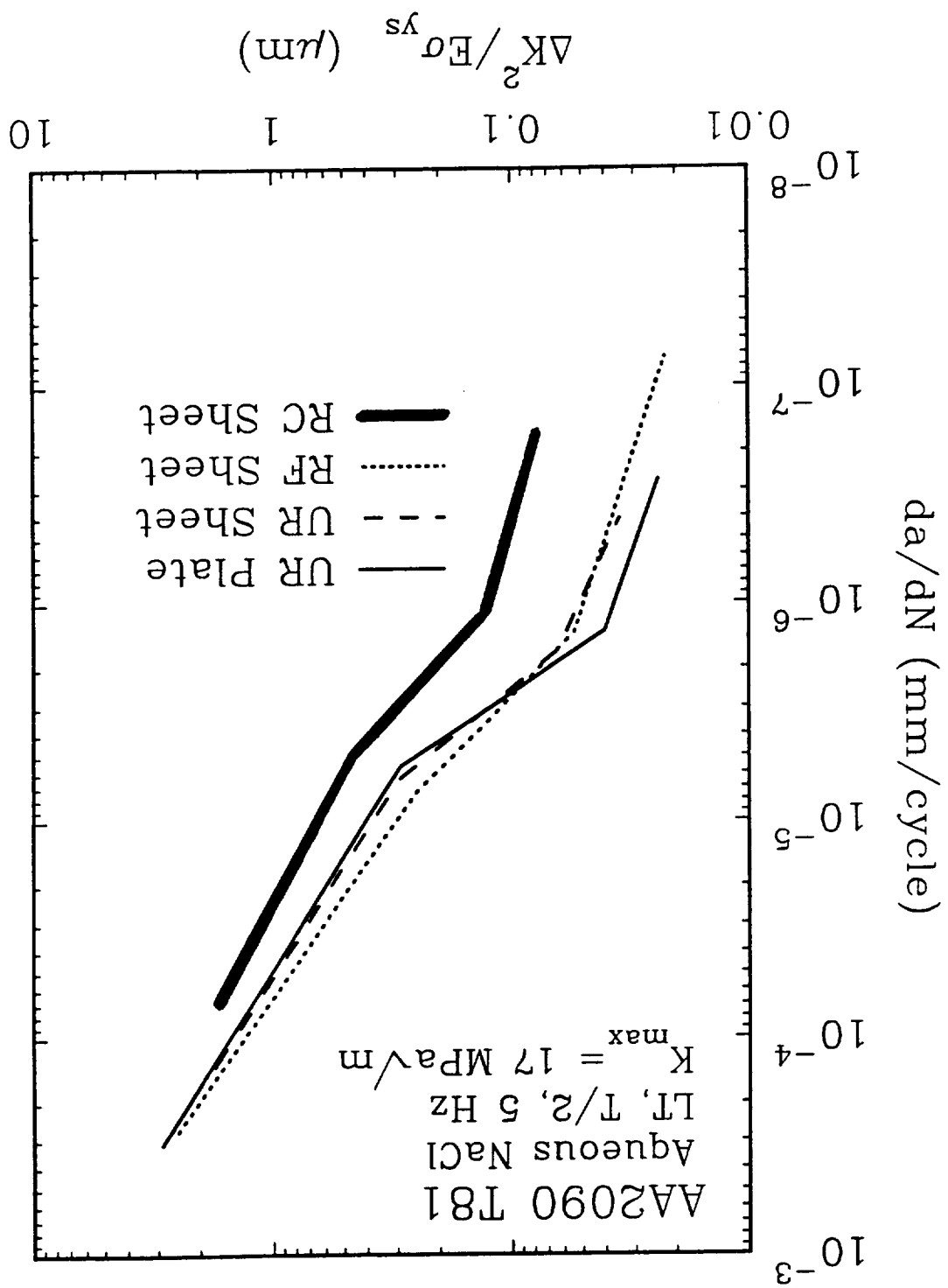
- o Fracture within deformation bands
  - not planar slip
  - bands not identically  $\{111\}$
- o Deformation bands complex dislocation structures even in uniaxial fatigue
  - bands cross subgrain boundaries
  - bands cross grain boundaries
- o Deformation bands at crack tip extremely complex
  - multiple slip predicted
  - high crack tip strains
  - complex dislocation structures



Tensile Test,  $\epsilon^p = 2\%$   
AA2090 UR Plate

## **Inert Environment Fatigue Damage Conclusions**

- o Fully quantitative fracture crystallography technique**
  - applicable for 5  $\mu\text{m}$  subgrains
  - global methods cannot distinguish  $\{100\}$  or  $\{111\}$  facets
- o Near- $\{111\}$  facets quantitatively identified**
  - implicates a deformation band cracking mechanism
  - facets form independent of texture and subgrains
- o Multiple  $\{111\}$  facets within single grains**
  - multiple  $\{111\}$  oriented for slip
  - $60^\circ$  intersecting angles at high and low-angle boundaries
- o Single cracking mechanisms and single  $da/dN$  correlating parameter**
  - $\Delta\epsilon_{\text{crack}} = \Delta K^2 / E \sigma_{ys} X$
  - similar trends for other aluminum alloys



A  $da/dN$ - $\Delta K$  power law transition is predicted when the cyclic plastic zone diameter equals the distance between microstructural ( $\lambda$ ) impediments to slip:

$$\lambda = 0.033 (\Delta K_{\text{TRANSITION}} / \sigma_{\text{ysc}})^2$$

$\lambda$	UR Plate	UR Sheet	RF Sheet	RC Sheet
$T_1$ Spacing	0.7**	0.6	0.6	0.4
$\beta'$ Spacing	1.3	1.1	1.2	0.8
Subgrain Width	10.7	5.7	----	----
Grain Width	> 80	> 25	13	49

\*\*  $\Delta K_{\text{TRANSITION}}$  in MPa $\sqrt{m}$

## Single Microscopic Damage Mode

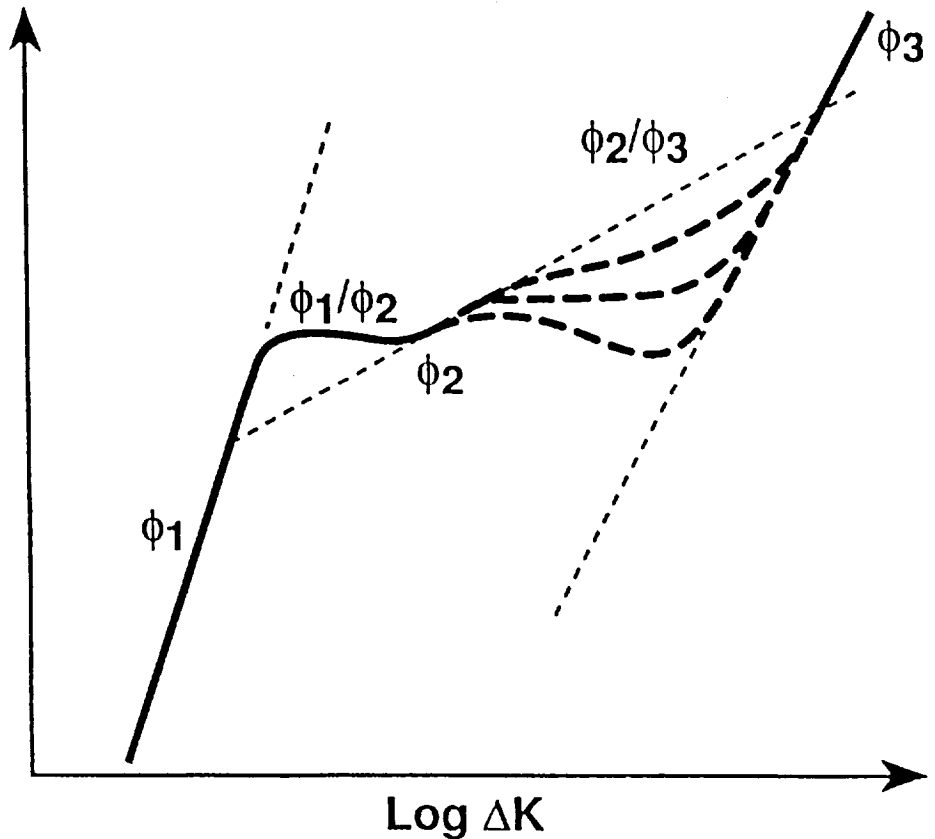
$$da/dN \propto \Delta K^{(2+4\phi)} / \sigma_{YS}^{(2+3\phi)} E^\phi$$

## Multiple Damage Modes in Parallel

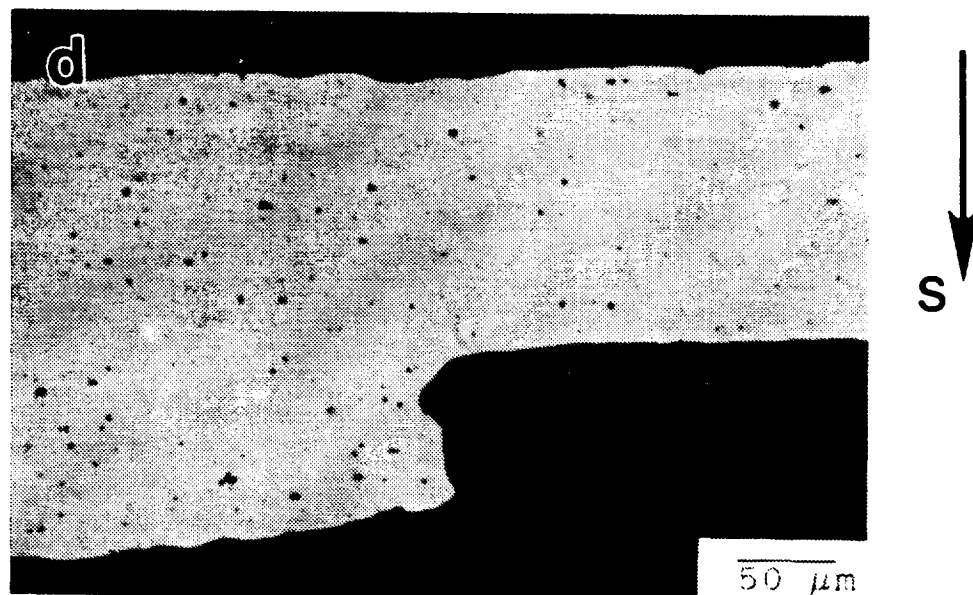
$$da/dN_{ENV} \propto \underbrace{\Theta_{\{111\}} \Delta K^{2/\beta}}_{\text{(Inert)}} + \underbrace{\Theta_{\{100\}} \Delta K^{(2+4\phi-\{100\})}}_{\text{(Hydrogen Enhanced \{100\})}} + \underbrace{\Theta_{ISGC} \Delta K^{(2+4\phi-ISGC)}}_{\text{+ ISGC}}$$

Complex  $da/dN$ - $\Delta K$  transitions controlled by proportion of each cracking mode ( $\Theta_i$ ), and intrinsic  $\Delta K$  dependence ( $\phi$ ,  $\gamma$ )

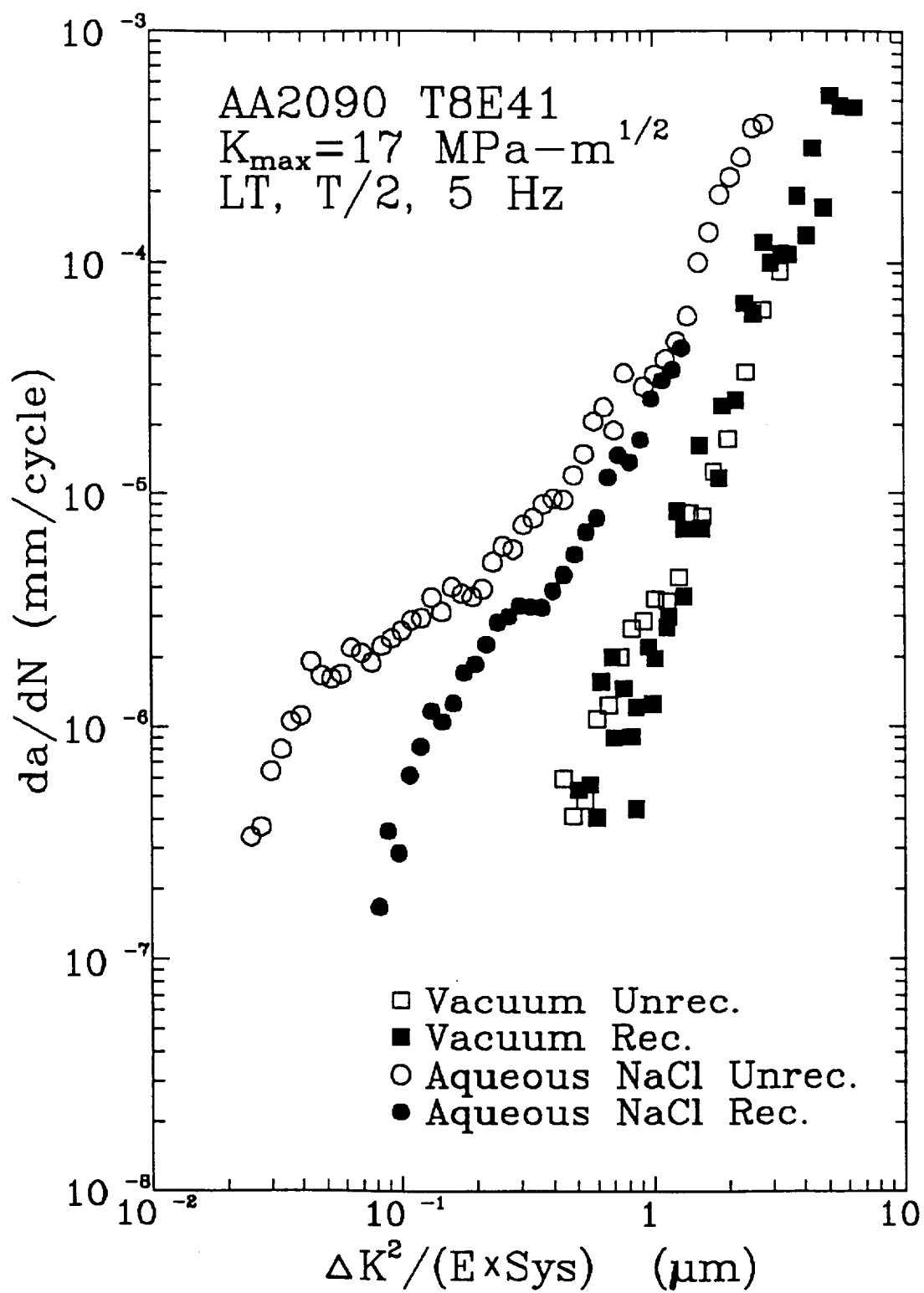
Absolute  $da/dN$  not predicted because of unknowns



## Recrystallized AA 2090 Sheet from Plate

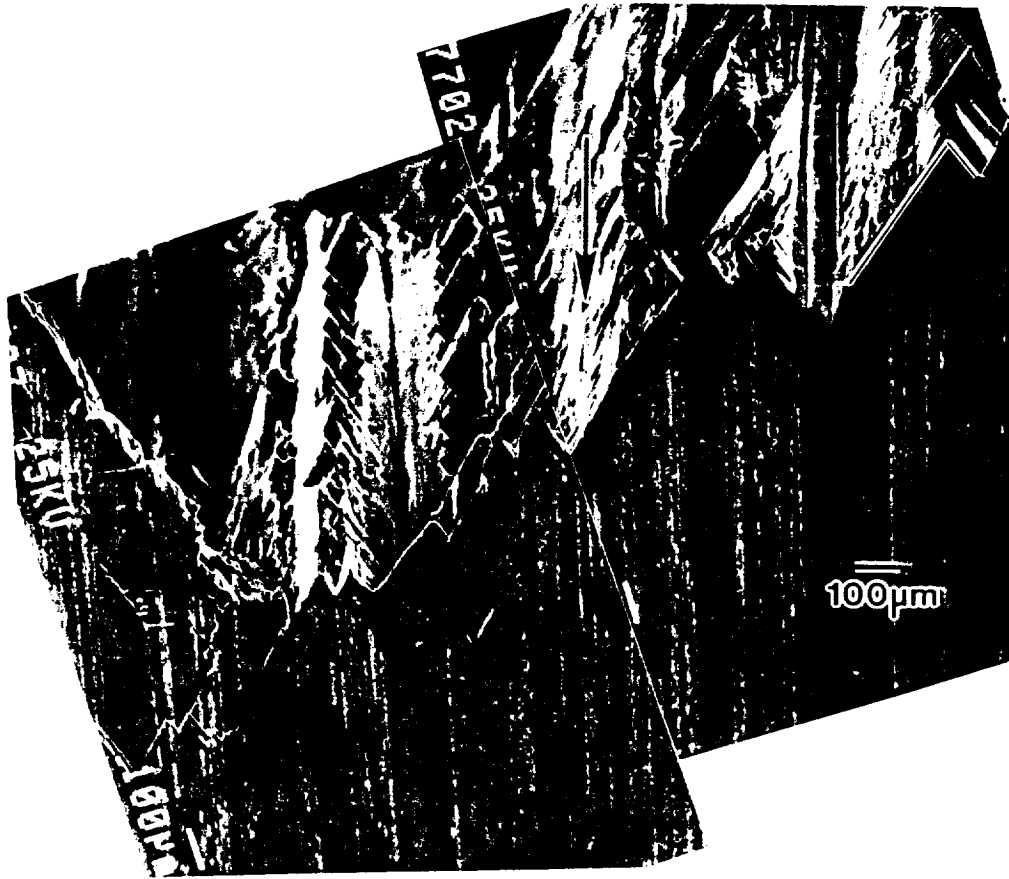




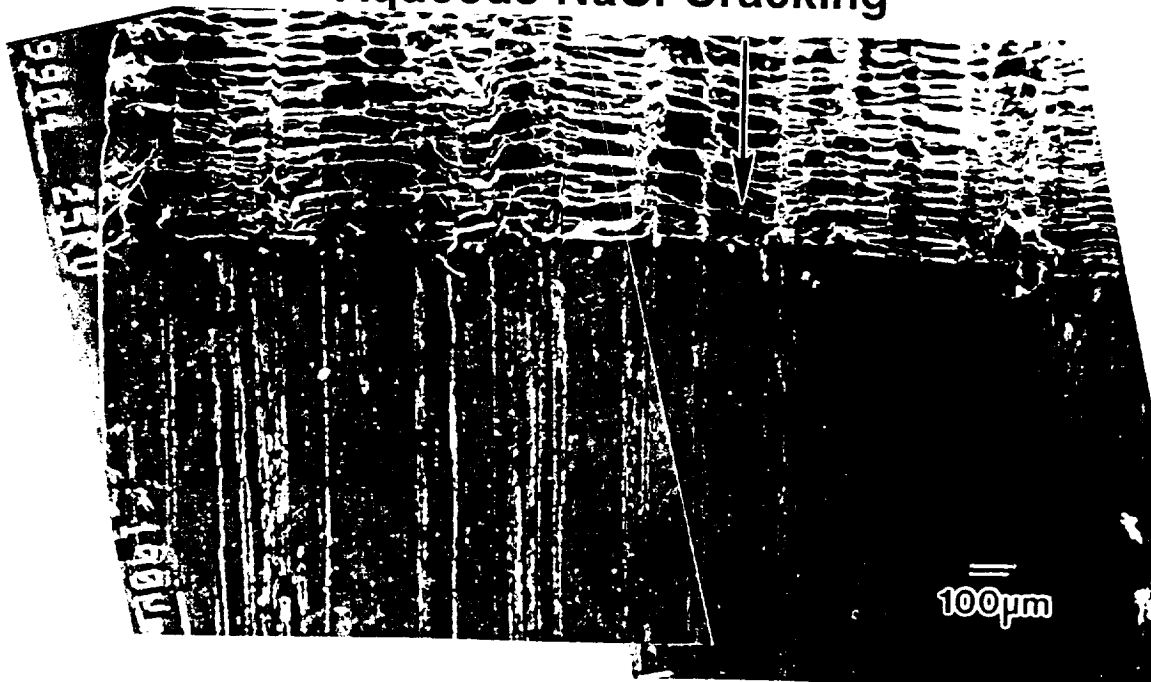


# Unrecrystallized Tilt Fractography

## Vacuum Cracking

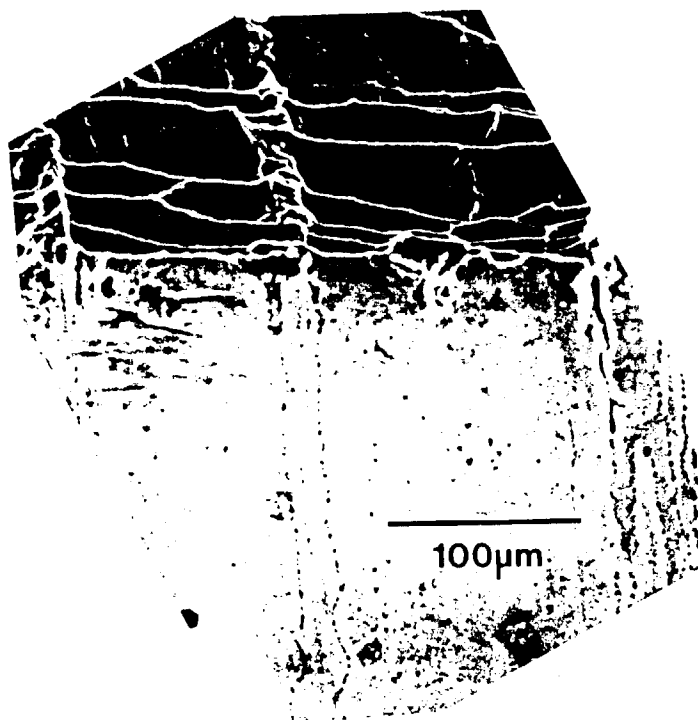


## Aqueous NaCl Cracking

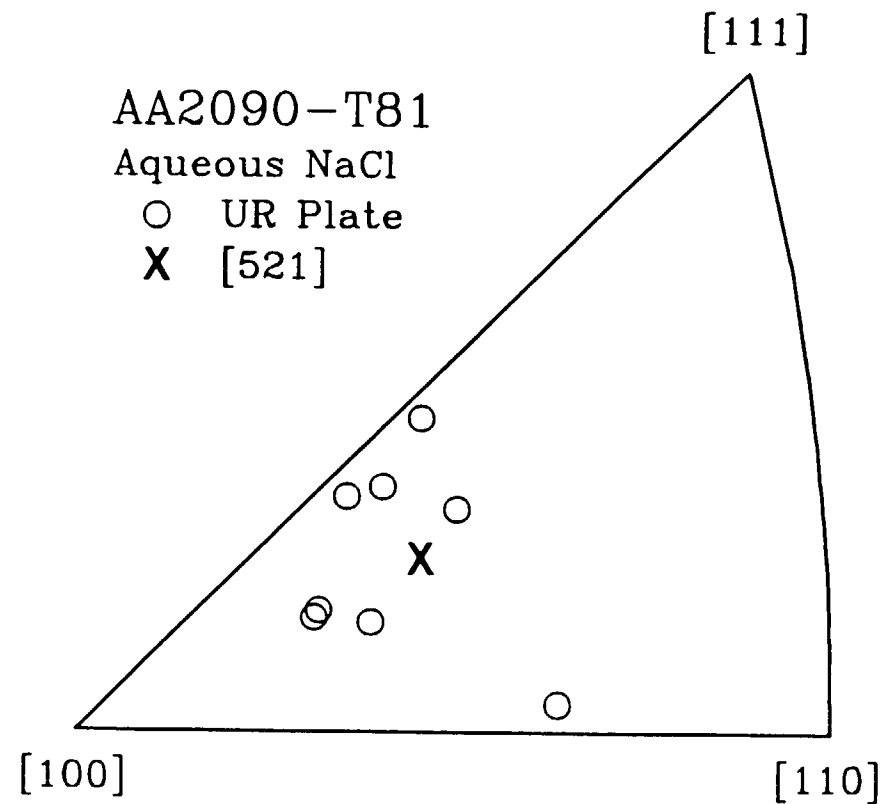


# Unrecrystallized Plate Aqueous NaCl Cracking

## Tilt Fractography



## Facet Crystallography

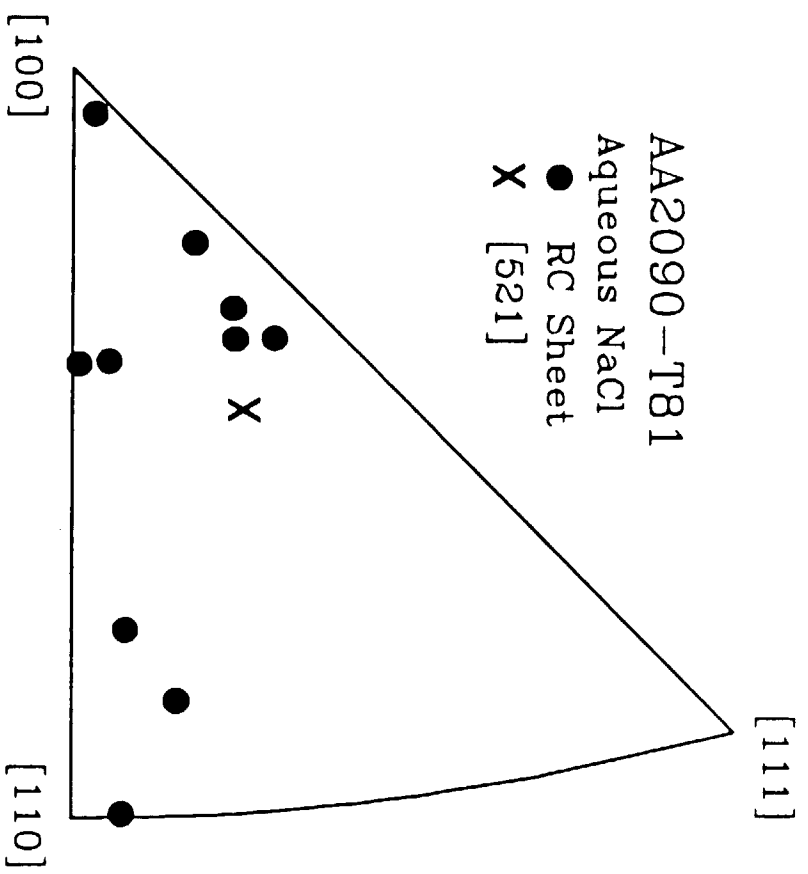


AA2090-T81

Aqueous NaCl

● RC Sheet

X [521]

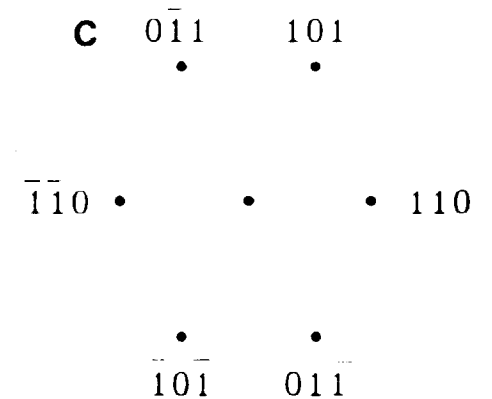
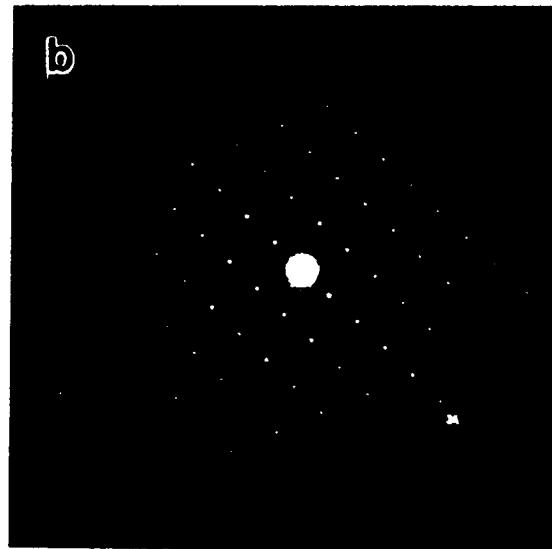
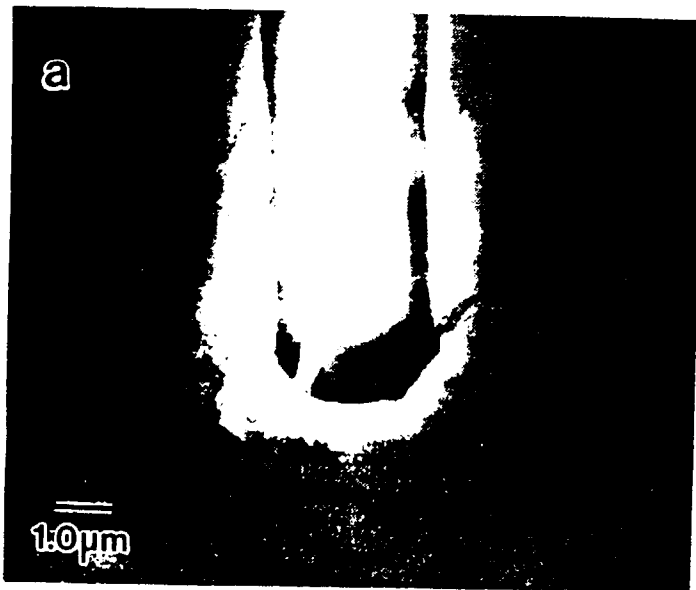


# Unlikely Aqueous NaCl Fatigue Damage Mechanisms

- o Facets are not macroscopically  $\{100\}/\{110\}$ 
  - $22^\circ$  from  $\{100\}$  for UR plate
  - $27^\circ$  from  $\{110\}$  for UR plate
  - not  $\{100\}$  when normal to  $\bar{L}$  for RC sheet
  - \* NOT  $\{100\}$  crystallographic decohesion
  - \* NOT  $\{100\}$  alternate slip
- o Facets are not macroscopically  $\{111\}$ 
  - $33^\circ$  from  $\{111\}$  for UR AA2090
  - \* NOT hydrogen enhanced deformation band cracking
  - \* NOT matrix  $T_1$  dissolution and decohesion
- o Facets are not randomly oriented
  - facet pole  $15^\circ$  from  $\bar{L}$  for UR plate
  - periodic facets for single UR plate grains
  - \* Facets crystallographic near  $\{521\}$

# Potential Aqueous NaCl Damage Mechanism

- o  $\text{LiAlH}_4$  identified in the literature
  - high purity Al-Li-Cu Alloys
  - $[421]$  beam direction



## **Aqueous NaCl Fatigue Conclusions**

- o Environmental influence dramatic compared to vacuum**
  - $\Delta K_{th}$  decreased**
  - multiple  $da/dN$ - $\Delta K$  power law slopes**
  - unique cracking profiles**
- o Microstructural dependence on cracking**
  - $\Delta K_{th}$  increased for RC sheet compared to other microstructures**
- o Facets crystallographic**
  - near  $\{521\}$  faceted cracking**
- o Cracking modes and  $da/dN$ - $\Delta K$  are not fully understood**
  - possibly explained with  $LiAlH_4$  fracture**
  - further work needed**
- o  $da/dN$ - $\Delta K$  modelling require an improved understanding of damage modes**





**Project #2    Elevated Temperature Damage Tolerance of Advanced Ingot Metallurgy Wrought Aluminum Alloys**

Michael J. Haynes and Richard P. Gangloff

**Objective**

The goal of this study is to characterize the flaw damage tolerance of emerging ingot metallurgy wrought aluminum alloys as a function of temperature and loading rate, to establish the underlying mechanisms for time-temperature dependent fracture, and to predict the initiation and growth toughness behavior through micromechanical modeling.

**Technical Approach**

Work for this reporting period concentrated on three 2000 series wrought aluminum alloys. Alcoa provided two variants of AA2519, modified with additions of either 0.3 wt% Mg or 0.3 wt% Mg + 0.5 wt% Ag, and in the form of 3.2 mm thick sheet. Pechiney provided 6 mm thick plate of AA2650. Precipitates and microstructure were characterized for each alloy through TEM and optical microscopy.

Slow rising load  $J$ - $\Delta a$  curves were obtained for each alloy as a function of temperature, over a testing period of approximately three hours, and employing 3.2 mm thick compact tension specimens with a width of 10.2 cm. Plane strain initiation toughness ( $K_{IC}$ ) was obtained for each alloy and temperature from  $J_i$ , the  $J$ -integral value corresponding to direct current potential difference (DCPD) detection of the onset of crack propagation. We believe that this measurement from a thin sheet specimen corresponds to a conventional plane strain fracture toughness from a sufficiently thick specimen. Crack growth toughness was estimated by the stress intensity level, from the total applied  $J$ -integral, at 5.0 mm of crack extension. This value should be proportional to  $K_C$  from a wide, cracked panel experiment. Fracture surfaces were analyzed to define the operating fracture mechanism(s).

UVA is participating in the NASA-LaRC sponsored interlaboratory experimental program to characterize the room temperature fracture toughness of AA2024-T3 sheet. Accordingly, we have tested 3.2 mm thick compact tension specimens of this alloy for  $K$ - $\Delta a$  curve comparison with data to be determined with wide centrally crack panels. Wide panel

measurements will be performed at a variety of laboratories.

### Current Status

Mr. Haynes joined the LA<sup>2</sup>ST program in September of 1992, and has completed six of the eight classes required for the Master of Science degree in Materials Science and Engineering. The following research results were obtained since January of 1993.

### Recent Results

TEM analysis revealed that the Ag addition to AA2519 promotes  $\Omega$  as the primary strengthening phase. In the AA2519 with additional Mg,  $\Omega$  is formed, but  $\Theta'$ ,  $S'$ , and  $\Omega$  phases collectively strengthen the alloy.  $S'$  formed as the primary strengthening phase in AA2650, analogous to precipitation in AA2618. Optical metallography showed a recrystallized grain structure for each alloy.

Room temperature J- $\Delta a$  results show that the  $K_{IC}$  values for the three advanced IM alloys are greater than AA2618 and RS P/M AA8009 (two alloys previously studied at UVa). The room temperature crack growth toughnesses (assessed by  $K_C$ ) of the two variants of AA2519 are superior to that of AA2024-T3, while the damage tolerance of AA2650 is slightly inferior.

$K_{IC}$  for 2519 + Ag is essentially independent of temperature between 25 and 175°C, while that of Mg modified AA2519 exhibits a mild maximum at about 100°C before declining at 175°C. The temperature dependence of  $K_{IC}$  for AA2650 is similar to that of Mg modified AA2519. The crack growth toughness of each AA2519 variant initially increases and then falls as temperature increases to 175°C. Toughness decreases less rapidly for the alloy with the Ag addition, suggesting that  $\Omega$  is more thermally stable than  $\Theta'$  in the context of time-temperature dependent crack growth. AA2650 showed an increased crack growth toughness at higher temperatures.

Microvoid coalescence was identified as the fracture mechanism for each alloy at all temperatures. Fracture surfaces contained a duplex distribution of voids; 10 to 30  $\mu m$  diameter dimples were associated with constituents or primary phases, and 1 to 5  $\mu m$  diameter dimples were possibly affiliated with dispersoids or precipitates. SEM fractography revealed that as the temperature increased, the smaller sized dimples increased in size for AA2519 with Mg + Ag. This implies an expanded role of void sheeting in the fracture

process which may possibly account for the lower crack growth toughnesses at high temperatures.

### Milestones

Future work will be aimed at characterizing the time-temperature dependence of crack growth, with particular attention towards the role of creep deformation in the fracture process. Consequently, the initiation and growth toughnesses will be assessed over a range of grip displacement rates at 150°C for AA2519 (Mg + Ag). Tests will vary in length from a few minutes to approximately a week. Fracture toughness tests will also be performed at cryogenic temperatures for each alloy.

Uniaxial compression and Bridgman notched bar tensile experiments will be employed to provide input for modeling the initiation and crack growth toughnesses. Each test will be applied over the full range of temperatures, the compression test utilizing a recently built high temperature compression fixture.

### Presentation Viewgraphs

1. Title.
2. The challenge for HSCT materials: develop an aluminum alloy that is thermally stable to high temperatures and maintains a high level of toughness. This is a summary plot of AA8009 data showing the deleterious decrease in toughness with increasing temperature.
3. Project objective and presentation outline.
4. Schematic drawing depicting the experimental set up for fracture toughness testing of C(T) specimens. Load, crack length from electrical potential and crack mouth opening displacement are digitally recorded for input to the calculation of J versus  $\Delta a$ .
5. Linear elastic stress intensity (K) versus crack extension ( $\Delta a$ ) R-curves for the NASA sponsored round robin characterization of AA2024-T3, derived from the small scale yielding analogy of the J- $\Delta a$  curve. Note the reproducibility of the J- $\Delta a$  measurements.
6. Compositions of the alloys studied (AA2024, AA2650, AA2519 w/Mg, and AA2519 w/Mg + Ag).
7. Optical micrographs of the AA2519 variants at magnifications of 50X and 200X, showing the recrystallized grain structure and distribution of constituents.

8. TEM micrograph of AA2519 w/0.5 wt% Mg + 0.5 wt% Ag, showing the high density of  $\Omega$  phase.
9. Bright Field and Dark Field TEM micrographs showing the strong presence of  $S'$ ,  $\Theta'$ , and  $\Omega$  phases in AA2519 with additional Mg.
10. Optical and TEM micrographs of AA2650 showing recrystallized grain structure and  $S'$  strengthening phase, respectively.
11. Table summarizing the major strengthening phases, grain structure, room temperature yield strength, and ageing practices for the three alloy systems. The characteristics of the three precipitates are also shown.
12. Room temperature J- $\Delta a$  curves for the four alloys tested, demonstrating the greater crack growth toughness of the modified 2519 alloys. The change in shape of the initial portion of the R-curve may be due to a decrease in the proportion of plane strain cracking and an increase in plane stress crack growth. Substantial plane strain crack growth, normal to the applied loading axis, was observed for the crack initiation and early growth stages of the R-curve. Crack growth was entirely along planes inclined at about  $45^\circ$  to the loading axis for  $\Delta a$  values above the upper inflection point for each curve.
13. Table of plane strain fracture toughnesses,  $K_{IC}$ , as a function of temperature for five aluminum alloys, as characterized by the rising load J- $\Delta a$  method at UVa. All  $K_{IC}$  values are derived from the J-integral value at the onset of crack growth measured by DCPD.
14. Ranking of the room temperature plane stress crack growth toughness of each of the four alloys tested, based on a linear elastic plane stress  $K_C$  value corresponding to a crack growth of 5 mm.
15. SEM fractography of room temperature crack surfaces within the plane strain initiation region for the three advanced alloys. The fracture mode is microvoid coalescence with a duplex distribution of dimple sizes. The low magnification SEM micrograph (upper left) shows the transition from plane strain fracture at the precrack to fully plane stress fracture.
16. J- $\Delta a$  data for AA2519 w/Mg & Ag as a function of temperature. These data demonstrate a decrease in crack growth toughness at high temperatures.
17.  $K_{IC}$  values for each alloy composition and temperature. Note that Ag bearing AA2519 retains  $K_{IC}$  at elevated temperature, at least for a three hour loading period.
18. Slide #2, including  $K_{IC}$  data for AA2519 w/Mg & Ag plotted with triangles.
19. Summary of  $K_C$  values for each alloy and temperature. Note the superior high temperature crack growth toughness of the AA2650 alloy. Also note the better

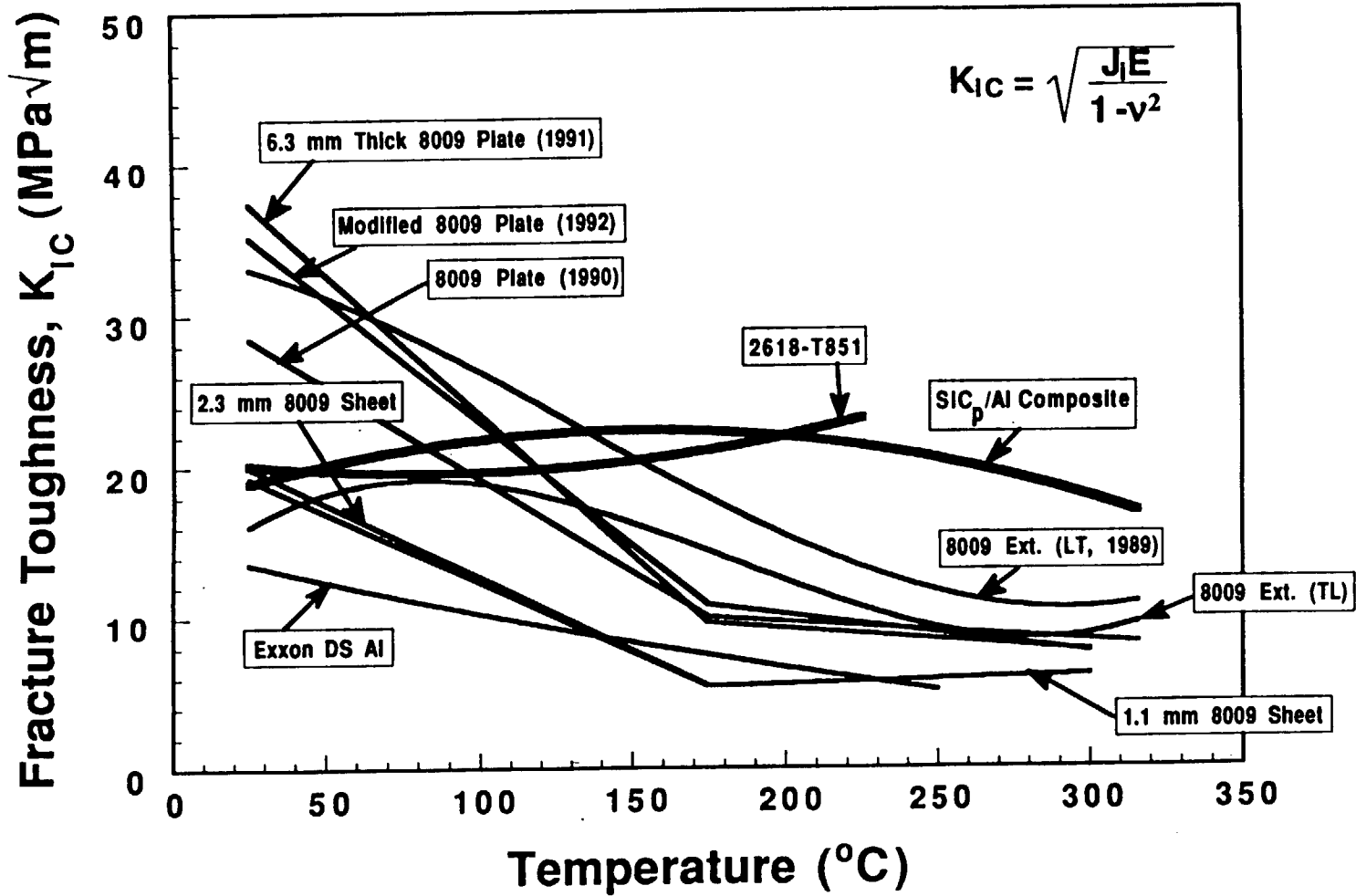
thermal behavior of Ag bearing AA2519 relative to the non-Ag bearing variant.

20. SEM fractographs of AA2519 w/Mg + Ag showing the morphology of the plane strain initiation region as a function of temperature. Note the increased size of the smaller sized population of dimples as temperature increases, implying an expanded role of void sheeting in crack growth.
21. Micromechanical modeling based on the critical plastic strain controlled model (after McClintock, MacKenzie et al. and Ritchie et al.). Simplified expressions from the model utilize tensile reduction in area and a constraint factor to predict the temperature dependence of  $K_{IC}$ .
22. Predicted  $K_{IC}$  versus temperature compared to measured  $K_{IC}$  values for AA2519 w/Mg & Ag.
23. Conclusions
24. Future Work

# **ELEVATED TEMPERATURE DAMAGE TOLERANCE OF ADVANCED INGOT METALLURGY WROUGHT ALUMINUM ALLOYS**

**Michael J. Haynes and Richard P. Gangloff**

**Funded by NASA Langley Research Center  
W.B. Lisagor, Project Monitor**



## **Objective**

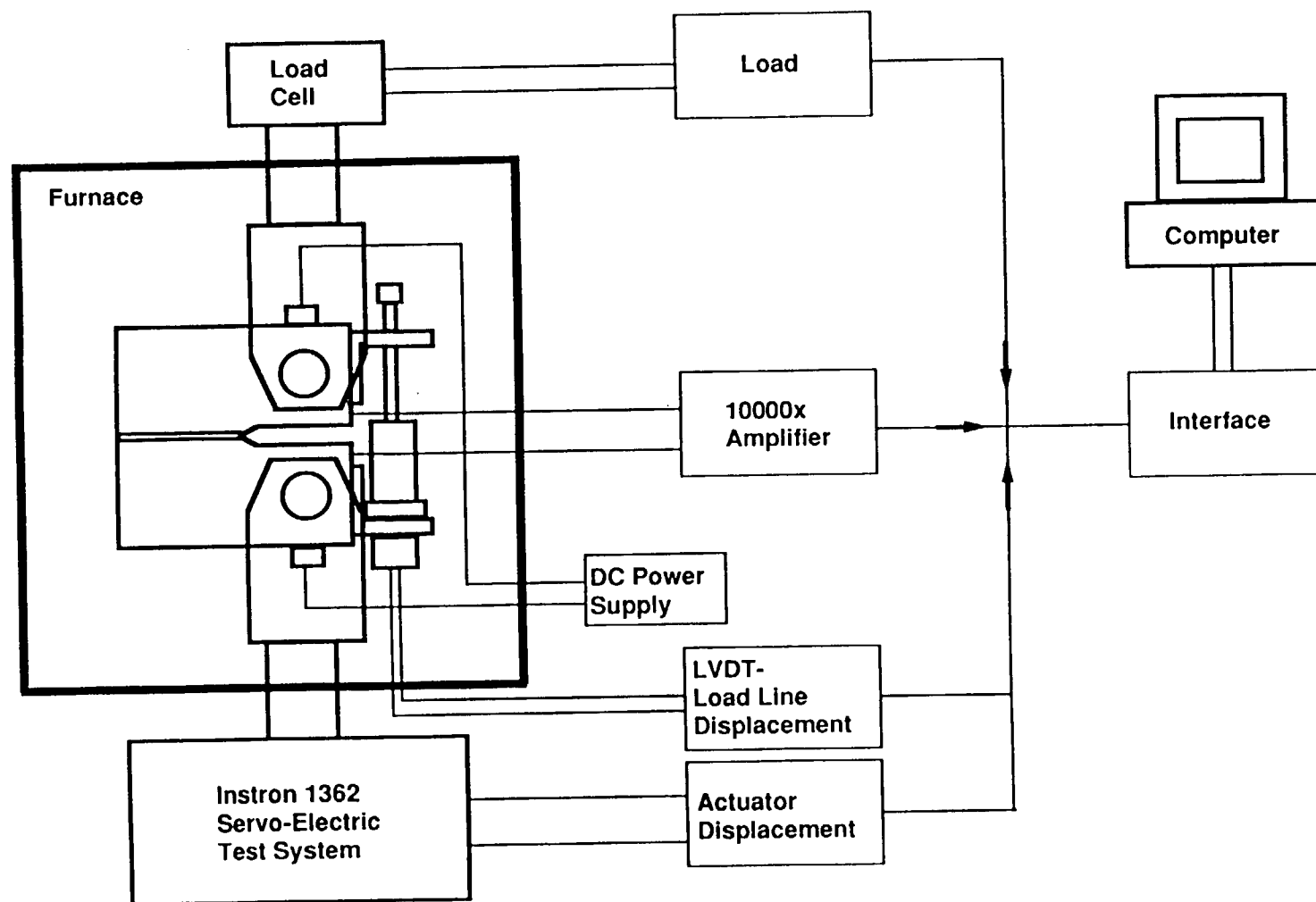
- **Characterize the flaw damage tolerance of advanced ingot metallurgy aluminum alloys as a function of temperature and loading rate, and establish the underlying damage mechanisms**

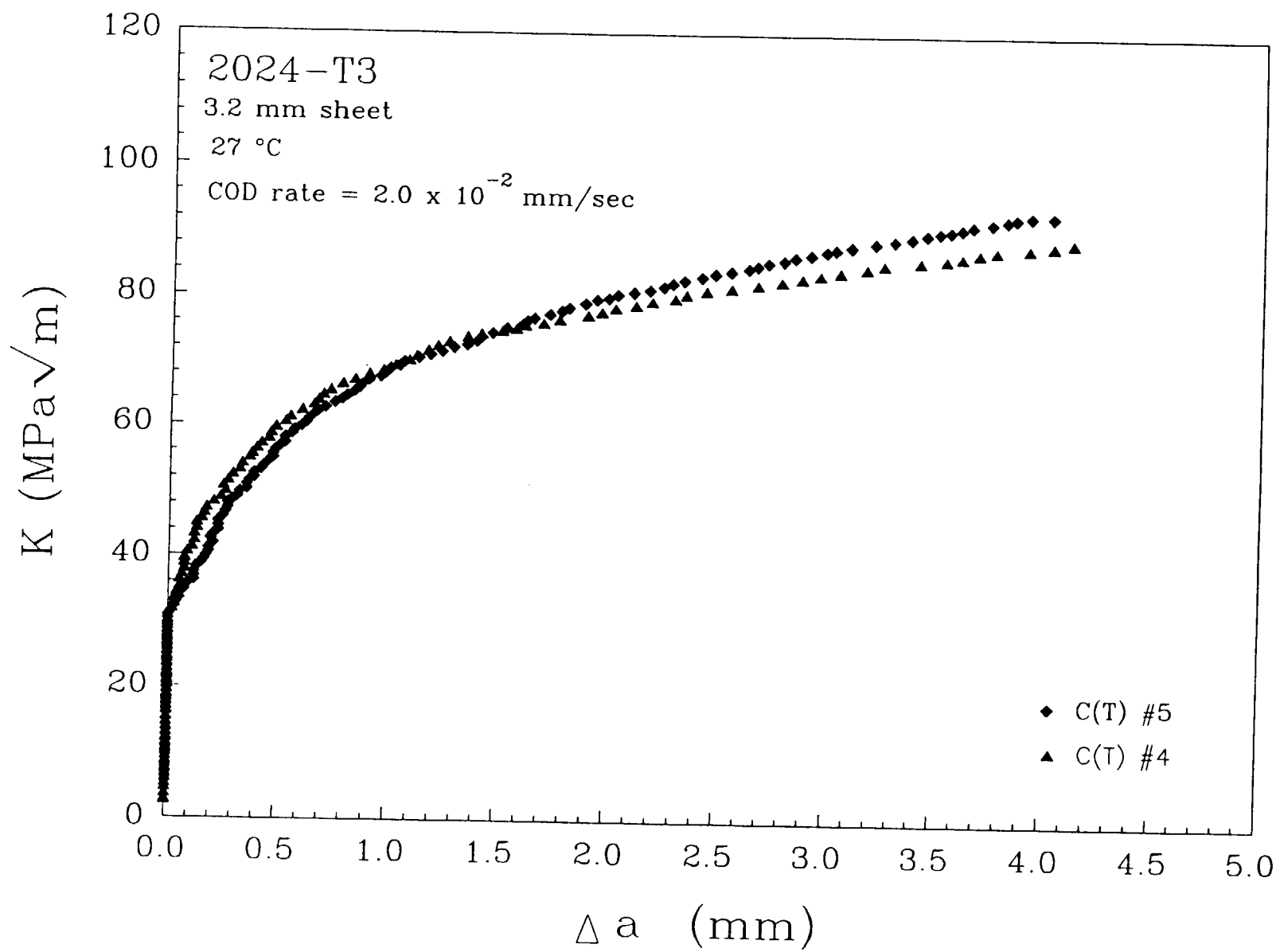
## **Outline**

- **Experimental Procedures**
- **Materials and Microstructural Characterization**
- **Toughness Results and Fractography**
- **Conclusions**
- **Future Work**



# Schematic of Fracture Toughness Experimental Setup



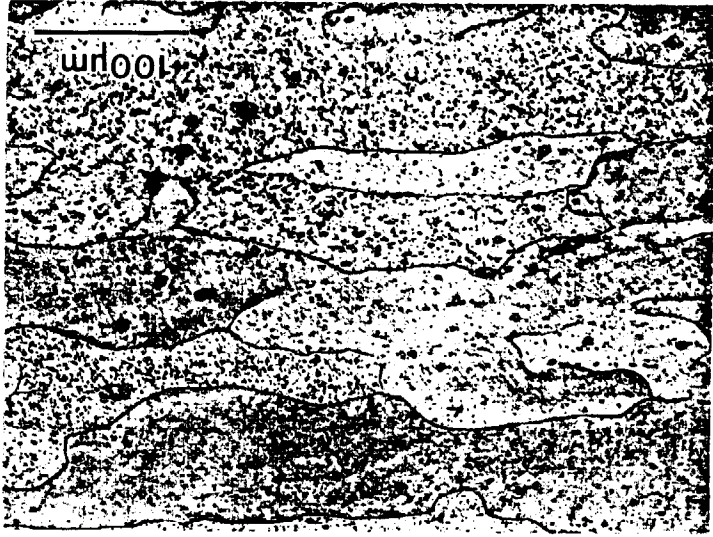


### Alloy Compositions

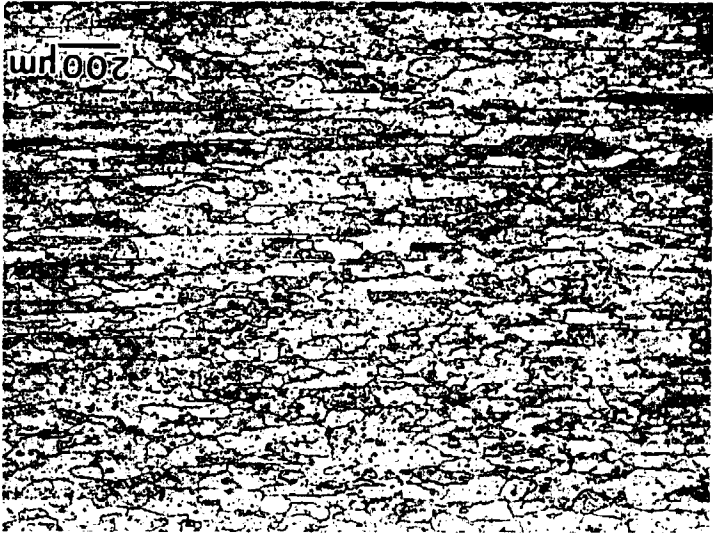
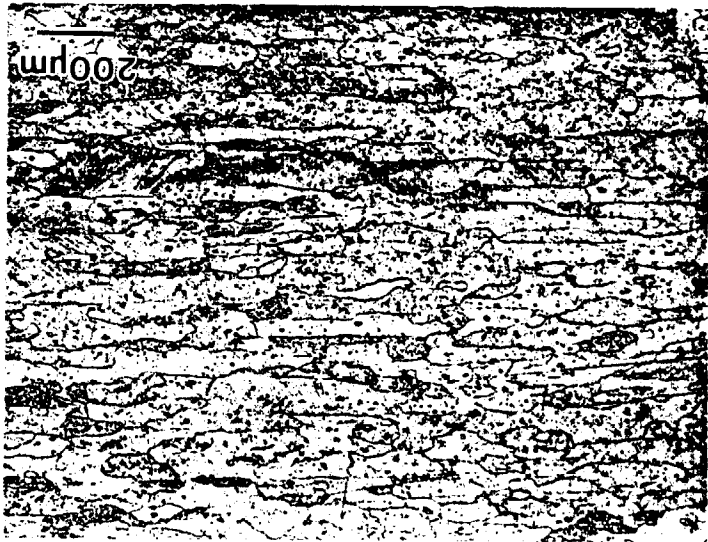
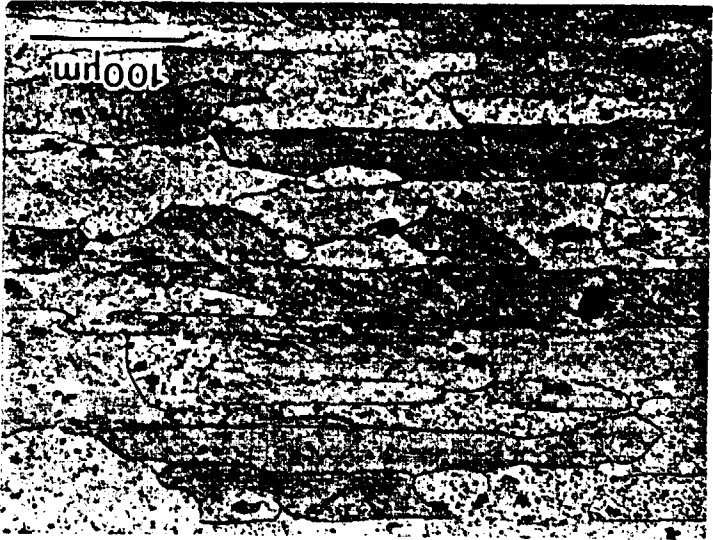
	Cu	Mg	Mn	Ag	Zr	V	Fe	Ni	Si
AA2024-T3	4.4	1.5	0.6	---	---	---	---	---	---
AA2519-T87 w/ Mg	5.83	0.52	0.30	---	0.15	0.10	---	---	---
AA2519-T87 w/ Mg, Ag	5.75	0.52	0.30	0.5	0.16	0.09	---	---	---
AA2650-T6	2.71	1.64	---	---	---	---	0.20	0.21	0.21

AA2519

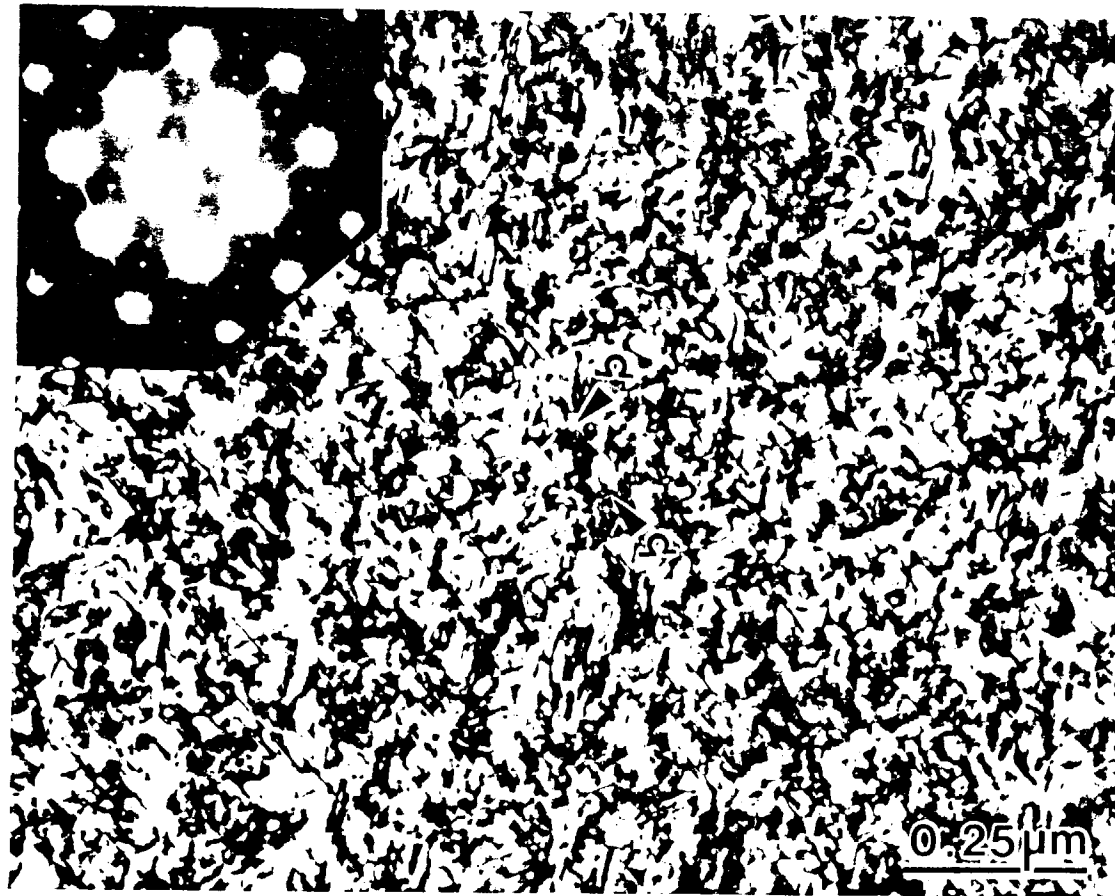
w/ 0.5 Wt% Mg



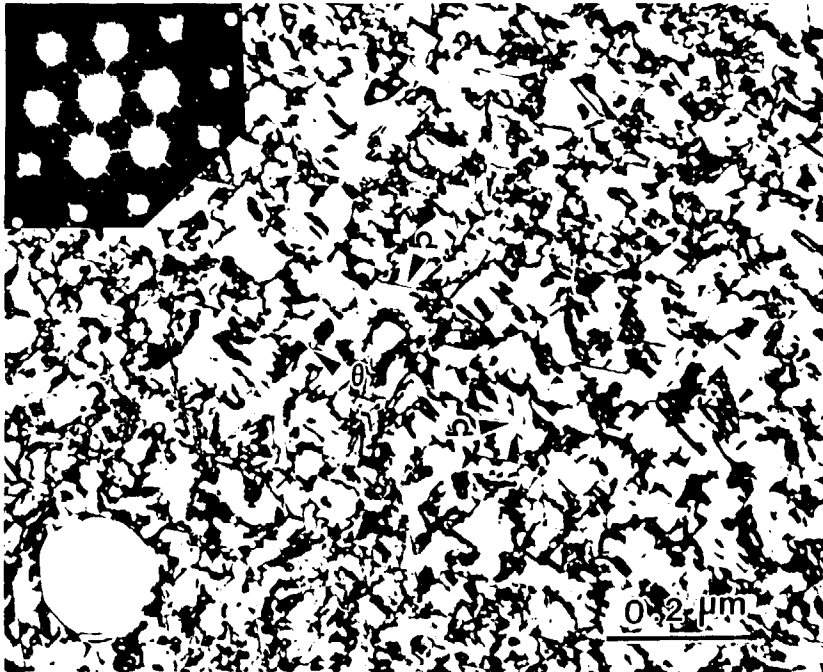
w/ 0.5 Wt% Mg + 0.5 Wt% Ag



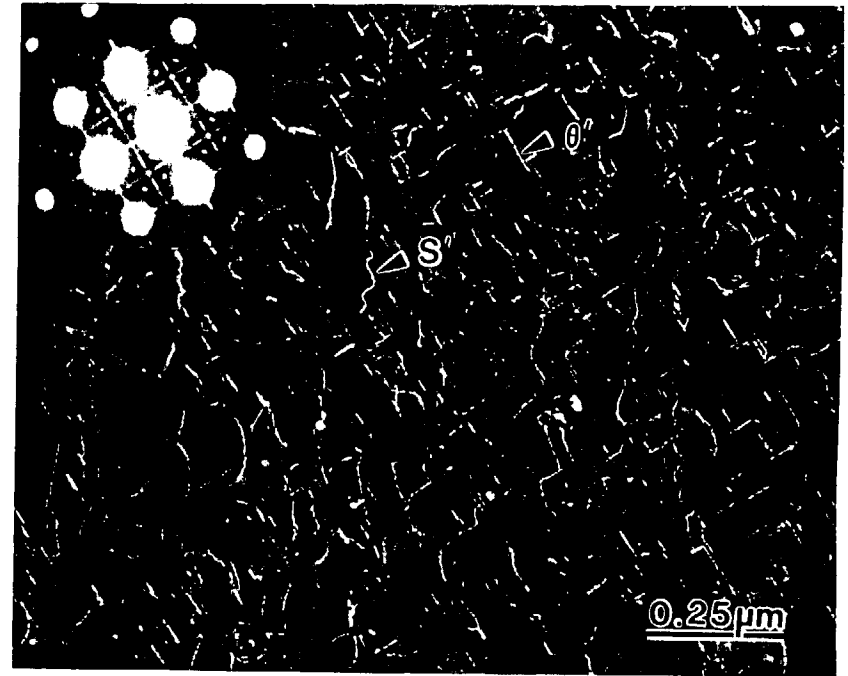
# AA2519 w/ 0.5Wt% Mg + 0.5Wt% Ag



## AA2519 w/ 0.5 Wt% Mg

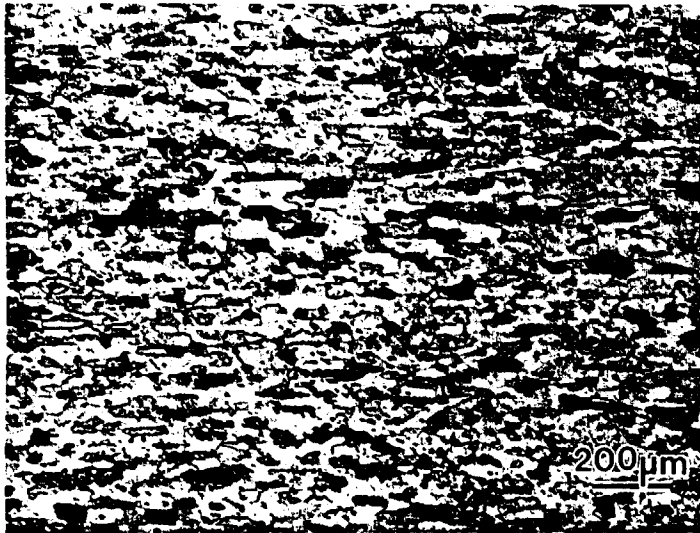


Bright Field

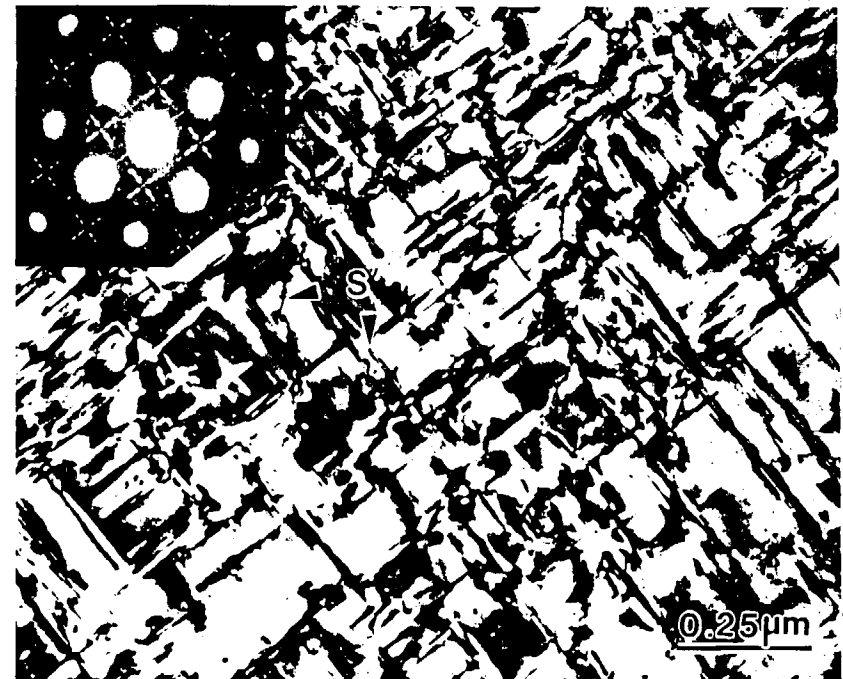


Dark Field

# AA2650



Optical



TEM

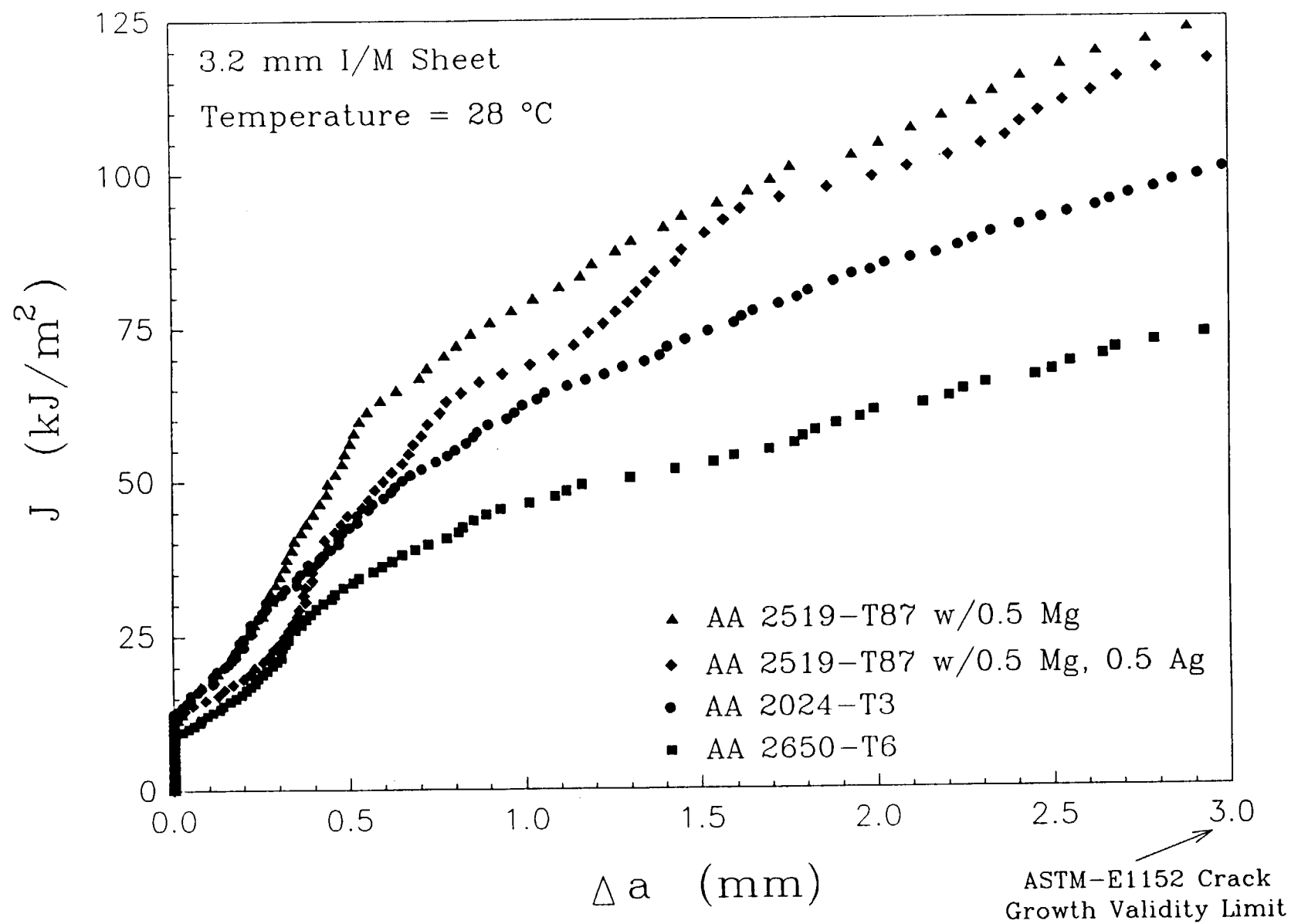
Alloy	2024-T3	2519-T87 w/ Mg	2519-T87 w/ Mg,Ag	2650-T6
Strengthening Phase(s)	S'	S', $\theta'$ , $\Omega$	$\Omega$	S'
Other Precipitates	$\theta'$	---	$\theta'$ , S'	$\theta'$
Grain Structure	--	RX	RX	RX
$\sigma_{ys}$ at 27 °C (MPa)	390	476	485	405
Aging Time/Temperature	---	3hrs/ 177°C	3hrs/ 177°C	20hrs/ 190°C

$\theta'$  -  $\text{Al}_2\text{Cu}$  Plates, {001}

$\Omega$  -  $\text{Al}_2\text{Cu}$  Plates, {111}

S' -  $\text{Al}_2\text{CuMg}$  Needles, {012}; {001}





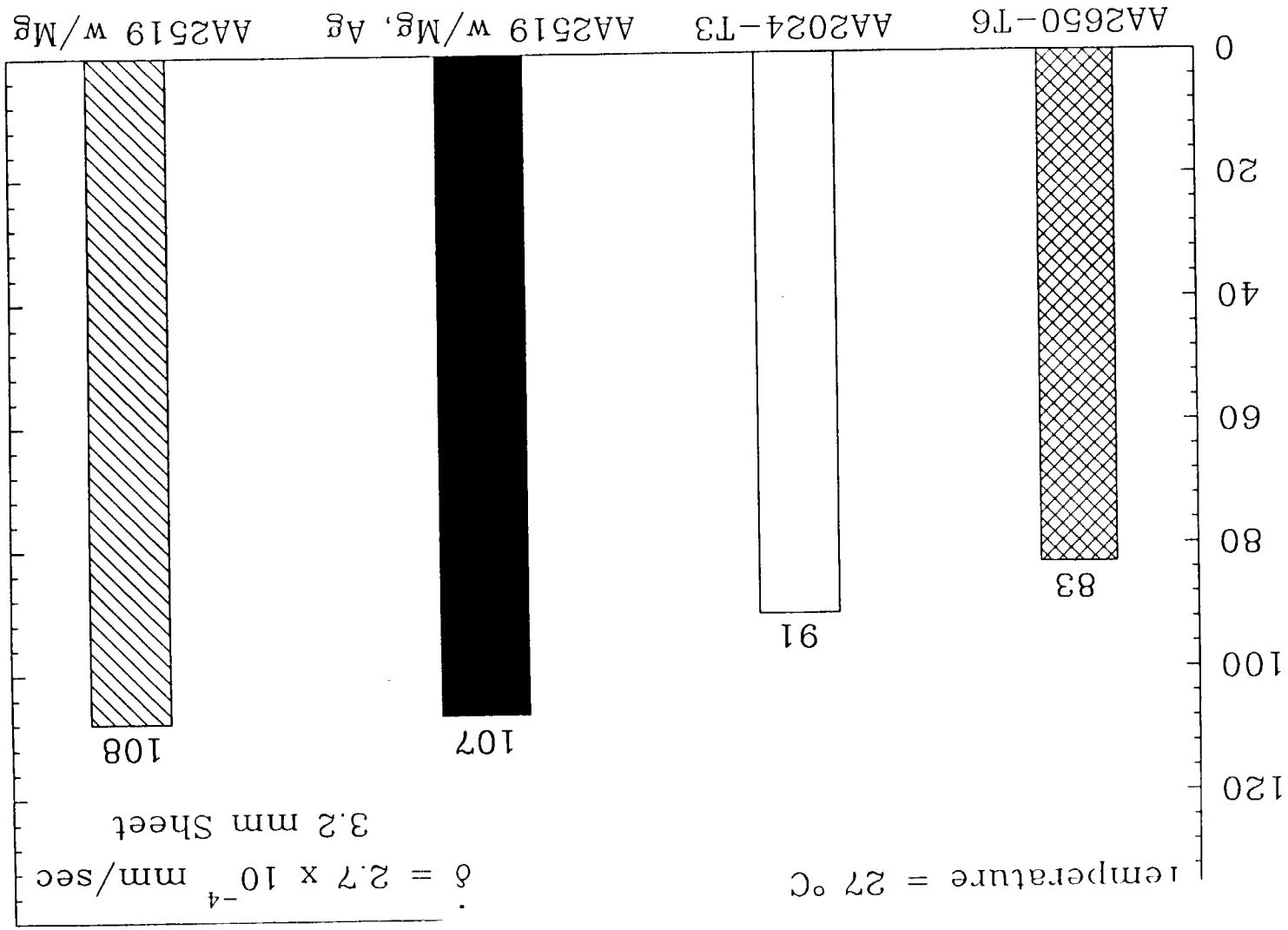
# Plane Strain Fracture Toughnesses of Aluminum Alloys

$K_{IC}$  (MPa√m)

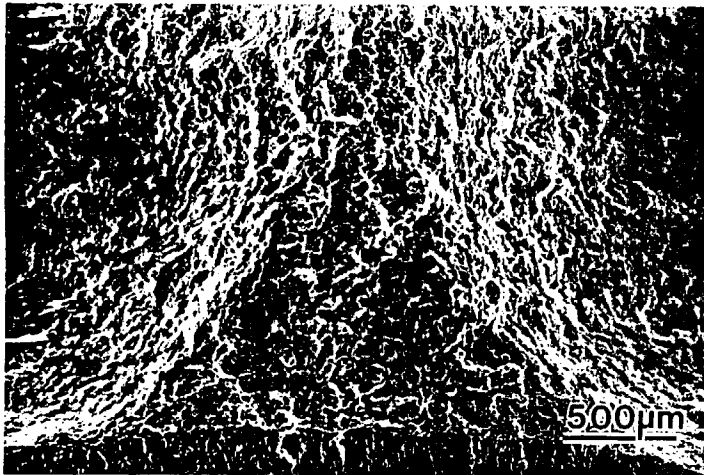
Test Temperature (°C)	8009 Plate	2618 Plate	2650 Sheet	2519 w/ Mg Sheet	2519 w/ Mg,Ag Sheet
27	27.4	20.1	27.8	30.5	30.9
75					31.9
100		20.0	29.3	34.1	
150					31.7
175	10.1	20.0	25.1	25.4	30.9
Test Time	15 Minutes	15 Minutes	3 Hours	3 Hours	3 Hours

- All  $K_{IC}$  values are derived from DCPD  $J_I$  values

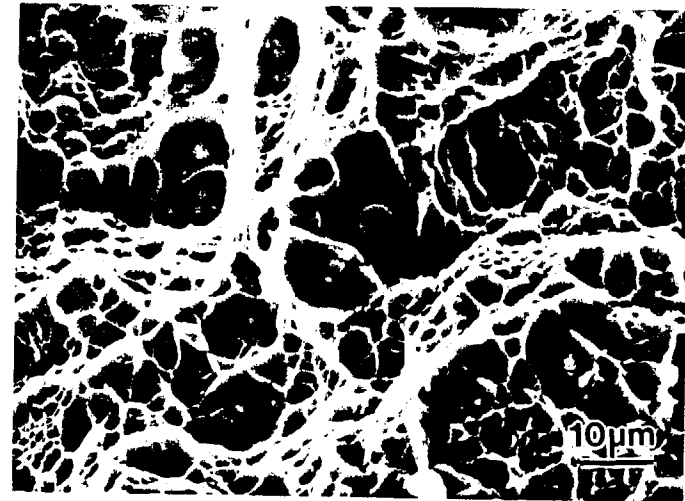
$K_C$  (MPa $\sqrt{m}$ ) at  $\Delta a = 5$  mm



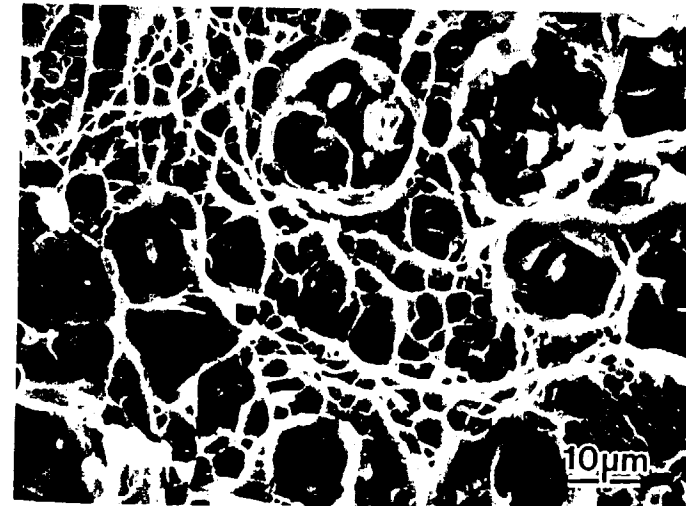
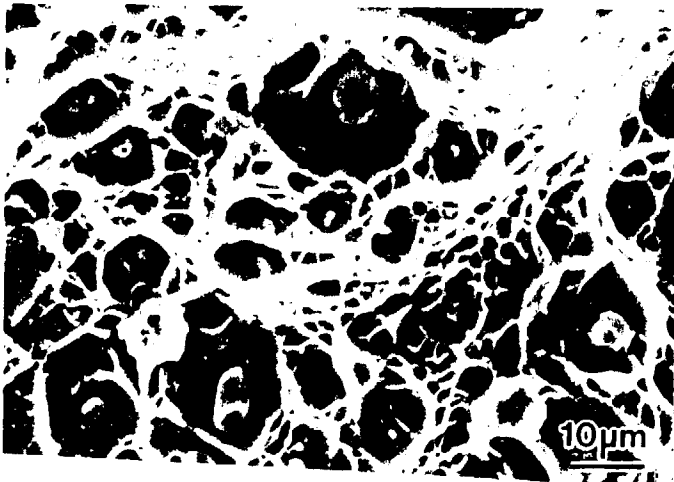
## Room Temperature SEM Fractographs

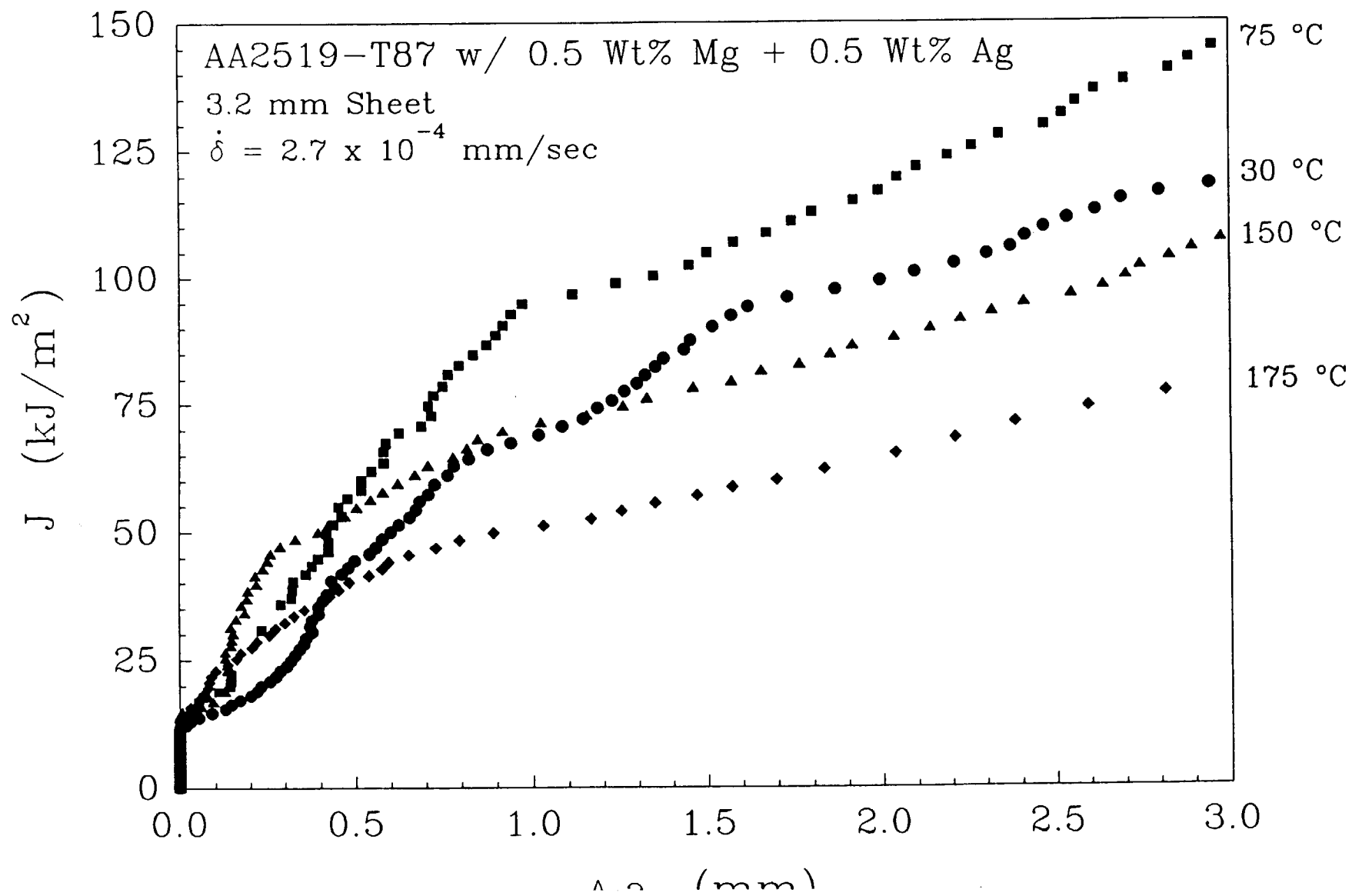


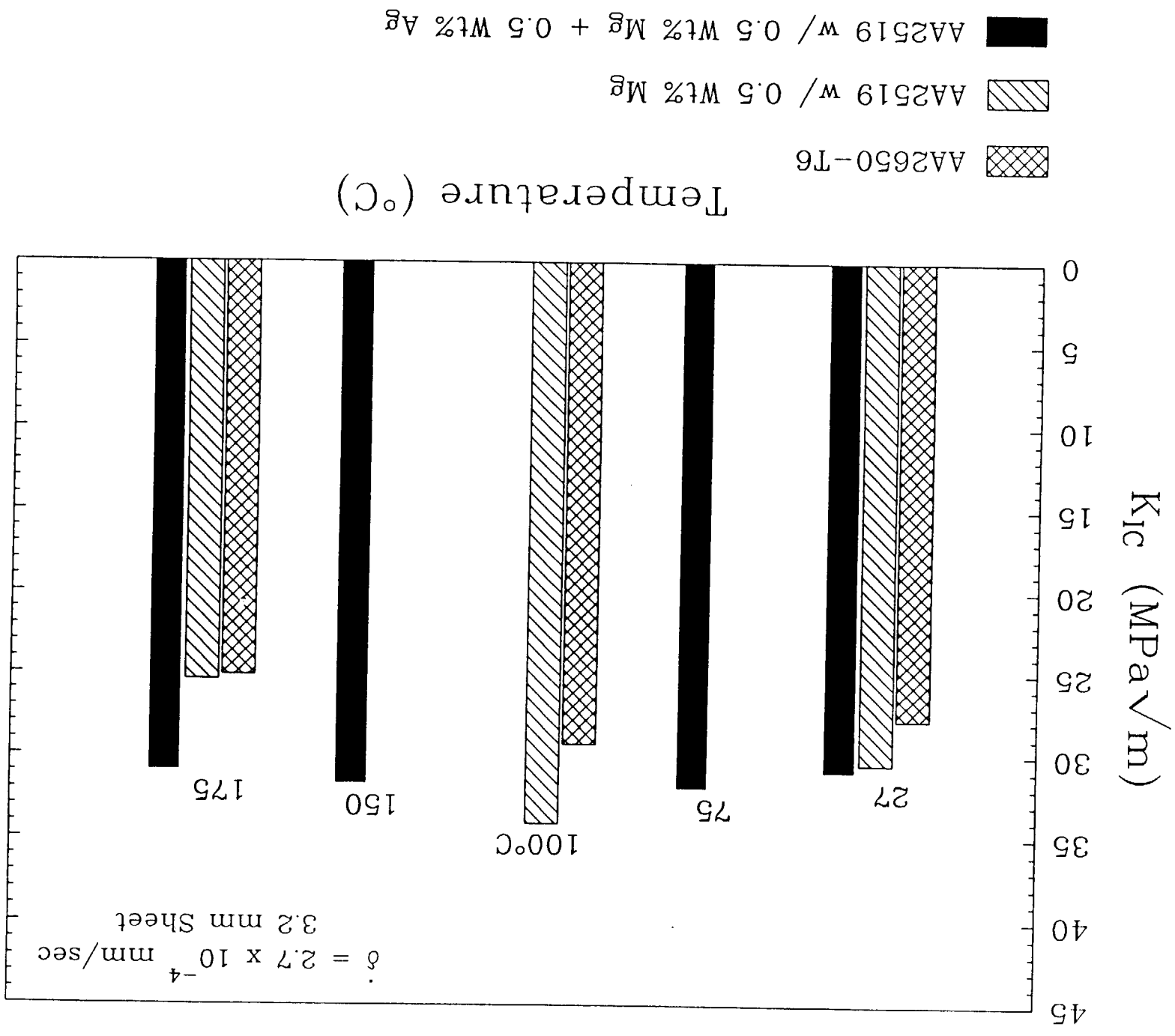
Low Magnification

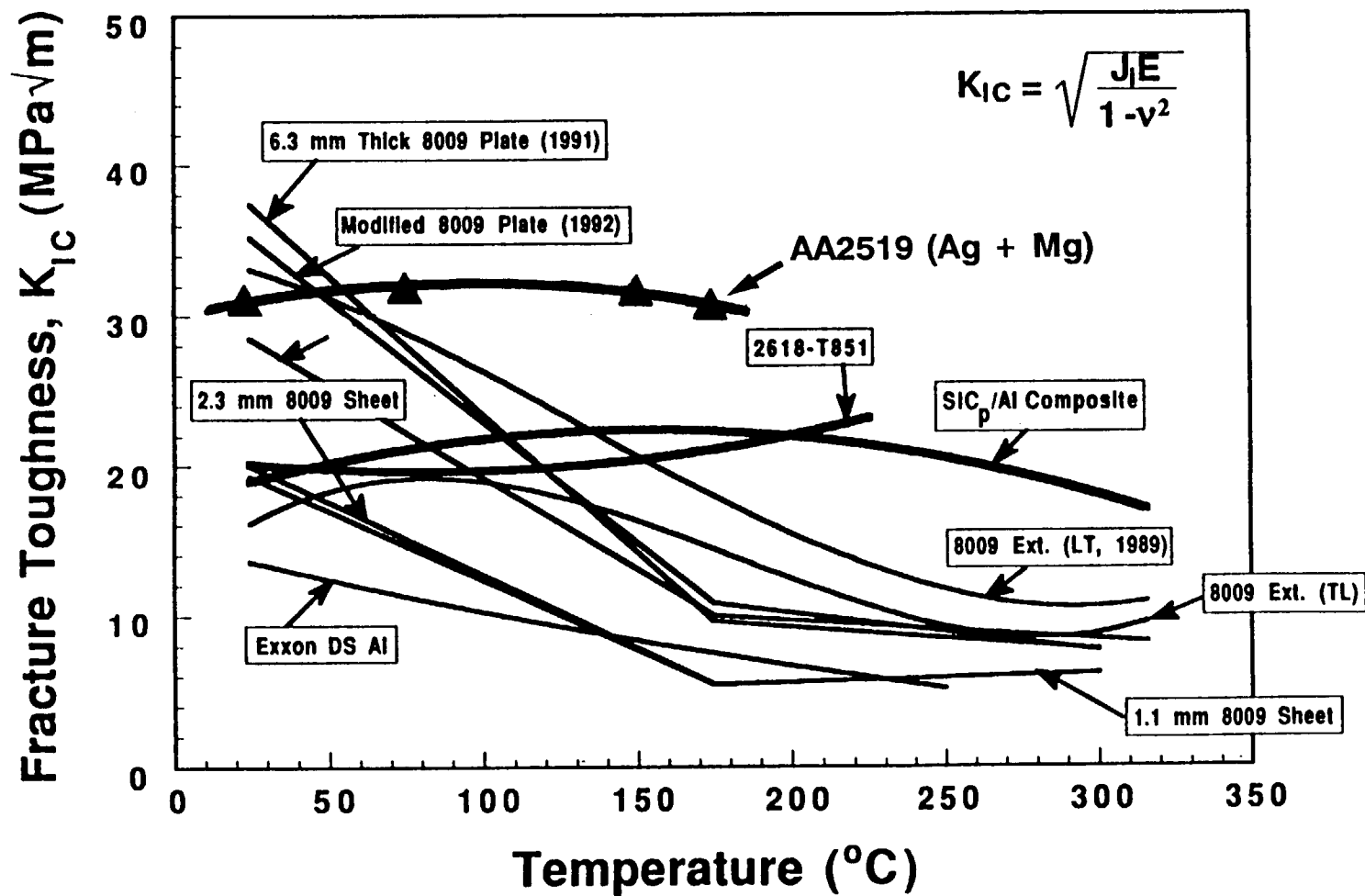


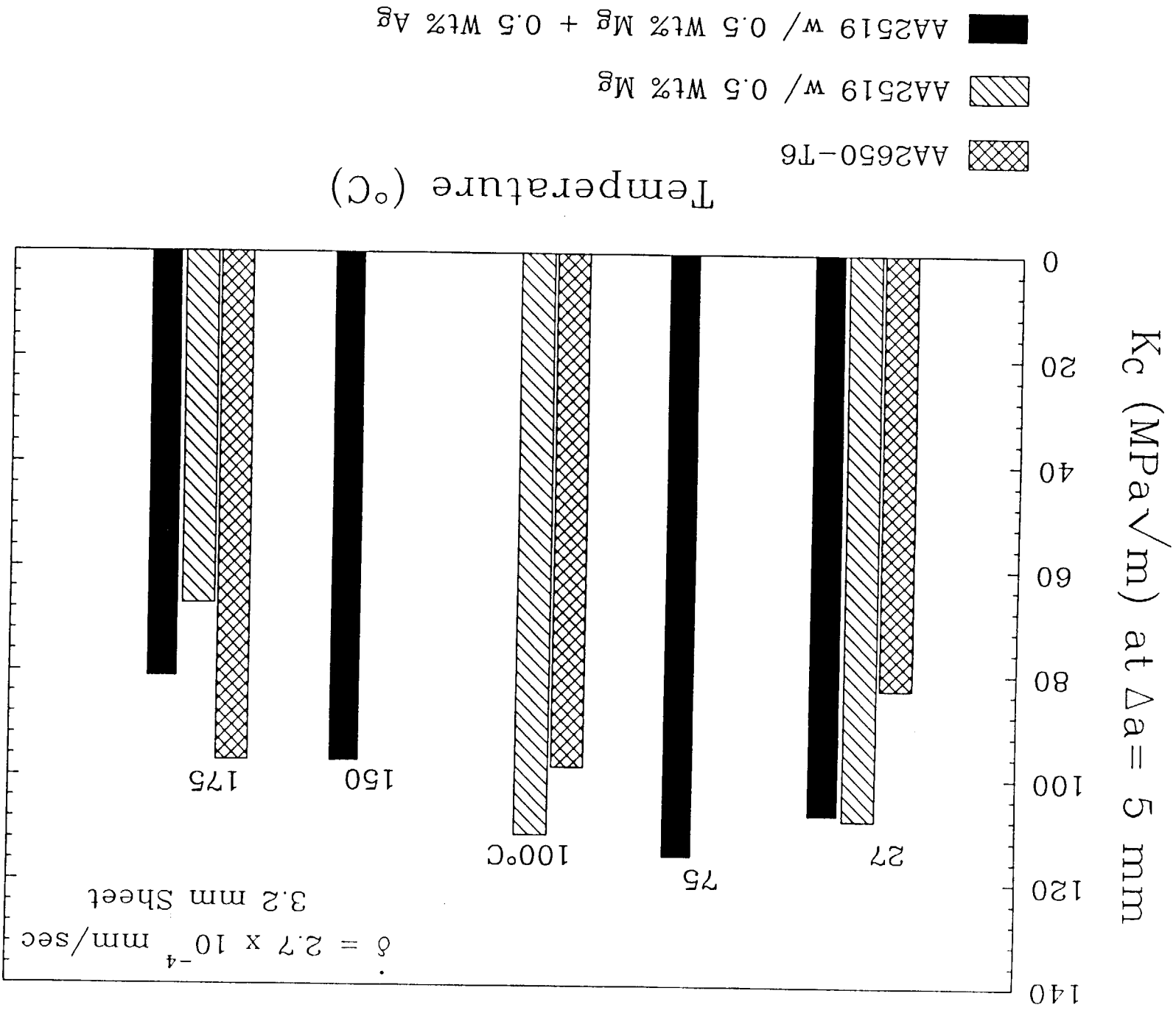
AA2519 w/ 0.5 Wt% Mg + 0.5 Wt% Ag



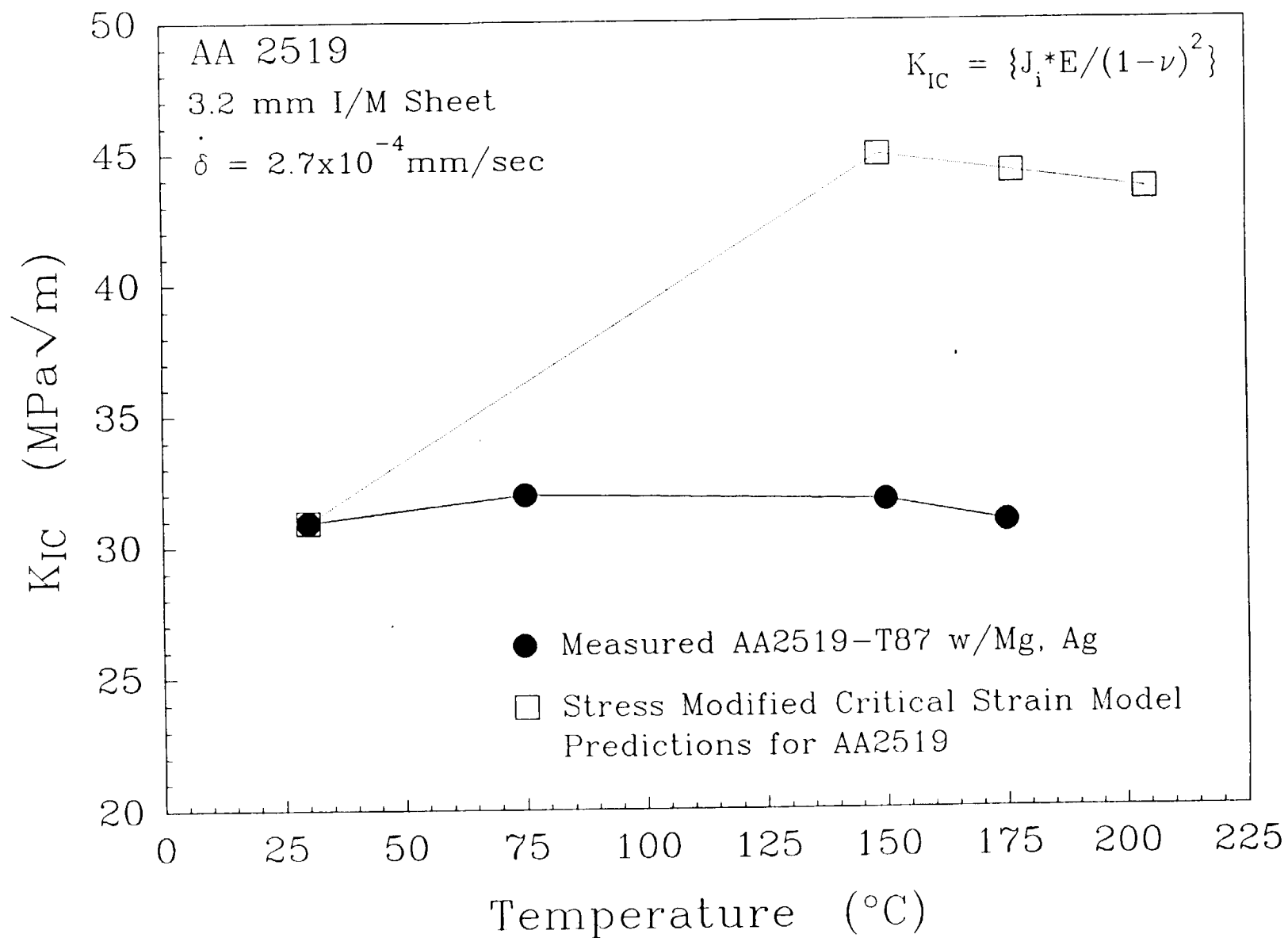






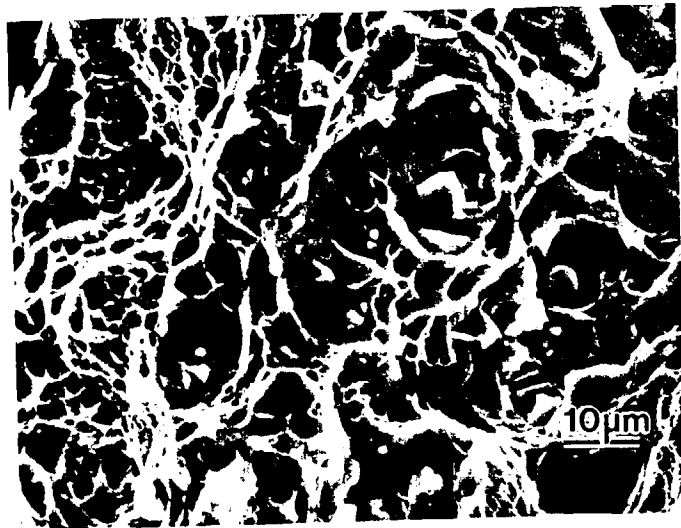




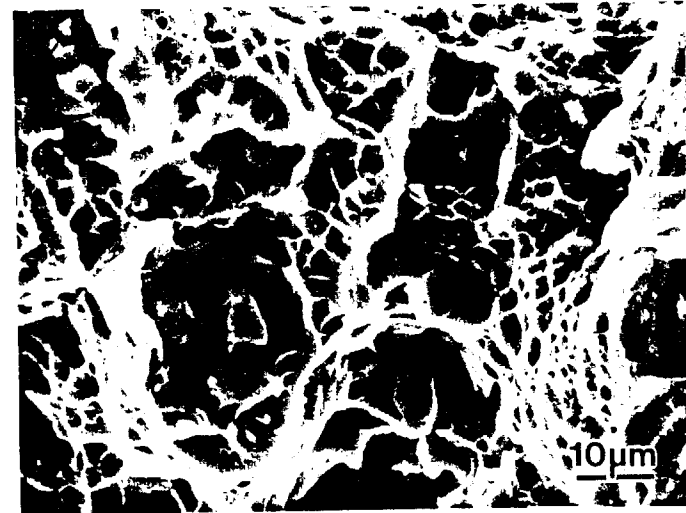




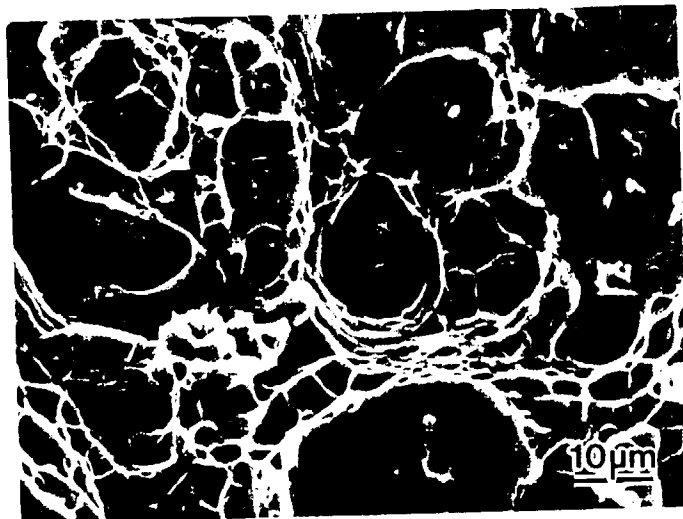
**AA2519 w/ 0.5 Wt% Mg + 0.5 Wt% Ag**  
**2.3 mm Sheet**



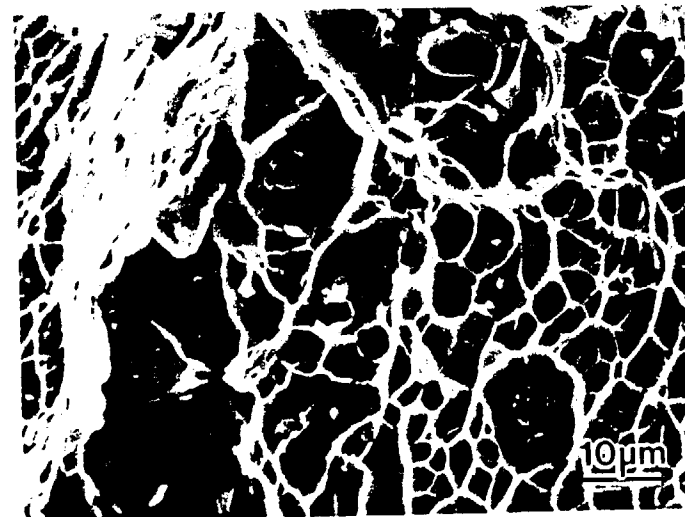
**30 °C**



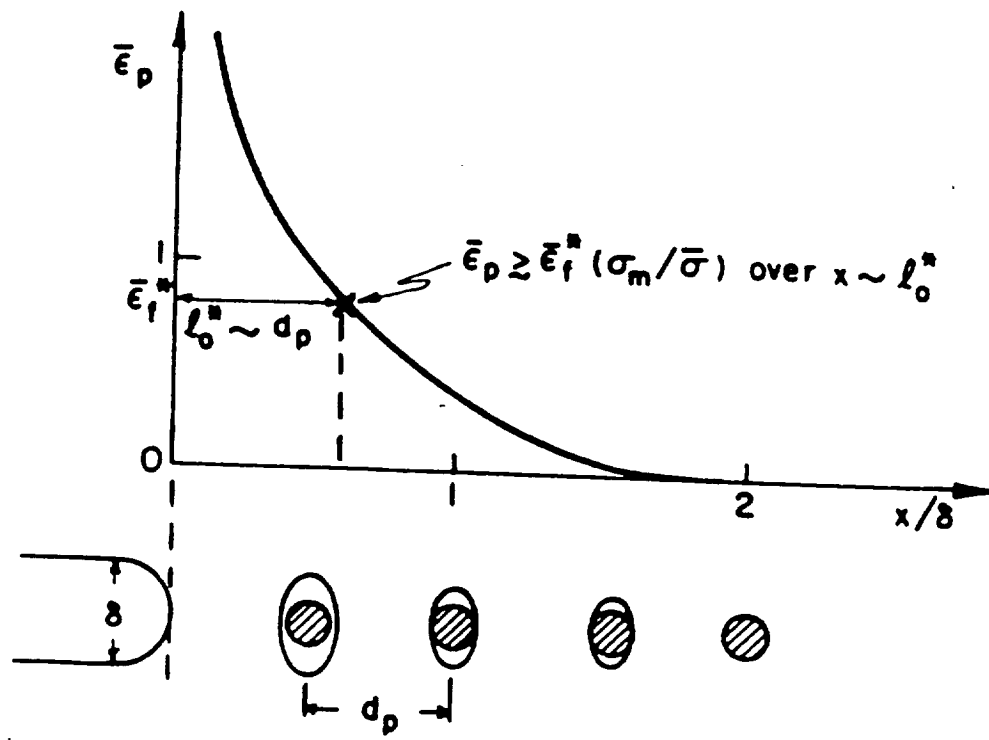
**75 °C**



**150 °C**



**175 °C**



Critical Plastic Strain-Controlled Model

$$K_{IC} \propto (l^* \sigma_{ys} E \bar{\epsilon}_F)^{1/2}$$

$$\bar{\epsilon}_F = (1/\gamma) \{-\ln (1 - RA)\}$$

## **Conclusions**

- **Modified AA2519 alloys show highest damage tolerance at 25 °C.**
- **At 175 °C, AA2650 exhibits superior damage tolerance.**
- **$\Omega$  phase strengthened AA2519 displays significantly higher initiation and crack growth toughnesses than  $\theta'$  strengthened AA2519 at 175°C.**
- **The fracture mechanism for all alloys at every temperature was microvoid coalescence for test times of 3 hrs.**
- **Fracture surfaces contain a duplex distribution of dimples; 10-30  $\mu\text{m}$  dimples associated with 5-10  $\mu\text{m}$  constituents and 1-5  $\mu\text{m}$  dimples possibly affiliated with dispersoids/precipitates.**
- **The smaller sized population of dimples increased in size as temperature increased, implying an augmented role of void sheeting in crack growth.**

## Future Work

- Perform slow strain rate tests at high temperatures to identify the role of time-temperature dependent "creep" crack growth in the fracture process
- Correlate the initial slope of the  $J-\Delta a$  curve to the plane strain-plane stress transition in fracture mode
- Perform notched bar and compression tests to model initiation and growth fracture toughnesses
- Characterize fracture toughness of AA2650 and AA2519 alloys at cryogenic temperatures

**Project #3      Cryogenic Temperature Effects on the Deformation and Fracture of Al-Li-Cu and Al-Li-Cu-In Alloys**

John A. Wagner and R.P. Gangloff

**Objective**

The objective of this PhD research is to characterize and optimize the crack initiation and growth fracture resistance of Al-Li-Cu (alloy 2090) and Al-Li-Cu-In (alloy 2090 + In) for cryogenic tank applications. The program aims to understand microscopic fracture events; as influenced by ambient to cryogenic temperatures, stress state and microstructure. A specific goal is to determine the mechanism of transgranular shear (TGS) fracture.

**Status**

Work in this project has been focusing on the details of the mechanisms associated with fracture of 2090 at ambient and cryogenic temperatures. Crack growth resistance was correlated with fracture and grain morphology under nominal plane stress and plain strain conditions for tests conducted at 25 and -185°C to define the physical basis for fracture. Relative grain orientation in the region of TGS fracture was investigated to gain insight about the underlying fracture mechanisms.

**Recent Results**

The 2090-T81 plate studied in this investigation exhibited four different fracture modes:

- High angle grain boundary delamination
- TGS fracture
- Intersubgranular (ISG) cracking
- Slip band cracking SBC)

Delaminations occur along high angle boundaries at both 25 and -185°C for 12.0 mm thick compact tension specimens in the LT orientation. At both temperatures there is a dual distribution of delamination depths. However, at -185°C there are fewer but deeper large

delaminations and more numerous small delaminations. The increased tendency for delamination fracture at  $-185^{\circ}\text{C}$  is attributed to increased through-thickness stresses and possibly to a change in the interaction of slip bands with grain boundaries at cryogenic temperatures.

TGS occurred between delaminations, traversing numerous grains of apparently different orientations as shown by backscattered electron (BSe<sup>-</sup>) and cross polarized light imaging techniques. The initiation of TGS fracture presumably occurred due to SBC. Localized SBC was more apparent at cryogenic temperatures.

In regions in which the subgrain boundaries were heavily decorated with precipitation, fracture was typically intersubgranular.

### Milestones

Future work will focus on completing the development of a physical model to describe the evolution of fracture in 2090-T81 at ambient and cryogenic temperatures.

### Presentation Viewgraphs

1. Title.
2. Problem statement and program objective.
3. Presentation outline.
4. The microstructure of the 2090-T81 19.0 mm plate is unrecrystallized with pancake-shaped grains elongated in the rolling direction. The 2090 + In-T6 also has an unrecrystallized microstructure, but with copious boundary and subgrain boundary precipitation.
5. Summary of the salient findings on the tensile and fracture behavior of 2090 + In-T6.
6. The primary focus for this reporting period is on 2090-T81. The microstructure about the midplane was investigated by electropolishing specimens and examining in the SEM under BSe<sup>-</sup> conditions.
7. Fracture toughness behavior of 2090-T81 was investigated using the J-Integral single specimen unloading compliance technique. This chart shows the results of specimens tested under primarily plane stress conditions with their corresponding full-thickness fracture cross sections. For the 1.6 mm specimens, there is a modest increase in the initiation and growth toughnesses,  $J_{Ic}$  and  $T_R$ , at  $-185^{\circ}\text{C}$ .



8. Similar to the results on 1.6 mm specimens, 12.0 mm specimens with side grooves exhibit an increase in initiation toughness and growth toughnesses at cryogenic temperatures. However, the magnitude in the increase of  $J_{Ic}$  and  $T_R$  for the 12.0 mm specimens from 25 to  $-185^{\circ}\text{C}$  was significantly greater compared to 1.6 mm specimens.
9. To compare the fracture stress of grain boundaries, subsized tensile specimens were tested in the ST orientation. Results indicate that the strength of the boundaries does not decrease at  $-185^{\circ}\text{C}$ , but actually increases slightly.
10. Fracture in 2090-T81 exhibits four dominant fracture modes:
  - Delamination
  - Transgranular shear (TGS) fracture
  - Intersubgranular (ISG) fracture
  - Slip band cracking (SBC)

This chart shows delaminations along with TGS fracture in matched pairs of SEM fractographs together with the corresponding etched cross sections of the grain structure. In the location marked A is a small delamination with shear fracture across two grains. Location B is also a region of TGS fracture which shows that the shear fracture can propagate across several grains before arresting.

11. To qualitatively examine the orientation of grains in the region of fracture where TGS was the dominate fracture mode, cross sections of 12.0 mm specimens tested at  $25^{\circ}\text{C}$  were electroetched and examined in cross polarized light or electropolished and examined in the SEM BSe- mode. The figure shows that in the region of TGS fracture several grains of apparently differing orientation have been traversed by a shear crack.
12. Electron Back Scattering Pattern analysis of grain orientation has been used previously to study 2090-T81 plate. This is a result from the work by Slavik on a different lot of 19.0 mm plate, nominally processed in the same manner as the material in the current investigation. The chart is the intersection of a fatigue fracture surface with the grain structure and shows the large orientation difference between grains.
13. Fracture in areas which had a well defined substructure, in general, was characterized by ISG fracture. On the right side of cross sections in the figure is a region where fracture has been confined to a single grain in which the subboundaries are, in comparison, not decorated.
14. At  $-185^{\circ}\text{C}$ , the yield strength of 2090-T81 is elevated and results in an increase in the through-thickness stresses. Higher stresses build up at grain boundaries and result in more numerous grain boundary delaminations at cryogenic temperatures.
15. To study the progression of fracture in alloy 2090-T81 at  $-185^{\circ}\text{C}$ , notched tensile specimens were tested in the longitudinal direction. Specimens were loaded close to the failure load and then sectioned at the midplane for examination.

16. These are sectioned notched tensile optical and BSe<sup>-</sup> images. The bottom three photomicrographs are of the smaller crack which is more centrally located. The crack tends to primarily follow grain boundaries typical of delamination fracture.
17. More insight into the progression of fracture was obtained by examining the cross section of specimens tested to failure. The bottom left photomicrograph shows two delamination cracks along boundaries being linked up by a shear crack similar to what was observed in fracture toughness specimens. The photomicrograph on the right shows cracking along decorated substructure.
18. Individual fracture toughness tests were conducted at intermediate temperatures between 25 and 185°C. The largest increase in toughness, as suggested by the R-curve behavior occurs between -155 and -185°C.
19.  $K_{Ic}$  values calculated from  $J_{Ic}$  values plotted against temperature again show the largest increase in toughness at -185°C.
20. The tearing resistance which is related to the slope of the R-curve in the region of stable crack growth is plotted against temperature in this chart. There is a more gradual increase in the tearing modulus with decreasing temperature compared to the initiation toughness.
21. Summary.

**FRACTURE OF Al-Li ALLOYS  
2090 AND 2090+In AT  
CRYOGENIC TEMPERATURES**

**John A. Wagner  
LA<sup>2</sup>ST Program Review  
NASA Langley Research Center  
July 20-21, 1993**

# **FRACTURE OF 2090 AND 2090+In ALLOYS**

## **Problem**

- No systematic investigation conducted to determine the interactive effects of:
  - Temperature
  - Delamination
  - Indium addition
  - Microstructure

on the fracture of 2090-based alloys

## **Objective**

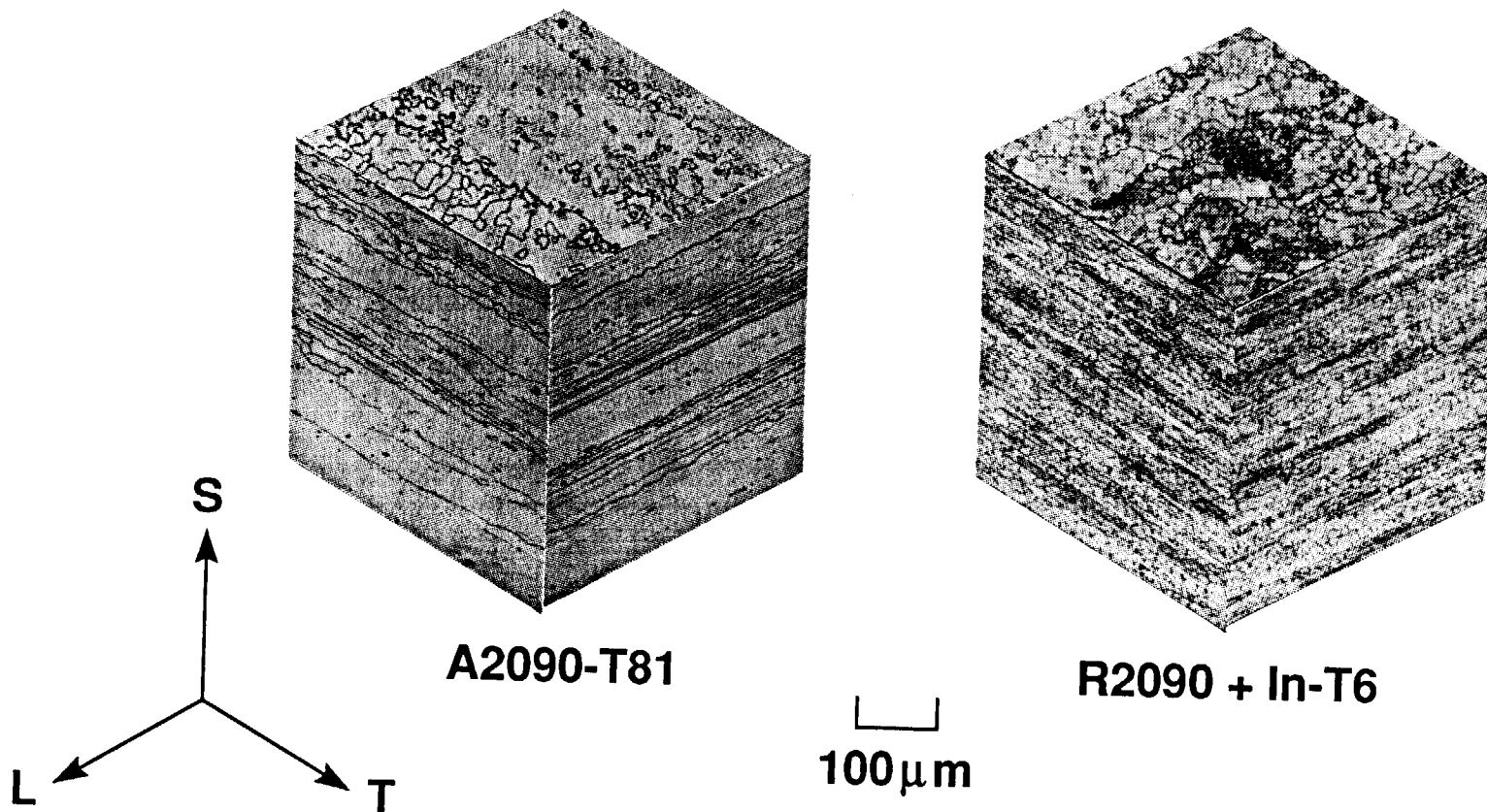
- Determine the influences of microstructure, stress state and temperature on the occurrence of various fracture modes in Al-Li-Cu-X alloys. Understand the mechanism(s) associated with transgranular shear fracture

# **FRACTURE OF 2090 AND 2090+In ALLOYS AT CRYOGENIC TEMPERATURES**

## **Outline**

- **Summary of tensile and fracture properties of 2090+In-T6**
- **Correlation of structure/property/fracture morphology of 2090-T81**
- **Intermediate temperature tests**
- **Future direction**

# MICROSTRUCTURES OF PLATE ALLOYS

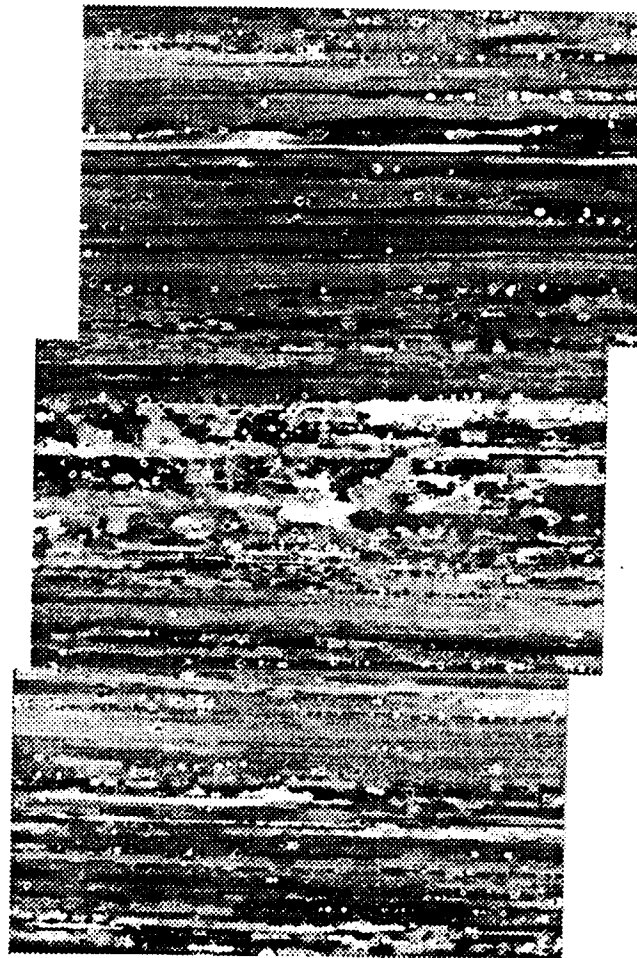


# **TENSILE AND FRACTURE BEHAVIOR OF 2090+In-T6**

## **Summary**

- Indium additions to 2090-based alloys increase  $T_1$  number density with no change in yield strength
- Toughness of 2090+In-T6 at ambient and cryogenic is low and characterized by intersubgranular fracture
- Delamination fracture occurs at cryogenic temperature for plane strain case, but does not change the fracture toughness
- Thermal treatments employed to increase toughness of 2090+In-T6 were unsuccessful

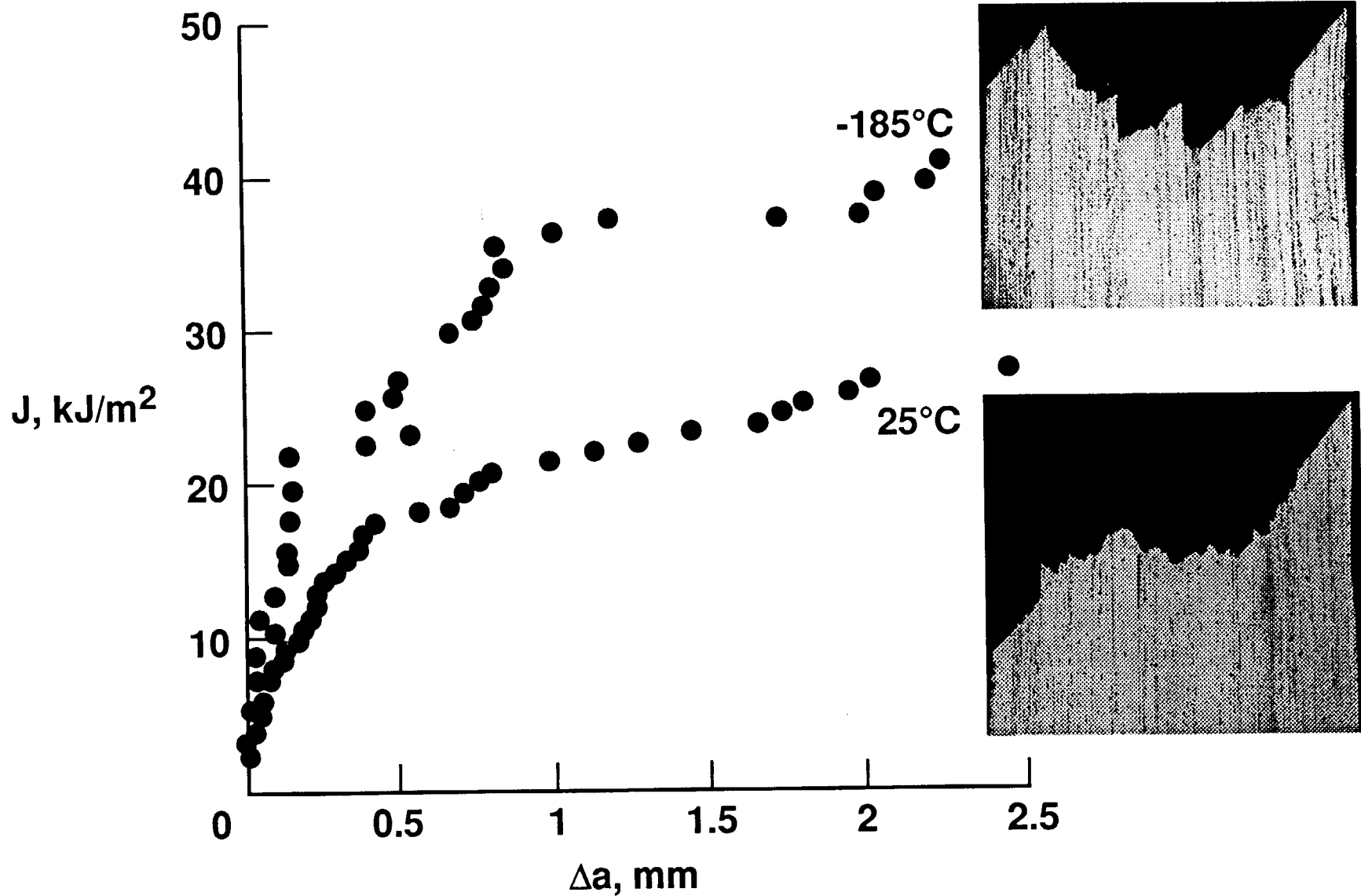
# THROUGH THICKNESS GRAIN STRUCTURE OF 2090-T81



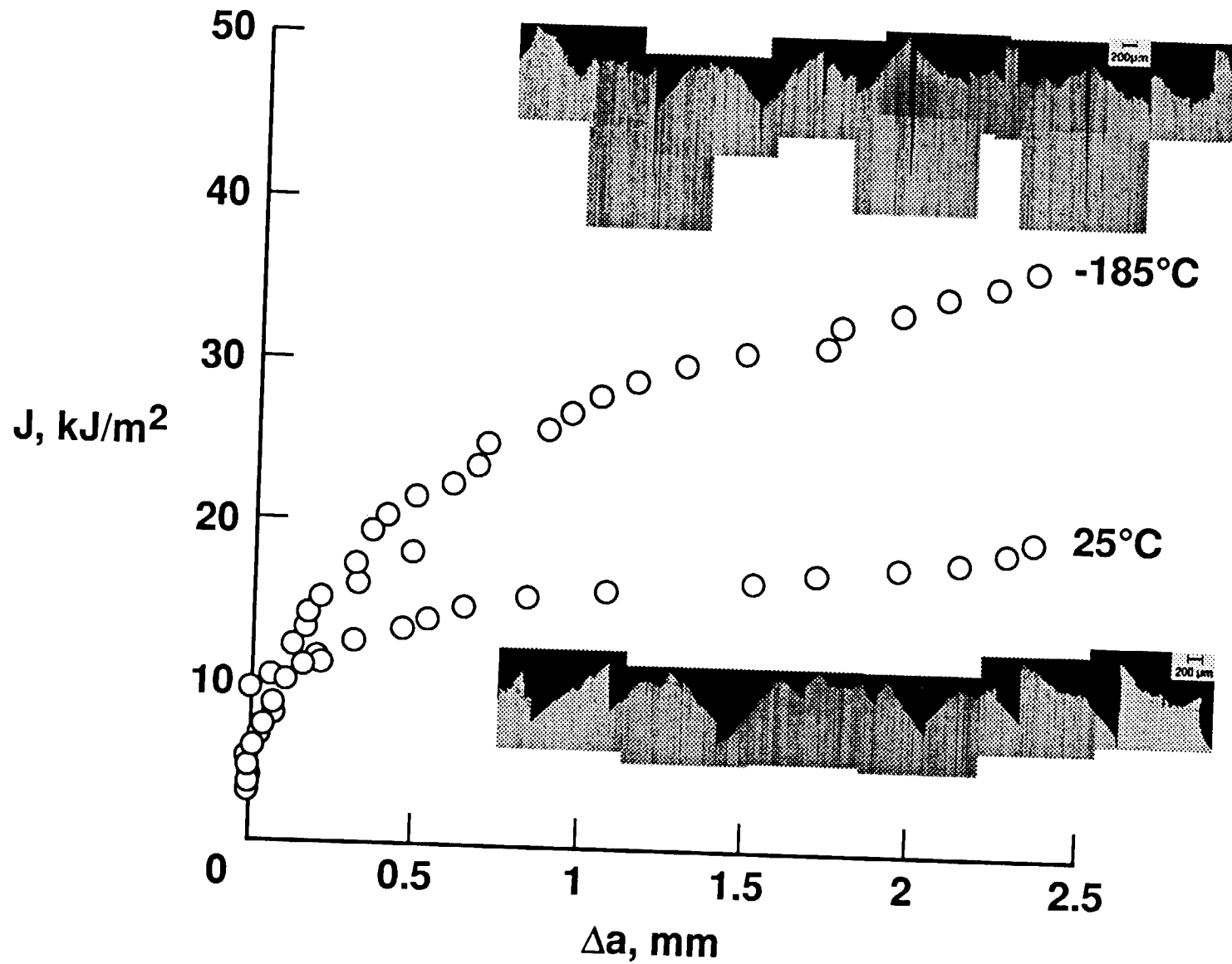
100μm



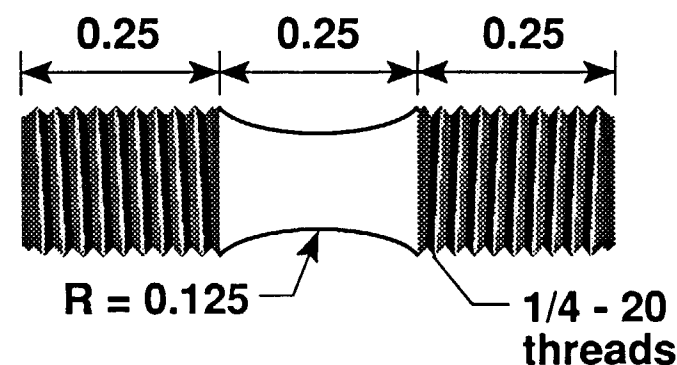
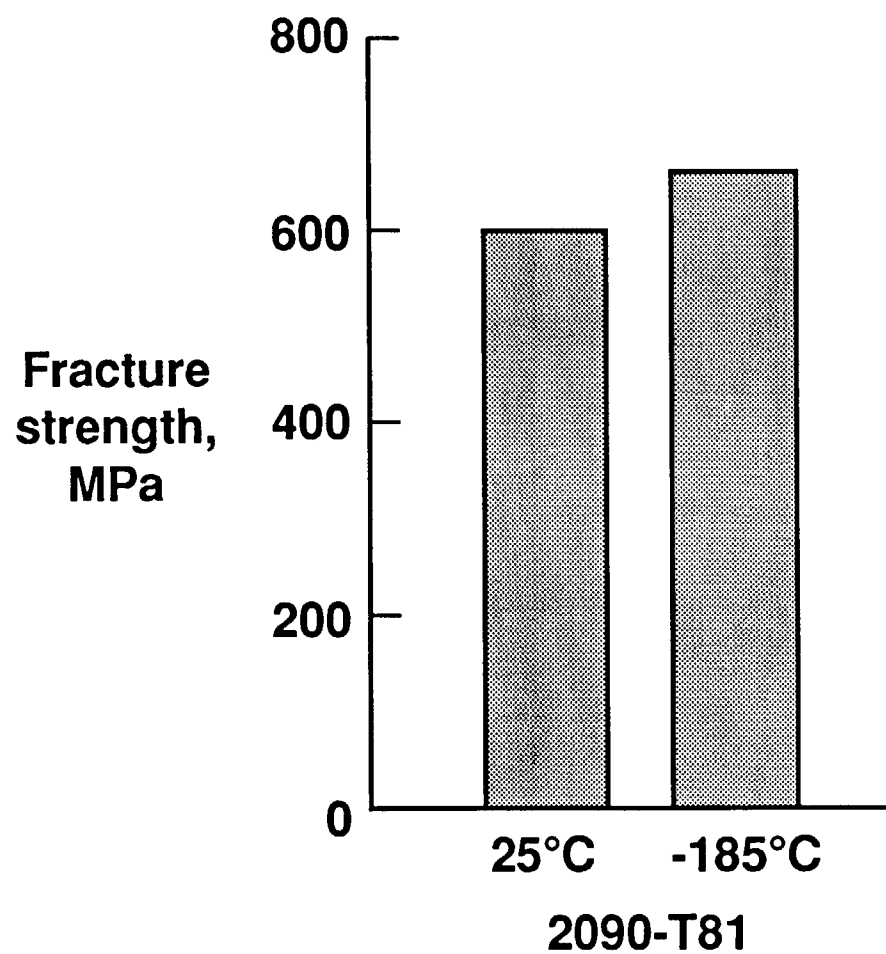
# R-CURVES FOR 1.6MM 2090-T81 SPECIMENS TESTED AT 25°C AND -185°C



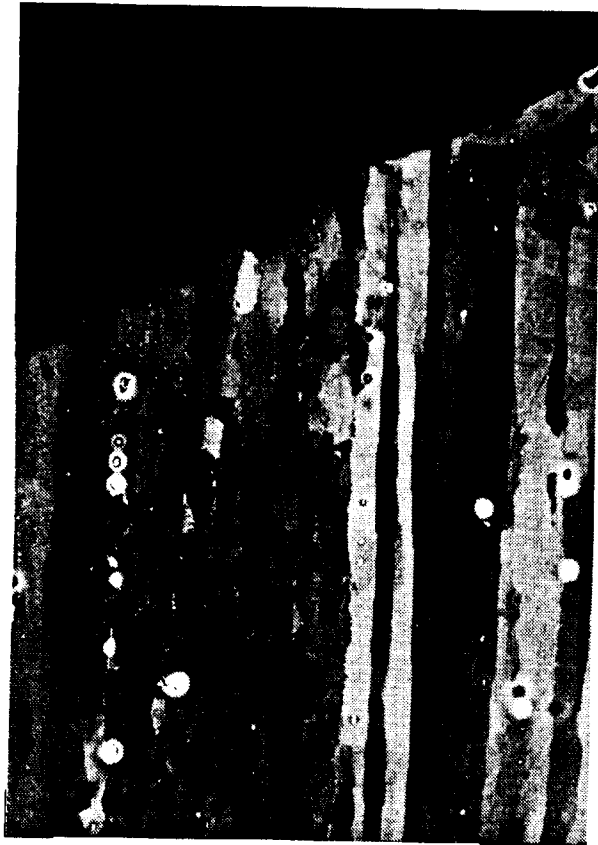
# R-CURVES FOR 12MM 2090-T81 SPECIMENS TESTED AT 25°C AND -185°C



# SHORT TRANSVERSE TENSILE PROPERTIES OF 2090 AT 25° AND -185°C



# **CROSS SECTIONS OF TRANSGRANULAR SHEAR FRACTURE REGION IN 2090-T81**



20 $\mu$ m

**Backscattered  
electron image**

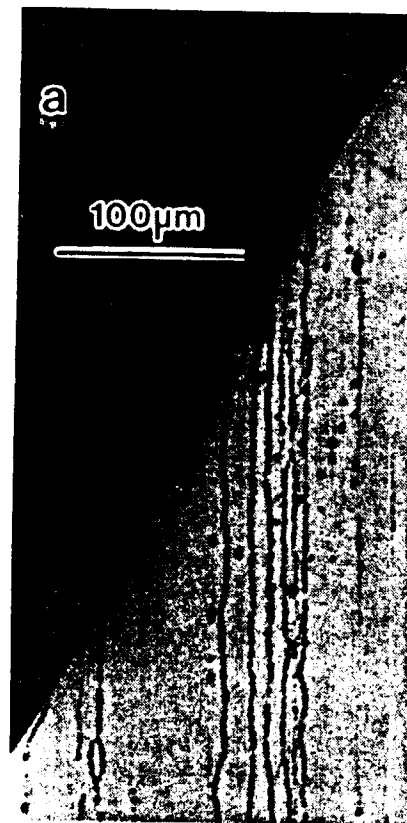


10 $\mu$ m

**Cross polarized light image**

Figure 5

# ETCHED GRAIN BOUNDARY MISORIENTATIONS IN 2090-T81 FROM SLAVIK



59° 29° 44°  
57° 43°

# INTERSUBGRANULAR FRACTURE AND AND SLIP BAND CRACKING 2090-T81

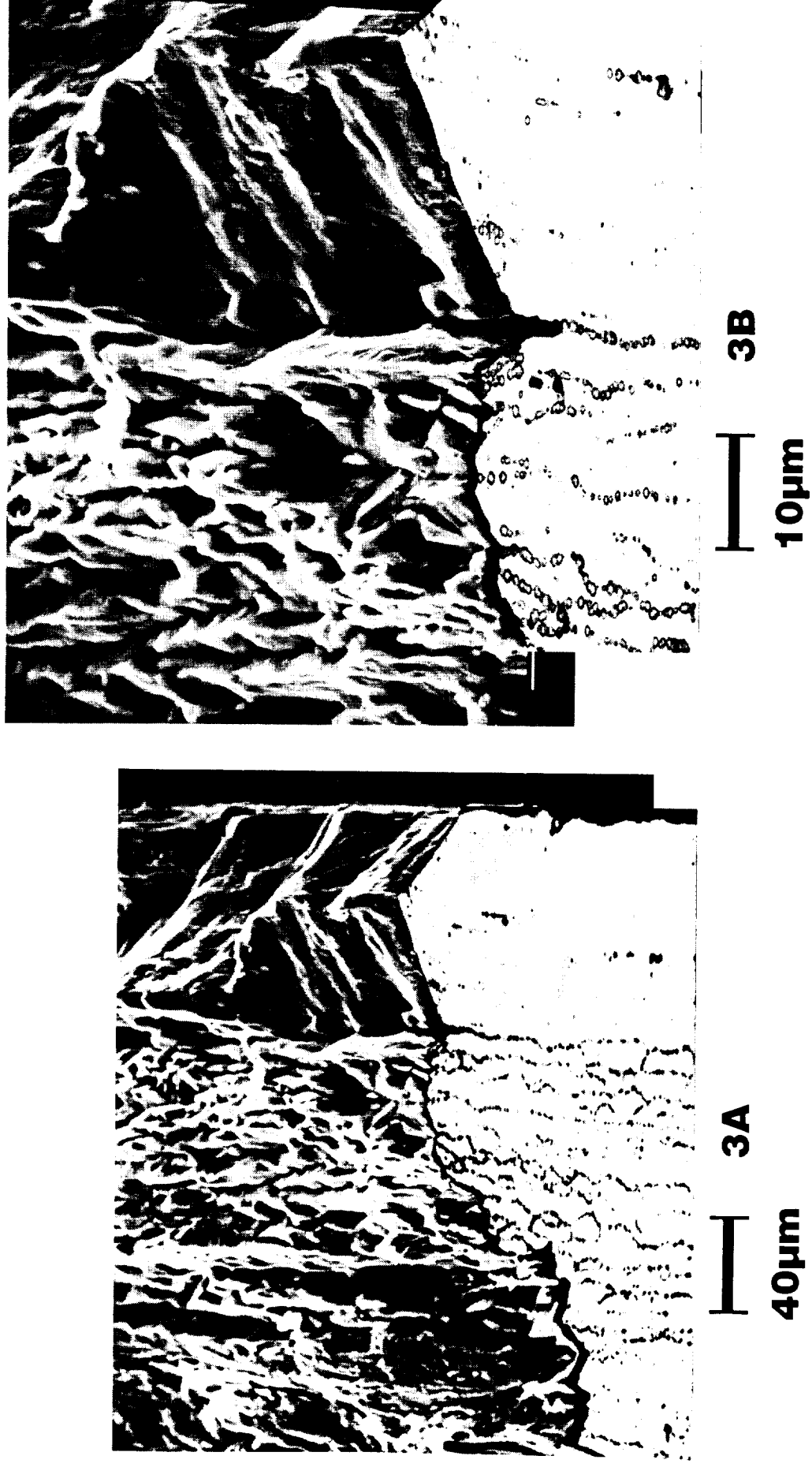
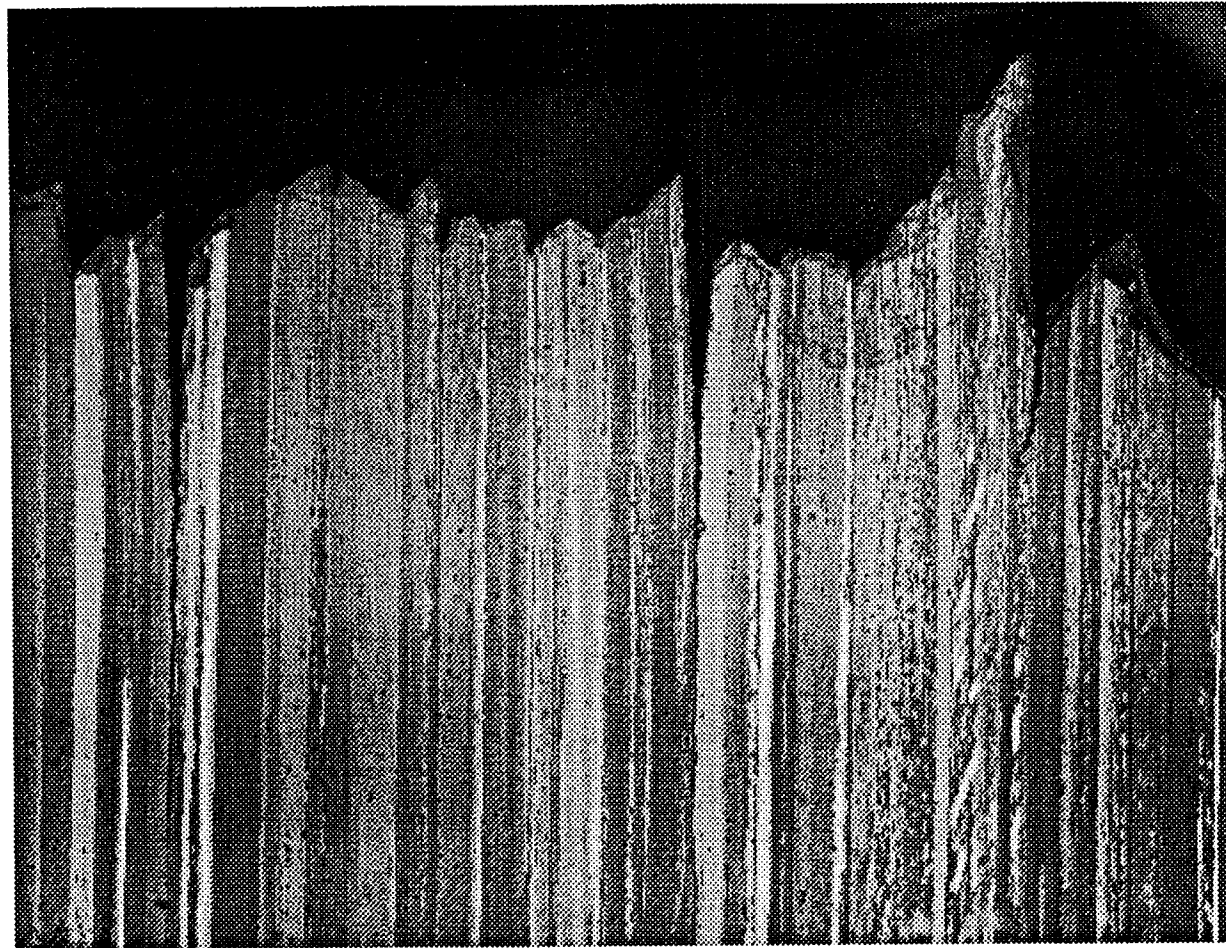


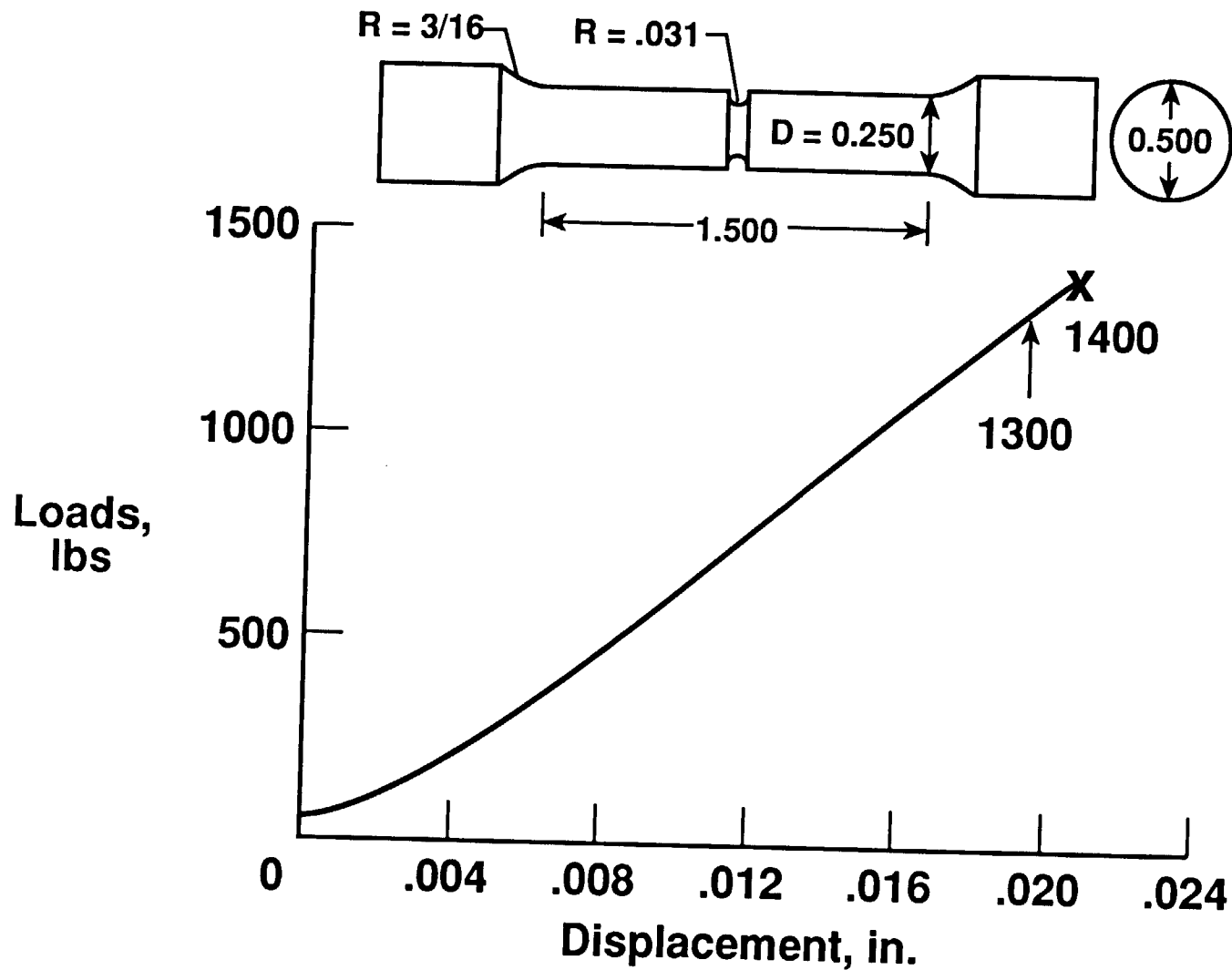
Figure 3

**FRACTURE CROSS SECTION  
OF 2090-T81 TESTED AT -185°C,  
CROSS POLARIZED LIGHT IMAGE**



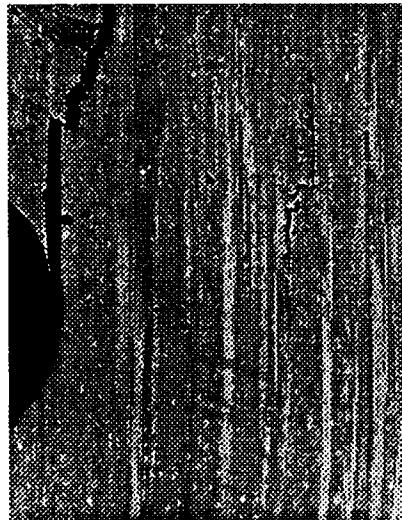
400μm

# NOTCHED TENSILE SPECIMEN AND TYPICAL LOAD-DISPLACEMENT PLOT





# OPTICAL AND BACK SCATTERED IMAGES OF THE MIDPLANE OF INTERRUPTED NOTCH TENSILE TEST AT -185°C



400μm

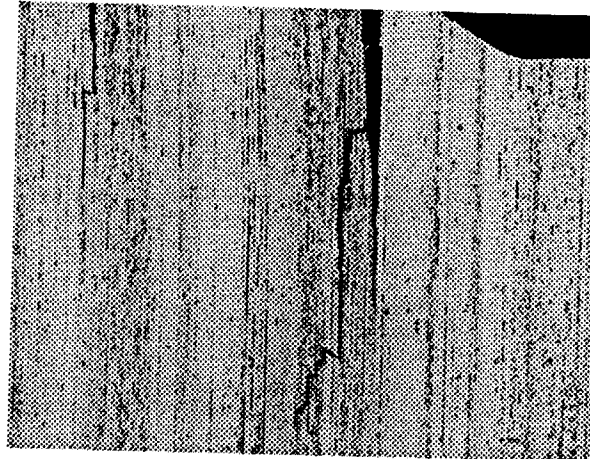


200μm

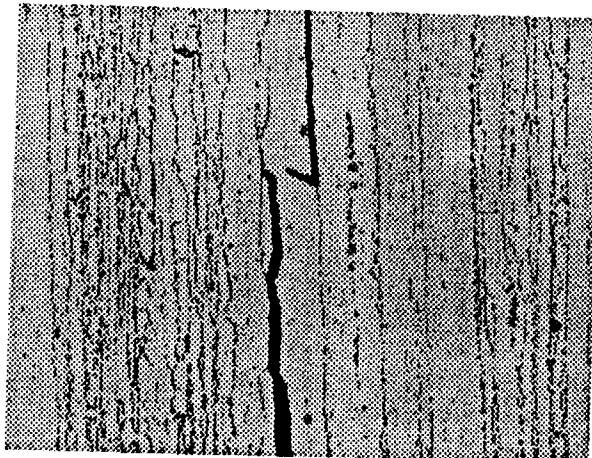


10μm

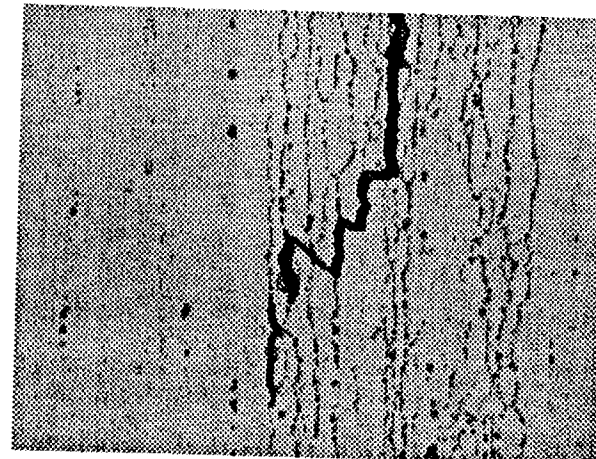
# **CROSS SECTION OF NOTCHED TENSILE SPECIMEN TESTED TO FAILURE AT -185°C**



200μm

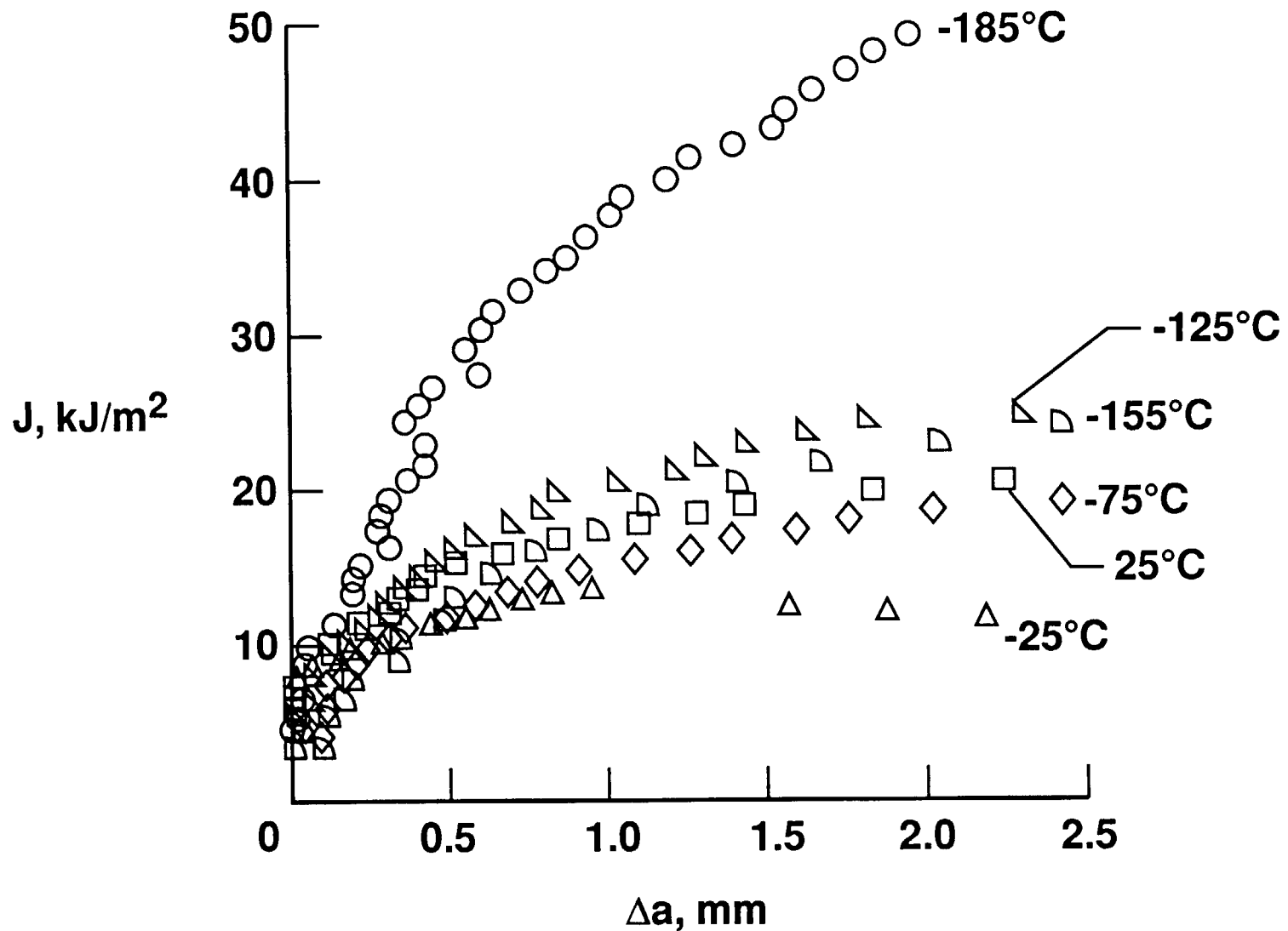


50μm

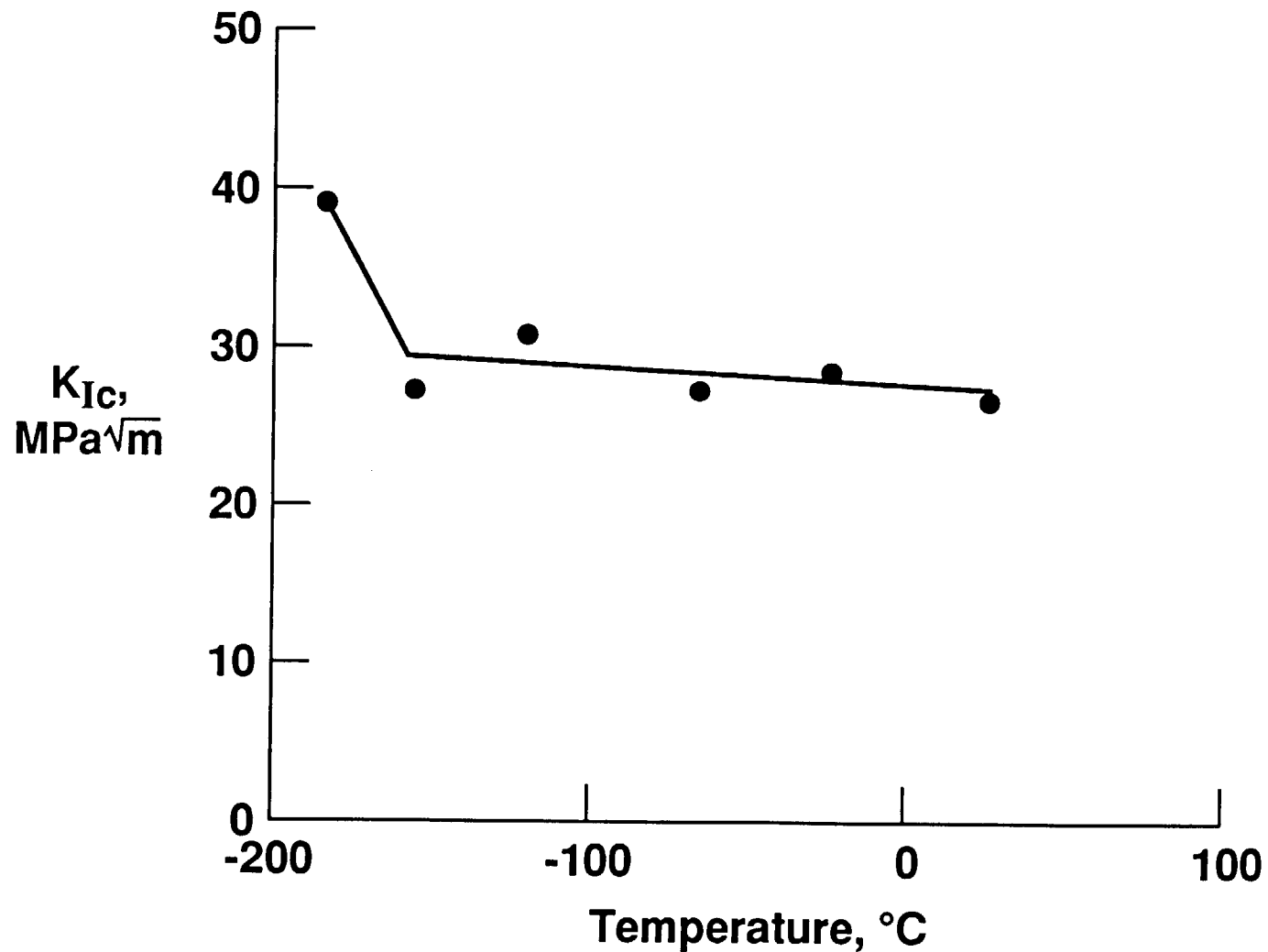


20μm

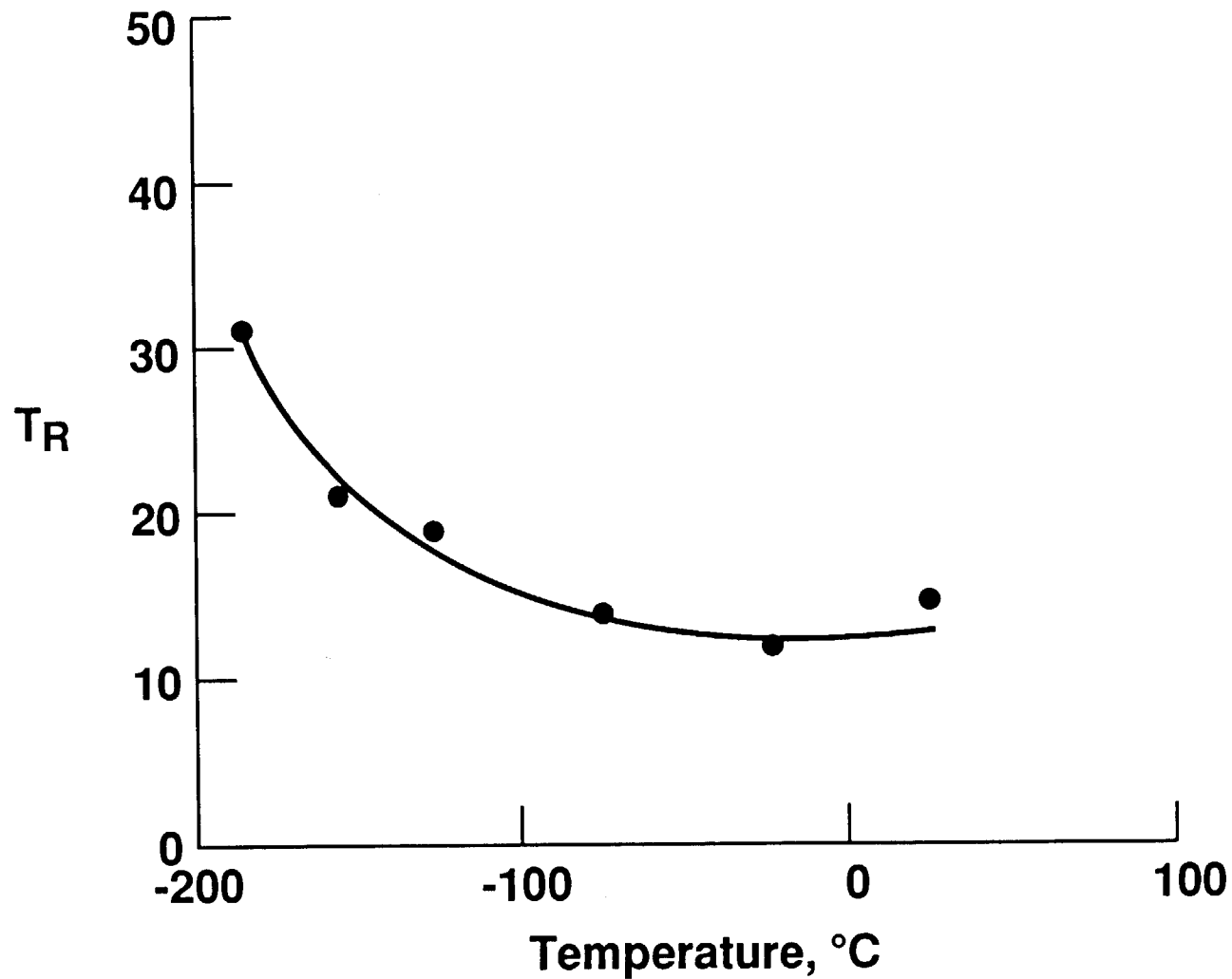
# R-CURVES OF 12MM THICK SPECIMENS AT -185°C TO 25°C



# **FRACTURE TOUGHNESS, $K_{Ic}$ , OF 12MM THICK 2090-T81 AS A FUNCTION OF TEMPERATURE**



# TEAR RESISTANCE OF 12MM THICK 2090-T81 AS A FUNCTION OF TEMPERATURE



# **FRACTURE OF 2090-T81 AT CRYOGENIC TEMPERATURES**

## **Summary**

- **Fracture in 2090-T81 is characterized by four fracture modes:**
  - Intersubgranular
  - Slip band cracking
  - Delamination
  - Transgranular shear
- **For a given thickness, the difference in toughness from 25° to -185°C is related to a change in fracture mode**
- **All 2090-T81 specimens exhibit an increase in toughness at -185°C and is primarily associated with an increase in the level of delamination**
- **Transgranular shear fracture across multiple grains of different orientations suggests a macroscopic shearing event and not cooperative slip band cracking**

# **TRANSGRANULAR SHEAR FRACTURE IN 2090-T81 AT -185°C**

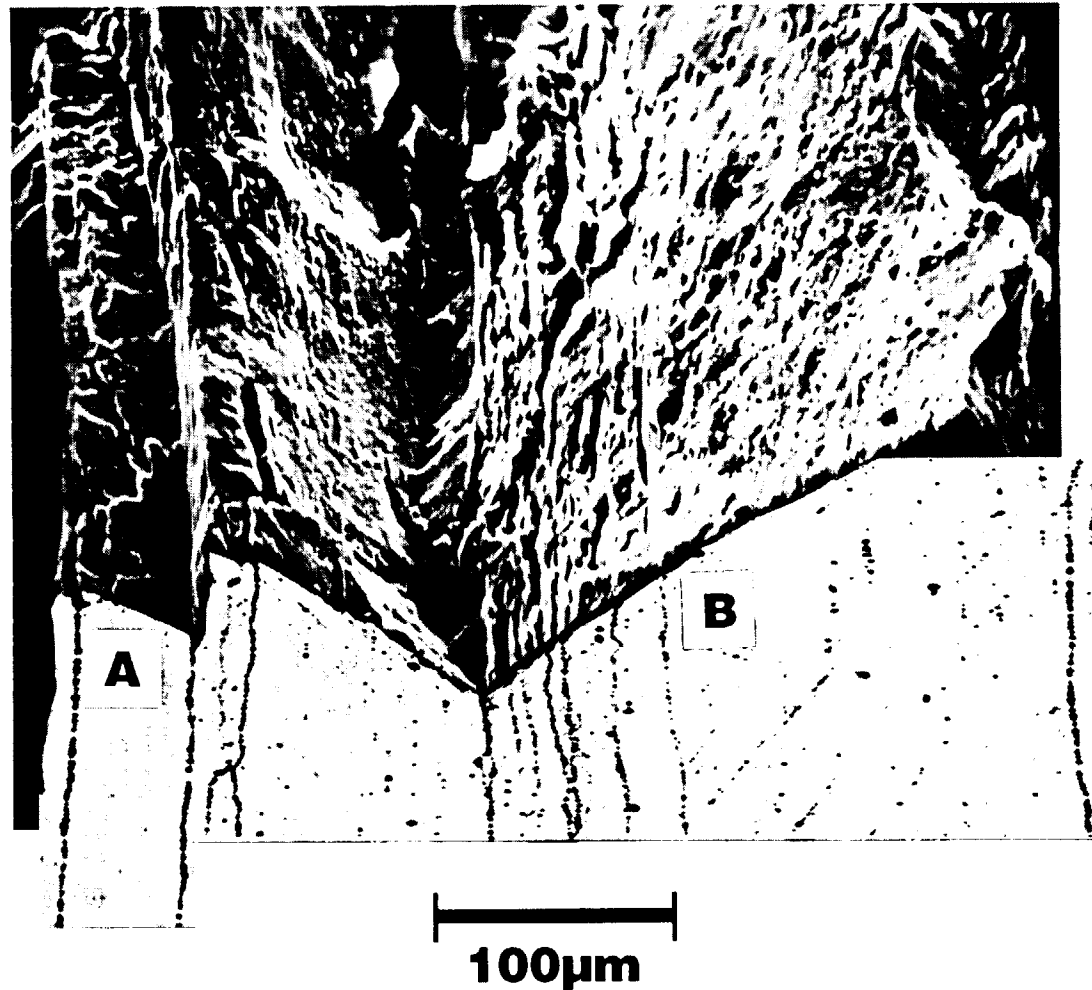


Figure 4





**Project #4     The Effect of Cryogenic Temperature on the Fracture Toughness of Weldalite™ X2095**

Cynthia L. Lach and Richard P. Gangloff

**Objective**

The objective of this research is to characterize the effect of cryogenic to mildly elevated temperature on the tensile fracture toughness of an emerging composition of Weldalite™-type alloys. We will determine quantitative initiation and growth fracture toughness data, and associated microscopic fracture mechanisms.

**Current Status**

The graduate student was on leave during this reporting period and there has been no progress since the July to December of 1992 report. The student recently returned to work at LaRC and resumed experiments on the temperature dependence of the fracture toughness of two compositions of Weldalite™ alloy X2095.



## Project #5     **Mechanisms of Localized Corrosion in Alloys 2090 and X2095**

F. Douglas Wall and Glenn E. Stoner

### Objective

The overall goal of this research project is to determine the roles of microstructure and electrochemistry in the failure of advanced Al-Cu-Li alloys.

### Current Status

At present, the project is focussed on examining the development of solution chemistry in the localized corrosion of Al-Cu-Li alloys and the resulting electrochemical interactions between a Cu-depleted region and the matrix alloy material.

### Recent Findings

To date experiments have been performed which suggest environmental conditions may exist which result in the failure of Al-Li-Cu alloys due to the anodic dissolution of an active path likely defined by the presence of a Cu-depleted zone. Scratching electrode experiments in two environments (NaCl/Na<sub>2</sub>CrO<sub>4</sub>, NaCl/Li<sub>2</sub>CO<sub>3</sub>) have shown that there is a significant difference between the potentials at which spontaneous repassivation is observed for the matrix phase and a copper depleted zone (modelled by 99.99 Al). Straining electrode experiments support these data. Heat-treated Al-Li-Cu alloys display rapid environmental fracture when held at constant load and polarized between the repassivation potentials for the matrix and Cu-depleted zone. Furthermore, in the carbonate environment the open circuit potential for both 2095 and 2090 lies within the potential window of susceptibility. Electrochemical testing has been initiated with Al-Cu binaries which shows that the critical repassivation potential increases with copper content. A similar increase in critical potential is observed as the aging time for Al-Li-Cu alloys is increased.

The role for a Cu-depleted region outlined above is strongly dependent on the environment that develops in an occluded cell. An alkaline 0.6M NaCl + 0.1M Li<sub>2</sub>CO<sub>3</sub> environment has been used thus far as a crude estimation of a possible chemistry. To validate this choice and/or determine a better candidate, solution analysis has been performed to determine the lithium ion concentration and pH that develop when a large area of material

is exposed to a small volume of aqueous NaCl solution. Several configurations of experiments have shown that an alkaline chemistry develops and that lithium ions become detectable within a short (less than one day) exposure period. The analysis to determine ion concentrations has been performed using capillary electrophoresis.

The combination of electrochemical and chemical information that has been acquired suggests that local chemistries can develop which lead to the preferential dissolution of a Cu depleted zone. This mechanism is being evaluated as a possible cause of environmental fracture for Al-Li-Cu alloys. Although recent work has focussed on the Cu-depleted region, the highly active  $T_1$  phase has not been discounted as a primary contribution to the anodic dissolution processes.

#### Future Work

- (1) Continue to evaluate the solution chemistries that develop in occluded environments.
- (2) Complete the characterization of the Al-Cu binaries in several environments to more clearly describe the effects of the Cu additions.
- (3) Use electrochemical impedance spectroscopy to determine if a significant change in polarization resistance can be linked to a specific  $Li_2CO_3$  concentration.
- (4) Rank various alloys and tempers according to crack growth kinetics by performing in-situ rising and static K tests on compact tension samples. If the growth rates are distinguishable it may be possible to find a correlation with a microstructural feature.

#### Presentation Slides

**Mechanisms of Localized Corrosion  
in Alloys 2090 and 2095**

**F. D. Wall  
G. E. Stoner**

**Department of Materials Science and Engineering  
University of Virginia  
Charlottesville, Virginia 22901**

**NASA - LaRC Contact : Marsha Domac**

**Co-sponsor : Reynolds Metals Corporation  
Technical Contact : Alex Cho**

## **OUTLINE OF PRESENTATION**

- I. Objectives**
- II. Materials**
- III. Electrochemical Characterization and Environmental Fracture**
- IV. Occluded Chemistry Analysis**
- V. Future work**

## **OBJECTIVES**

**Overall:** Determine the roles of microstructure and environment in the SCC behavior of aluminum-lithium-copper alloys.

**Recent:** Examine the possible role of a Cu-depleted zone in the SCC behavior of 2095 and 2090.

Begin to determine the occluded environment that develops during localized corrosion of the research materials.

**Future:** Tie together the electrochemical and chemical analysis with microstructure and crack growth rate information.

## **MATERIALS UNDER INVESTIGATION**

### **Primary Al-Li-Cu alloys**

**2095      composition : Al-4 Cu-1 Li-0.25 Mg-0.25 Ag**  
**tempers        : 20 hrs at 290°F, 36 hrs at 290°F**

**2090      composition : Al-2 Li-2.5 Cu**  
**temper         : T8**

### **Other materials**

**2124, 7075, 99.99 Al, Al-0.1 Cu, Al-0.98 Cu, Al-3.96 Cu**



## **ELECTROCHEMICAL CHARACTERIZATION AND ENVIRONMENTAL FRACTURE**

**Determine the electrochemical behavior of microstructural features and of the bulk alloy.**

- \* Potentiodynamic polarization**
- \* Scratching electrode experiments**
- \* Straining electrode experiments**

**Determine the combined effects of load, potential and environment on the alloys.**

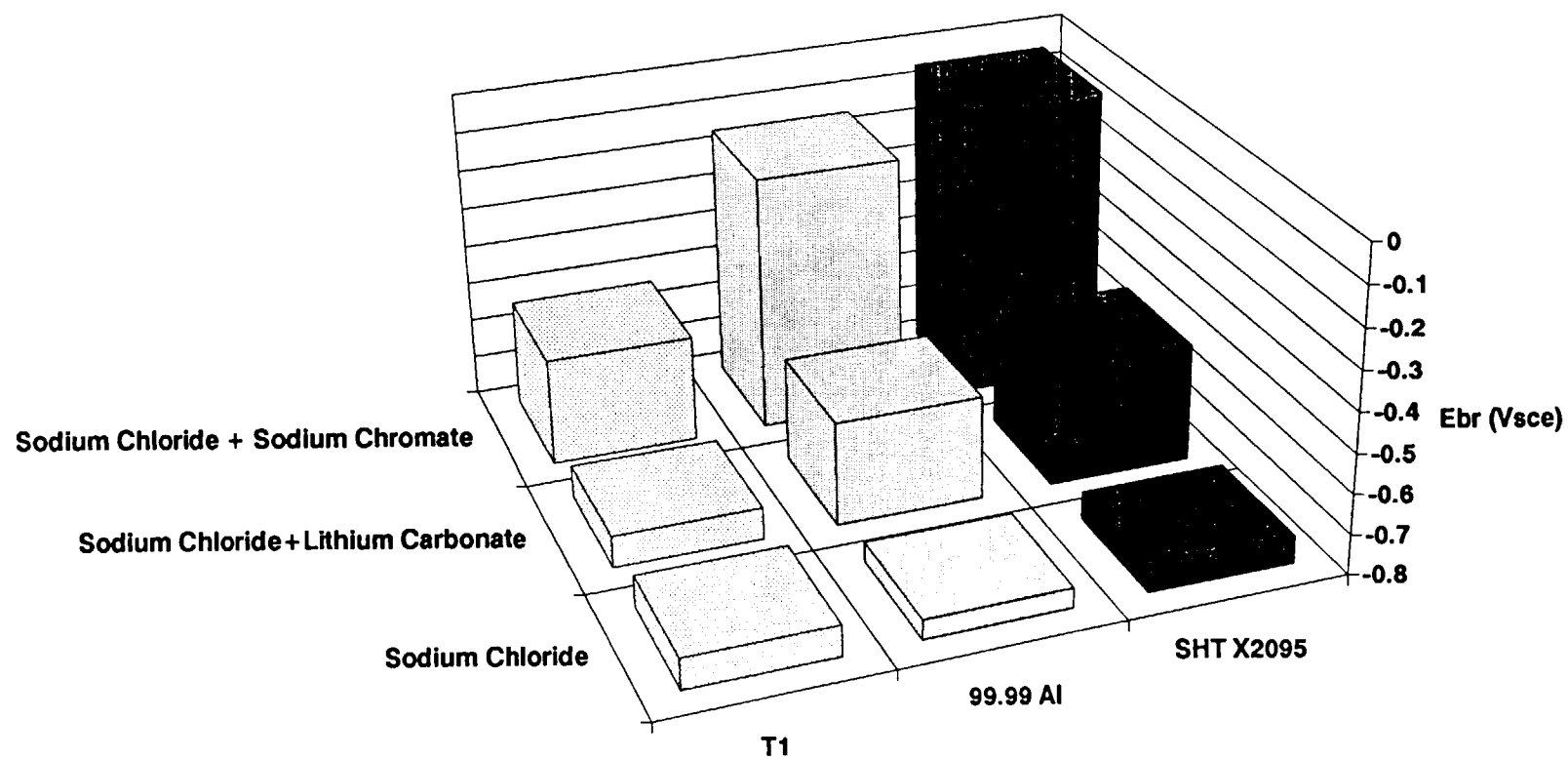
- \* In situ constant load testing under potentiostatic control.**

**Is there a correlation between the behavior of the mechanically stressed specimens and the electrochemistry observed for the microstructural phases?**

**Is there a likely active pathway for localized corrosion?**

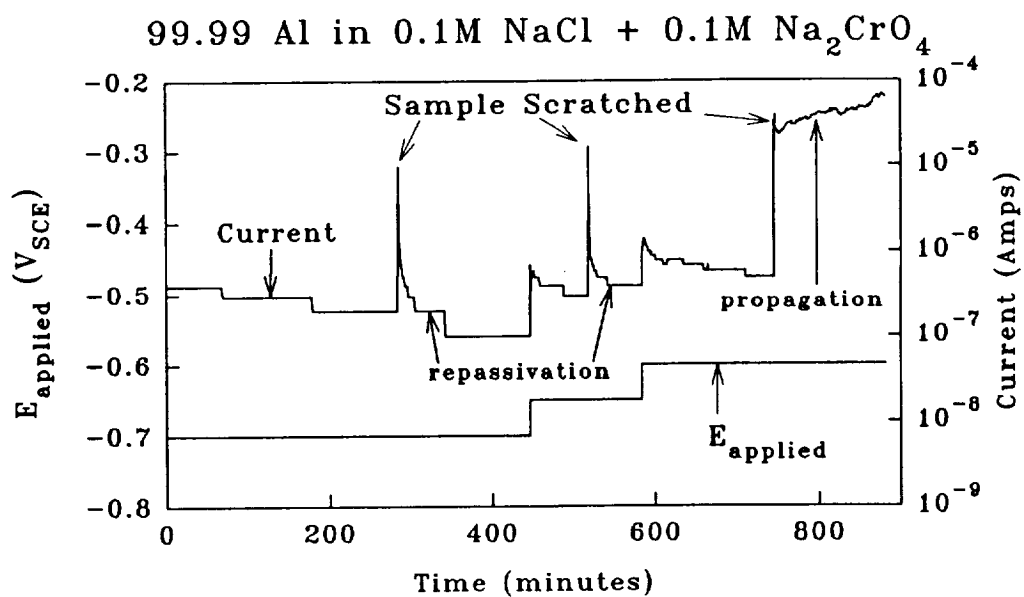
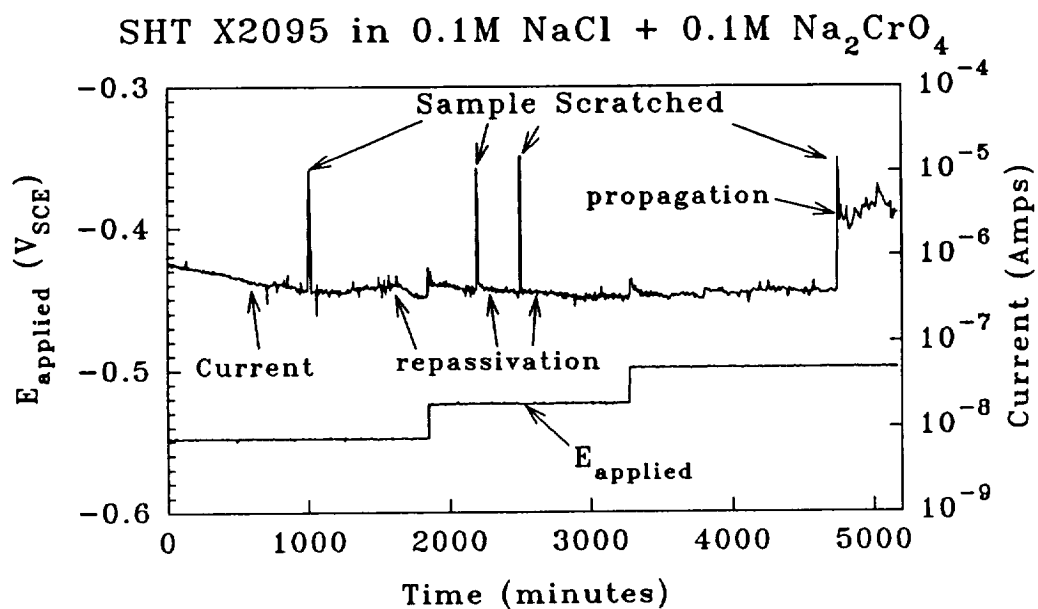
**Two methods were used to determine the potential corresponding to a change from passive to active behavior for the boundary phases in Al-Li-Cu alloys. The breakdown potentials ( $E_{BR}$ ) from potentiodynamic polarization experiments are shown on the following page.**

## Breakaway Potentials Determined By Potentiodynamic Polarization at 0.1mV/sec



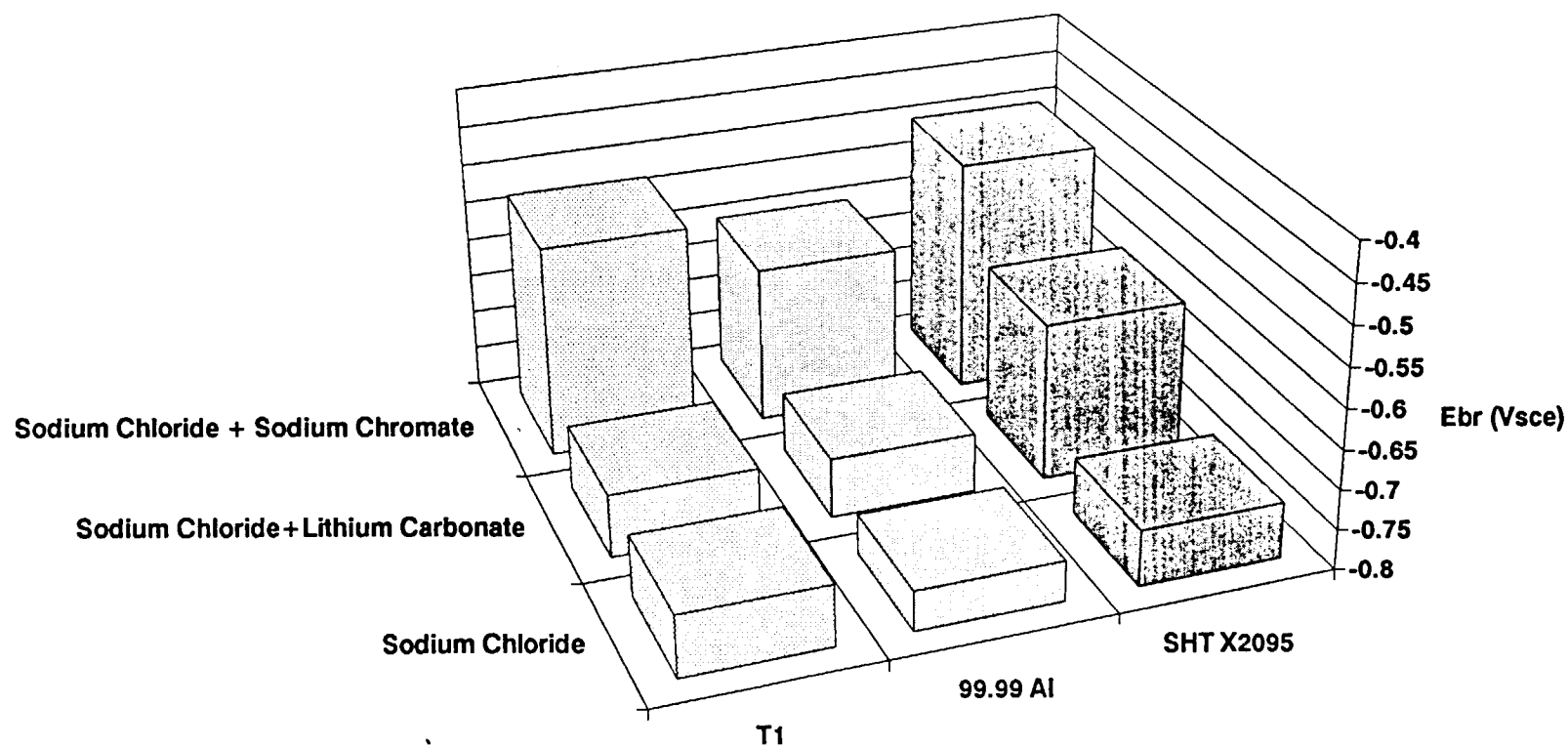
Potentiodynamic experiments are performed on a static material surface and may not reflect the conditions at the tip of an advancing crack where the material is plastically deformed exposing oxide-free material to the environment. To determine the potential at which a mechanically damaged material would spontaneously repassivate, scratching electrode experiments were performed. In these experiments a flat sample under no applied load is potentiostatically polarized then scratched with a sharp glass rod. If the sample repassivates the potential is increased and the process repeated. When a potential is reached where the scratch results in the propagation of corrosion, that potential is defined as the critical transition potential. Propagation of corrosion is determined by visual inspection of the surface and monitoring of the corrosion current. The next figure shows the response of SHT 2095 and 99.99 Al in the NaCl/Na<sub>2</sub>CrO<sub>4</sub> environment. Note that the critical potential differs by approximately 100 mV for these materials.

# DETERMINATION OF CRITICAL POTENTIALS VIA SCRATCHING ELECTRODE



The critical potentials for the matrix phase (SHT 2095), the Cu-depleted zone (99.99 Al) and the  $T_1$  ( $Al_2CuLi$ ) phase (bulk ingot) are shown on the next page. Note the discrepancy between these values and those determined by potentiodynamic polarization. The scratching electrode results indicate that the transition for the matrix phase occurs at a more noble potential than for the Cu-depleted region and the  $T_1$  phase. A material polarized between these potentials would have a passivated matrix and at least two rapidly corroding sub-grain boundary phases suggesting a sharp path for localized attack.

## Critical Potentials Determined by Scratching Electrode Experiments\*



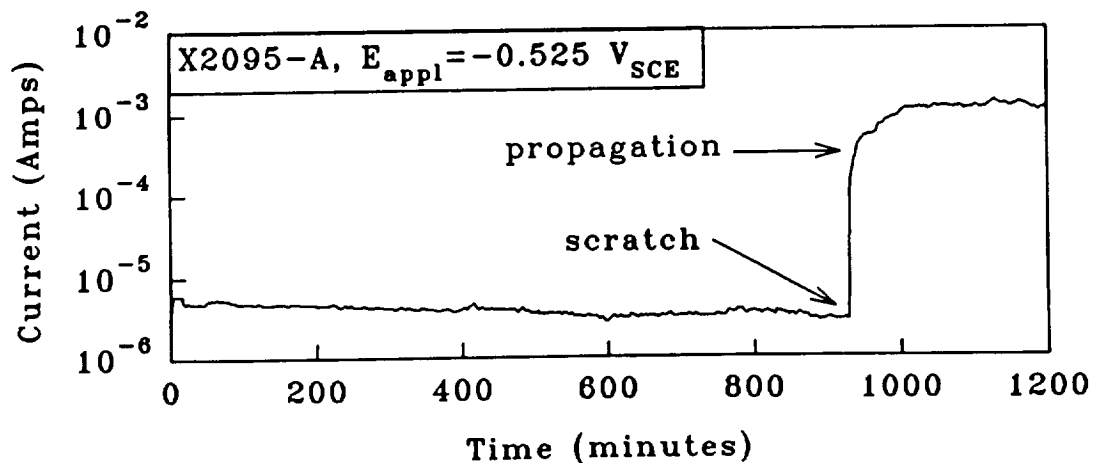
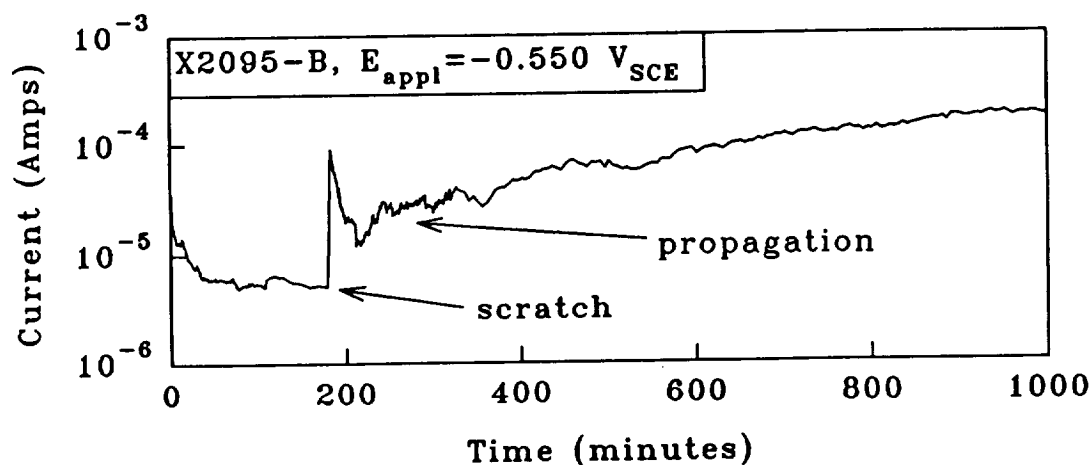
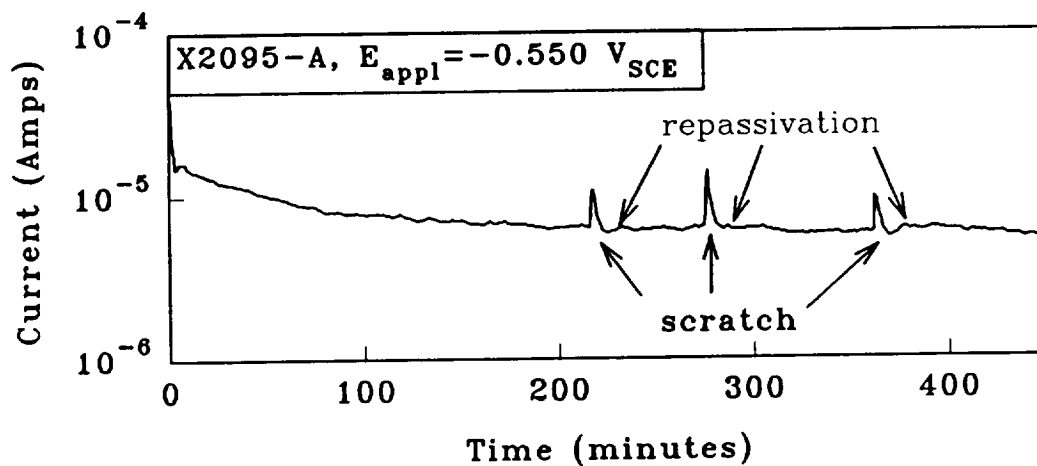
\* T1 values from potentiodynamic scans

The following figure shows responses for two tempers of 2095 polarized between the critical potentials defined for 99.99 Al and SHT 2095. Note that at  $-0.550 V_{SCE}$  the "B" temper (peakaged) corrodes while the "A" temper (underaged) remains passive. Only after being scratched at  $-0.525 V_{SCE}$  does the "A" temper become active. This behavior favors a Cu-depleted zone as an active pathway since increased aging (more Cu depletion) tends to shift the transition potential cathodic (toward that observed for 99.99 Al).



# RESPONSES OF TWO X2095 TEMPEERS TO SCRATCHING EXPERIMENT

(0.1M NaCl + 0.1M Na<sub>2</sub>CrO<sub>4</sub>)



Constant load experiments were performed to determine if the transition potentials determined for flat, unstressed samples correlate to behavior of materials under load. Smooth, short transverse specimens were loaded to 60% YS then critical potentials were determined in the same manner applied to unstressed specimens. For mechanically loaded specimens the transition potential corresponds to rapid failure of the specimen due to the propagation of localized corrosion.

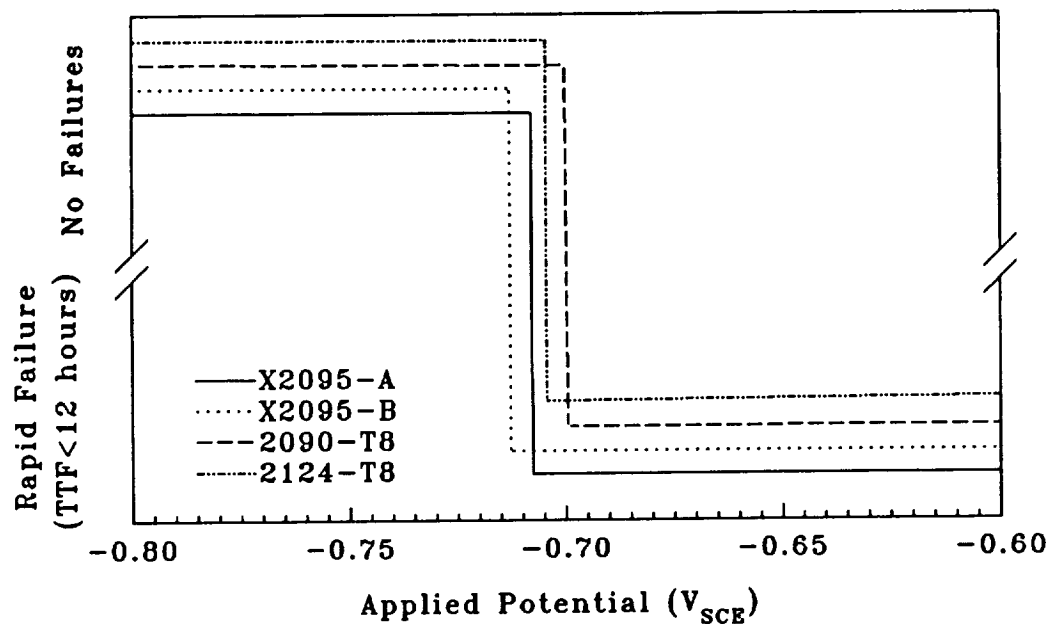
The graph on the next page shows the transition potentials for four Al-Cu-X materials as a change in time-to-failure behavior. Note that all of the transitions occur in a potential range bracketed by the critical potentials determined for the Cu-depleted zone (99.99 Al) and the grain interiors (SHT 2095).

Another interesting piece of information shown by these data is that there is a critical potential associated with 2124 Al in the same range as the other alloys. However, 2124 contains no Li and thus no  $T_1$  phase on the boundaries; therefore it is impossible that the activation of  $T_1$  is responsible for the change in behavior of this material.

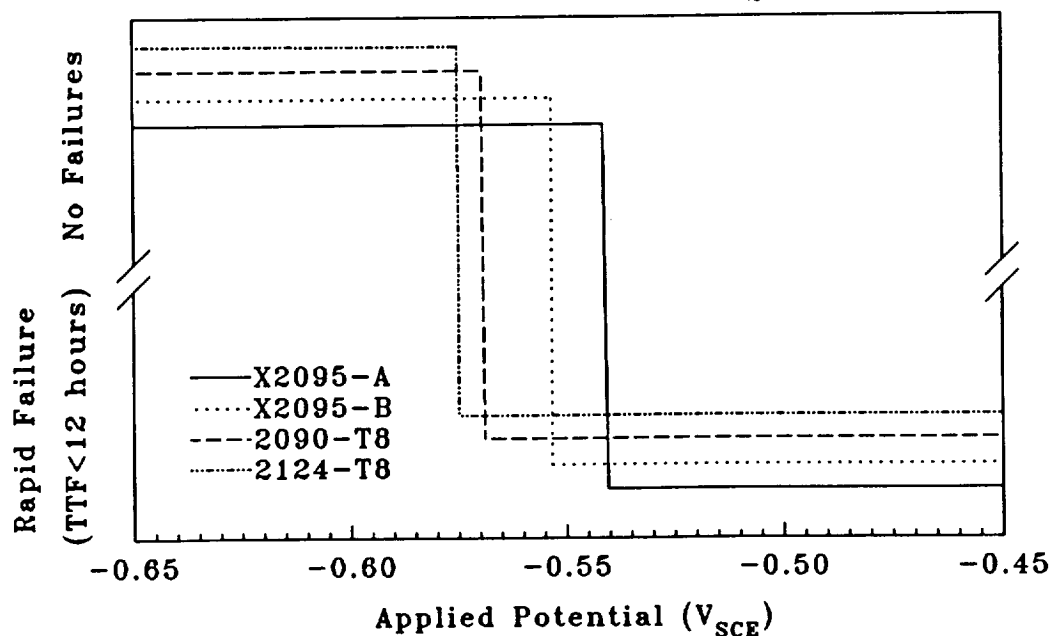
Also note the separation of the critical potentials for the two tempers of 2095. In these experiments the potentials were determined within the resolution defined by the stability of the reference electrode (saturated calomel) which is one or two millivolts. The observed difference of about 25 mV supports the proposed correlation between aging condition and transition potential.

# CRITICAL POTENTIALS FOR TTF BEHAVIOR OF SEVERAL AL-LI-X ALLOYS

0.6M NaCl + 0.1M  $\text{Li}_2\text{CO}_3$



0.1M NaCl + 0.1M  $\text{Na}_2\text{CrO}_4$

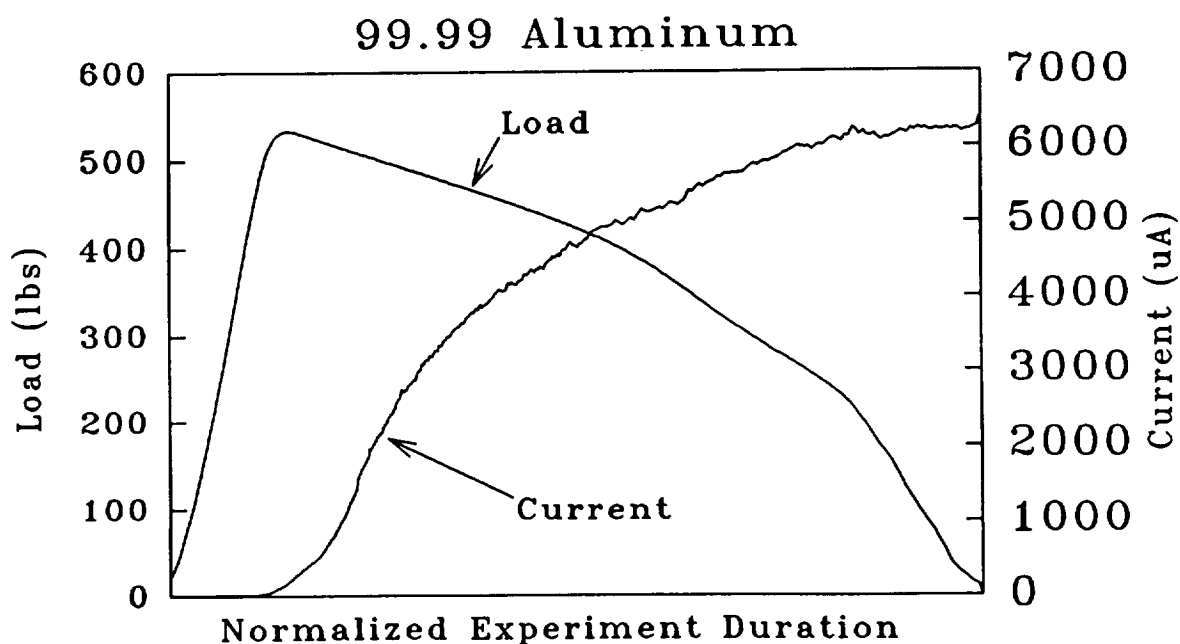
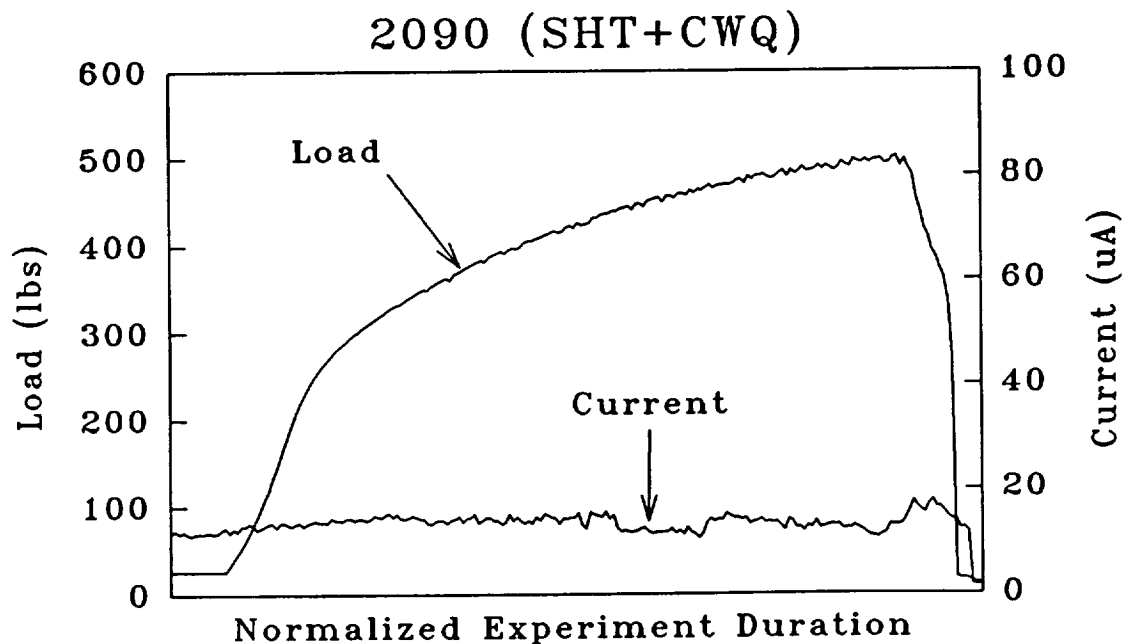


**Although the electrochemical studies of the boundary phases agree with the constant load experiments performed on the tempered alloys, no data has been presented for boundary phases under actual dynamic strain.**

**The corrosion responses of the matrix material and Cu-depleted zone under conditions of plastic deformation were determined for a potential where the tempered alloys are active. The following graphs show that under plastic strain the 99.99 Al is highly active while the solutionized material (matrix) remains passive.**

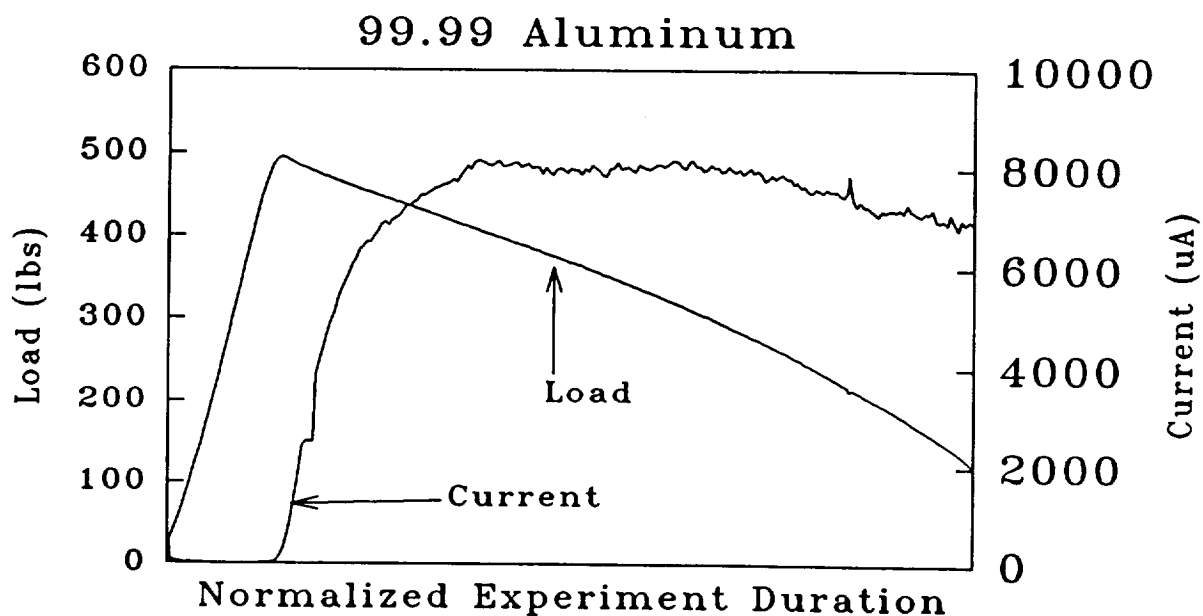
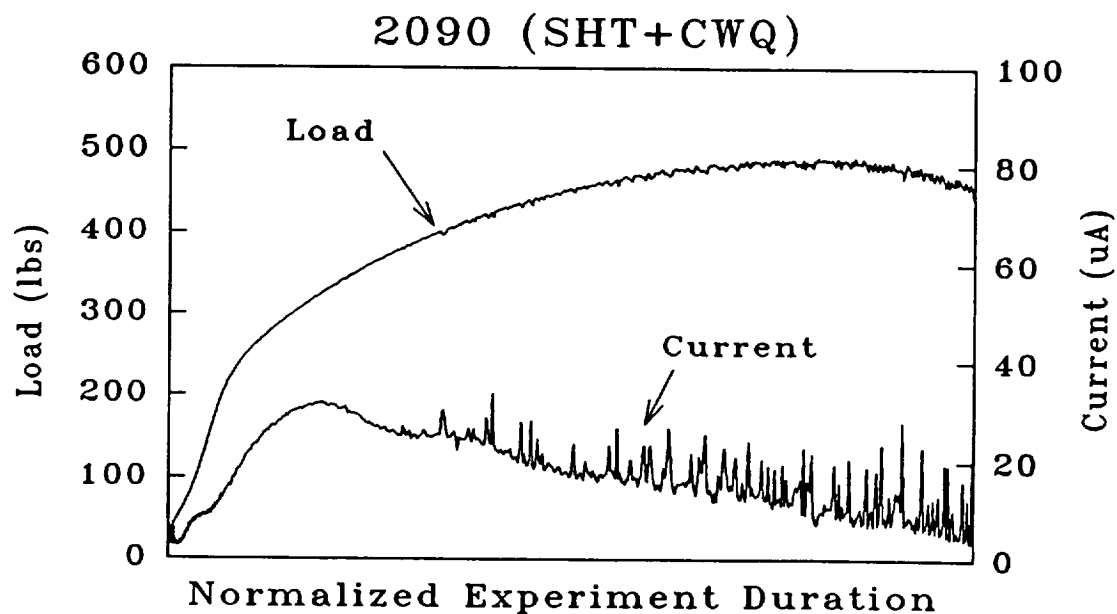
# ELECTROCHEMICAL RESPONSE OF MATERIALS DURING PLASTIC DEFORMATION

0.1M NaCl + 0.1M Na<sub>2</sub>CrO<sub>4</sub>  
Applied Potential = -0.550 V<sub>SCE</sub>



# ELECTROCHEMICAL RESPONSE OF MATERIALS DURING PLASTIC DEFORMATION

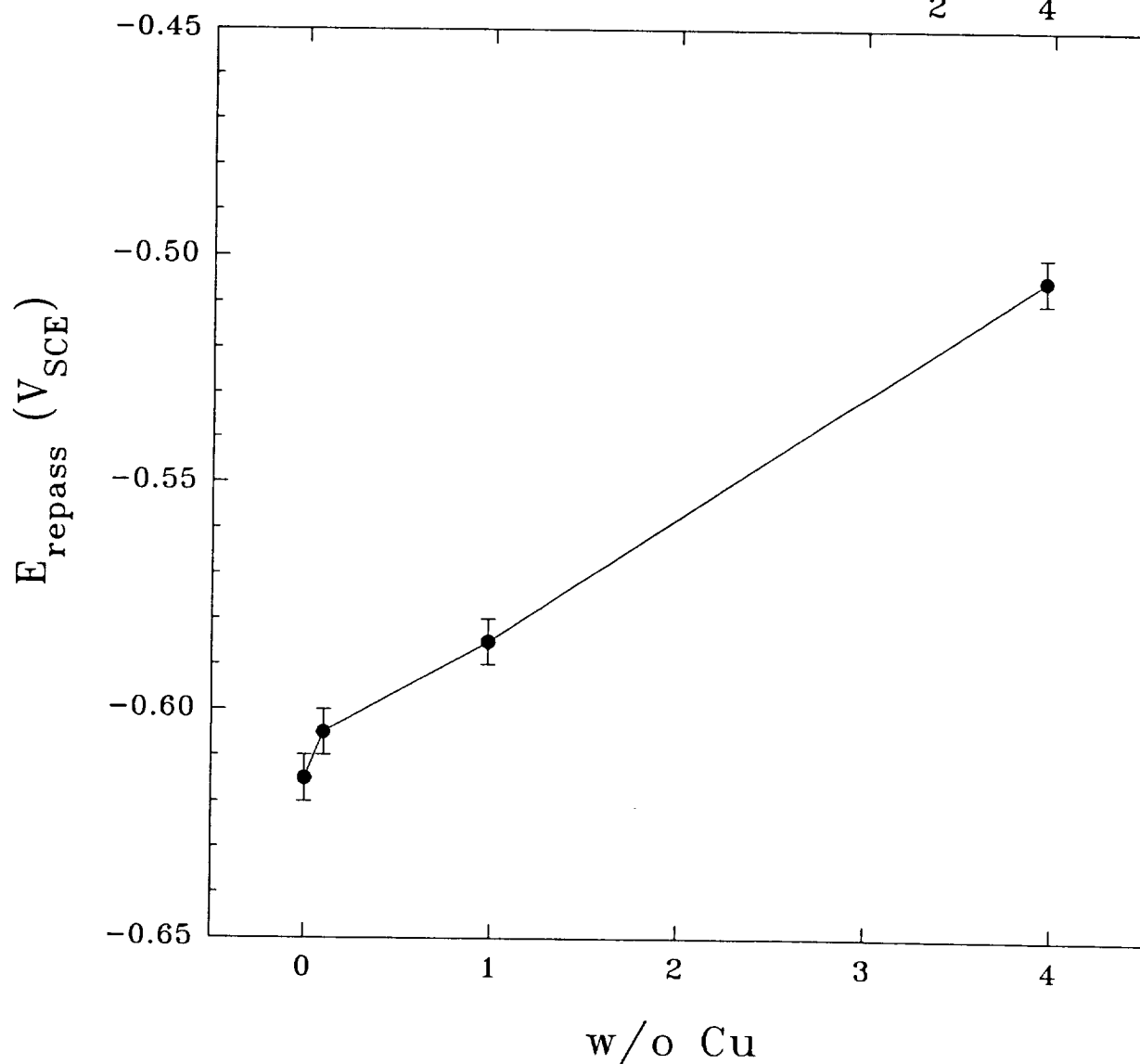
0.6M NaCl + 0.1M Li<sub>2</sub>CO<sub>3</sub>  
Applied Potential = -0.700 V<sub>SCE</sub>



(Initial Strain Rate of Approximately  $10^{-4}$ /sec)

Since a Cu-depleted zone in an alloy is more likely to lie between the compositions of the matrix and 99.99 Al, Al-Cu binaries were used to map out transition potential as a function of copper content. The following graph shows the response determined in the NaCl/Na<sub>2</sub>CrO<sub>4</sub> environment. Identical work is currently being performed in the NaCl/Li<sub>2</sub>CO<sub>3</sub> environment.

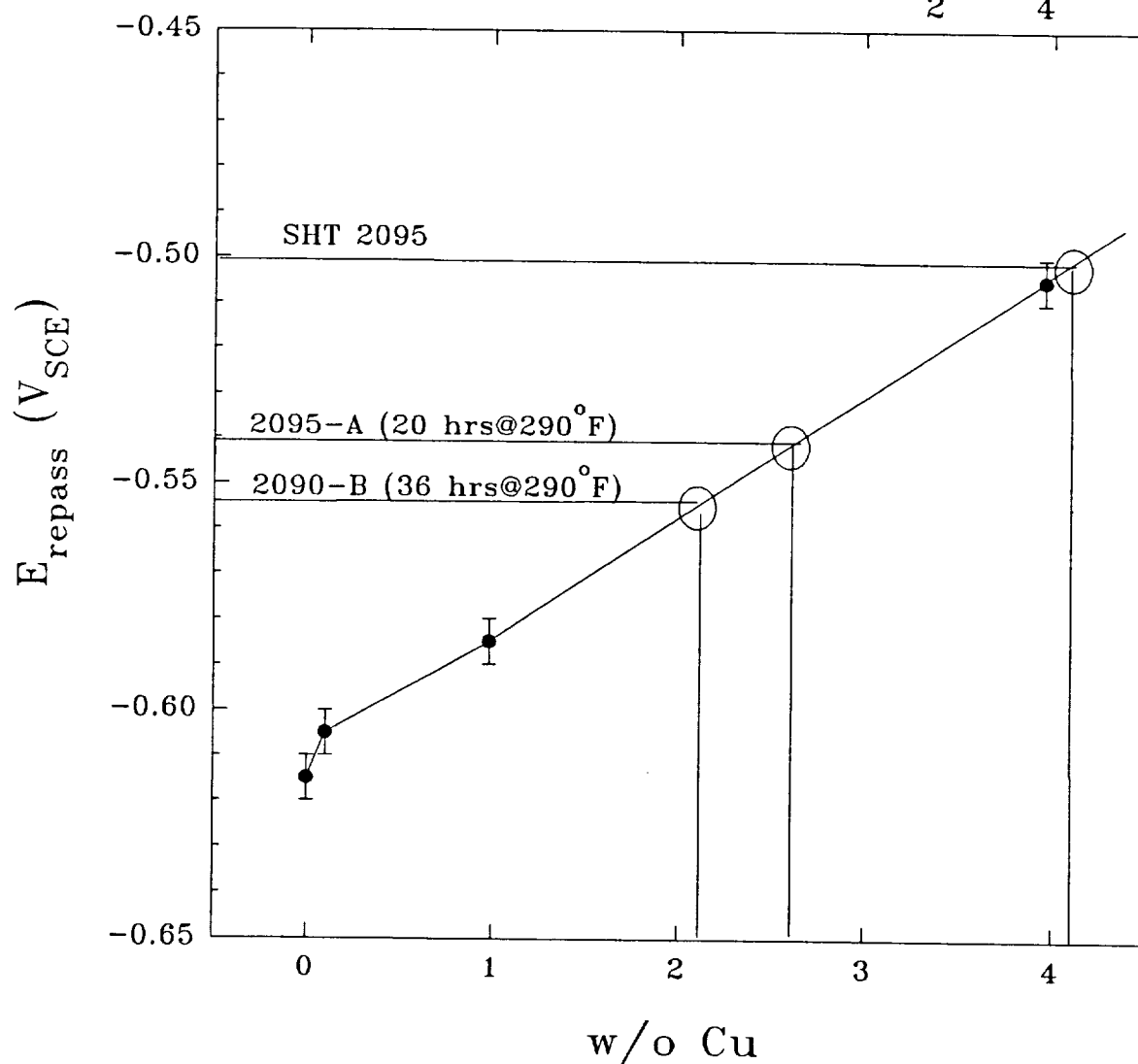
Spontaneous Repassivation Potentials  
of Aluminum–Copper Binaries  
Determined by Mechanical Scratch  
in 0.1M NaCl + 0.1M Na<sub>2</sub>CrO<sub>4</sub>





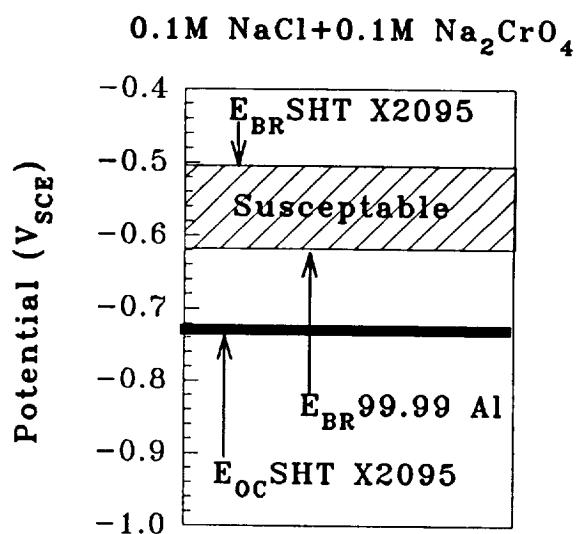
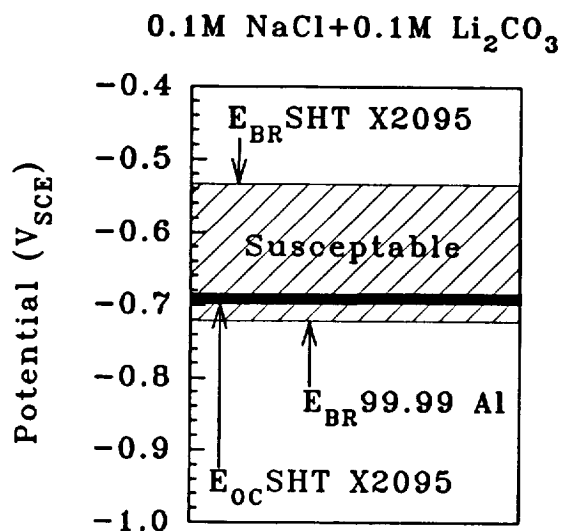
**On the next graph the critical potentials for 2095 A and B and SHT 2095 are superimposed on the plot of critical potential vs Cu-content. Note that the alloy is 4.0 w/o in Cu and the SHT value lines up almost perfectly with the Al-3.96 Cu value. This graph also reemphasizes the idea of temper affecting transition potential. Note the different Cu-depleted concentrations predicted electrochemically for the two tempers of 2095.**

Comparison of Spontaneous  
Repassivation Potentials of 2095 and  
Aluminum-Copper Binaries  
Determined by Mechanical Scratch  
in 0.1M NaCl + 0.1M Na<sub>2</sub>CrO<sub>4</sub>



Although data have been presented that favor active path dissolution in two environments under potentiostatic polarization, it has not been shown if these potentials are realized under free corrosion conditions. The following graph shows the open circuit potential of SHT 2095 in relationship to the critical potentials for the matrix and Cu-depleted region. In the carbonate environment it appears likely that the Cu-depleted region can be active under free corroding conditions; whereas in the chromate environment the Cu-depleted region would remain passive since  $E_{OC}$  is cathodic to the critical potential of this region.

# **LIKELY RANGES OF SUSCEPTABILITY TO PREFERENTIAL BOUNDARY CORROSION IN RELATION TO OBSERVED OPEN CIRCUIT POTENTIALS**



## **SUMMARY OF ELECTROCHEMICAL CHARACTERIZATION**

- \* Critical potentials determined via scratching electrode experiments correspond well with behavior observed for mechanically loaded tensile specimens.**
- \* Straining electrode experiments indicate that there are combinations of potential, environment and plastic strain in which the Cu-depleted region will be highly active while the matrix phase remains passive.**
- \* Aging condition in Al-Cu-Li alloys influences the transition potentials possibly do to the degree of Cu-depletion along microstructural boundaries.**
- \* Scratch testing of Al-Cu binaries suggests a strong correlation between Cu content and transition potential.**
- \* The critical potentials determined for sub-grain boundary phases in Al-Cu-Li alloys suggests that there are at least two possible contributions to an active path for corrosion - the highly active  $T_1$  phase and a Cu-depleted region.**

**In order for the preceding electrochemical analysis to be valid for a freely corroding system exposed to a sodium chloride environment, it must be determined if a lithium carbonate solution chemistry can develop in an occluded cell.**

## **OCCLUDED CHEMISTRY ANALYSIS**

**Determine the pH response resulting from a large ratio of material surface area to solution volume.**

- \* Shavings experiments**
- \* Occluded chemistry experiments**
- \* Flat sample experiment**

**Examine solution chemistries to determine the possible  $\text{Li}^+$  levels that might develop in an occluded environment.**

- \* Analysis of solutions from pH experiments**
- \*  $\text{Li}^+$  accumulation under galvanostatic polarization**

**Are there conditions favoring the development of an alkaline environment containing lithium ions from exposure of an Al-Cu-Li alloy to an NaCl environment?**

## **PH MEASUREMENTS**

### **Material Shavings**

- \* Samples of various materials were milled to produce fine turnings.**
- \* Enough NaCl solution was added to a test-tube of turnings to just cover the material.**
- \* Some turnings were cleaned in 0.1 M NaOH prior to the experiment.**
- \* The pH is monitored for up to a week.**

### **Occluded Chemistry**

- \* A small hole was bored into a block of material.**
- \* Several drops of NaCl solution were added.**
- \* A snug fitting pH electrode was inserted into the hole and pH monitored for 1 to 2 days.**

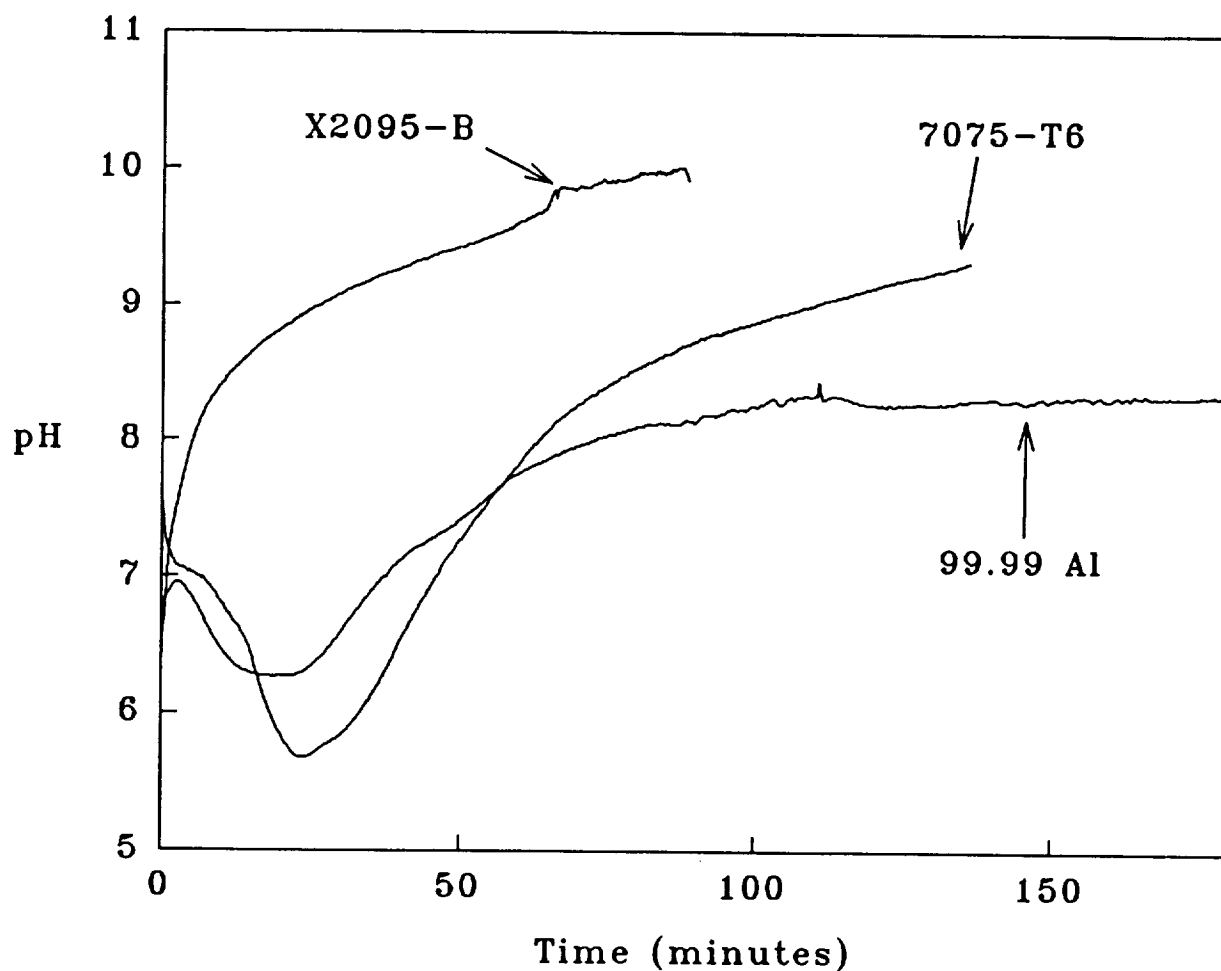
### **Flat Sample Experiments**

- \* A small coupon of material was polished and cleaned.**
- \* A tiny "puddle" of solution was deposited on the surface.**
- \* A microelectrode was used to monitor the pH for 2 or 3 hours.**
- \* Experiment length was initially limited by evaporation of electrolyte.**



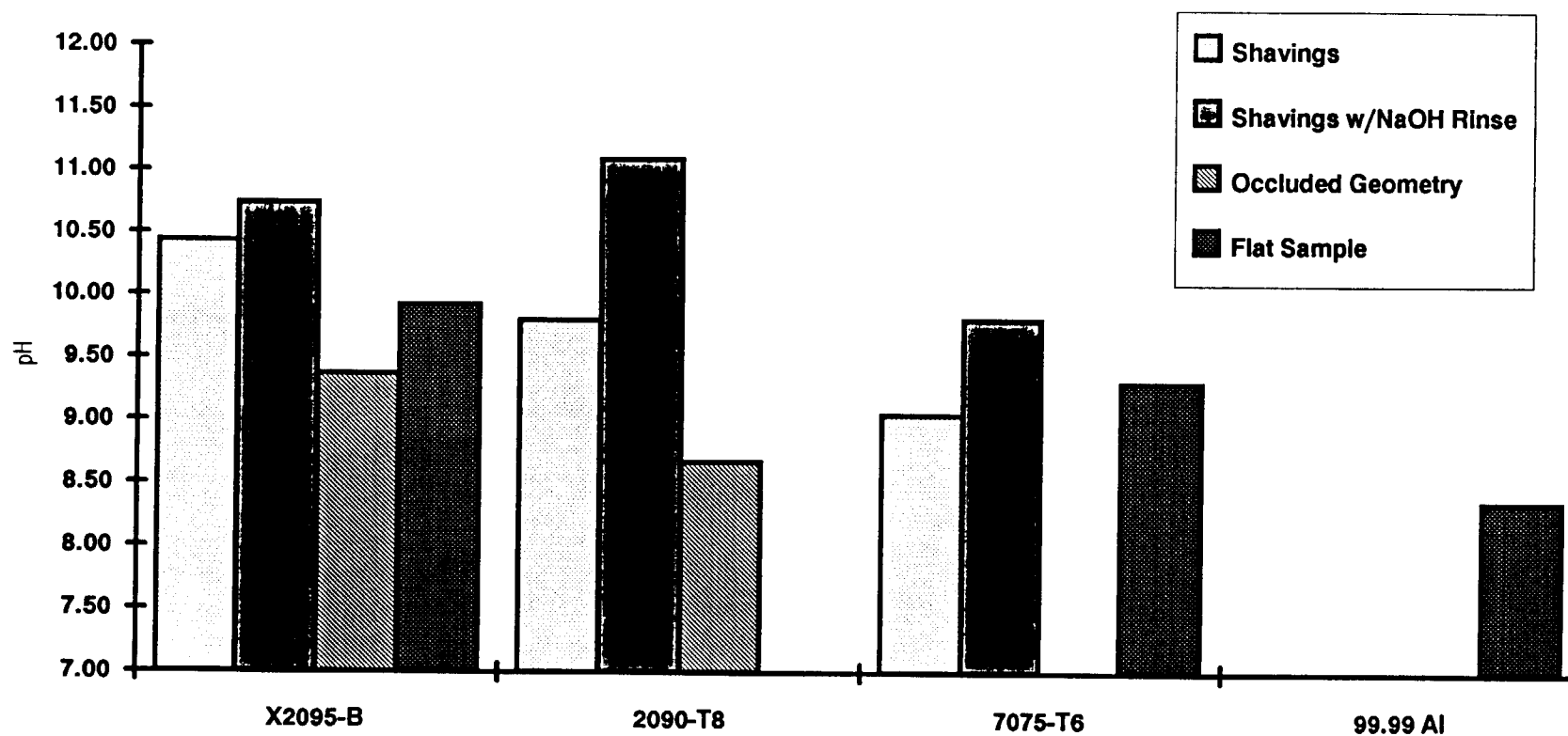
**The pH vs time responses for 2095-B, 7075-T6 and 99.99 Al in flat sample experiments are shown on the following page. Within the short duration of these experiments all materials tended to produce an alkaline environment. Evaporation of the solution limited the length of the experiment. Data will be presented from a slightly improved experimental set-up which allowed data collection over a twenty-four hour period.**

# PH RESPONSES OF MATERIALS EXPOSED TO A SMALL VOLUME OF 0.1M NaCl SOLUTION



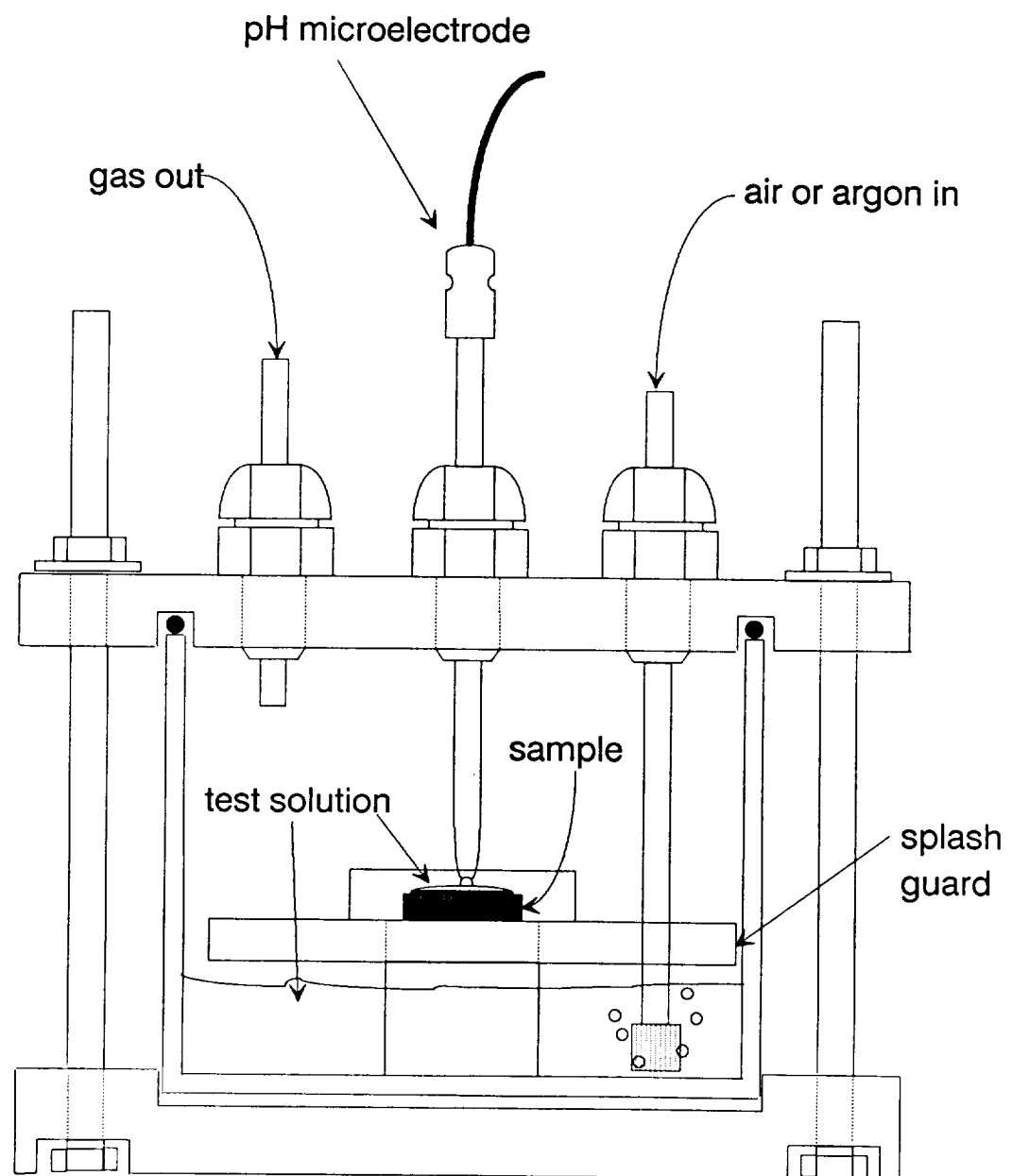
**The next figure shows the pH values from all three types of experiments and a variety of materials. The tendency is towards an alkaline environment independent of material or experimental configuration.**

## Final pH Values For Materials Exposed to 0.1M NaCl Solution



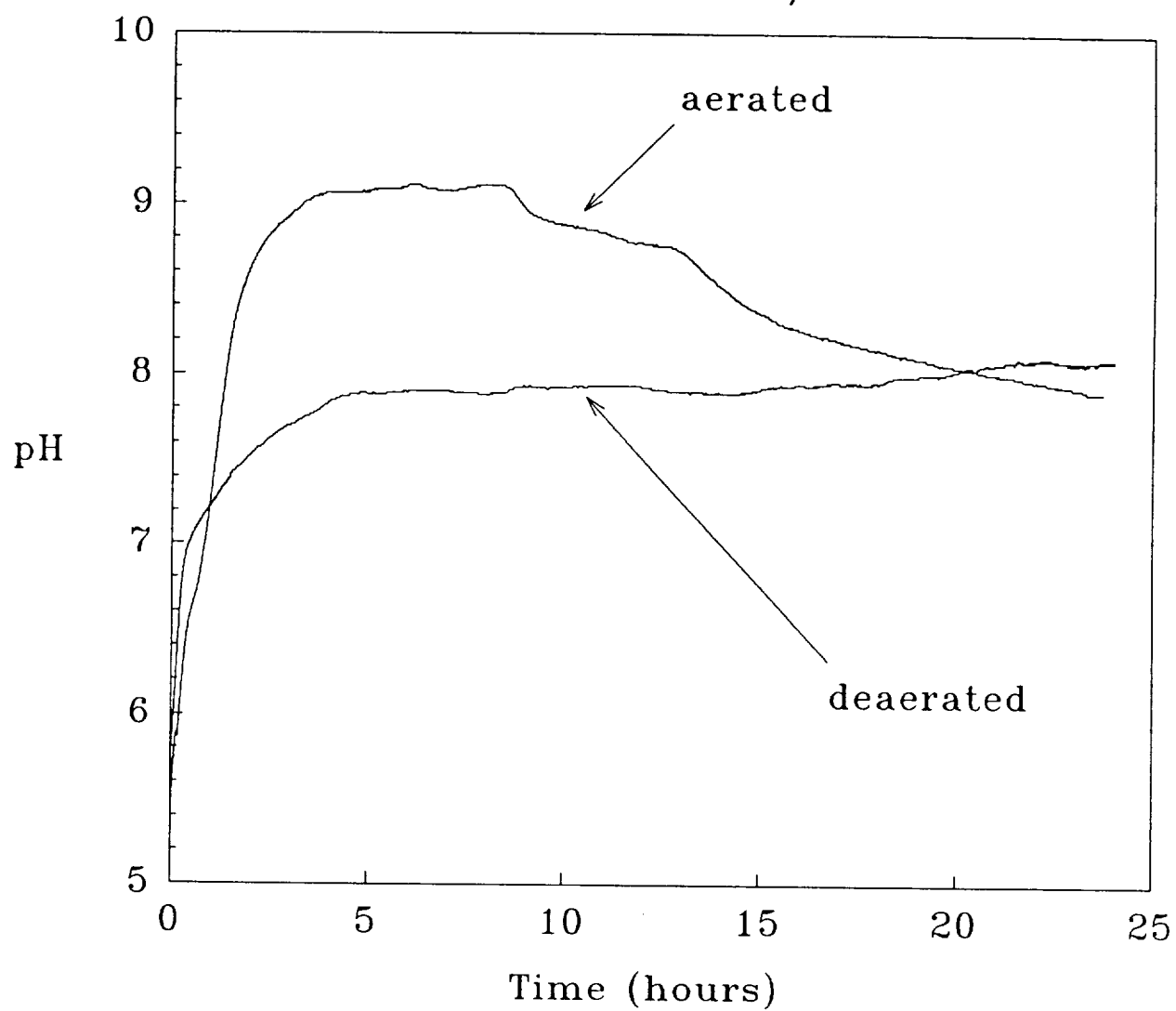
The schematic drawing on the following page shows the experimental cell used to extend the lifetime of flat sample type pH experiments. There are two key characteristics. First the high humidity environment prevents evaporation of the electrolyte. Second, the ability to deaerate the chamber with an inert gas allows for the effect of dissolved oxygen to be taken into account.

# Experimental set-up for long term pH measurements on flat samples with small solution volume



**The following graph shows the pH vs time response of 2095-B exposed to 3.5w/o NaCl for 24 hours. The presence or absence of oxygen changes the initial response but it is unclear if the steady-state pH value is affected.**

pH vs Time for 2095-B  
Small Volume 3.5 w/o NaCl

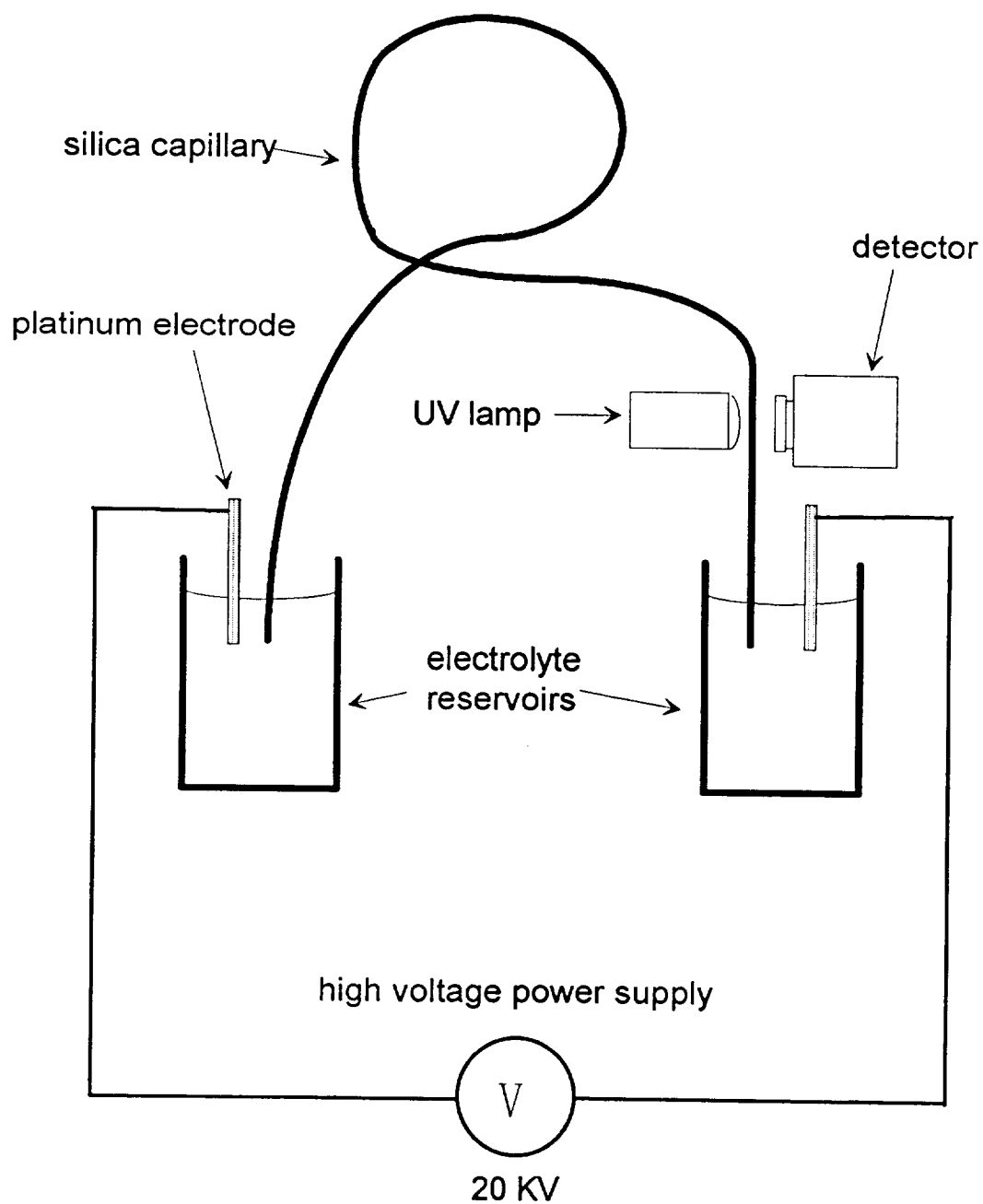




**Analysis of some of the chemistries generated by high surface area to volume ratios has been performed using Capillary Electrophoresis (CE). The following page shows a schematic representation of a CE system. In this technique ions are separated based on differences in mobility in an electric field. Both the size and the charge of the species determines its mobility. The basic scheme for this technique is as follows:**

- \* The ends of a silica capillary are placed in two reservoirs of electrolyte which also contain electrodes for applying an electric field.**
- \* The capillary is filled with solution by applying a vacuum to one end.**
- \* The test solution is sampled by placing one end of the capillary into a reservoir of the solution. Loading is performed either hydrostatically or electrostatically. The capillary end is subsequently returned to the electrolyte reservoir.**
- \* Electrodes in the reservoir are used to apply a large electric field (e.g. 20 KV) across the capillary.**
- \* Ions in solution separate according to mobility and are detected by indirect UV absorbance.**
- \* Absorbance is plotted vs time and ions are identified by migration time which is compared to a known standard solution also run through the system. Since the concentrations of the standards are known, the unknown concentrations can be determined by comparisons of peak heights.**

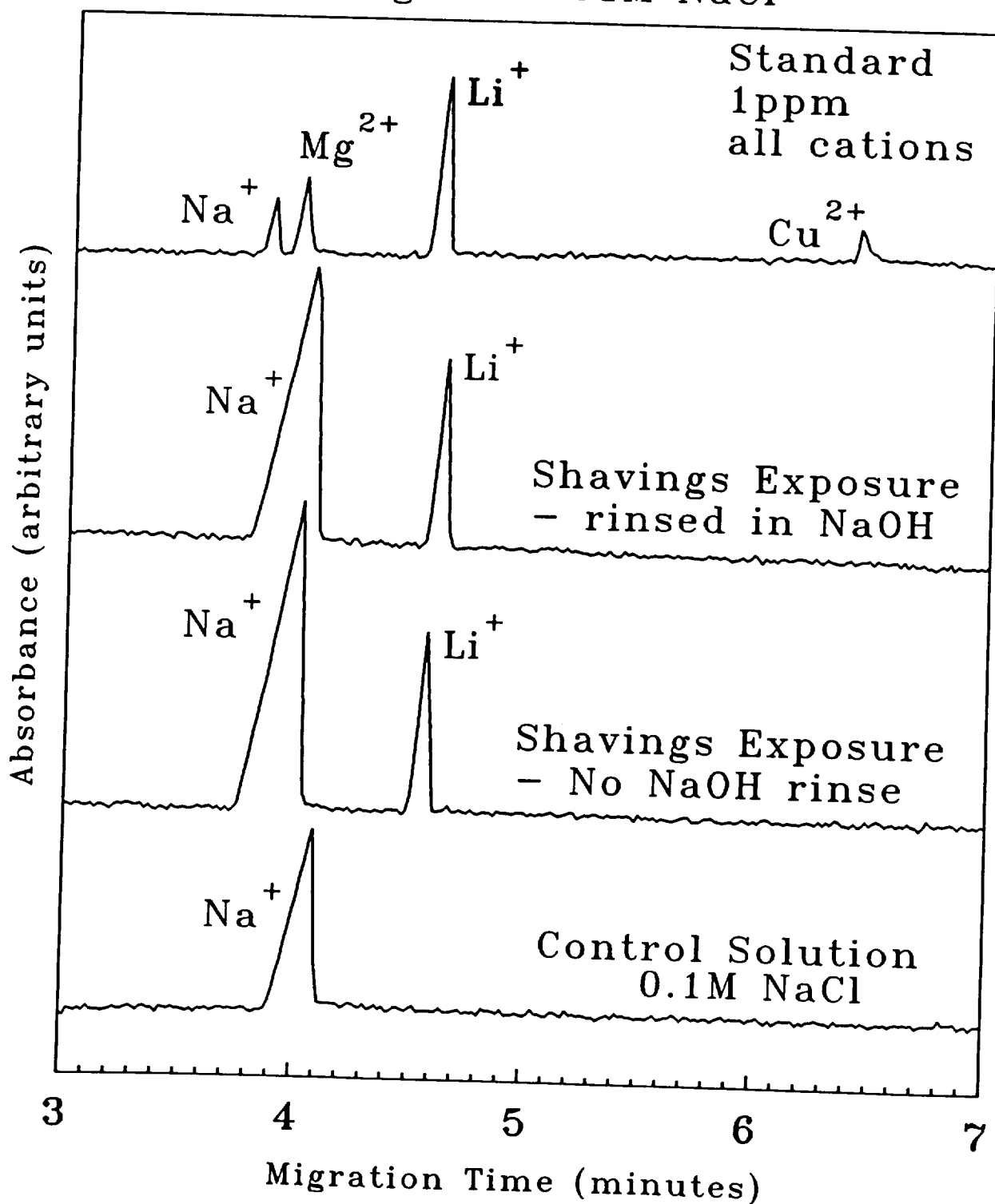
# Schematic Setup for the Capillary Electrophoresis Technique



**On the following page absorbance vs migration time is plotted for solution from 2095—B shavings exposed to 0.01 M NaCl solution. Plots of known standards and control solutions are included for comparison. The peaks from the test solution correspond with the standards for sodium and lithium ions. These data indicate that lithium ions are present in the occluded environments under study.**

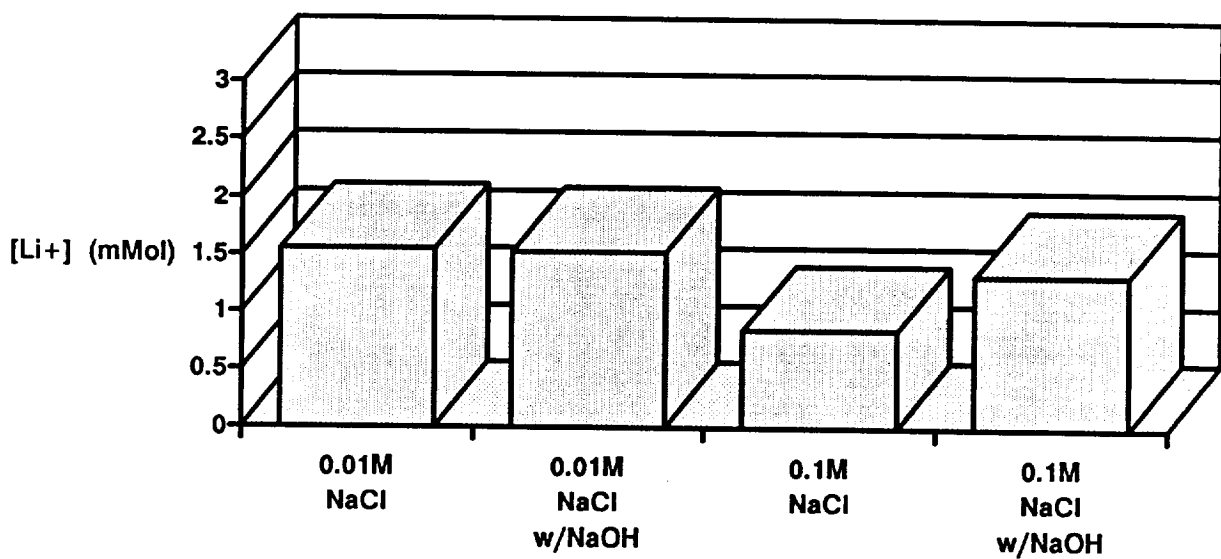
# CAPILLARY ELECTROPHORESIS

Results From X2095-B  
Shavings in 0.01M NaCl

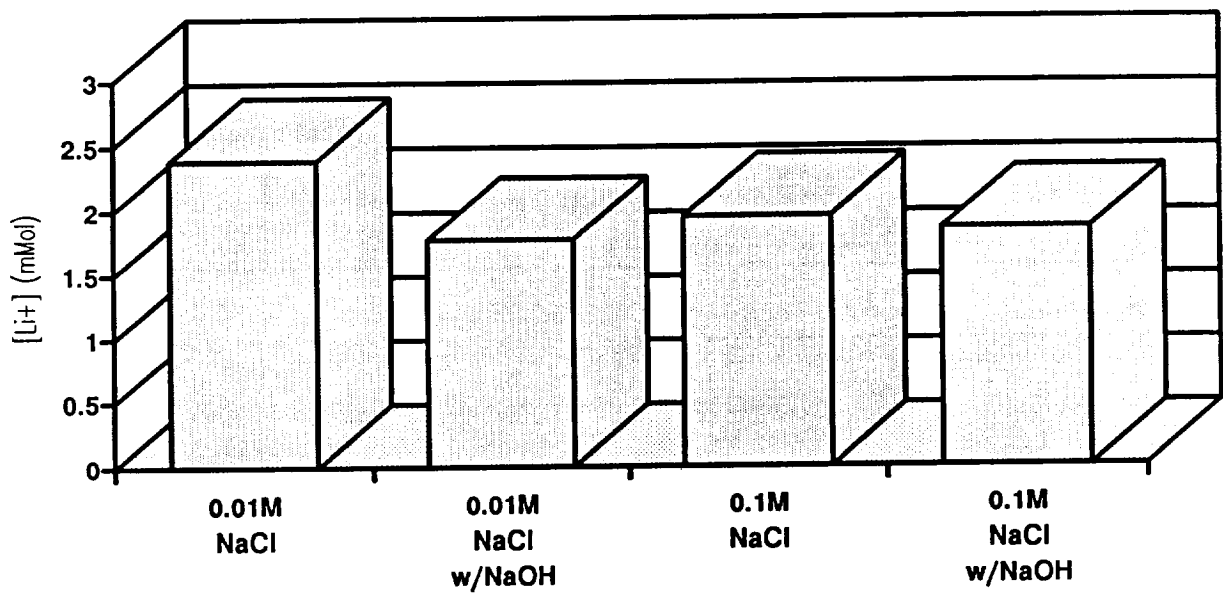


**The next two pages summarize the results of CE testing on solutions collected from shavings experiments. For both 2090 and 2095 the lithium levels appear to be in the millimolar range.**

**Lithium Ion Concentrations of X2095-B  
Shavings Exposed to Solution (Values  
based on one point calibration)**



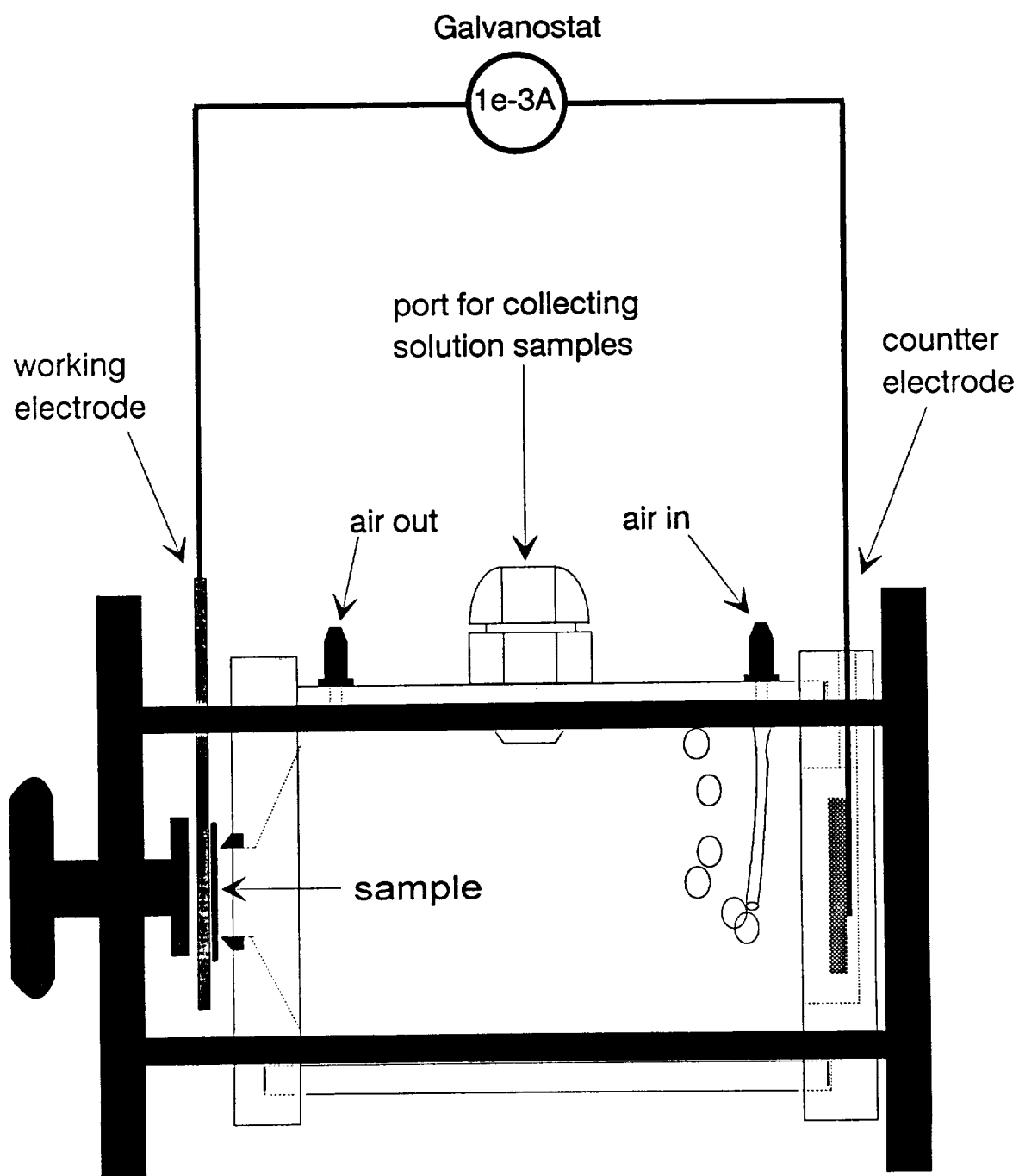
**Lithium Ion Concentrations of 2090-T8  
Shavings Exposed to Solution (Values  
based on one point calibration)**



**Galvanostatic polarization on 1 cm<sup>2</sup> 2095 A and B coupons was performed in 250 ml of 0.01 M NaCl and the bulk solution periodically analyzed for lithium ion concentration. The following schematic illustrates this experiment. The goal was to determine the rate of Li<sup>+</sup> ions into solution from each of the tempers and possibly characterize the material by the dissolution rate.**



# Setup for Galvanostatic Polarization Experiments

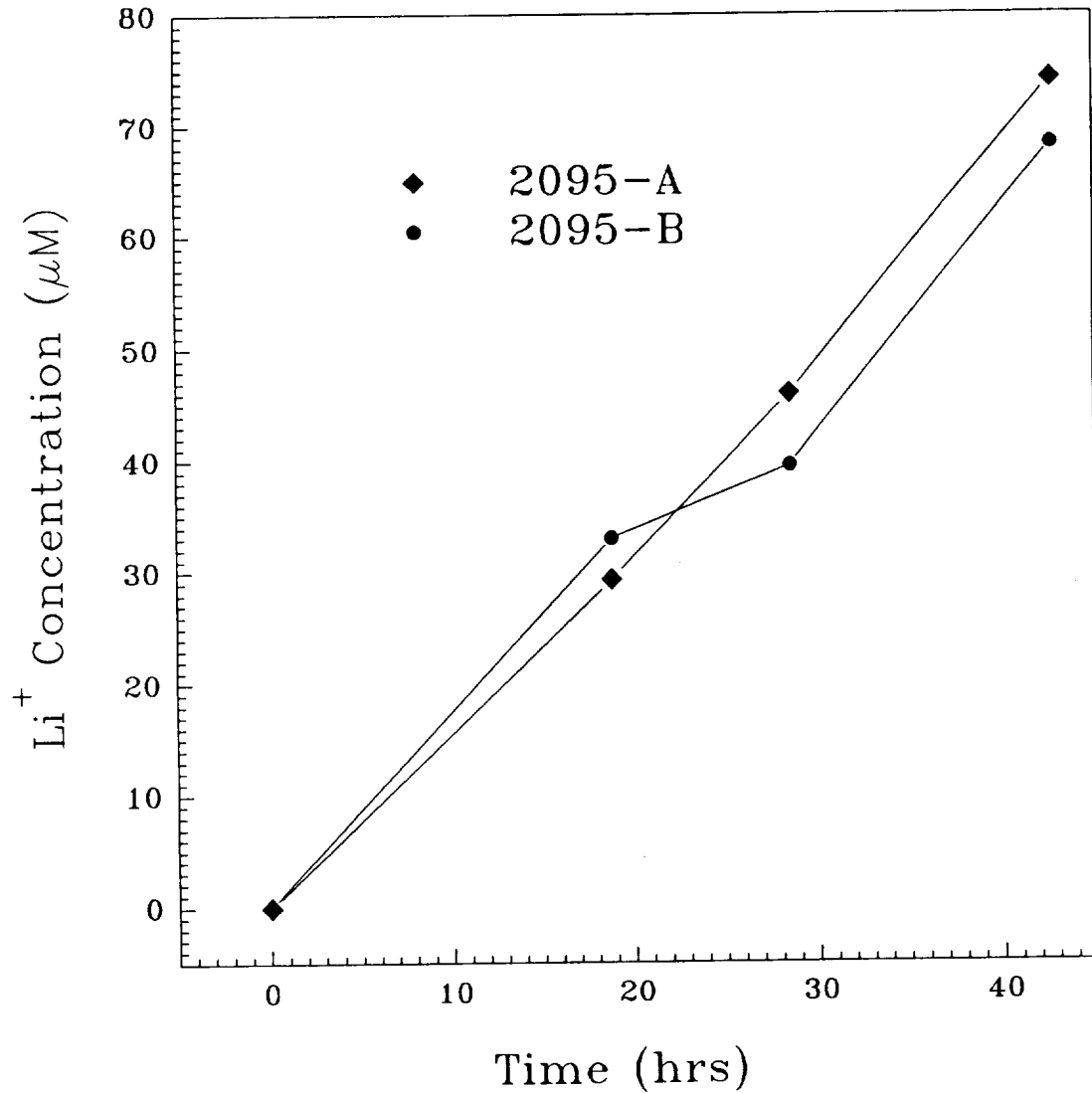


Results from the galvanostatic polarizations are shown on the following graph in terms of  $\text{Li}^+$  concentration as a function of time. It appears that the rates of dissolution for the two tempers cannot be resolved from one another with the available data. However, the dissolution rate can be applied to a theoretical crevice or crack to determine the length of time required to achieve significant  $\text{Li}^+$  levels. If the distance between crevice walls is assumed to be 5 microns and the dissolution rate  $1 \times 10^{-3} \text{ A/cm}^2$  then the rate of  $\text{Li}^+$  ion buildup is 0.016 moles/liter/hour. Even if the assumptions are changed by an order of magnitude or more, it is evident that significant levels of  $\text{Li}^+$  can be generated in an occluded environment in a relatively short amount of time.

Note the assumptions made in this calculation are:

- \* The dissolution rate is constant in the crevice.
- \* The measured  $\text{Li}^+$  concentrations are valid based on a one point calibration.
- \* The crevice is isolated from a bulk environment as would be the case in an alternate immersion test.
- \* Depletion of the lithium concentration due to complexation or reaction and precipitation has not been taken into account.

Bulk  $\text{Li}^+$  Concentrations  
for  $1\text{cm}^2$  2095-B Corroding at  
 $10^{-3}\text{A}$  in 250 ml of 3.5 w/o NaCl



Normalized rate of corrosion

$$1.67 \times 10^{-5} \text{ M/cm}^2/\text{hr} \times 250 \text{ ml} = 4 \times 10^{-6} \text{ mol/cm}^2/\text{hr}$$

For a crevice of width  $5\mu\text{m}$ :  $0.016 \text{ M/hr}$

## **SUMMARY OF OCCLUDED CHEMISTRY ANALYSIS**

- \* Three configurations of pH monitoring experiments have indicated that an alkaline occluded chemistry is possible for several aluminum alloys.**
- \* The absence of O<sub>2</sub> has an affect on the initial pH response of a sample exposed to low solution volumes but does not appear to significantly alter the pH observed after a 24 hour exposure.**
- \* Capillary electrophoresis analysis of shavings solutions shows that a high surface area to volume ratio may result in significant Li<sup>+</sup> concentrations when an Al-Li-X alloy is exposed to a chloride environment.**
- \* Projection of Li dissolution rates from galvanostatic experiments onto restricted geometries suggests that significant Li concentrations may be generated in a short period of time.**

## **FUTURE WORK**

- \* Continue to evaluate the solution chemistries that develop in occluded environments.**
- \* Complete the characterization of the Al-Cu binaries in several environments to more clearly describe the effects of the Cu additions.**
- \* Use electrochemical impedance spectroscopy to determine if a significant change in polarization resistance can be linked to a specific  $\text{Li}_2\text{CO}_3$  concentration.**
- \* Rank various alloys and tempers according to crack growth kinetics by performing in-situ rising and static K tests on compact tension samples. If the growth rates are distinguishable it may be possible to find a correlation with a microstructural feature.**

**Mech. Prop. of X2095-A: 290°F for 20 hrs (S. No. 65662)**

	<u>UTS(ksi)</u>	<u>TYS(ksi)</u>	<u>EL(%)</u>	<u>Kic (Ksi√in)</u>
at T/2				
L	86.4	83.2	10.0	
LT	82.4	76.4	10.0	
at T/4				
L	78.3	75.1	12.0	
LT	77.5	70.0	12.0	30.2
at T/8				
L	80.5	76.9	16.0	

**Mech. Prop. of X2095-B: 290°F for 36 hrs (S. No. 65663)**

	<u>UTS(ksi)</u>	<u>TYS(ksi)</u>	<u>EL(%)</u>	<u>Kic (Ksi√in)</u>
at T/2				
L	88.9	86.5	8.0	
LT	87.6	82.9	6.0	
ST	84.9	71.4	5.5	21.2
at T/4				
L	82.8	80.1	10.5	35.8
LT	83.8	78.0	7.0	24.6
at T/8				
L	--	--	--	--
LT	83.8	73.3	10.0	
ST	85.8	75.1	4.0	

Project #6     **The Effects of Zinc Additions on the Precipitation and Stress Corrosion Cracking Behavior of Alloy 8090**

Raymond J. Kilmer and G.E. Stoner

Objectives

The objectives of the PhD research are to document and characterize the effects of Zn additions on the microstructure of alloy 8090 under different aging conditions, and to correlate SCC behavioral changes with changes in alloy composition and microstructure. Emphasis will be placed on optimizing SCC behavior and alloy density.

Current Status

Ray Kilmer successfully defended his dissertation in June of 1993. The revisions recommended by his committee are still underway and two additional publication manuscripts will be submitted by the end of calendar year 1993.

Recent Important Findings

- A. Significant progress was made concerning hydrogen effects on recrystallized AA 2090 in collaboration with Scully and Smith. These results will be presented by Smith.
- B. Several significant findings concerning additions of zinc to AA 8090 type alloys are listed below.
  - 1. Zinc additions alter the boundary phase precipitates and the precipitation sequence. Mechanical properties are retained if zinc additions are in the range of 0.5-1 weight percent and proper heat treatment practices are followed.
  - 2. Zinc additions result in a significant improvement in the SCC resistance of UA tempers based on ASTM time to failure tests.
  - 3. Slow rising load testing of susceptible and resistant tempers of AA 8090 and AA 8090 plus zinc indicate substantial crack growth occurred primarily in the susceptible tempers of these alloys.
  - 4. Hydrogen charging studies of nickel coated samples indicated a degradation of the initiation toughness  $J_i$  of the susceptible tempers of both AA 8090 and AA 8090 plus zinc.

The summary of these findings indicates that when AA 8090 is alloyed with small (~1 w/o) amounts of zinc, satisfactory mechanical properties are retained and the alloy, when aged to a suitable temper is resistant to premature failure by ASTM alternate immersion tests, slow rising loads/SCC tests, and extensive hydrogen charging.

#### Presentation Slides



**The Effect of Zn Additions to the Microstructure and  
SCC Behavior of 8090 and 8090-type Alloys**

**R. J. Kilmer  
G. E. Stoner**

**Department of Materials Science and Engineering  
University of Virginia  
Charlottesville, Virginia 22903**

**Sponsored by:**

**NASA-Langley Research Center  
Contact: M. Domack**

**and**

**Aluminum Company of America  
Contact: J. M. Newman**

# **OUTLINE OF PRESENTATION**

## **I. Objectives**

## **II. Summary of Previous Work**

### **A. Materials**

### **B. Test Procedures and Results**

## **III. Recent Results**

### **A. Test Procedures**

### **B. Results**

## **IV. Summary and Conclusions**

## **I. OBJECTIVES (AA 8090 AND AA 8090 + Zn)**

**To document and characterize the effects of Zinc additions on the microstructure of alloy 8090 under different aging conditions, and to correlate SCC behavioral changes with changes in alloy composition and microstructure. Emphasis will be placed on optimizing SCC behavior and alloy density.**

## **II. SUMMARY OF PREVIOUS WORK**

### **A. MATERIALS**

**The AA 8090-type alloys studied by Kilmer and some of their microstructure and mechanical properties are given in the next three slides.**

**Compositions of alloys employed in microstructural characterization:**

Alloy	Product	Li	Cu	Mg	Zn	Zr
A	Sheet	2.27	1.07	0.60	0.21	0.10
B	Plate	2.45	1.20	0.67	0.20	0.10
C	Sheet	1.91	1.07	0.62	0.58	0.10
D	Sheet	2.09	1.00	0.59	1.07	0.10
E	Plate	2.54	1.23	0.49	1.00	0.12
F	Plate	2.53	1.22	0.67	1.36	0.12
G	Plate	2.47	1.23	0.74	0.99	0.12
H	Plate (B)	2.55	1.16	0.69	0.02	0.12
I	Sheet (B)	2.44	1.06	0.63	0.00	0.10

Note: (B) denotes baseline alloy

## Results to Date:

### Microstructural Characterization:

Alloy 8090 (Al-2.45Li-1.2Cu-0.7Mg-0.1Zr)

#### Matrix:

- $\delta'$  ( $\text{Al}_3\text{Li}$ ).....spherical, homogeneously nucleated
- $S'$  ( $\text{Al}_2\text{CuMg}$ ).....needle shaped, heterogeneously nucleated
- $T_1$  ( $\text{Al}_2\text{CuLi}$ ).....plate shaped, heterogeneously nucleated

#### Boundaries:

- $T_2$  ( $\text{Al}_6\text{CuLi}_3$ ).....globular, grain and subgrain boundaries
- $S'$  ( $\text{Al}_2\text{CuMg}$ ).....subgrain boundaries
- $T_1$  ( $\text{Al}_2\text{CuLi}$ ).....subgrain boundaries

Zn additions to alloy 8090 decrease the solubility of Li, Cu and Mg in Al and depending on the relative amount of solute present

#### Matrix:

- increased v/o ..... $\delta'$  ( $\text{Al}_3\text{Li}$ )
- ..... $S'$  ( $\text{Al}_2\text{CuMg}$ )

#### Boundaries:

- Predominant boundary phase changes from  $T_2$  to  $T$  ( $\text{Mg}_{32}(\text{Al,Cu,Zn})_{49}$ ) as Zn content increases

### Microstructure:

- Zn additions (from 0.2 to 1.36 w/o) dramatically influence precipitation
- Characterization methods:
  - TEM with CBED, EDS and SAD
  - DSC and solution potential measurements

**Alloy A** • **Low Zn** ( $\sim 0.2$  w/o), **low solute** ( $\text{Li} + \text{Cu} + \text{Mg} = 3.94$  w/o) **Sheet**  
• decreased boundary precipitation wrt 8090 baseline  
• S' not qualitatively affected

**Alloy B** • **Low Zn** ( $\sim 0.2$  w/o), **high solute** ( $\text{Li} + \text{Cu} + \text{Mg} = 4.32$  w/o) **Plate**  
• enhanced boundary precipitation wrt 8090 baseline  
• little apparent change in matrix precipitation  
• improved S-T TYS, UTS and % el. values

**Alloy C** • **Medium Zn** ( $\sim 0.6$  w/o), **low solute** ( $\text{Li} + \text{Cu} + \text{Mg} = 3.60$  w/o) **Sheet**  
• boundary precipitation less than 8090 baseline (fewer  $\delta'$ -FZ's)  
• S' enhanced

**Alloy D** • **High Zn** ( $\geq 1.0$  w/o), **low solute** ( $\text{Li} + \text{Cu} + \text{Mg} = 3.68$  w/o) **Sheet**  
• coarse intermetallic T phase precipitates on grain and subgrain boundaries upon artificial aging  
• S' enhanced

**Alloy E** • **High Zn** ( $\geq 1.0$  w/o), **high solute** ( $\text{Li} + \text{Cu} + \text{Mg} = 4.26$  w/o) **Plate**

**Alloy F** ( $\text{Li} + \text{Cu} + \text{Mg} = 4.42$  w/o)

**Alloy G** ( $\text{Li} + \text{Cu} + \text{Mg} = 4.44$  w/o)

- coarse T phase evident on grain boundaries at T3 condition (*inappropriate SHT practice employed*)
- S' enhanced
- TYS, UTS improved, % el. and  $K_{IC}$  degraded with magnitude of degradation dependent on Mg content and total solute supersaturation
- $\delta$  (AlLi) promoted with Zn additions (seen only at grain interiors)

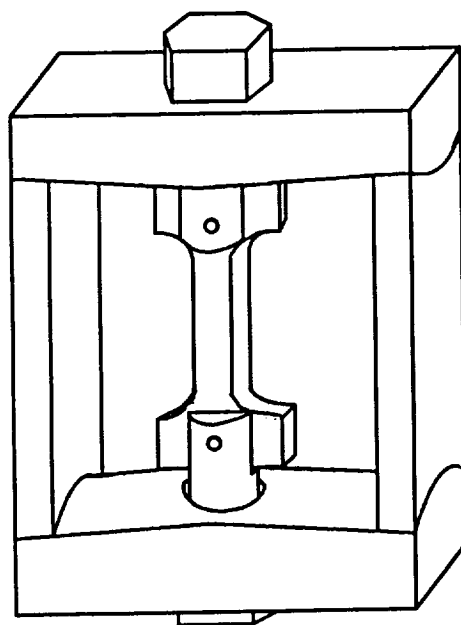
## **II. SUMMARY OF PREVIOUS WORK**

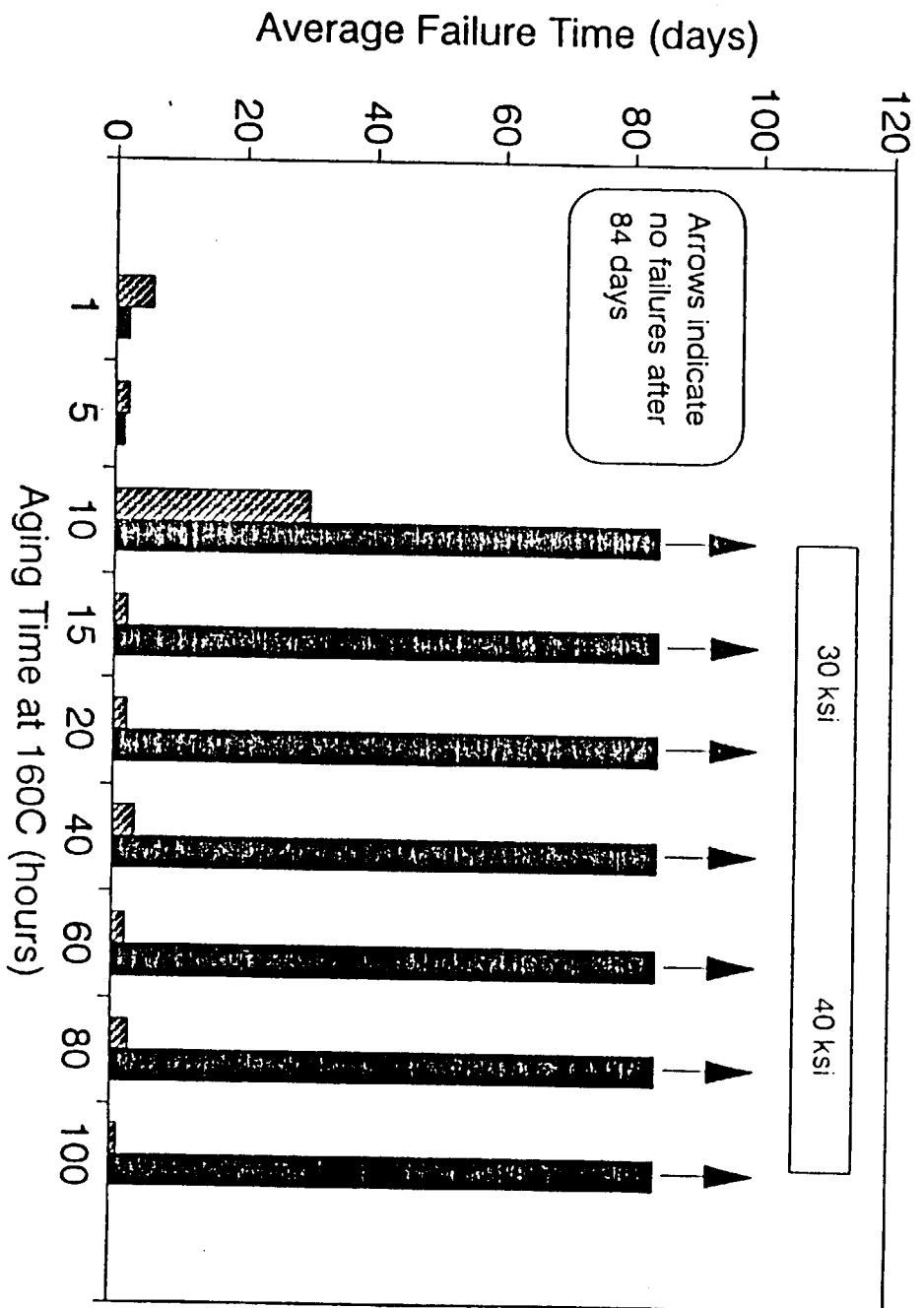
### **B. TEST PROCEDURES AND RESULTS**

The initial SCC screening of the AA 8090 and AA 8090+Zn alloys was done by employing an ASTM G44 alternate immersion time to failure test. The results of these tests are summarized in the next four slides.



To assess the aqueous EAC susceptibility,  
Alternate immersion time-to-failure tests  
were performed

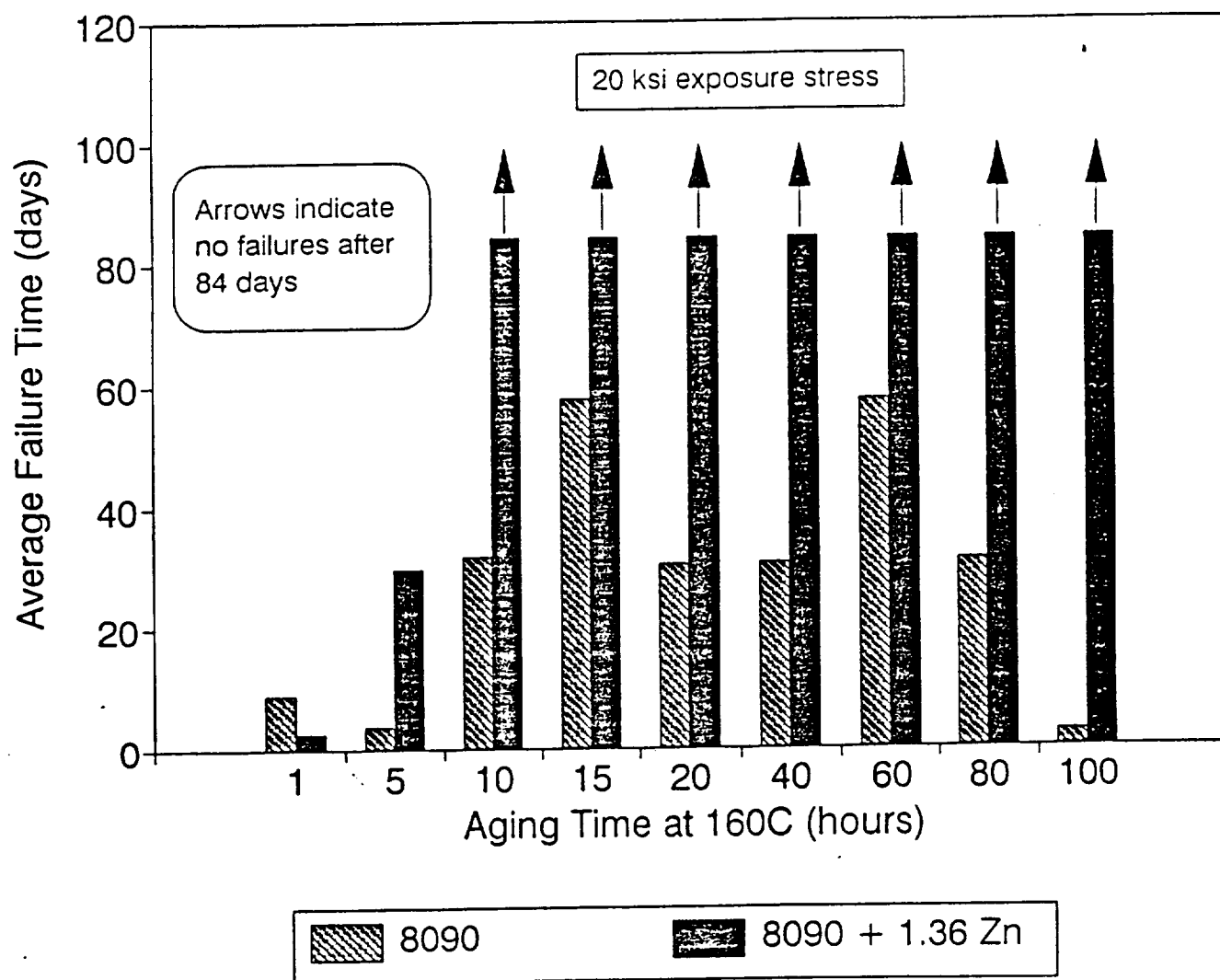




8090

8090 + 1.36 Zn

ALLOY F



ALLOY F

**AI Results: Al-Li-Cu-Mg AA8090 and Al-Li-Cu-Mg-Zn Al1**

Alloy	Temper	138 MPa		207 MPa	
		F/N	Days	F/N	Days
Al-Li-Cu-Mg (AA8090)	UT1	3/3	3,3,5	3/3	1,2,3
	UT3	2/3	3,5	3/3	3,3,4
Al-Li-Cu-Mg-Zn	UT1	3/3	2,2,3	3/3	1,2,2
	UT3	0/3	----	0/3	---

### **III. RECENT WORK**

#### **A. TEST PROCEDURES**

- **The Aqueous Slow Rising Load Method**

**Method was performed to assess the response of the alloy to the application of a rising stress intensity in an aqueous chloride environment.**

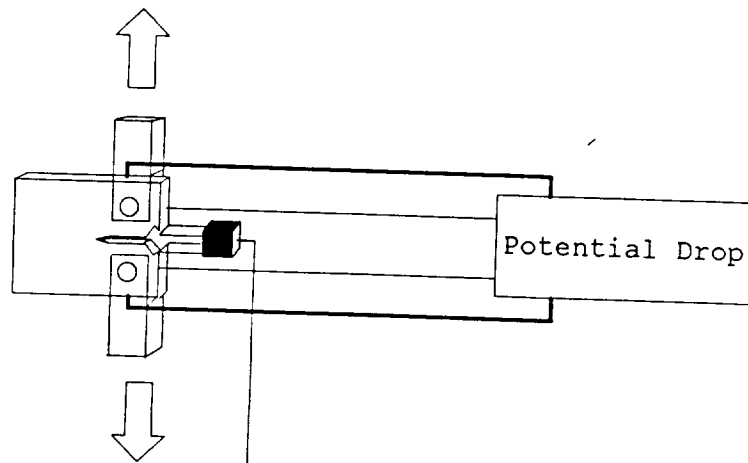
**Testing was performed with an MTS 810 servohydraulic machine in crack opening displacement control (strain control) at a constant CMOD rate of:**

$$8.4 \times 10^{-7} \text{ mm/sec.}$$

$$(\approx 7.0 \times 10^{-7} \text{ mm/sec.})$$

**Load Line Displacement**

## Aqueous Slow Rising Load Testing



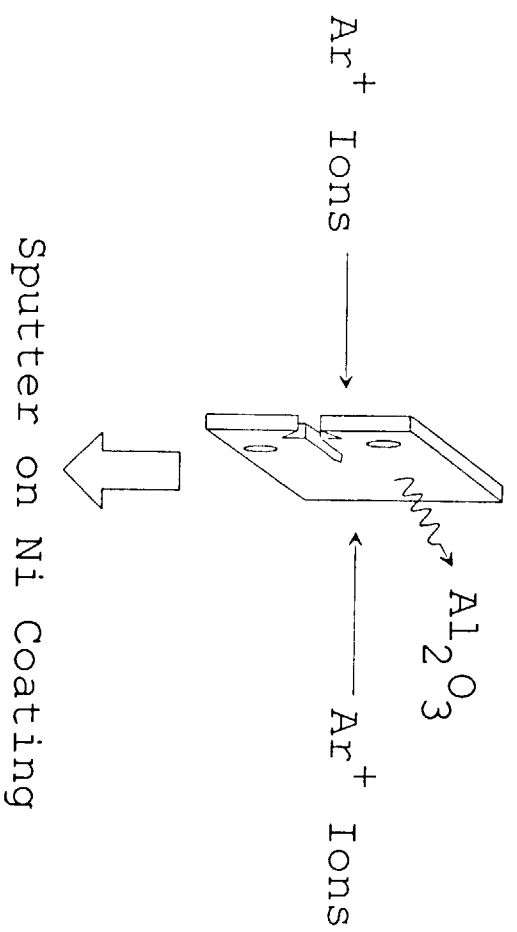
### **III. RECENT WORK**

#### **A. TEST PROCEDURES**

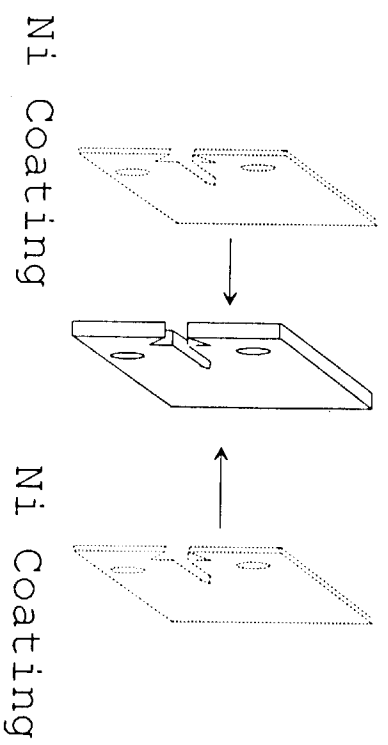
- **Hydrogen Charging Experiments**

**Experiments to determine the effects of hydrogen charging on resultant mechanical properties were developed by John Scully and Steve Smith. A schematic description of this procedure follows in the next two figures.**

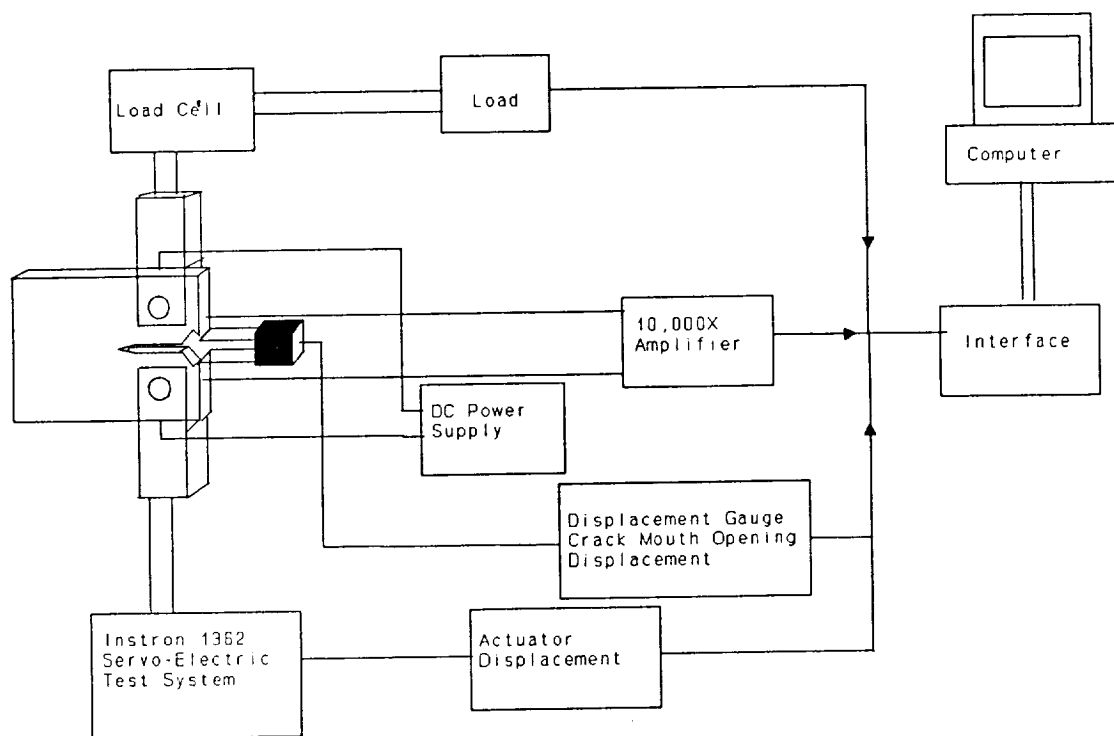
## Sputter off Oxide Layer



## Sputter on Ni Coating







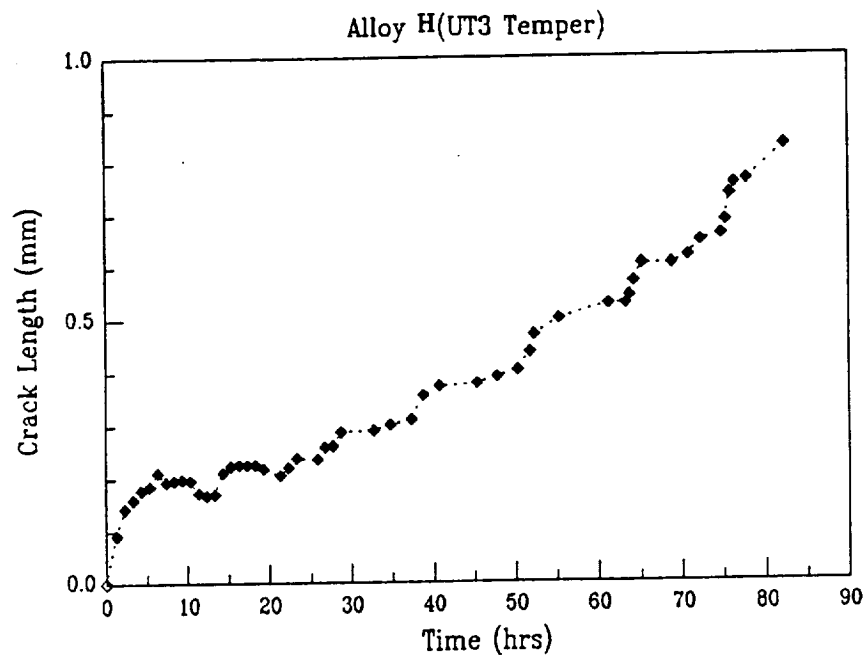
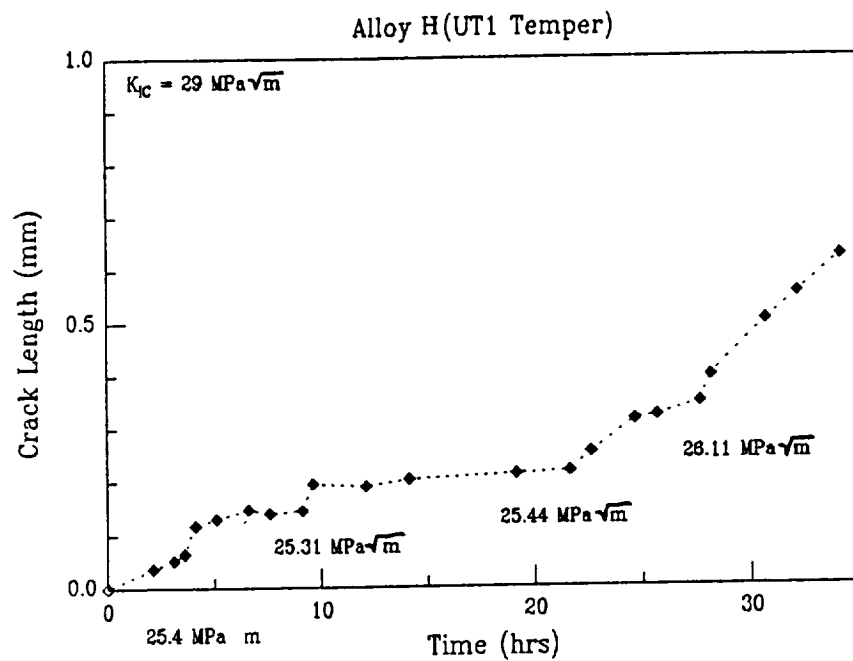
### **III. RECENT WORK**

#### **B. RESULTS**

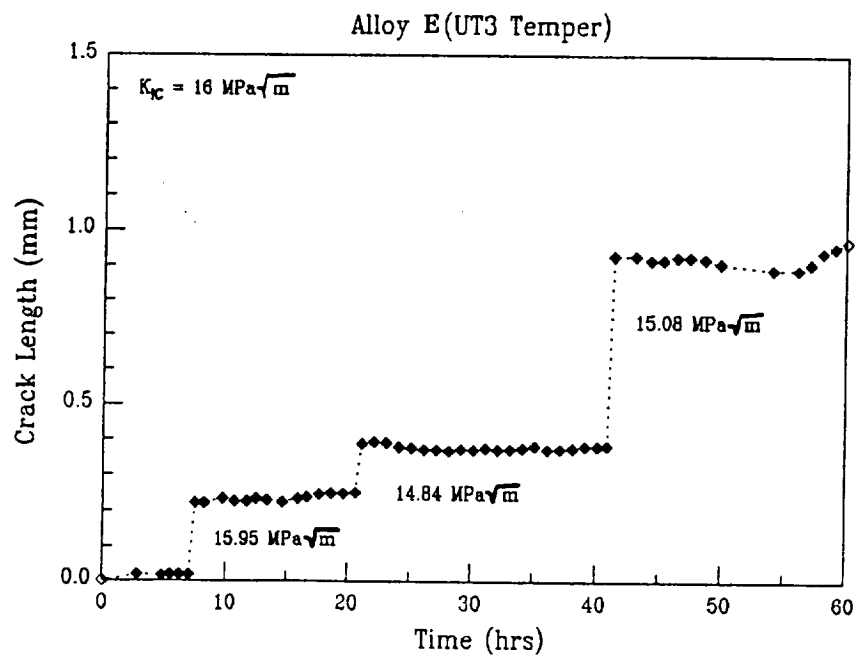
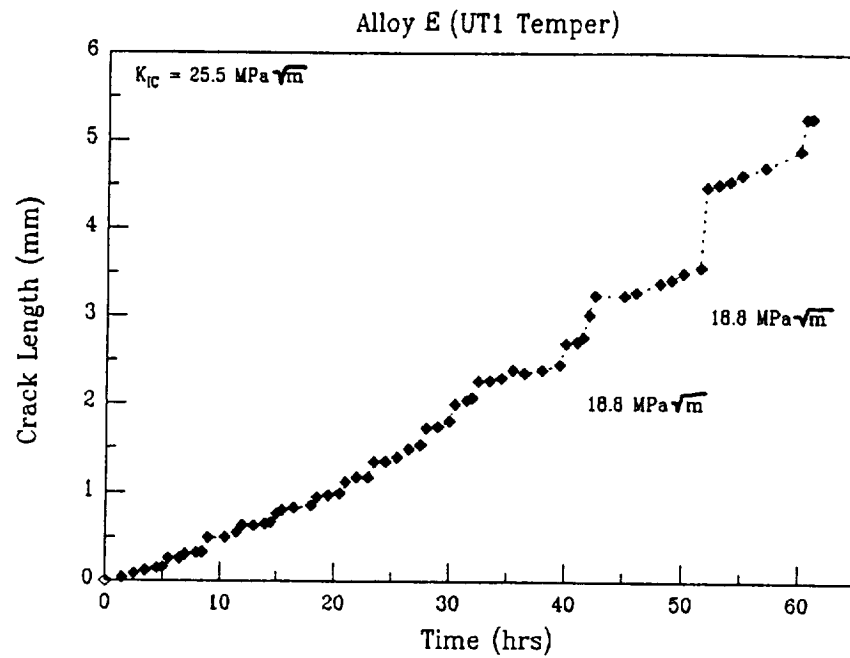
**The results of the slow rising load aqueous tests and the hydrogen charging tests are given in the next four slides.**

**A fifth slide compares the combined results of the two methods.**

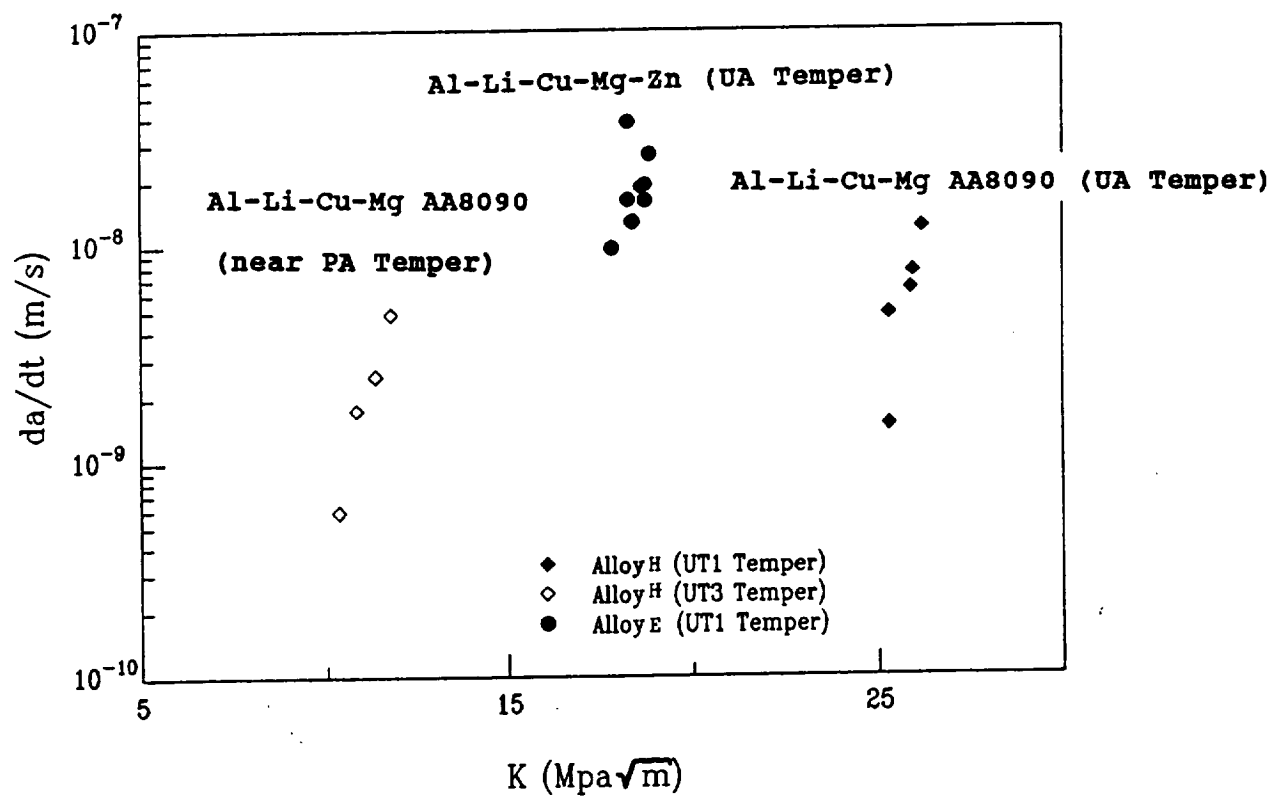
# Aqueous Slow Rising Load Tests: Al-Li-Cu-Mg AA8090



# Aqueous Slow Rising Load Tests: Al-Li-Cu-Mg-Zn Alloy



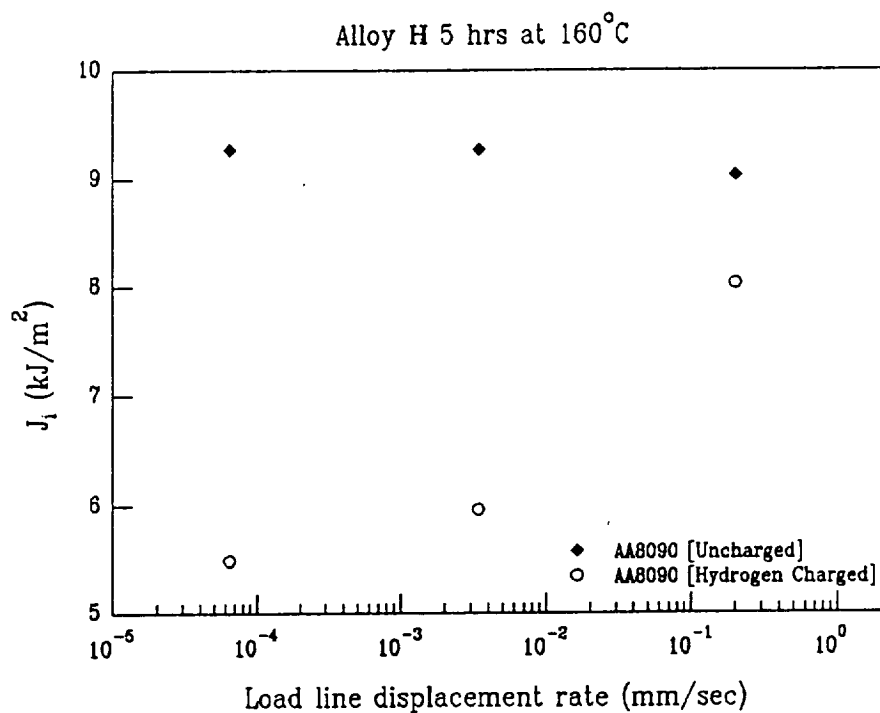
**Aqueous Slow Rising Load Tests: Al-Li-Cu-Mg AA8090  
& Al-Li-Cu-Mg-Zn Alloys**



**Aqueous Slow Rising Load Tests: Al-Li-Cu-Mg AA8090  
& Al-Li-Cu-Mg-Zn Alloys**

Alloy	TTF @ 138 MPa	Peak $da/dt$ m/s	$K_{th}$ MPa/m
Al-Li-Cu-Mg-Zn-UA	2,2,3 days	$3.8 \times 10^{-8}$	15
Al-Li-Cu-Mg-UA (AA8090)	3,3,5 days	$1.2 \times 10^{-8}$	24
-PA	3,5 days	$4.8 \times 10^{-9}$	9

# Hydrogen Charging Results: Al-Li-Cu-Mg AA8090

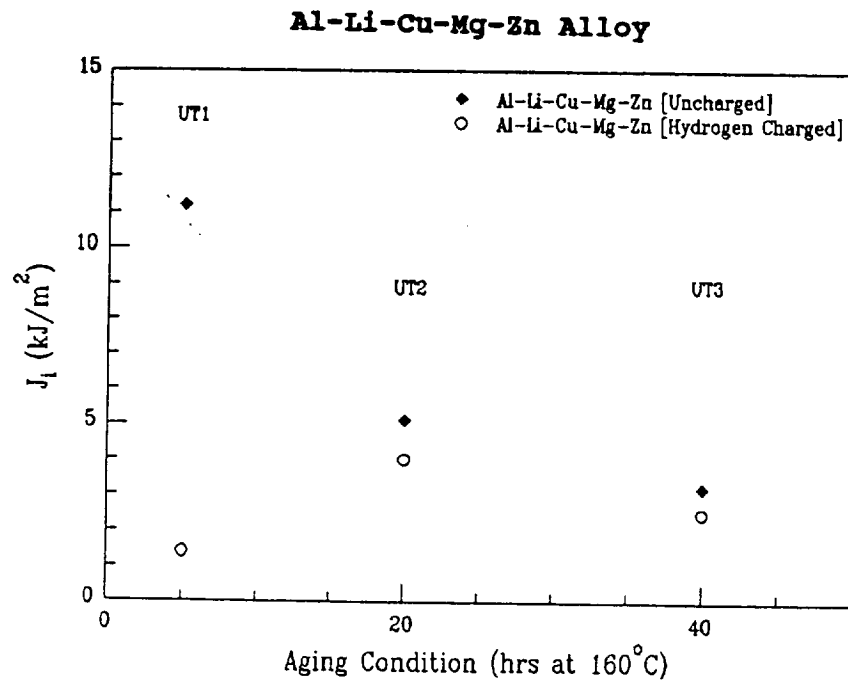
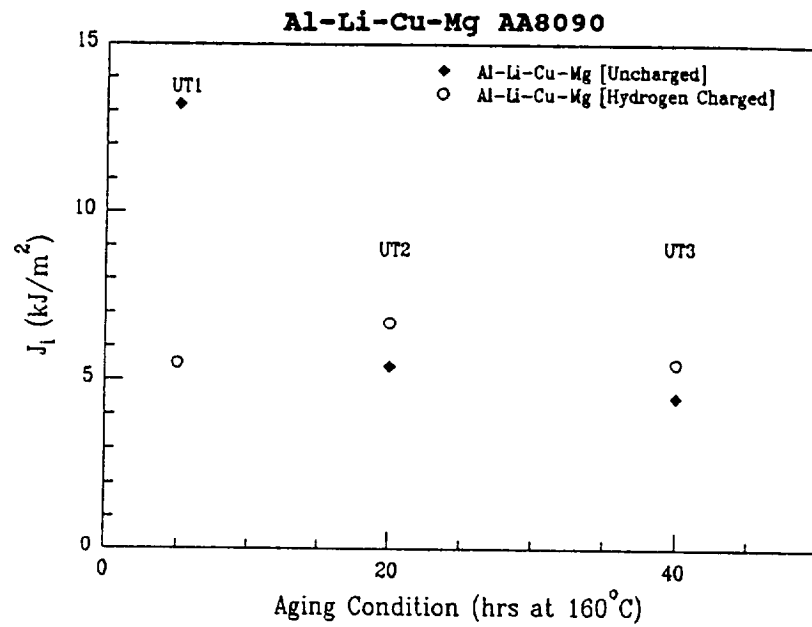



---

Alloy	v <sub>ll</sub> (mm/sec)	Uncharged	Charged
		$J_i$ (kJ/m <sup>2</sup> )	$J_i$ (kJ/m <sup>2</sup> )
Al-Li-Cu-Mg	$6.4 \times 10^{-5}$	9.27	5.49
AA8090	$3.4 \times 10^{-3}$	9.27	5.96
	$2.0 \times 10^{-1}$	9.03	8.03

---

# Hydrogen Charging Results: Al-Li-Cu-Mg AA8090 & Al-Li-Cu-Mg-Zn Alloys





# Comparison of Hydrogen Charging Results and Aqueous Slow Rising Load Experiments

		Hydrogen Charging Results		Aqueous Slow Rising Load Tests
Alloy	Temper	<u>Uncharged</u> $K_I$ (MPa/m)	<u>Charged</u> $K_I$ (MPa/m)	Aqueous $K_{th}$ (MPa/m)
Al-Li-Cu-Mg (AA8090)	UA	32.2	20.8	24
	near PA	18.8	20.8	9
Al-Li-Cu-Mg-Zn	UA	29.7	10.5	14
	near PA	15.9	14.0	n/a
SL orientation				

#### **IV. SUMMARY AND CONCLUSIONS**

- **Zinc additions alter the boundary phase precipitates and the precipitation sequence of AA 8090.**
- **Suitable mechanical properties can be retained for low to medium zinc additions with appropriate SHT procedures.**
- **Zinc additions result in significant improvement in the SCC resistance of intermediate (UA) tempers based on ASTM-AI tests.**
- **Slow rising load testing of susceptible and resistant tempers of AA 8090 and AA 8090 plus zinc indicate that substantial crack growth occurred in the susceptible tempers.**
- **In general, hydrogen charging studies of nickel coated samples indicated a degradation of the initiation toughness  $J_i$  of the susceptible tempers of both AA 8090 and AA 8090 plus zinc.**
- **Although Region II behavior (of crack growth rate vs.  $\Delta K$ ) was not observed in the aqueous slow rising load tests, for the susceptible tempers, the maximum crack growth rates seemed to be consistent with time to failure data.**

**The summary of these findings indicates that when AA 8090 is properly alloyed with small ( $\sim 1$  w/o) amounts of zinc, satisfactory mechanical properties are retained and the alloy, when aged to a suitable temper, is resistant to premature failure under the conditions of alternate immersion, slow rising load SCC tests, and extensive hydrogen charging.**



**Project #7     Hydrogen Interactions in Aluminum-Lithium Alloy 2090 and Selected Model Alloys**

S.W. Smith and J.R. Scully

**Objective**

The role hydrogen plays in the environmentally assisted cracking of aluminum-lithium alloys has not been fully established. This issue must be addressed since hydrogen environmentally assisted cracking (HEAC) is an important issue concerning alloys intended for utilization in advanced aerospace applications. To date the hydrogen absorption, internal transport, trapping and resultant effects on mechanical properties have not been characterized for these alloys. We seek to develop a fundamental understanding of the effects of dissolved and trapped hydrogen on the mechanical properties of selected Al-Li-Cu-X alloys. In order to reach this goal we will study the behavior of alloy 2090.

We have established three major goals in this study. We propose to (a) distinguish HEAC from aqueous dissolution controlled EAC, (b) correlate internal hydrogen embrittlement (IHE) with mobile and trapped hydrogen concentrations, and (c) identify significant trap sites and hydride phases (if any do exist). The ultimate goal of this project is to develop deterministic models which define the effect of absorbed hydrogen on the mechanical properties of aluminum lithium alloys.

**Current Status**

The research to be conducted has been separated into three major phases (a) hydrogen analysis of electrochemically pre-charged samples, (b) examination of mechanical properties under the influence of absorbed hydrogen, and (c) correlation of hydrogen trapping analysis results with mechanical properties. Over the last reporting period research has been conducted on the analysis of absorbed hydrogen with the use of thermal desorption spectroscopy (TDS) and the effects of absorbed hydrogen on the mechanical properties of alloy 2090. Mechanical tests were performed on hydrogen charged and uncharged materials in three different tempers, as well as four unique microstructures. The alloys studied consisted of one commercially available unrecrystallized sheet product and three model recrystallized sheet products of varying grain size. Continuous extension rate testing was performed on the unrecrystallized material, while J-integral resistance curve testing was

performed on all four of the alloys. In all cases the alloys were tested in both the charged and uncharged conditions. The charging is performed prior to mechanical testing.

By using pre-charged specimens and performing tests in a dry environment we are able to separate the effects of hydrogen induced cracking from any operative aqueous dissolution mechanisms, which often mask HEAC when tests are performed in aqueous solutions.

Work on the construction of a thermal desorption spectroscopy unit at the university has been completed during the last reporting period and measurements have been conducted on pure aluminum as well as the commercial 2090 product. Several other researchers who have attempted to make desorption measurements of absorbed hydrogen in aluminum and aluminum-lithium alloys in the past have not met with great success due to the relatively high hydrogen partial pressures present in their systems and due to the fact that the measurements are often performed with total pressure devices that are not mass sensitive. The TDS system that we have constructed is capable of reaching hydrogen partial pressure below  $1 \times 10^{-9}$  torr and uses a quadrupole mass spectrometer capable of distinguishing hydrogen from other desorbed gases.

### Recent Findings

The mechanical tests that have been performed to date clearly indicate internal hydrogen embrittlement (IHE) of alloy 2090 in the T3 (naturally aged) and underaged condition (T3 + 5 hrs. @ 160°C). IHE is found for both tempers for continuous extension rate testing by examining the effect of absorbed hydrogen on elongation to failure, reduction in area and fracture energy, in both the LT and TL orientations. The J-integral tests have shown a significant drop in the  $J_{\text{initiation}}$  for the underaged temper, when there is a favorable high angle grain boundary path for crack propagation. A favorable path is present in commercial sheet tested in the TL orientation as well as fine grain recrystallized LT. No reduction in  $J_i$  was found for specimens tested in the T8 temper. The trends found through J-integral testing roughly follow the results of alternate immersion SCC testing.

TDS tests have resulted in very reproducible results for pure aluminum as well as 2090-T3. The experiments run to date show the presence of three major trapping sites in the T3 temper and have allowed us to determine approximate total hydrogen concentrations.

### Future Work

To date the J-integral results presented consist of only one test for the UA and PA tempers. No tests have been performed on samples in the T3 temper. More testing will be done in order to have duplicate tests for all the materials (heat treatments and orientations) being studied. In an attempt to obtain higher hydrogen concentrations in the test specimens, potentiostatic charging will be performed at higher cathodic overpotentials as well as for longer time periods. Exact hydrogen levels for these tests will be evaluated with the use of the TDS system.

In addition to using the TDS system to evaluate total absorbed hydrogen levels, we will try to determine the trapping sites present in these materials. A complete trap site analysis will be conducted with the use of some model binary Al-Cu and Al-Li alloys produced at UVA and Alcoa Technical Center. These alloys will be processed in order to vary the grain size, cold work and secondary phases present. These microstructural variations will allow us to identify potential trapping sites.

### List of Slides

1. Title
2. Objectives
3. Compositions for the two variants of 2090 being studied. (Table 1)
4. Mechanical data for the four different 2090 microstructures studied. (Table 2)
5. Composite optical micrograph of 2090 - T3 alloy being used. (Figure 1)
6. Testing procedure followed for mechanical tests. (Figure 2)
7. Continuous extension rate test results for 2090-T3-LT. specimens were charged at  $-1 V_{SCE}$  in 0.25 M  $Na_2SO_4$  pH 7 for various times. (Figure 3)
8. Results for CERT testing of unrecrystallized 2090. All testing was performed at a strain rate of  $2.5 \times 10^{-6} \text{ sec}^{-1}$ . (Table 3)
9. J-R curve generated for charged and uncharged 2090 CT specimens. The specimens are underaged and tested in the LT orientation. Results for fine grain recrystallized specimens are shown in Figure 4a and the results for the unrecrystallized material are represented in Figure 4b. (Figure 4a,b)

10. Results for  $J_{\text{initiation}}$  values obtained from J-integral testing for all 2090 alloys studied. (Table 4)
11. SEM micrographs for alloy C in the UA temper. Micrographs taken in the region of high constraint produced during a J-Integral test. The figure on the left is charged and the one on the right is uncharged. (Figure 5a, b)
12. Conclusions for mechanical testing.
13. Schematic drawing of the thermal desorption spectroscopy system, being used for hydrogen analysis. (Figure 6)
14. Hydrogen partial pressure vs. time curve. Specimen is unrecrystallized 2090-T3. The furnace was programmed for a 5°C/min ramp rate. (Figure 7)
15. Mass balance equations used to solve for desorption rate and absorbed hydrogen concentration during a thermal desorption experiment.
16. Hydrogen desorption rate vs. time curve. Desorption rate was calculated from the partial pressure data shown in Figure 7. Specimen is unrecrystallized 2090-T3. (Figure 8)
17. Hydrogen desorption rate vs. time curves. The specimen used to compile the data shown in Figures 7 and 8, was removed from the vacuum system after one desorption spectra was conducted. The surface was prepared in the same manor as before the first bake and then returned to the TDS system. The second bake is performed to determine how much adsorbed hydrogen is being detected and to also make sure that all the hydrogen was released during the first bake. (Figure 9)
18. Binding energy calculations used to solve trap binding energies when performing thermal desorption experiments.
19. Hydrogen desorption rate vs. time curve, showing the points of maximum hydrogen desorption rate. (Figure 10)
20. Hydrogen desorption rate vs. temperature curves. All data is for 2090-T3 specimens charged in the same manner. The three curves represent programmed ramp rates of 5, 7.5 and 10 °C/min. (Figure 11)
21. Results of binding energies obtained for unrecrystallized 2090-T3 alloy. The data obtained for peak one did not result in a good fit and is therefore not supplied. (Table 5)
22. Conclusion for thermal desorption spectroscopy.
23. Future work



# **Hydrogen Interactions in Aluminum-Lithium Alloys and Hydrogen Embrittlement of AA2090**

Stephen W. Smith

and

John R. Scully

University of Virginia

Department of Materials Science and Engineering

Center for Electrochemical Sciences and Engineering

Charlottesville, VA 22903

Sponsors:

NASA Langley Research Center

Virginia Center for Innovative Technology

Alcoa Technical Center

## **Objective**

We seek to develop a fundamental understanding of the effects dissolved and trapped hydrogen have on the mechanical properties of selected Al-Li-Cu-X alloys. In order to reach this goal work will be centered around three major areas: 1) distinguish hydrogen induced EAC from aqueous dissolution controlled EAC, 2) correlate hydrogen induced EAC with mobile and trapped hydrogen concentrations, and 3) identify significant trap sites and hydride phases (if any).

### Alloys Studied

Table 1: Chemical compositions of alloys being studied.

	Cu (wt. %)*	Li (wt. %)*	Zr (wt. %)*	Al
Unrecrystallized Alloy D	2.56	2.15	0.12	bal.
Recrystallized Alloys A-C	2.27	2.05	0.09	bal

\* Cu and Zr contents of alloys determined by quantometer analysis.

# Li contents determined by atomic absorption analysis.

Table 2: Mechanical properties of alloys being studied

Alloy	Temper	Product Form	Grain Dimensions ( $\mu\text{m}$ )	$\sigma_{ys}$ (Mpa)	$\sigma_{UTS}$ (MPa)
A	UA	Recrystallized	1200 x 1100 x 250	296	393
	PA			379	434
B	UA	Recrystallized	800 x 800 x 100	241	379
	PA			400	490
C	UA	Recrystallized	30 x 30 x 20	303	421
	PA			400	496
D	T3	Unrecrystallized	4400 x 600 x 10	255	303
	UA			296	476
	PA			434	572

Figure 1: Optical micrograph of 2090-T3 unrecrystallized.

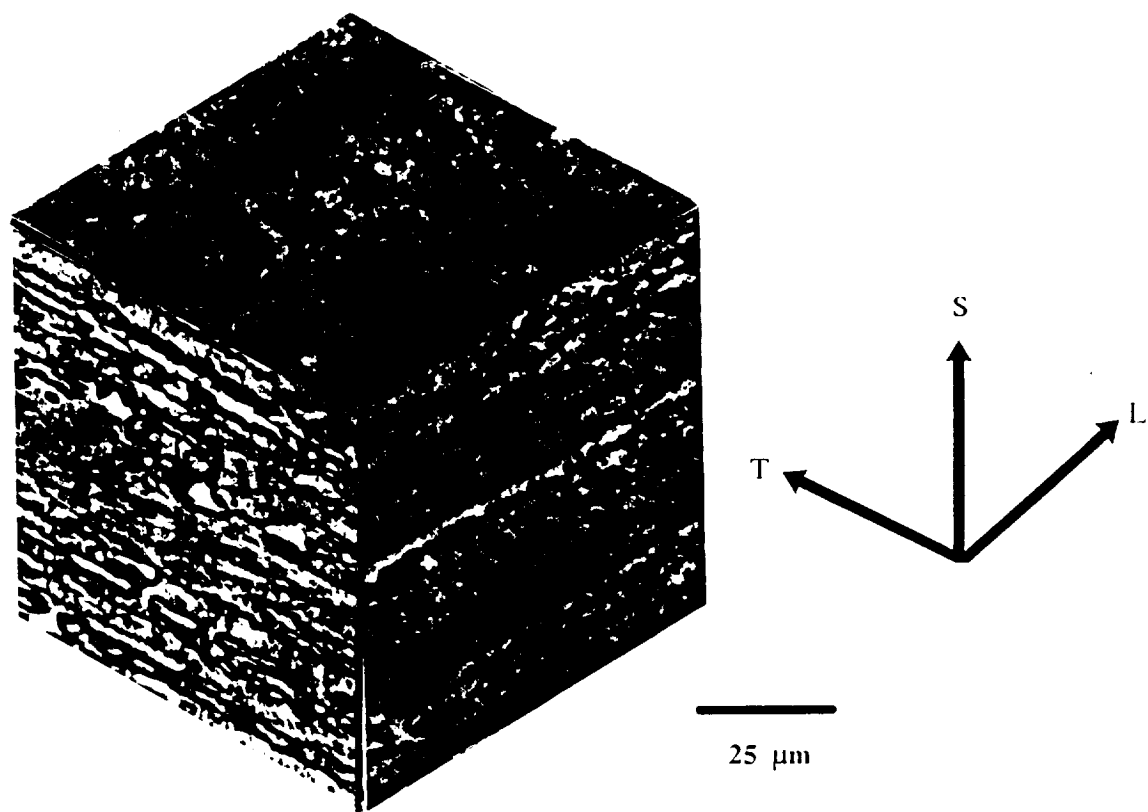


Figure 2: Testing procedure used for mechanical testing.

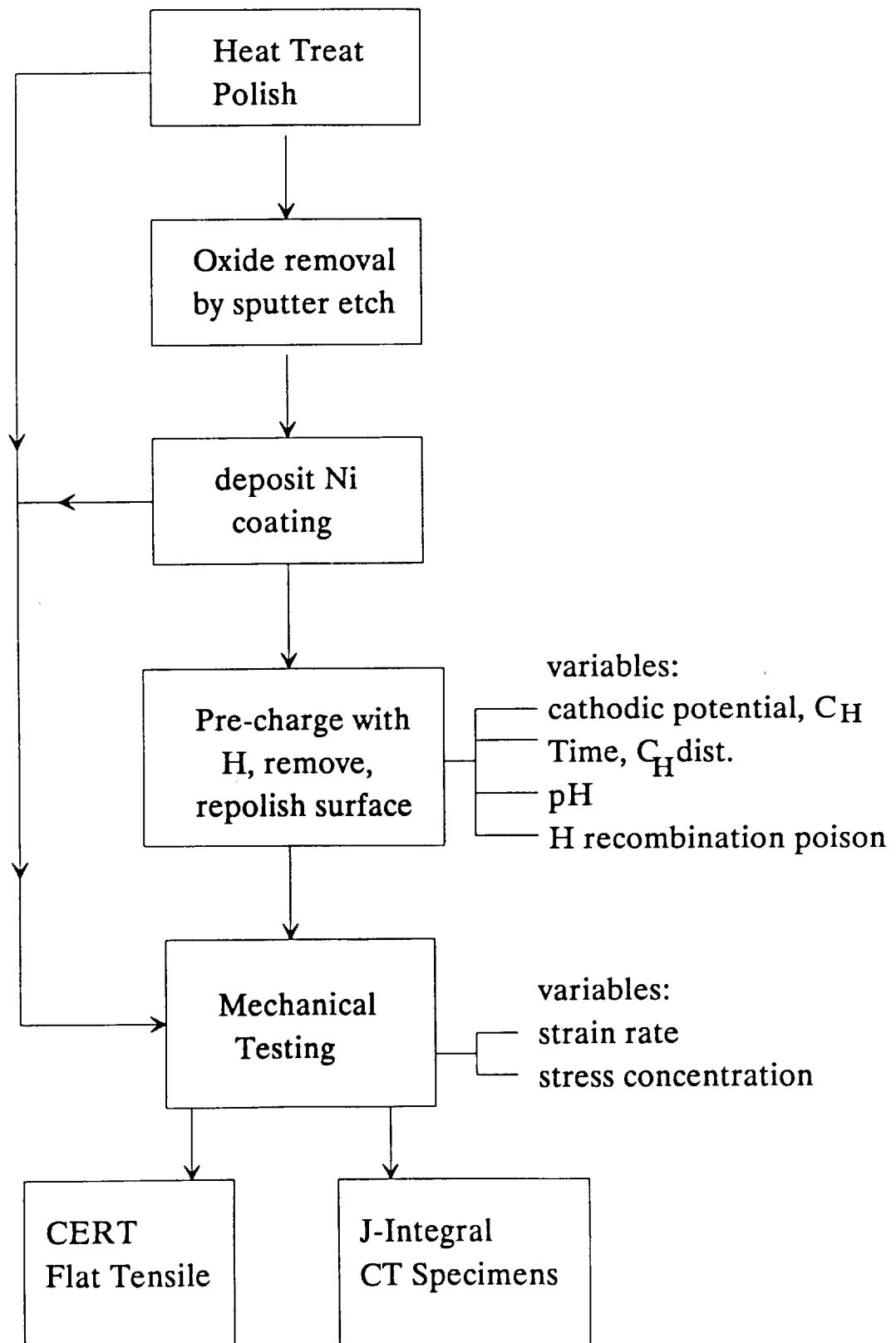
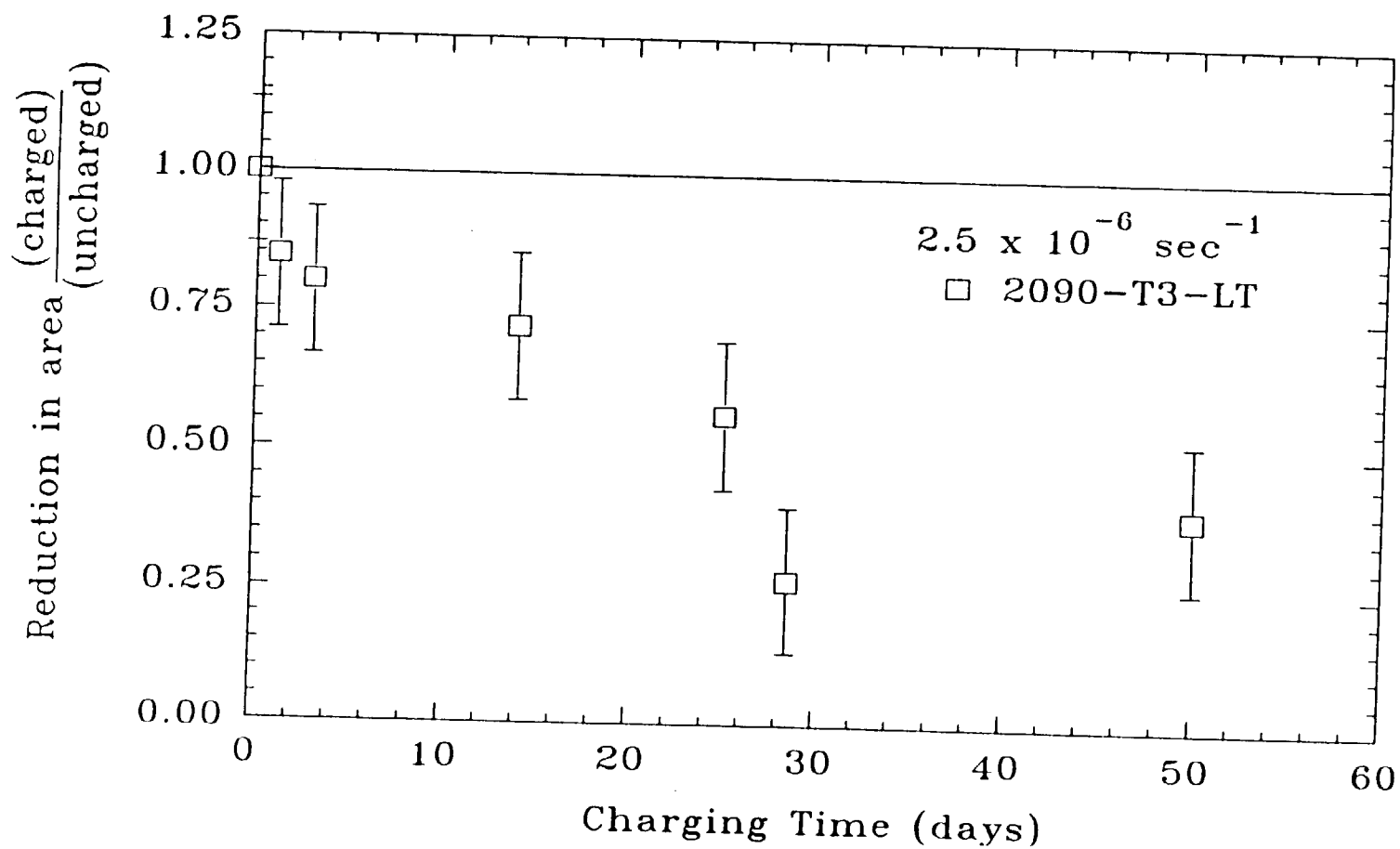


Figure 3. Continuous extension rate test results for 2090-T3-LT specimens charged at  $-1\text{ V}_{\text{SCE}}$ .



**Table 3: CERT RESULTS**  
**Unrecrystallized 2090 Sheet**

Temper	Orientation	Charging Condition	Reduction in Area (% loss)	Fracture Mode
T3	TL	Uncharged	27.98 <sup>#</sup>	transgranular shear
		28 days @ -1V <sub>SCE</sub>	17.49 <sup>#</sup>	TGS + intersubgranular
T3	LT	Uncharged	19.97 <sup>#</sup>	transgranular shear
		28 days @ -1V <sub>SCE</sub>	9.63 <sup>#</sup>	hydrogen affected TGS
UA	TL	Uncharged	20.68 <sup>*</sup>	transgranular shear
		28 days @ -1V <sub>SCE</sub>	13.85 <sup>*</sup>	TGS + intersubgranular
UA	LT	Uncharged	13.35 <sup>*</sup>	transgranular shear
		28 days @ -1V <sub>SCE</sub>	11.94 <sup>*</sup>	hydrogen affected TGS
PA	TL	Uncharged	32.27 <sup>#</sup>	transgranular shear
		28 days @ -1V <sub>SCE</sub>	38.40 <sup>#</sup>	transgranular shear
PA	LT	Uncharged	16.30 <sup>#</sup>	transgranular shear
		28 days @ -1V <sub>SCE</sub>	14.85 <sup>#</sup>	transgranular shear

All specimens charged in 0.25 M Na<sub>2</sub>SO<sub>4</sub> buffered to pH 7.

temper designations:

T3 - as received (solution heat treated, cold worked, naturally aged)

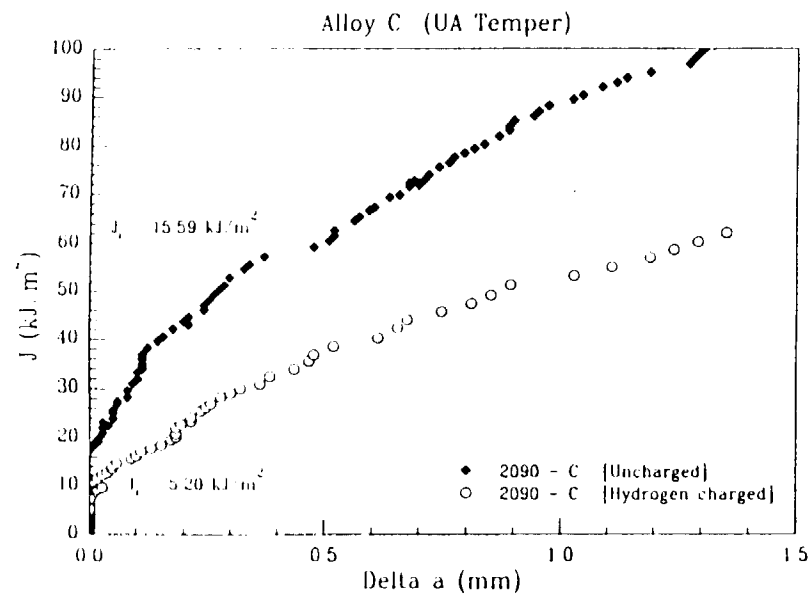
UA - T3 + 5 hrs. at 160°C

PA - T3 + 25 hrs. at 160°C

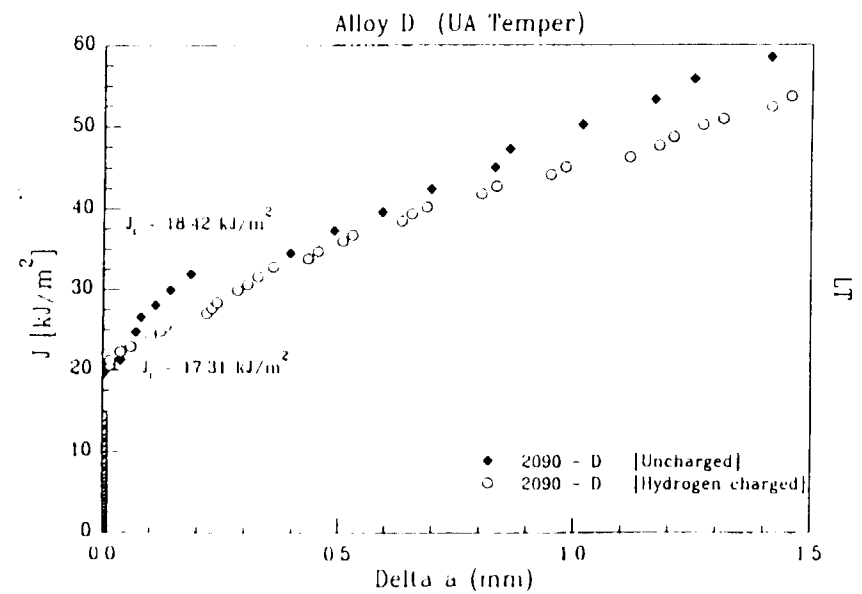
# - average of 3 specimens

\* - single specimen tested

Figure 4 a,b. J-R curves for underaged alloys charged and uncharged, tested in the LT orientation



4a) Alloy C  
(fine grain recrystallized)



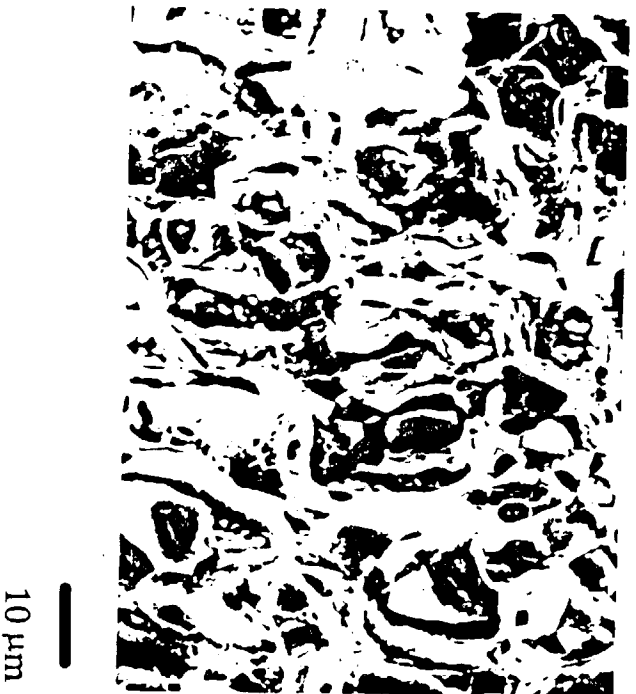
4b) Alloy D  
(Unrecrystallized)



**Table 4: Results of J-Integral Testing for 2090 alloys.**

Alloy (orientation)	Fracture Mode	$J_i(\text{kJ/m}^2)$			
		$U A_{\text{uncharged}}$	$U A_{\text{charged}}$	$P A_{\text{uncharged}}$	$P A_{\text{charged}}$
A (LT)	Transgranular	6.70	9.47	10.51	11.02
B (LT)	Transgranular + Intergranular	13.71	6.87	9.86	15.12
C (LT)	Intergranular	15.59	5.20	4.77	3.98
D (LT)	Transgranular + Intersubgranular	18.42	17.31	5.35	5.12
D (TL)	Transgranular + Intergranular	27.70	18.60	--	--

Figure 5 a, b. SEM micrographs of alloy C UA temper, a) charged with hydrogen and b) uncharged.



5a



5b

## **Conclusions: Mechanical Testing**

- AA 2090 is susceptible to Hydrogen Environmentally Assisted Cracking in the underaged and T3 tempers. This behavior agrees with alternate immersion testing of these alloys.
- HEAC correlates well with the favorable orientation of high angle grain boundaries with respect to the crack plane. The fine grain recrystallized (equiaxed) material was found to be the most susceptible material.
- Intergranular fracture processes were significantly degraded with hydrogen charging.
- $J_i$  was not significantly degraded upon charging when the operative fracture processes were transgranular shear and intersubgranular fracture.

Figure 6. Schematic of thermal desorption spectroscopy system

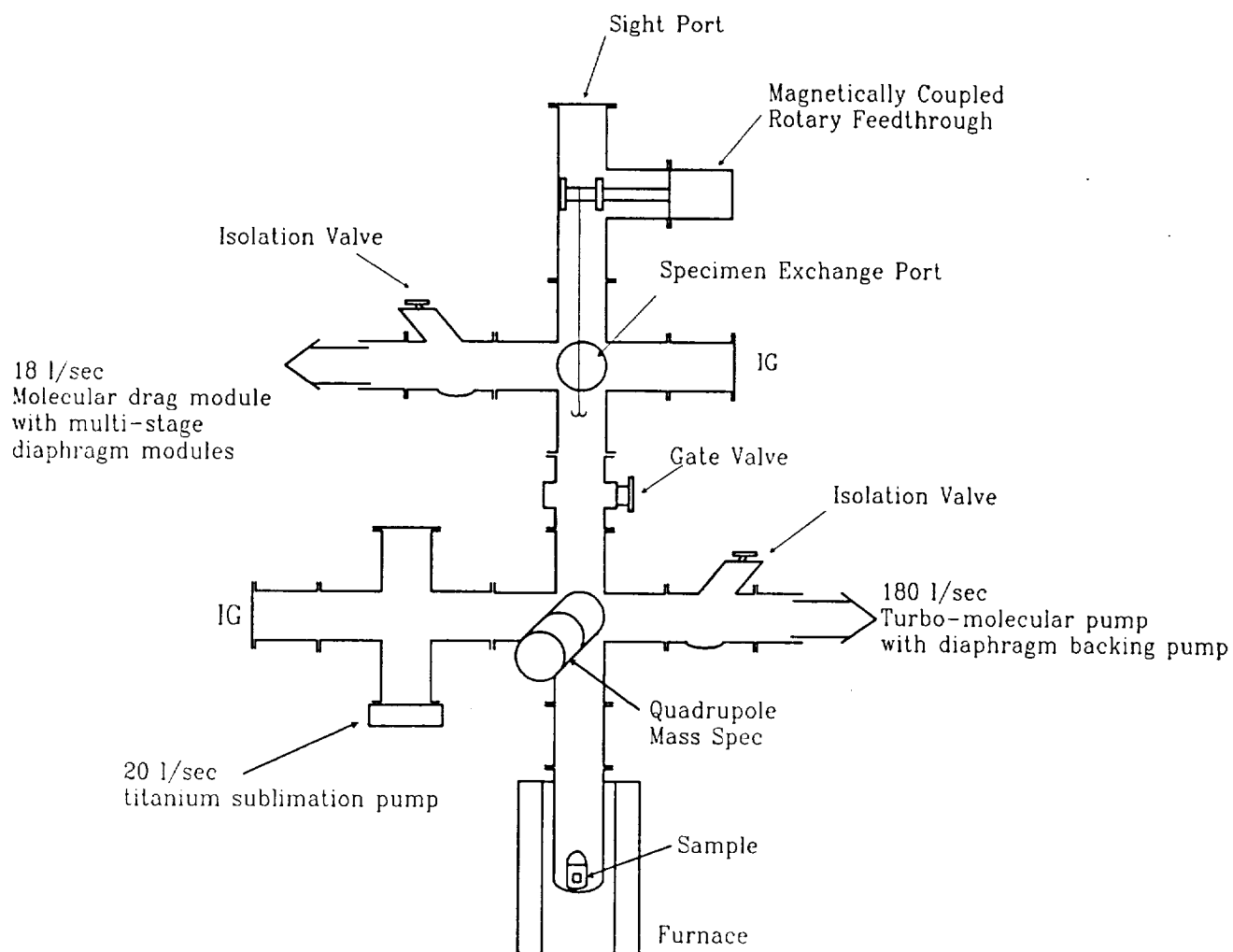
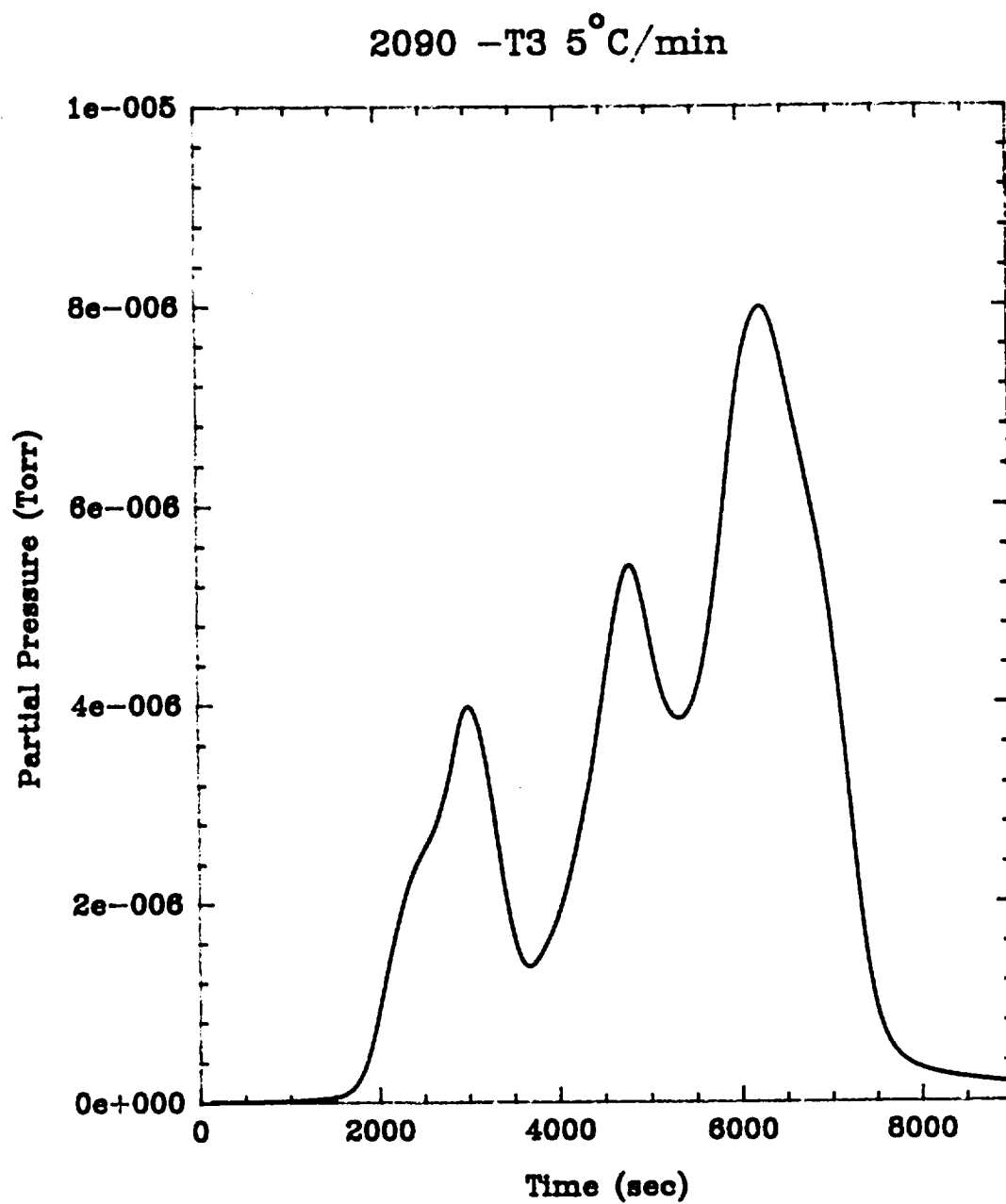


Figure 7. Hydrogen partial pressure vs. time curve for a charged 2090-T3 specimen tested at a ramp rate of 5°C/min.



## Mass Balance During Desorption Experiments

$$V \frac{dp}{dt} = F_d - F_r + L - Sp$$

where:

$V$  → Volume of analysis chamber (known)

$p$  →  $H_2$  partial pressure (measured)

$F_d$  → instantaneous desorption rate (solve)

$F_r$  → instantaneous re-adsorption rate ( $F_r \ll F_d$ )

$L$  → leak rate ( $L \ll F_d$ )

$S$  → pumping speed (known for  $H_2$ )

$$F_{d_{H_2}} = V \frac{dp_{H_2}}{dt} + S_{H_2} p_{H_2}$$

$$C_{H_2} = \int F_{d_{H_2}} dt$$

Figure 8. Hydrogen desorption rate vs. time curve for a charged 2090-T3 specimen tested at a ramp rate of 5°C/min.

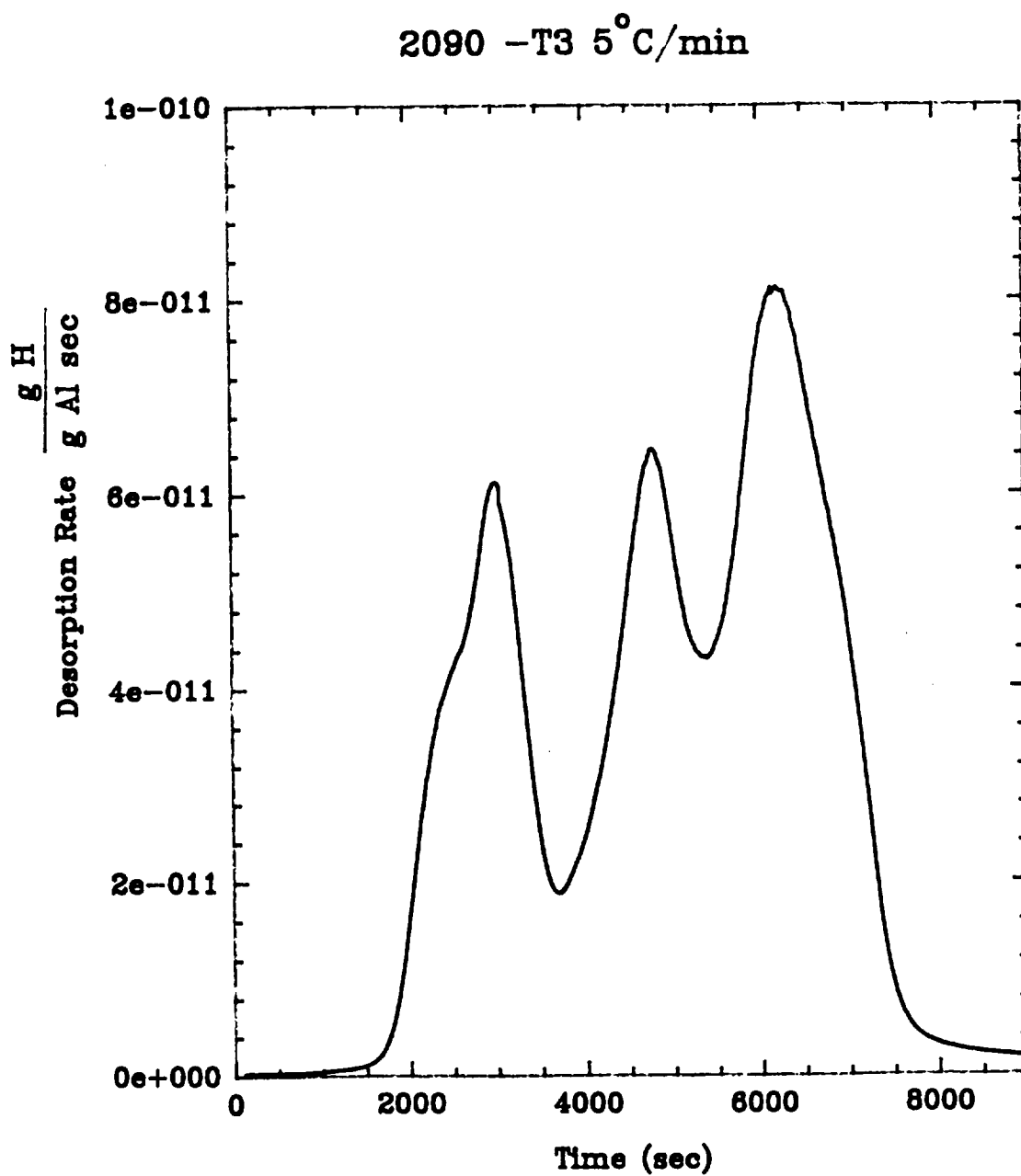
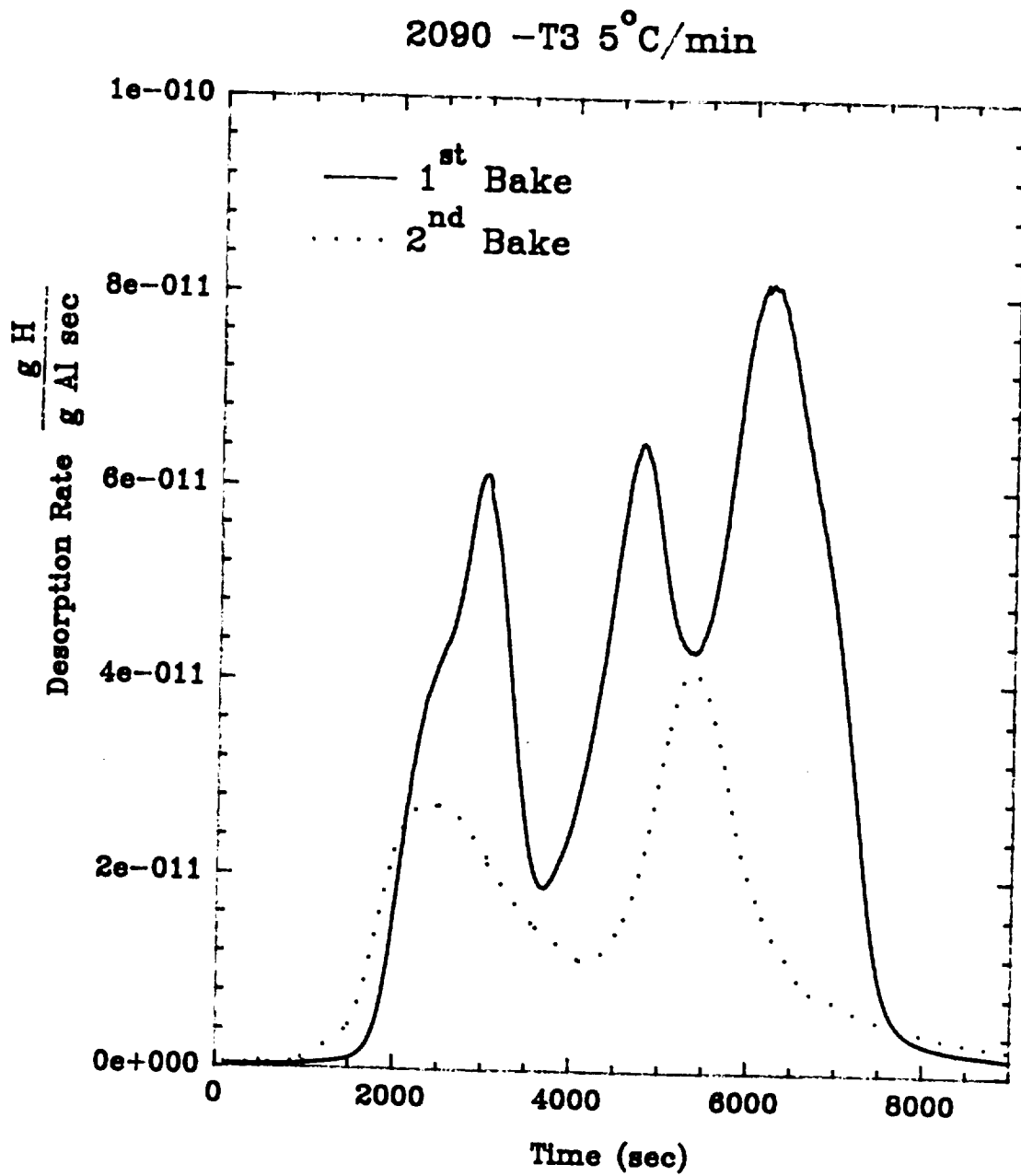


Figure 9. Hydrogen desorption rate vs. time curve for a charged 2090-T3 specimen tested at a ramp rate of 5°C/min. Data is shown for two separate desorption scans of the same specimen.





## Binding Energy Calculation

$$H_{trap} \rightleftharpoons \frac{E_B}{RT} + H_{abs} \rightleftharpoons H_{ads}$$

$$2 H_{ads} \rightleftharpoons H_2$$

$$\frac{dC(t)}{dt} = -\frac{e^{-E_B/N_0 kT}}{\tau_0} C(t)^2$$

$$\frac{d}{dt} \frac{d(X(t))}{dt} = -\left[ \frac{E_B}{RT^2} \frac{dT}{dt} - A \exp^{-E_B/RT} \right] [2(1-X(t)) \left( -\frac{d(X(t))}{dt} \right)]$$

solve for :

$$\frac{d}{dt} \frac{d(X(t))}{dt} = 0$$

$$\frac{\partial \ln(\Phi/T_c^2)}{\partial (1/T_c)} = -\frac{E_B}{R} \quad \text{where: } \Phi = \frac{dT}{dt}$$

Figure 10. Hydrogen desorption rate vs. time curve for a charged 2090-T3 specimen. The temperatures that correspond to maximum desorption rates are shown.

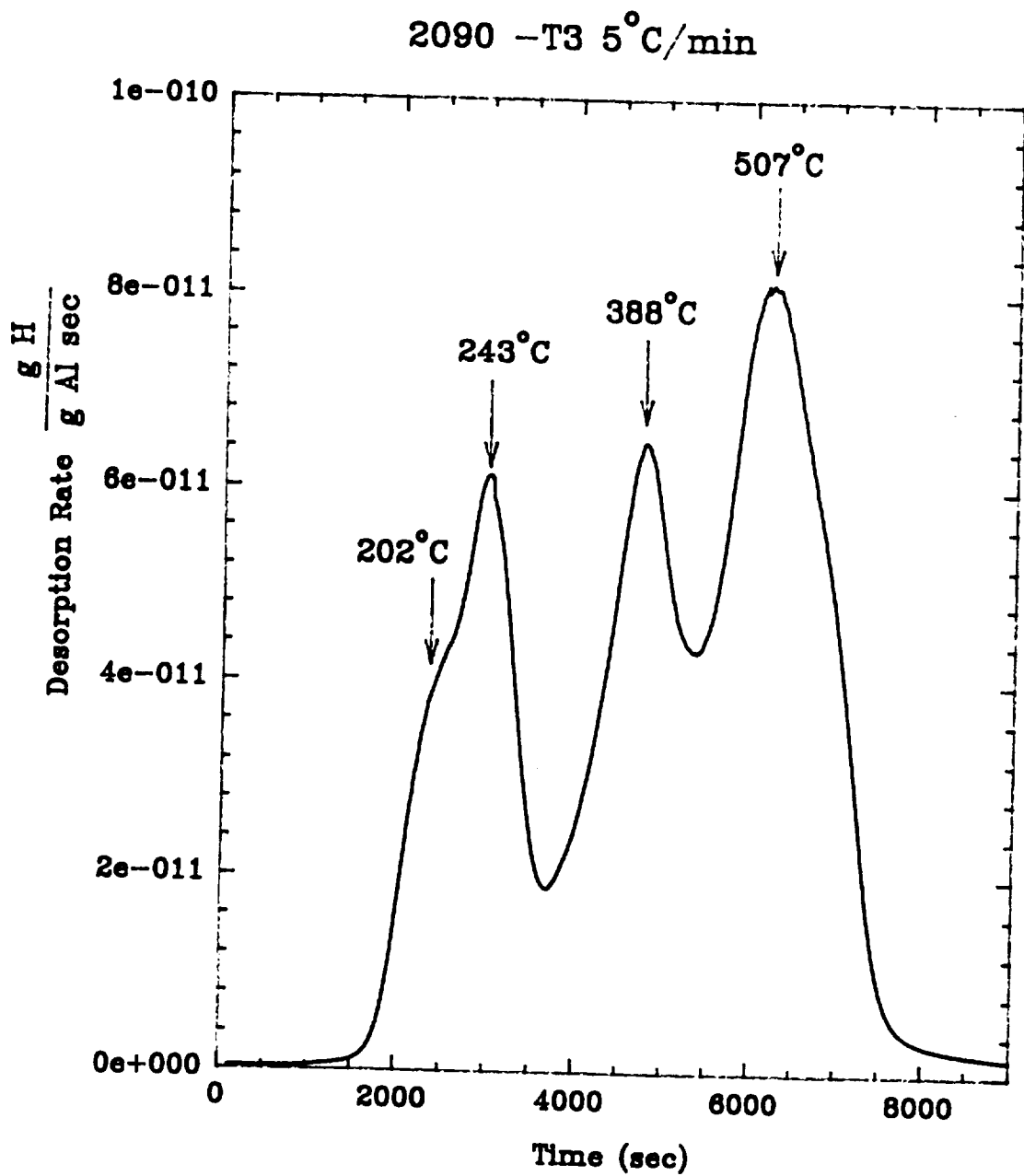
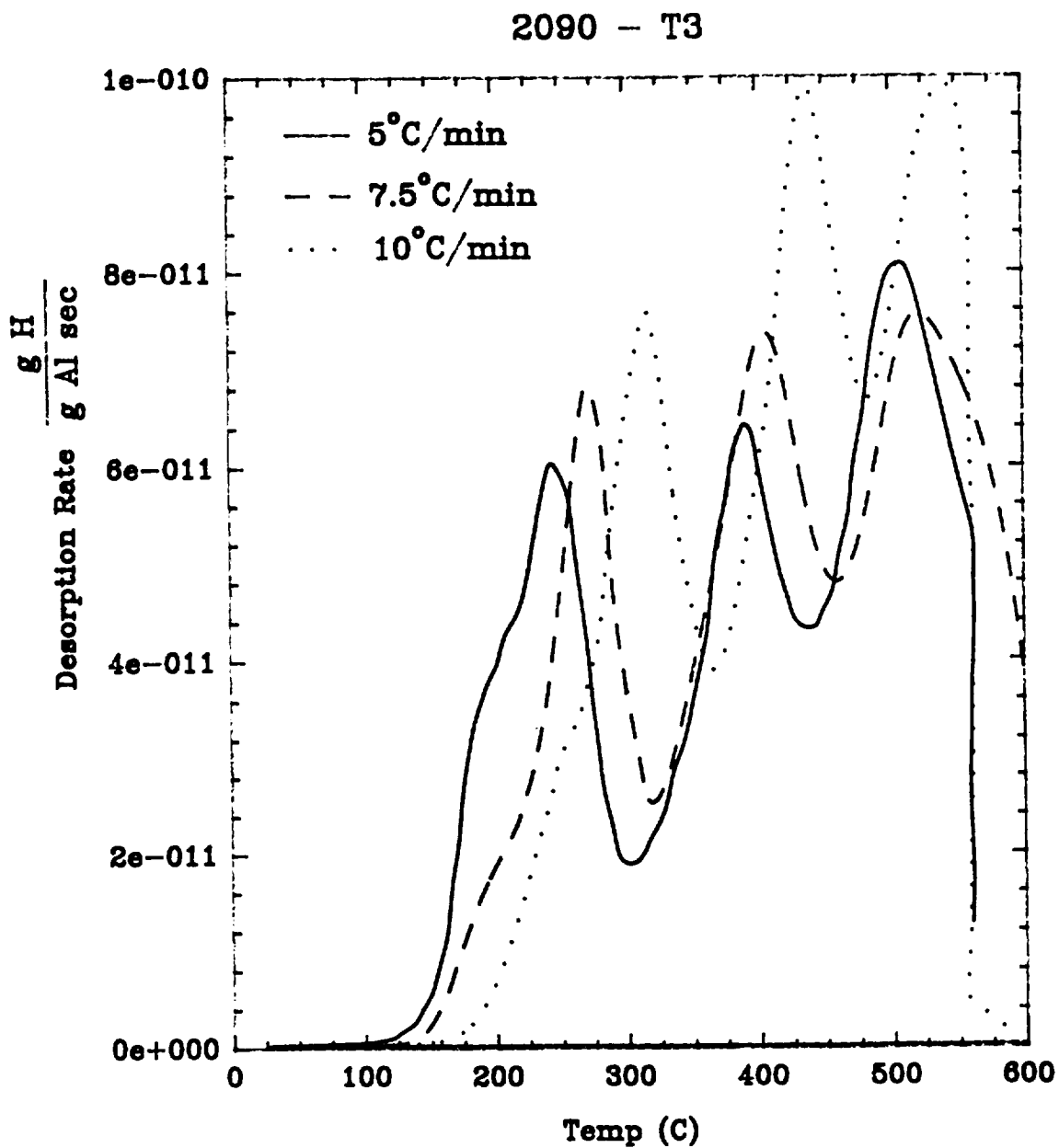


Figure 11. Hydrogen desorption rate vs. time curves for charged 2090-T3 specimens that were tested at three different ramp rates.



**Table 5: Binding Energy Calculations for 2090-T3  
charged at  $-1V_{SCE}$  pH 7 for 28 days**

peak	T <sub>m</sub> (°C) ( $\phi = 4.89$ )	T <sub>m</sub> (°C) ( $\phi = 7.34$ )	T <sub>m</sub> (°C) ( $\phi = 9.58$ )	E <sub>B</sub> (kJ/mol)
1	202	212	249	--
2	243	269	315	13.668
3	388	405	438	38.673
4	507	519	540	88.727

## **Future Work**

- Run duplicate J-integral resistance curve tests to verify results.
- Develop more severe charging conditions (increase  $\eta_c$  and increase charging time).
- Determine total hydrogen concentrations in alloys under various charging conditions.
- Use Al-Li binaries and Al-Cu binaries as well as 2090 recrystallized and unrecrystallized materials to identify operative trap sites.
- Correlate trap sites to fracture trends.

## **Conclusions: Thermal Desorption Spectroscopy**

- The TDS unit constructed at UVA is capable of resolving the hydrogen concentrations present in aluminum and aluminum alloys.
- We are able to detect several trap sites present in AA2090 and to calculate their binding energies.
- With the use of several model alloys (Al-Li, and Al-Cu) as well as the recrystallized and commercial 2090 materials, we should be able to identify several of the operative trap sites available during different stages of aging for 2090.

## Project #8     **Metastable Pitting of Al Alloys in Halide Solutions**

S.T. Pride<sup>1</sup>, J.R. Scully and J.L. Hudson<sup>1</sup>

### Objective

Metastable pitting of high purity Al and an aged Al-2%Cu alloy was characterized by analyzing electrochemical transients. Studies were conducted in room temperature aqueous halide solutions. Many studies cited in the literature focus on stable pit propagation at high positive potentials. Consequently, little is understood about pit nucleation and the factors responsible for stabilizing pit growth. For instance, factors which influence the metastable pit nucleation process and govern the transition from metastable to stable pit growth remain unclear. Is the dissolution rate observed in metastable pits different from that associated with stable pits or are there other important differences? What critical factors promote the survival and growth of pits for extended periods at applied potentials above the pitting potential but not below? The answer to these questions has significant implications with regard to the design of corrosion resistant alloys and aqueous phase inhibitors.

The aim of this work is to obtain some insight into these questions using various electrochemical techniques.

### Current Status

Several electrochemical test configurations have been utilized. (1) Open circuit potential (OCP) transients were investigated for aged Al-2%Cu (wt. %) as a function of halide concentration. Rapid negative excursions OCP's signaled the nucleation and growth of pits. A slow rise in potential signaled repassivation of pits and recharging of the adjacent oxide covered metal. (2) Anodic current transients were investigated as a function of halide concentration and potentiostatically applied potentials for high purity Al (99.999%). High purity Al is used to simulate the Cu depleted grain boundary zones present in aged Al-Cu alloys. Results are emphasized for pure Al wires.

The dependencies of a variety of metastable pitting parameters on potential, halide

---

<sup>1</sup> Department of Chemical Engineering, University of Virginia, Charlottesville, VA.

concentration, and exposure time were examined. These included metastable pit nucleation rates, pit lifetimes, apparent pit current densities, and apparent pit sizes at various stages of the pit propagation process. However, a few comparisons are made with sputter deposited high purity Al and Al-2%Cu thin films with film thicknesses of approximately 1  $\mu\text{m}$ . (3) Anodic current transients associated with the galvanic coupling between two identical Al-2%Cu thin films via a zero resistant ammeter were also investigated.

### Recent Findings

A finite range of pitting potentials exists for duplicate Al specimens potentiodynamically polarized to determine the pitting potentials at the same halide concentration. High purity Al specimens consisted of looped wires. Consequently, the origin of the range of pitting potentials can not be traced to inadvertent crevicing between the Al and some mounting material. Evidence suggests that this distribution of pitting potentials may be brought about by a several factors. These include a distribution of both metastable pit current densities and the rate at which the metastable pit current rises with time for a population of metastable pits formed within the range of pitting potentials observed.

It is interesting to note that at applied potentials below the pitting potential range, both metastable pit nucleation rates and apparent pit current densities at the peak anodic current associated with metastable pits are significantly lower than those observed within or above the pitting potential range described. Also, the rate at which the pit current rises with time increases when the applied potential is raised to levels within the pitting potential range. This results in larger apparent pit sizes for pits that eventually do stabilize even within time periods equivalent to the lifetimes of metastable pits which do not stabilize.

This finding is significant since larger pits provide a greater diffusional barrier to dilution of the pit environment, thereby promoting pit stabilization. Therefore, it is hypothesized that pit stabilization is more favorable with higher pit current densities, more rapid rise in pit currents, and, possibly, re-entrant pit geometries. The cumulative number of metastable pitting events increases with both increasing  $\text{Cl}^-$  ion concentration and applied potential at potentials below the pitting potential. At a constant applied potential below the pitting potential, the metastable pit nucleation rate decreased with exposure time.

In view of these findings, two beneficial roles of alloying additions or aqueous phase inhibitors would be to lower the pit current density and rate of current rise with time for



metastable pits and hence limit the ability of pits to stabilize. Another beneficial role of alloying additions and inhibitors would be to lower the metastable pit nucleation rate at a given potential, thus limiting the population of micropits available for stabilization. This effect is observed in the case of the addition of  $\text{KNO}_3$  and  $\text{NaCrO}_4$  to halide containing solutions.

### Milestones

In the next 6 months the methods of non-linear signal analyses will be explored as a means of examining electrochemical transients associated with the metastable pitting process. The emphasis of this phase of the work is to determine if the processes that give rise to the metastable pitting transients are the result of a deterministic chaotic process or a stochastic process. Attractor reconstruction, dimension calculation, and next maximum maps are some of the techniques from the time series analyses which are being used. Similar type of analysis will also be performed on the electrochemical transients associated with the metastable pitting of 2024 T3.

### Presentation Graphic Captions

1. Title page.
2. Objectives.
3. Experimental system for metastable pitting of pure Al electrodes.
4. Pitting and repassivation potentials for pure Al electrodes vs. NaCl concentration. Pitting potentials can be fitted with a logarithmic function. Repassivation potentials are independent of  $\text{Cl}^-$  concentration.
5. Time series showing metastable pitting of pure Al at various NaCl concentrations. Applied potential =  $-0.6 \text{ V (SCE)}$ . The number of metastable pitting events increase with increasing  $\text{Cl}^-$  concentrations. The  $10^{-2} \text{ M}$  transient is stable pitting.
6. Time series showing metastable pitting of pure Al at various applied potentials. NaCl concentration =  $10^{-3} \text{ M}$ . The number of metastable pitting events increase with increasing applied potentials.
7. Cumulative number of pitting events for pure Al at various applied potentials. NaCl concentration =  $10^{-3} \text{ M}$ .

8. Faraday Law relationship used to calculate pit sizes. Hemispherical pit geometry was assumed.
9. Time series showing the transition from metastable to stable pitting. Pure Al electrode in  $10^{-4}$  M NaCl at  $E_{app} = -0.05$  V (SCE).
10. Peak pit current vs. pit radius at peak pit current for pure Al at various applied potentials in  $10^{-4}$  M NaCl. The data corresponding to potentials between -0.75 V and -0.1 V (SCE) are metastable pit. The data corresponding to potentials between 0.1 V and 1 V (SCE) are stable pit. The average pitting potential for pure Al in  $10^{-4}$  M Cl<sup>-</sup> is -0.3 V(SCE). The lines are lines of constant pit radii.
11. Peak pit current vs. pit current density at peak pit current for pure Al at various applied potentials in  $10^{-4}$  M NaCl. Same data that is in Figure 10. The  $I_{pit}/r_{pit}$  line is the criterion for stable pit formation.
12. Criterion for maintenance of pit chemistry assuming spherical diffusion and H<sub>2</sub> production. For formation of a pit the pit concentration must be 1 to 3 M.
13. Critical pits sizes for maintenance of pit chemistry. The smaller the pit current density the larger the pit size must be to maintain the concentrated pit environment.
14. Factors contributing to the stabilization of micro-pits leading to stable pit propagation.
15. Anodic polarization curves for pure Al electrodes in NaCl/NaCrO<sub>4</sub> solution. The pitting potential is increased with increasing CrO<sub>4</sub><sup>-</sup> concentration.
16. Effect of NaCrO<sub>4</sub> on pure Al electrodes metastable pit formation. The number of metastable pitting events decrease with increasing CrO<sub>4</sub><sup>-</sup> concentrations.
17. Effect of NaCrO<sub>4</sub> on cumulative number of pitting events for pure Al. NaCl concentration =  $10^{-3}$  M. Applied potential = -0.5 V (SCE).
18. Effect of NaCrO<sub>4</sub> on metastable pit properties. Peak pit current vs. pit current density at peak pit current. On average the larger metastable pit current density are removed with the addition of CrO<sub>4</sub><sup>-</sup>.
19. Conclusions
20. Experiment system for studying metastable pitting of Al-2%Cu (1 mm thick). Galvanic coupling experiments.
21. Time series showing galvanic coupling of two identical Al-2%Cu in 0.1 M NaCl.
22. Time series showing galvanic coupling of two identical Al-2%Cu in 1 M NaCl. Note the increase in the number of events compared to the 0.1 M time series.

23. Next maximum map of peak pit currents. Positive currents only corresponding to the pitting of only one of the Al-2%Cu samples in 1M NaCl. Note for large  $I_{pit}(n)$  that  $I_{pit}(n+1)$  is smaller.
24. Next  $\Delta$ time map. The time interval between each pitting event. Positive currents only corresponding to the pitting of only one of the Al-2%Cu samples in 1 M NaCl.
25. Preliminary observation for the galvanic coupling of two identical Al-2%Cu.
26. Future work.



# **Metastable Pitting in Aluminum Alloys and Criteria for the Transition to Stable Pitting**

**S.T. Pride, J.L. Hudson, J.R. Scully**

**Center for Electrochemical Sciences and Engineering  
University of Virginia  
Charlottesville, VA 22903**

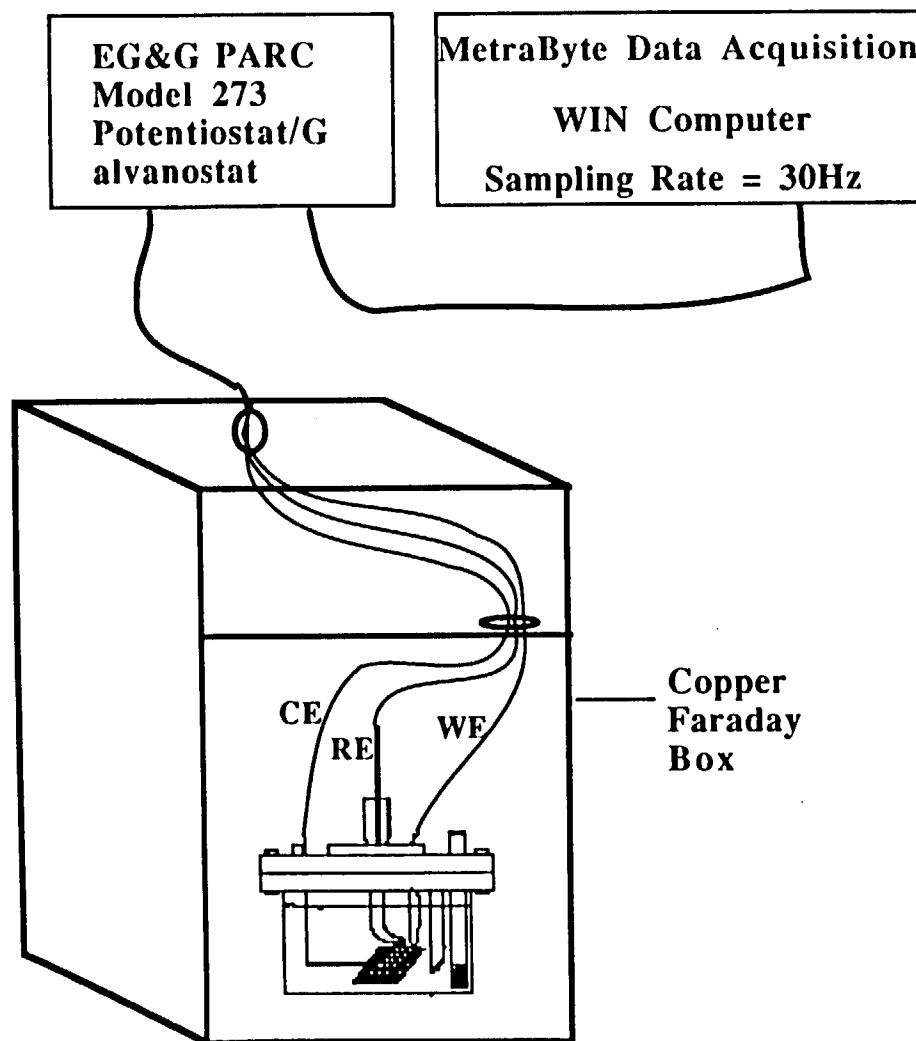
## *Acknowledgments*

*Defense Advance Research Projects Agency  
NASA-Langley Research Center*

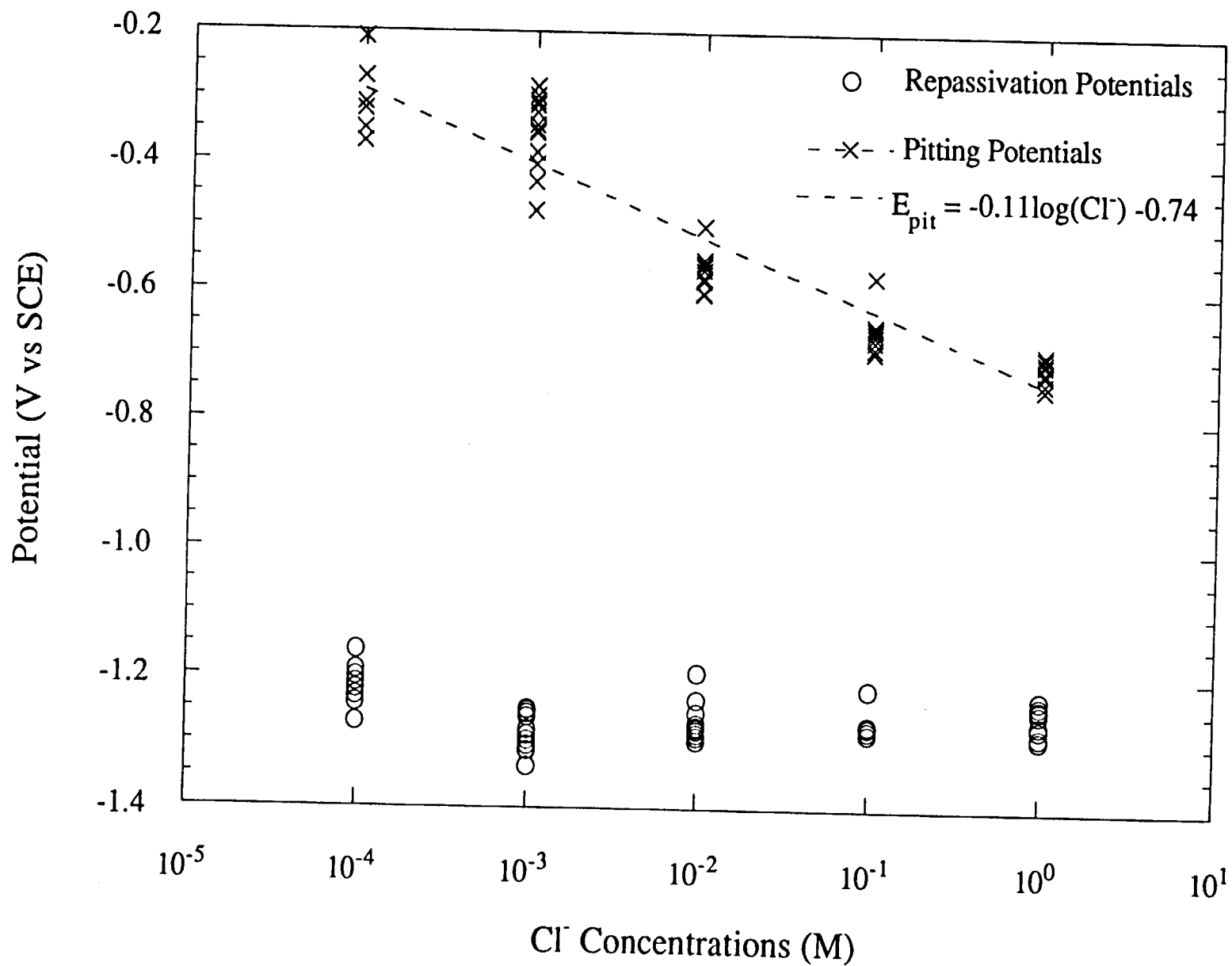
## Objectives

- Examine factors which contribute to the stabilization of micro-pits, leading to stable pit propagation (and the observation of breakdown potentials).
- Re-examine the role of pitting inhibitors (e.g. chromate) in the context of these factors.
- Utilize non-linear dynamic techniques to examine spatial and temporal aspects of pit initiation, growth, and repassivation.

# Experimental System for Studying Metastable Pitting using Pure Al Looped Wire Electrodes



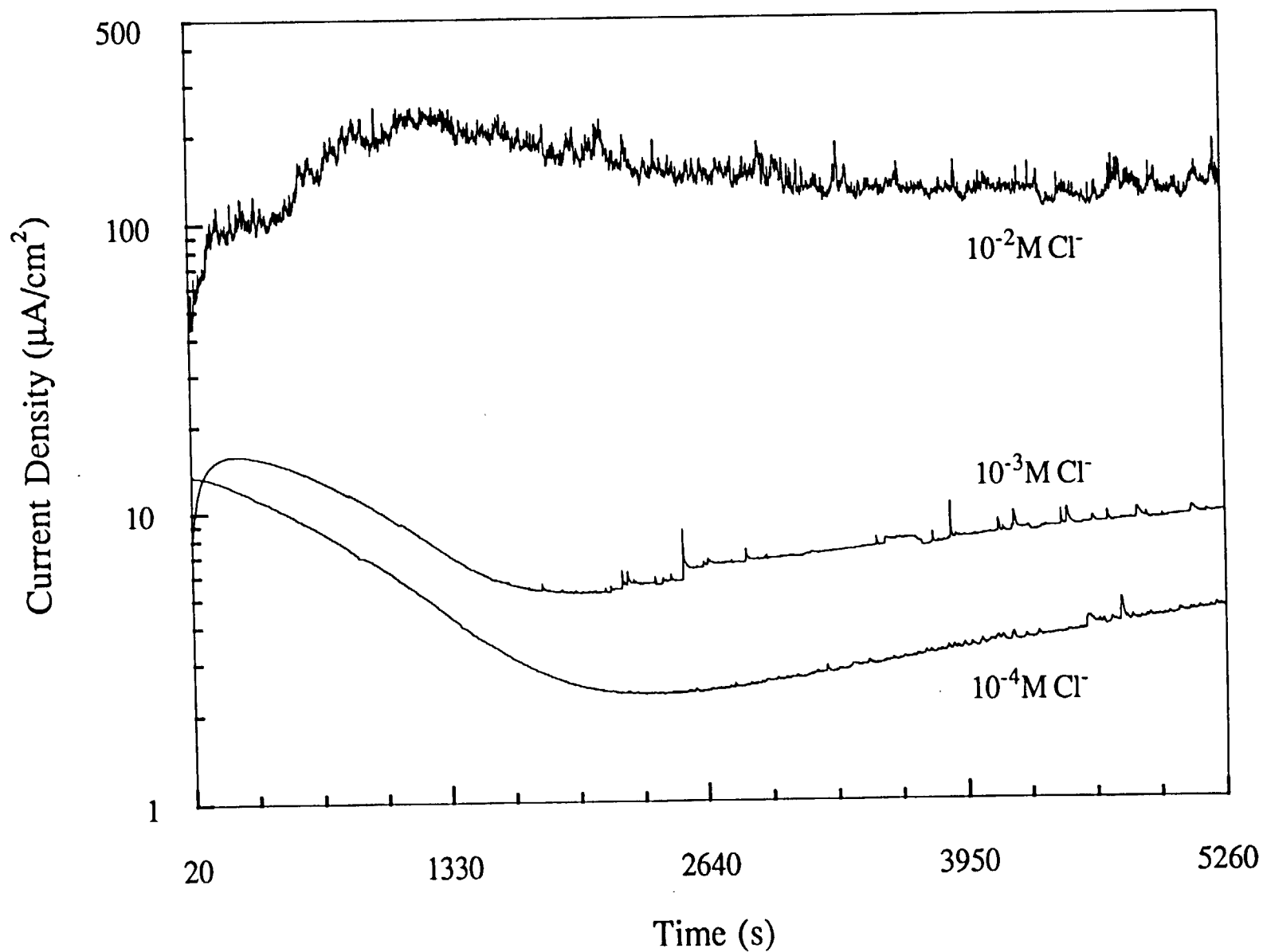
# Pitting and Repassivation Potentials for Pure Al vs NaCl Concentrations





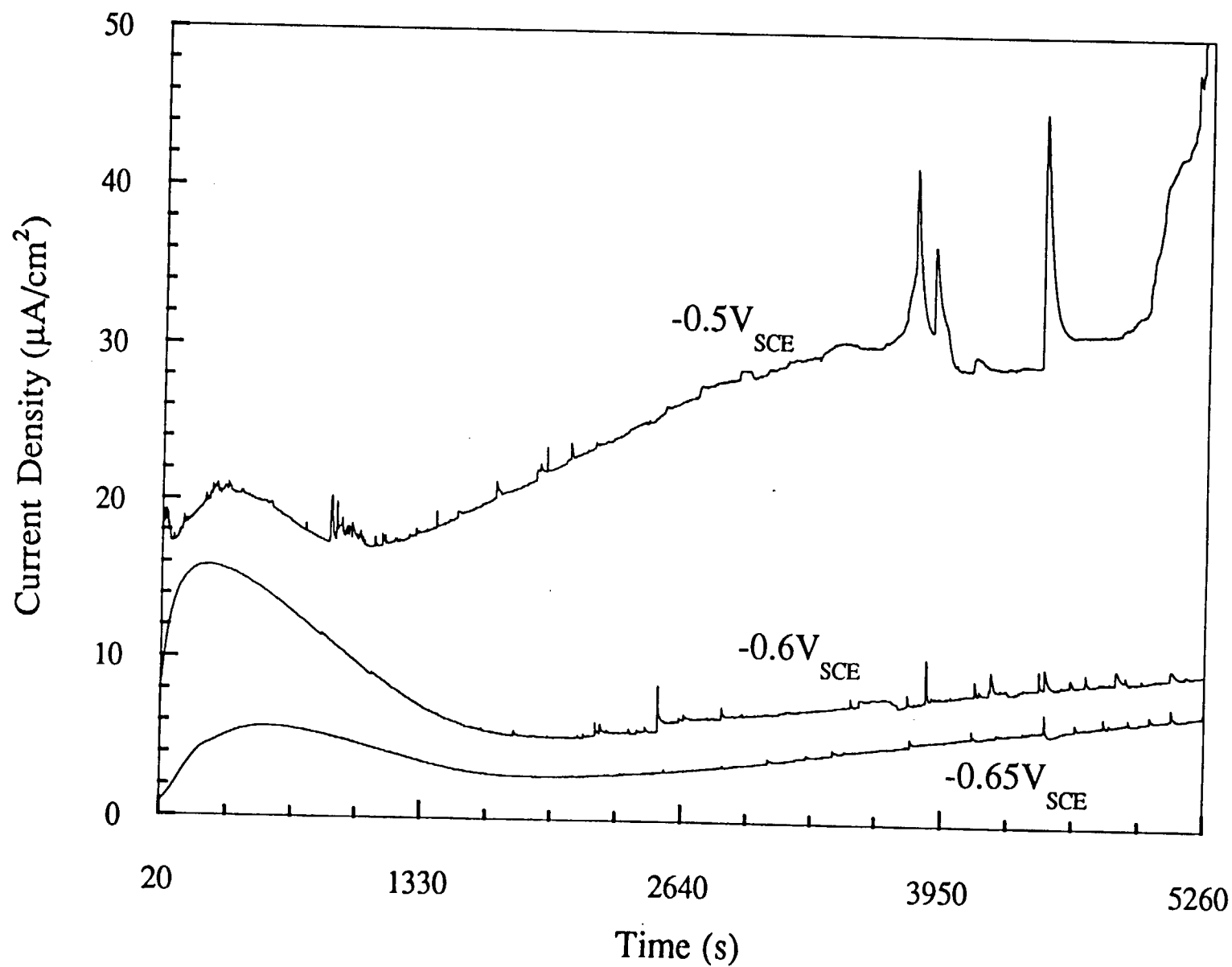
**Time Series Showing Metastable Pitting of Pure Al  
at Various NaCl Concentrations**

$$E_{\text{app}} = -0.6\text{V (SCE)}$$

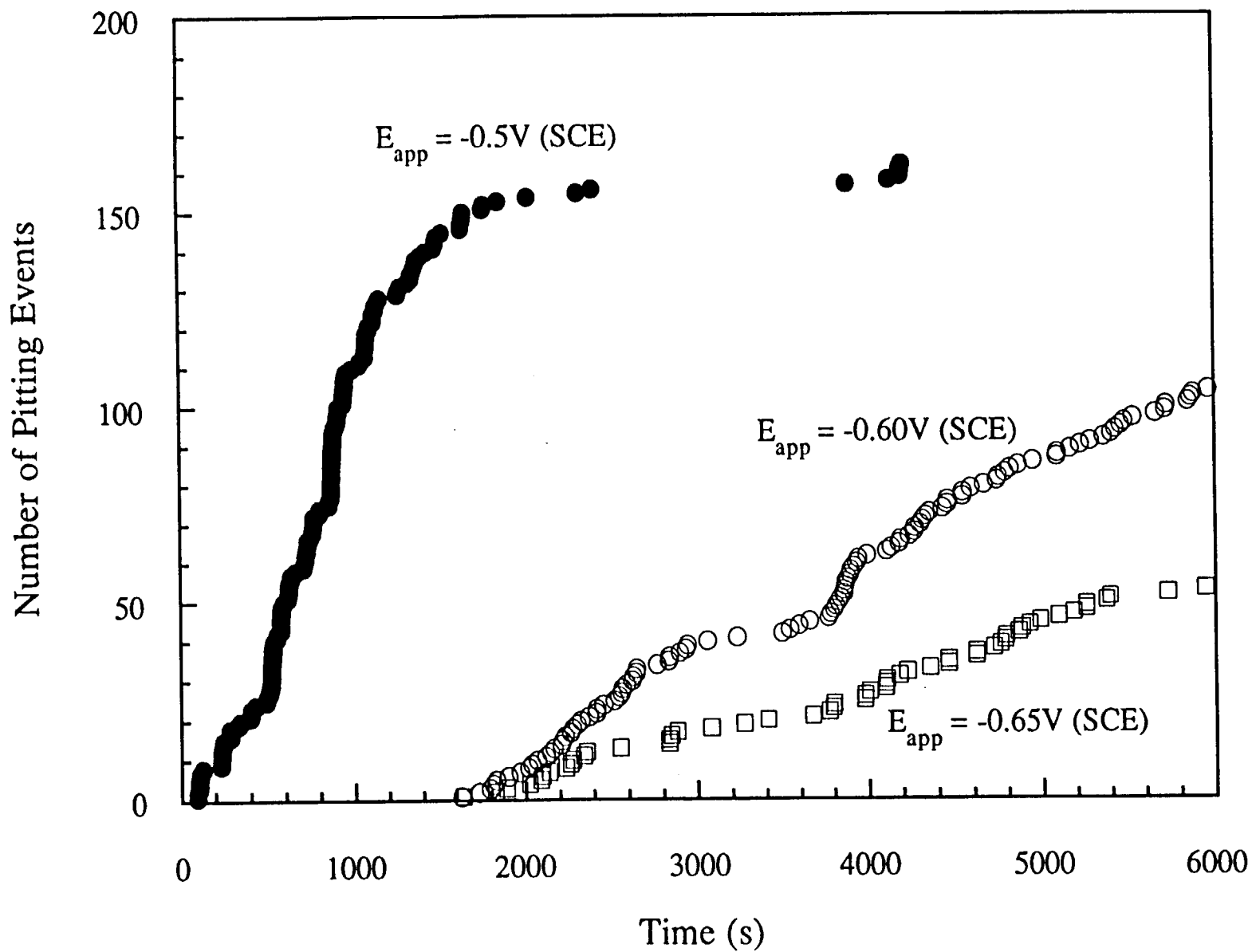


**Time Series Showing Metastable Pitting of Pure Al  
at Various Applied Potentials**

**$10^{-3}\text{M NaCl}$**



Cumulative Number of Pitting Events for Pure Al  
at Various Applied Potentials  
 $10^{-3}\text{M NaCl}$



**Faraday Law relationship**  
**Assuming hemispherical pits**

$$r_{\text{pit}} = \left( \frac{3AW}{2\pi zF\rho} \right)^{\frac{1}{3}} \left( \int (I_{\text{app}} - I_{\text{ox}}) dt \right)^{\frac{1}{3}}$$

$r_{\text{pit}}$  - pit radius

$AW$  - atomic weight

$z$  - valence

$F$  - Faraday's constant

$\rho$  - density of Al

$I_{\text{app}}$  - applied anodic current

$I_{\text{ox}}$  - passive current

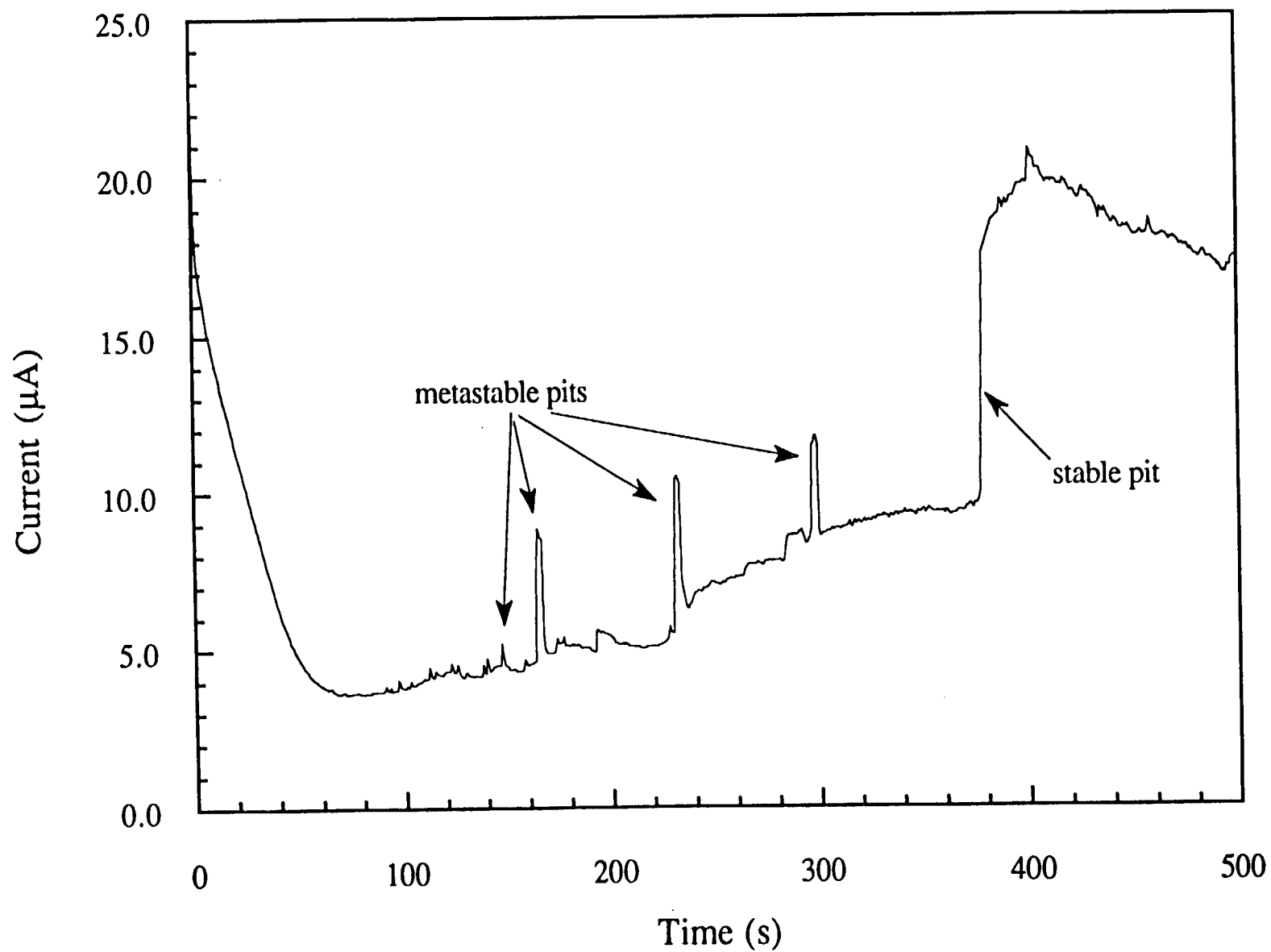
$t$  - time

$$I_{\text{app}} - I_{\text{ox}} = I(\text{pit})_{\text{an}} - I(\text{pit})_{\text{cath}}$$

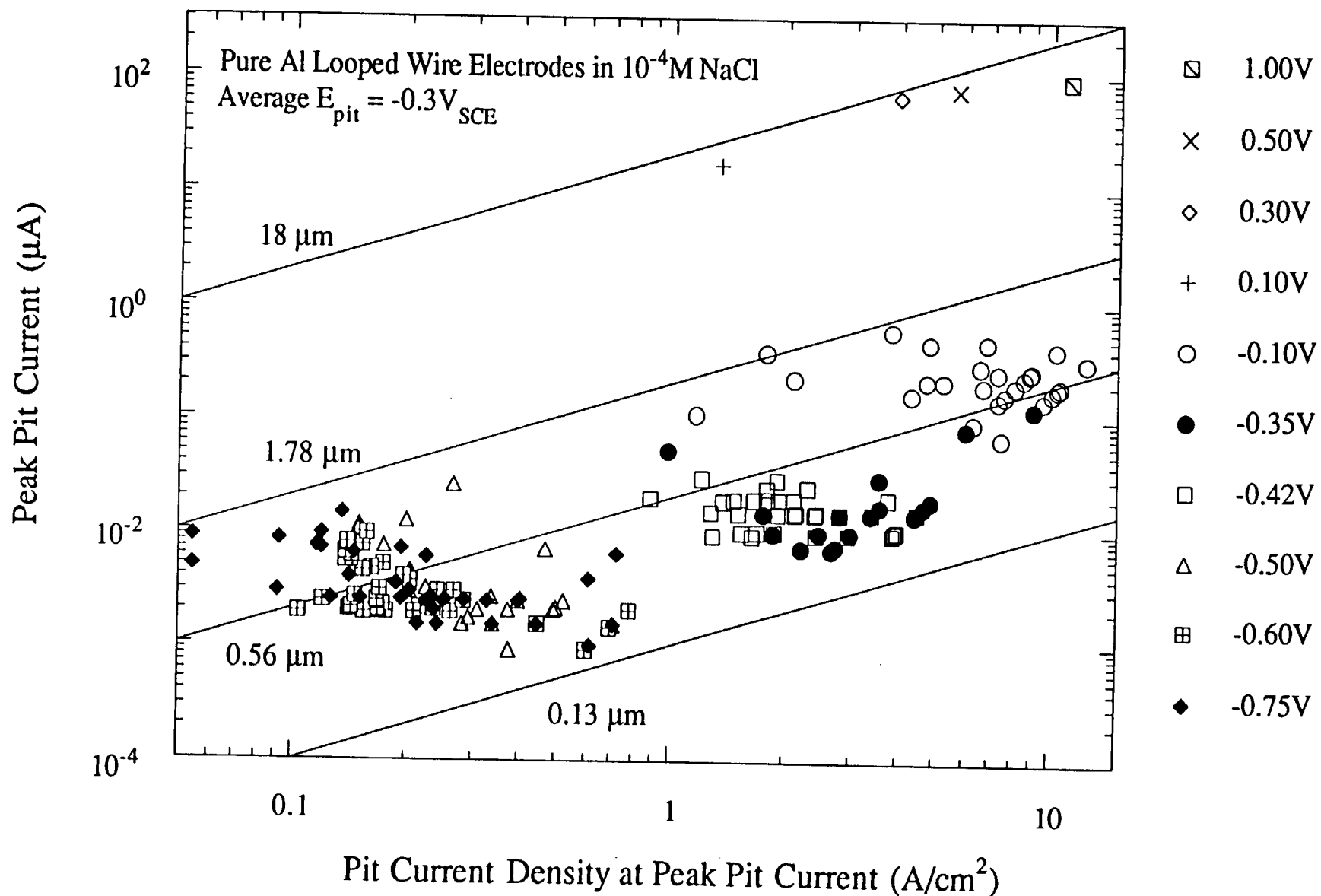
$I(\text{pit})_{\text{an}}$  - anodic pit current

$I(\text{pit})_{\text{cath}}$  - cathodic pit current

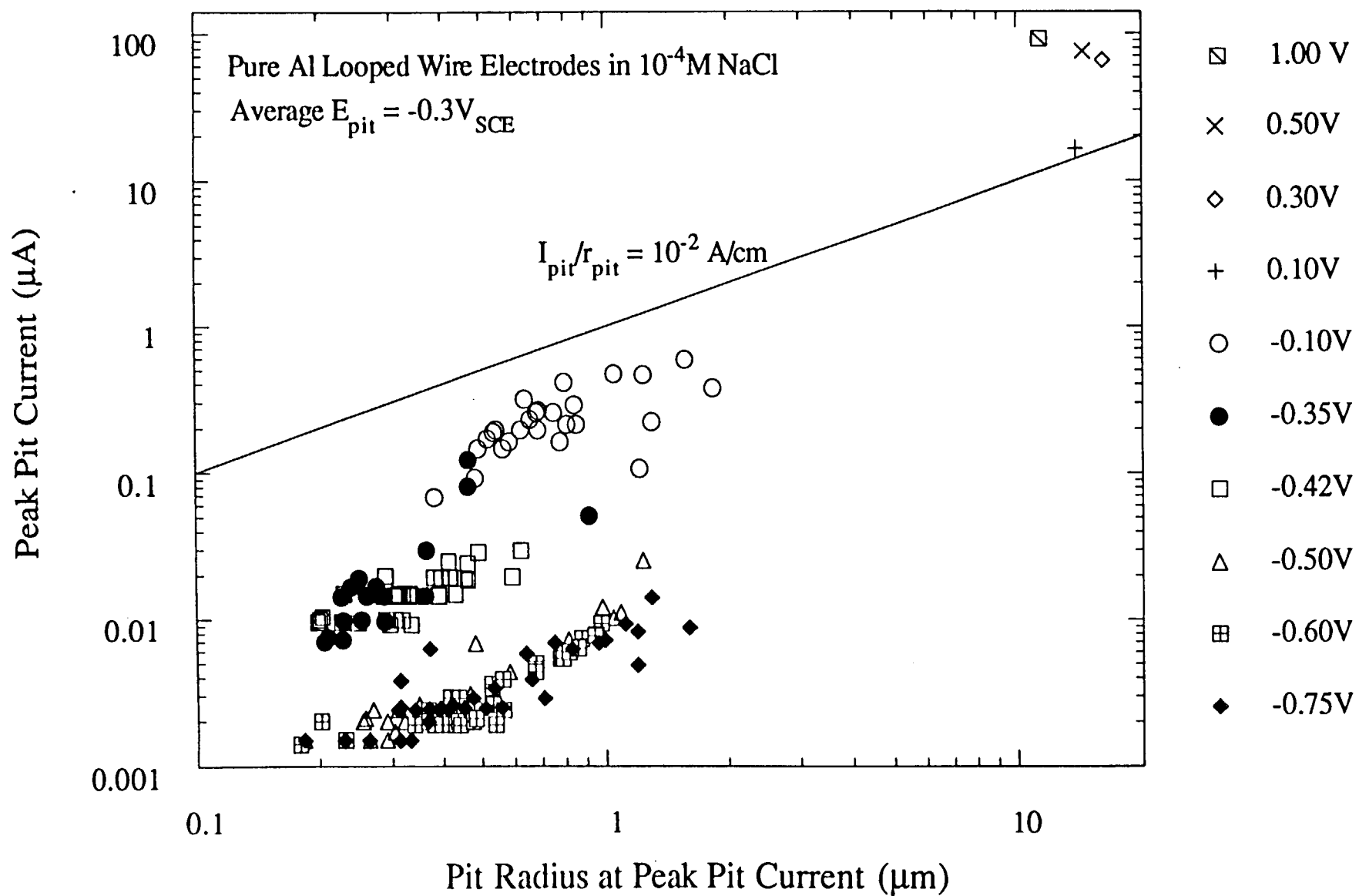
**Pitting of Pure Al in  $10^{-4}$  M NaCl**  
 **$E_{app} = -0.05$  V (SCE)**



# Metastable Pit Peak Currents vs Pit Current Density for Pure Al at Various Applied Potentials

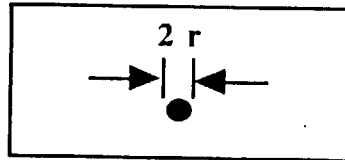


## Possible Criterion for Metastable Pit Stabilization



# Criterion For Maintenance of Pit Chemistry

## Spherical Diffusion

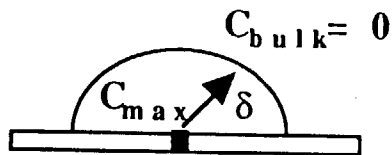


Criterion:

$$i_{pit} = nFD_{max} \left[ \frac{1}{(\pi Dt)^{1/2}} + \frac{1}{r_{pit}} \right]$$

Modification for Hydrogen Evolution:

$$\delta \propto (\pi Dt)^{1/2} \quad \delta = \frac{D}{A} v^{-0.53} \quad (N. Ibl)$$



$$\frac{D}{A} v^{-0.53} \gg r_{pit}$$

$$i_{pit} = \frac{nFDC_{max}}{r_{pit}}$$



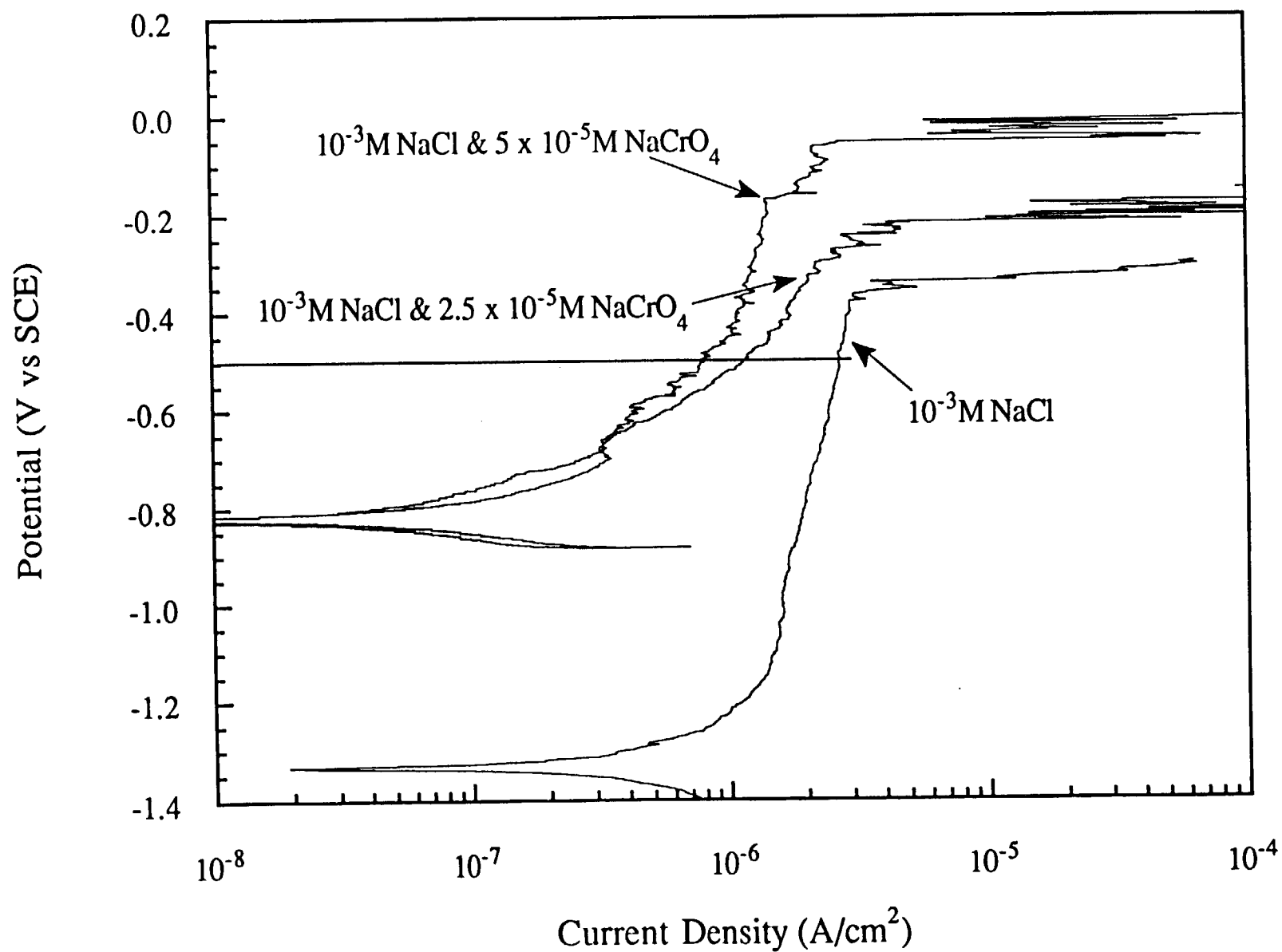
## Critical Pit Sizes for Maintenance of Pit Chemistry

$i_{\text{pit}}$ (A/cm <sup>2</sup> )	critical pit sizes for stabilization ( $\Delta C = 3M$ )	$I_{\text{pit}}/r_{\text{critical}}$ (A/cm)
	( $\mu\text{m}$ )	stable > $10^{-2}\text{A/cm}$
0.1	174	$10^{-2}$
1.0	17.4	$10^{-2}$
10	1.74	$10^{-2}$

## **Factors contributing to the stabilization of micro-pits leading to stable pit propagation**

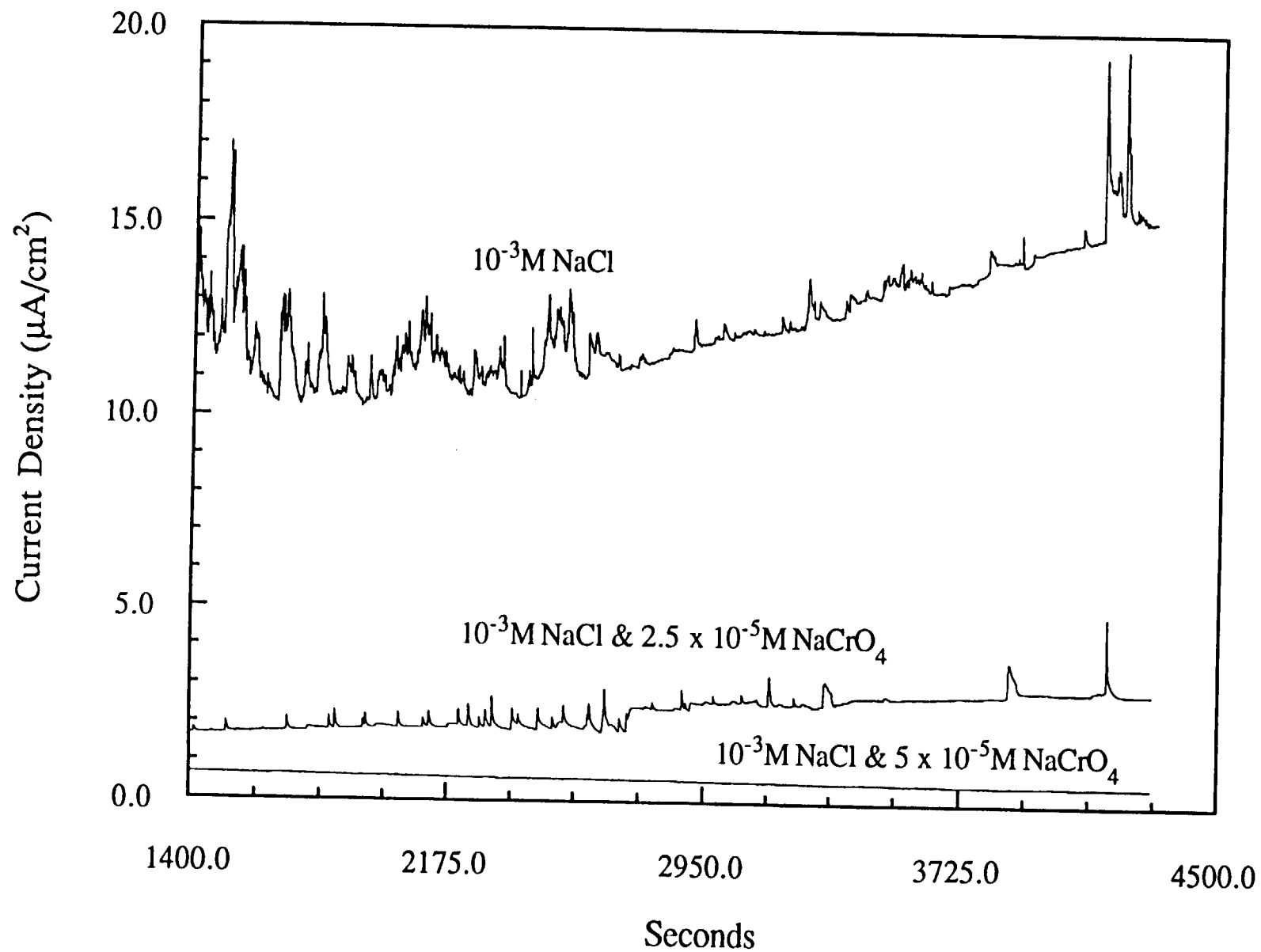
- 1. Current densities  $> 1 \text{ A/cm}^2$  early in micropit growth, or  $I_{\text{pit}}/r_{\text{pit}} > 10^{-2} \text{ A/cm}$ .**
- 2. Rapid rate of rise in pit current with time.**
- 3. A re-entrant pit geometry, or micropit formation at the bottom of a repassivated metastable pit.**

# Anodic Polarization Behavior of Pure Al in NaCl/NaCrO<sub>4</sub> Solutions

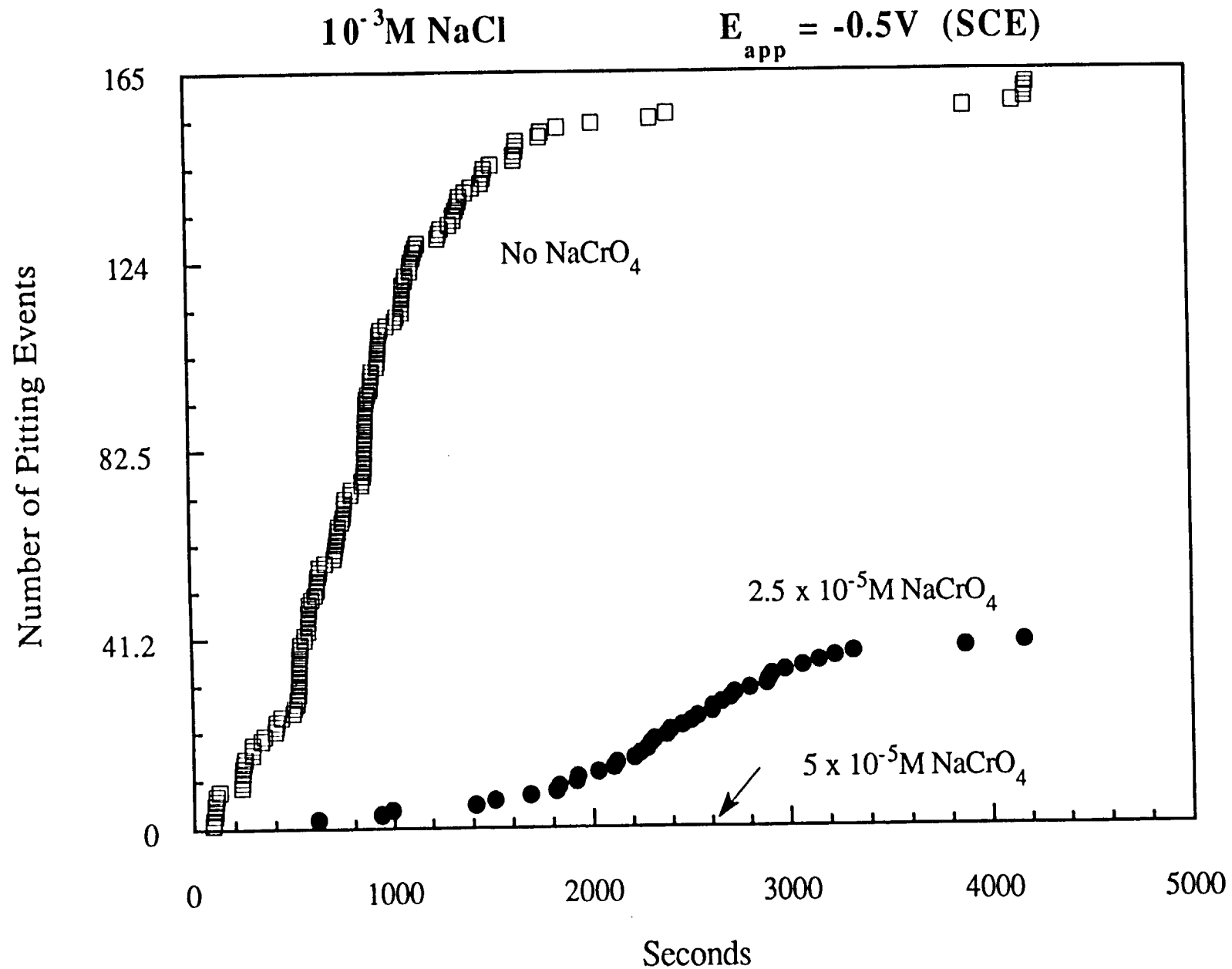


# Effect of $\text{NaCrO}_4$ on Pure Al Metastable Pit Formation

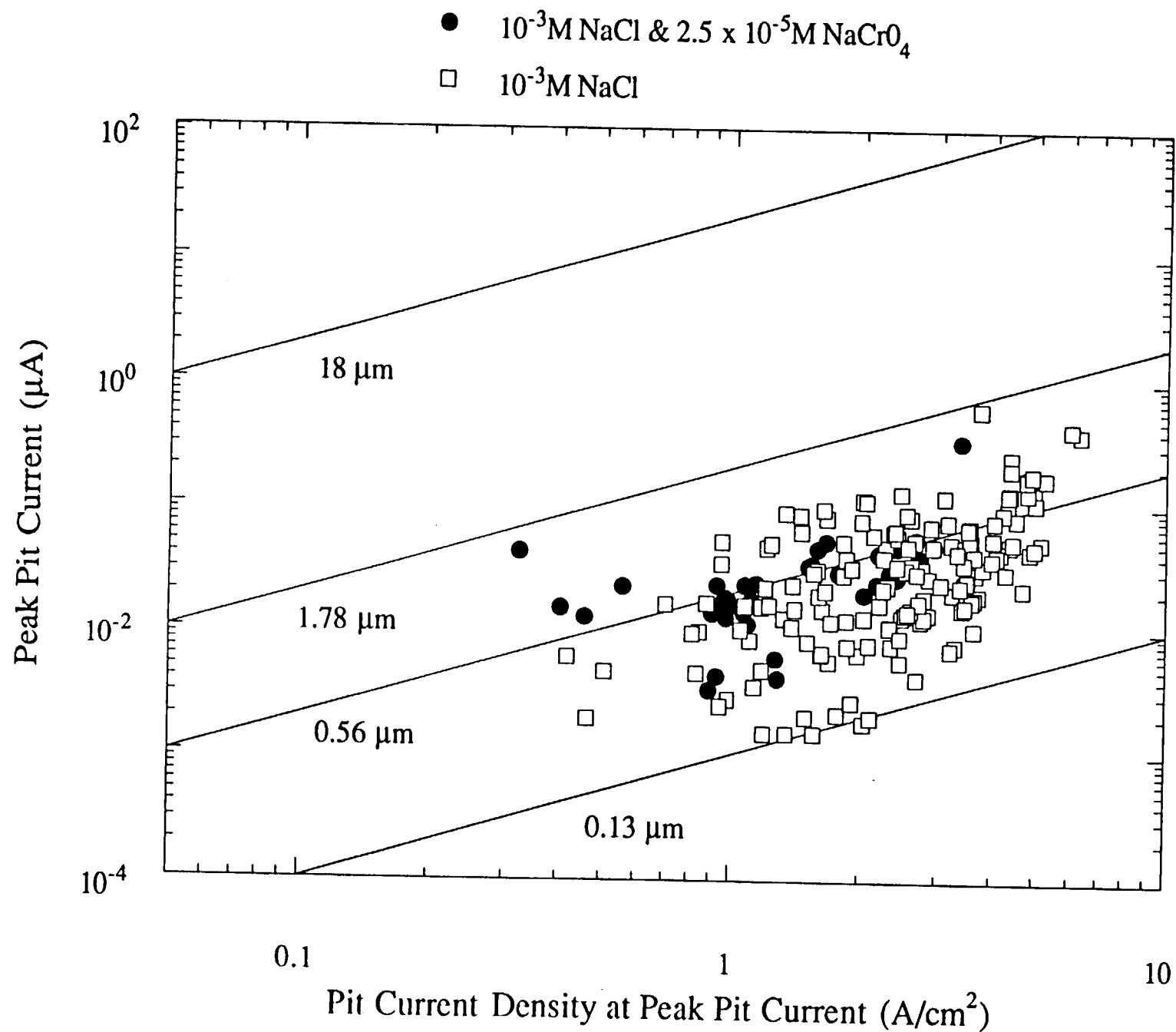
$$E_{\text{app}} = -0.5\text{V (SCE)}$$



# Effect of $\text{NaCrO}_4$ on Cumulative Number of Pitting Events for Pure Al



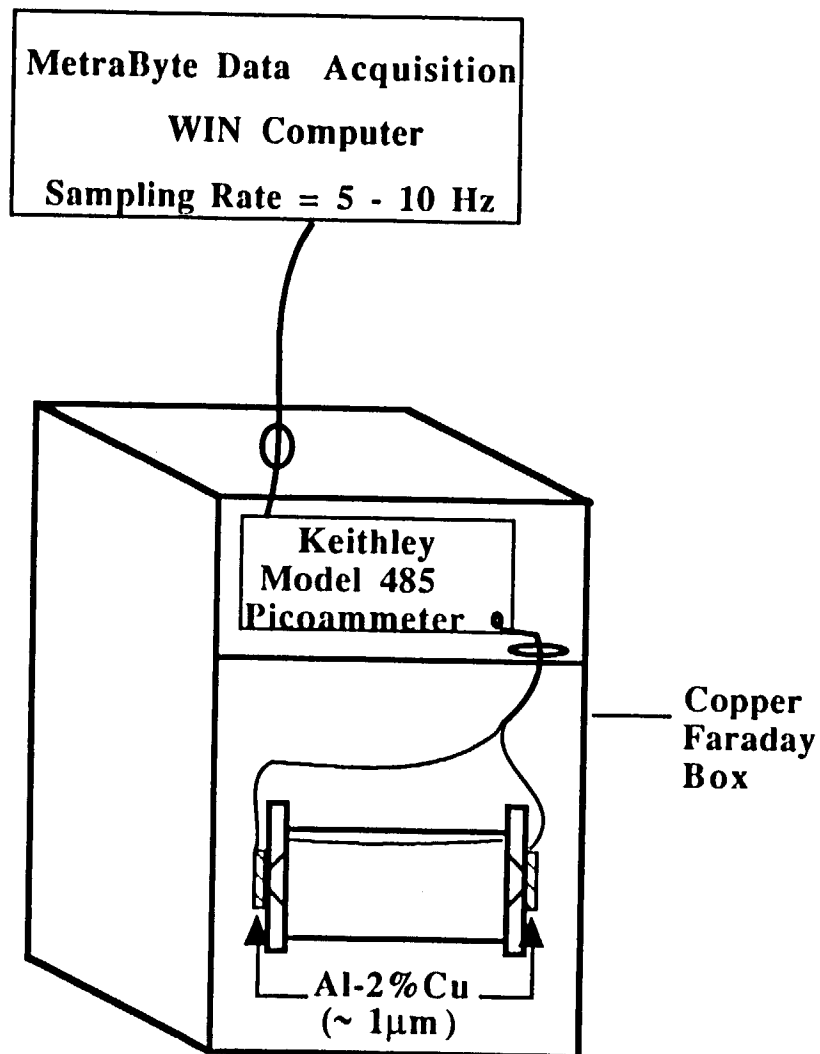
# Effect of NaCrO<sub>4</sub> on Metastable Pit Properties



## **Overall Conclusions**

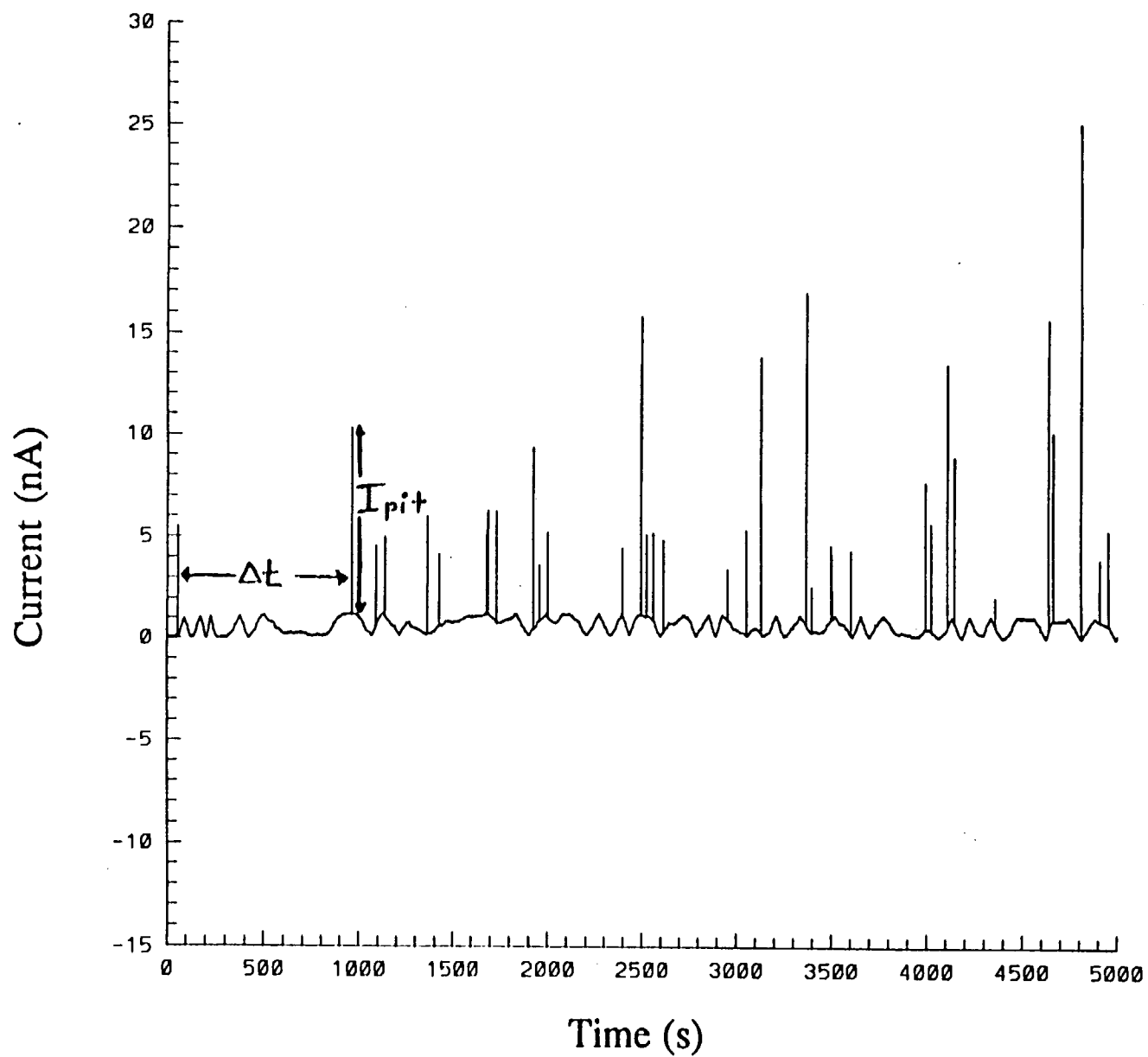
- 1. Factors have been identified which promote the transition from metastable to stable pitting for pure Al.**
- 2. A variety of factors contribute to pitting inhibition.**
  - the micropit nucleation frequency is lowered at a given  $\text{Cl}^-$  concentration and applied potential.**
  - micropits with high pit current densities are selectively eliminated. Pit chemistry maintenance is more difficult making micro-pit survival less likely.**
  - repassivation occurs more readily.**

# Experimental System for Studying Metastable Pitting of Al-2%Cu (1 $\mu$ m Thick)

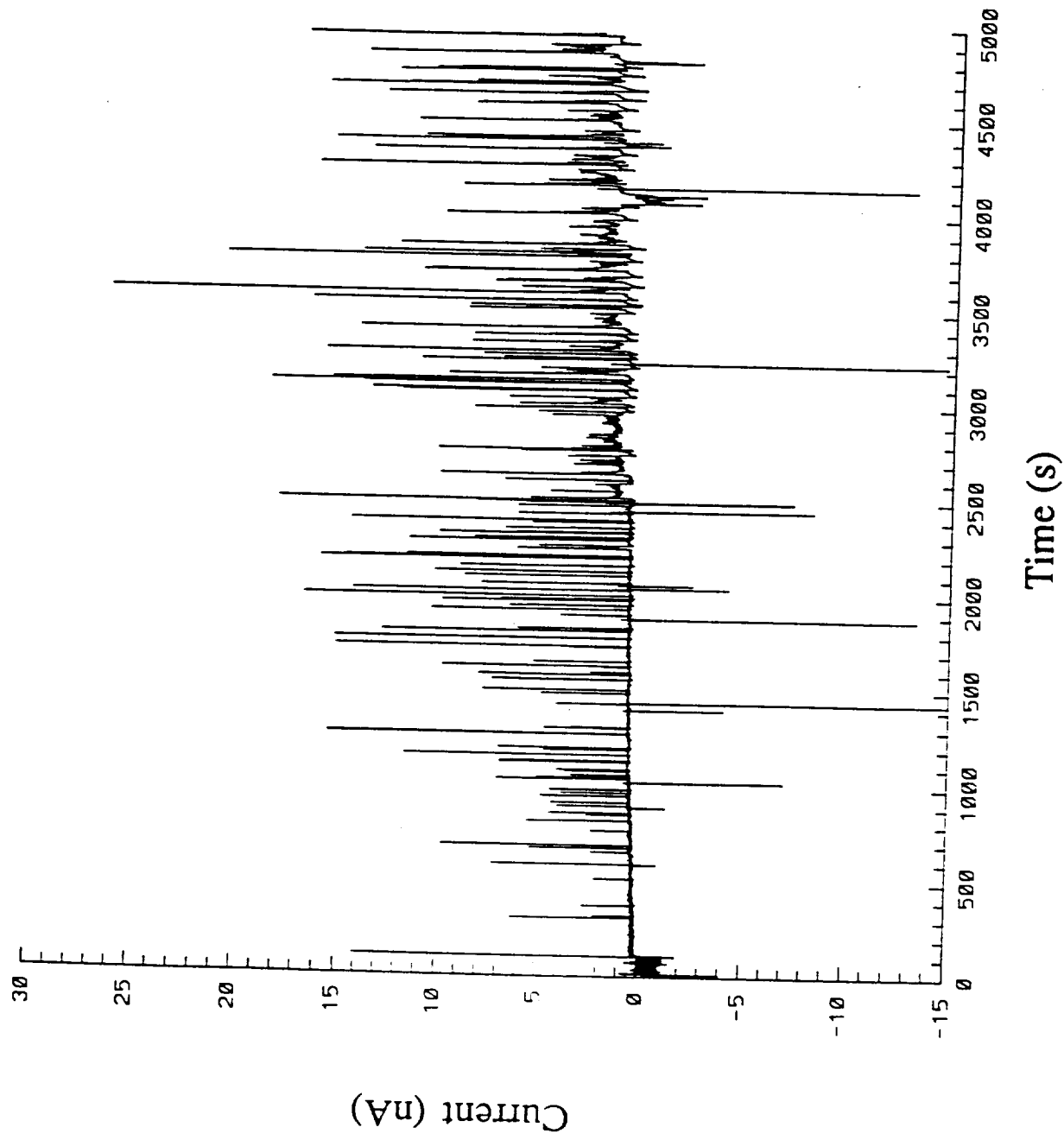




# Time Series Showing Coupled Al-2%Cu in 0.1M NaCl

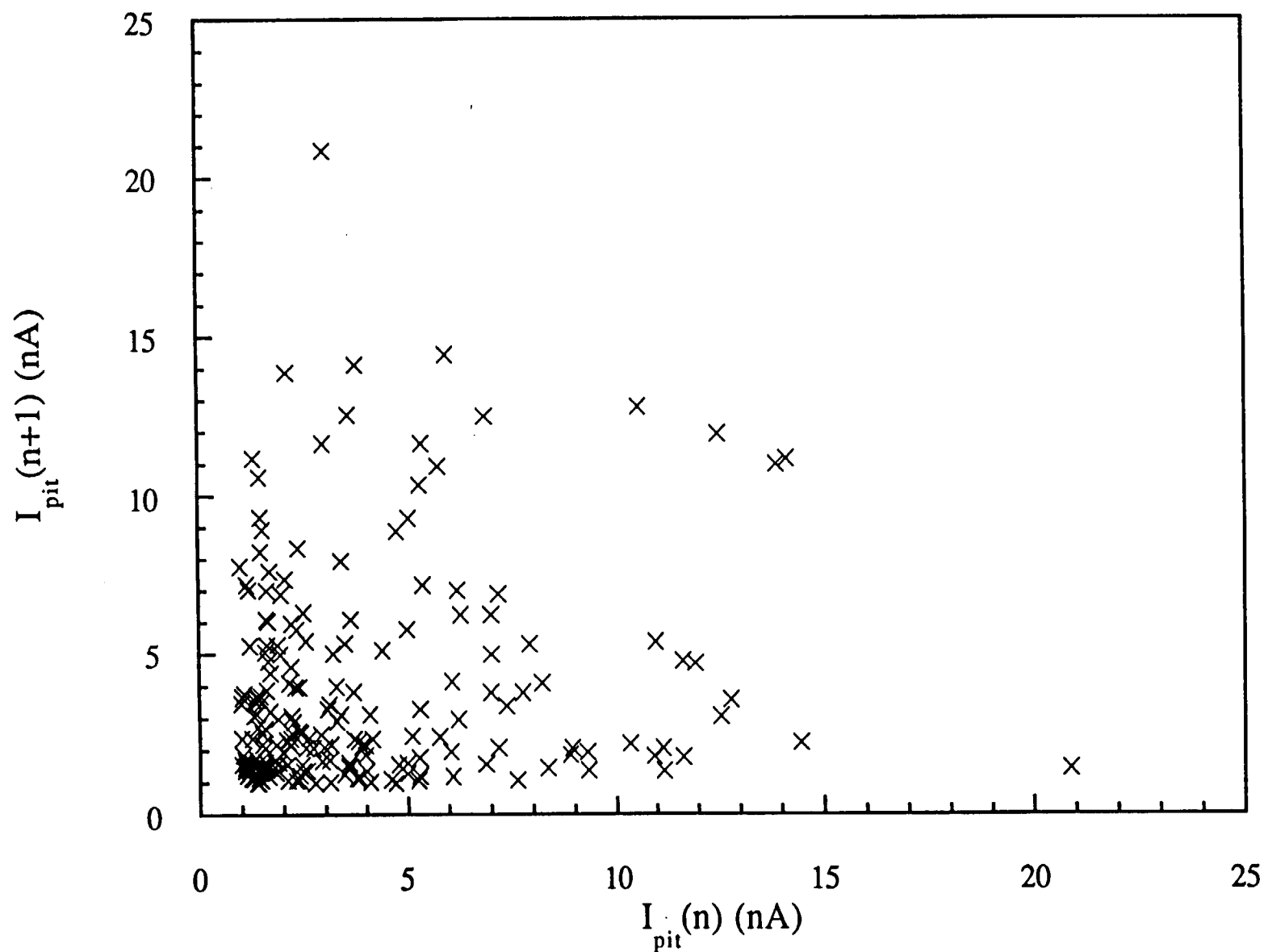


**Time Series Showing Coupled Al-2%Cu in 1M NaCl**

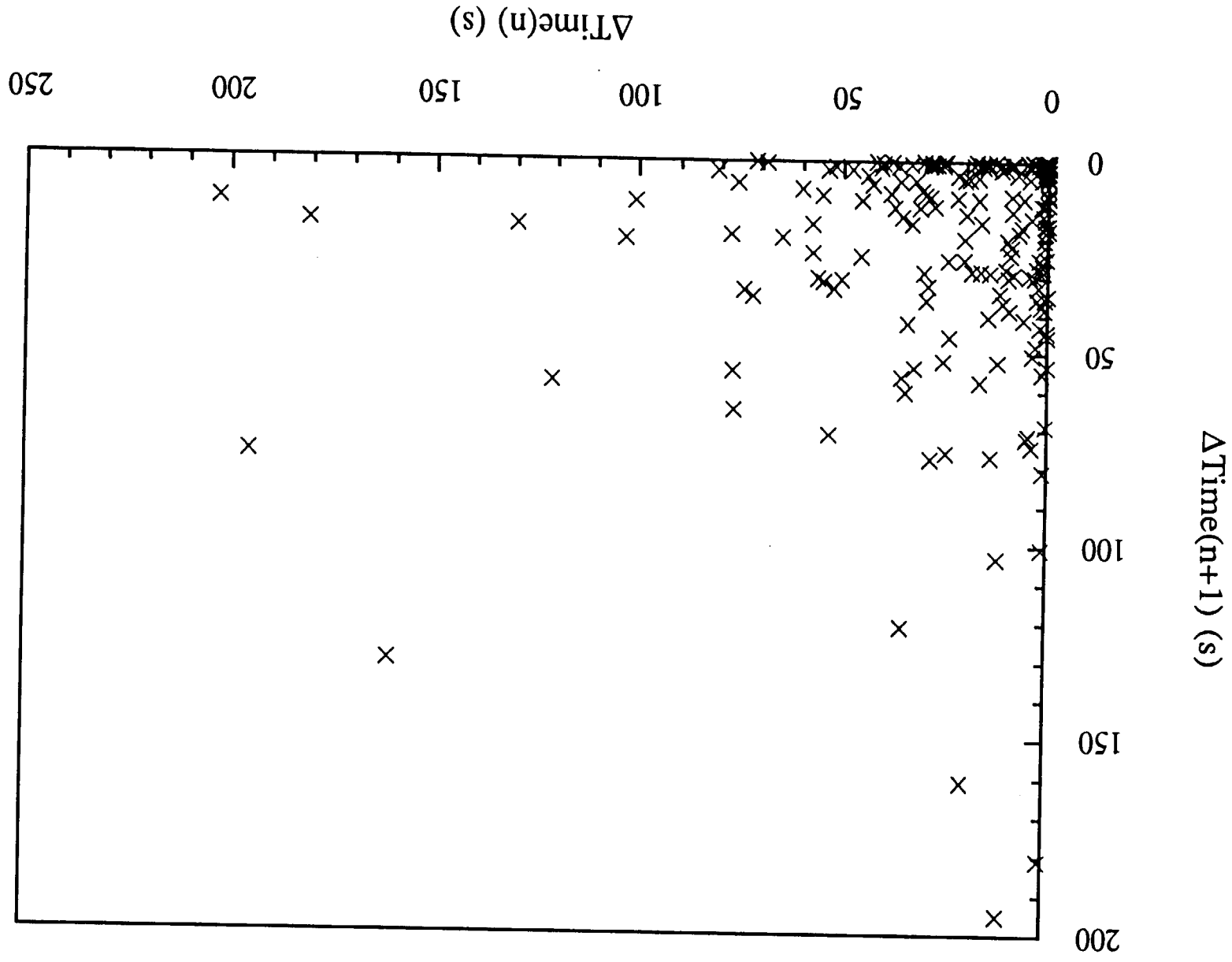


# Next Maximum Map for Coupled Al-2%Cu in 1M NaCl

Positive Current Sample  
Exposure Time = 5000 sec



Next  $\Delta\text{Time}$  Map for Coupled Al-2%Cu in 1M NaCl



## **Galvanic Coupling Preliminary Observations**

- **Metastable pitting is not totally random.**
- **Next Maximum Map using Ipit show that the formation of smaller pits can be followed by the formation of both smaller and larger pits.**
- **However formation of larger pits are only followed by the formation of smaller pits.**

## **Future Work**

- **Continue time series analysis of galvanically coupled Al-2%Cu thin films.**
- **Test the validity of increasing aggressive conditions leads more ordered metastable pitting due to interaction between pit sites.**
- **Similar types of analysis will also be performed on the electrochemical transients associated with the metastable pitting of 2024 T3.**

**Project #9      Investigation of the Effect of Thermal Treatment on the Mechanical Properties of Ti-1100/SCS-6 Composites**

Douglas B. Gundel and F.E. Wawner

**Objective**

The overall objective of this research is to investigate the influence of thermal exposure, both isothermal and cyclic, on the microstructure and mechanical properties of Ti-1100/SCS-6 composites.

**Current Status**

An evaluation of the influence of fabrication on the response of Ti-1100/SCS-6 composites to elevated temperature exposure has been completed. This included the effect of poor matrix-ply bonding on longitudinal properties, and the effect of fiber-fiber contact on transverse properties. Future work will focus on the prediction and determination of the response of well-consolidated composites to thermal exposure.

**Recent Important Findings**

The degradation of the composite during high temperature exposure in air has been attributed primarily to the embrittlement of the titanium matrix. Poor matrix-ply bonding in the case of longitudinal samples, and fiber-fiber contact in the case of transverse samples allowed a much greater volume of titanium to be embrittled during the exposures, and hence reduced the composite strength. Poor matrix-ply bonding not only allowed significant matrix embrittlement, but also resulted in limited fiber-matrix contact. The diffusion of embrittling species from the air (oxygen, nitrogen) along the fiber-matrix interface was observed. Fiber contact allowed the matrix to be embrittled and the fiber-matrix bond to be degraded to a much greater depth by this process than it was along individual, isolated fibers.

**Next 6-Month Milestones**

The work in the next reporting period will be centered around the modelling and measurement of the property degradation of well-consolidated composites (in both orientations) during elevated temperature exposure in air. The models will be verified at a

relatively high temperature ( $\approx 800^{\circ}\text{C}$ ), in the interest limiting the exposure time, but limited testing will also be carried out at lower temperatures ( $\leq 700^{\circ}\text{C}$ ). The effect of sample oxidation on the properties of the fiber and the fiber-matrix interface will also be measured. The influence of stresses generated by thermal cycling in conjunction with the thermal exposure will be evaluated.

#### Presentation Viewgraphs

1. Title Slide
2. Overall research objective and the components of the composites under study.
3. A subsurface layer grows in the titanium during elevated temperature exposure in air, and fails in a tensile test to yield a flat fracture surface. This layer is observable in polished and etched cross sections in the scanning electron and optical microscopes.
4. The effect of the embrittled layer on the sample tensile properties is dependent on the thickness of the exposed sample. This is a result of the higher volume percent of embrittled material in the thinner samples.
5. A description of the composite panels and the heat treatments performed.
6. A comparison of the fiber spacing in the two groups of panels supplied by NASA-LaRC.
7. A comparison of the histograms describing the fiber spacing distribution in the two groups of panels. The spacing in the original panels is skewed toward the low end of the distribution, whereas that of the new panels is well-distributed about the mean.
8. Chart of the strength, exposure performed, and position of transverse samples from a panel with poor fiber spacing. Exposure in argon had no influence, while exposures in air degraded the strength. Cycling to  $800^{\circ}\text{C}$  500 times in air had the greatest effect. The isothermal exposure was designed to give the equivalent thermal exposure to the sample as cycling to  $800^{\circ}\text{C}$ .
9. Stress-strain curves for the transverse samples from the panel with poor fiber spacing. The initial modulus of the samples was also degraded by the exposure.
10. Chart of the strength of transverse samples from a panel with good fiber spacing. The strength was degraded by the exposure, but not as severely as in the samples with poor fiber spacing.
11. Stress-strain curves of the transverse samples from the panel with good fiber spacing. The knee in the curve is still apparent after cycling.



12. Fracture surfaces of cycled samples from the two panels indicate a great deal of matrix embrittlement inside the sample with poor spacing, and only limited matrix embrittlement in the sample with well-spaced fibers.
13. Sectioning of the cycled sample with poor spacing revealed that the touching fibers were surrounded by embrittled titanium to a greater depth than individual, isolated fibers.
14. The point of fiber contact seemed to be easily degraded, thereby creating a pathway for the direct transport of air into the sample.
15. The fracture surface of a cycled transverse sample, 27% through the sample (or  $\approx 0.17$  cm from the surface), indicating that the crack that caused final failure of the sample propagated through the embrittled titanium. Also, touching fibers are surrounded by embrittled titanium, while single fibers are not.
16. The depth of penetration of the embrittling species along touching fibers following cycling to  $800^{\circ}\text{C}$  500 times is of interest. These micrographs indicate that enhanced matrix embrittlement takes place along touching fibers for depths at least up to 1 cm.
17. The depth of embrittlement along single fibers has been investigated for an isothermal exposure at  $800^{\circ}\text{C}$  for 10 hours. This micrograph indicates that the titanium is embrittled and the SCS layer on the fiber is degraded to a depth of approximately 1.5 mm.
18. Ultrasonic C-scans of the panels indicated areas of poor bonding, as indicated by the accompanying micrographs. These area included regions of incomplete consolidation, matrix-ply debonding, and severe cracking at the matrix-ply interfaces.
19. These two panels were subsequently sectioned into longitudinal samples, thermally exposed, and tensile tested. The C-scans indicate that the outer samples may contain poor matrix-ply bonding.
20. All of the samples from Panel C were cycled to  $800^{\circ}\text{C}$  500 times. The results indicate that the outer samples were more severely degraded by the thermal treatment.
21. The combined results from samples from Panels C and D indicate that cycling severely degraded the samples from near the panel edge, whereas those from the center were only slightly affected. Isothermal exposure seemed to have a similar effect on the well and poorly-consolidated samples.
22. Ultrasonic C-scan of Panel E indicating the position of the samples and their relative quality of fabrication.
23. Tensile test results of the samples from Panel E in the as-fabricated and cycled condition. These results also indicate that poorly-consolidated samples were degraded by the thermal cycling, while well-consolidated samples were not greatly affected.

**INVESTIGATION OF THE EFFECT OF THERMAL  
EXPOSURE ON THE MECHANICAL PROPERTIES  
OF Ti-1100/SCS-6 COMPOSITES**

**DOUGLAS GUNDEL**

**F. E. WAWNER**

**UNIVERSITY OF VIRGINIA, CHARLOTTESVILLE**

**SPONSORED BY NASA LaRC  
D.L. DICUS, W.D. BREWER, CONTRACT MONITORS  
GRANT NO. NAG-1-745**

## Research Objective

The objective of this research is to investigate the influence of thermal exposure, both isothermal and cyclic, on the microstructure and mechanical properties of Ti-1100/SiC composites.

## Constituents

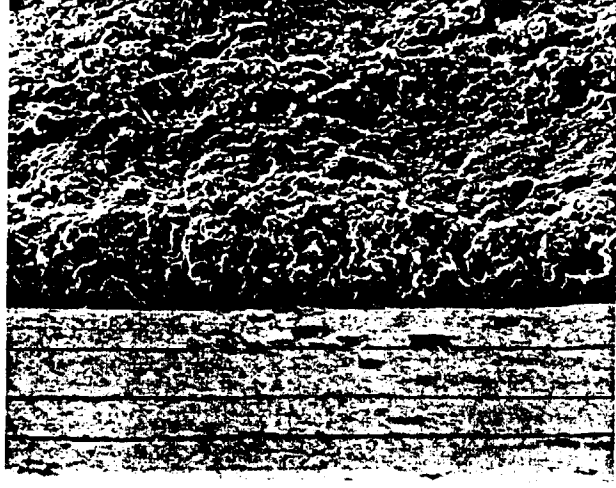
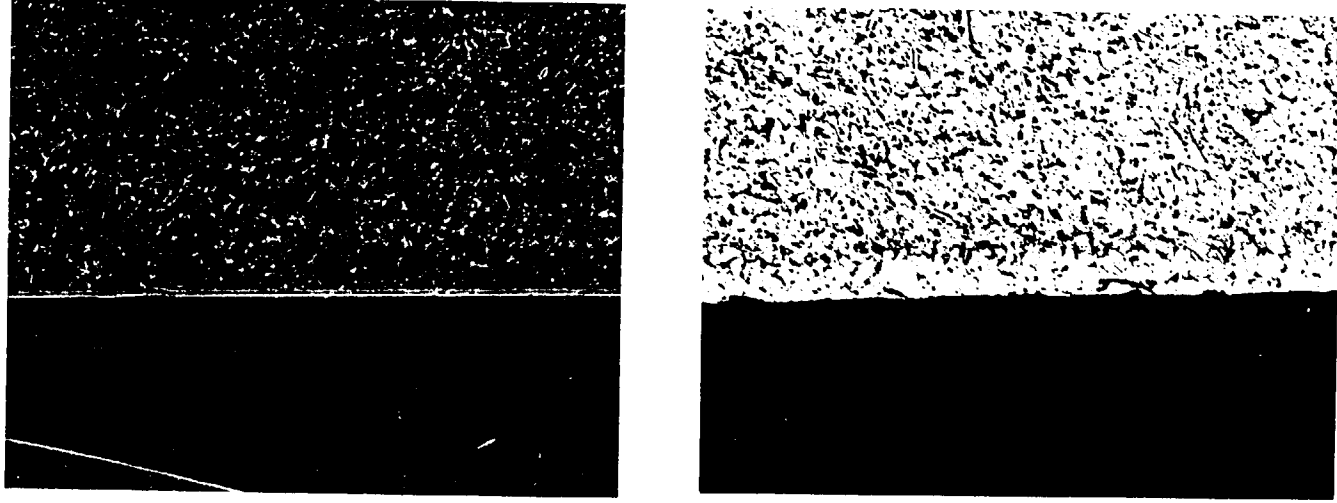
### Ti-1100

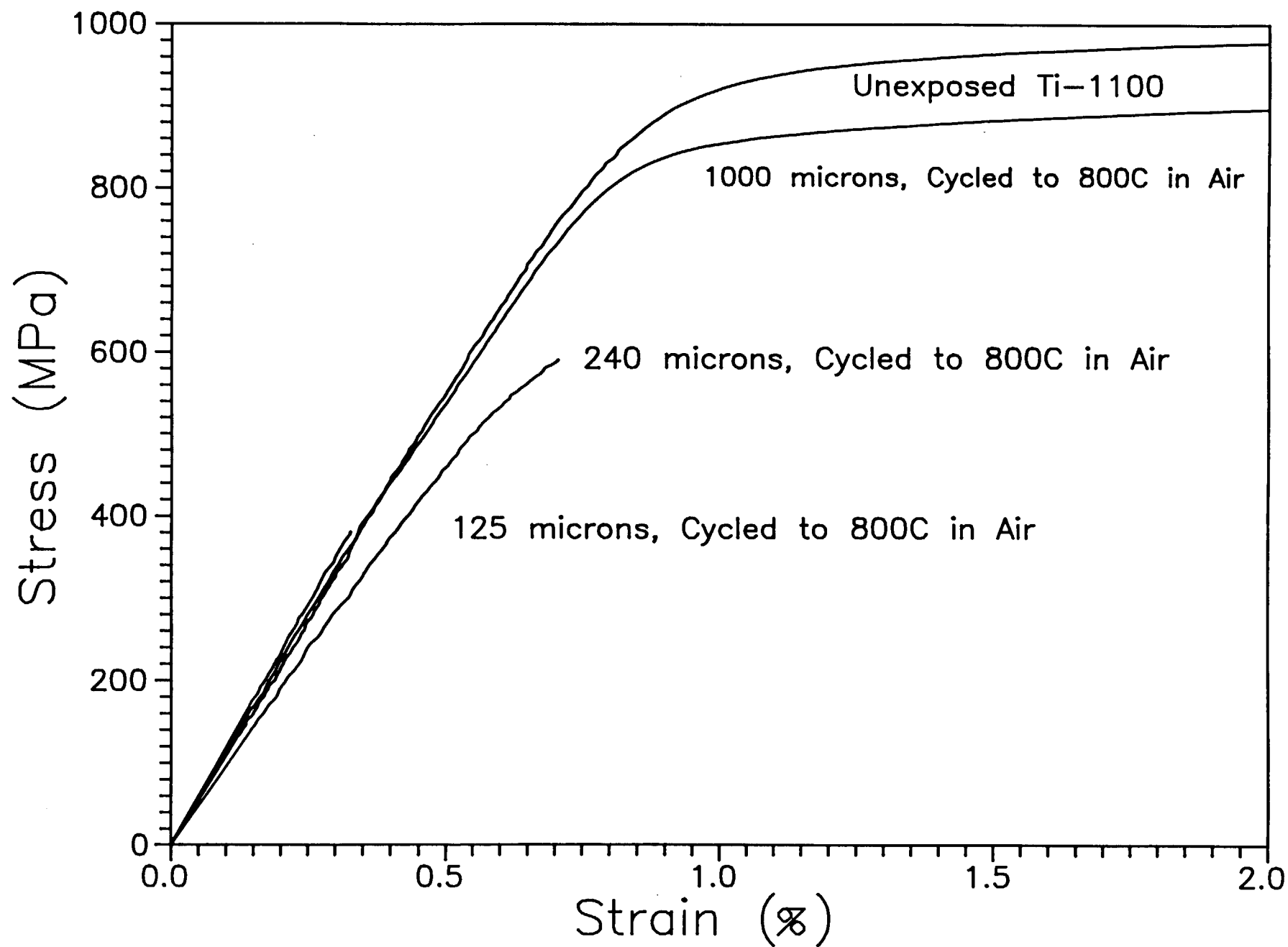
- Ti-6Al-2.8Sn-4Zr-0.4Mo-0.45Si
- Near-alpha alloy
- Designed for use to 593C (1100F)

### SCS-6

- Produced by Textron Specialty Materials using CVD
- 140 micron diameter fiber
- 33 micron carbon core
- Carbon-rich "SCS" coating

# Ti-1100 Embrittlement 800C, 10 hours in air

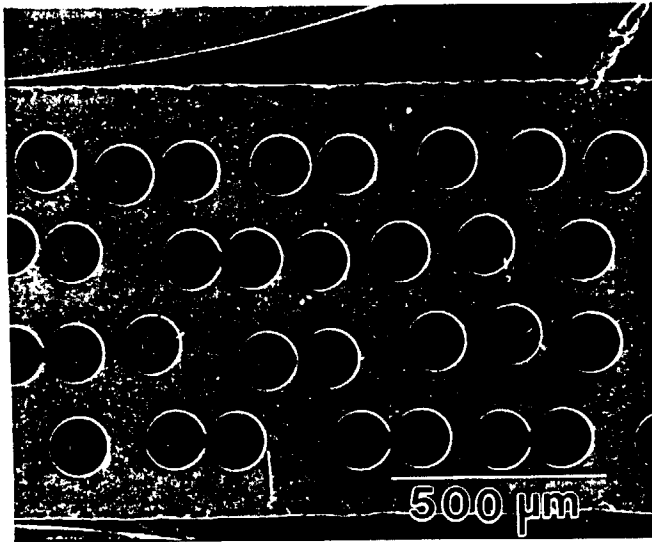




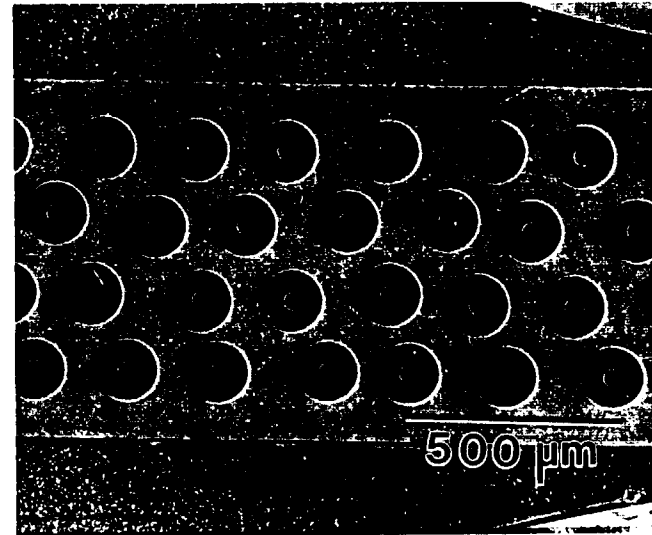
# Ti-1100/SCS-6 Composite Panels

- Fabricated at NASA LaRC by VHP'ing foil/fiber/foil layups.
- 4-ply, unidirectional panels sectioned into 0.25 inch wide samples prior to exposure.
- Original Panels - Panel A
  - 7 mil foil
  - 28 volume percent fiber
  - average fiber spacing = 190 microns
- New Panels - Panels B,C,D,E
  - 4 mil foil
  - 37 volume percent fiber
  - average fiber spacing = 210 microns
- Thermal Exposures Performed
  - Cycled 150 to 800C 500 times in air.
  - Cycled 150 to 800C 500 times in argon.
  - Cycled 150 to 700C 500 times in air.
  - Isothermally Exposed at 735C in air.

# Fiber Spacing



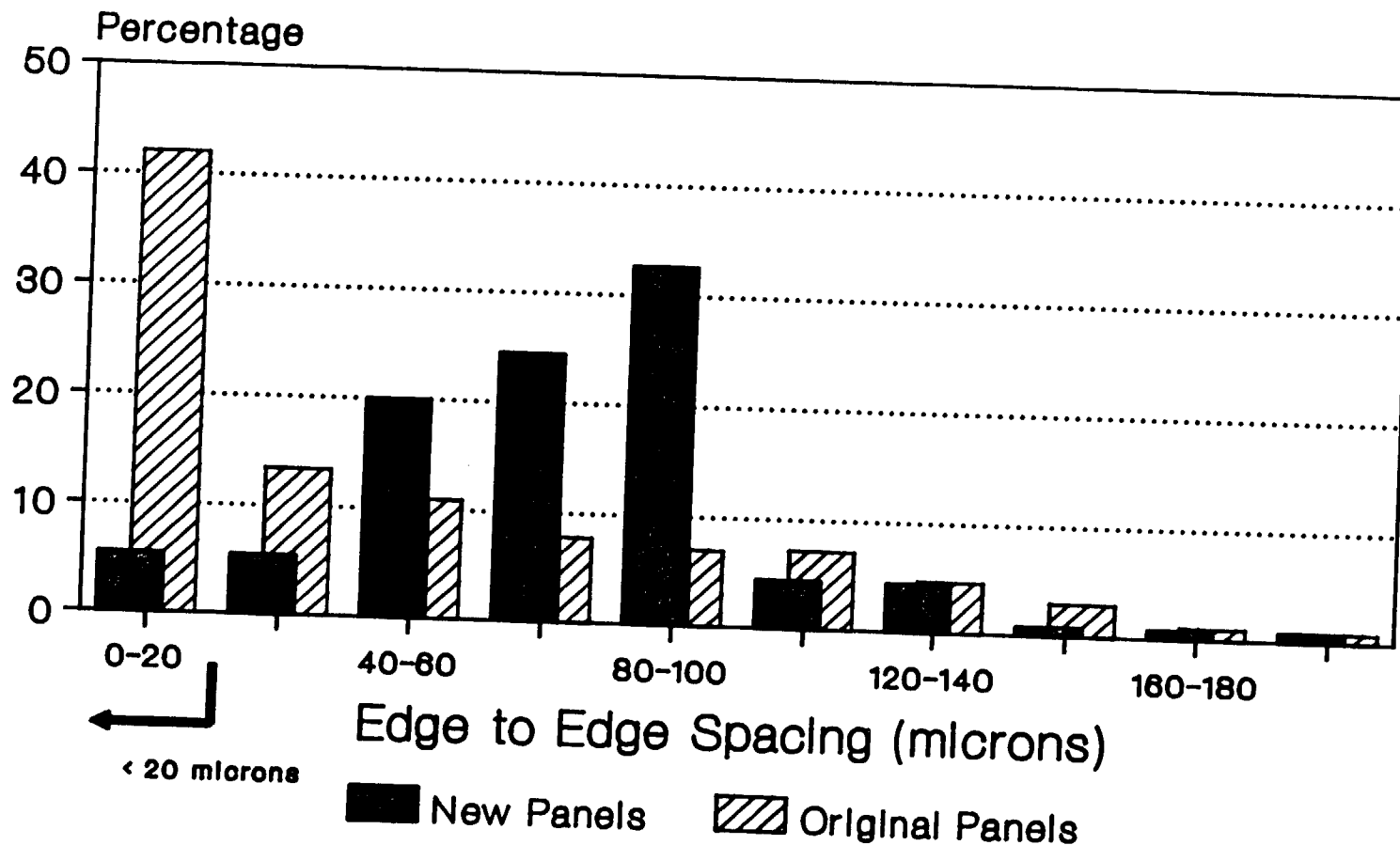
Original Panels



New Panels

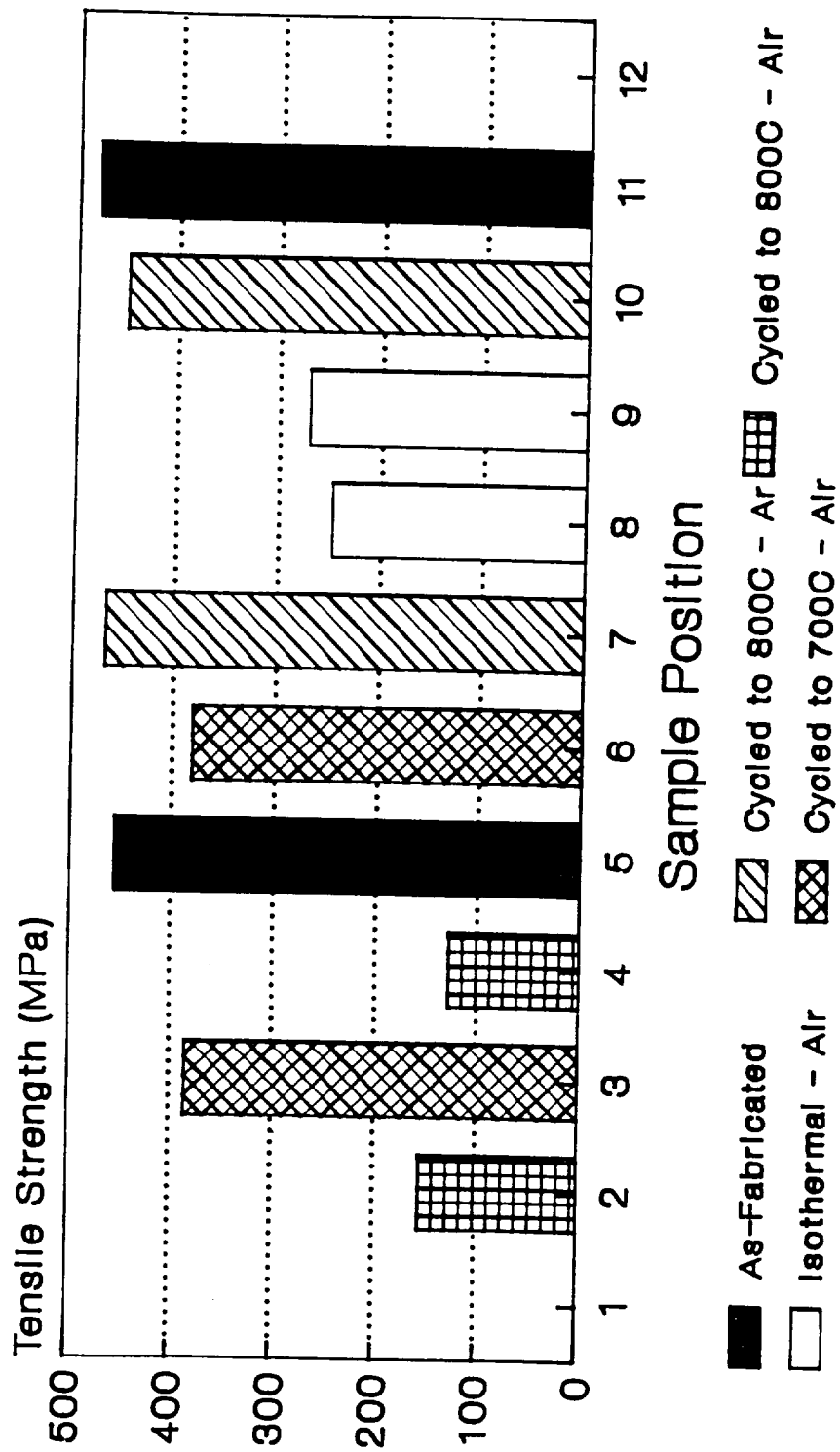
# Fiber Spacing Distribution

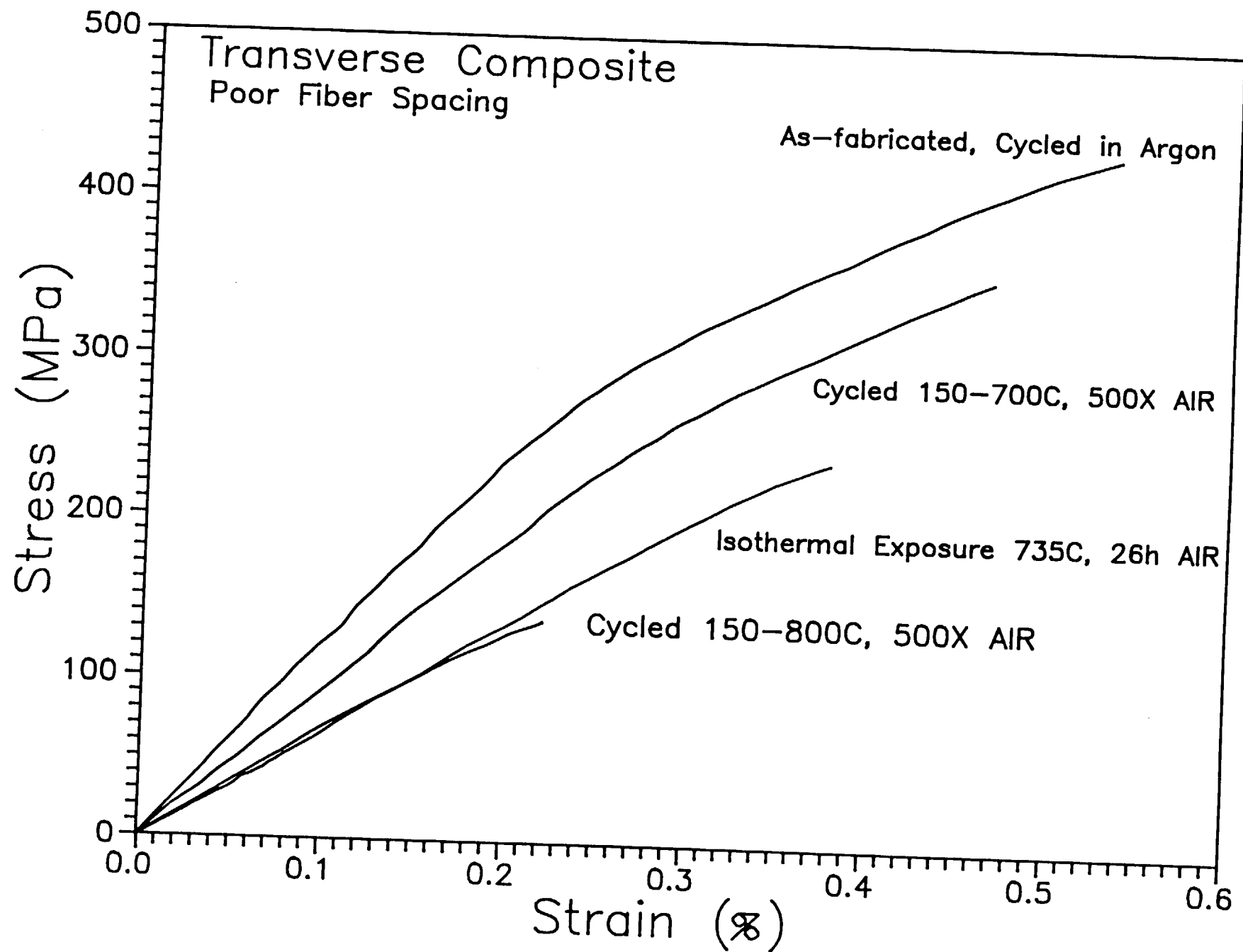
## Original vs. New Panels





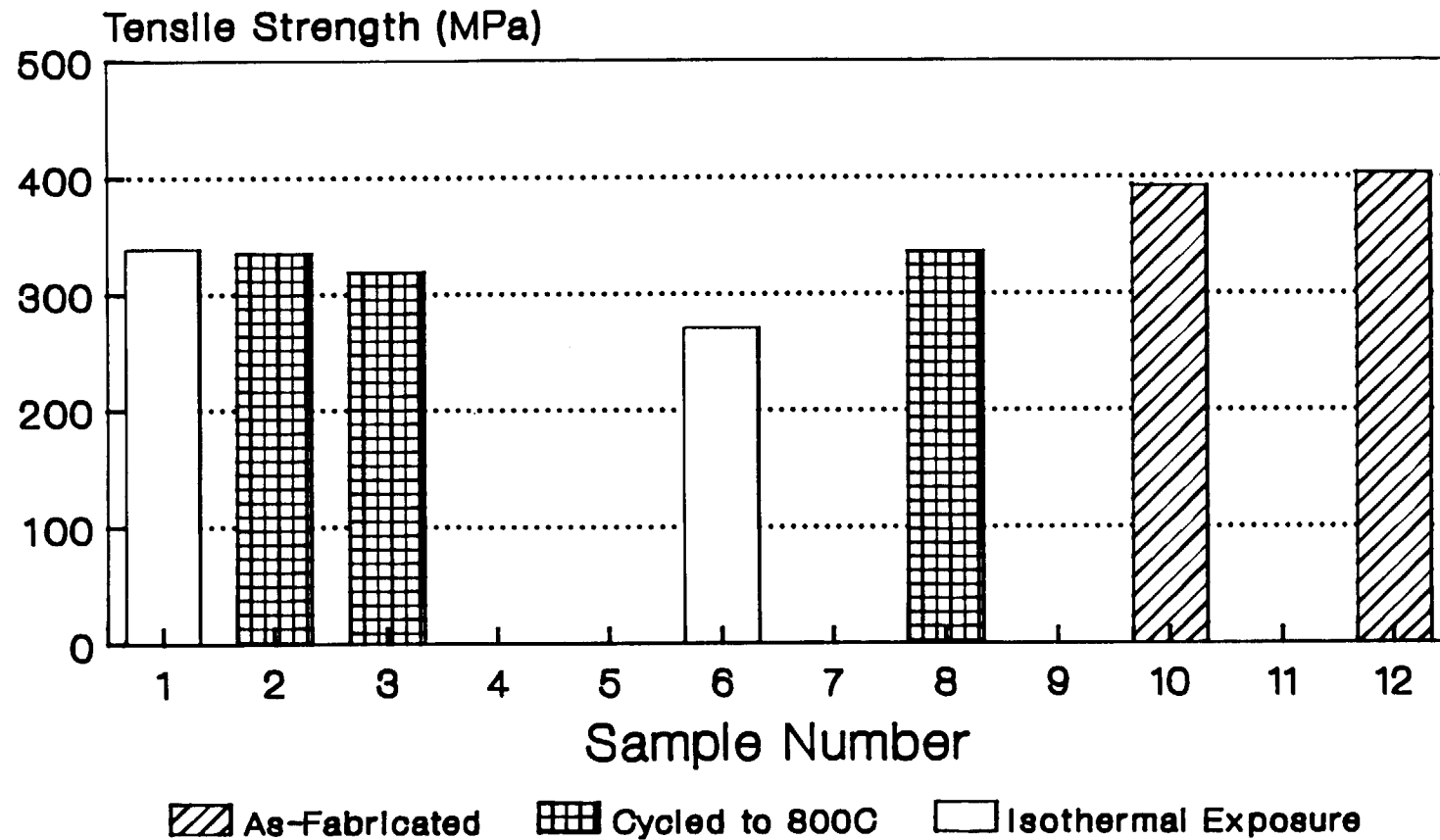
# Tranverse Samples Poor Fiber Spacing

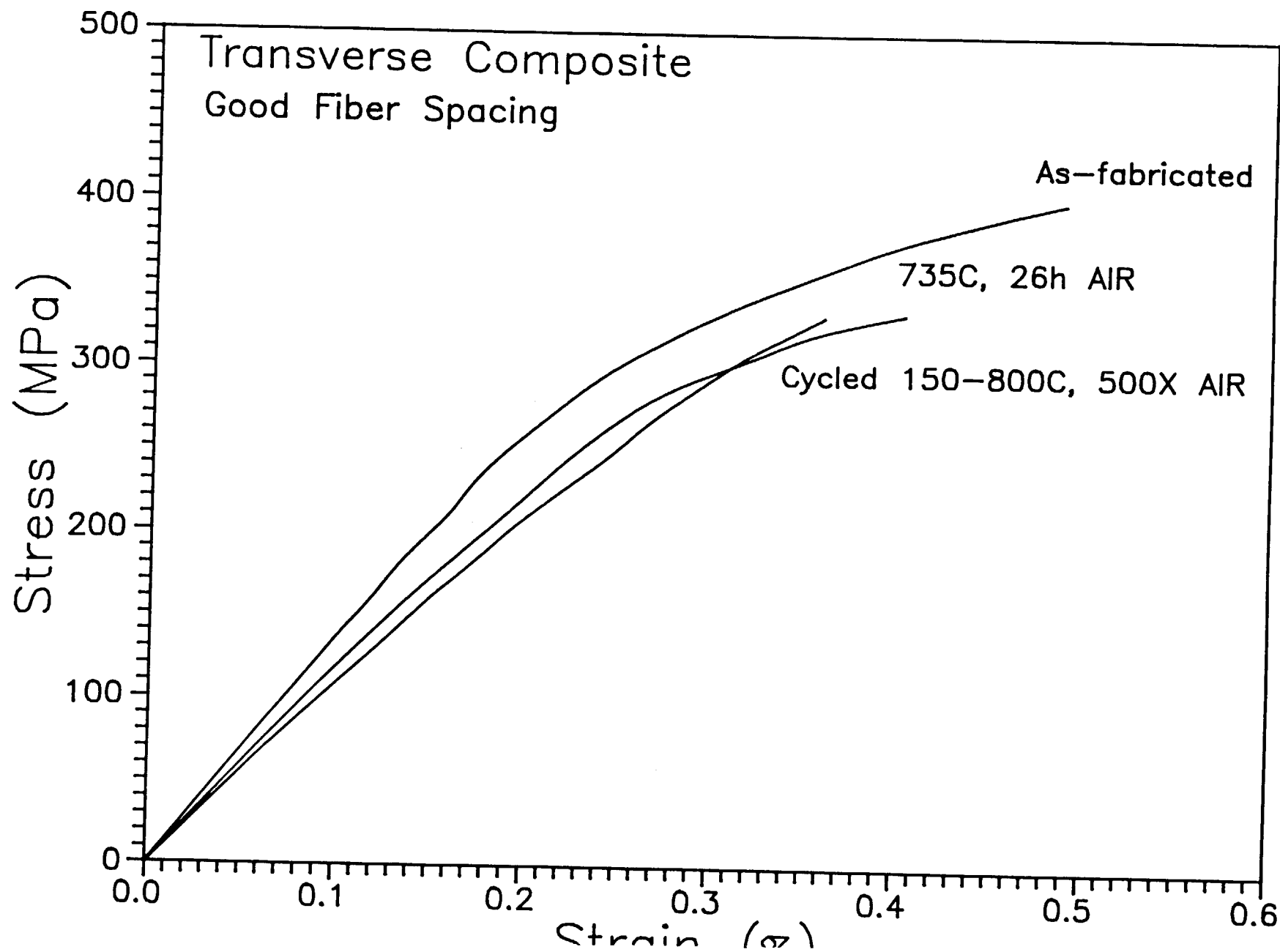




# Transverse Samples

## Good Fiber Spacing



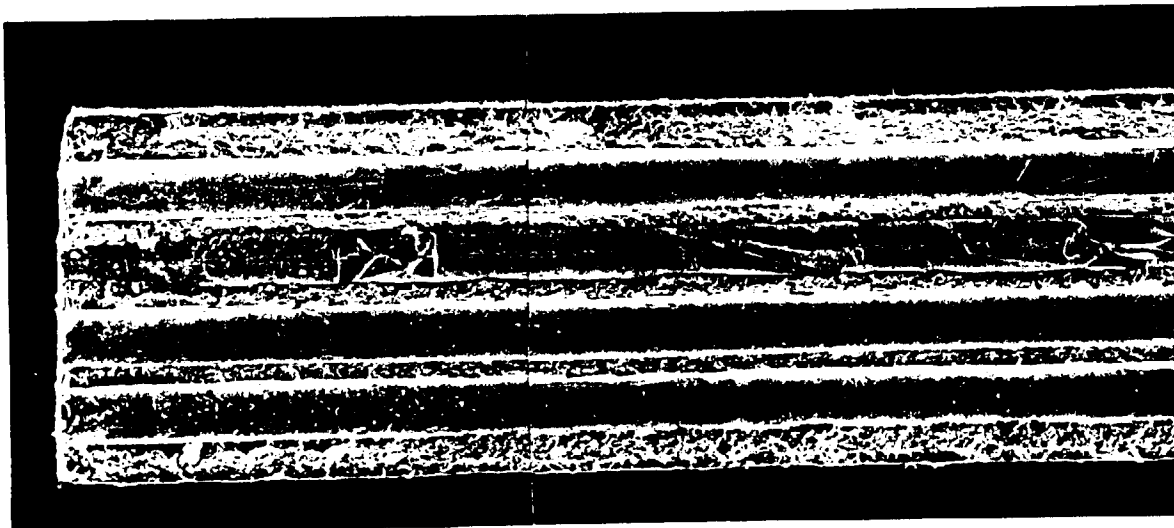


# Transverse Fracture Surfaces

Cycled 150-800C 500X

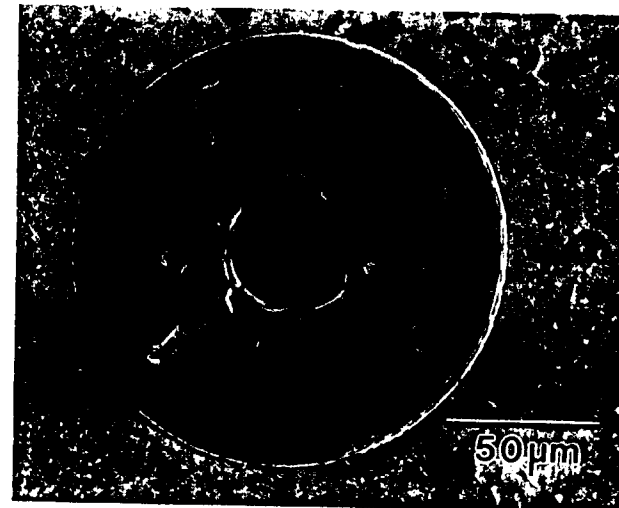
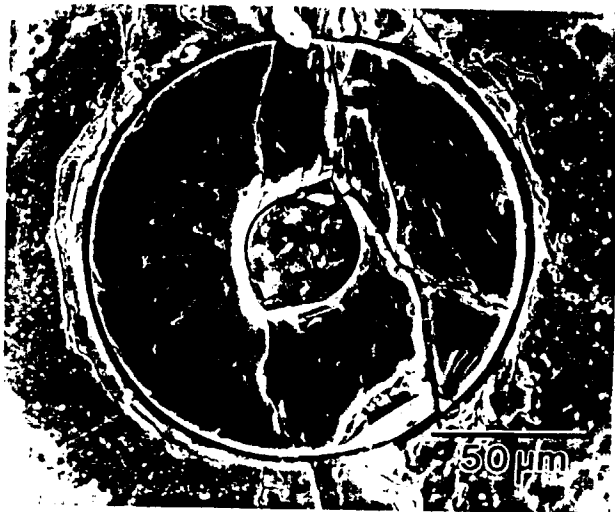
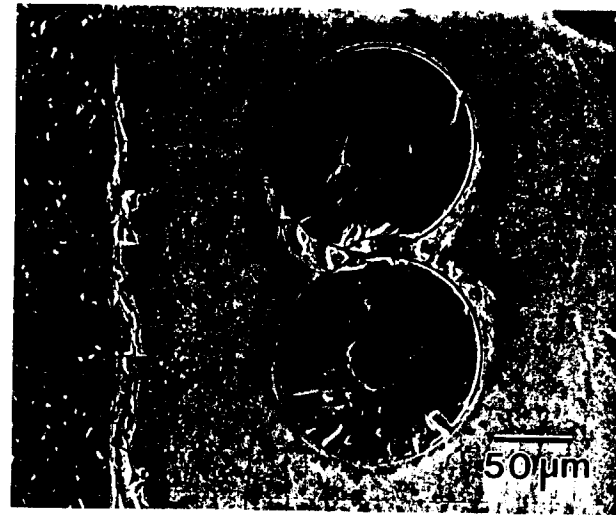
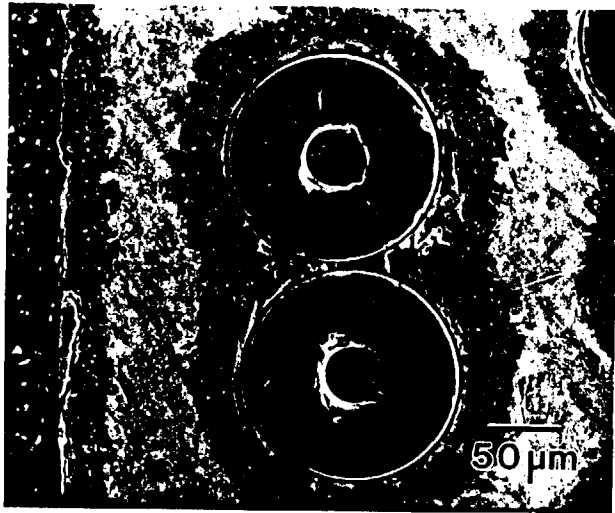


Original Panel

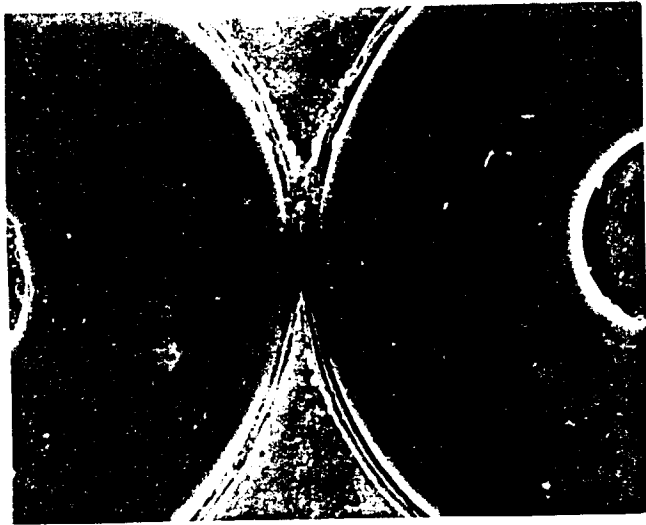


# Transverse – Poor Spacing

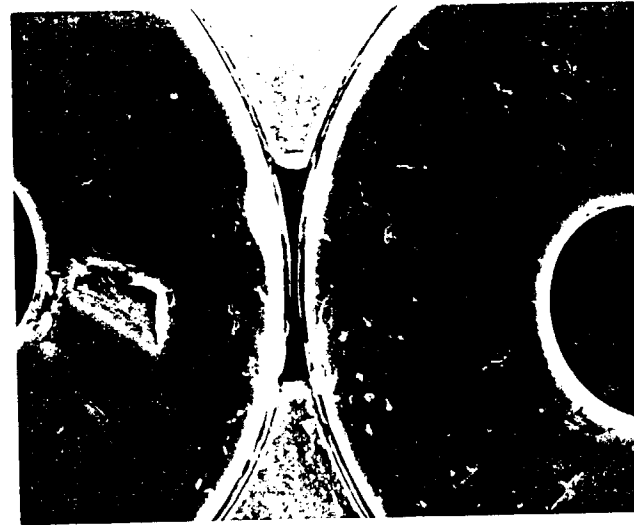
Cycled 150–800C 500X



# Transverse – Poor Spacing



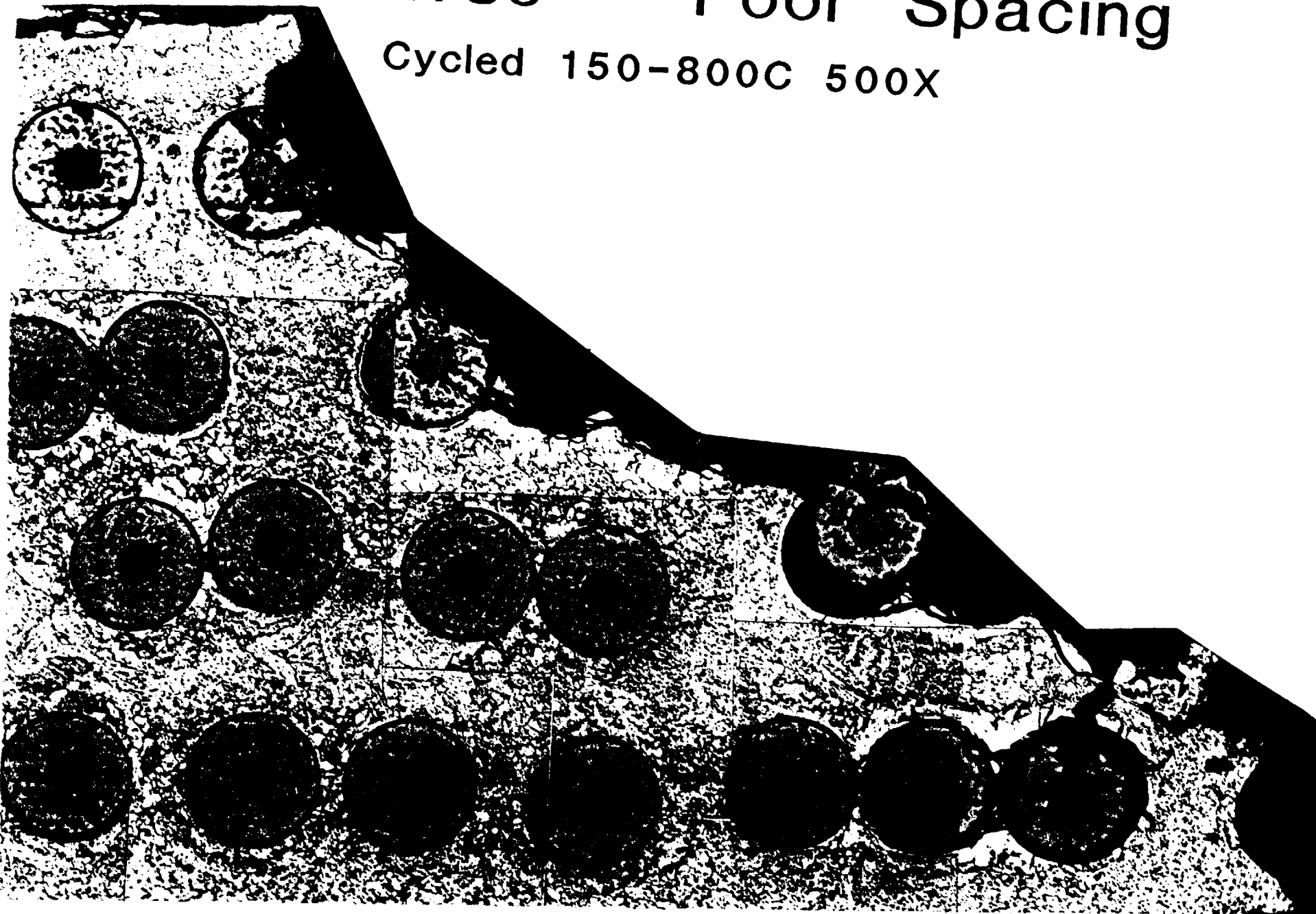
**As-Fabricated**



**Cycled**

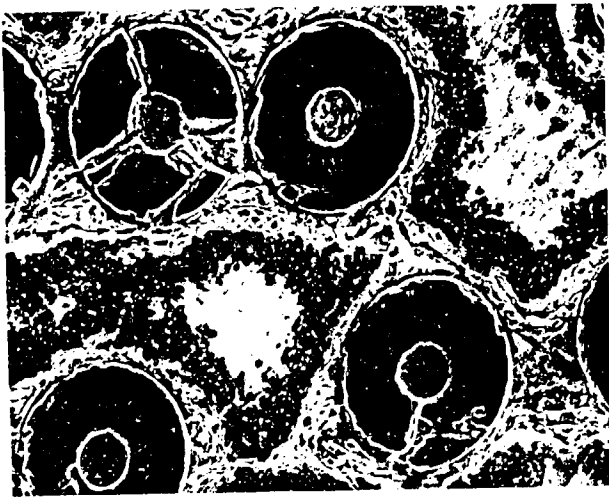
# Transverse - Poor Spacing

Cycled 150-800C 500X

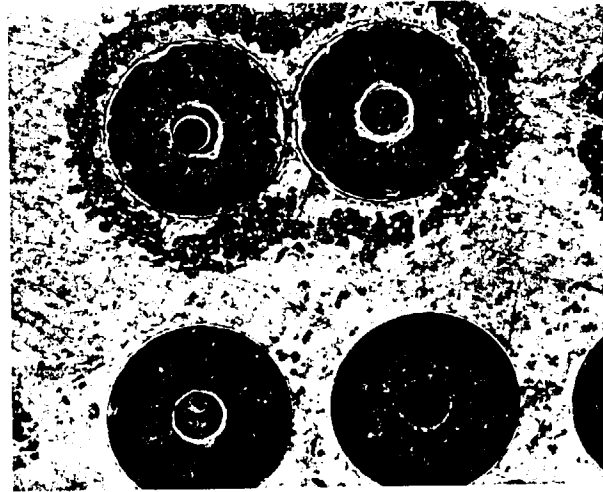




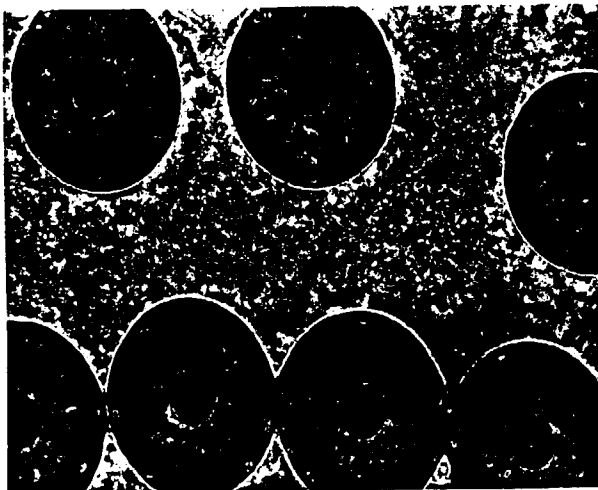
# Depth of Environmental Interaction Along Touching Fibers



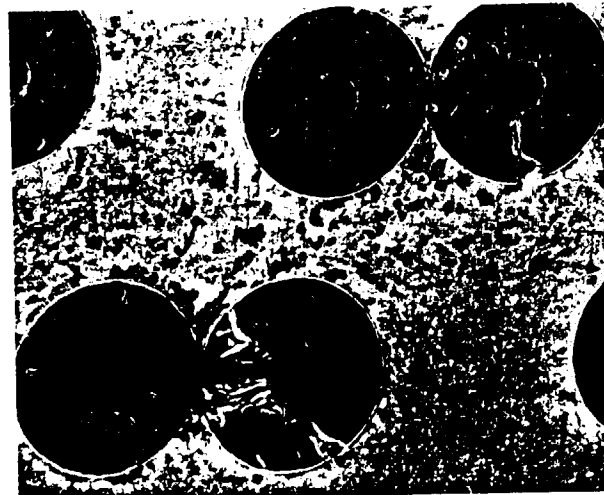
0 cm



0.33 cm



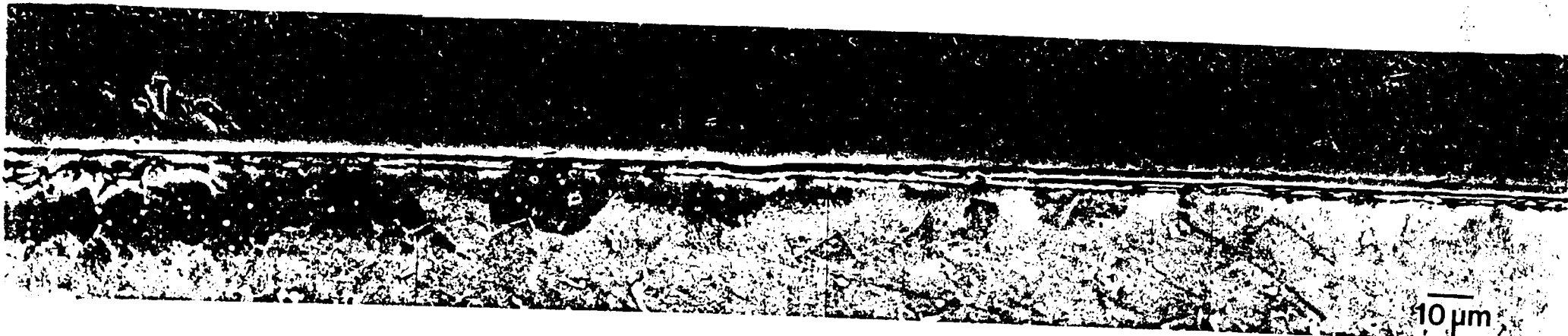
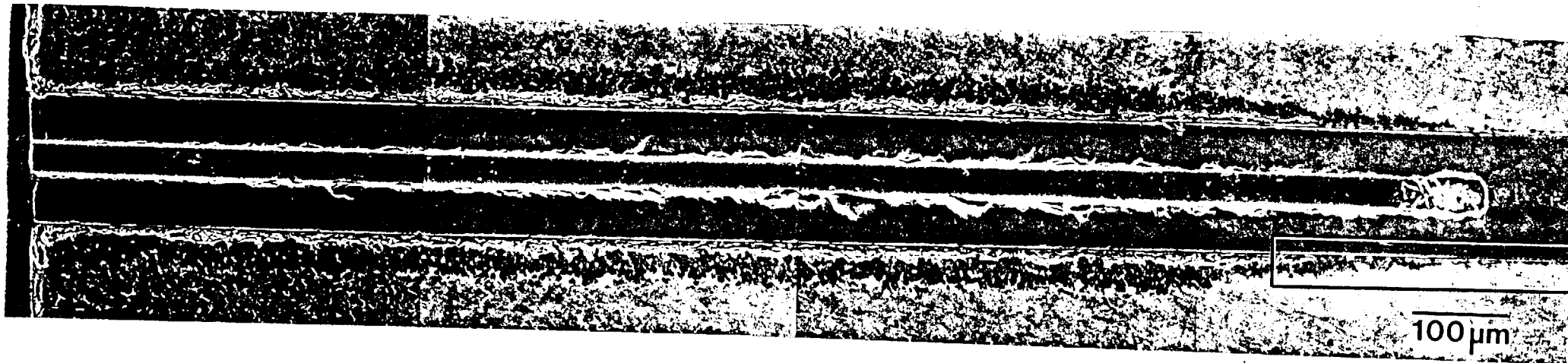
0.67 cm

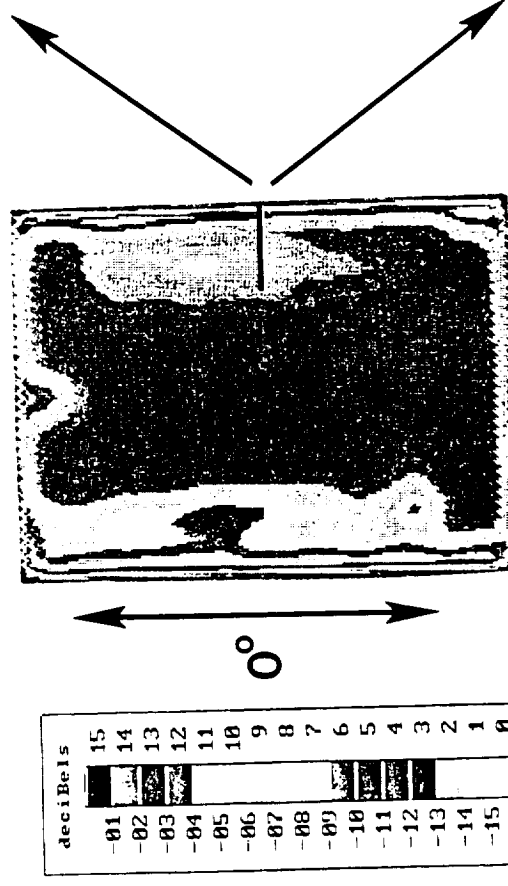


1.0 cm

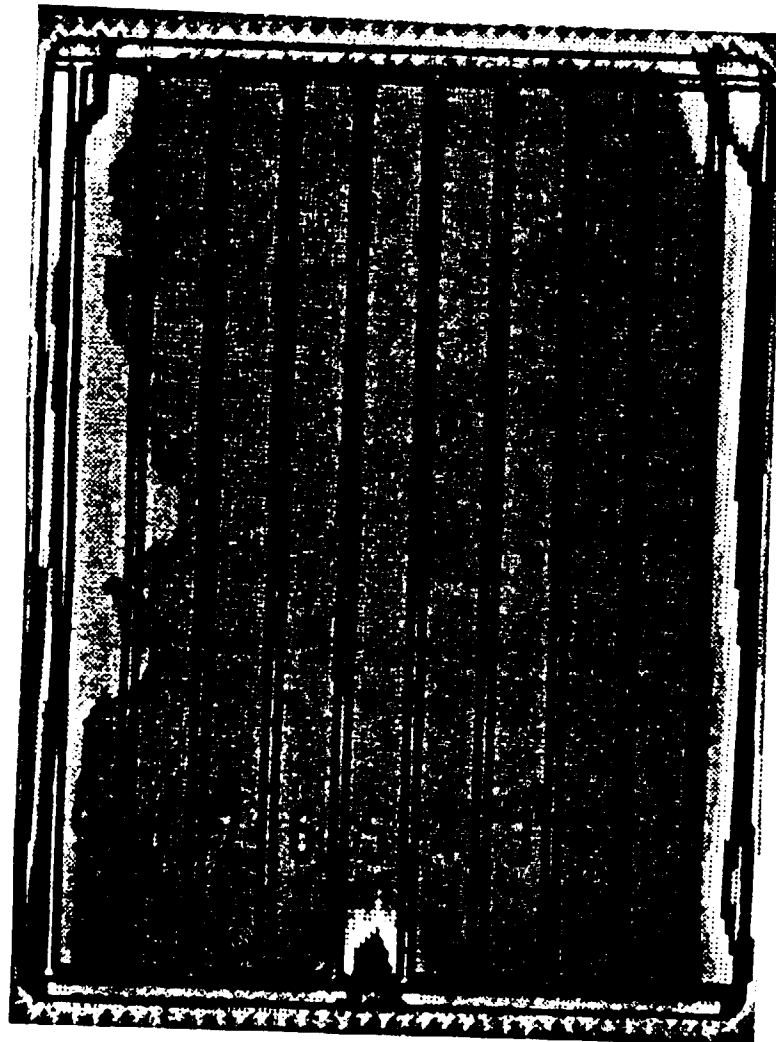
# Interfacial Diffusion

800C 10h

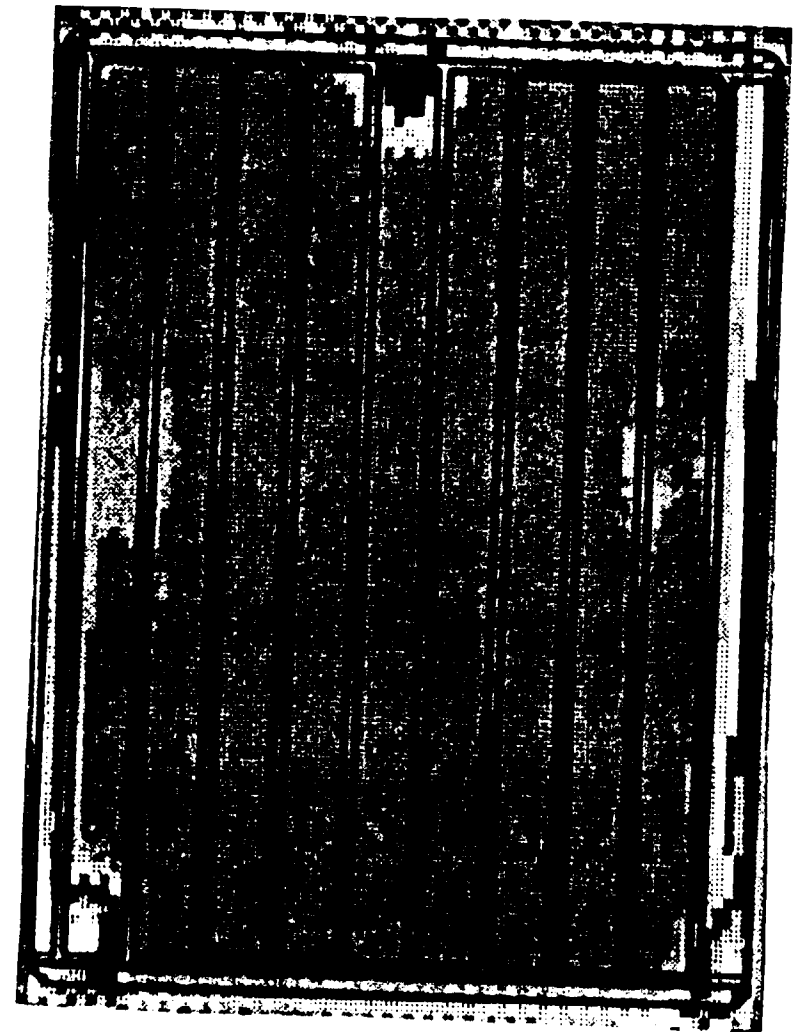
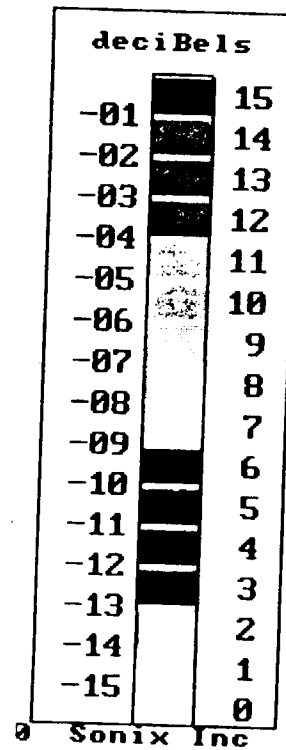




# C-Scans of Panels C and D

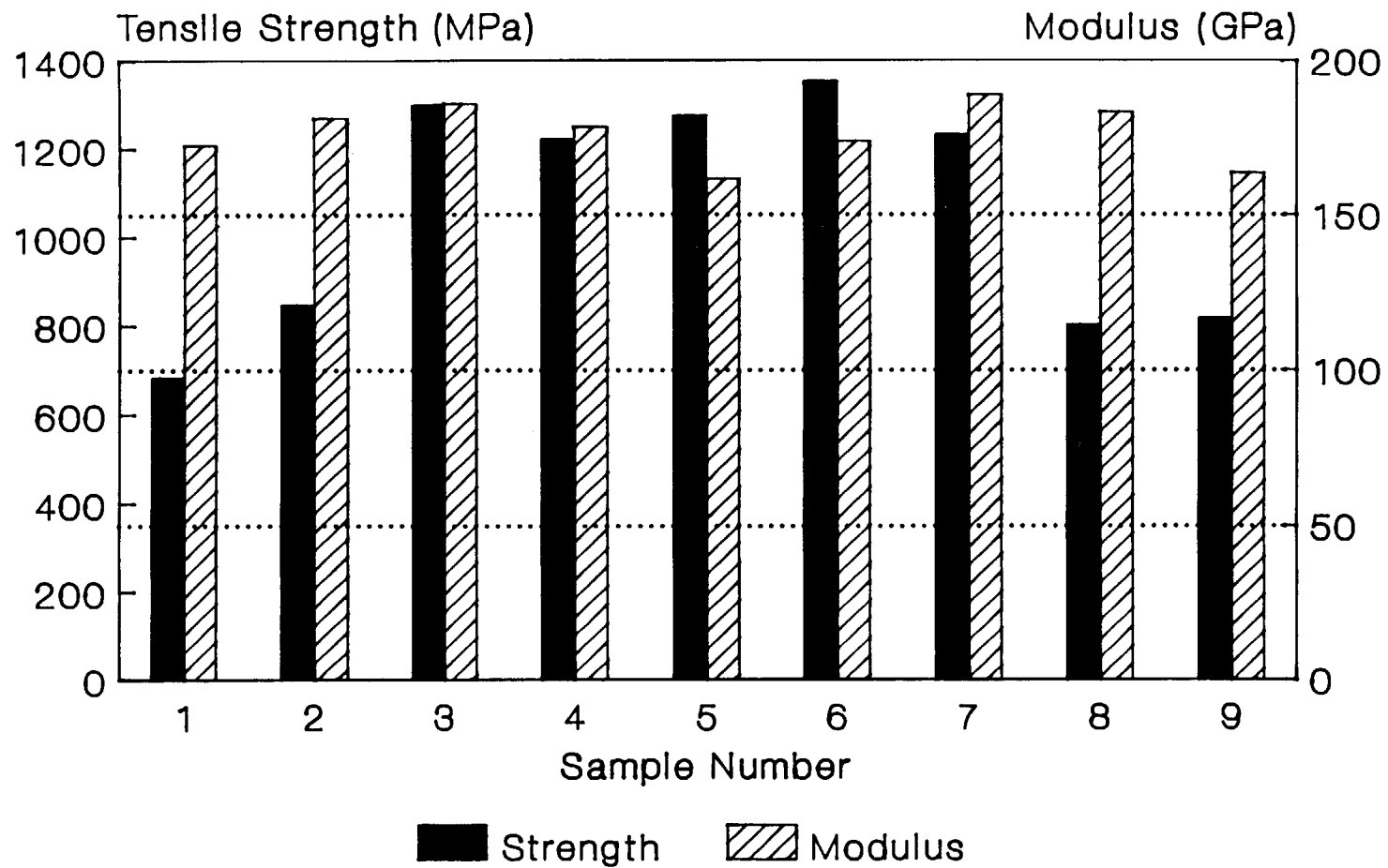


Panel C

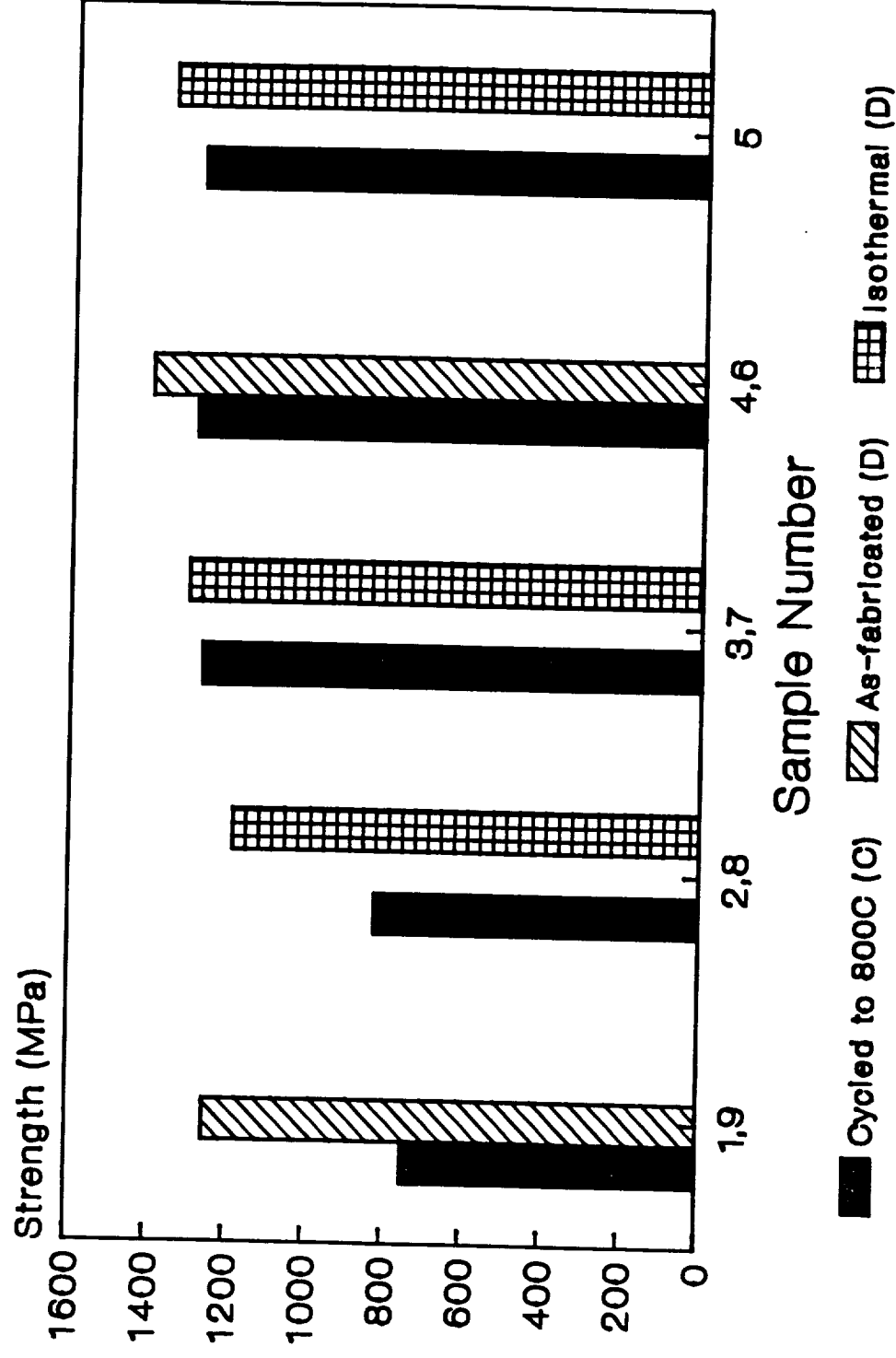


Panel D

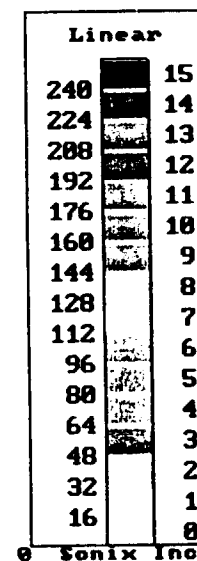
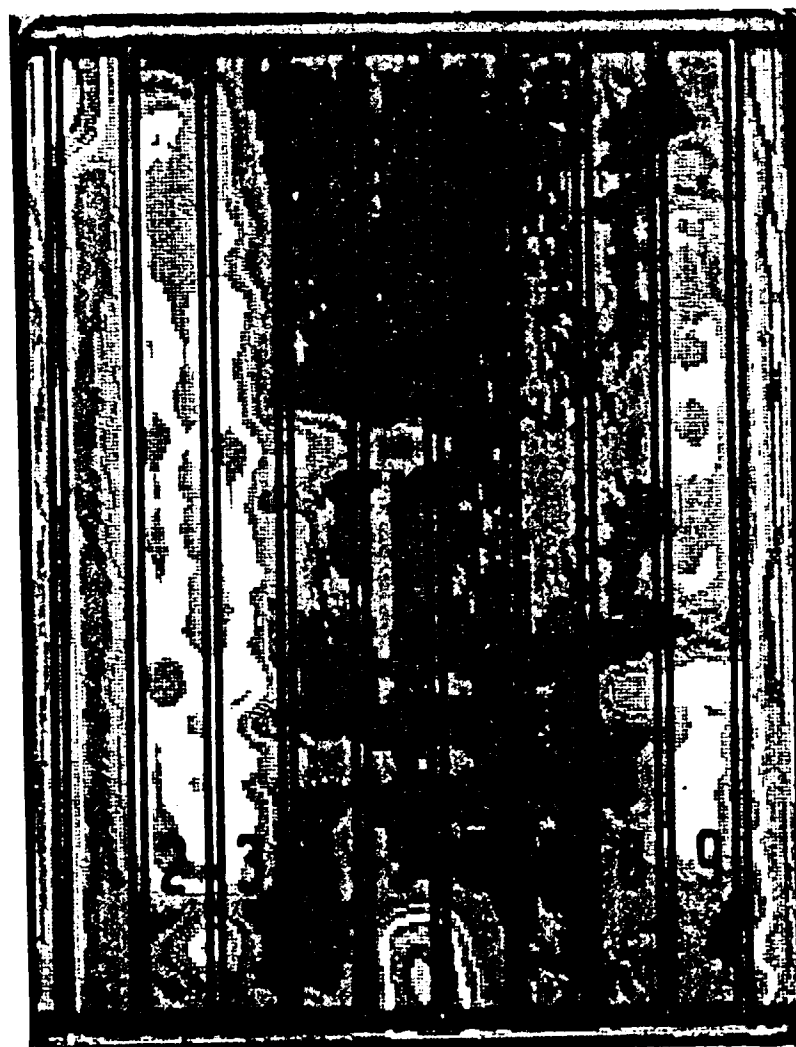
# Tensile Properties vs. Position Cycled 150-800C 500X (Panel C)



# Tensile Strength vs. Position

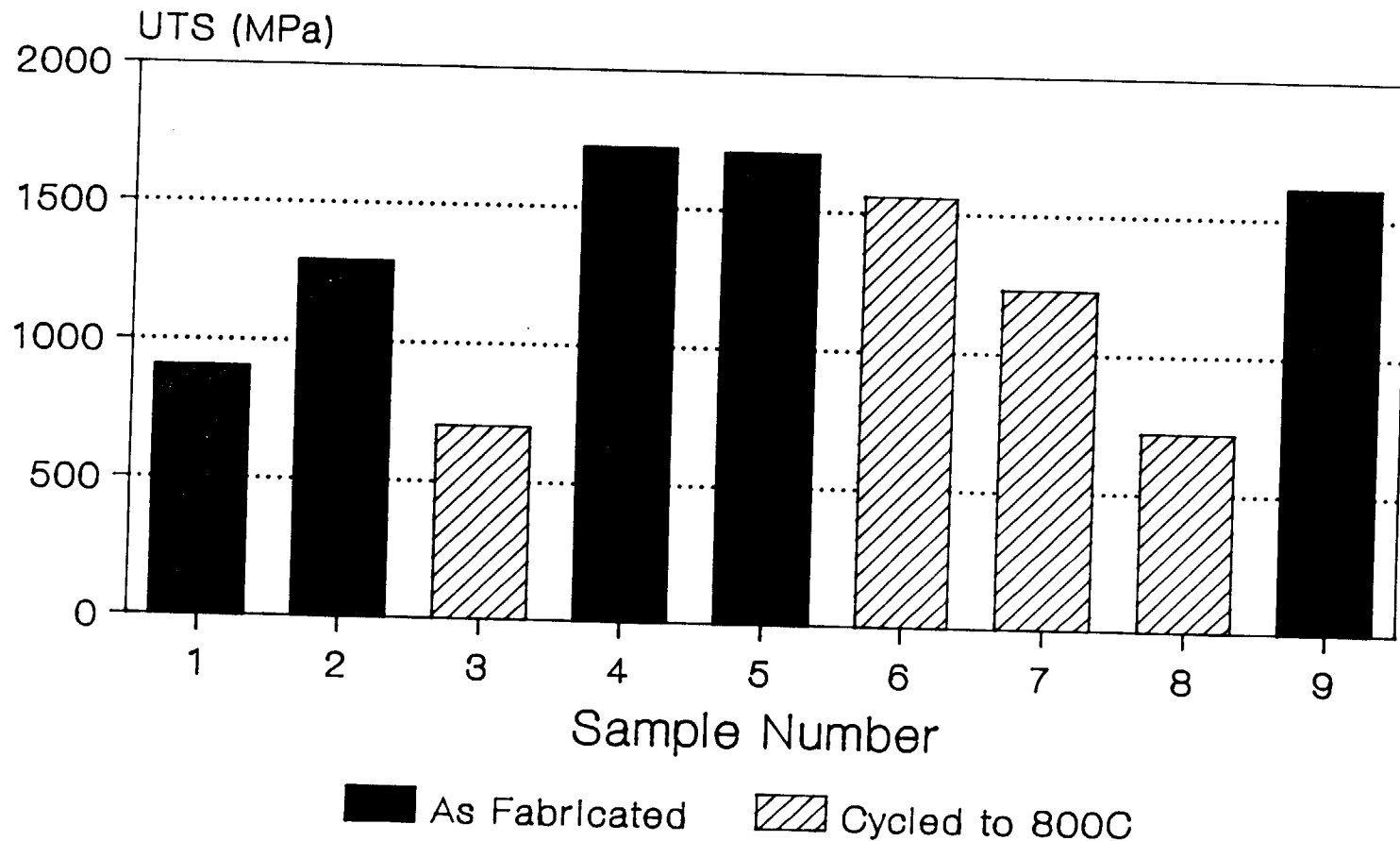


# C-Scan of Panel E



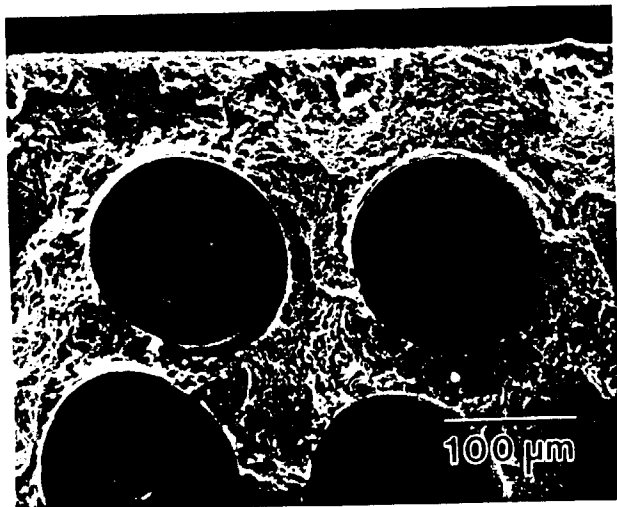
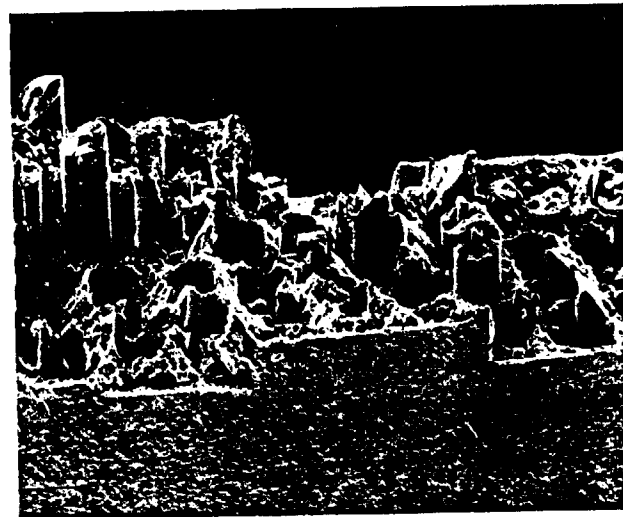
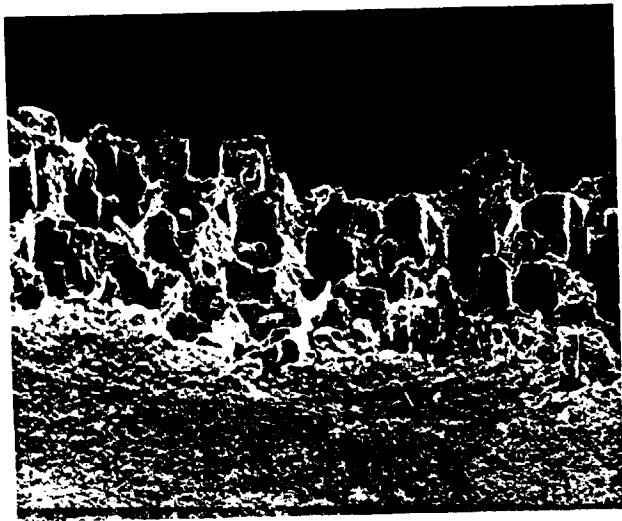
# Tensile Strength (Panel E)

## Cycled and As-Fabricated

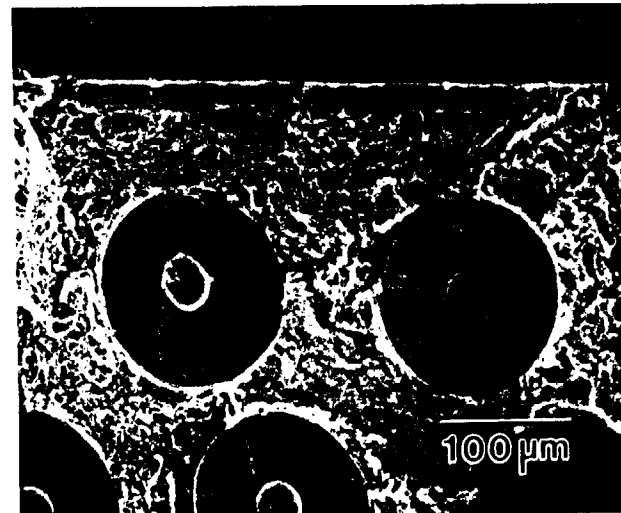




# Well-Consolidated

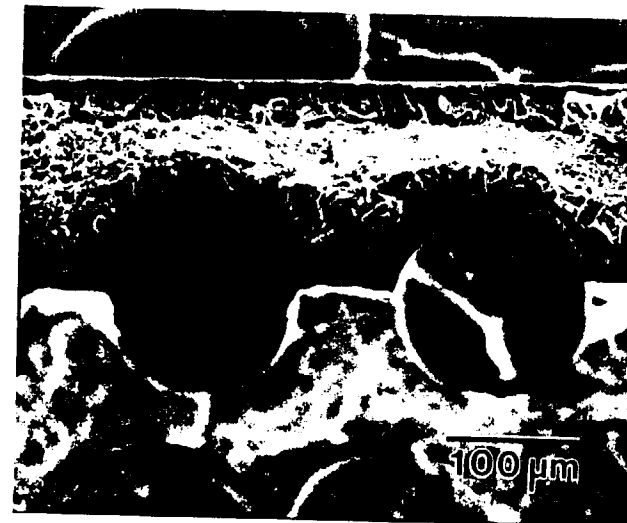
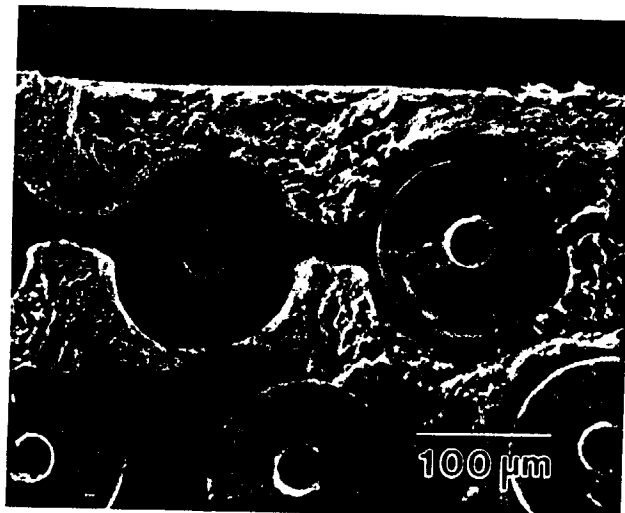
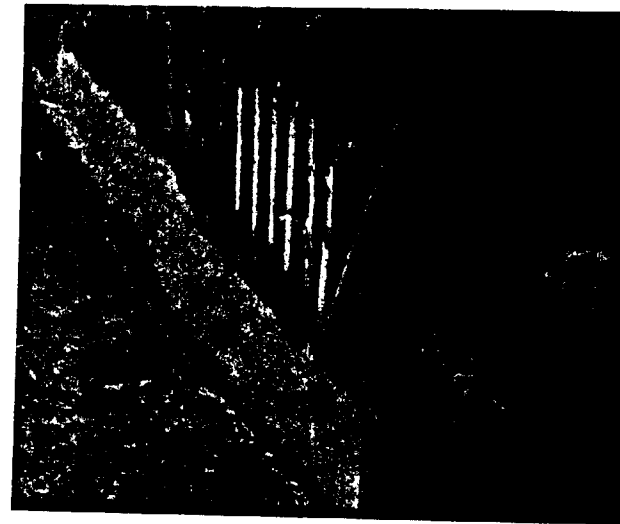


As-Fabricated  
1721 MPa



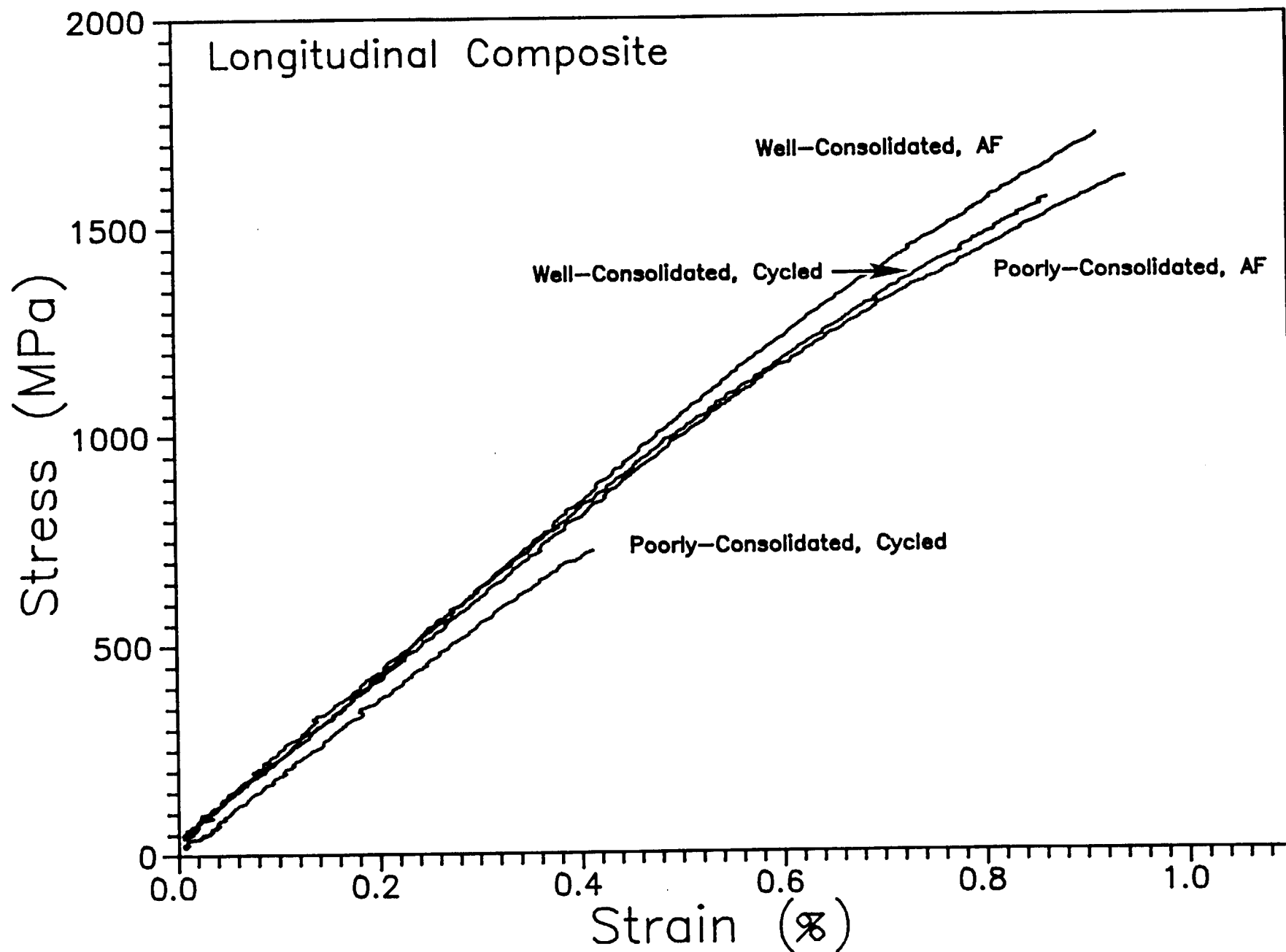
Cycled  
1560 MPa

# Poorly Consolidated



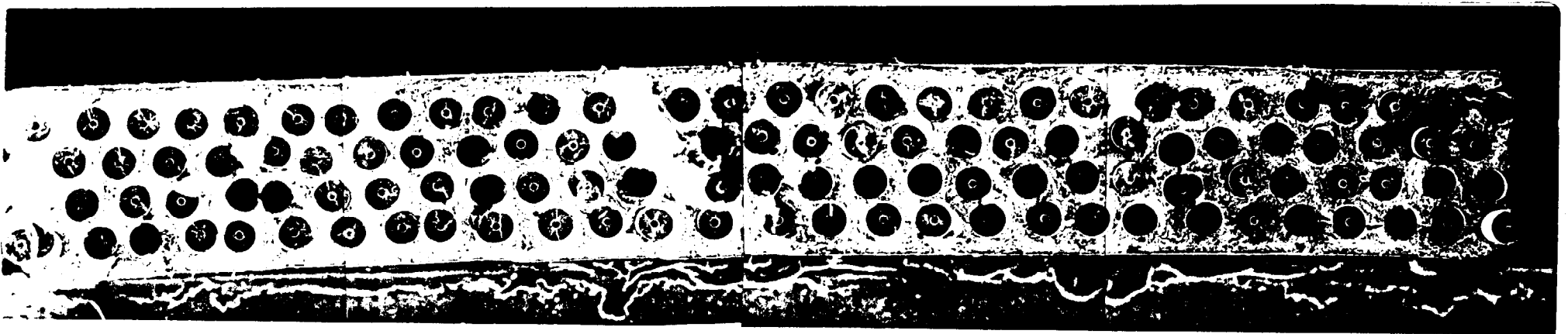
As-Fabricated

Cycled

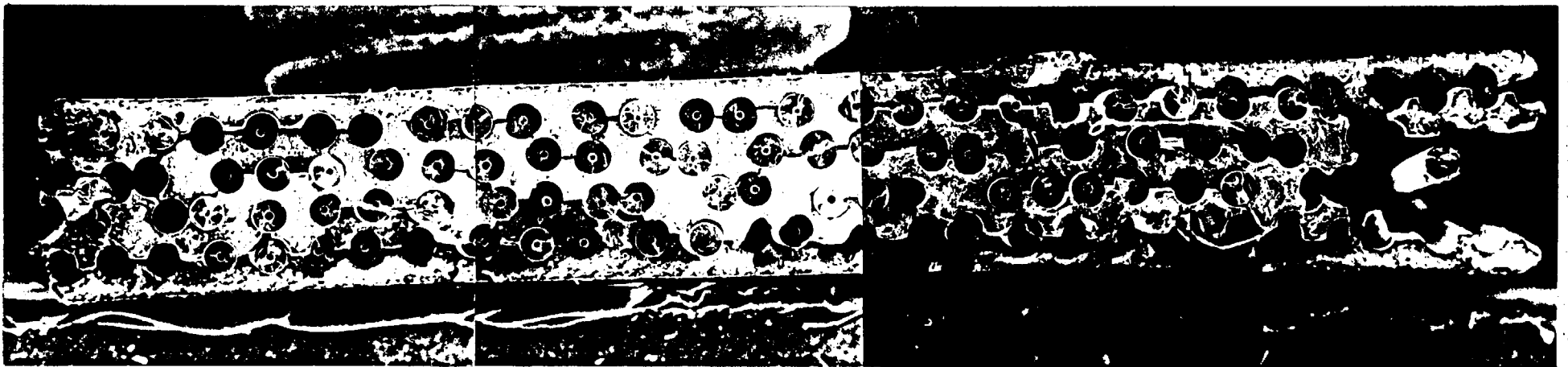


# Longitudinal Fracture Surfaces

Cycled 150-800C 500X



Well-Consolidated



Poorly Consolidated

# Summary

- A brittle subsurface layer grows in Ti-1100 during thermal exposure in air.
- Ultrasonic c-scans of the composite panels revealed poorly-consolidated areas.

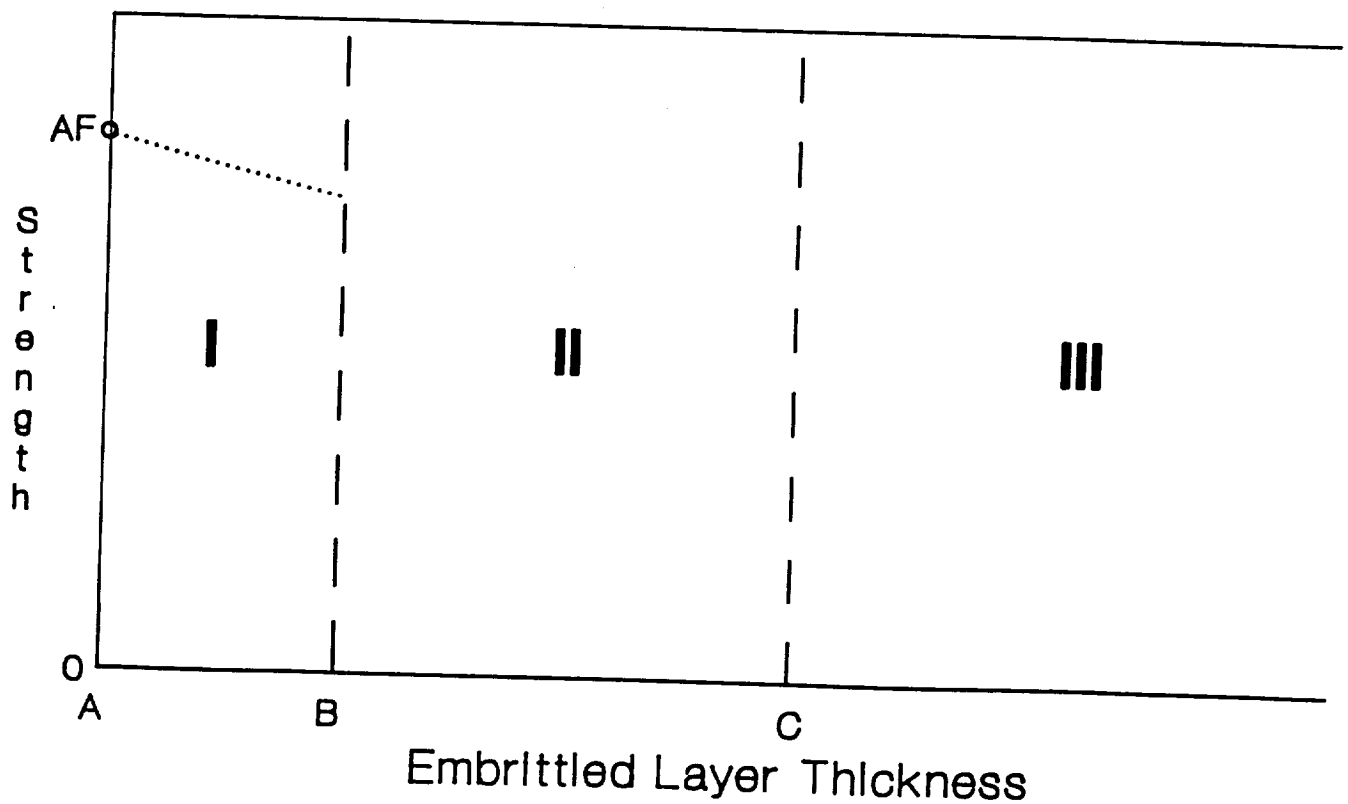
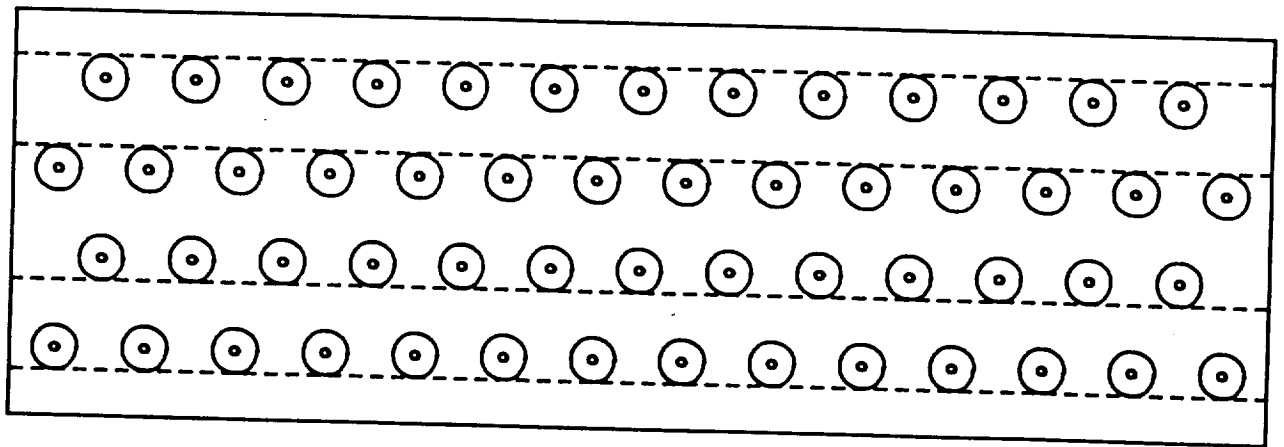
## TRANSVERSE

- Samples containing a great deal of fiber-fiber contact exhibited drastic strength losses following cyclic thermal and isothermal exposure in air.
- Fiber contact allowed significant embrittlement of the matrix well into the sample.
- Samples with well-spaced fibers retained over 80% of their tensile strength following cycling in air.

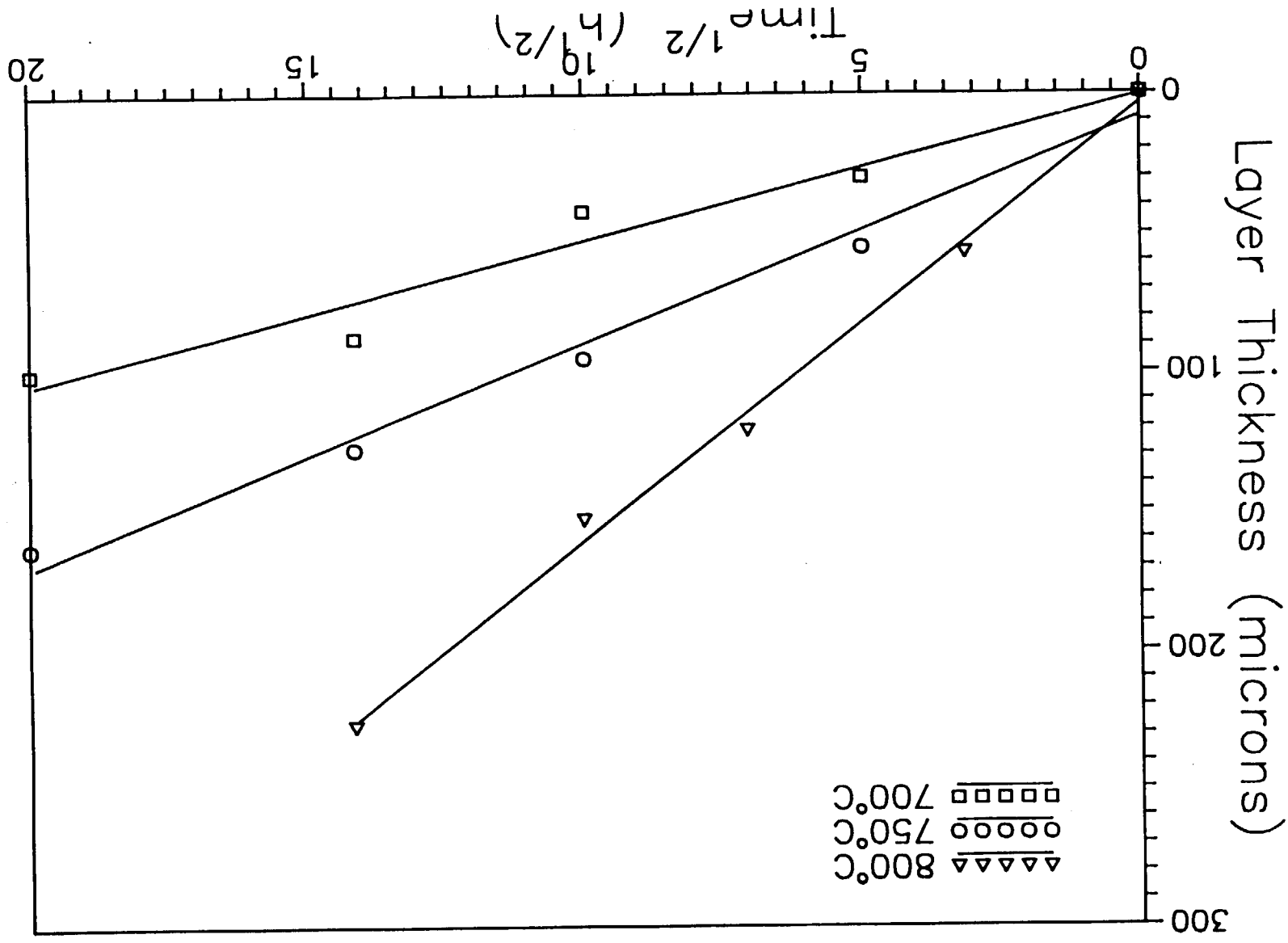
## LONGITUDINAL

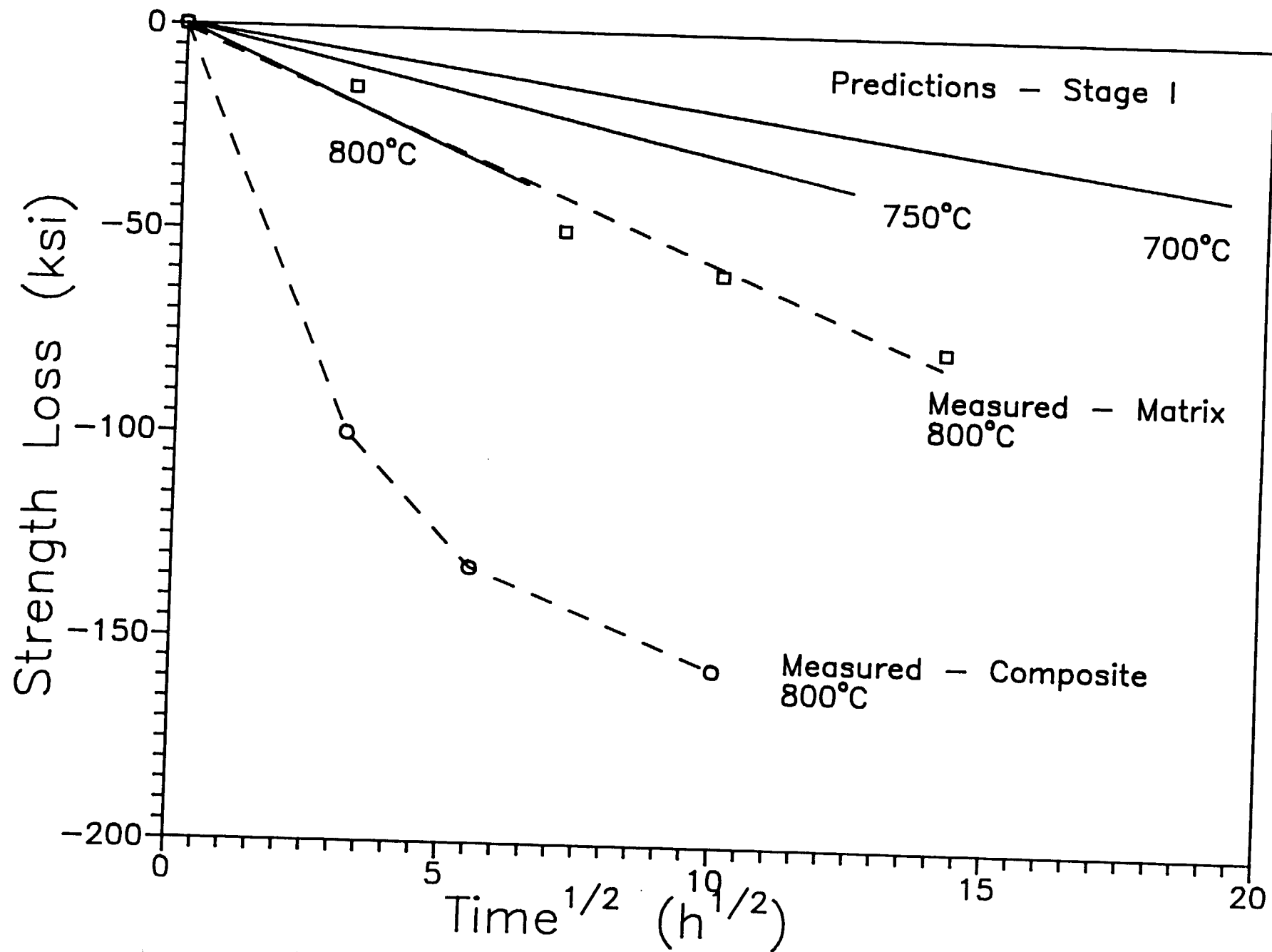
- Samples from poorly consolidated areas of the composite sometimes exhibited low as-fabricated strength, but were always severely degraded by thermal exposure.
- Damage to the poorly-consolidated samples included matrix ply delamination, matrix embrittlement, and fiber-matrix interfacial degradation.
- Cyclic thermal or isothermal exposure of well-consolidated samples in air only slightly degraded their strength.

# Effect of Matrix Embrittlement on Longitudinal Composite Strength



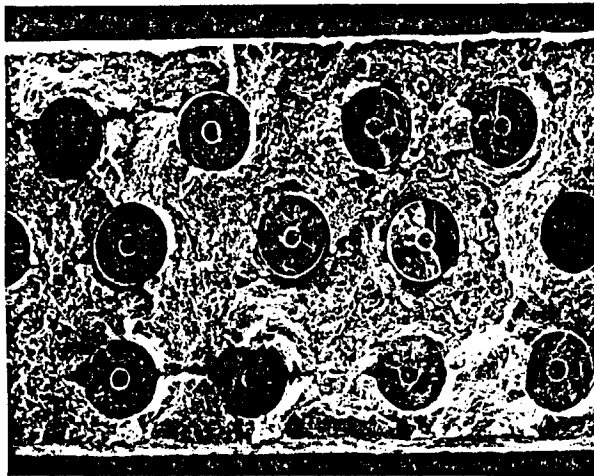
# Embrittled Layer Growth Rate



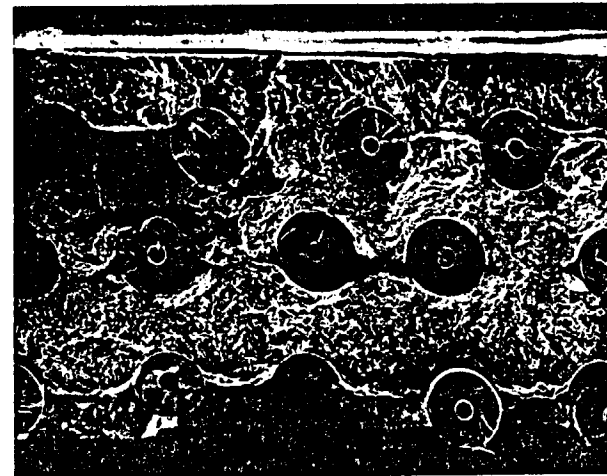




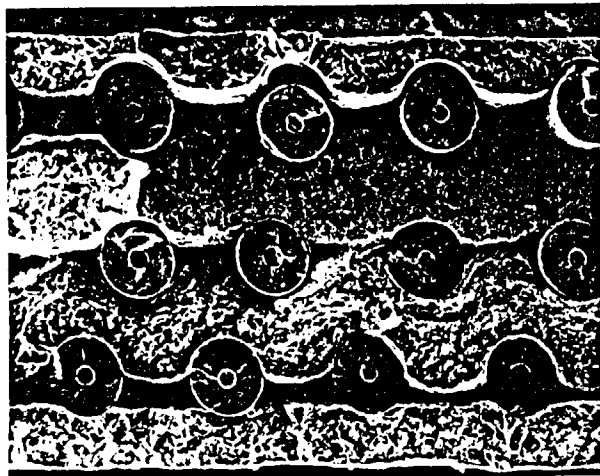
# Longitudinal Composite Fracture Surfaces



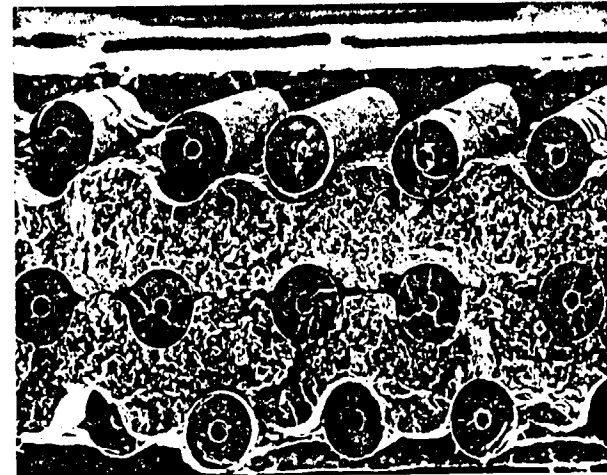
As-Fabricated



800C 30h



800C 10h



800C 100h



## **Project #10    Processing and Superplastic Properties of Weldalite™ Sheet**

Mark Lyttle and John A. Wert

### **Objective**

The objectives of this research are to observe the effect of tensile axis orientation on the superplastic formability of Weldalite™ sheet and to isolate, using simulative models and other techniques, the important microstructural elements and deformation mechanisms that impart superplastic properties to aluminum alloys via continuous recrystallization.

### **Current Status**

To examine the anisotropy of the superplastic properties of Weldalite™, uniaxial tensile tests have been performed on two sets of specimens, one oriented with the tensile axis parallel to the rolling direction and the other parallel to the transverse direction. The tensile tests were stopped at various strains during the initial stages of superplastic deformation and the resulting microstructural evolution was interpreted through the observation of boundary misorientation angle characteristics, microtexture evolution, and grain growth rate.

### **Important Findings**

The anisotropy of the Weldalite™ sheet during superplastic forming processes is easily observable and can be quantified in many ways. By comparison of stress-strain curves during forming, the flow stress of the transverse-oriented samples is seen to be almost twice that observed in the rolling direction-oriented specimens. However, elongations of greater than 800% occurred during tests to failure for both orientations, which indicates that the increased forming stress does not necessarily lead directly to a reduction in attainable superplastic strain.

TEM investigation and subsequent Kikuchi pattern analyses of the grip (unstrained) portions of the tensile specimens revealed that the microstructure initially contains predominantly low-angle boundaries in both experimental orientations. As strain increases in the gauge sections, the fraction of high-angle boundaries is observed to increase, eventually generating a predominantly high-angle microstructure suitable for superplastic

forming. This microstructural evolution is characteristic of that observed in other continuously recrystallized aluminum alloys.

Several differences were observed in the evolution of mean linear intercept grain sizes determined from micrograph montages of grain clusters at various strains and tensile orientations. The initial grain structure of the ST plane was more equiaxed than that of the LS plane. During forming, strain enhanced grain growth occurred in all specimens and the rate was roughly the same for the two tensile specimen orientations.

Application of simulative models to the initial experimental observations indicated that for both compositions of Weldalite™ and for both specimen orientations, grain boundary sliding was the predominant mechanism that facilitated superplastic elongations. No significant evidence was seen to support a major role of dislocation motion as an accommodation process. Eventual differences during superplastic forming can be directly attributed to the initial as-rolled microstructure and the degree to which the grains are elongated in the original microstructure.

#### Presentation Viewgraphs

1. Introduction and Topics
2. Objectives
3. Overview of Superplasticity. A short review of how continuous recrystallization facilitates superplastic elongations.
4. Continuous Recrystallization. A schematic of the microstructural evolution occurring during concurrent straining and annealing.
5. Composition and Experimental Tests. Composition of specimens and a description of the tensile tests performed.
6. TEM Grain Misorientation Map for x2095 Transverse Grip. Micrograph of a grip section which reveals a traditional as-rolled microstructure. Boundary misorientations are indicated on the micrograph.
7. TEM Grain Misorientation Map for x2095 Transverse Gauge (Strain = 0.21). The effect of continuous recrystallization is evident. There is a lower fraction of low angle boundaries, and high angle boundaries have lost some of their identity with the rolled direction.

8. Histograms of Misorientations in 049 Rolling. A series of histograms that show the evolution from a predominantly low angle microstructure to one favorable for superplastic elongations.
9. Histograms of Misorientations in X2095 Rolling. A series of histograms that show the evolution from a predominantly low angle microstructure to one favorable for superplastic elongations.
10. Histograms of Misorientations in 049 Transverse. A series of histograms that show the evolution from a predominantly low angle microstructure to one favorable for superplastic elongations.
11. Histograms of Misorientations in x2095 Transverse. A series of histograms that show the evolution from a predominantly low angle microstructure to one favorable for superplastic elongations.
12. Strain Enhanced Grain Growth. All specimens were subject to basically the same heat exposure during forming. The samples deformed to higher strains had an increased grain growth rate.
13. Experimental Summary. A review of all direct experimental observations.
14. Modeling of Continuous Recrystallization. A brief review of the two models developed last year for this project.
15. Grain Boundary Switching. A description of a model developed this year that simulates the amount of grain rearrangement that occurs during large strains. a) micrograph of a grip section. b) tessellation representation of the grip section. c) tessellation representation of grip section strained to 0.41. Note the increase in very high angle boundaries ( $> 50$  degrees) represented by the thickest lines.
16. Application of Models to 049 Rolling. Comparison of experimental and modeled results. There is a good correspondence between 5 degree rotation and strain = 0.11 and also between 10 degree rotation and strain = 0.21.
17. Application of Models to x2095 Transverse. Comparison of experimental and modeled results. At a strain of 0.11, it appears that an average 10 degree rotation has already occurred. This indicates grain boundary sliding is responsible for a higher fraction of the total strain in the transverse specimens.
18. Conclusions.



# **Effect of Specimen Orientation on the Superplasticity of Weldalite**

**M. T. Lyttle and J. A. Wert**

**Department of Materials Science and Engineering  
University of Virginia**

---

## **Topics**

- Introduction and Objective
- Conditions for Superplasticity
- Maximum Elongation Testing
- Microstructural Evolution During Superplastic Forming
- Strain Enhanced Grain Growth
- Interpretation of Microstructural Evolution Using Models
- Conclusions

## Objectives

---

- Observe the effect of tensile axis orientation on the microstructural evolution occurring during continuous recrystallization
- Develop and apply simulative models to determine the relative role of various deformation mechanisms during concurrent straining and annealing
- Evaluate the significance of any anisotropy of the superplastic properties



# Overview of Superplasticity

---

## Necessary Characteristics for Superplasticity

- Small Grain Size
- High Angle Grain Boundaries

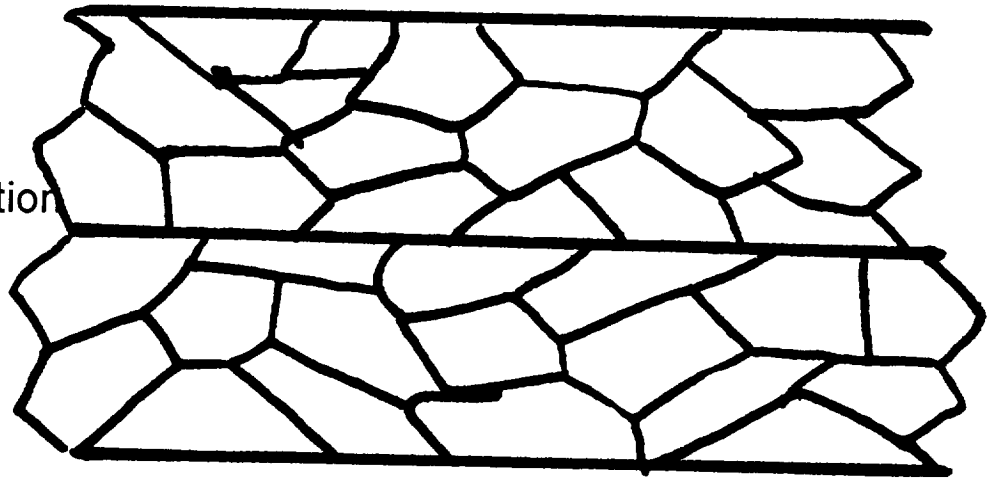
## Continuous Recrystallization

- Initial Structure Contains Mostly Low Angle Boundaries
- Concurrent Straining and Annealing
- Grain Rotations Accumulate
- High Angle Grain Boundaries Result

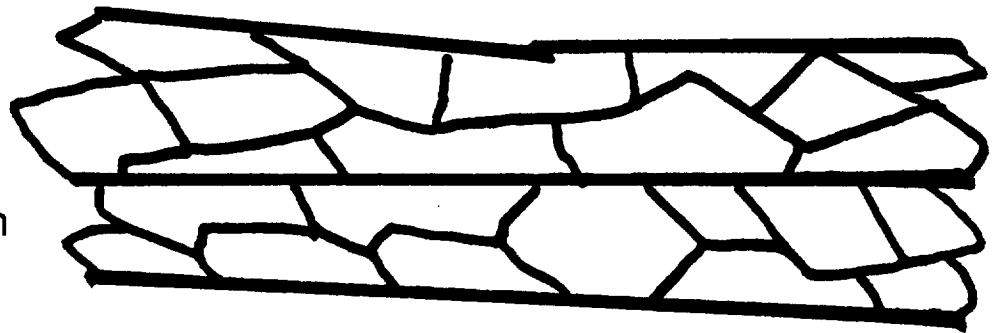
# Continuous Recrystallization

---

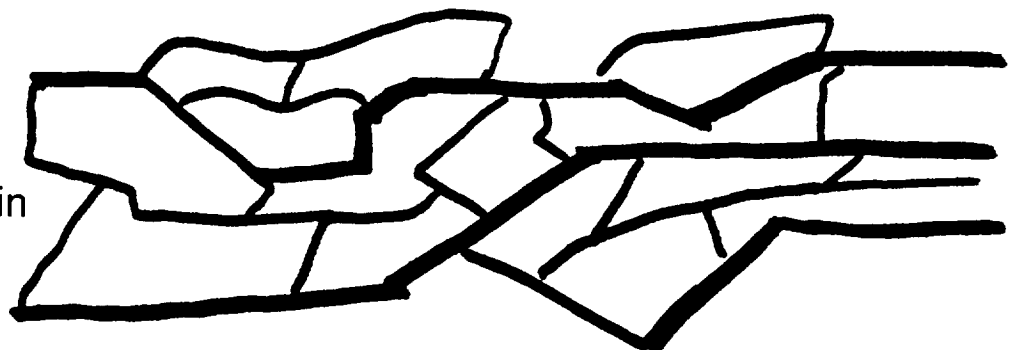
Grip Section



Low Strain



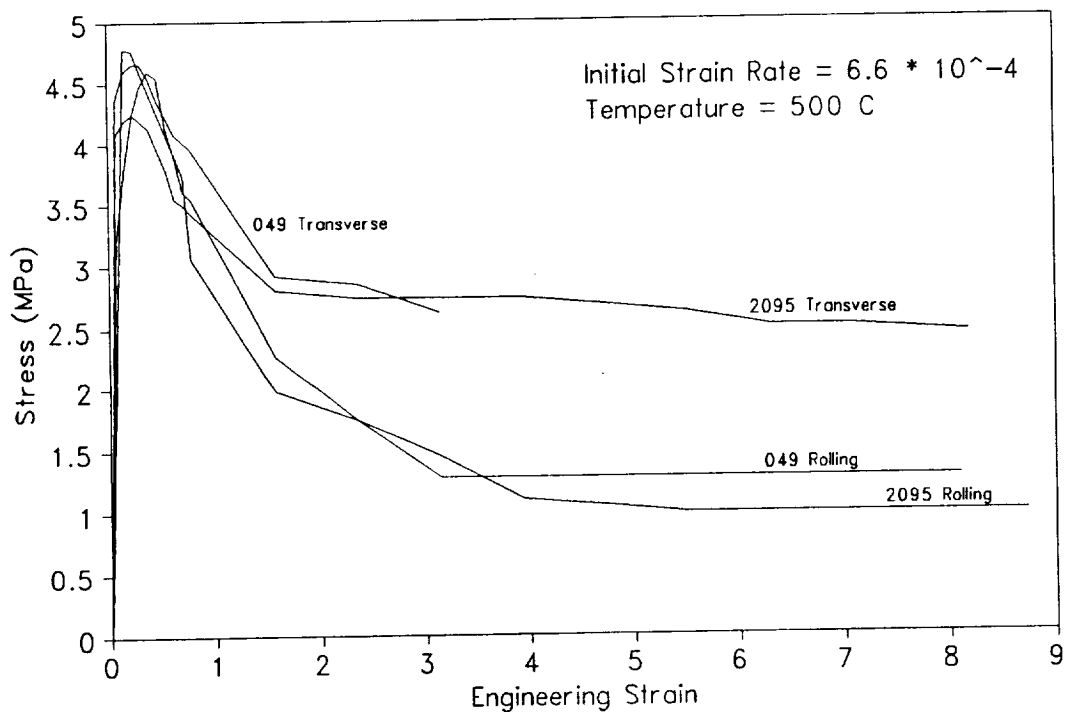
High Strain



## Composition and Experimental Tests

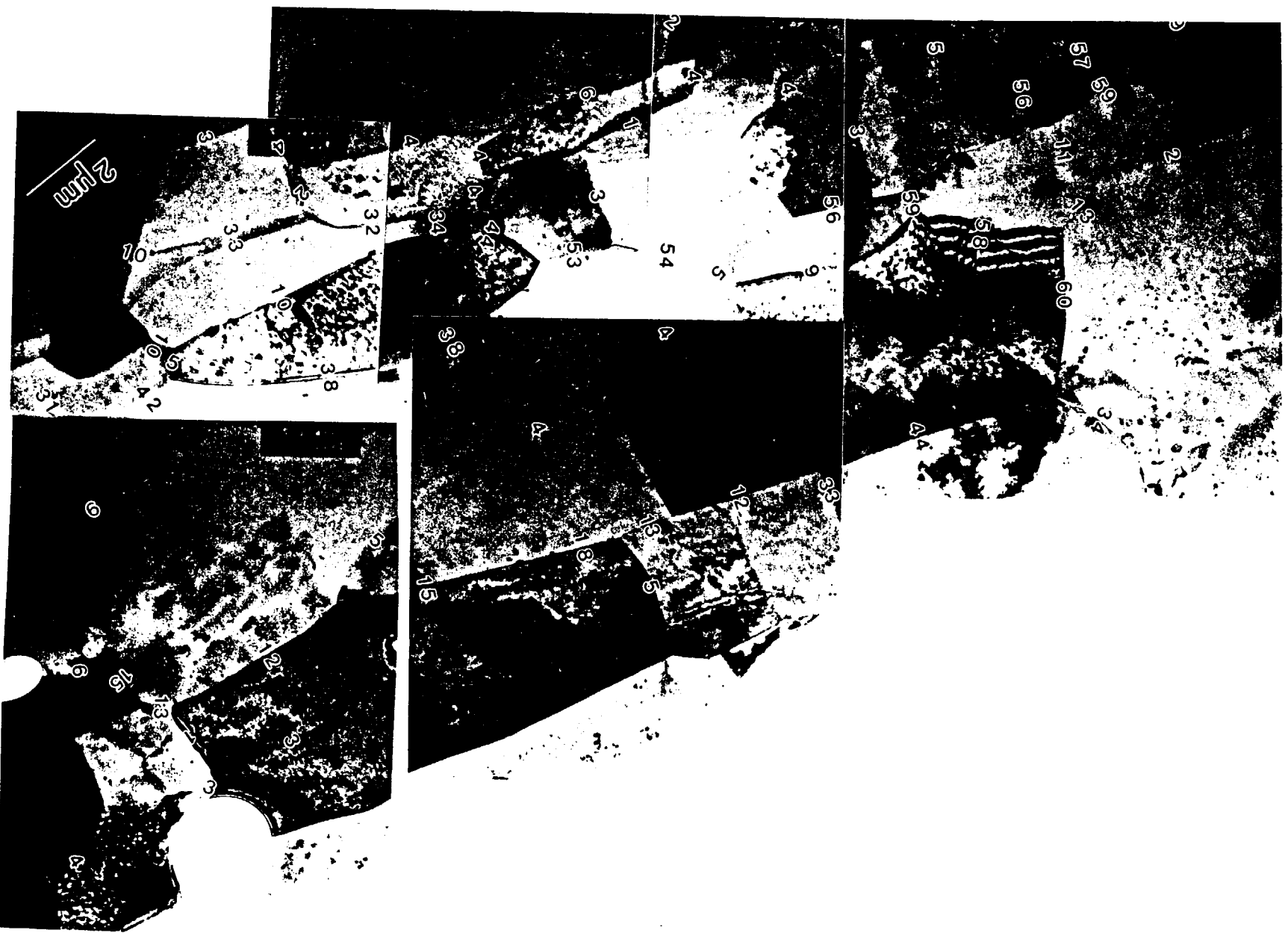
	Cu	Li	Ag	Mg	Zr
x2095	4.49	1.15	.4	.37	.17
049	4.76	1.27	.37	.33	.13

- Tensile specimens machined from as-rolled sheet
- Tensile axis oriented parallel to
  - 1) Rolling direction
  - 2) Transverse direction
- Interrupted tests at strain = 0.11, 0.21, 0.47 and failure
- Concurrent Straining and Annealing



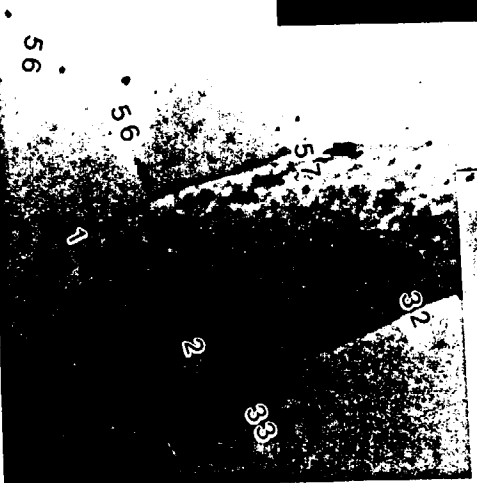
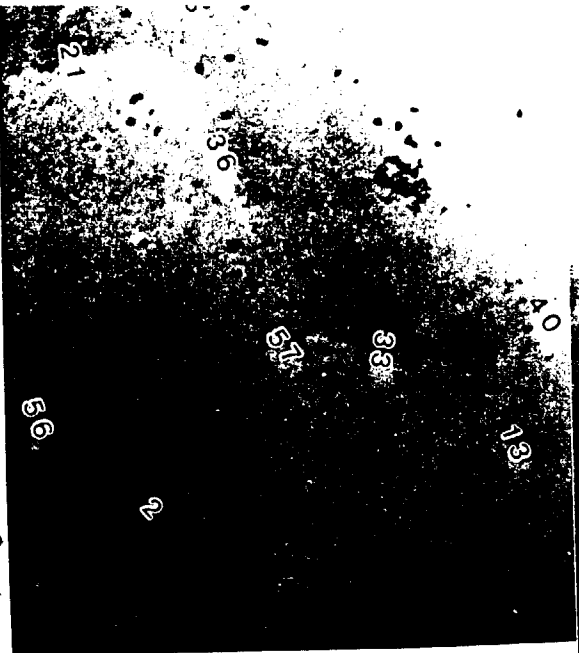
TEM Grain Misorientation Map for x2095 Transverse Grip

---



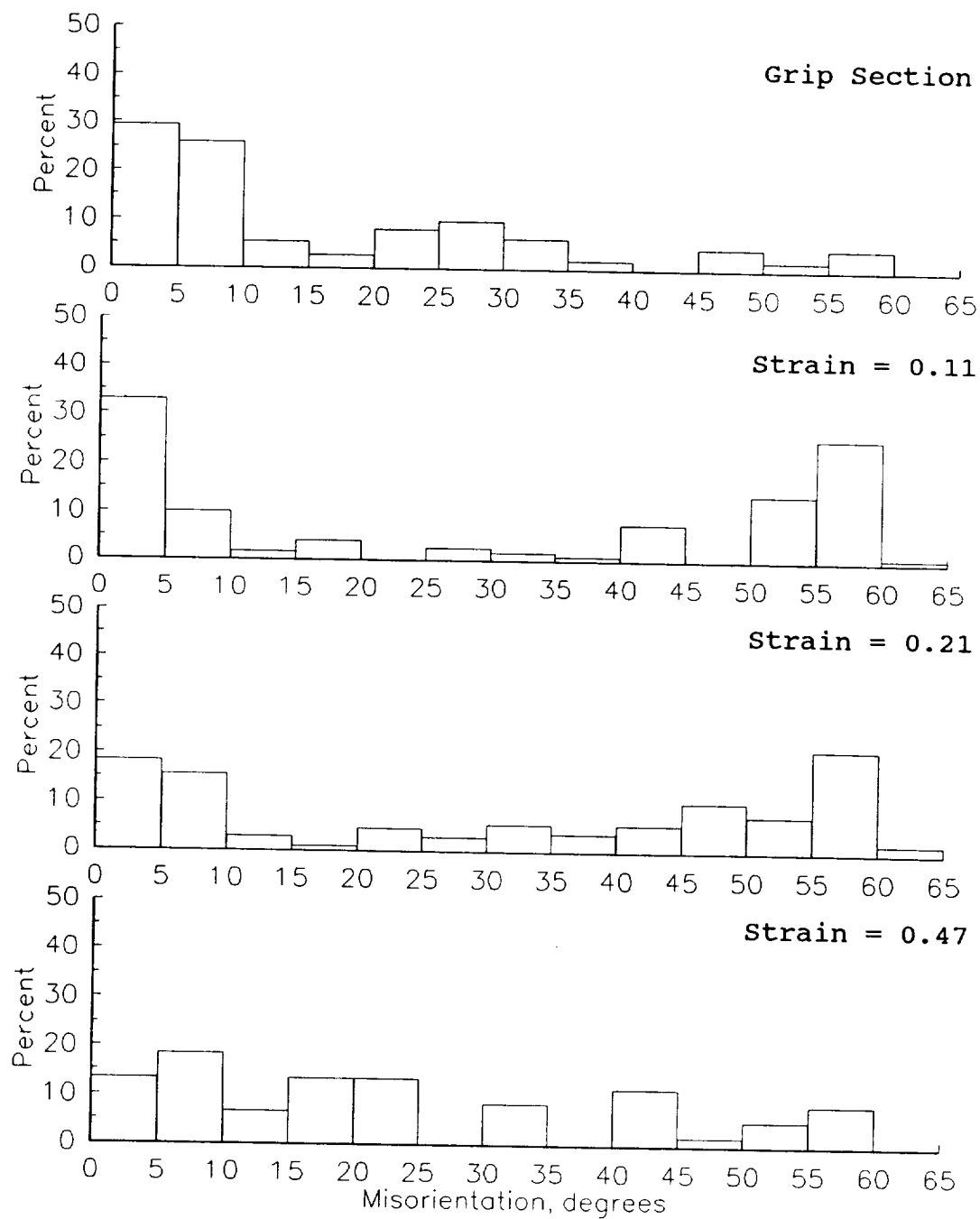
# TEM Grain Misorientation Map for x2095 Transverse Gauge

Strain = 0.21

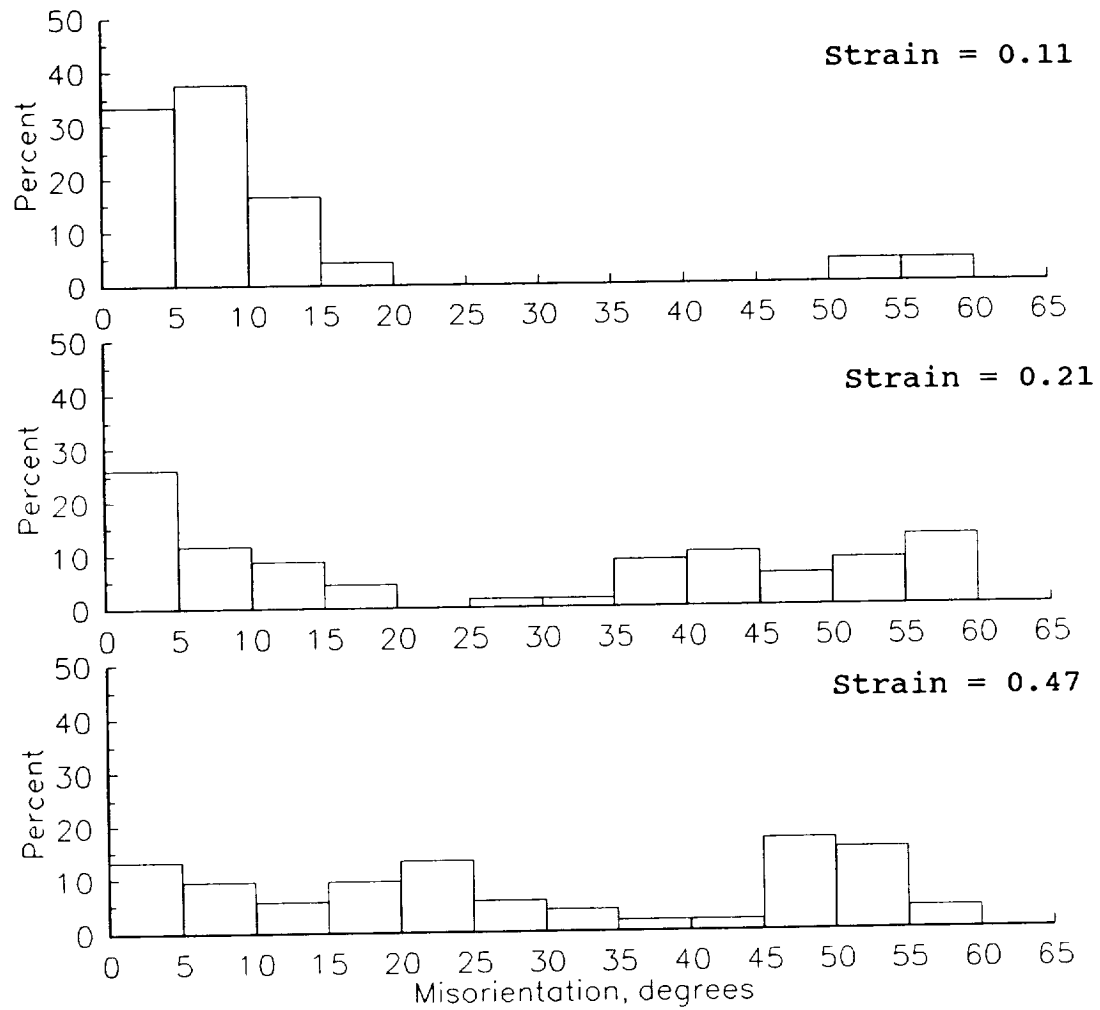


ORIGINAL PAGE IS  
OF POOR QUALITY

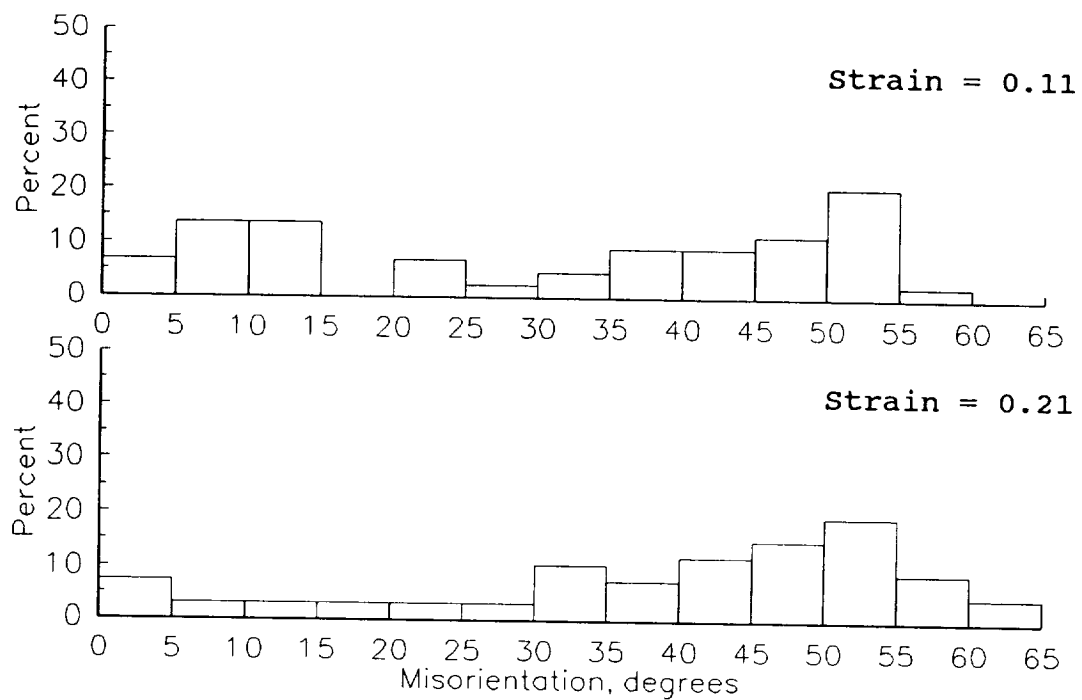
# Histogram of Misorientations in 049 Rolling



## Histogram of Misorientations in x2095 Rolling



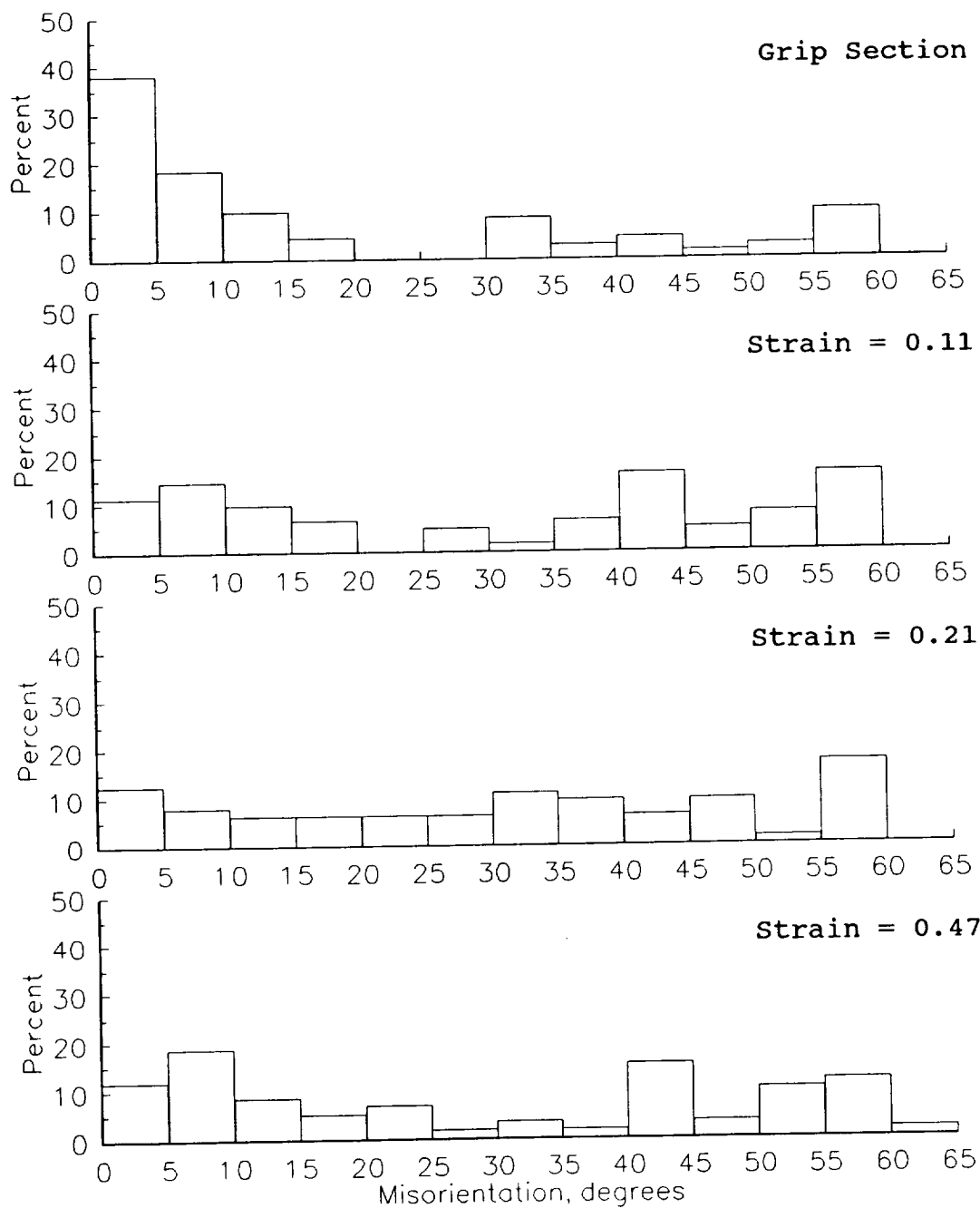
## Histogram of Misorientations in 049 Transverse





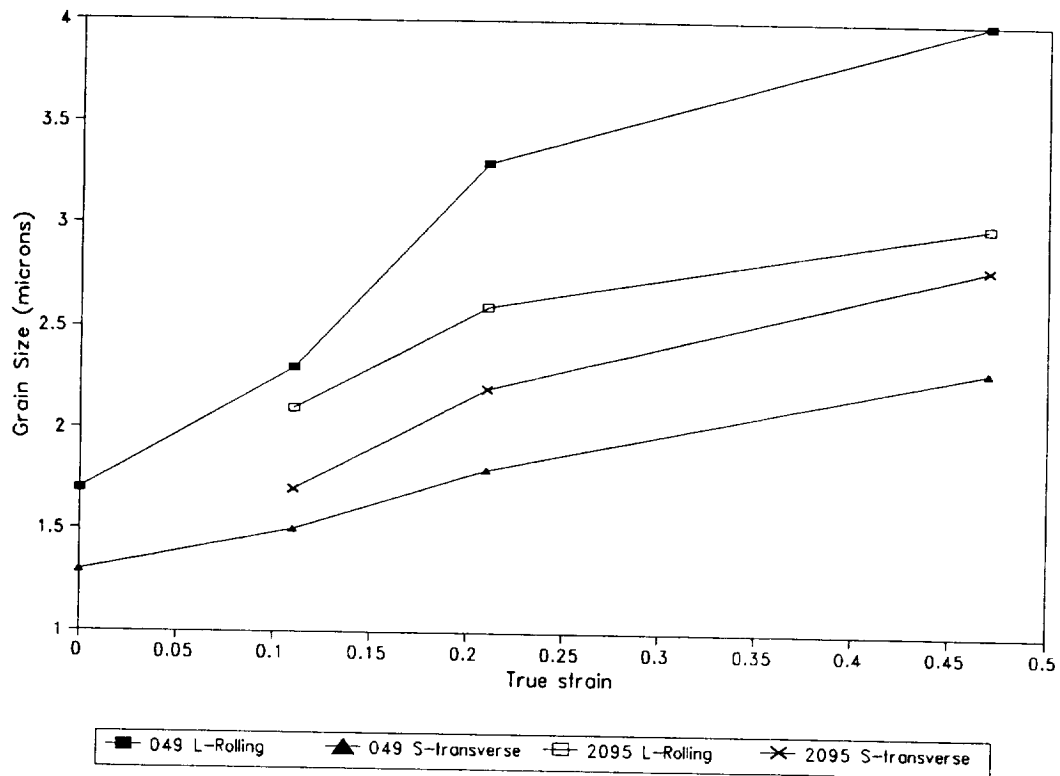
## Histogram of Misorientations in x2095 Transverse

---

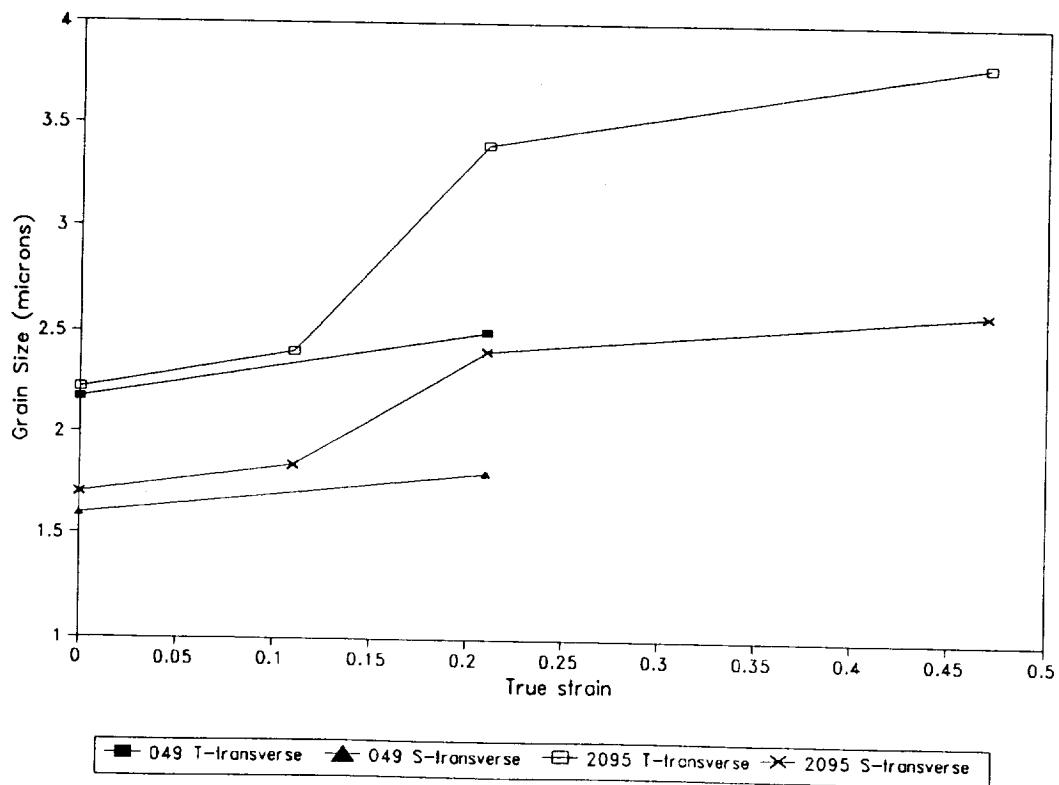


# Strain Enhanced Grain Growth

## Tensile axis parallel to rolling direction



## Tensile axis parallel to transverse direction



## **Experimental Summary**

---

<b>Misorientation</b>	<b>Evolution toward a microstructure with predominantly high-angle boundaries. Occurs slightly faster in transverse specimens implying that the mechanism for continuous recrystallization produces a larger fraction of total strain</b>
<b>Grain Size</b>	<b>Strain enhanced grain growth is observed. Similar growth in both orientations indicates little dependence of continuous recrystallization on rate of grain growth. Larger initial grain size in transverse specimens possibly detrimental</b>
<b>Flow Stress</b>	<b>Nearly twice as high in transverse specimens. Transverse specimens develop a microstructure more resistant to superplastic forming.</b>

# **Modelling of Changes in Microstructure During Superplastic Forming**

---

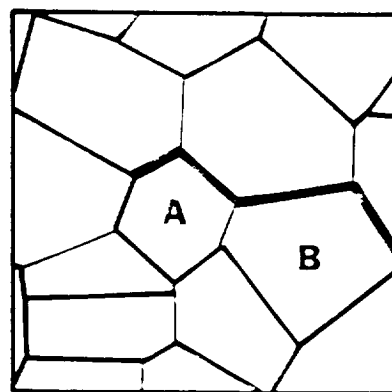
## **Model 1: Rigid Body Rotation of Grains**

- **Rotation Occurs by Sliding Along Grain Boundaries**
- **Use Initial Experimental Data for Grip Sections**
- **Fix an Arbitrary Angle of Rotation**
- **Perform Rotation Around Random Axis For Each Grain**
- **Examine Final Grain Orientation**

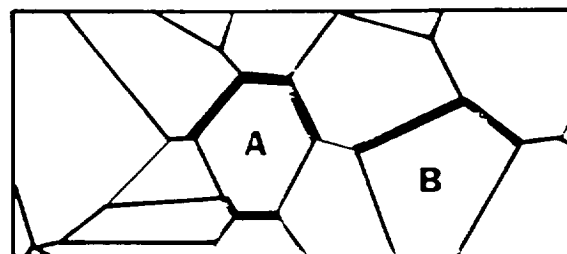
## **Model 2: Grain Rotation Caused by Slip Within Grains**

- **Rotation Occurs by Intragrain Slip**
- **Use Initial Experimental Data from Grip Sections**
- **Simple Model Allows Up To Two Slip Systems In Each Grain**
- **Allow Each Grain To Rotate as a Single Crystal**
- **Examine Final Grain Orientation**

\_\_\_\_\_



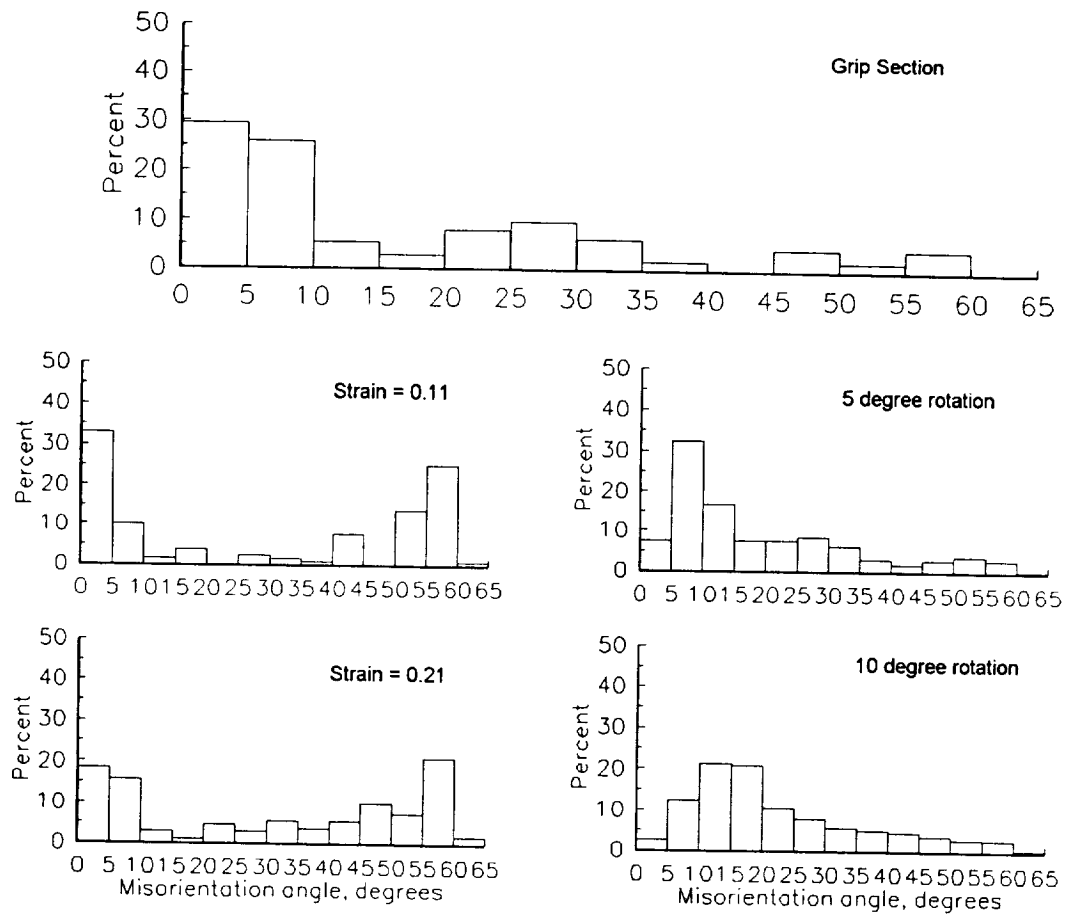
(b)



(C)

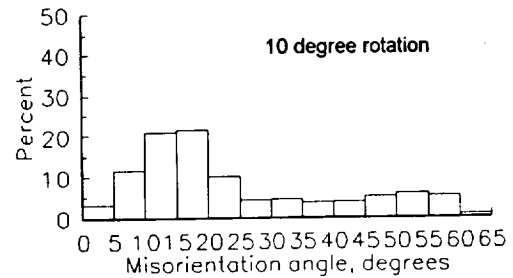
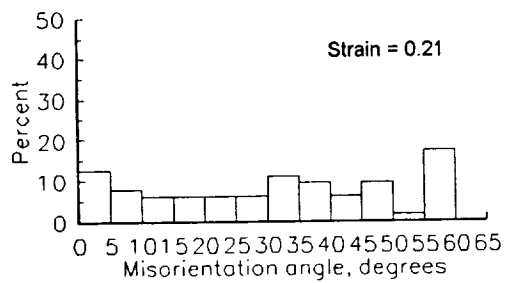
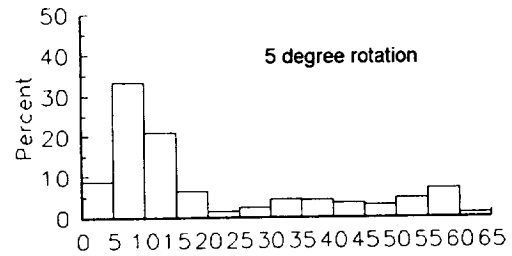
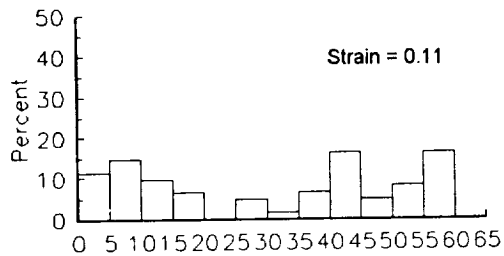
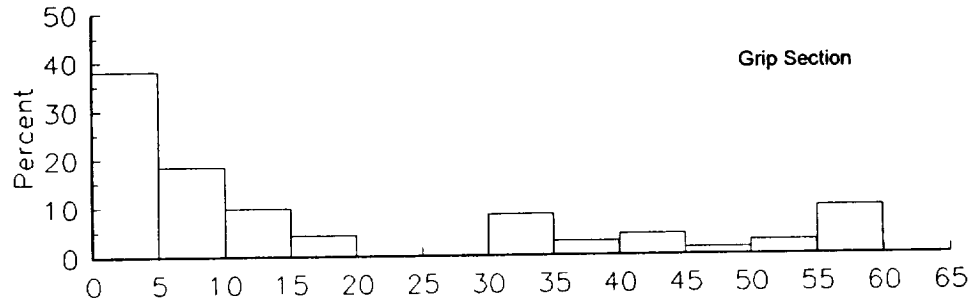
ORIGINAL PAGE IS  
OF POOR QUALITY

# Application of Models to 049 Rolling



## Application of Models to x2095 Transverse

---



## Conclusions

- Flow stress of Wieldalite™ during uniaxial superplastic forming is strongly dependent on its tensile orientation
- Similar maximum elongations are attained for all specimen orientations
- Initial microstructure in transverse specimens is not as conducive to superplastic forming. Mechanisms of continuous recrystallization contribute more to the total strain, which yields a suitable microstructure enabling superplastic elongations
- Grain boundary sliding is the dominant deformation mechanism during concurrent straining and annealing



**Project #11 Environmental Effects in Fatigue Life Prediction: Modeling Crack Propagation in Light Aerospace Alloys**

Mark Mason, Sang-Shik Kim and Richard P. Gangloff

**Objectives**

The long term objective of this project is to establish data and models for predicting environment enhanced fatigue crack propagation (FCP) kinetics for light aerospace structural alloys, particularly titanium and high strength aluminum alloys. As outlined in the 1993 renewal proposal, there are two approaches to this goal. One task is focusing on environmental-crack closure interactions in Ti-6Al-4V and a second task emphasizes linear superposition predictions of FCP in the AA7075/aqueous NaCl system

**Project #11A Dynamic Strain Rate Effects on Cracking in AA7075-T651**

Mark Mason and Richard P. Gangloff

**Project Objective**

The objective of this research is to enhance the predictive capability of existing damage tolerant fatigue life prediction codes, particularly NASA-FLAGRO. This effort concentrates on determining relevant quantitative inputs to a superposition model which accurately model environmental fatigue crack growth.

**Current Status**

Well characterized AA7075 was provided by Alcoa in both the environmentally sensitive peak aged T651 temper and in the environmentally resistive overaged T7651 temper. All environmental crack growth experiments are being conducted with the precracked wedge-opening-load specimen, machined in the cracking susceptible short-transverse orientation. Experiments are in aqueous 2.5% NaCl, modified with HCl to pH 3 and a chromate inhibitor to protect fracture surfaces, and with full immersion.

An environmental cell was successfully designed for fatigue, static load/displacement

and variable displacement rate fracture mechanics experiments. This cell allows measurement of crack mouth opening displacement, direct current potential difference, applied load, and electrochemical variables such as open-circuit potential or applied potential/current. Environmental cracking experiments with these alloys and apparatus were initiated in March of 1993.

Messrs. Allen Wilson, Edward Richie and Jonathan Pope, undergraduates in Mechanical and Aerospace Engineering at UVa, have developed various Fortran 77 computer programs to support environmental fatigue life prediction. This work was jointly supported by the UVa Academic Enhancement Program and the LA<sup>2</sup>ST Grant, and began in January of 1993. Pope developed a program to digitize literature crack growth rate data for subsequent analysis. Richie developed programs to curve fit  $da/dN$  vs  $\Delta K$  and  $da/dt$  vs  $K$  data based on the Forman-Newman equation, a hyperbolic sine approach, and a modified sigmoidal equation. Wilson programmed the Wei-Landes linear superposition model, incorporating the Richie results to curve fit crack growth rate data. These capabilities will be fully developed by the end of August, 1993, and were employed in the current research.

### Recent Findings

AA7075-T651 is sensitive to static displacement environmental crack growth when fully immersed in NaCl, however, the characteristic plateau  $da/dt$  is relatively slow and below that seen in alternate immersion experiments. Despite this noted sensitivity, including a relatively low threshold stress intensity for environmental crack growth ( $K_{ISCC} = 5$  MPa/m), the linear superposition model does not work for this system. The model predicts an extremely modest environmental enhancement of  $da/dN$  (of order 20% increase at 0.01 Hz), while environmental fatigue data show a significant effect of environment (25-fold increase in  $da/dN$  relative to vacuum and a 5-fold increase relative to FCP in moist air). Linear superposition predicts that the environmental fatigue crack growth rate is proportional to the inverse of loading frequency, while a greatly reduced time dependence of environmental FCP was observed. Time-based environmental crack growth rates, input into the model, are an order of magnitude too small to predict a significant effect of environment on fatigue crack growth.

There are at least two reasons why linear superposition modeling fails to predict environmental FCP kinetics for AA7075-T651 in NaCl. First, static load/displacement crack

tip strain rates may be substantially slower than those rates typical of the fatigue crack tip process zone. Strain rate should affect both environmental hydrogen production and atomic hydrogen entry into the crack tip process zone. Second, environmental fatigue crack propagation may compete with static load cracking and occur by a wholly different crack tip damage mechanism unique to cyclic deformation. The former hypothesis is being examined in this research.

In an effort to determine the effect of strain rate on crack growth rates, threshold stress intensity was measured as a function of applied loading rate and the resulting crack tip strain rate. Crack growth rate data were determined after the onset of environmental crack propagation. The initial results of these experiments indicate that increasing strain rate, from the static displacement case, does not markedly enhance environmental cracking. Similar slow  $da/dt$  were observed, which greatly complicated detection of the threshold for crack growth.

#### Milestones

The measurement of  $da/dt(K)$  at constant load-line displacement for 7075-T651 in 2.5% NaCl (full immersion) will be finalized to obtain crack growth rates over a wider range of stress intensities. Fatigue crack propagation experiments will be conducted to fully characterize the effects of stress ratio, frequency, and waveform at a single  $\Delta K$ , for the environmentally sensitive temper.

Dynamic load testing and crack tip strain rate modeling will seek to clarify the role of crack tip strain rate in  $da/dt$  measuring methods and to relate these rates to crack tip strain rates in fatigue. Ripple load testing and further constant displacement rate testing will be conducted to quantify the effect of crack tip strain rate on both fatigue and monotonic load crack growth.

#### Presentation Slides

1. Title.
2. Objective and Current Work.

3. Quantitative models for predicting environmental effects on FCP rate,  $da/dN$ . Approaches include linear superposition, empirical curve-fitting, and mechanism-base methods.
4. Schematic of the elements and application of the Wei-Landes and Bucci-Paris superposition model to predict environmental fatigue crack growth kinetics from static load or displacement time-based environmental crack growth; after Hertzberg.
5. Stress corrosion crack growth rates for commercial Al-Zn-Mg-Cu alloys in 3.5% NaCl, generally with full immersion; after Holroyd.
6. This slide shows the material properties of AA7075 for the T651 and T7651 tempers, and the susceptible short-transverse specimen orientation. The plot at the bottom shows the effect of temper on 7075 aluminum plate SCC performance for a given exposure time; after Lukasak et al.
7. A schematic of the environmental testing set-up used in this research.
8. A plateau crack growth rate is determined from a least squares fit of a plot of crack length verses time for a constant displacement experiment. The crack lengths for this test were determined from compliance calculations. The alloy was AA7075-T651 and the environment was the full immersion chloride solution at the free corrosion potential.
9. Comparison of crack growth rates for the two tempers of AA7075. The fastest rate was acquired from data reported by Speidel for constant displacement tests in 3.5% NaCl.
10. Faster plateau crack growth rates are reported for the susceptible T651 temper of AA7075 in an alternate immersion chloride environment with initially smooth uniaxial tensile specimens.
11. The linear superposition model, as applied utilizing measured crack growth rates with baseline air and argon fatigue data, predicts modest environmental effects at various loading frequencies.
12. Comparison of model results with corrosion fatigue data for AA7075-T651 in aqueous chloride. The linear superposition model predictions of a modest environmental effect are inadequate.
13. The measured frequency dependence of environmental fatigue crack growth rate in the AA7075-T651/NaCl system at a fixed  $\Delta K$  of 7.5 MPa/m is weak based on our data compared to the expected dependence of  $da/dN$  on inverse loading frequency from the linear superposition concept. Higher plateau crack growth rate inputs would produce the strong frequency dependence.

14. There are at least two reasons why the linear superposition approach does not work for the "susceptible" AA7075-T651/NaCl system.
15. Schematic of the constant displacement rate testing method; after Young.
16. Threshold stress intensities for AA7075-T651 in the standard aqueous chloride environment show a transition between static and high displacement rate experiments.
17. Threshold stress intensities as a function of displacement rate for AA2024 in NaCl; after Dietzel and Schwalbe.
18. Crack growth during rising loading of AA7075-T651 in 2.5% NaCl and at the slowest applied rate in the previous slide. These data are consistent with the results from the literature and static displacement experiments. Environmental crack growth in fact occurs at very slow rates above a low  $K_{ISCC}$  (or  $K_{TH}$ ), but is not enhanced by the applied crack tip strain rate.
19. Conclusions.
20. Future work.



**Environmental Effects in Fatigue Life Prediction:  
Dynamic Strain Rate Effects on Cracking  
in AA7075-T651**

**Mark Mason and Richard P. Gangloff**

**Department of Materials Science and Engineering  
University of Virginia**

**Robert S. Piascik  
and  
James C. Newman**

**NASA-LaRC**

## **Objective**

**Quantitatively model environmental fatigue,  $da/dN(\Delta K, R, f, \text{ waveform, ..})$ , for use in NASA-FLAGRO life predictions.**

## **Current work**

- 00      Apply linear superposition (LS) to an EAC sensitive system; and speculate why LS does not work.**
- 00      Examine the role of crack tip strain rate in  $da/dt$  measurements.**
- 00      Identify input  $da/dt$  for LS that is descriptive of the stress corrosion system and models  $da/dN$ .**
- 00      Understand mechanisms for EAC damage.**



## **Quantitative Crack Growth Models**

- oo **Models to interpolate and predict  $da/dN$ -( $\Delta K$ ,  $R$ ,  $f$ , waveform,...) have been developed from several perspectives**

### **A. Linear Superposition**

$$\frac{da}{dN} = \frac{da}{dN_m} + \frac{da}{dN_{SCC}}$$

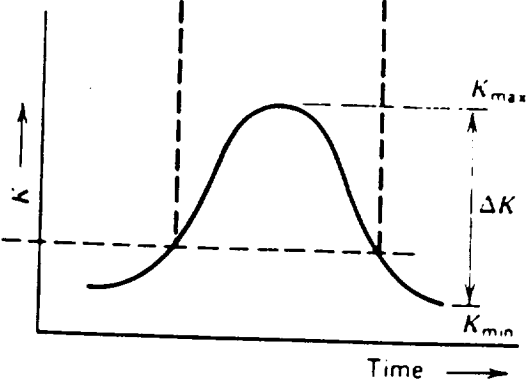
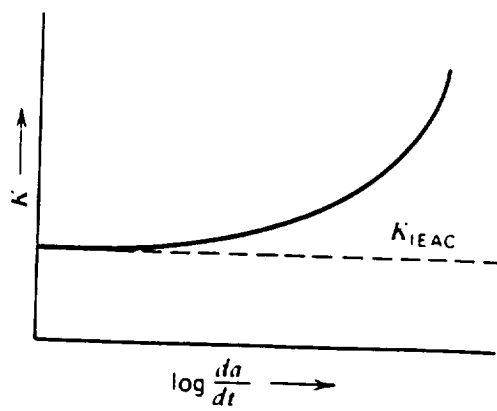
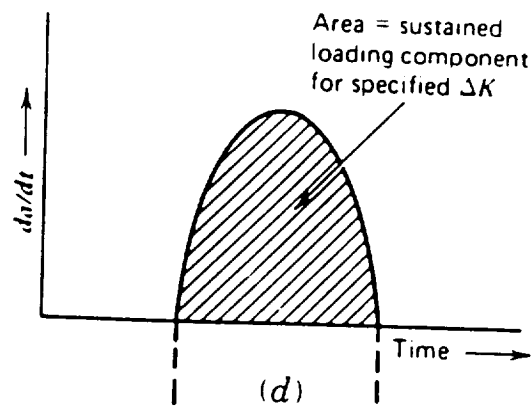
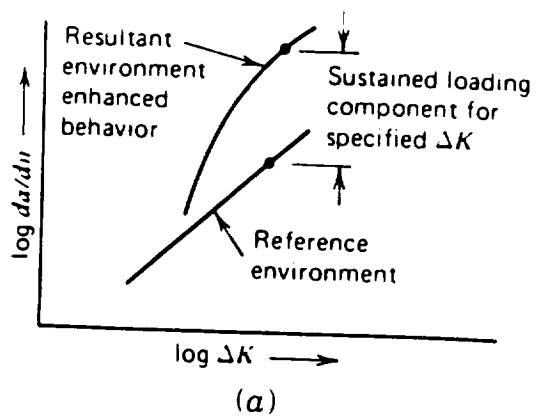
### **B. Empirical Curve Fitting (Forman)**

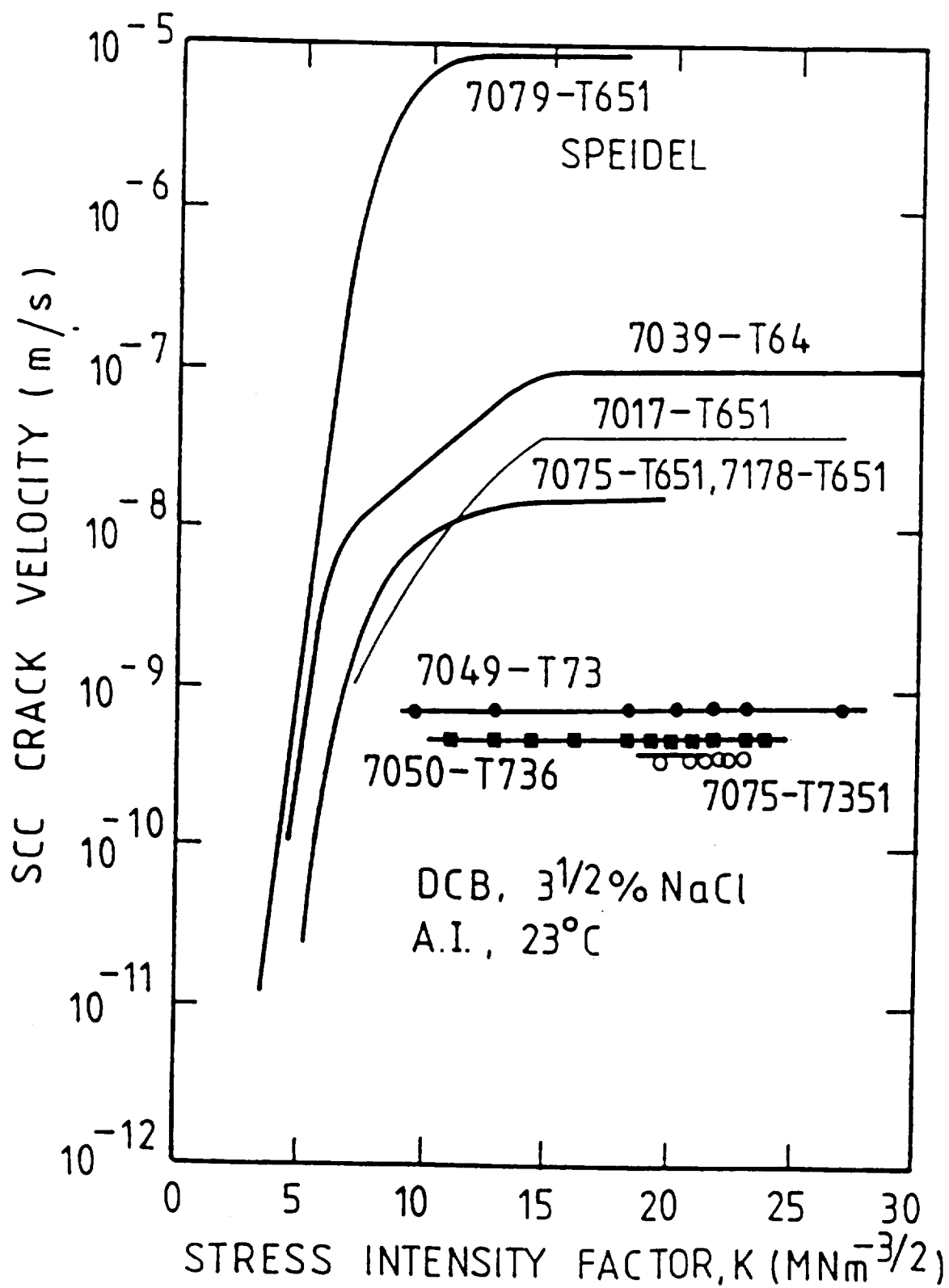
$$\frac{da}{dN} = \frac{[C(1 - R)^m \Delta K^n (\Delta K - \Delta K_{th})]^p}{[(1 - R)K_c - \Delta K]^q}$$

### **C. Mechanism Based Model**

$$\frac{da}{dN} = \frac{da}{dN_m} + \frac{da}{dN_{SCC}} + \frac{da}{dN_{cf}}$$

- oo **Each approach is limited**

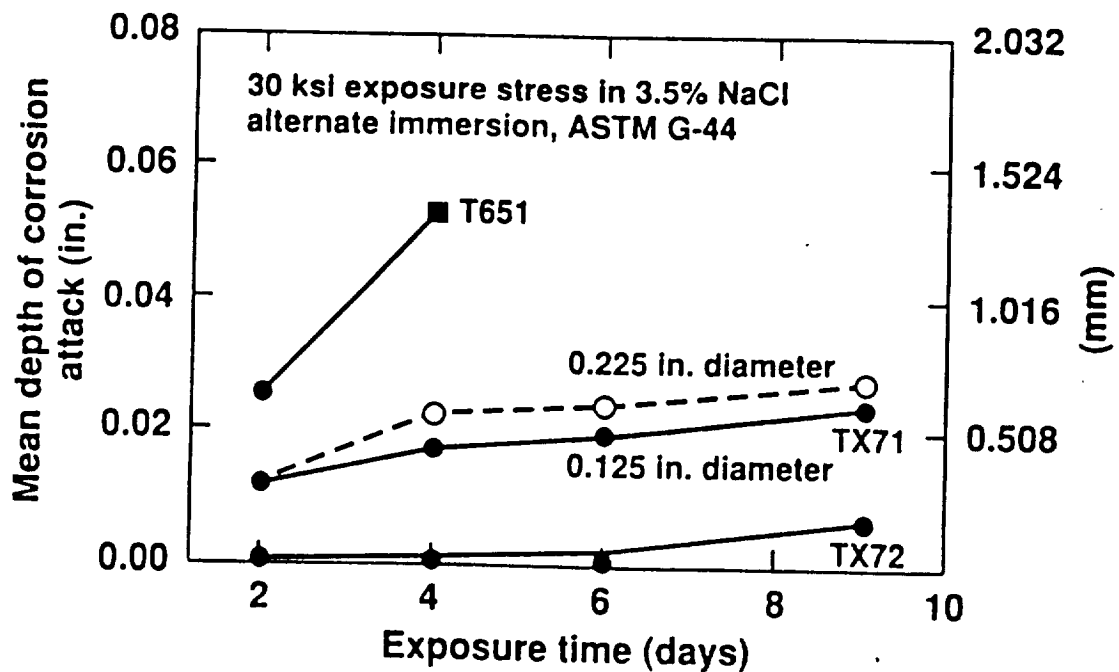




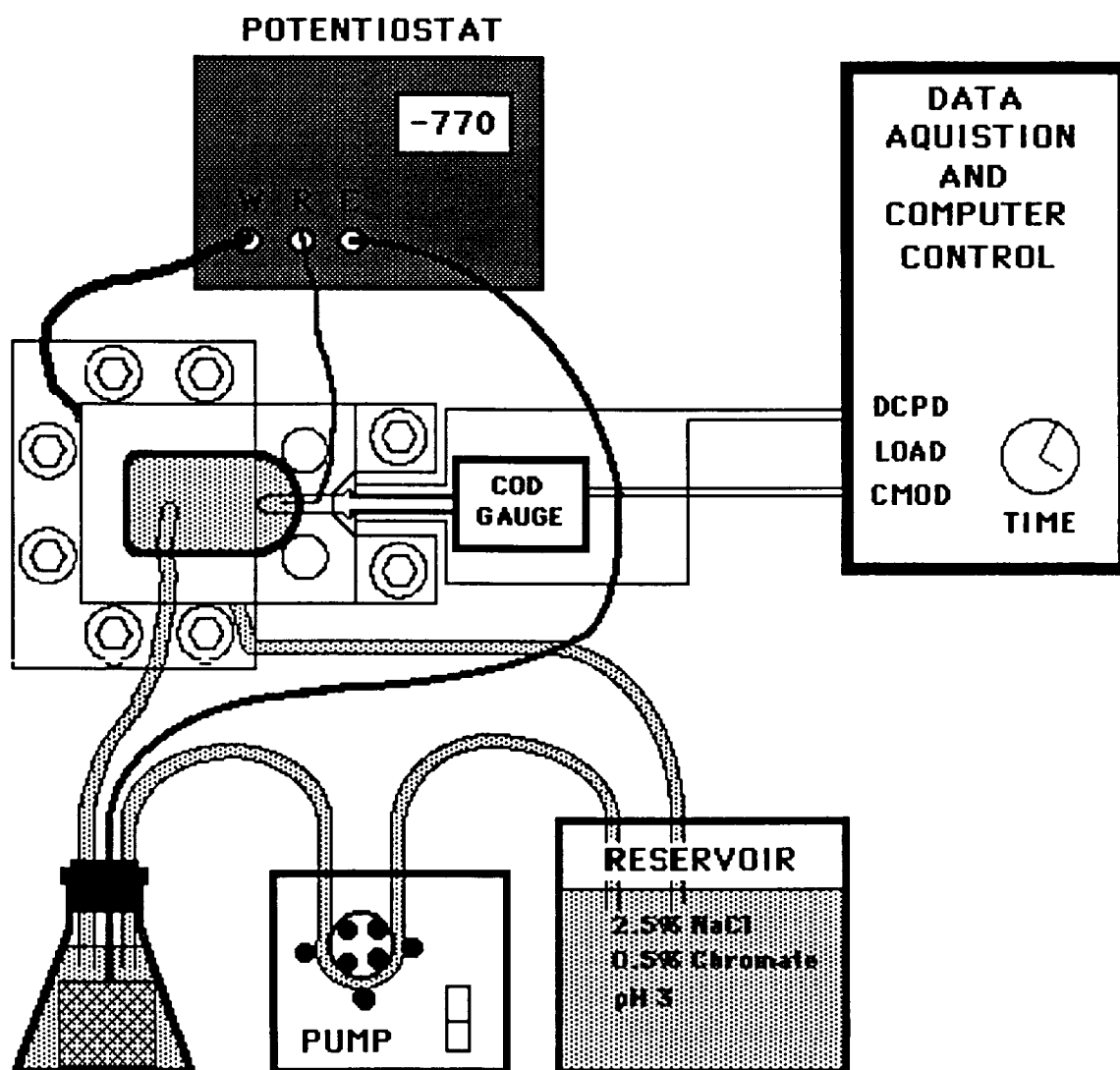
## AA7075

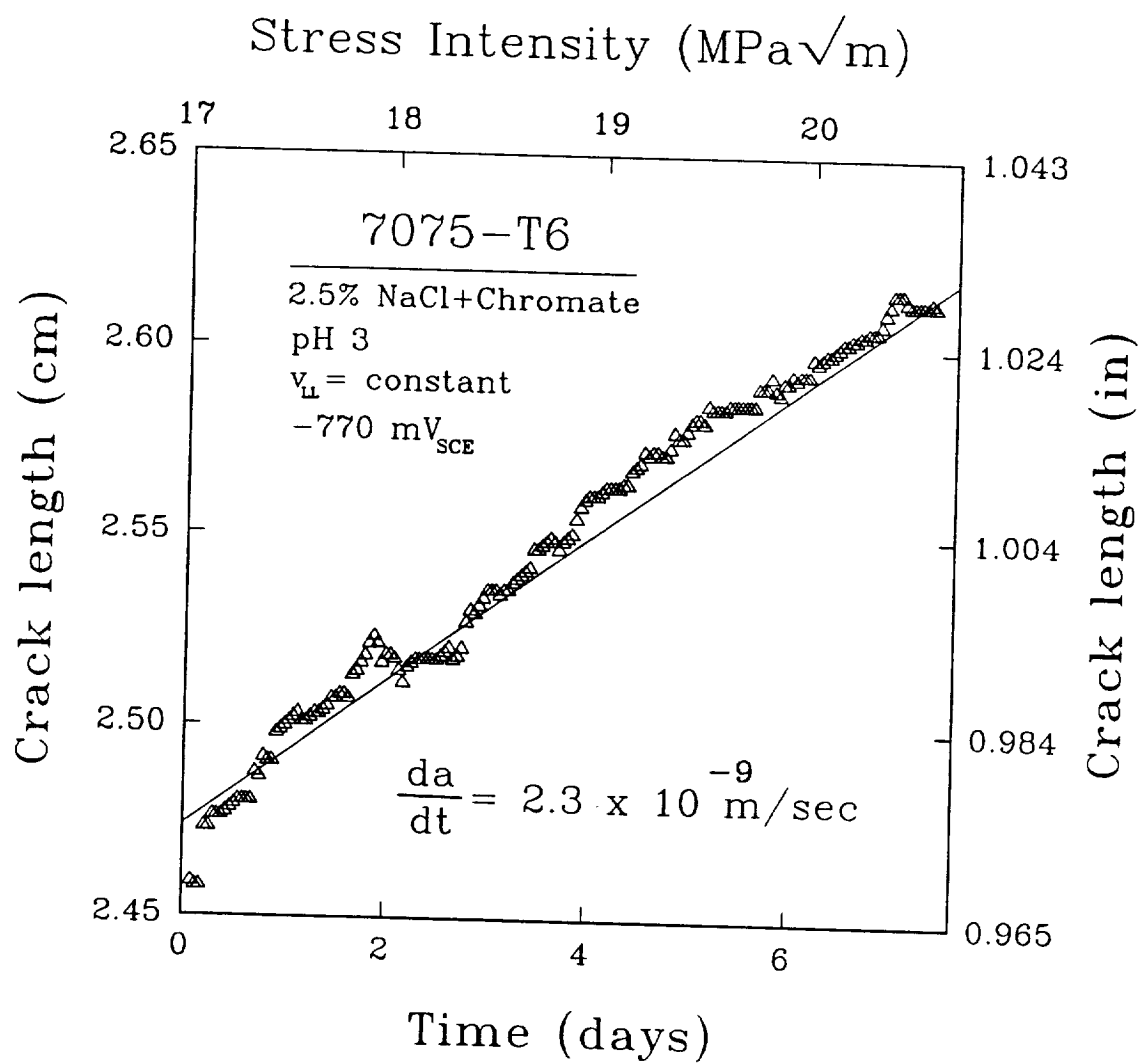
- Al - 5.6 Zn - 3.1 Mg - 1.6 Cu (wt%)
- 5.2 cm plate
- WOL Specimen
- S-L orientation

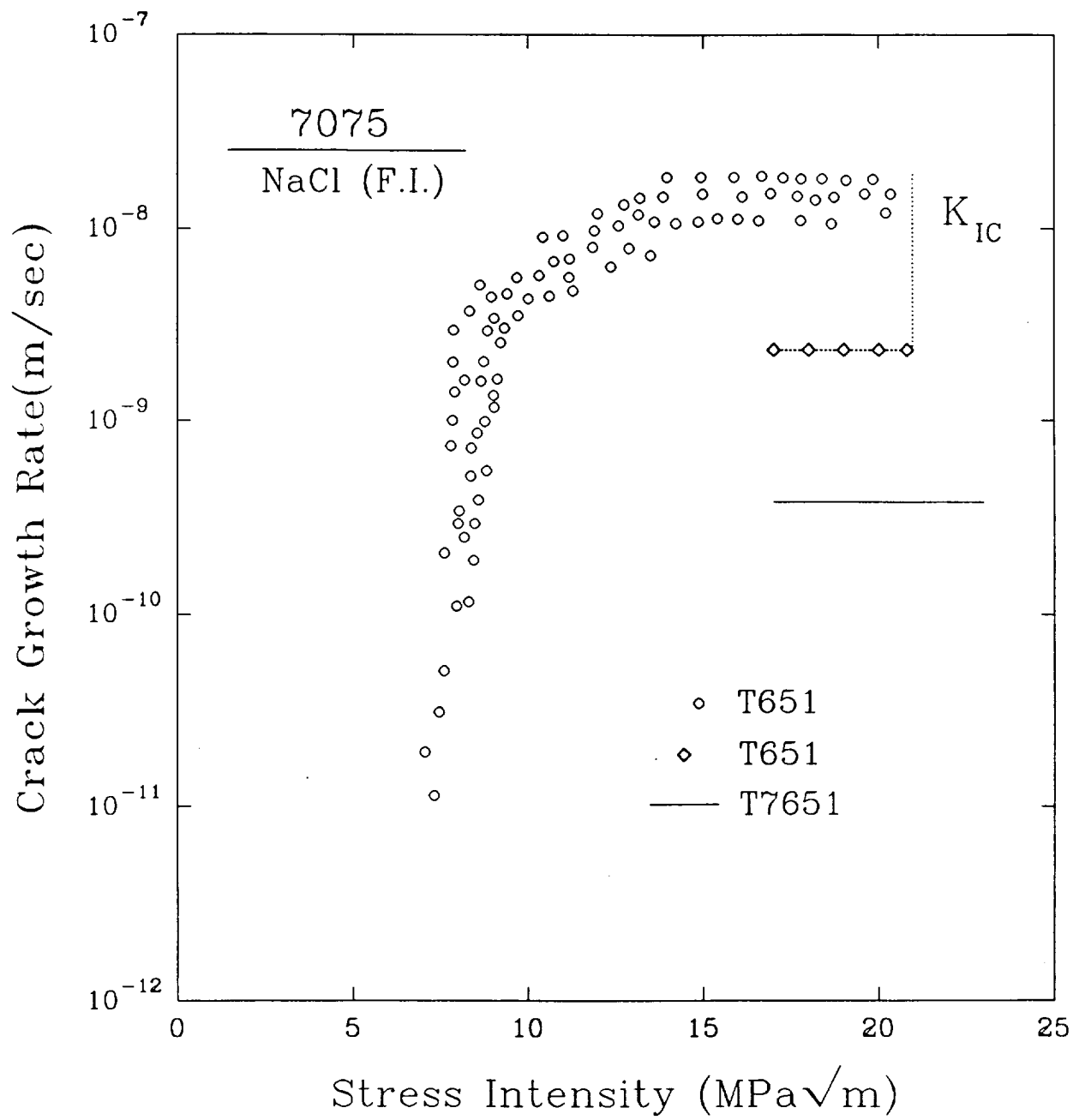
Property	T651	T7651
$\sigma_{YS}$ (MPa)	469	441
$\sigma_{UTS}$ (MPa)	538	517
Elongation %	4	6
KIC (MPa $\sqrt{m}$ )	21.2	21.3



# Environmental Testing Set-up





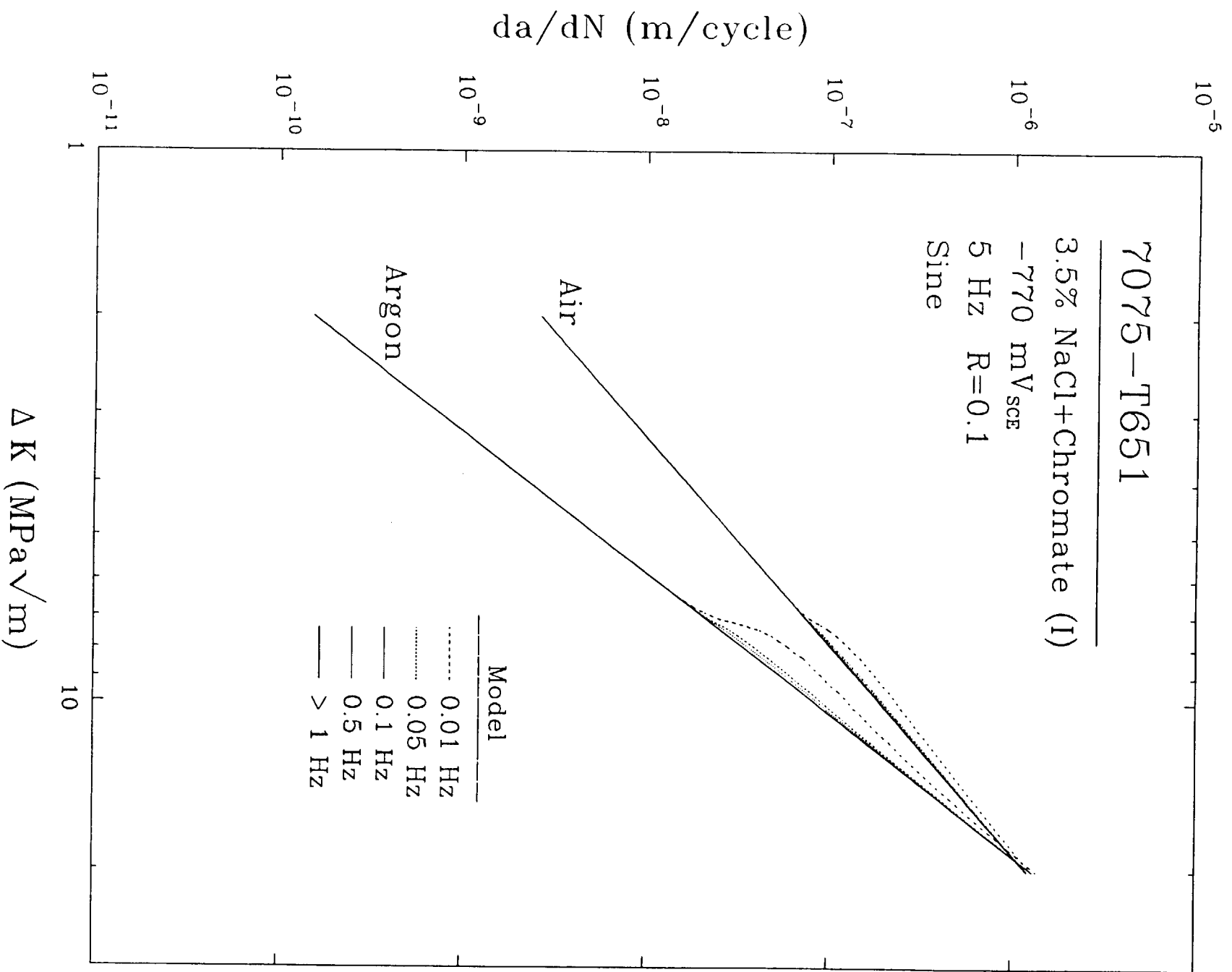


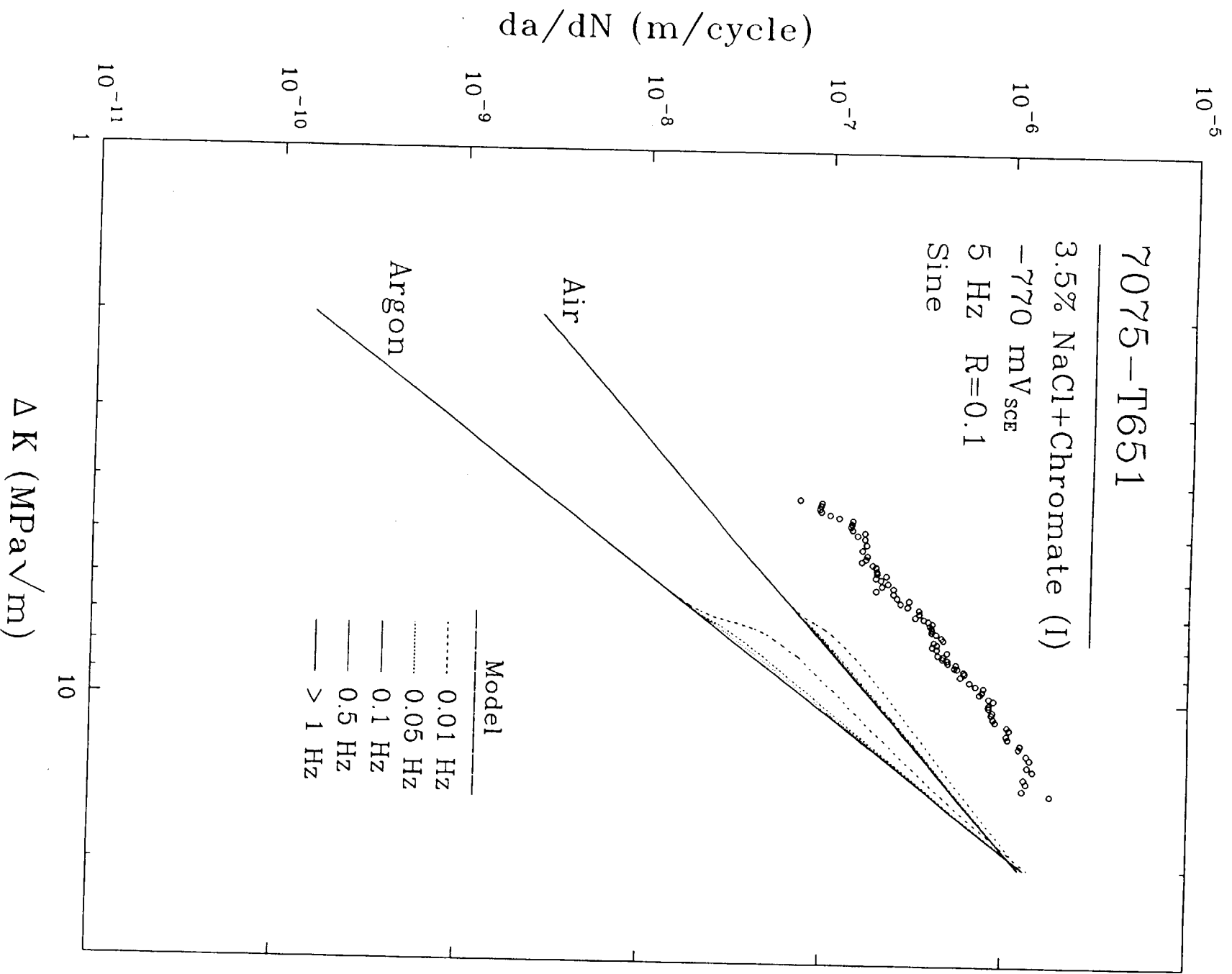
## AA7075

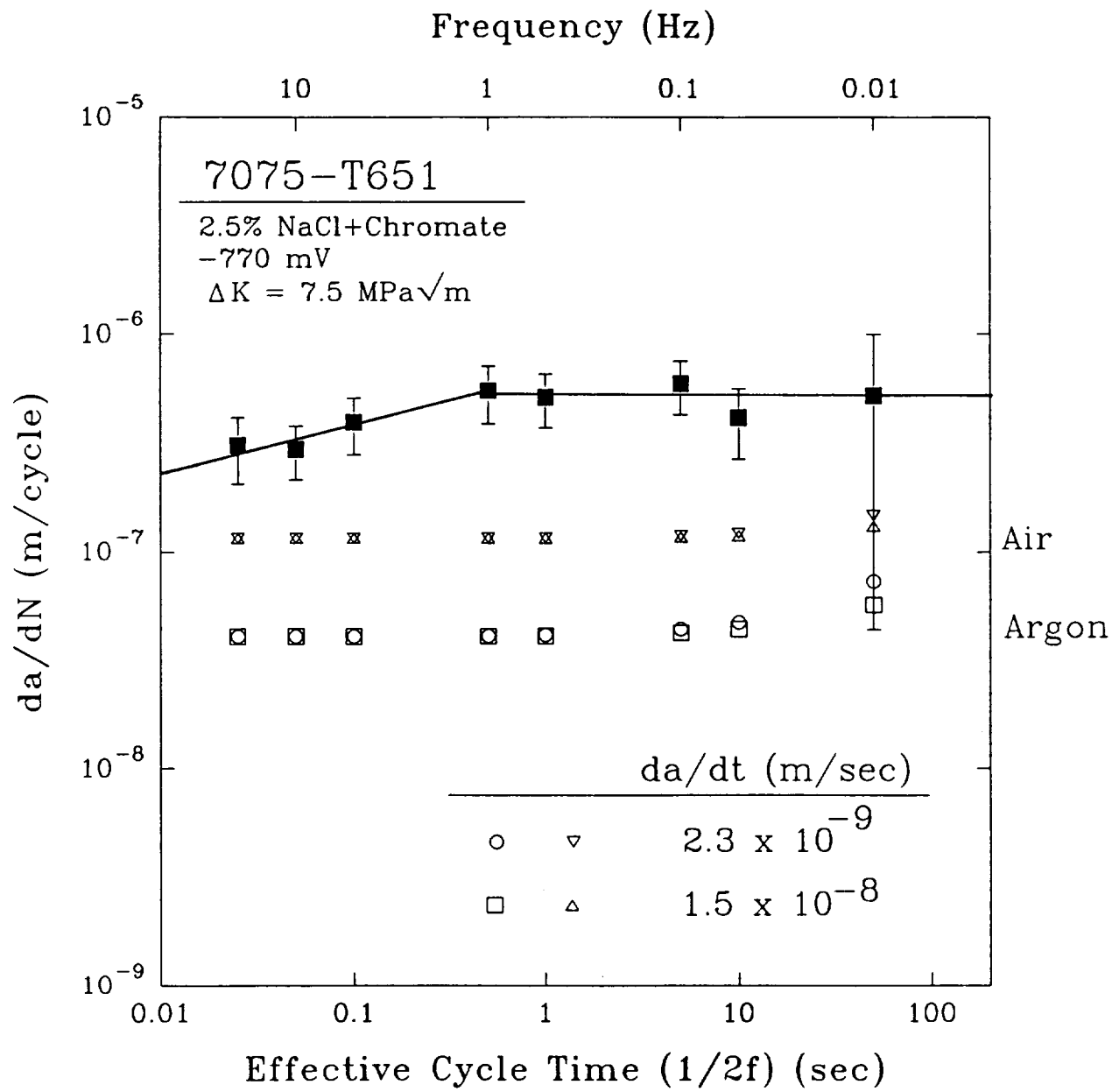
### Plateau Stress Corrosion Crack Velocities

	Environment	Plateau da/dt (m/sec)	Plateau da/dt (m/sec)
Temper		T651	T7651
Mason	2.5% NaCl (I)	$2.3 \times 10^{-9}$	
Colvin et al.	Alt. Immersion	$5.6 \times 10^{-9}$	$7.3 \times 10^{-10}$
Speidel	3.5% NaCl (I)	$1.5 \times 10^{-8}$	$3.8 \times 10^{-10}$



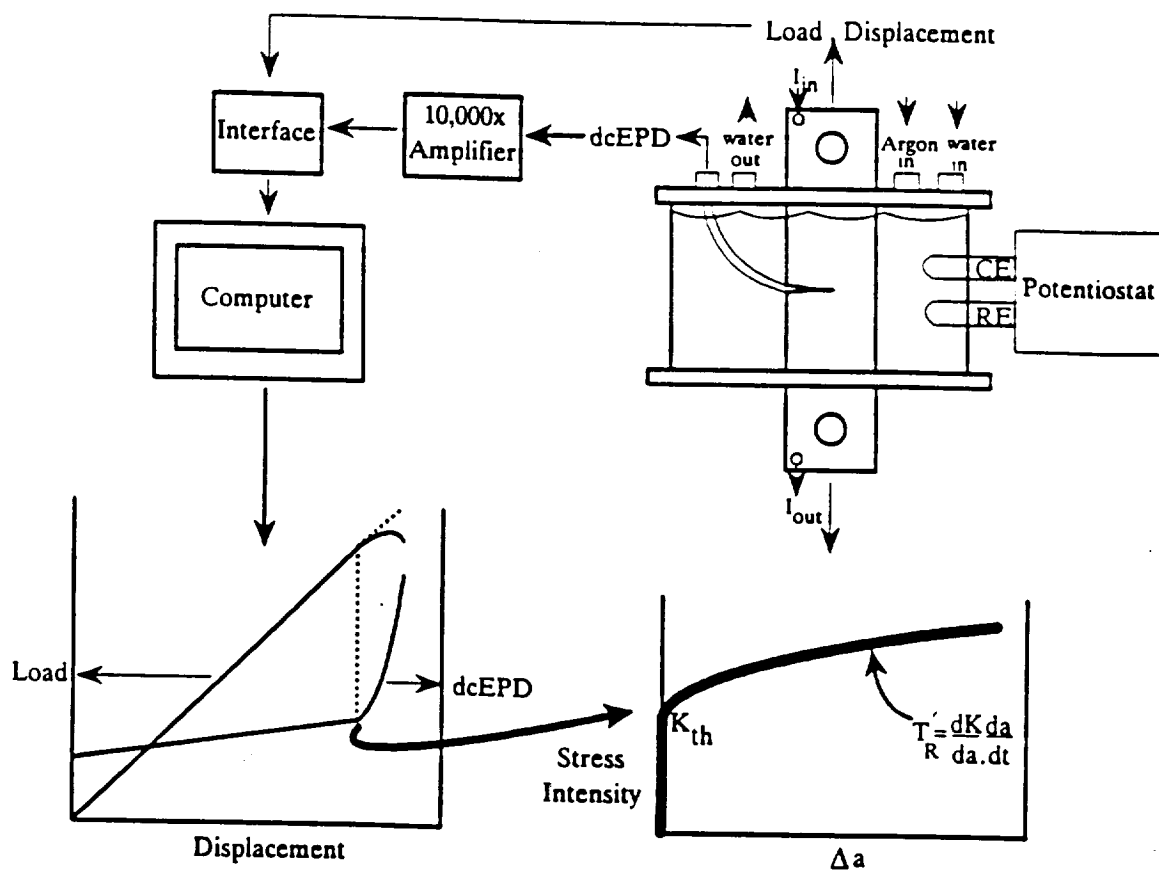


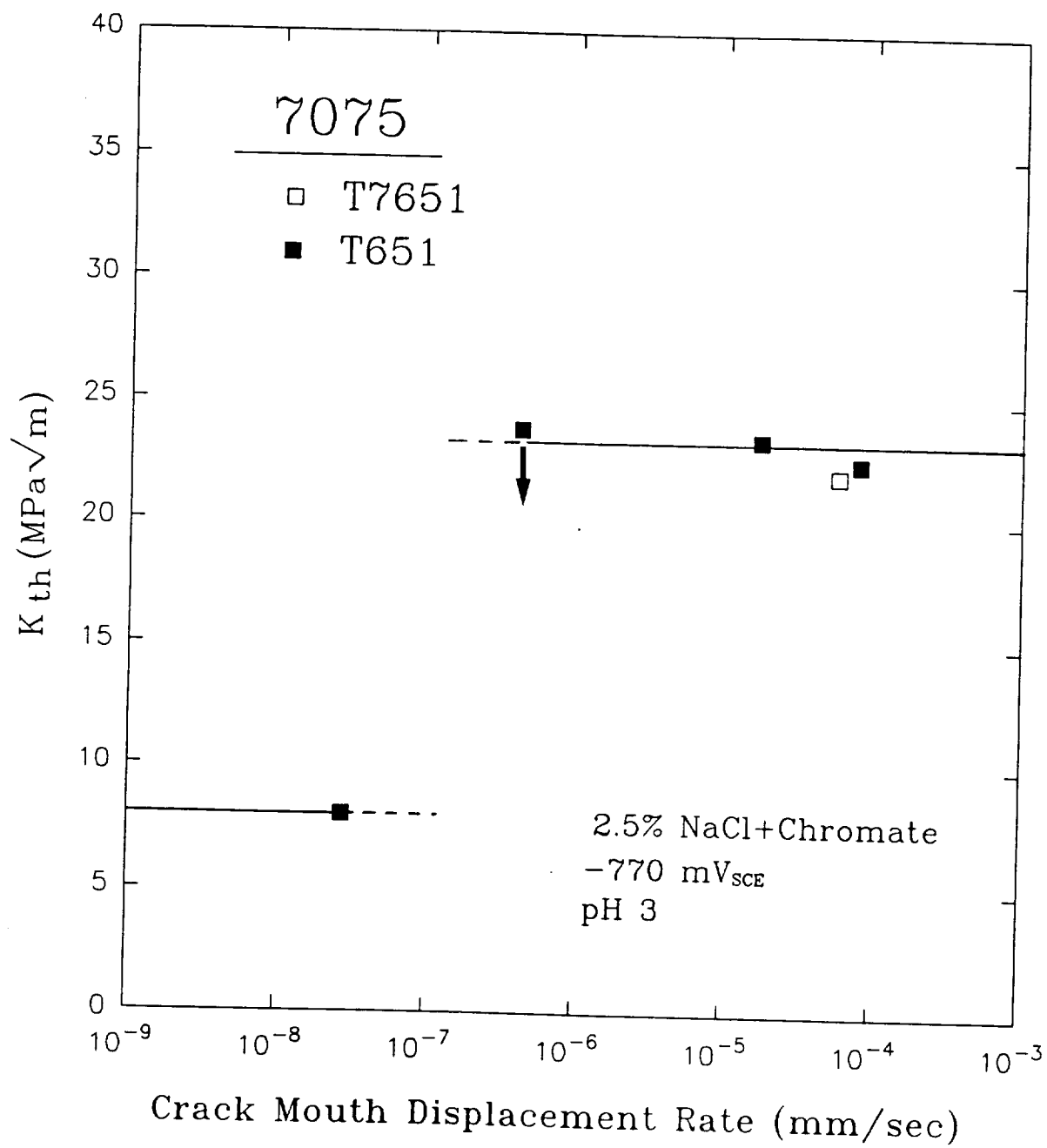


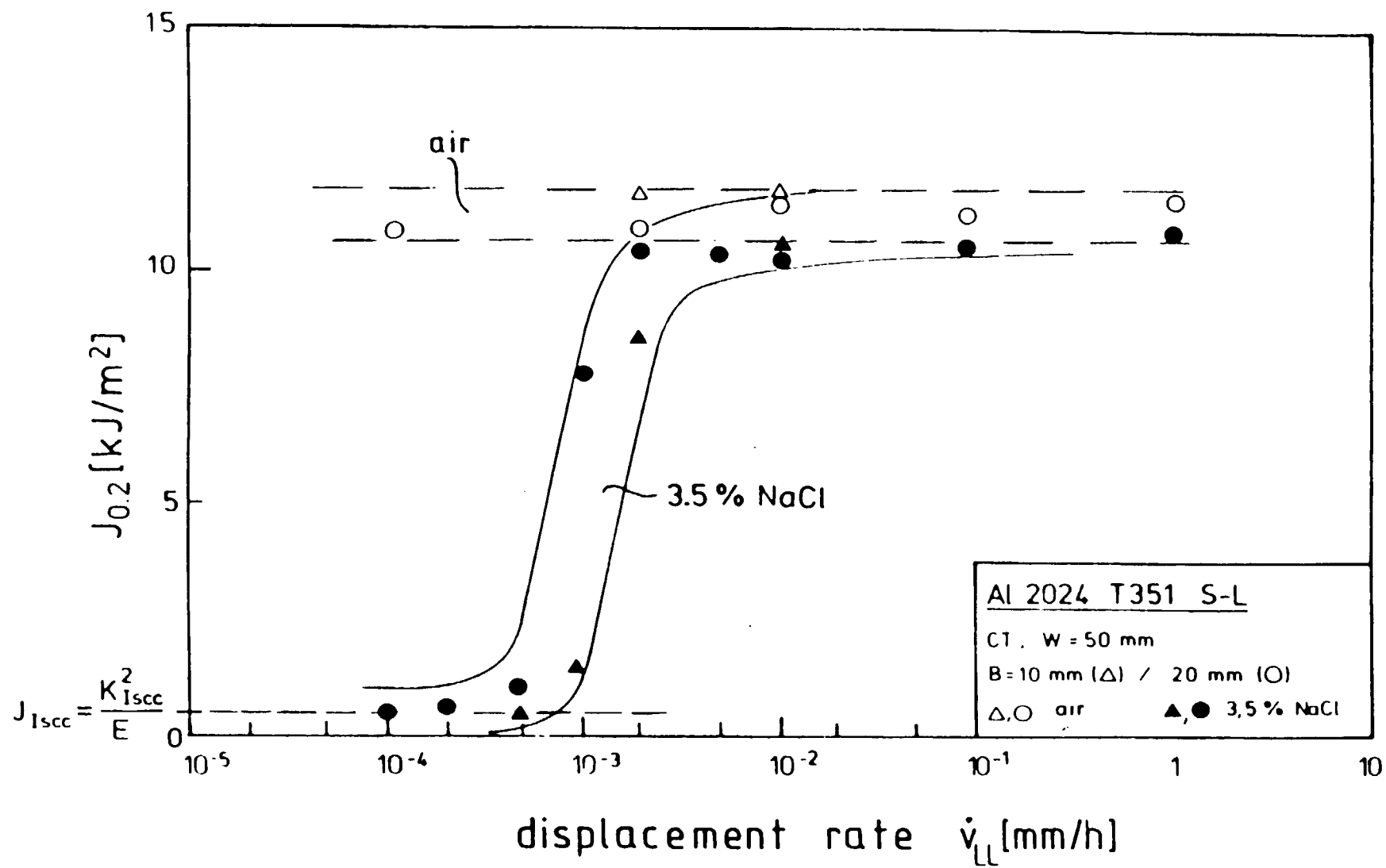


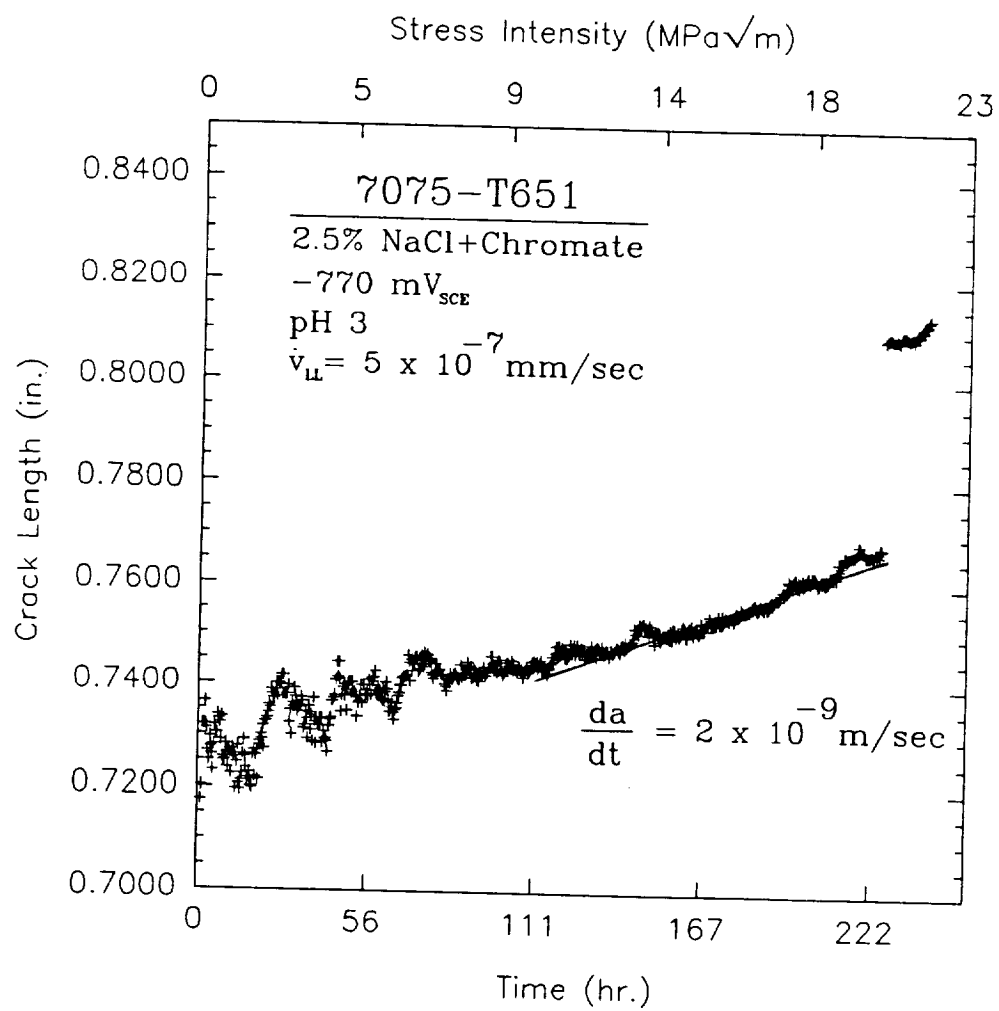
**Two reasons why linear superposition fails to predict environmental FCP kinetics for AA7075-T651/NaCl:**

- Static load/displacement crack tip strain rates are slower than dynamic rates in the fatigue crack tip process zone, affecting hydrogen uptake.**
- Environmental FCP competes with static load cracking and occurs by a different crack tip damage mechanism unique to cyclic deformation.**











## Conclusions

- oo AA7075-T651 is sensitive to static displacement environmental crack growth in NaCl (F.I.). The characteristic plateau  $da/dt$  is below that expected from AI experiments.
- oo Superposition does not work for this environment sensitive system. The model predicts extremely modest environmental enhancement of  $da/dN$ .
- oo Crack propagation rates for corrosion fatigue of 7075-T651 in this environment depend weakly on frequency. Slow  $da/dt$  precludes a significant contribution by  $da/dN_{SCC}$  to the model and the expected strong  $(1/2f)$  frequency dependence.
- oo Increasing strain rate from the static displacement case does not enhance environmental cracking.

## **Future Work**

- oo    **Finalize measurement of  $da/dt[K]$  at constant  $v_{LL}$  for 7075-T651**
- oo    **Conduct full characterization of effects of  $R$ ,  $f$ , waveform at a single  $\Delta K$  for the EAC sensitive temper.**
- oo    **Clarify the role of crack tip strain rate in  $da/dt$  measuring methods. Relate these rates to crack tip strain rates in fatigue by dynamic load testing.**

## Project #11B Environmental Effects on Fatigue Crack Propagation and Closure in Titanium Alloys

Sang-Shik Kim and Richard P. Gangloff

### Objective

The objective of this ongoing research is to enhance the predictive capability of existing damage tolerance fatigue life prediction codes, particularly NASA FLAGRO, by incorporating environmental effects on FCP behavior. Specific goals are to:

- oo Review and critically evaluate both environmental FCP data and the predictive capabilities of crack growth rate models.
- oo Characterize intrinsic and extrinsic environmental  $da/dN$ - $\Delta K$  kinetics for titanium alloys, as a function of R ratio.
- oo Understand environment-sensitive crack closure phenomena and mechanisms, including the effects of  $\Delta K$  and R ratio.

### Current Status

A chamber was designed and built to contain aqueous solutions about the crack in a compact tension specimen. The aim of the design is to control the environment chemistry (controlled electrode potential and environment purity) during FCP, while enabling compliance-based measurement of fatigue crack closure without interference from the chamber.

FCP experiments were conducted on Ti-6-4 in moist air and 1% NaCl at  $-500 \text{ mV}_{\text{SCE}}$  at R ratios of 0.1, 0.4 and 0.7 and constant  $K_{\text{max}}$  of 27.5 MPa/m. Crack length and crack closure were measured by the global compliance technique with a standard gauge mounted across the notch mouth in both environments.

Crack growth rate ( $da/dN$ ) versus applied and effective stress intensity range ( $\Delta K$  and  $\Delta K_{\text{EFF}}$ , respectively) data for Ti-6-4 at R ratio of 0.1 in moist air and 1% NaCl were analyzed by NASA-FLAGRO interpolative curve fitting model.  $Da/dN$ - $\Delta K$  at R ratios of 0.4 and 0.7, respectively, were extrapolated based on the empirical constants derived at an R ratio of 0.1.

### Recent Results

The following conclusions are drawn from the present research.

- oo FCP resistance for Ti-6-4 decreases with increasing R ratio in air and 1 % NaCl. In each environment, The R ratio effect mostly disappears after accounting for crack closure based on  $\Delta K_{EFF}$ .
- oo Crack closure for Ti-6-4 is strongly affected by  $\Delta K$ , R and environment. Crack closure in 1 % NaCl appears to be slightly higher than in air. Enhanced roughness-induced closure due to reduced slip reversibility in 1 % NaCl compared to air may be responsible for the trend. Further confirmation is required.
- oo 1 % NaCl degrades FCP resistance compared to air at each R ratio. Crack closure as affected by environment is not solely responsible for the observed difference.
- oo  $Da/dN$ - $\Delta K$  for Ti-6-4 in both air and 1 % NaCl reflects a complex shape as a function of  $\Delta K$ . The complexity exists as a function of  $\Delta K_{eff}$ , indicating that it is not due to crack closure.
- oo The aqueous environmental effect does not increase with increasing R ratio. The magnitude of hydrogen environment embrittlement appears to be unaffected by R ratio.
- oo  $Da/dN$ - $\Delta K$ , predicted by NASA FLAGRO for Ti-6-4 with library materials constants, does not agree with measured  $da/dN$ .

### Milestones

In the next six months, several critical experiments will be conducted to understand and quantify environment-closure interactions in Ti alloys in various environments.

$Da/dN$  and closure will be measured for Ti-6-4 in vacuum to understand if and how enhanced slip reversibility in vacuum affects intrinsic FCP resistance and closure. A thorough metallographic examination will be conducted on fatigued specimens to quantify the changes in roughness and oxide thickness. Existing closure models will be utilized to understand the contribution from each closure mechanism. To understand crack tip damage relevant to closure, a fractographic examination will be performed as a function of  $\Delta K$ .

## Presentation Slides

1. Title.
2. Objectives.
3. Experimental parameters and the environmental fatigue set-up.
4. Crack closure mechanisms; after Suresh and Ritchie.
5.  $Da/dN$  vs applied  $\Delta K$  for Ti-6Al-4V in moist air and 1% NaCl at R ratios of 0.1, 0.4 and 0.7, and at constant  $K_{max}$  of 27.5 MPa $\sqrt{m}$ . R ratio strongly affects FCP kinetics in both environments.
6.  $K_{CL}/K_{MAX}$  vs  $\Delta K$  for Ti-6Al-4V in moist air and 1% NaCl at various R ratios, indicating that crack closure depends on  $\Delta K$ , R and environment.
7. SEM characterization of the effect of R ratio and environment on the fatigue fracture surface morphology for Ti-6Al-4V in the near- $\Delta K_{TH}$  region.
8. SEM characterization of the effect of  $\Delta K$  and environment on the fatigue fracture surface morphology for Ti-6Al-4V at  $R = 0.1$ .
9. Possible environment-crack closure interactions for Ti-6Al-4V in 1% NaCl.
10.  $Da/dN$  vs  $\Delta K_{EFF}$  ( $K_{MAX} - K_{CLOSURE}$ ) for Ti-6Al-4V in moist air and 1% NaCl at R ratios of 0.1, 0.4 and 0.7. The R ratio effect mostly disappears after accounting for closure by an approximate remote method.
11. Comparison of  $da/dN$  vs  $\Delta K$  for Ti-6Al-4V in moist air and 1% NaCl at R ratios of 0.1, 0.4 and 0.7, respectively.
12. Comparison of  $da/dN$  vs  $\Delta K_{EFF}$  for Ti-6Al-4V in moist air and 1% NaCl at R ratios of 0.1, 0.4 and 0.7, respectively.
13. Effect of R ratio on  $\Delta K$  and  $\Delta K_{EFF}$  at  $da/dN = 1 \times 10^{-6}$  mm/cycle for Ti-6Al-4V in moist air and 1% NaCl. The environmental effect does not increase with increasing R ratio.
14.  $Da/dN$  vs  $\Delta K$  and  $da/dN - \Delta K_{EFF}$  for Ti-6Al-4V in 1% NaCl at an R ratio of 0.1, showing that the complex shape in FCP curve is not due to crack closure.
15. Conclusions on environment-R ratio-closure interactions for Ti-6Al-4V.
16. NASA FLAGRO 2.0 equation.

17. Formulations for the crack opening function ( $f$ ),  $\Delta K_{TH}$  and  $K_C$  used in NASA FLAGRO 2.0.
18. Comparison of predicted  $da/dN$  by FLAGRO with experimental data for Ti-6Al-4V in moist air at R ratios of 0.1, 0.4 and 0.7.
19. Comparison of predicted  $da/dN$  by FLAGRO, obtained with empirically derived C and n at an R ratio of 0.1, with experimental data for Ti-6Al-4V in air and 1 % NaCl, respectively, at various R ratios.
20. Problems associated with NASA FLAGRO.
21. Future work.

**ENVIRONMENTAL EFFECTS ON FATIGUE CRACK  
PROPAGATION AND CLOSURE IN TITANIUM ALLOYS**

**Sang-Shik Kim and Richard P. Gangloff**

**Department of Materials Science and Engineering  
University of Virginia**

**Drs. R.S. Piascik and J.C. Newman**

**Mechanics of Materials Branch  
NASA-Langley Research Center**

## Objectives

### *Incorporating Environmental Effects in NASA FLAGRO*

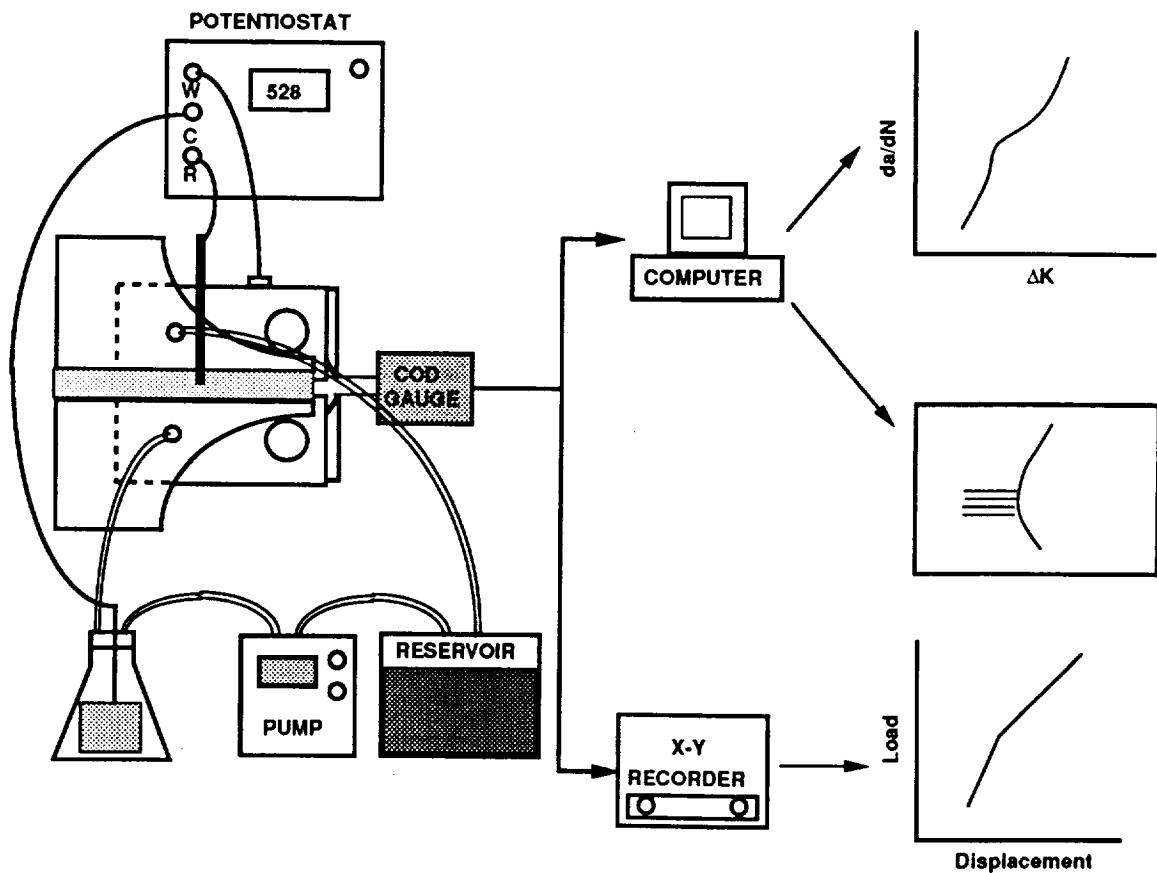
- Review and critically evaluate both EEFCP data and the predictive capabilities of crack growth rate models.
- Characterize intrinsic and extrinsic environmental  $da/dN-\Delta K$  kinetics for titanium alloys, as a function of R ratio.
- Understand environment-sensitive crack closure phenomena and mechanisms, including the effects of  $\Delta K$  and R ratio.



## Experimental Parameters

- **Material:** Ti-6Al-4V ELI (MA)
- **Compact Tension Specimen:** L-T Orientation
- **Stress Ratio :** 0.1, 0.4, 0.7 & const.  $K_{max}$
- **Frequency:** 5 Hz
- **Environments:** Air & 1% NaCl at  $-500 \text{ mV}_{SCE}$
- **Crack Closure Measurement:** Compliance Technique

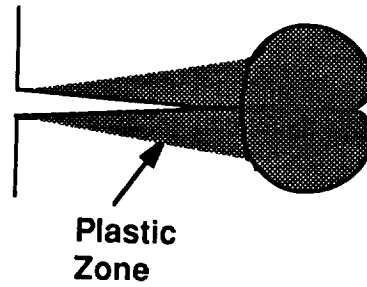
### Environmental Fatigue Set-up



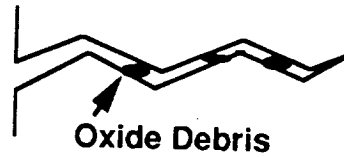
# CRACK CLOSURE MECHANISMS

(Suresh and Ritchie)

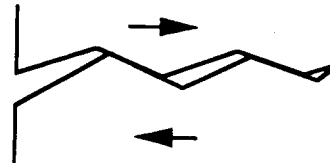
Plasticity-induced  
Closure



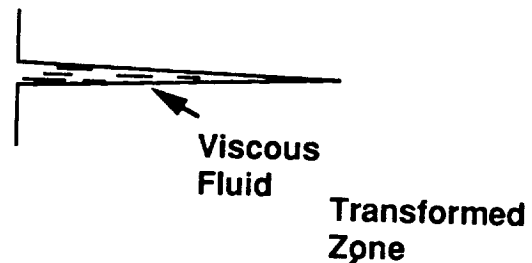
Oxide-induced



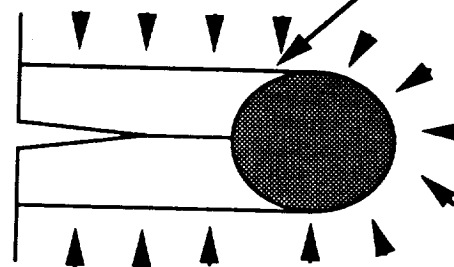
Roughness-induced



Viscous Fluid-induced



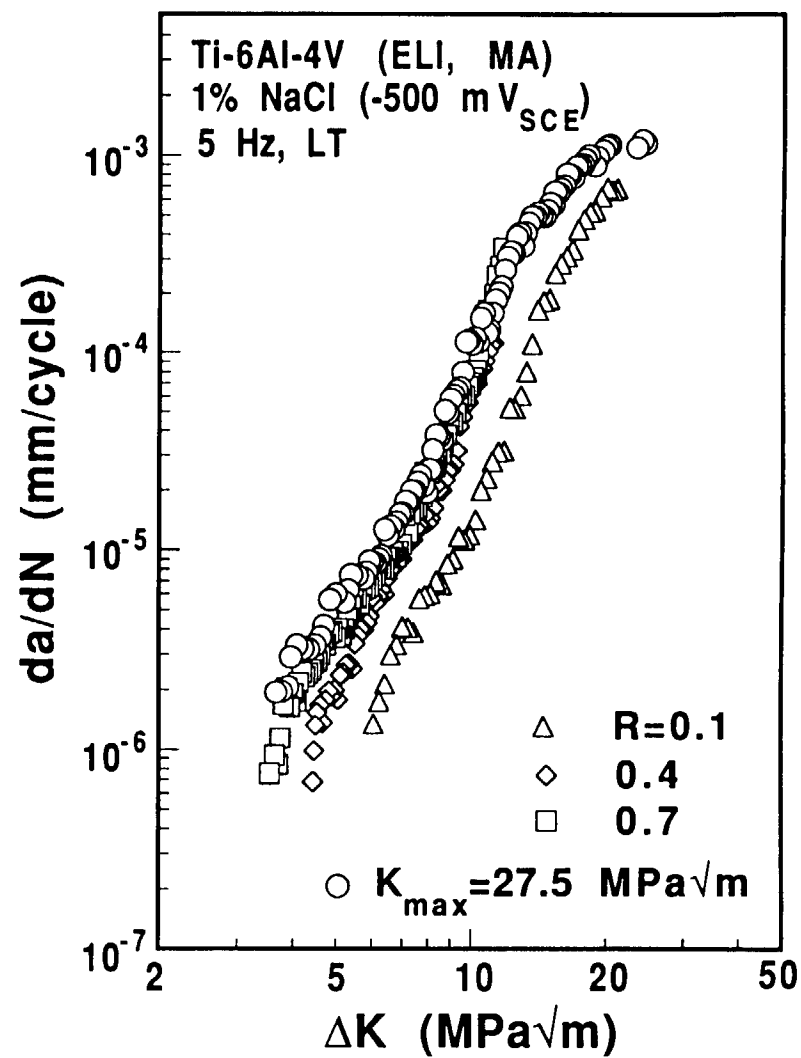
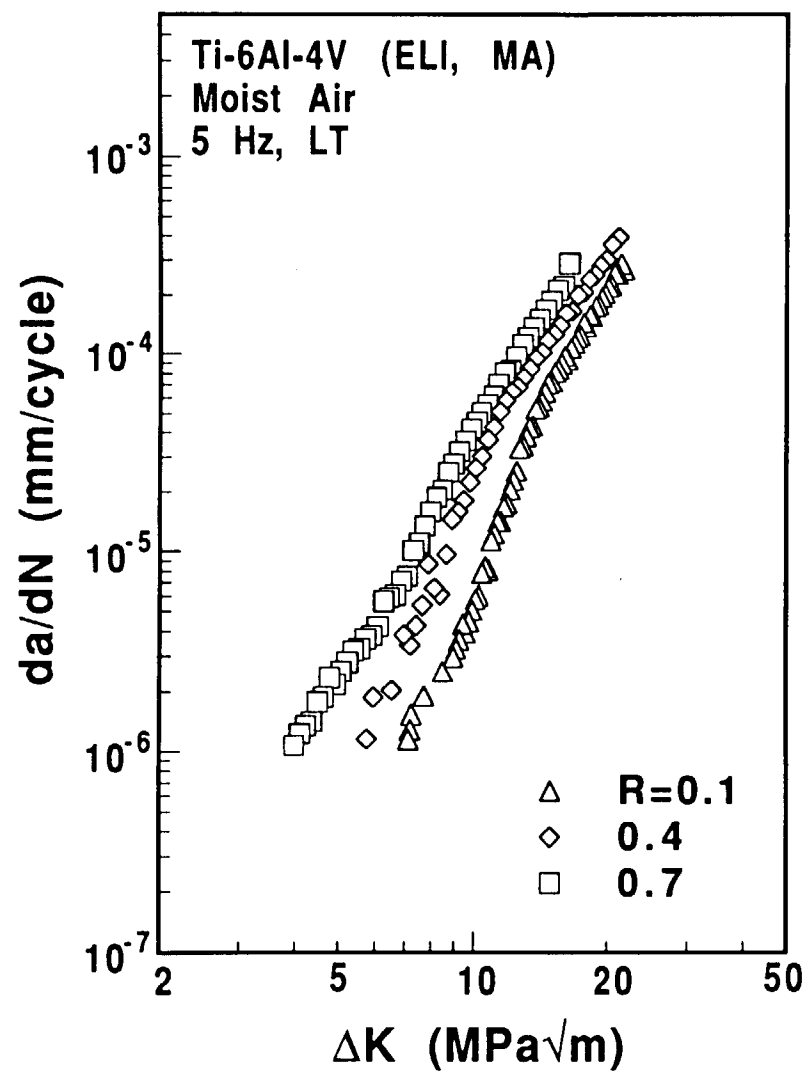
Phase Transformation-  
induced

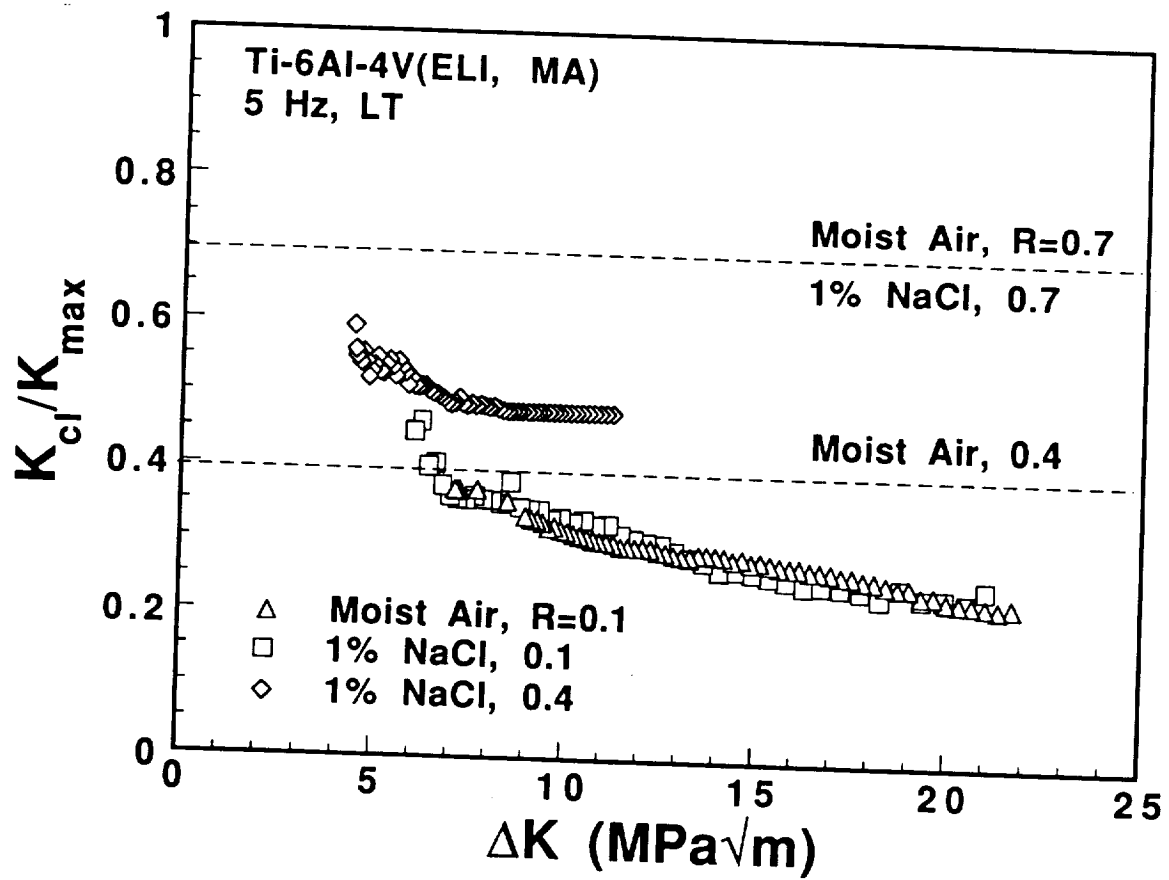


$$\Delta K = K_{\max} - K_{\min}$$

$$\Delta K_{\text{eff}} = K_{\max} - K_{\text{cl}}$$

$$\frac{da}{dN} = C(\Delta K_{\text{eff}})^m$$



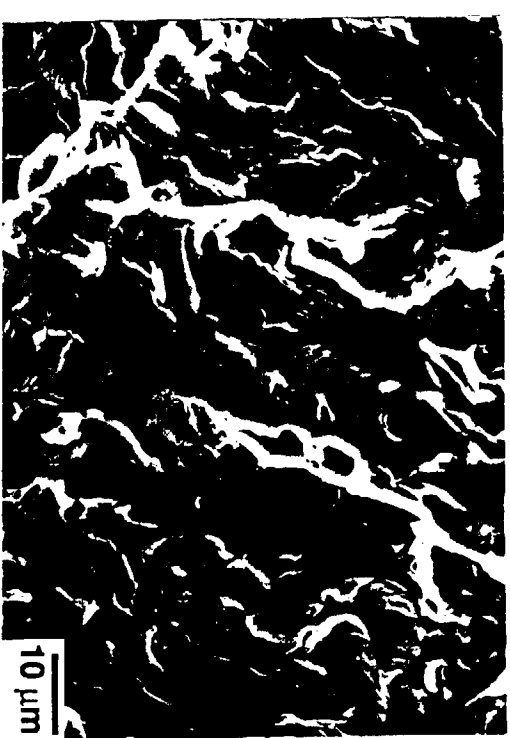


Moist Air



1% NaCl

$R=0.1$



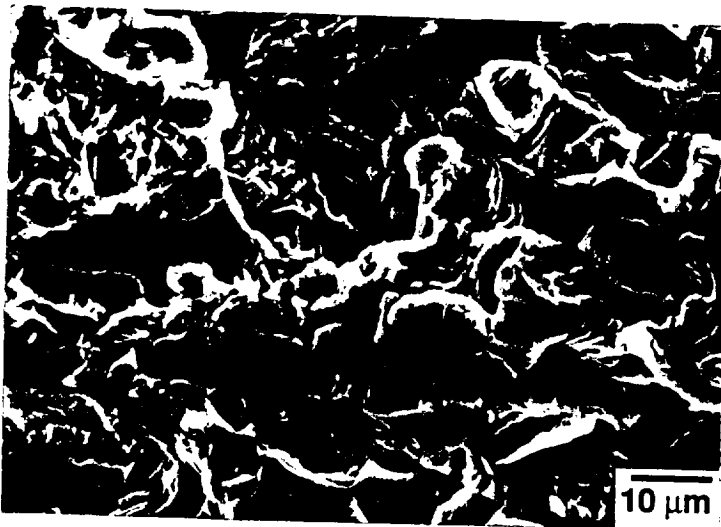
$R=0.4$



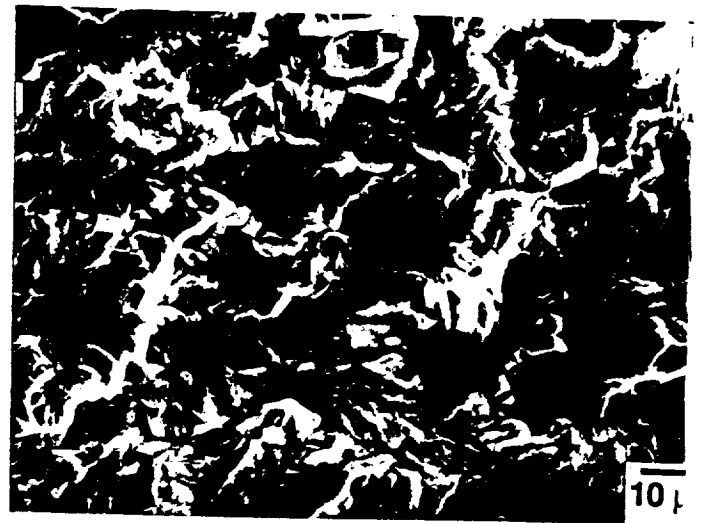
$R=0.7$

Near- $\Delta K_{th}$

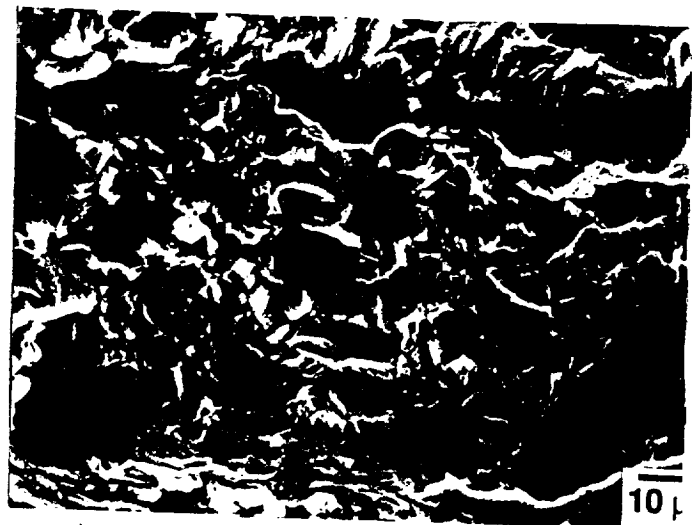
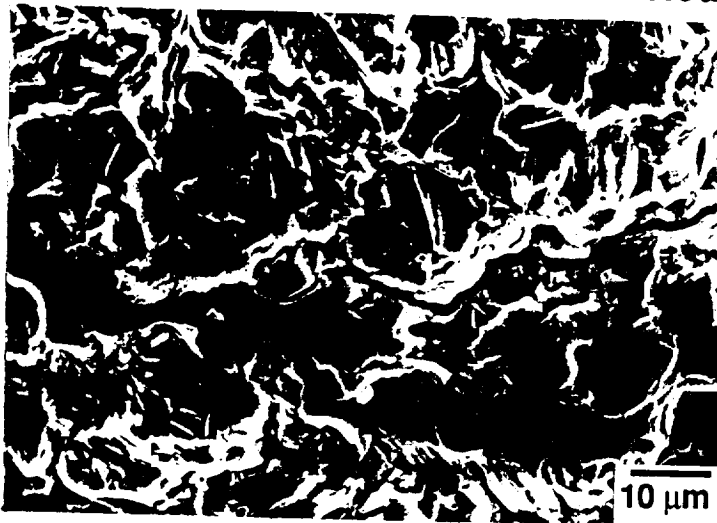
Moist Air



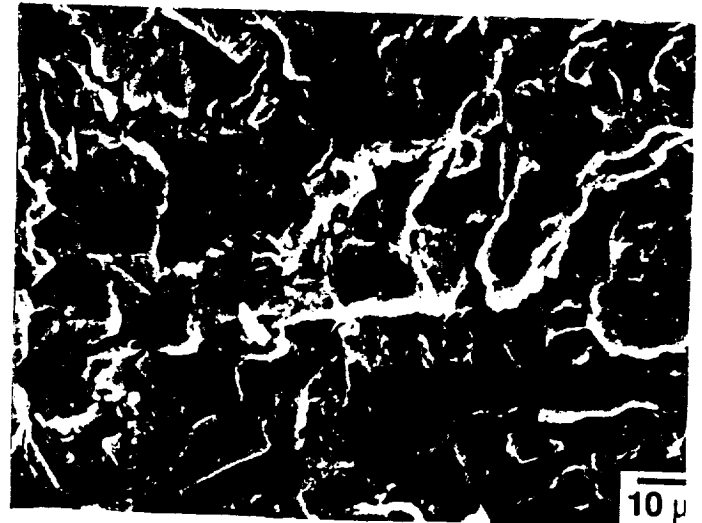
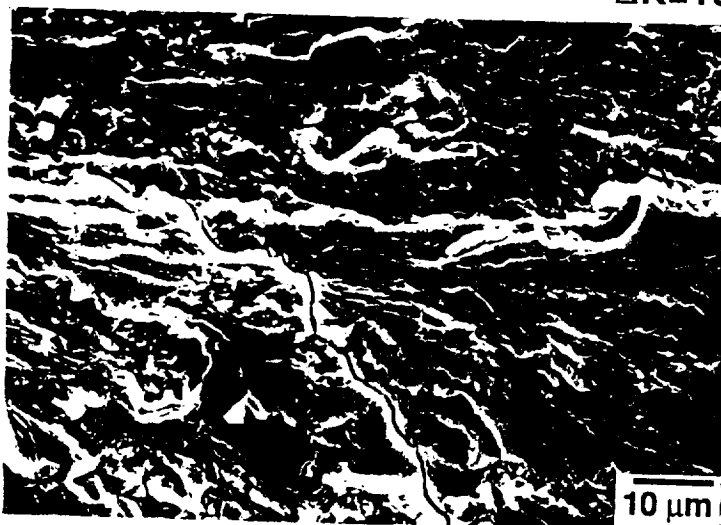
1% NaCl



Near- $\Delta K_{th}$



$\Delta K=10 \text{ MPa}\sqrt{\text{m}}$



$\Delta K=15 \text{ MPa}\sqrt{\text{m}}$

$R=0.1$

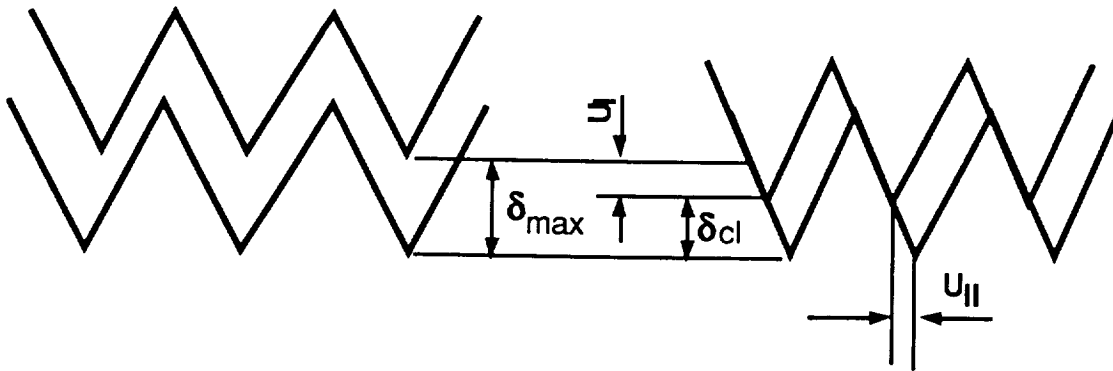
## Possible Environment-Crack Closure Interactions

### Oxide-induced :

- Wedging by corrosion product  
Cyclic CTOD  $\approx 180\text{\AA}$  at near- $\Delta K_{th}$  in 1% NaCl  
Oxide layer thickness  $< 10\text{ \AA}$

### Roughness-induced :

- Reduced slip reversibility in NaCl



- Reduced surface roughness due to transgranular cracking
- Enhanced surface roughness due to intergranular cracking

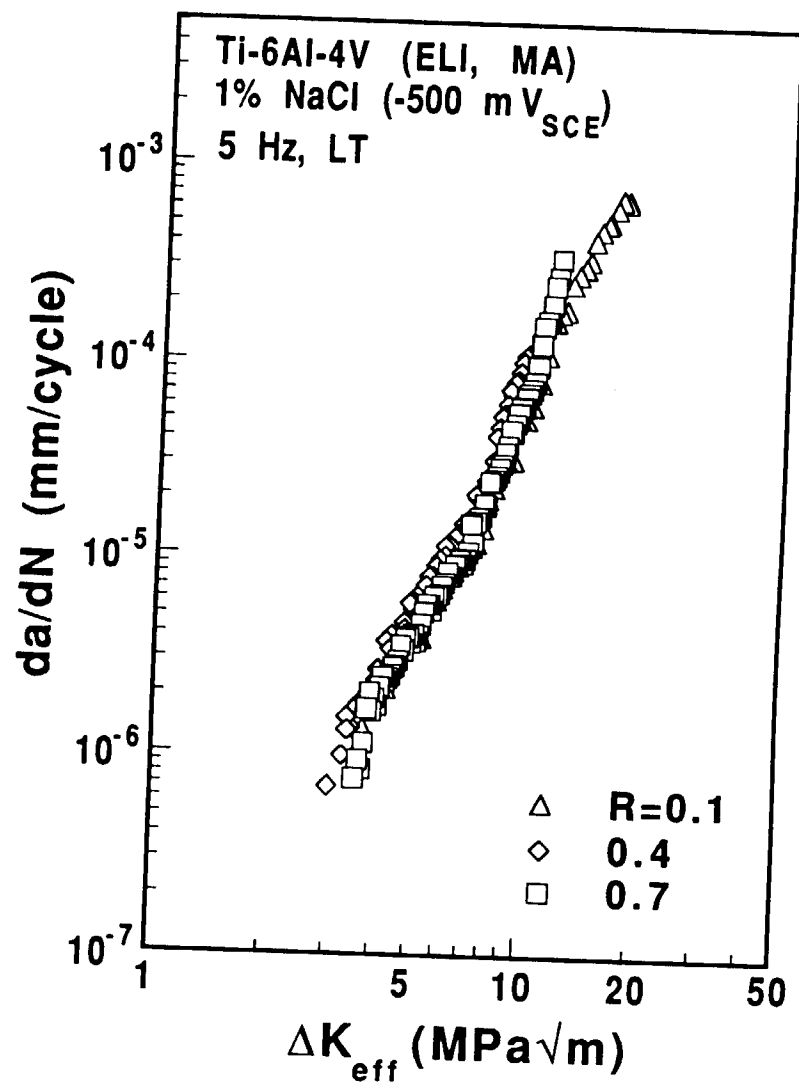
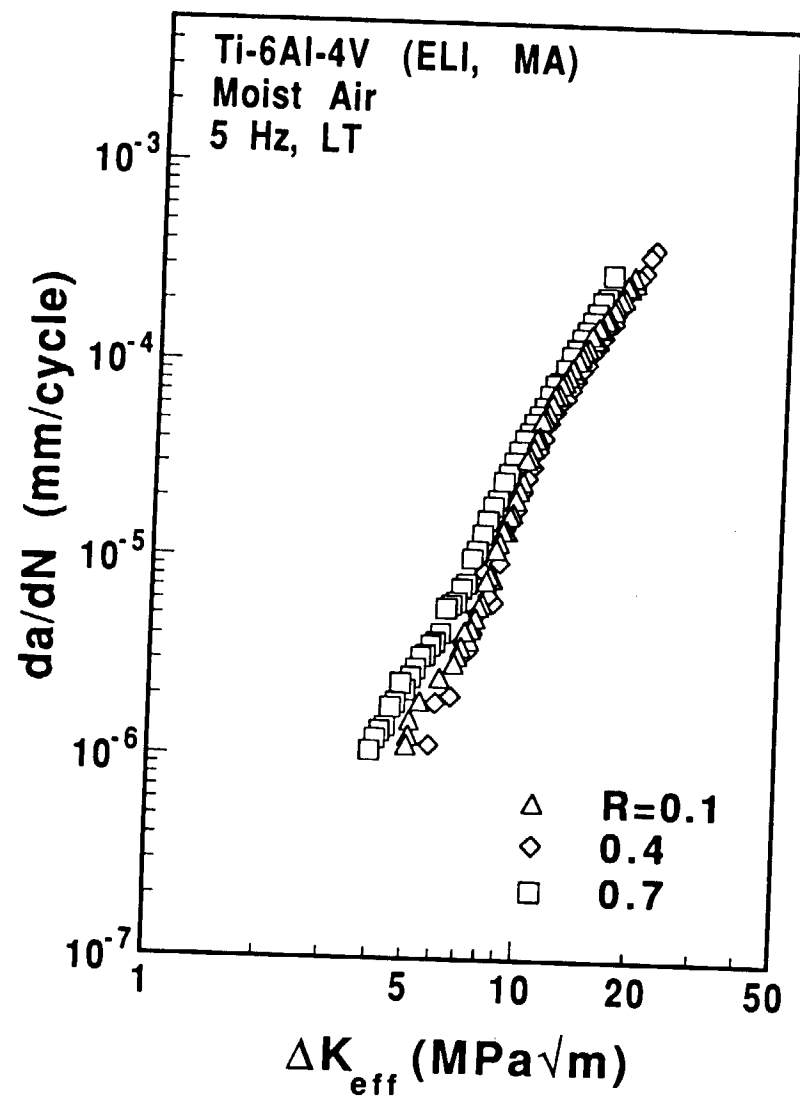
### Plasticity-induced :

- Environment enhanced crack wake plasticity

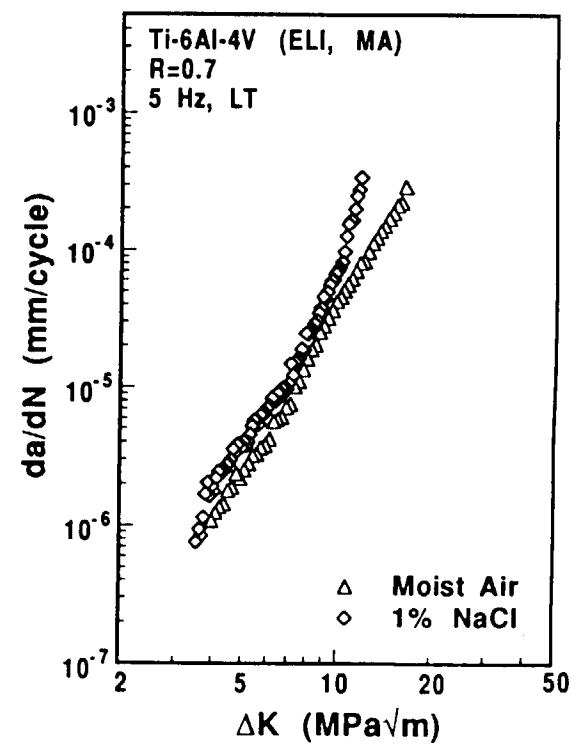
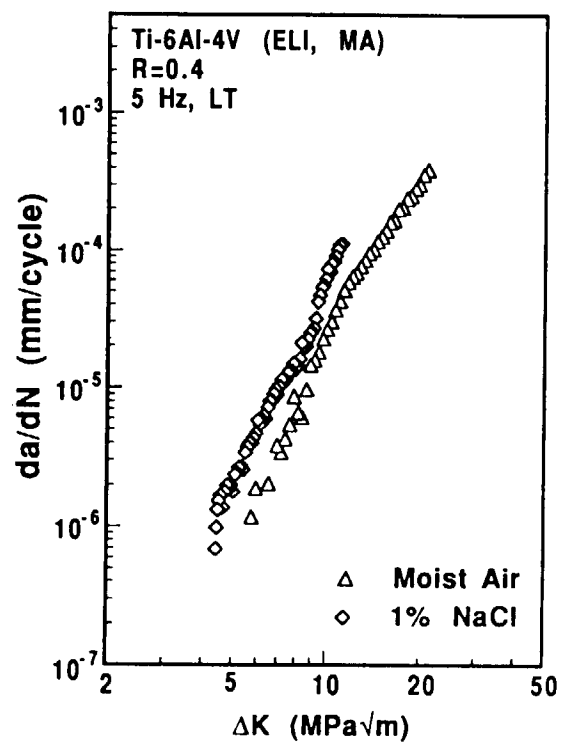
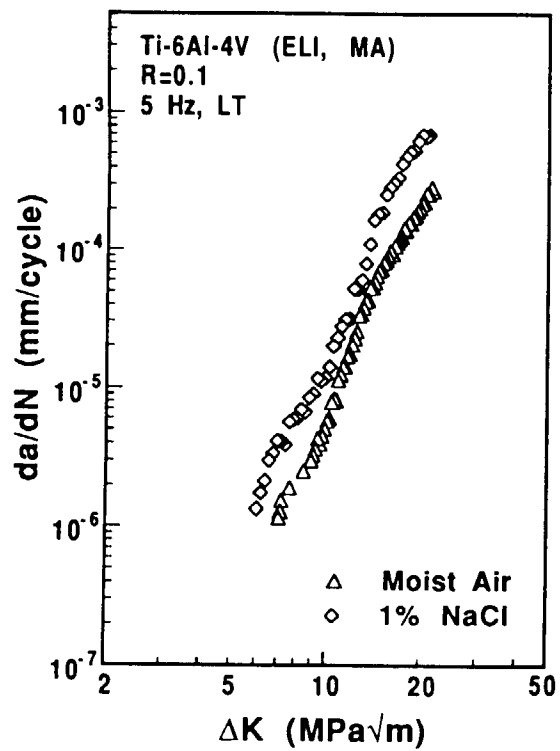
### Phase transformation-induced :

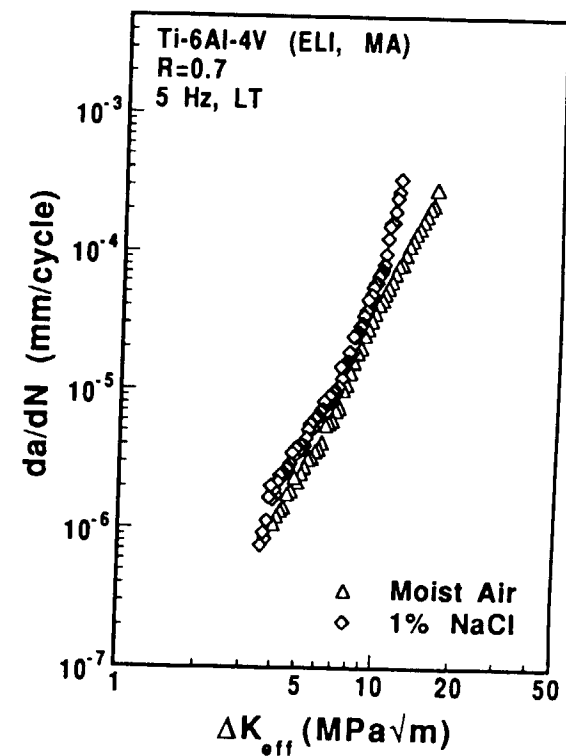
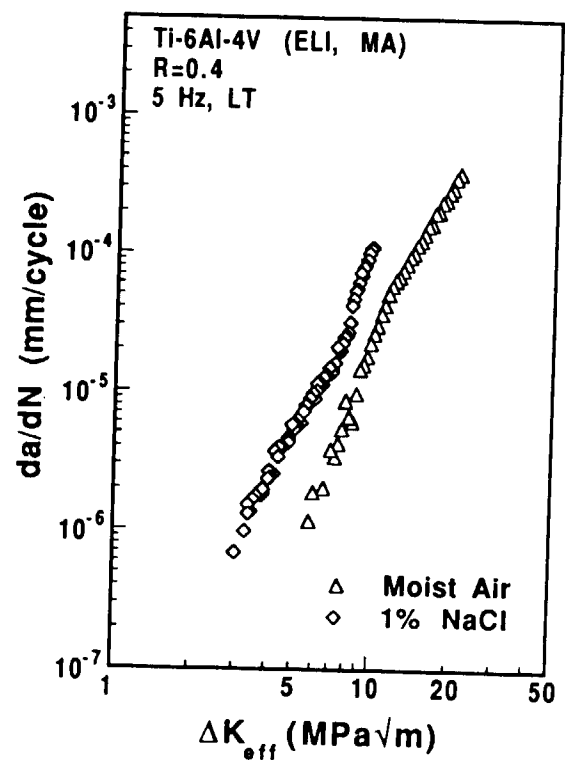
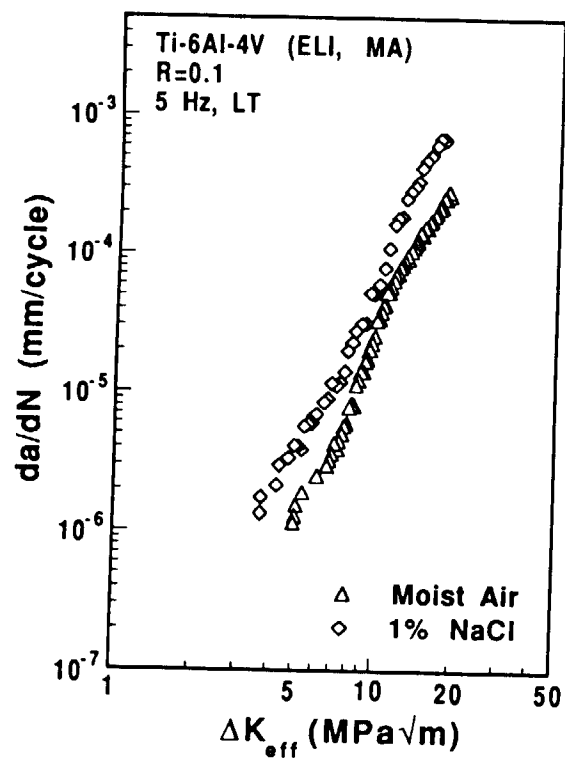
- Formation of hydride

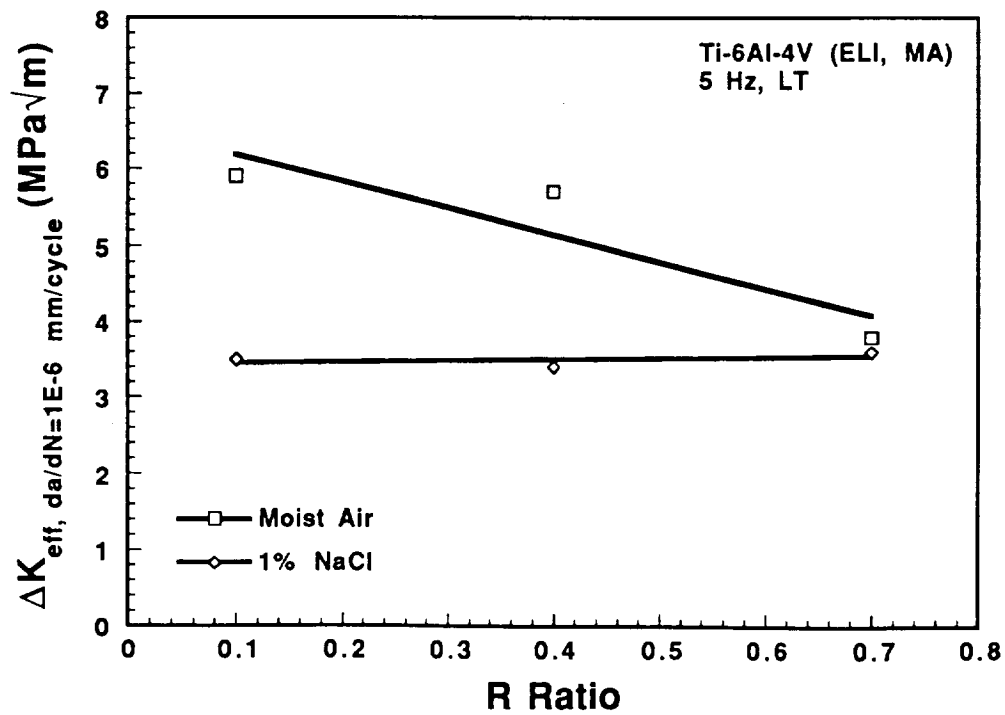
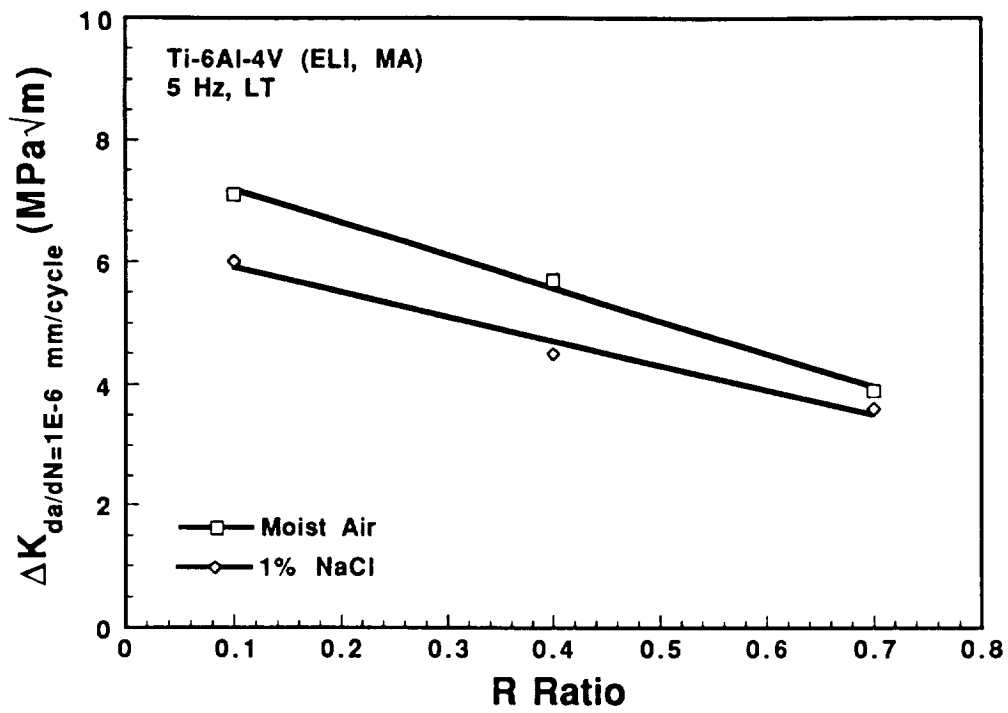
### Fluid pressure-induced :

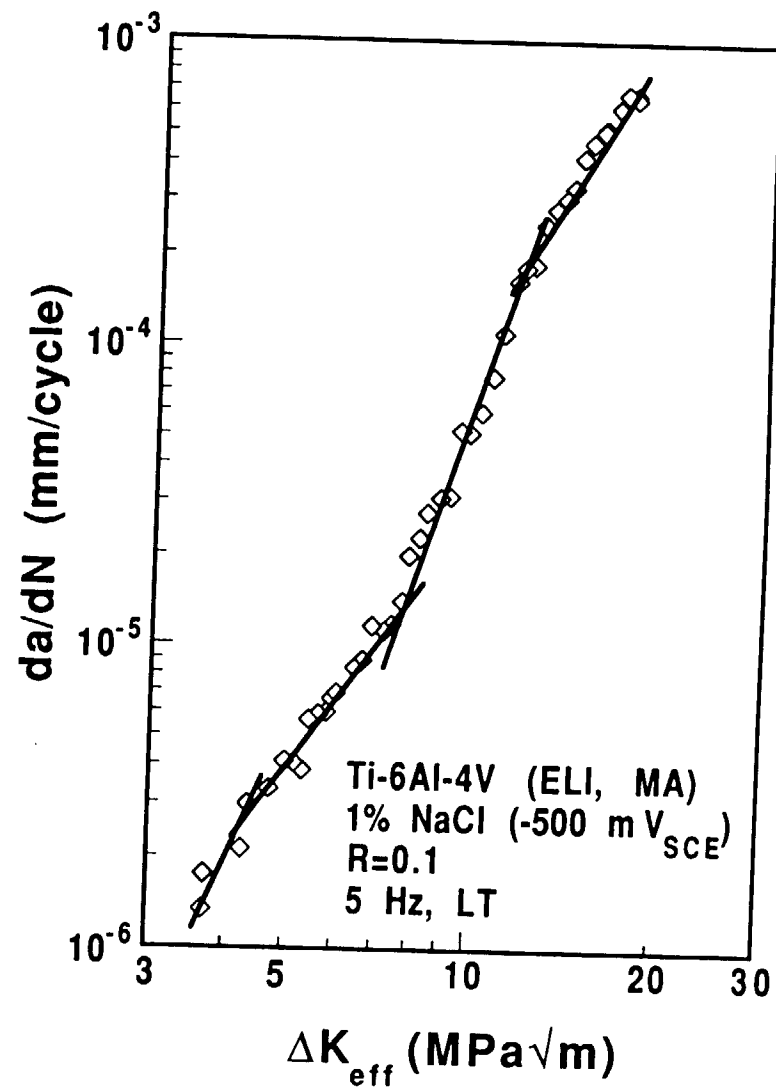
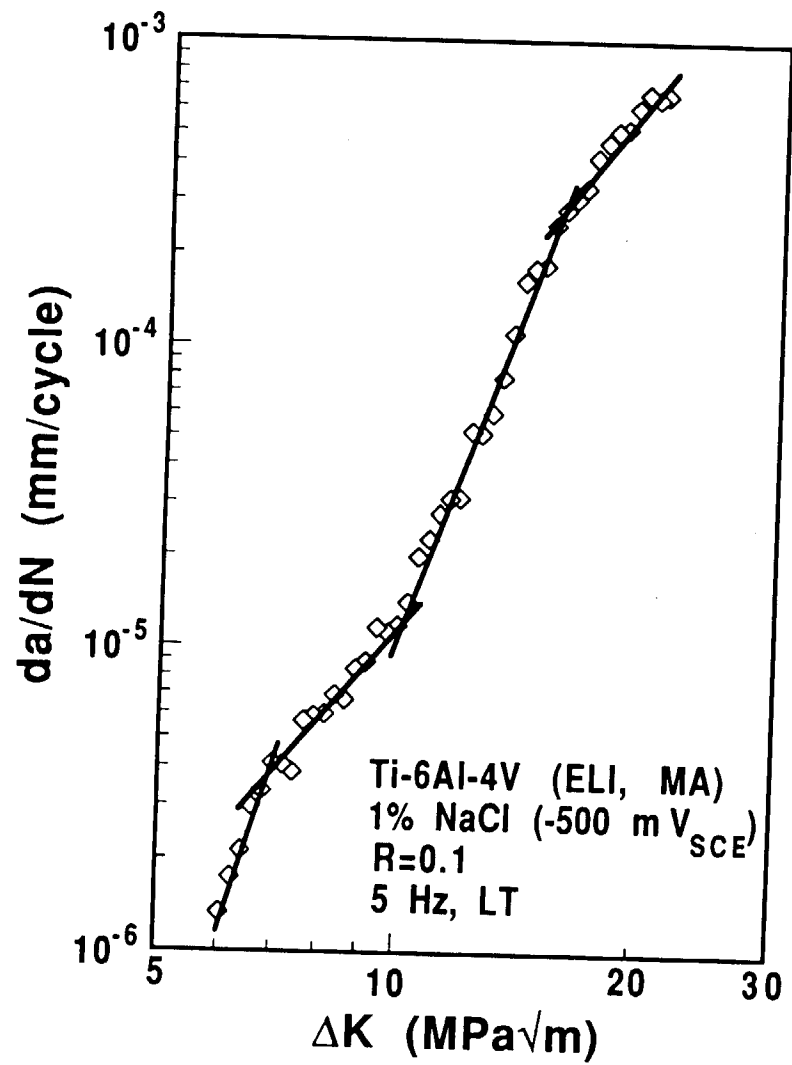












## **Conclusions**

### **Effect of Environment**

- **FCP resistance is higher in air than in NaCl.**
- **Complex shapes of  $da/dN-\Delta K$  for Ti-6-4 are not due to crack closure.**
- **Environmental effect does not increase with increasing R ratio.**

### **Effect of R Ratio**

- **FCP resistance decreases with increasing R ratio in air and NaCl.**
- **R ratio effect appears to be more severe in air than in NaCl : need confirmation.**
- **R ratio effect cannot be explained solely by crack closure.**

### **Crack Closure**

- **Crack closure is strongly affected by  $\Delta K$ , R and environment.**
- **Crack closure is slightly higher in NaCl than in air.**

## NASGRO 2.0 EQUATION

$$\frac{da}{dN} = \frac{C(1-f)^n \Delta K^n \left(1 - \frac{\Delta K_{th}}{\Delta K}\right)^p}{(1-R)^n \left(1 - \frac{\Delta K}{(1-R)K_C}\right)^q}$$

<b>C, n, p, q :</b>	<b>Empirical Constants</b>
<b>R :</b>	<b>Stress Ratio</b>
<b>f :</b>	<b>Crack Opening Function</b>
<b><math>\Delta K_{th}</math> :</b>	<b>Threshold Stress Intensity Range</b>
<b><math>K_C</math> :</b>	<b>Critical Stress Intensity</b>

$$f = \frac{K_{op}}{K_{max}}$$

$$= \max(R, A_0 + A_1 R + A_2 R^2 + A_3 R^3) \quad R \geq 0$$

$$= A_0 + A_1 R \quad -2 \leq R < 0$$

$$A_0 = (0.825 - 0.34\alpha + 0.05\alpha^2) \left[ \cos \left( \frac{\pi S_{max}}{2 \sigma_0} \right) \right]^\alpha$$

$$A_1 = (0.415 - 0.071\alpha) \frac{S_{max}}{\sigma_0}$$

$$A_2 = 1 - A_0 - A_1 - A_3$$

$$A_3 = 2A_0 + A_1 - 1$$

$\alpha$  : Plane Stress/strain Constraint Factor

$S_{max}$  : Maximum Applied Stress

$\sigma_0$  : Flow Stress

$$\Delta K_{th} = \Delta K_0 \left[ \frac{4}{\pi} \tan^{-1} (1-R) \right] \sqrt{\frac{a}{a+a_0}}$$

$\Delta K_0$  :  $\Delta K_{th}$  at  $R=0$

$a$  : Crack Length

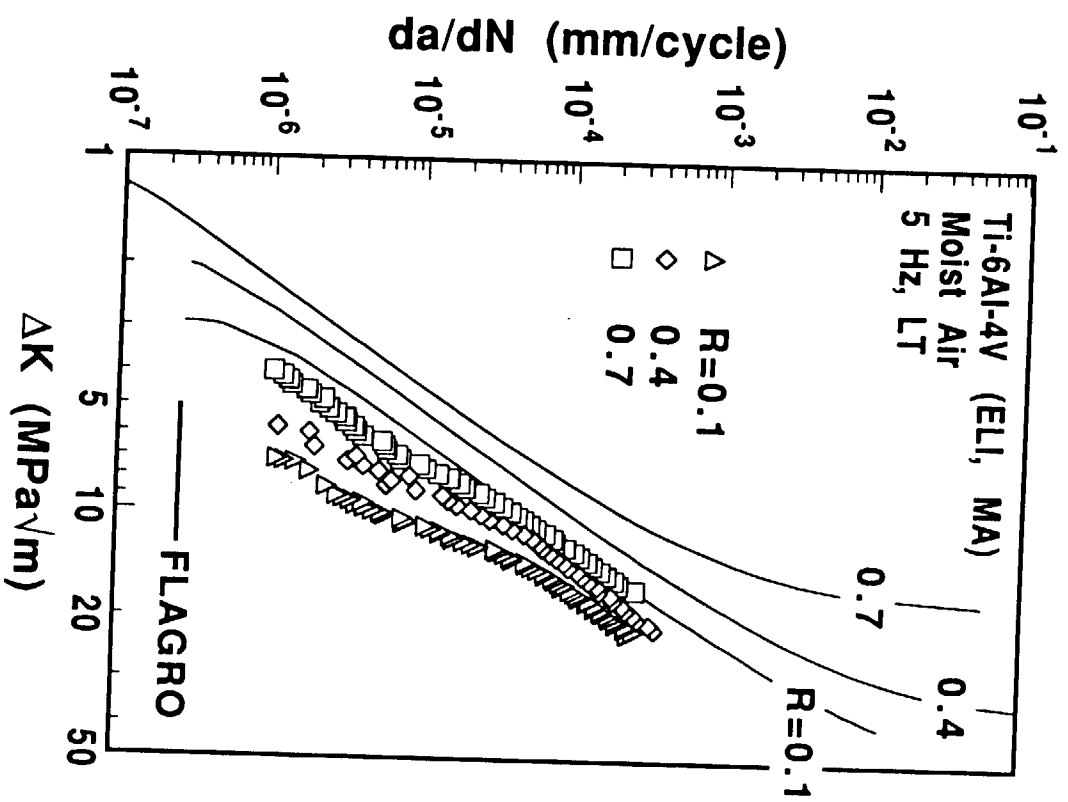
$a_0$  : Intrinsic Crack Length

$$K_C/K_{IC} = 1 + B_K e^{-(A_K t/t_0)^2}$$

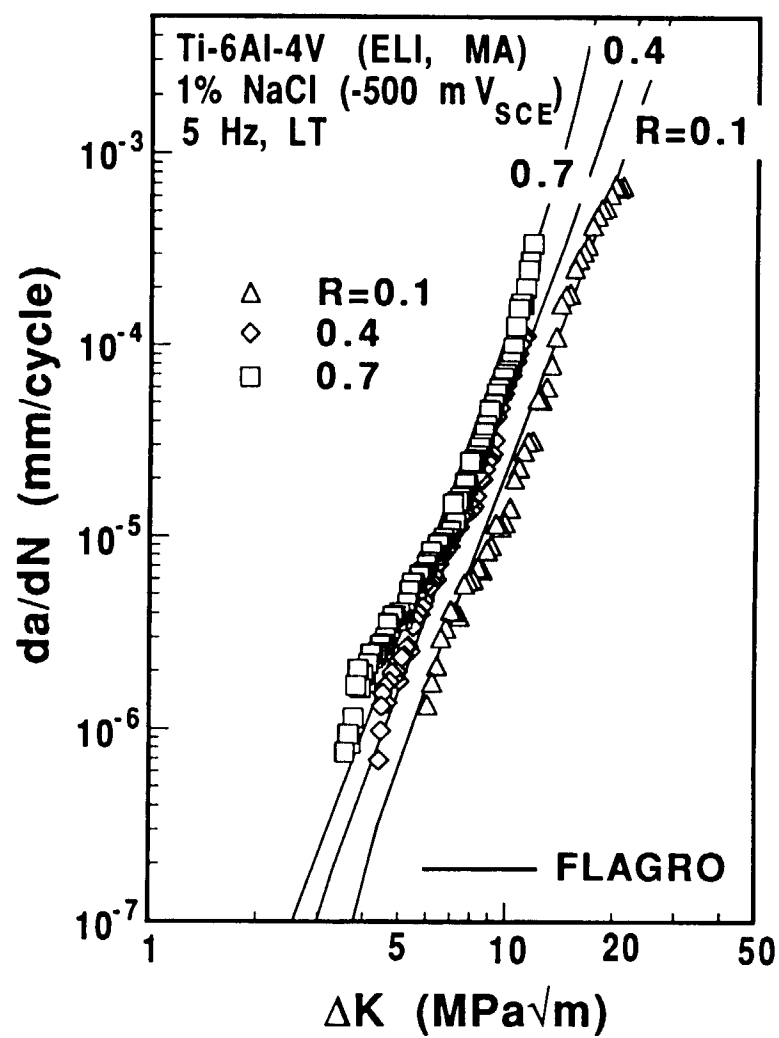
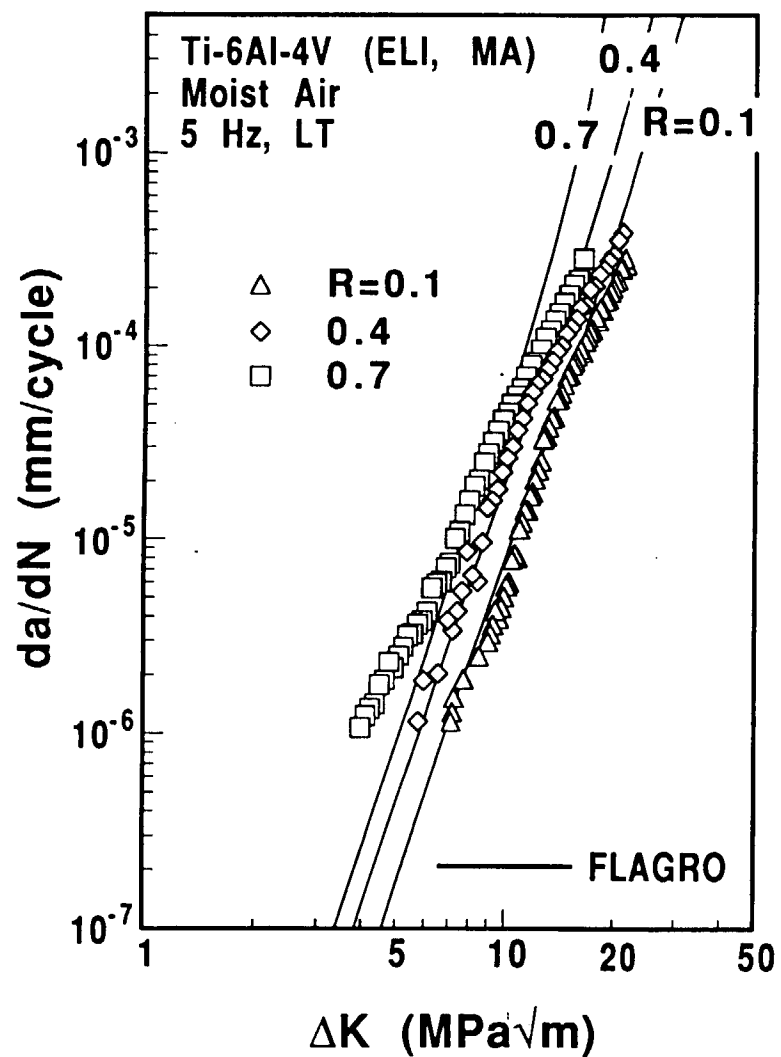
$$t_0 = 2.5 (K_{IC}/\sigma_{ys})^2$$

$A_K, B_K$  : Constants

$t$  : Thickness





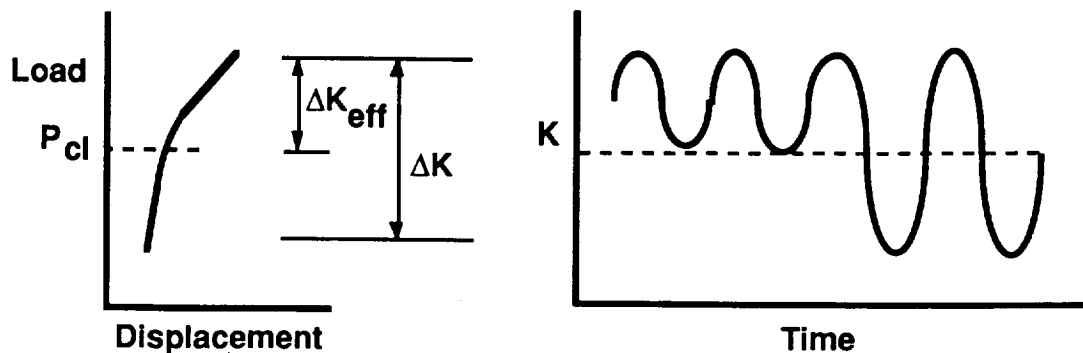


## **Problems Associated with NASA FLAGRO**

- **Lack of materials constants in various environments.**
- **Limited predictive capabilities.**
- **Crack opening function,  $f$ , needs to account for environment-sensitive crack closure.**

## Future Work

- How does vacuum affect intrinsic FCP and closure?
  - ⇒ Measure  $da/dN$  and crack closure for Ti-6-4 in vacuum.
- Try to understand crack tip damage relevant to closure
  - ⇒ Perform fractographic examination as a function of  $\Delta K$ .
- How does each closure mechanism contribute to the measured closure in Ti-6-4 in various environments?
  - ⇒ Perform metallographic examination to quantify the changes in roughness and oxide thickness.
  - ⇒ Apply the existing closure models.
- Alter microstructure as needed to affect closure for  $\alpha/\beta$  Ti alloys.
- How meaningful is  $\Delta K_{eff}$ ?





## **Project #12    Experimental Study of the Nonlinear Viscoplastic Response of High Temperature Structures**

Marshall F. Coyle, Mark A. Rowley and E.A. Thornton

### **Objectives**

The basic objective of this research program is to investigate experimentally the viscoplastic response of thermal structures for high speed flight. An additional objective of the experimental program is to provide high quality data for validation of finite element analysis using unified viscoplastic constitutive models.

### **Status and Recent Results**

Recent progress, of a research program focused on understanding the thermoviscoplastic behavior of structural panels, is described. The program has three tasks: (1) finite element simulations of geometric and nonlinear material behavior, (2) experimental determination of parameters for Bodner-Partom constitutive models of panel materials, and (3) thermal-structural tests of panels subjected to localized heating.

Finite element analysis of nonlinear panel bending is under development. A finite element formulation for elastic panel bending described by the Von Karman equations has been completed. Correlation of predicted panel behavior with experimental results is underway. The extension of the finite element analysis to include thermoviscoplastic behavior is described and initial validation results are highlighted.

A research task, focused on the experimental determination of the constitutive model parameters, is in progress. This task will provide data for the panel materials for the range of temperatures and strain rates to be used in the thermal-structural test program. Initial tensile tests for Hastelloy-X have been completed, and material parameters for the Bodner-Partom constitutive model have been determined. Testing to develop materials parameters for aluminum alloy 2618, the Concorde structural material, have been completed and Bodner-Partom parameters were determined. A test program including compression and creep tests to determine Bodner-Partom material parameters for the 8009 aluminum alloy has been completed.

In the experimental study, rectangular plates are heated transiently by a quartz heat

lamp focused on the panel centerline. Parallel edges of the panel are maintained at constant temperature by chill water flow through coolant tubes. The panel is supported at only four points to provide well-defined thermal and structural boundary conditions. A heat lamp characterization study has been completed, and an empirical formula for the incident surface heat flux developed. The thermal buckling test procedure is described. Temperatures, displacements and strain results for elastic and inelastic tests are presented. The panels exhibit global buckling response in all tests. Recent efforts have been focused on test validation and determination of error ranges for the experimental data.

The tests reaffirm that localized heating can cause substantial out-of-plane bending of real panels. The global bending deformations were due to in-plane spatial temperature gradients and initial panel warpage. Small initial warpage with compressive membrane thermal forces was sufficient to initiate substantial transverse bending.

#### Milestones

Future plans include continued development of each of the research tasks. Within the next year, correlations of simulated thermoviscoplastic panel behavior with experimental data will be initiated.

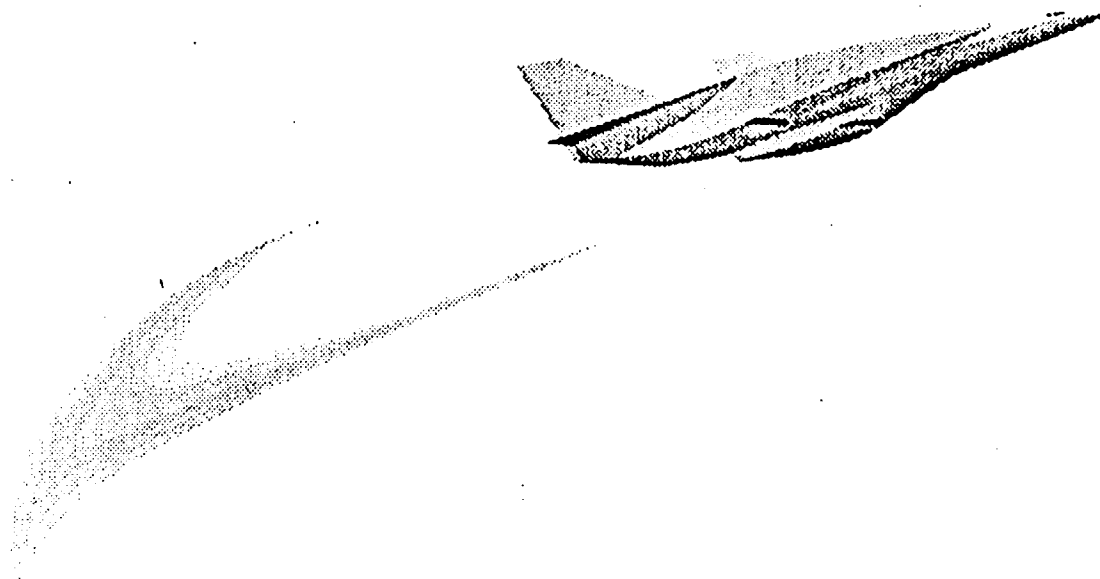
#### Presentation Slides

---

## ***RESEARCH OBJECTIVES***

---

- Investigate Thermoviscoplastic (TVP) response of thin panels subject to intense local heating.
- Evaluate finite element Thermal-Structural analyses with unified TVP constitutive models by comparison with experimental data.







---

## ***THERMOVISCOPLASTIC RESEARCH PROGRAM***

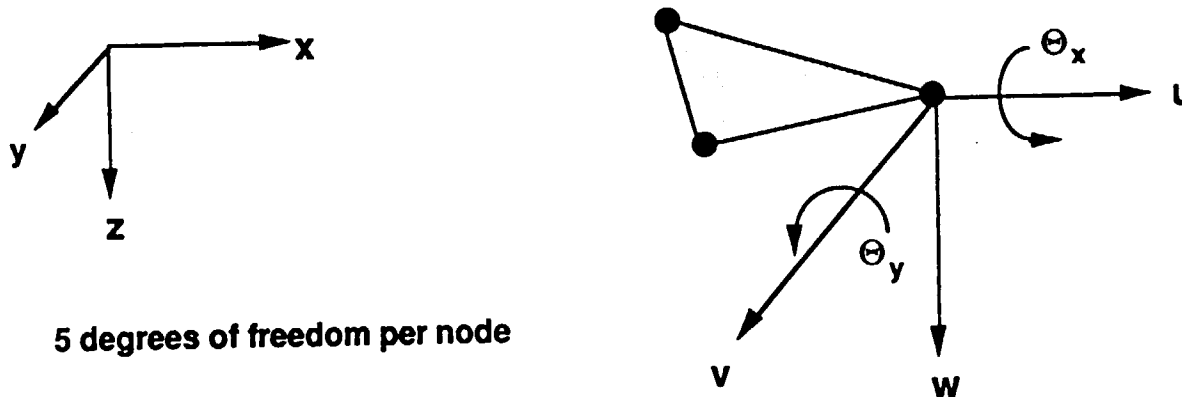
---

- **FINITE ELEMENT TVP ANALYSIS  
ROBERT P. MARINO**
- **BODNER-PARTOM CONSTITUTIVE MODELS  
MARK A. ROWLEY**
- **THERMAL-STRUCTURAL TESTS OF PANELS  
MARSHALL F. COYLE**

# **FINITE ELEMENT ANALYSIS**

# Computational Plate Analysis

- CST Plane Stress Element & DKT Bending Element



- Prescribed Nodal Temperature Histories
- Quasi-static Response
- Neglects Temperature Gradient Through Thickness
- Temperature Dependent Material Properties
- Newton-Raphson Iterative Equation Solver

# Governing Plate Equations

## Equilibrium

$$\frac{\partial^2 M_x}{\partial x^2} + 2 \frac{\partial^2 M_{xy}}{\partial x \partial y} + \frac{\partial^2 M_y}{\partial y^2} + \frac{\partial}{\partial x} \left( N_x \frac{\partial w}{\partial x} \right) + \frac{\partial}{\partial y} \left( N_{xy} \frac{\partial w}{\partial y} \right) + \frac{\partial}{\partial x} \left( N_{xy} \frac{\partial w}{\partial y} \right) + \frac{\partial}{\partial y} \left( N_y \frac{\partial w}{\partial y} \right) + q = 0$$

$$\frac{\partial N_x}{\partial x} + \frac{\partial N_{xy}}{\partial y} = 0$$

$$\frac{\partial N_{xy}}{\partial x} + \frac{\partial N_y}{\partial y} = 0$$

## Strain-Displacement

$$\{\epsilon_m\} = \begin{Bmatrix} \frac{\partial u_o}{\partial x} \\ \frac{\partial v_o}{\partial y} \\ \frac{\partial u_o}{\partial y} + \frac{\partial v_o}{\partial x} \end{Bmatrix} \quad \{\epsilon_b\} = z \begin{Bmatrix} -\frac{\partial^2 w}{\partial x^2} \\ -\frac{\partial^2 w}{\partial y^2} \\ -2 \frac{\partial^2 w}{\partial x \partial y} \end{Bmatrix} \quad \{\epsilon_m\} = \begin{Bmatrix} \frac{1}{2} \left( \frac{\partial w}{\partial x} \right)^2 \\ \frac{1}{2} \left( \frac{\partial w}{\partial y} \right)^2 \\ \frac{\partial w}{\partial x} \frac{\partial w}{\partial y} \end{Bmatrix}$$

$$\{\epsilon\} = \{\epsilon_m\} + \{\epsilon_b\} + \{\epsilon_m\}$$

## Stress-Strain

$$\{\sigma\} = [\sigma_x \quad \sigma_y \quad \tau_{xy}]^T = [E] \{\epsilon - \epsilon_o\}$$

## von Kármán Plate Theory Finite Element Formulation

$$\begin{bmatrix} [K_m] & \frac{1}{2}[K_{mb}] \\ \frac{1}{2}[K_{mb}]^T & [K_b] + \frac{1}{2}[K_{bl}] + \frac{1}{2}[K_{bml}] - [K_m] \end{bmatrix} \begin{Bmatrix} \delta_m \\ \delta_b \end{Bmatrix} = \begin{Bmatrix} R_T \\ R_{TM} + R_q \end{Bmatrix}$$

$[K_m] = \int_{\Omega} [B_m]^T [A] [B_m] d\Omega$	Membrane Stiffness
$[K_{mb}] = \int_{\Omega} [B_m]^T [A] [C] [G] d\Omega$	Coupling Stiffness
$[K_b] = \int_{\Omega} [B_b]^T [D] [B_b] d\Omega$	Bending Stiffness
$[K_{bl}] = \int_{\Omega} [G]^T [N_m] [G] d\Omega$	Linear Geometric Stiffness
$[K_{bml}] = \int_{\Omega} [G]^T [C]^T [A] [C] [G] d\Omega$	Nonlinear Geometric Stiffness
$[K_{bl}] = \int_{\Omega} [G]^T [N_T] [G] d\Omega$	Thermal Bending Stiffness
$\{R_T\} = \int_{\Omega} [B_m]^T \{N_T\} d\Omega$	Thermal Force
$\{R_{TM}\} = - \int_{\Omega} [B_b]^T \{M_T\} d\Omega$	Thermal Moment
$\{R_q\} = \int_{\Omega} q \{N\} d\Omega$	Pressure Load

# **Applications of Computational Plate Analysis**

## **Validation Studies**

- **Classical Small Deflection Plate**
- **Large Deflection Problems**
  - **Pressure Loaded Plate (Levy, Clough)**
  - **Simply Supported Movable & Immovable Edges**

## **Thermal Postbuckling of Plates with Initial Imperfections**

- **Aluminum Panel**
  - **Immovable & Movable Edges**
  - **Varying Initial Plate Imperfection**
- **Hastelloy-X Panel (UVa Experiment)**
  - **Point Supported**
  - **Initial Plate Imperfection**
  - **Slowly Heated**

***Presented at the AIAA 34th SDM in April 1993 at LaJolla***

# TVP Plate Formulation

- **Bodner - Partom Constitutive Model**

$$\dot{\sigma}_{ij} = E_{ijkl} \dot{\epsilon}_{kl}^E - E_{ijkl} \alpha_{kl} \Delta \dot{T}$$

$$\dot{\epsilon}_{ij}^P = f_{ij}(\sigma_{ij}, Z_k)$$

$$\dot{Z}_i = g_i(\sigma_{ij}, Z_k)$$

- **von Kármán Equations in Rate Form**

- **Solution Algorithm**

- Euler Time Marching
- Newton - Raphson Iteration

- **Computational Issues**

- Yielding Through Thickness
- Computational Time

# Thermo Visco-Plastic Rate Form Equations

$$\left[ \begin{array}{c|c} K_m & \frac{1}{2} K_{mb} \\ \hline \frac{1}{2} K_{bm} & K_b + \frac{1}{2} K_{bl} + \frac{1}{2} K_{bnl} - K_T - K_p \end{array} \right] \begin{Bmatrix} \dot{\delta}_m \\ \dot{\delta}_b \end{Bmatrix} + \left[ \begin{array}{c|c} 0 & \frac{1}{2} \dot{K}_{mb} \\ \hline \frac{1}{2} \dot{K}_{bm} & \frac{1}{2} \dot{K}_{bl} + \frac{1}{2} \dot{K}_{bnl} - \dot{K}_T - \dot{K}_p \end{array} \right] \begin{Bmatrix} \delta_m \\ \delta_b \end{Bmatrix} = \begin{Bmatrix} \dot{R}_T + \dot{R}_p \\ \dot{R}_q + \dot{R}_{pb} \end{Bmatrix}$$

$[K_m]$  Membrane Stiffness

$[K_{mb}]$  Coupling Stiffness  $[\dot{K}_{mb}]$

$[K_b]$  Constant Bending Stiffness

$[K_{bl}]$  Linearly Dependant Bending Stiffness  $[\dot{K}_{bl}]$

$[K_{bnl}]$  Non - Linearly Dependant Bending Stiffness  $[\dot{K}_{bnl}]$

$[K_T]$  Stiffness due to Thermal Force  $[\dot{K}_T]$

$[K_p]$  Stiffness due to Plasticity  $[\dot{K}_p]$

$\{\dot{R}_T\}$  Thermal Force Load Rate

$\{\dot{R}_p\}$  Equiv. Membrane Load Rate due to Plasticity

$\{\dot{R}_q\}$  Equiv. Bending Load Rate due to Transverse Pressure

$\{\dot{R}_{pb}\}$  Equiv. Bending Load Rate due to Plasticity Moment

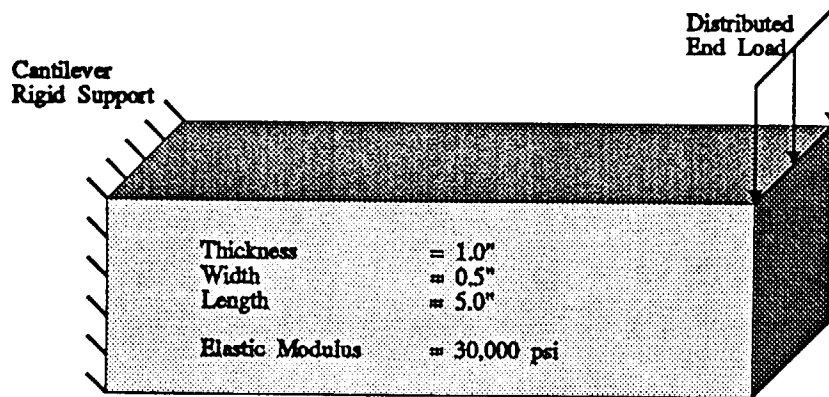


# **Current Status**

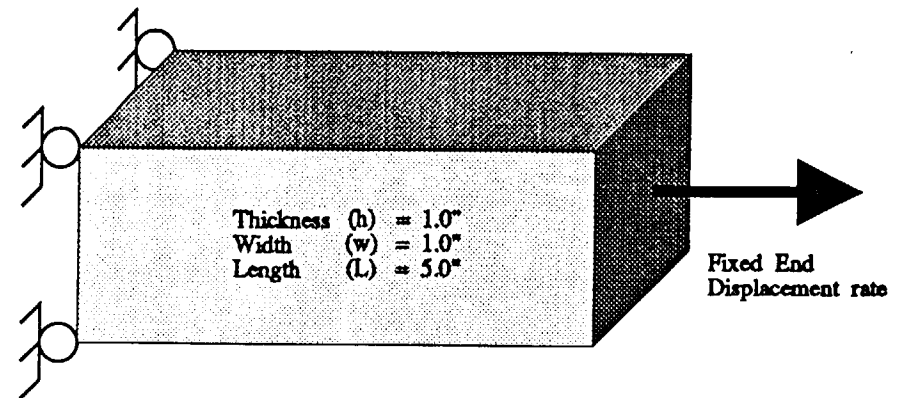
- **Computer Code Under Development**
- **Validation Testing Underway**
  - **Checked Elastic Thermal Buckling**
  - **Began Testing of Yielding**
    - \* **Axial Tension Test**
    - \* **Bending of Cantilever Beam  
with Yielding Progression**

# Validation Problems for Plastic Analysis

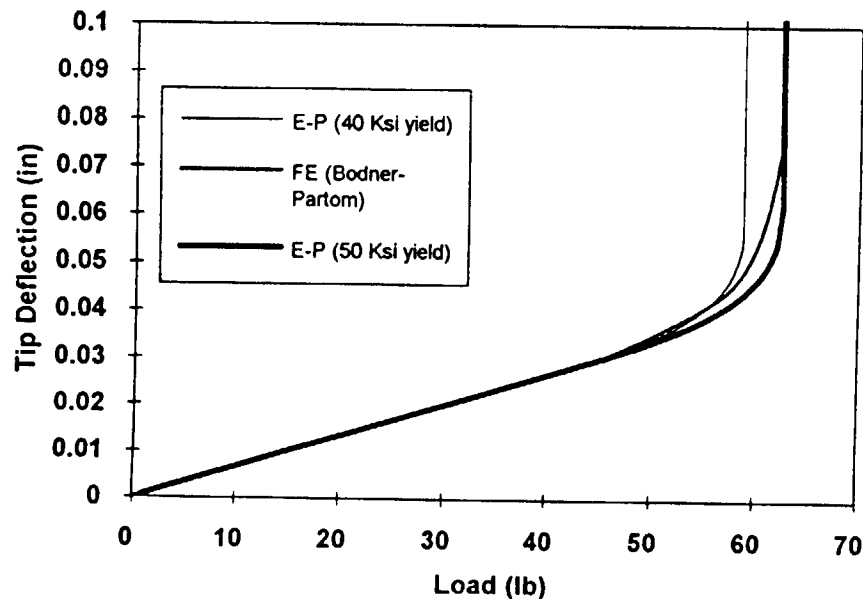
Cantilever Beam: Plastic model



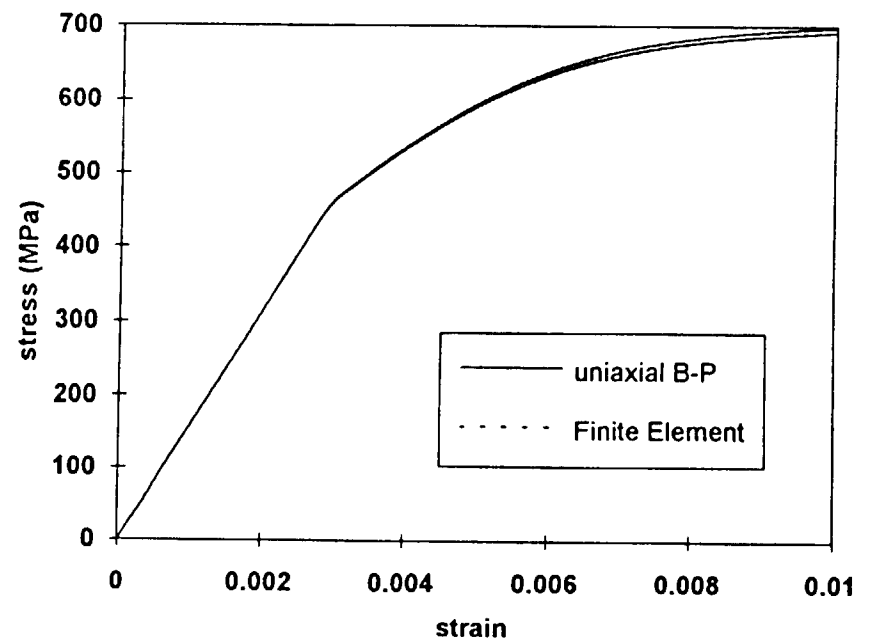
Uniaxial Tension Bar:



Analytic Elastic-Perfectly Plastic and Bodner-Partom F.E. Results



B1900+Hf Test Bar



# **Future Plans**

- **Comparision with Published Results**
  - **Byrom**
  - **Song**
- **Comparision with Coyle Buckling Tests**

**Characterization  
of the  
Viscoplastic  
Deformation Response  
of  
High Temperature Alloys**

**presented by**

**Mark A. Rowley**

**and**

**Earl A. Thornton**

# Overview

- ➡ Motivation
- ➡ Constitutive Model
- ➡ Testing
- ➡ Parameter Determination
- ➡ Results
- ➡ Concluding Remarks

# Motivation

## ➤ Unified Constitutive models

- Describe Elastic and Inelastic Behavior
- Include Both Time and Temperature Effects

## ➤ Materials

- The Thermal Structures Laboratory is Studying Inelastic Buckling of Hastelloy Panels
- Aluminum Alloy 8009 is a Candidate Material for Use in the High Speed Civil Transport

## ➤ Characterization

- Bodner Partom Constitutive Model
- Simple Mechanical Tests for Obtaining Model Parameters
- Wide Range of Temperatures and Strain Rates

# Model

## Essential Equations of the Uniaxial Bodner-Partom Unified Constitutive Law

### Flow Law

$$\dot{\epsilon} = \dot{\epsilon}^e + \dot{\epsilon}^p$$

### Kinetic Equation

$$\dot{\epsilon}^p = \frac{2}{\sqrt{3}} \left( \frac{\sigma}{|\sigma|} \right) D_0 \exp \left\{ -\frac{1}{2} \left[ \frac{Z}{\sigma} \right]^{2n} \right\}$$

### Evolution Equations

$$Z = Z^I + Z^D$$

$$\dot{Z}^I = m_1 [Z_1 - Z^I] \dot{W}_p - A_1 Z_1 \left[ \frac{Z^I - Z_2}{Z_1} \right]^n$$

$$\dot{Z}^D = m_2 [Z_3 - Z^D] \dot{W}_p - A_2 Z_1 \left[ \frac{Z^D}{Z_1} \right]^{n_2}$$

# Testing

## ☛ THREE KINDS OF MECHANICAL TESTS

Uniaxial, Isothermal Tension Tests

Uniaxial, Isothermal Compression Tests

Isothermal, Constant Load Creep Tests

## ☛ LOAD FRAMES

Universal Testing Machine

Creep Frame

## ☛ TEST FIXTURES

Wedge Grips

Compression Rams with Spherical Alignment  
adaptor

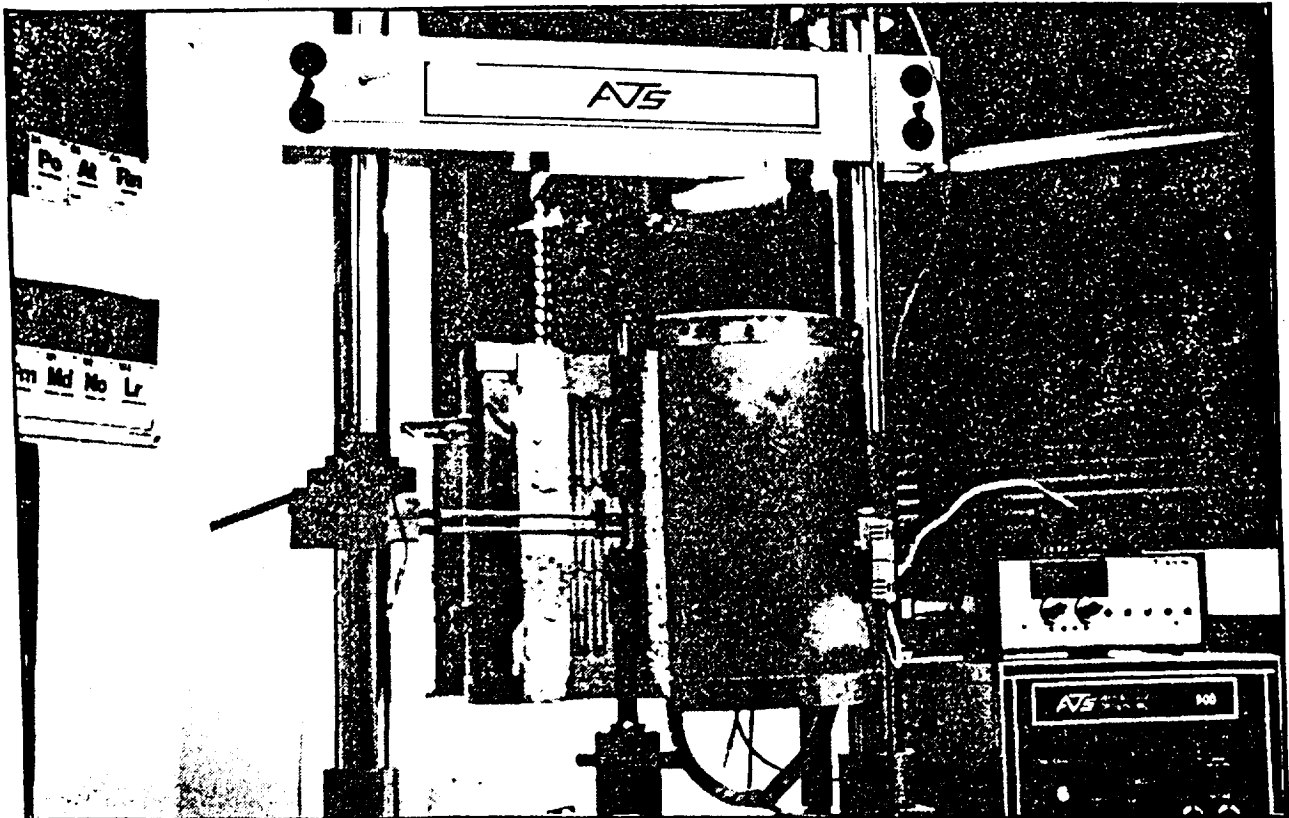
Extensometer

Furnace



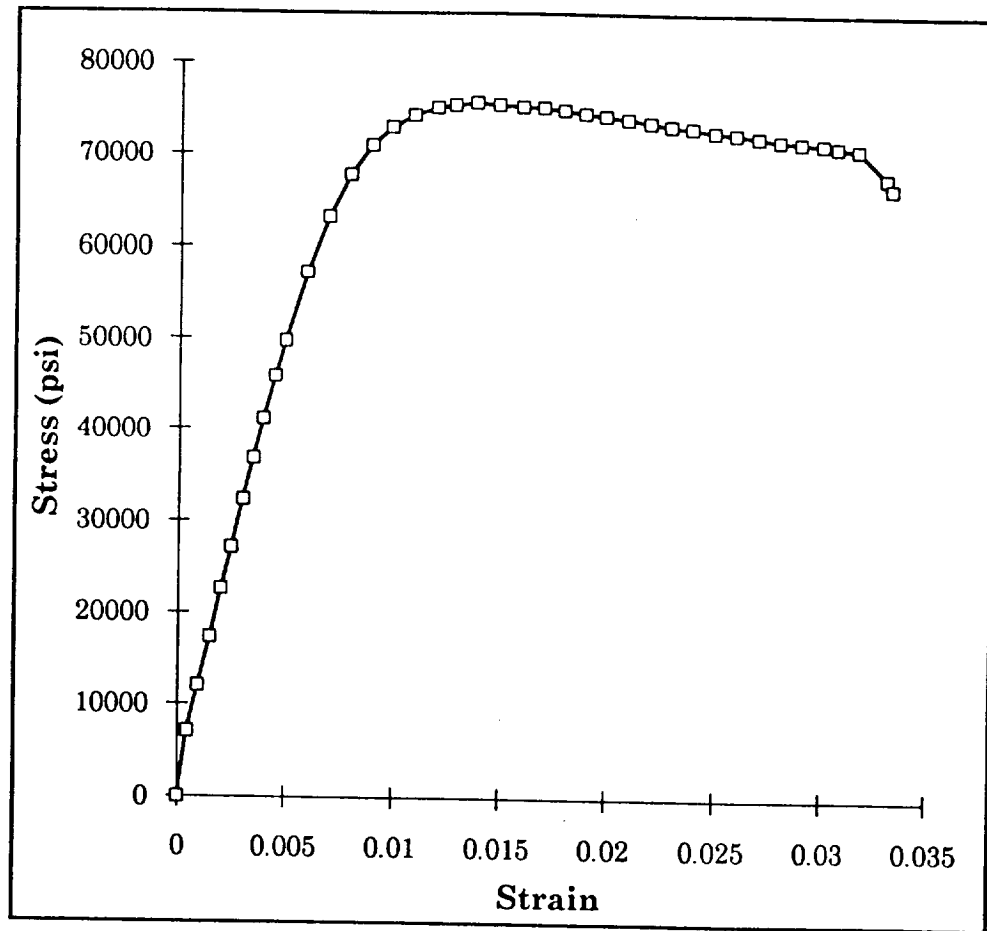
# Tension Tests of Hastelloy-X

Strain Rate	Temperature			
	77°F (25°C)	400°F (204°C)	700°F (371°C)	1000°F (538°C)
2.625E-3 1/s	2 Tests	2	2	2
2.625E-4 1/s	3	2	3	2
2.667E-5 1/s	0	1	0	1



# Engineering Stress-Strain curve for 8009 Al. in Tension

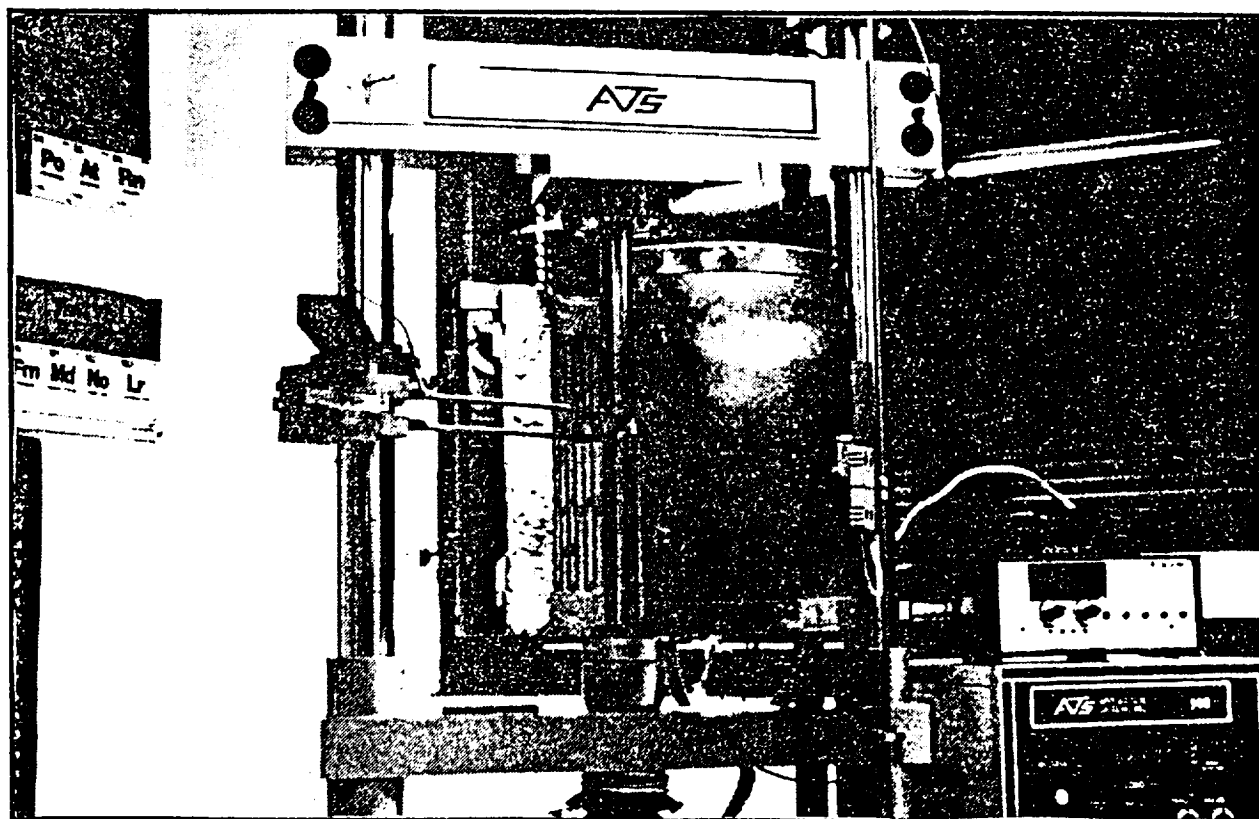
(Strain Rate =  $2.63 \times 10^{-4}$  1/s) (T = 77°F, 25°C)



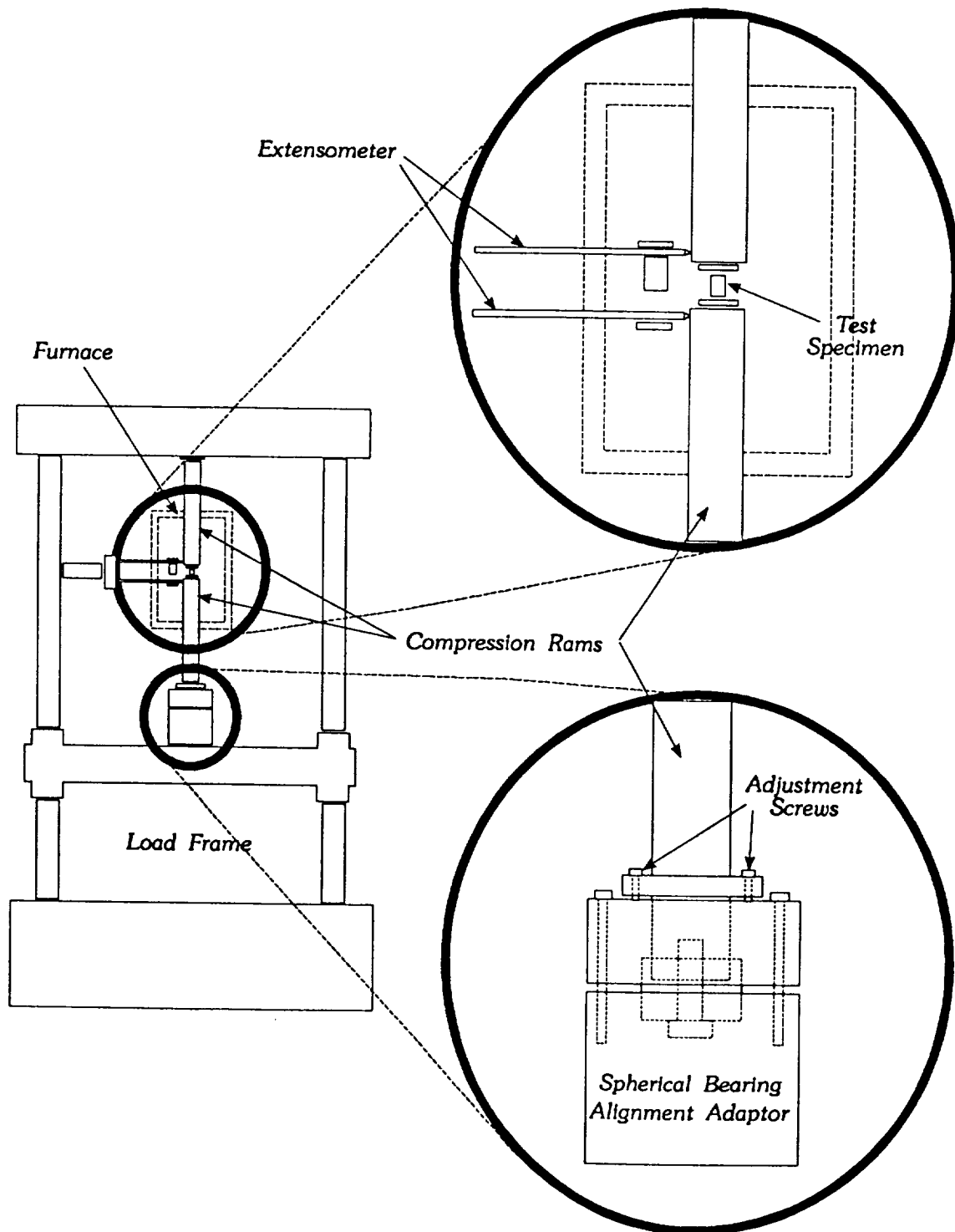
- Decrease in Load Levels in the Inelastic Range and Failure at Small Strains Possibly due to Localized Plastic Instability
- Alternate Mechanical Tests for Obtaining Uniaxial Hardening Data: Compression Tests

# Compression Tests of 8009 Aluminum

Strain Rate	Temperature				
	70°F (21°C)	212°F (100°C)	347°F (175°C)	437°F (225°C)	527°F (275°C)
5.333E-3 1/s	1 Test	1	1	1	1
5.333E-4 1/s	1	1	1	1	1
8.889E-5 1/s	1	1	1	1	1

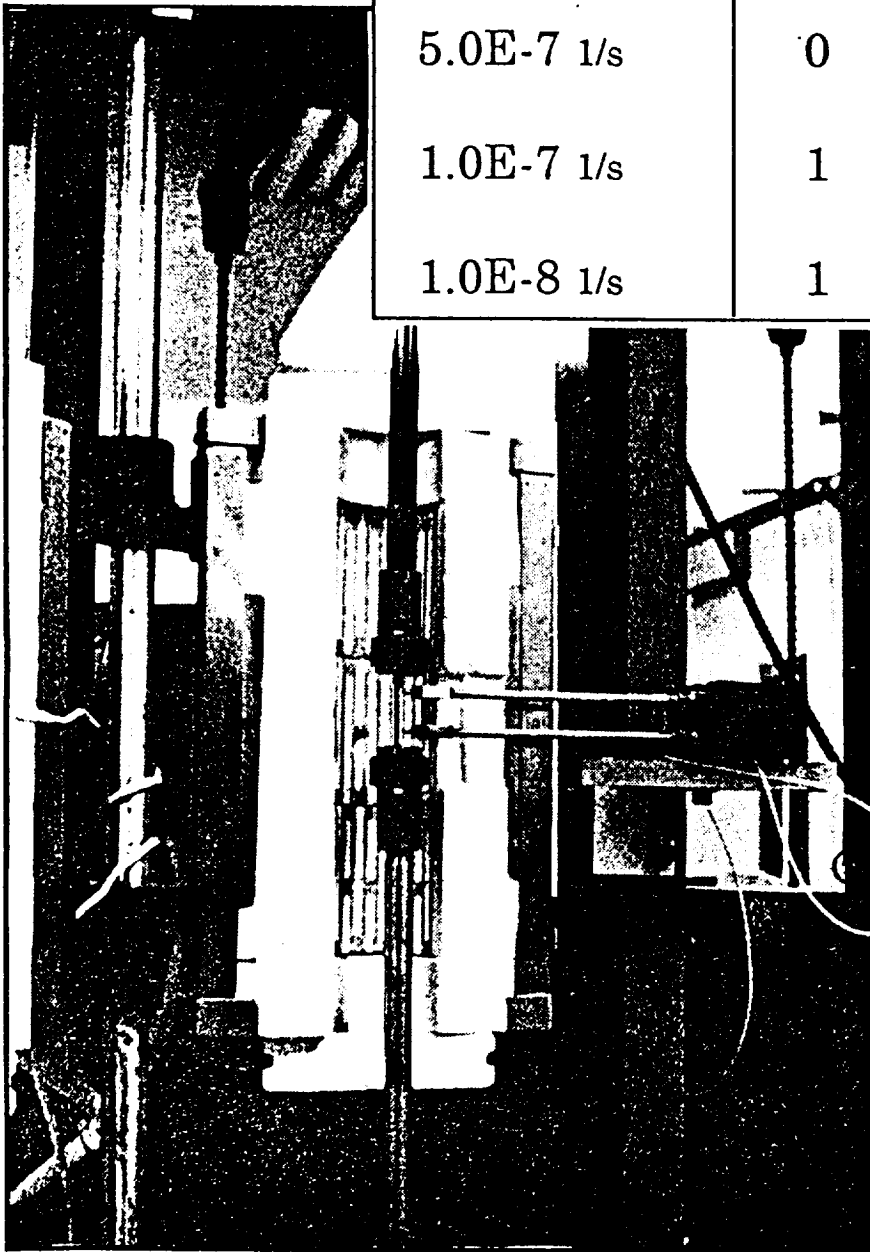


# Schematic of Compression Test Fixtures



# Creep Tests of 8009 Aluminum

Strain Rate	Temperature		
	347°F (175°C)	437°F (225°C)	527°F (275°C)
1.0E-6 1/s	1 Test	1	1
5.0E-7 1/s	0	1	1
1.0E-7 1/s	1	1	1
1.0E-8 1/s	1	0	0



# Parameter Determination

Conduct a series of tension or compression tests



Fit hardening data to a 9<sup>th</sup> order polynomial via non-linear least squares method

$$\sigma = a_0 + a_1 \epsilon_p + a_2 \epsilon_p^2 + a_3 \epsilon_p^3 + \dots$$



Obtain  $m_1$  and  $m_2$  from the slopes of the bilinear plot of  $\gamma$  vs.  $\sigma$  where

$$\gamma = \frac{1}{\sigma} \frac{d\sigma}{d\epsilon_p} = \frac{1}{\sigma} \{a_1 + 2a_2 \epsilon_p + 3a_3 \epsilon_p^2 + \dots\}$$



Set  $D_0 = 1 \times 10^4$



Make initial guess for  $n$



Calculate  $Z_0$ ,  $Z_1$ ,  $Z_2$ , and  $Z_3$  from the yield stress, the saturation stress,  $n$ , and  $\epsilon_p$



Conduct a series of creep tests to develop the recovery parameters  $A$  and  $r$

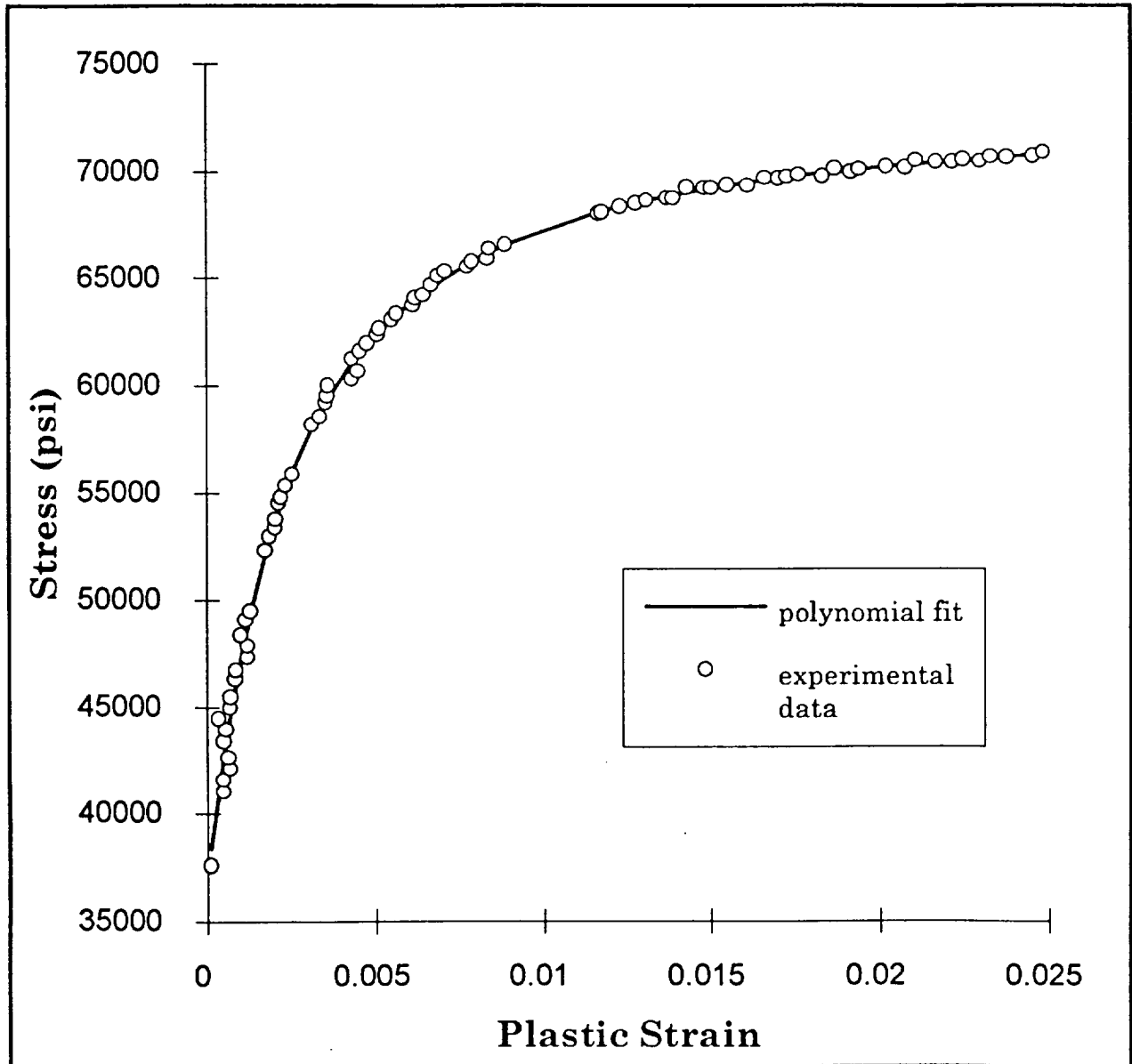


Obtain  $r$  from a plot of  $q$  vs  $\sigma_c - \sigma_0$  and calculate  $A$



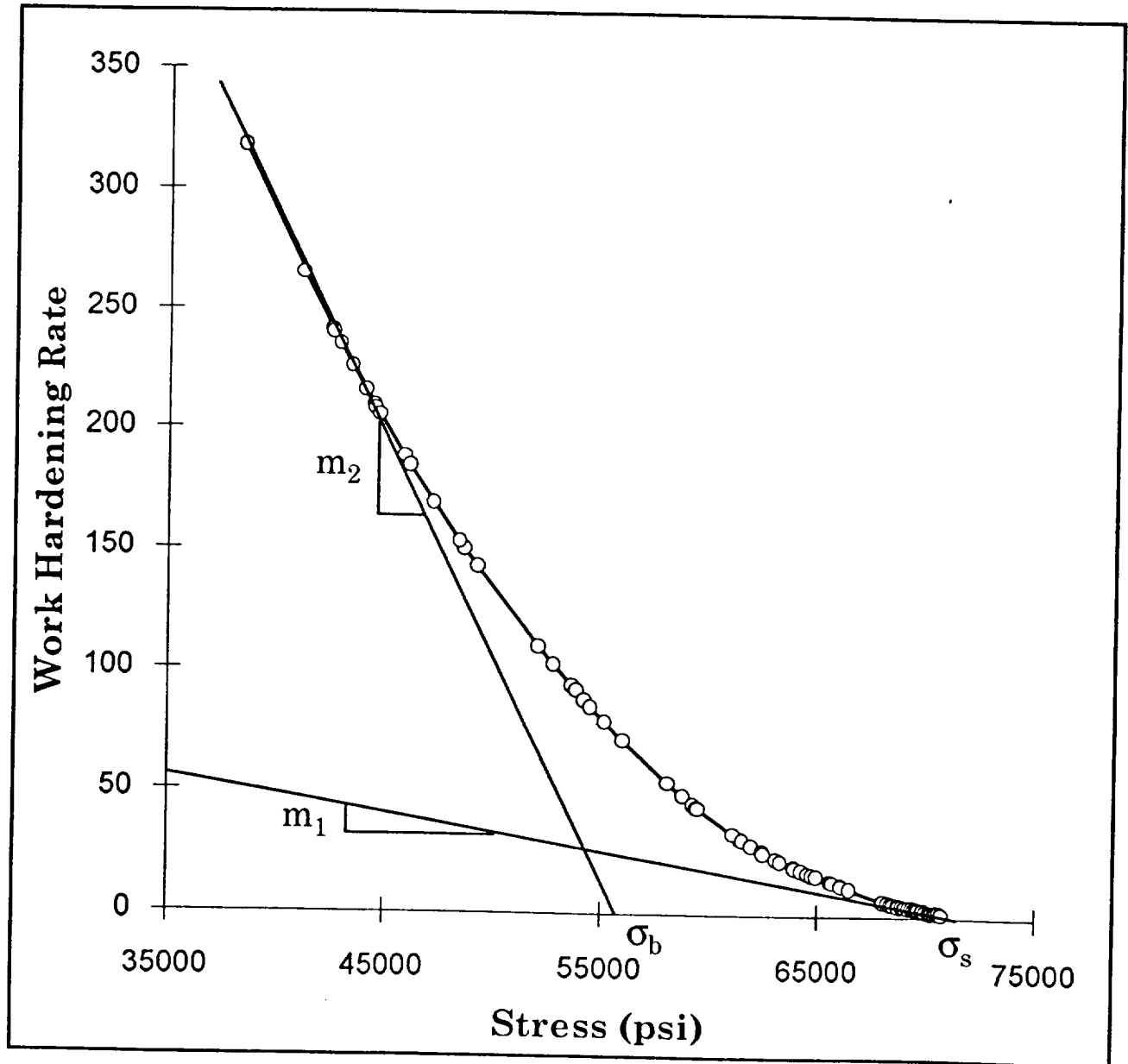
Curve fit for  $n$  and  $Z_0$

# Polynomial Fit of Experimental Test Data



$$\sigma = a_0 + a_1 \epsilon_p + a_2 \epsilon_p^2 + a_3 \epsilon_p^3 + \dots + a_9 \epsilon_p^9$$

# Plot of Hardening Rate, $\gamma$ vs. Stress, $\sigma$



$$\gamma = \frac{1}{\sigma} \frac{d\sigma}{d\epsilon_p} = \frac{1}{\sigma} \{a_1 + 2a_2\epsilon_p + 3a_3\epsilon_p^2 + \dots + 9a_9\epsilon_p^8\}$$



# Results

## Temperature-Independent Parameters

$D_0$	Assumed Value
$m_1$ $m_2$	From Work Hardening Data Obtained in Tension Tests
$Z_1$ $Z_3$	From Calculations based on Hardening Data and value of n

## Temperature-Dependent Parameters

E	From published Results
n	Initially 1.0, curve fitted for a 'best fit' over the range of strain rates and temperatures
$Z_0$ $Z_2$	From yield stress and initial value for n
A (A=A1=A2) r (r=r1=r2)	From Steady State Creep Data

# Material Parameters for Hastelloy-X

## Temperature Independent Parameters

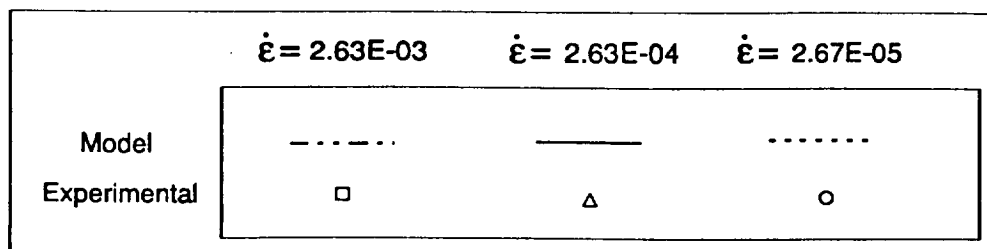
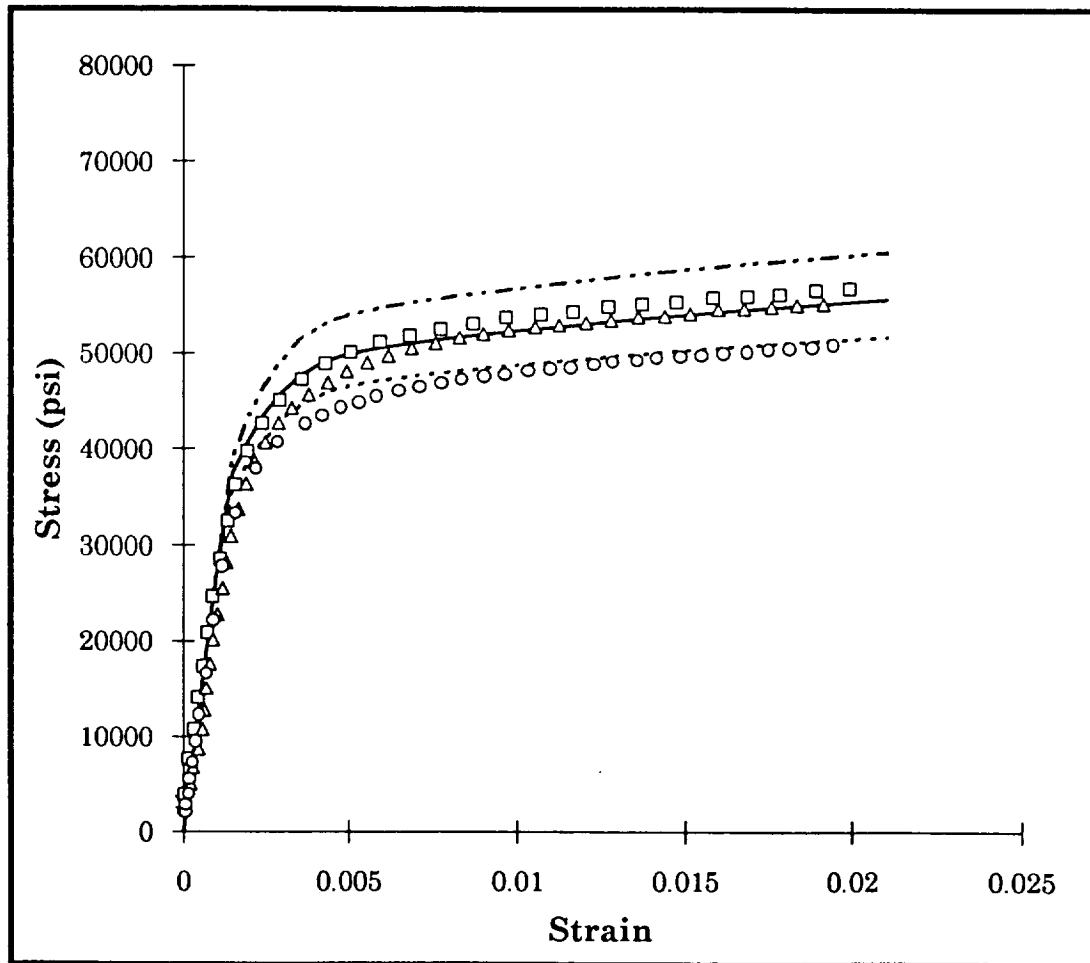
Parameter	Value
$D_0$ (sec <sup>-1</sup> )	1.00E4
$Z_1$ (psi)	3.46E5
$Z_3$ (psi)	8.75E4
$m_1$ (psi <sup>-1</sup> )	9.58E-4
$m_2$ (psi <sup>-1</sup> )	2.41E-2

## Temperature Dependent Parameters

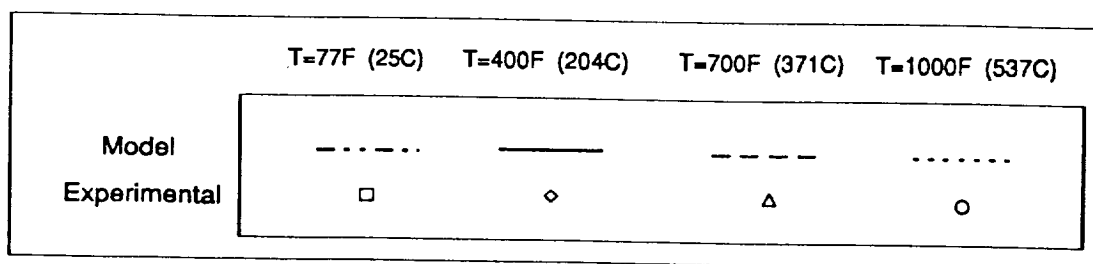
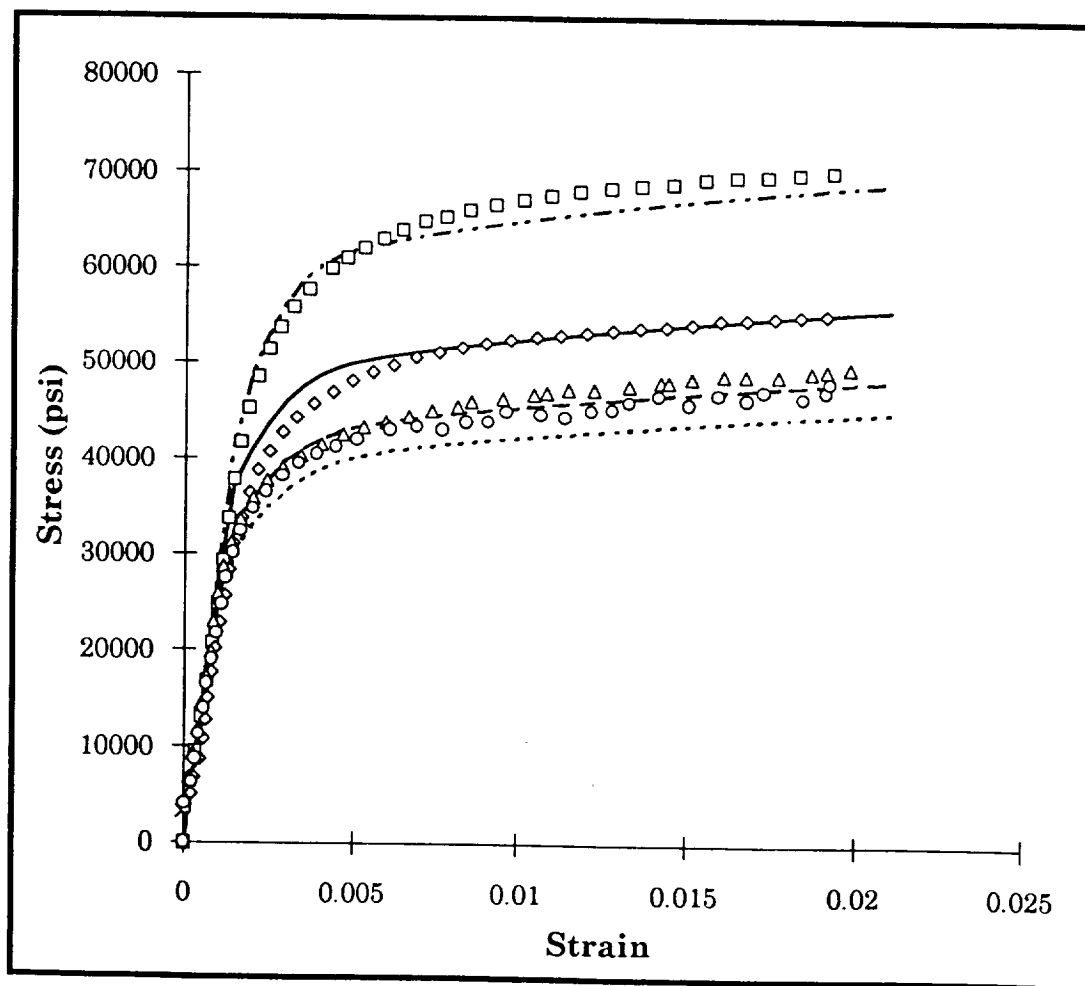
### Temperature

Parameters	77°F (25°C)	400°F (204°C)	700°F (371°C)	1000°F (538°C)
$E$ (psi)	28.5E6	27.1E6	25.3E6	23.4E6
$n$	1.000	0.901	0.847	0.824
$Z_0$ (psi)	2.70E5	2.65E5	2.60E5	2.55E5
$Z_2$ (psi)	2.70E5	2.65E5	2.60E5	2.55E5
$A$ (sec <sup>-1</sup> )	0.00	0.00	0.00	0.00
$r$	2	2	2	2

# Comparison of Model Predictions vs. Experimental Data for Hastelloy-X at T=400°F (204°C)



# Comparison of Model Predictions vs. Experimental Data for Hastelloy-X at constant Strain Rate = $2.625\text{E-}4$ 1/s



# Material Parameters for Aluminum Alloy 8009

## Temperature Independent Parameters

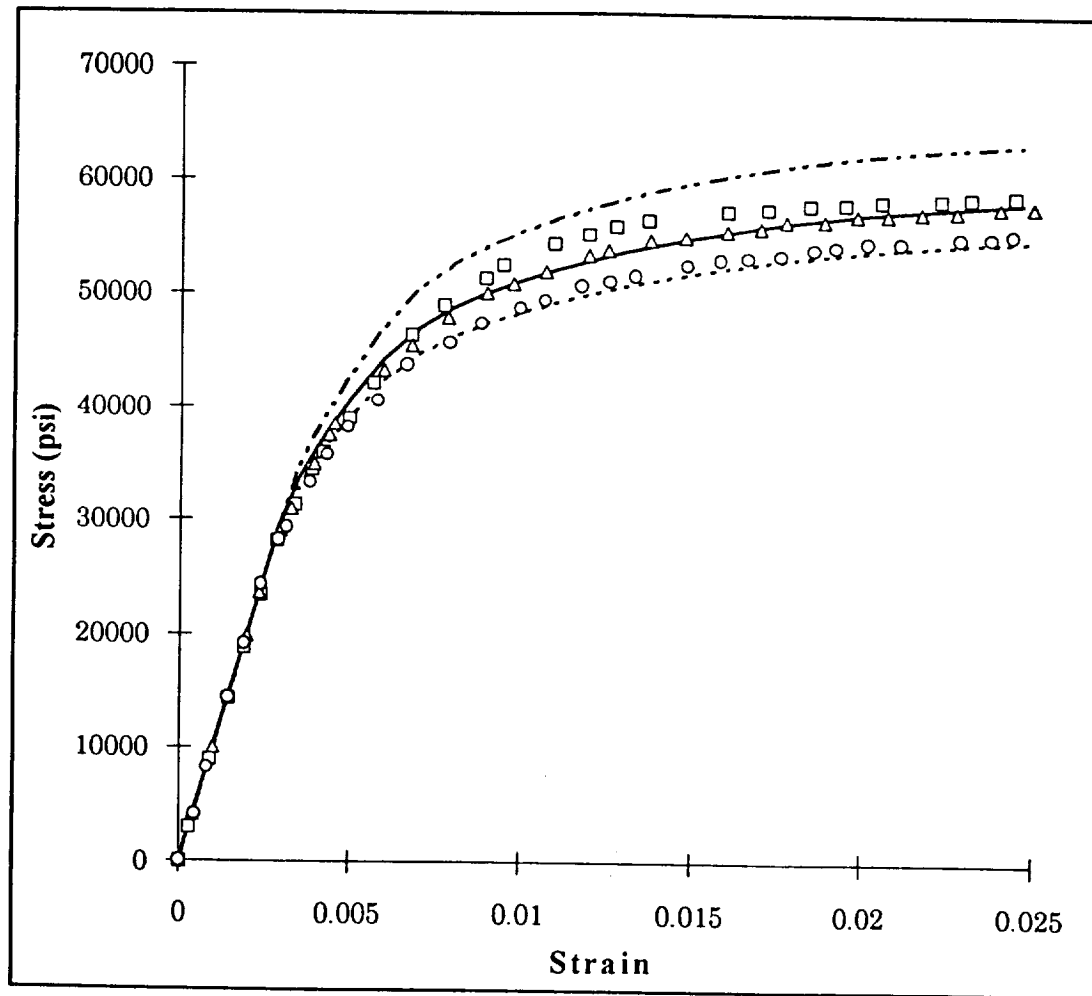
Parameter	Value
$D_0$ (sec <sup>-1</sup> )	1.00E4
$Z_1$ (psi)	3.42E5
$Z_3$ (psi)	9.07E4
$m_1$ (psi <sup>-1</sup> )	2.59E-3
$m_2$ (psi <sup>-1</sup> )	2.62E-2

## Temperature Dependent Parameters

### Temperature

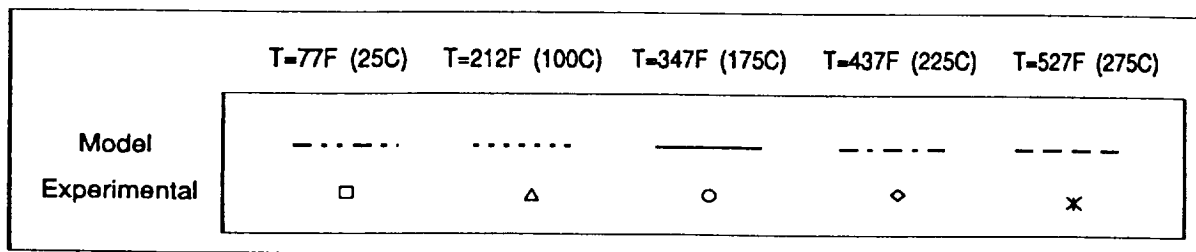
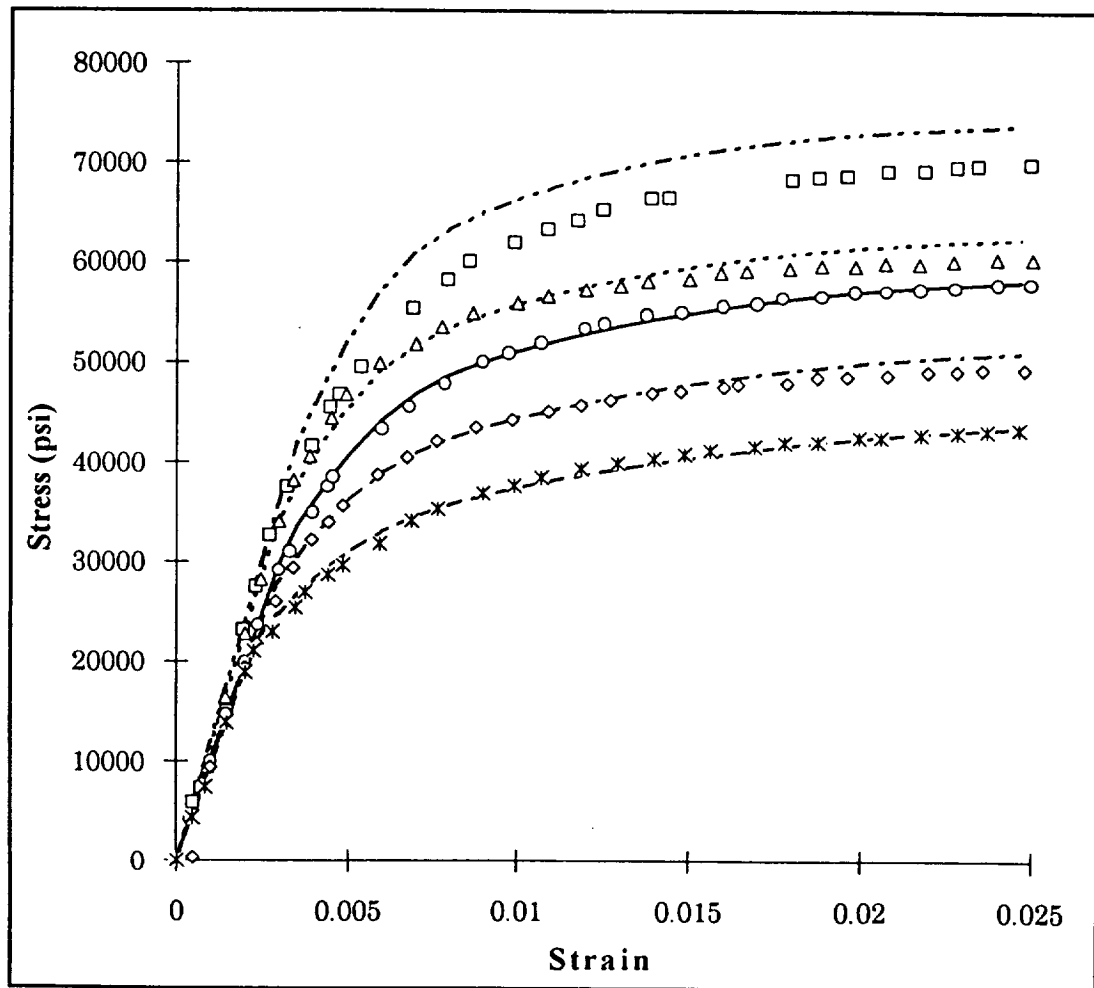
Parameters	77°F (25°C)	212°F (100°C)	347°F (175°C)	437°F (225°C)	527°F (275°C)
E (psi)	12.1E6	11.5E6	10.0E6	9.79E6	9.50E6
n	1.000	0.915	0.885	0.834	0.780
Z0 (psi)	2.50E5	2.45E5	2.40E5	2.30E5	2.20E5
Z2 (psi)	2.50E5	2.45E5	2.40E5	2.30E5	2.20E5
A (sec <sup>-1</sup> )	0.00	0.00	1.30E-3	1.13E-2	2.81E-1
r	2	2	2	2	2

# Comparison of Model Predictions vs. Experimental Data for 8009 Al. at T=347°F (175°C)



	$\dot{\epsilon} = 5.33E-03$	$\dot{\epsilon} = 5.33E-04$	$\dot{\epsilon} = 8.89E-05$
Model	-----	————	.....
Experimental	□	Δ	○

# Comparison of Model Predictions vs. Experimental Data for 8009 Al. at constant Strain Rate = $5.33\text{E-}4$



# Concluding Remarks

- A procedure has been outlined for the development of model parameters for the Bodner-Partom viscoplastic theory
- Model Parameters were obtained for both Hastelloy-X and 8009 aluminum using this procedure
- Model predictions were in good agreement with experimental results
- The Bodner-Partom viscoplastic model and the parameters for Hastelloy-X will be used with a finite element model for predicting the inelastic buckling of plates
- The Bodner-Partom theory can be used to characterize other materials. The procedure outlined in this thesis can be used to obtain model parameters for these materials



# **Experimental Study of Plate Buckling**

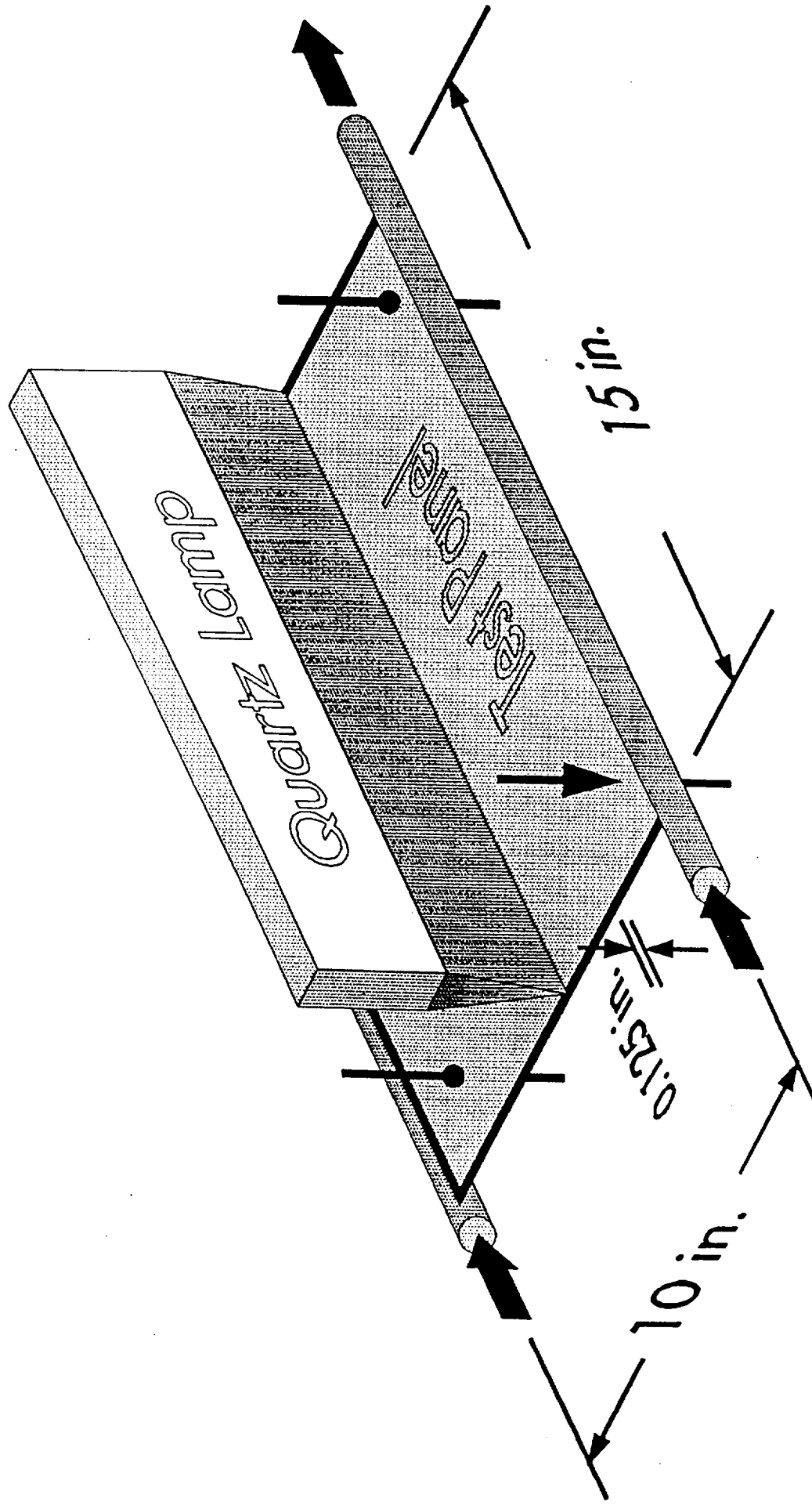
## **Objectives**

- Investigate experimentally the nonlinear response of panels subjected to localized heating
- Provide data for validation of finite element thermoviscoplastic analyses

## **Scope**

- Description of experimental program
- Presentation of results

# Test Panel Configuration



# **Lamp Characterization Tests**

- First test series showed lamp power and incident flux varied linearly with Power
- Second test series established (X,Y) spatial variation of incident flux
- Third test series established (X,Y,Z) spatial variation of incident flux



# **Heat Lamp Performance**

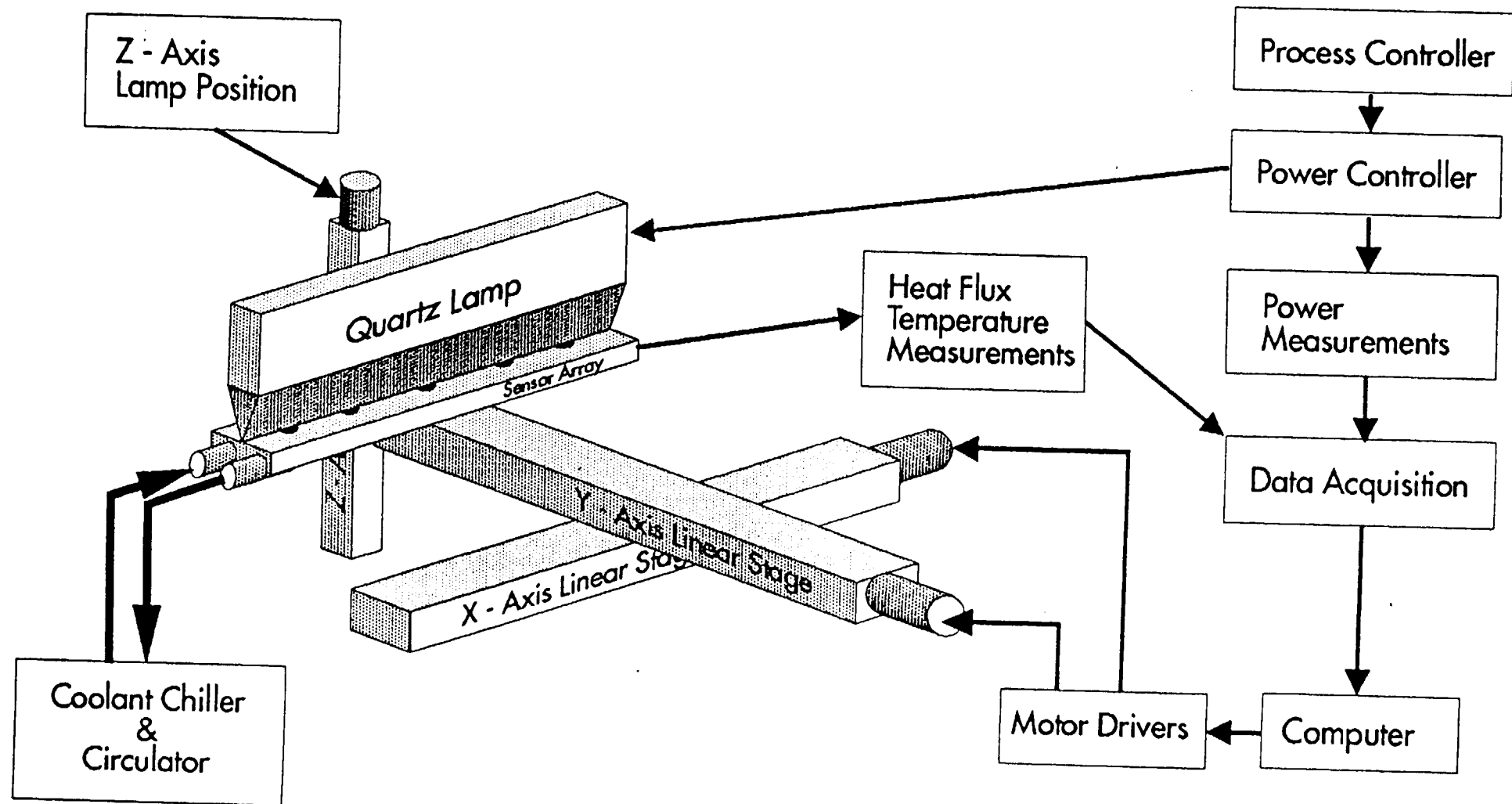
## **Commercial Lamps (Research, Inc.)**

- Tungsten filament quartz lamps
- Elliptical reflector concentrates incident flux on nominal width of 0.1 in.

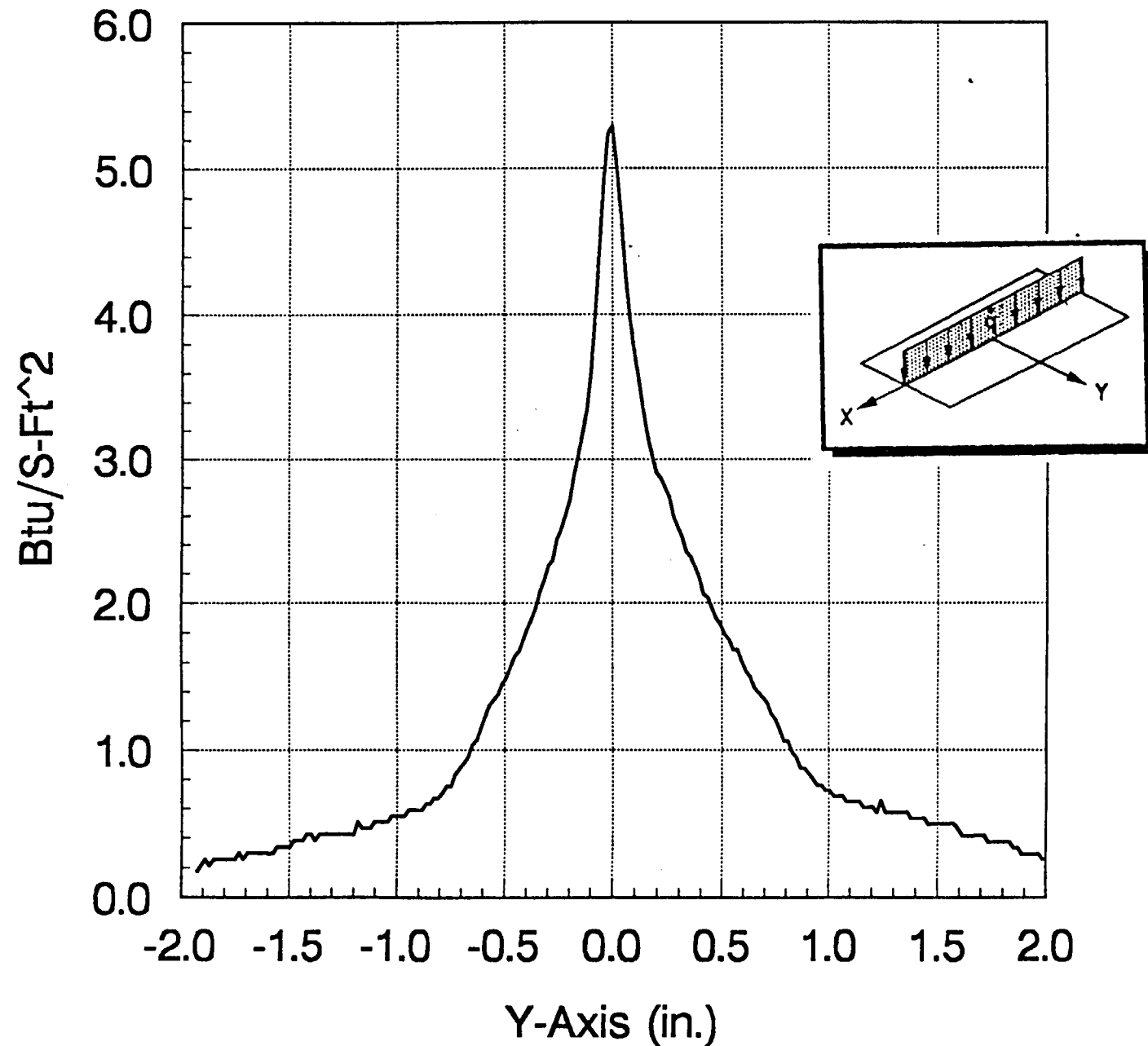
## **Orientation Tests**

- Significant heat flux levels outside of nominal width
- Variations along lamp length

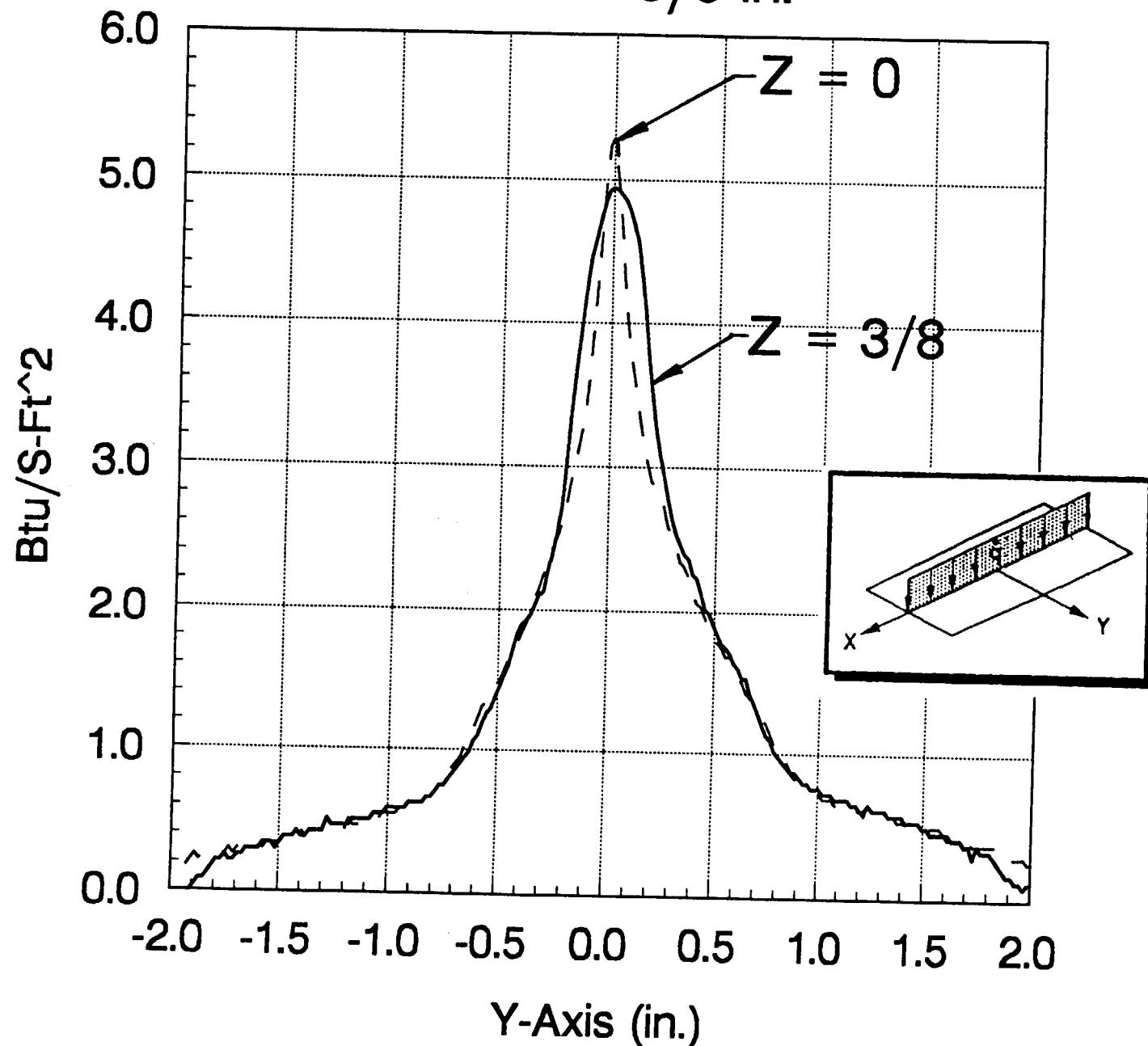
# Lamp Characterization Test Schematic



# Incident Heat Flux Distribution Along Y-Axis For $Z = 0$ in.

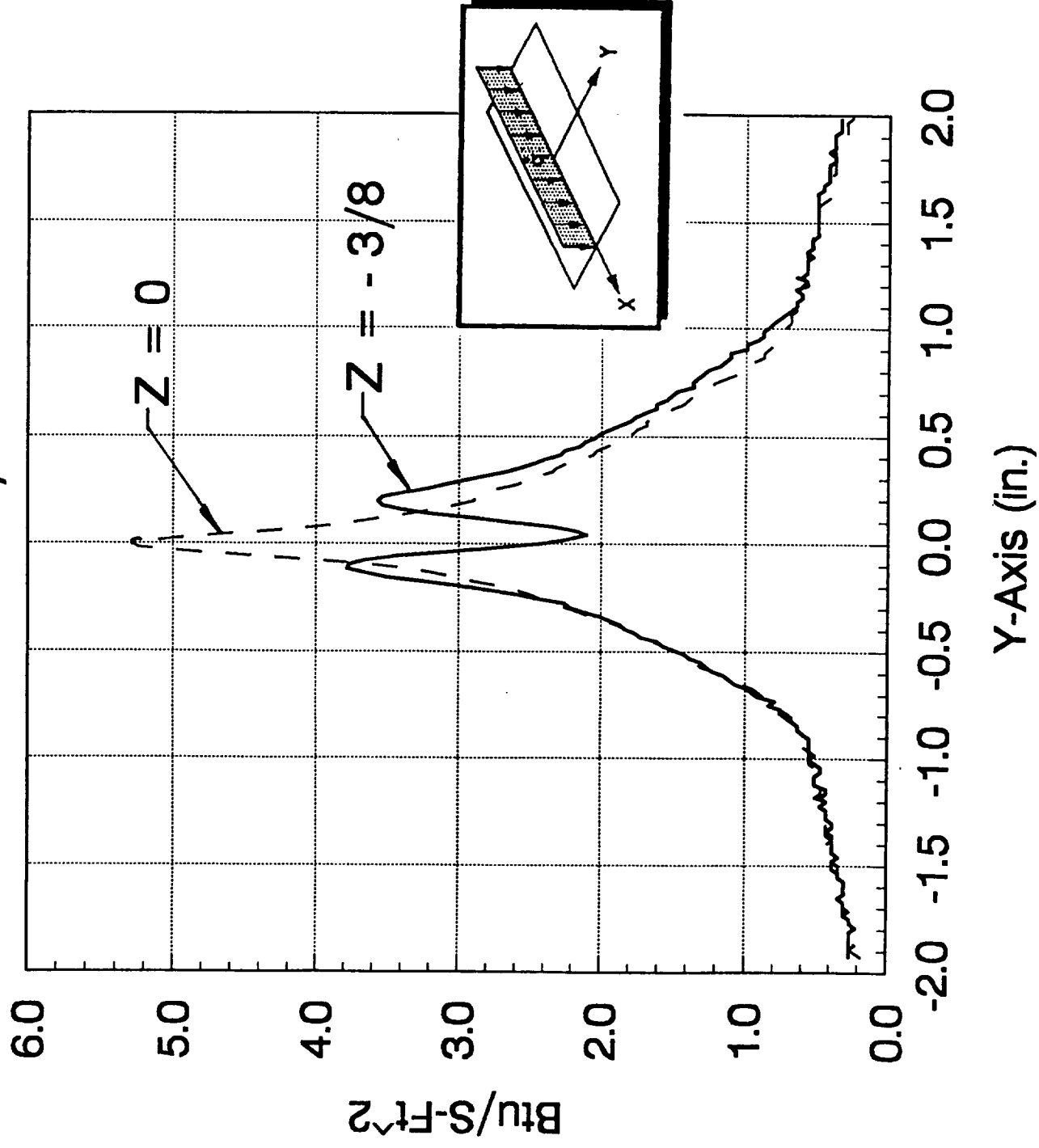


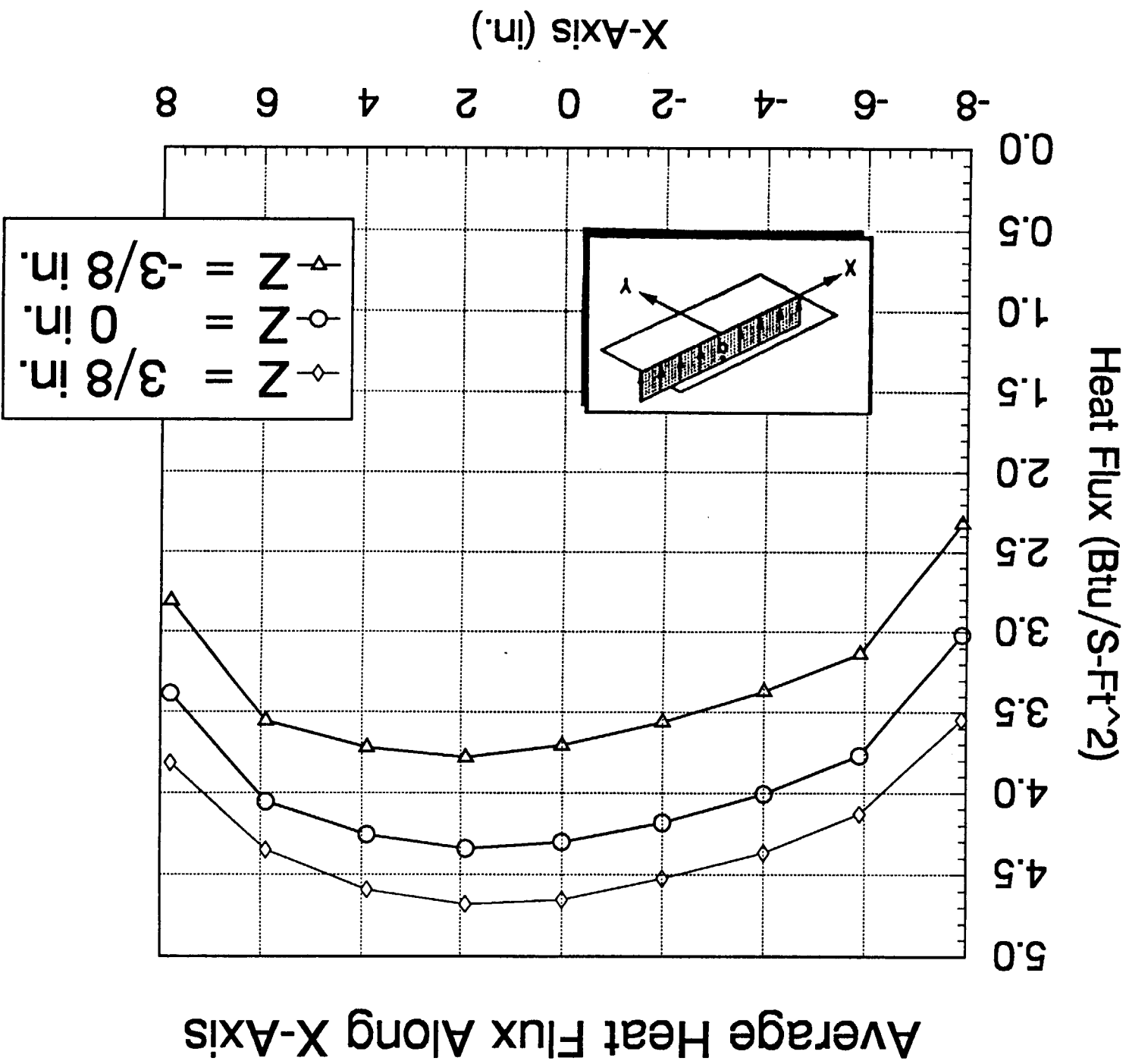
# Incident Heat Flux Distribution Along Y-Axis For $Z = 3/8$ in.



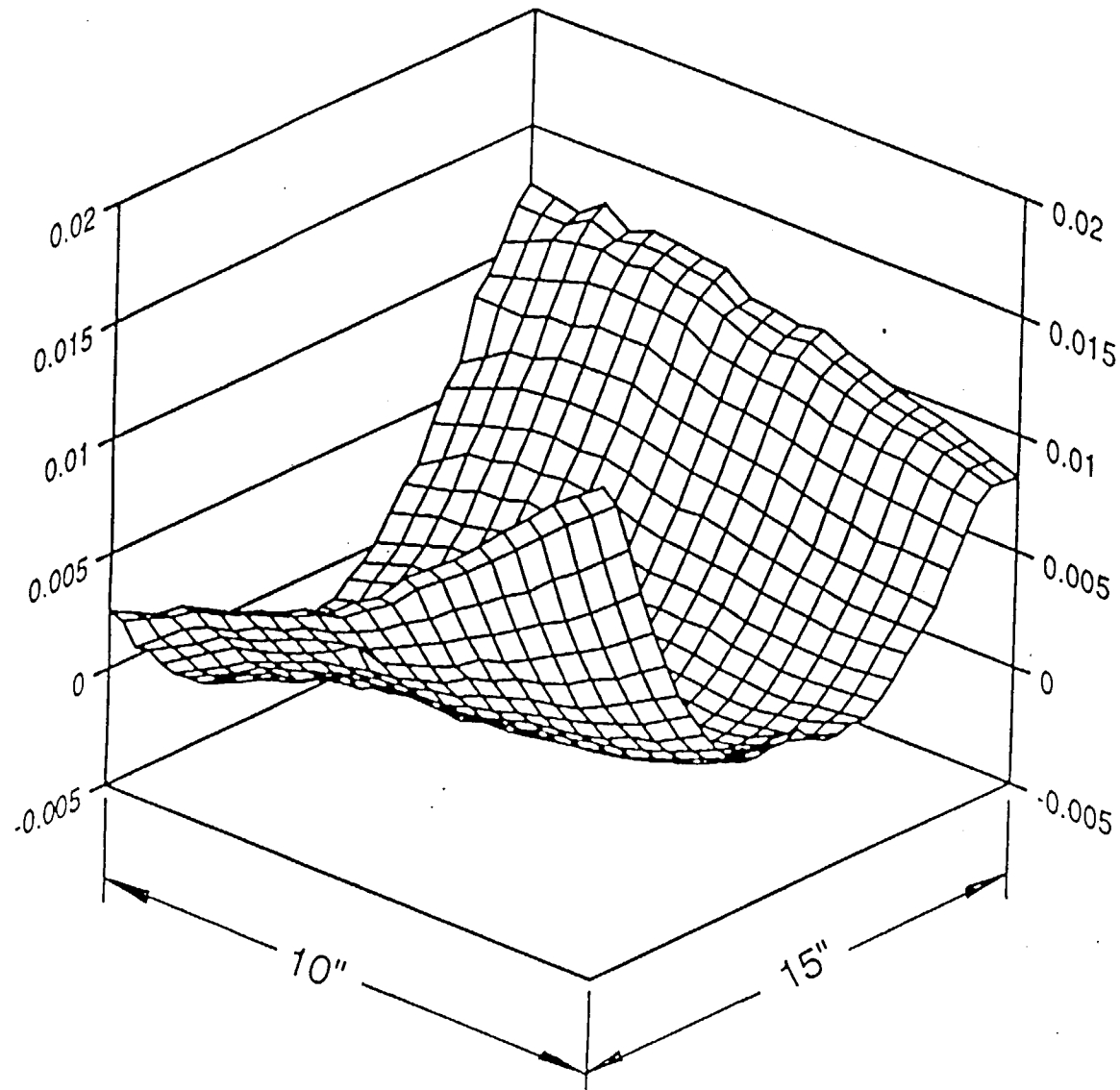


# Incident Heat Flux Distribution Along Y-Axis For $Z = -3/8$ in.



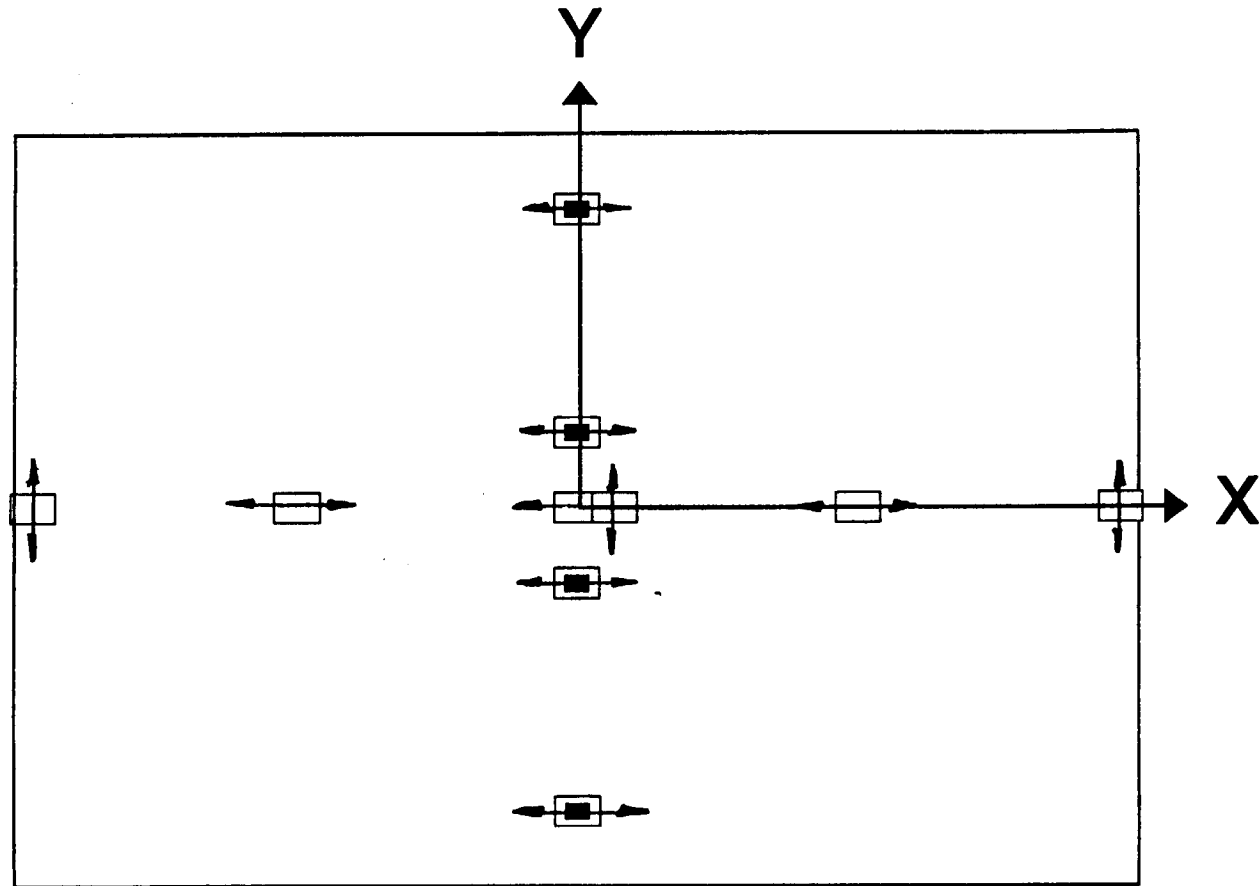


# Initial Transverse Deflection of Hastelloy-X Test



# STRAIN GAGE LOCATIONS

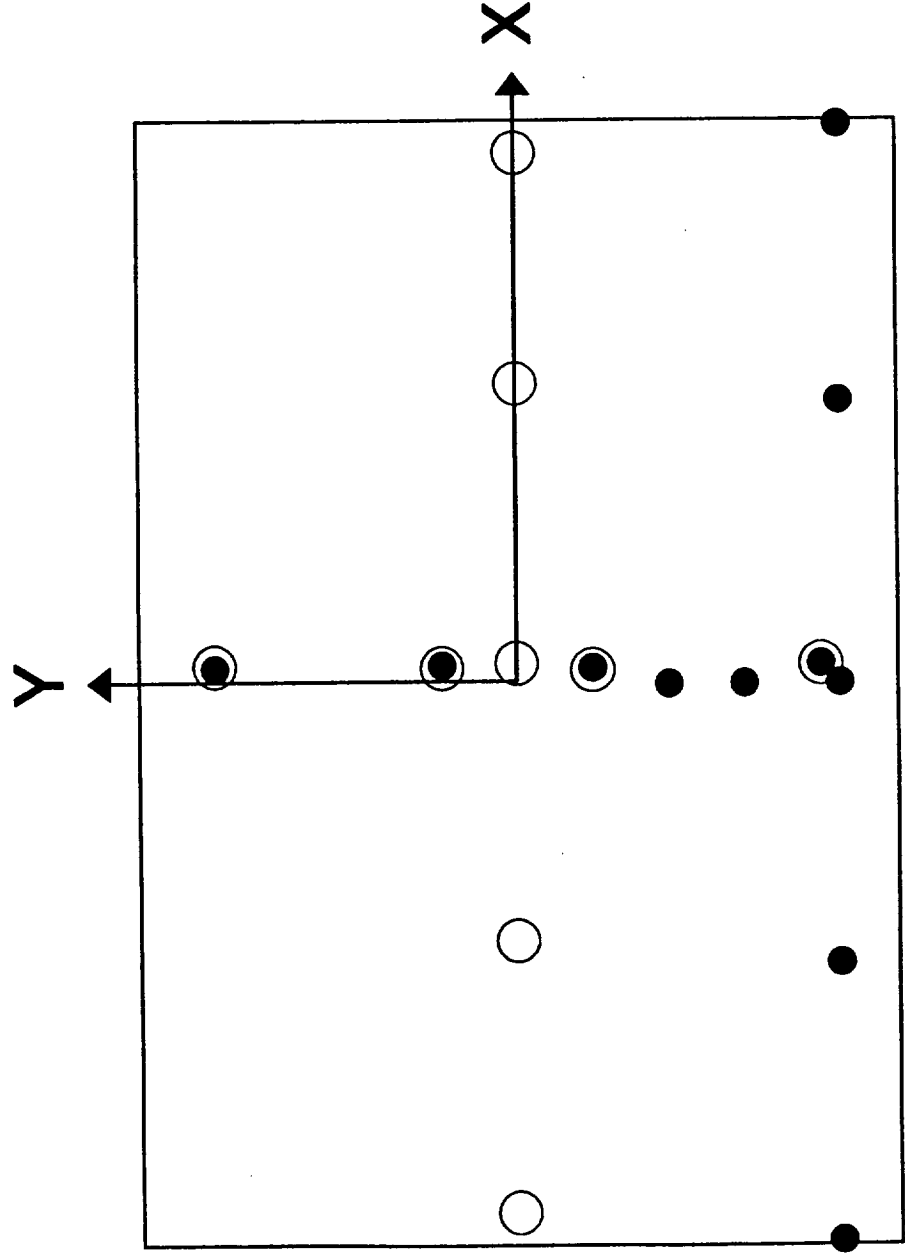
## 14 Strain Gages



□	BACK SIDE
■	HEATED SIDE

# THERMOCOUPLE LOCATIONS

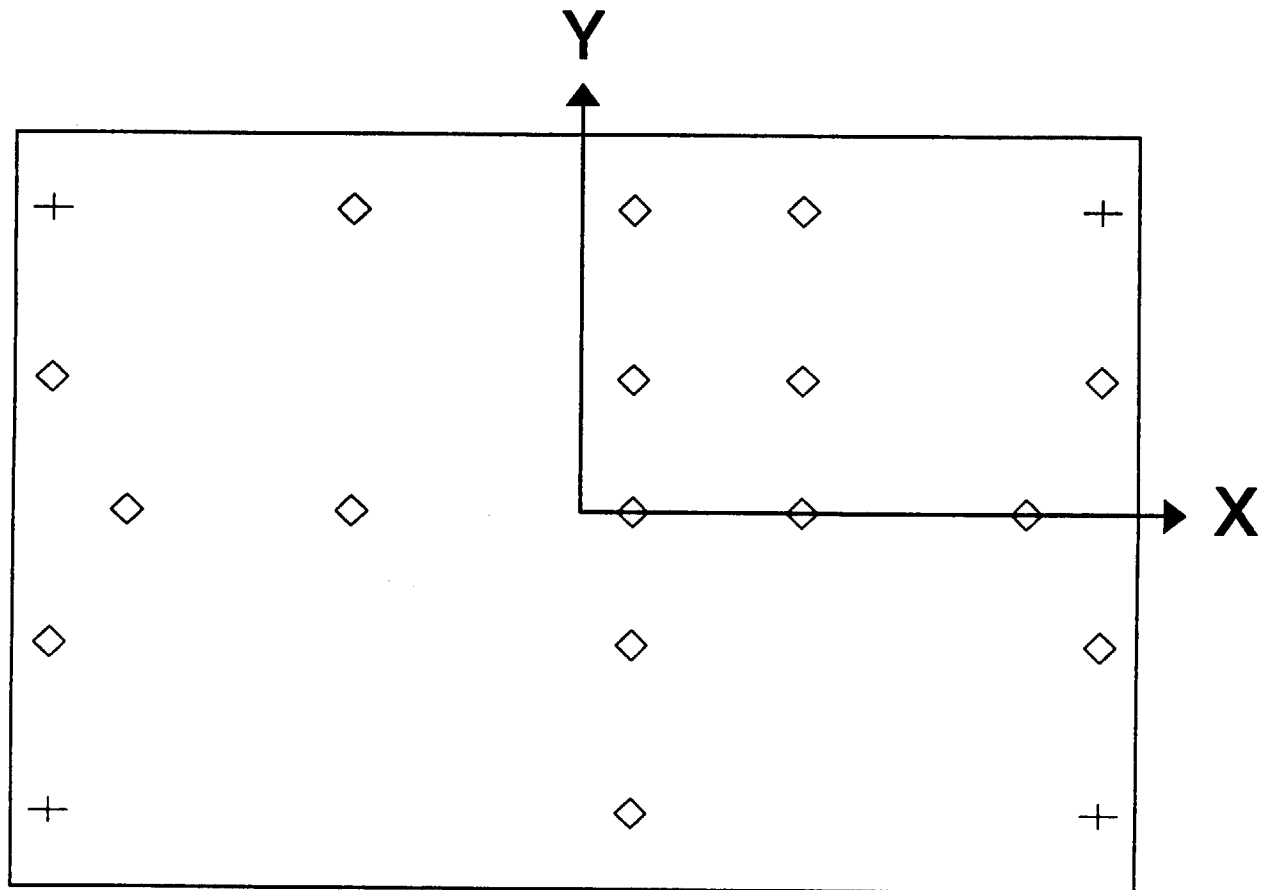
## 20 Thermocouples



○	BACK SIDE
●	HEATED SIDE

# LVDT LOCATIONS

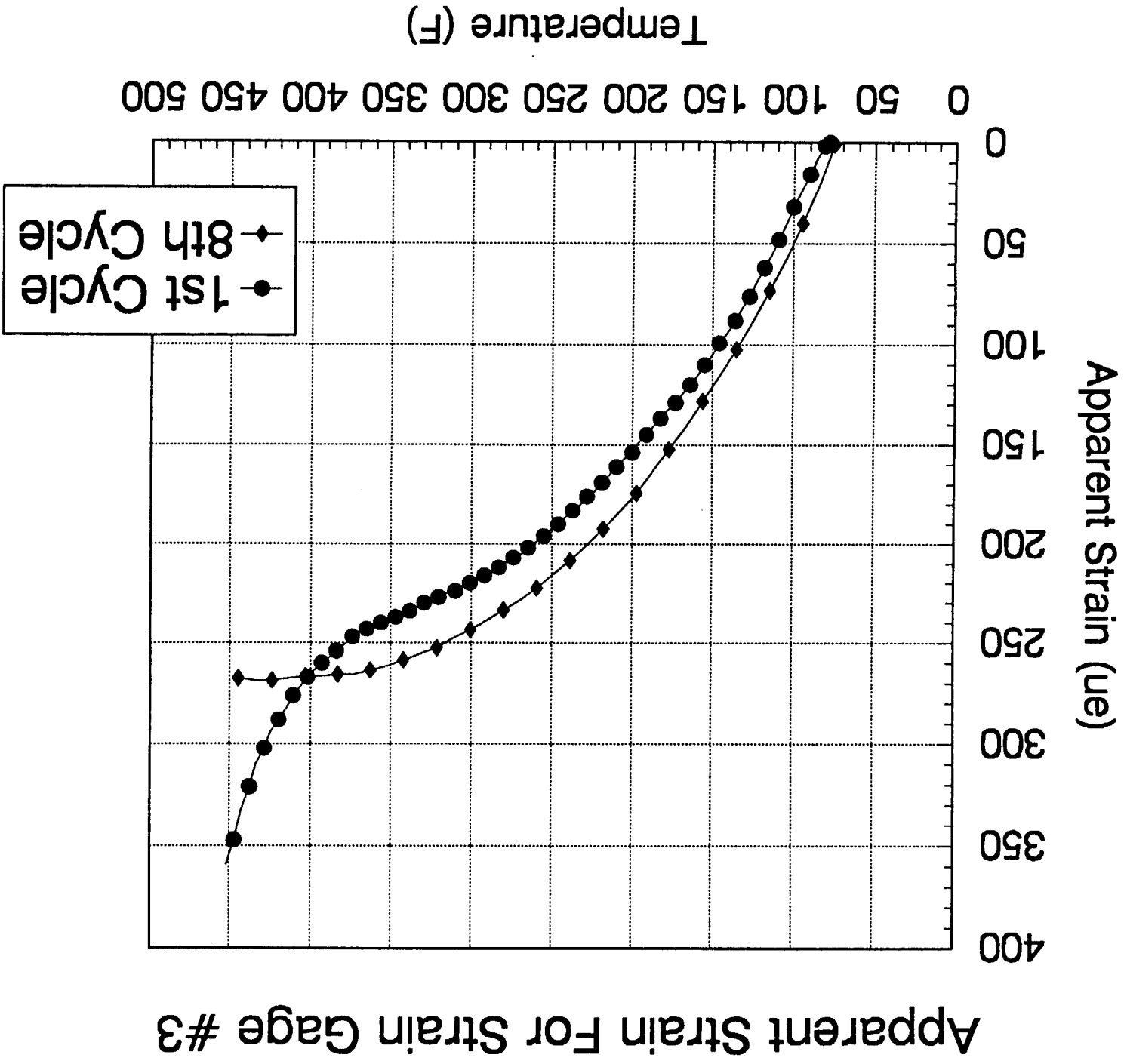
## 16 LVDT's



◇ LVDT (BACK SIDE)  
+ POINT SUPPORTS

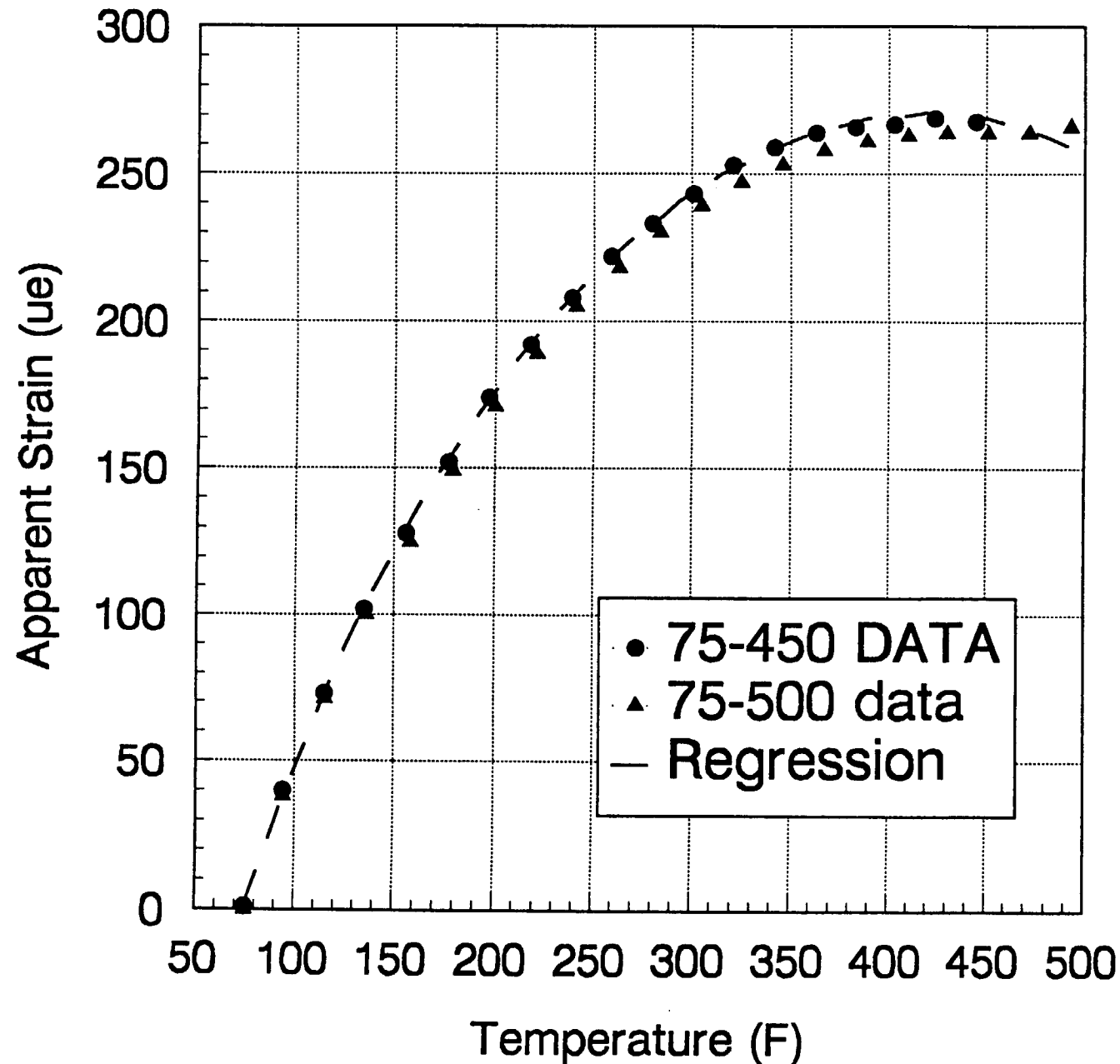
# **Apparent Strain Test Procedure**

- Instrumented panel was placed into an oven to control its temperature
- Oven was programmed to slowly ramp the panel's temperature from 75°F to 450°F in 9 hours
- A system 4000 data acquisition system was used to record strain gage and thermocouple outputs in 15 min. intervals
- Test panel required 8 thermal cycles to gain apparent strain versus temperature repeatability
- The apparent strain temperature data was used to develop regression curves for each strain gage

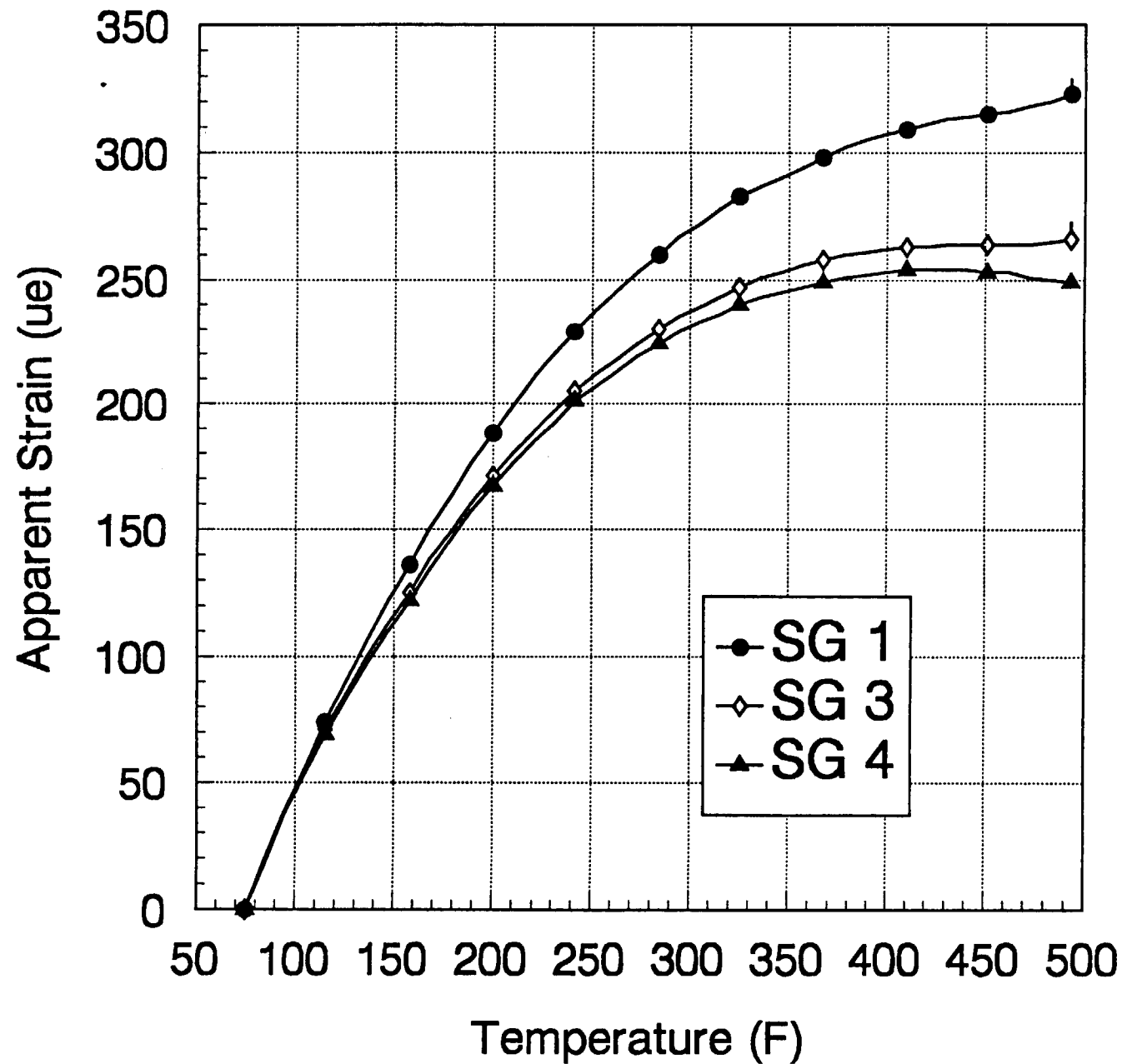




## APPARENT STRAIN FOR STRAIN GAGE #3

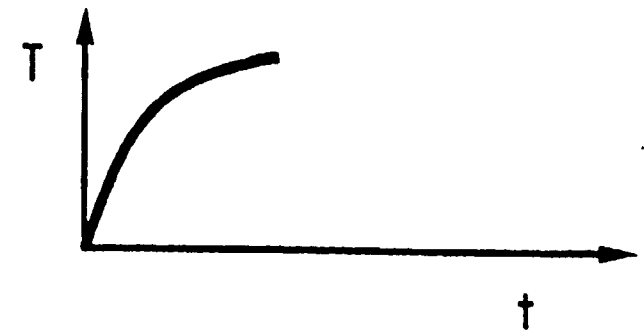
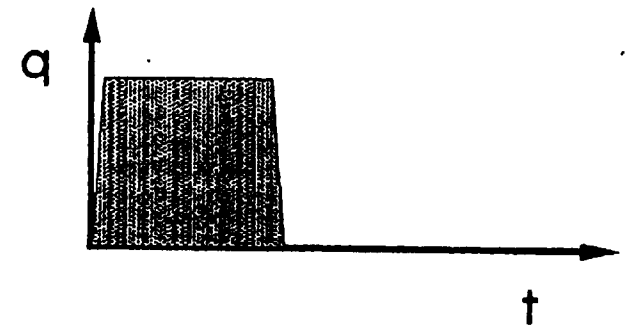


# APPARENT STRAIN



## Test Procedure

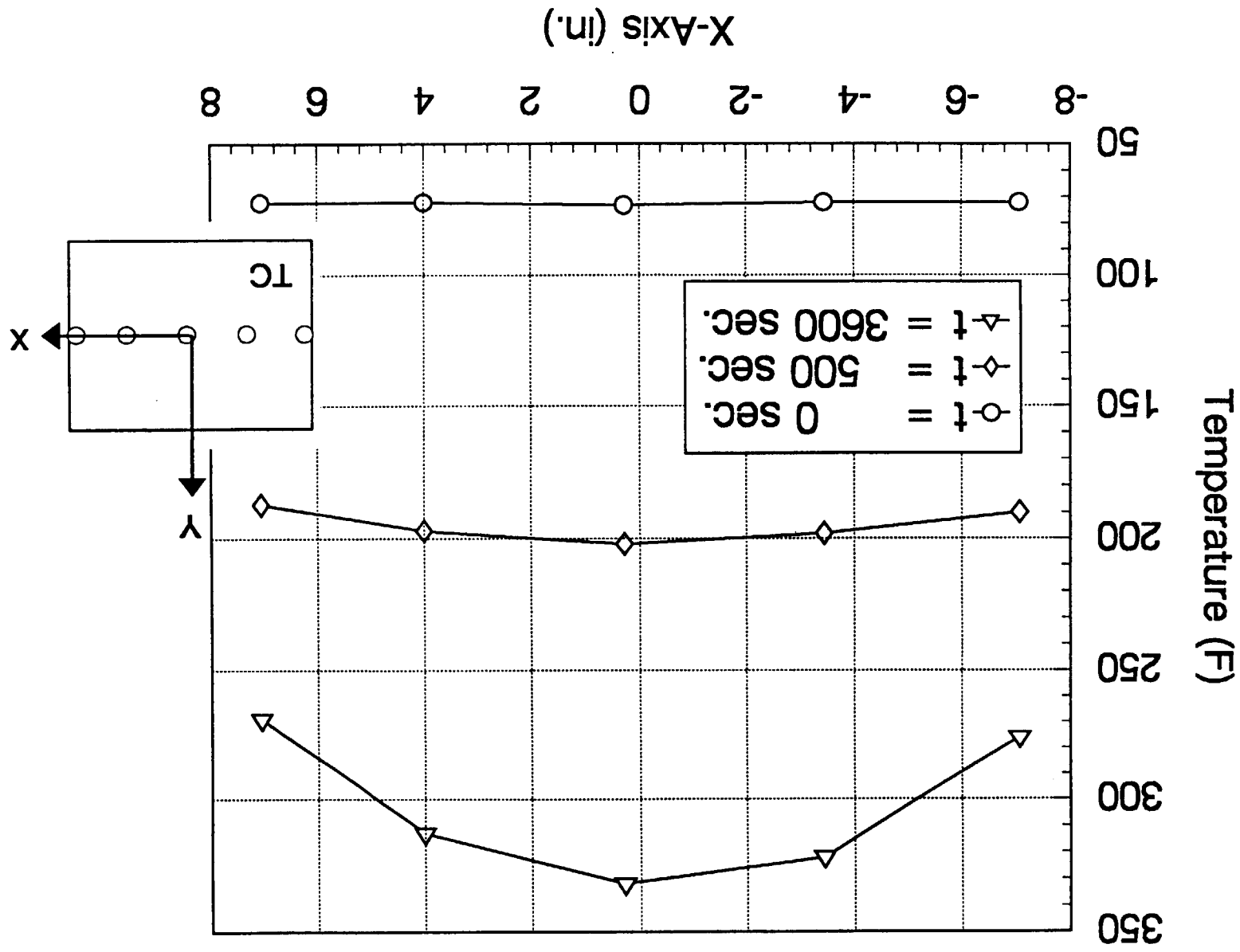
- Initialize panel temperatures with coolant flow for 30-60 minutes
- Conduct test with lamp at constant P % lamp output
- Shut off lamp when maximum desired panel temperature attained
- Record temperature and displacement data as panel temperatures return to steady state

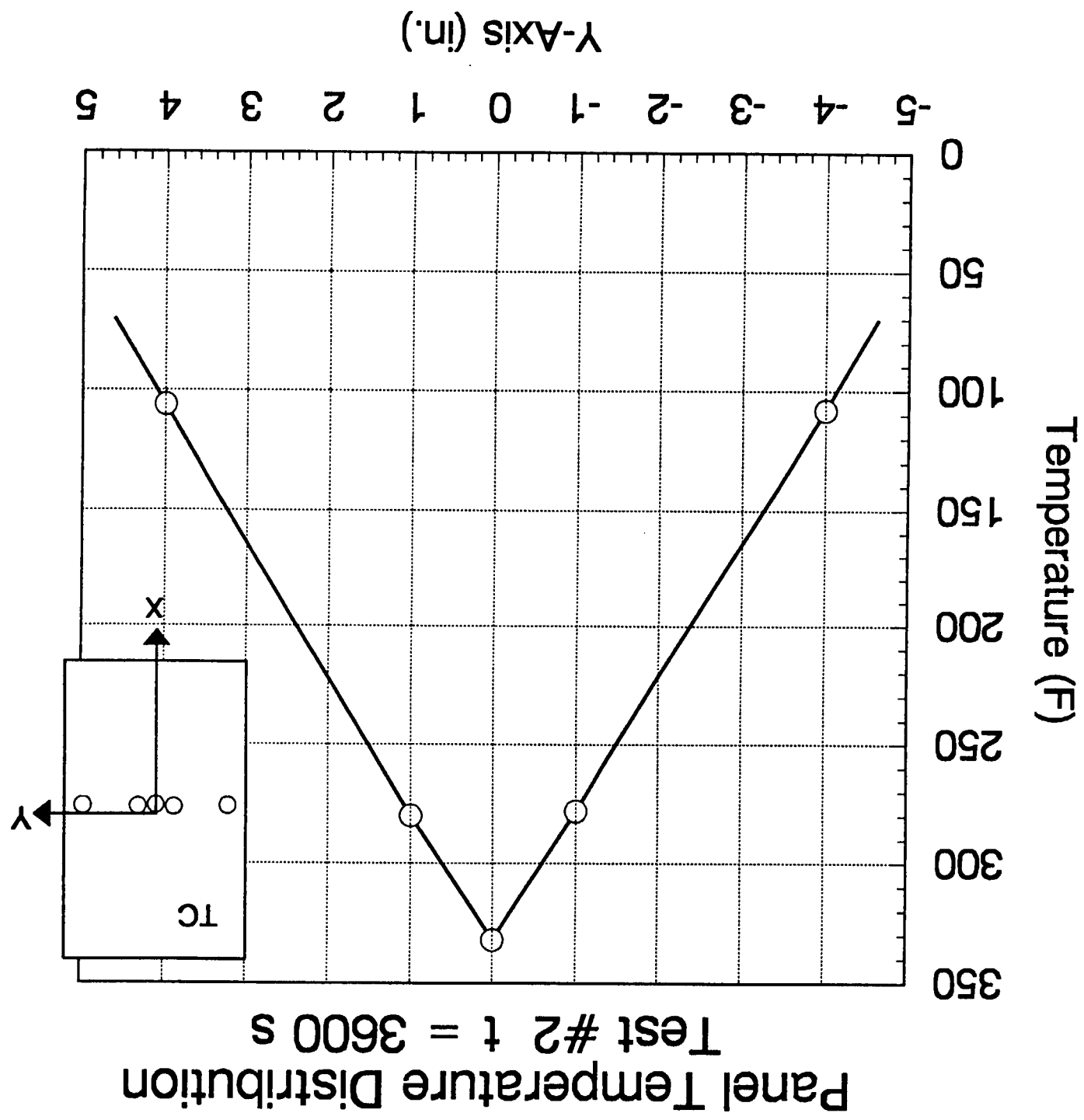


# Panel Buckling Tests

Test	P (%)	Max. Temp (°F)	Behavior
1	5	299	Elastic
2	5	332	Elastic
3	15	379	Elastic
4	15	502	Plastic
5	30	708	Plastic
6	70	732	Plastic

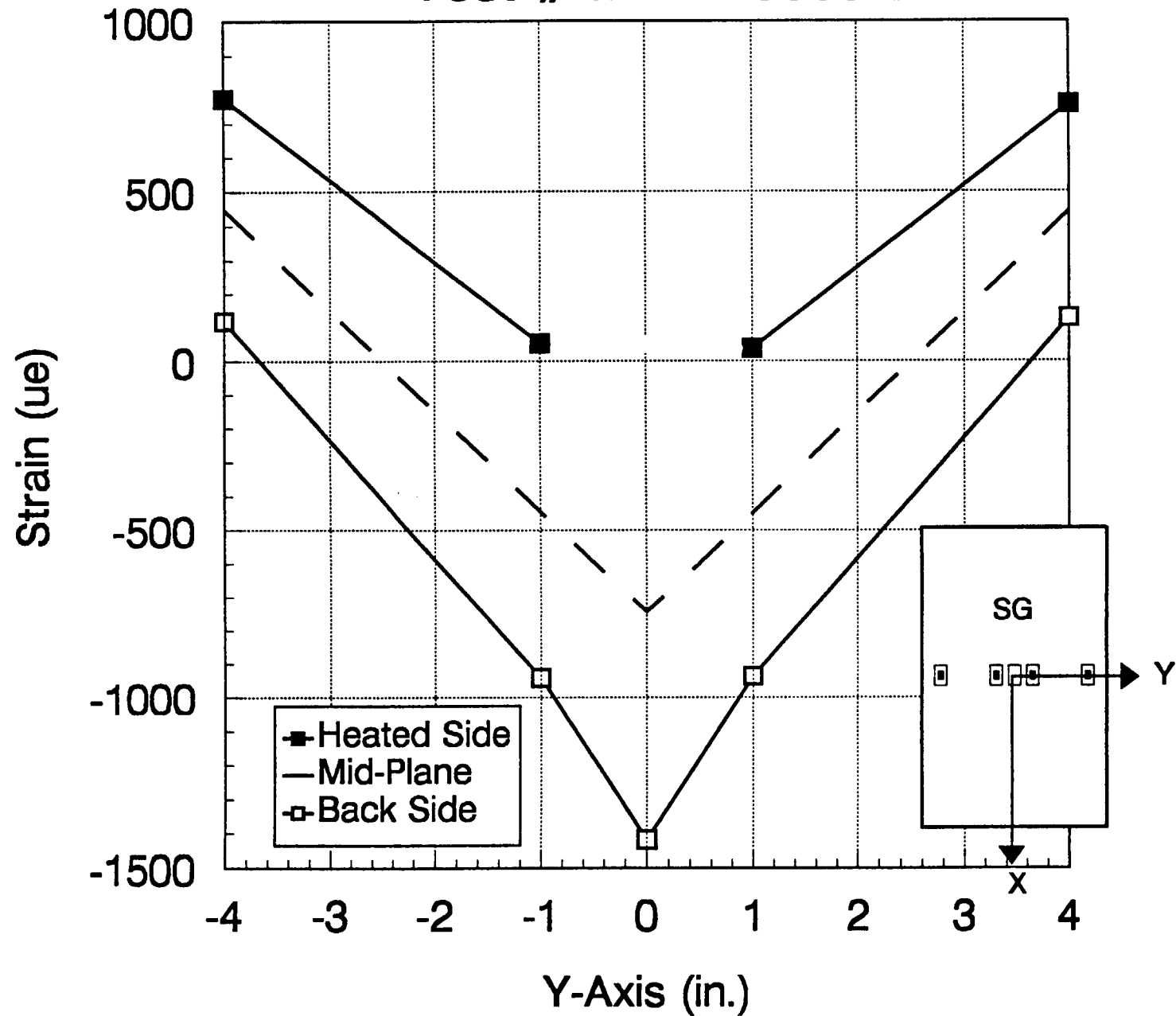
# Temperature Distribution Along X-Axis Test #2



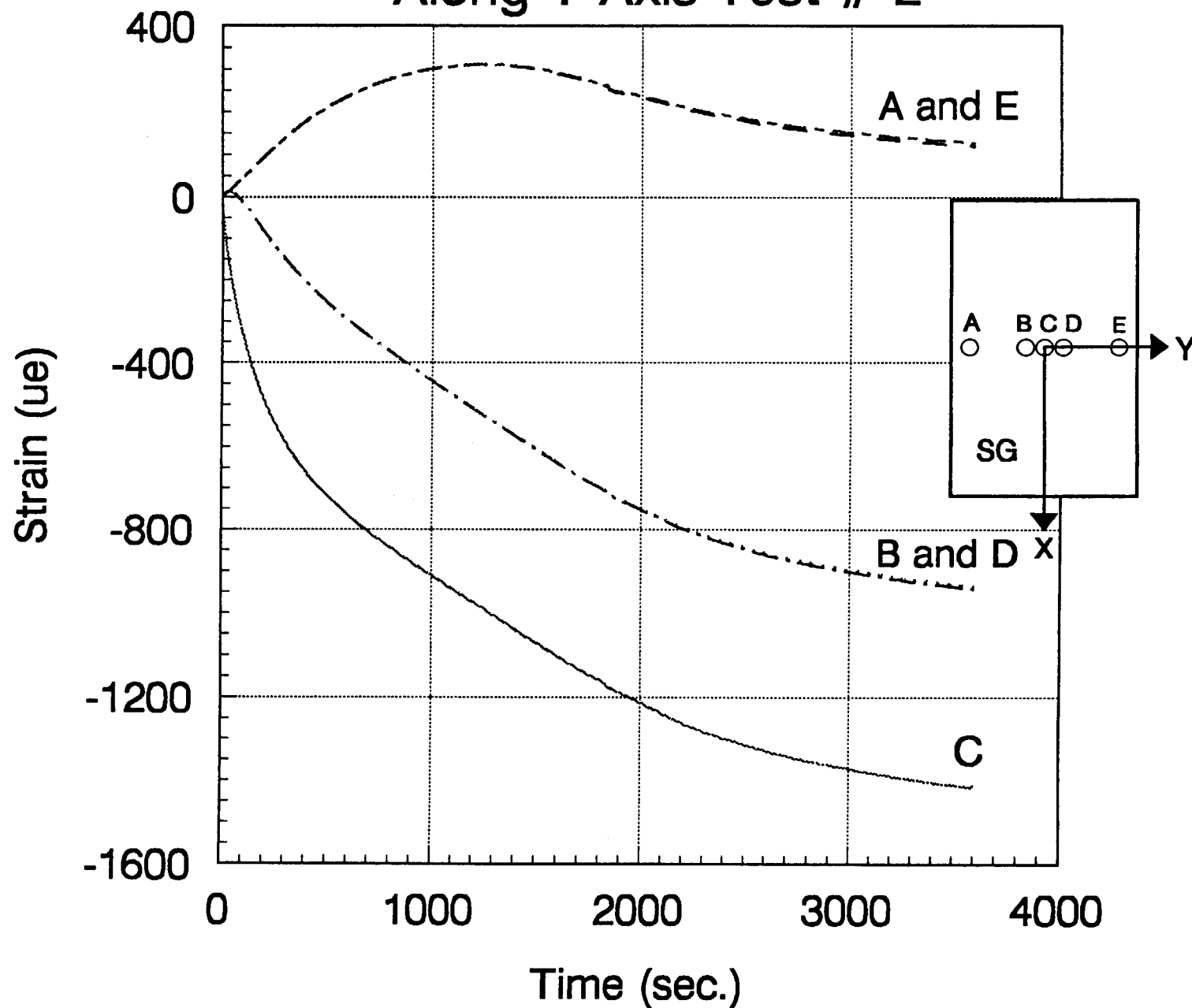


# Panel Strain Distribution

Test # 2  $t = 3600$  s

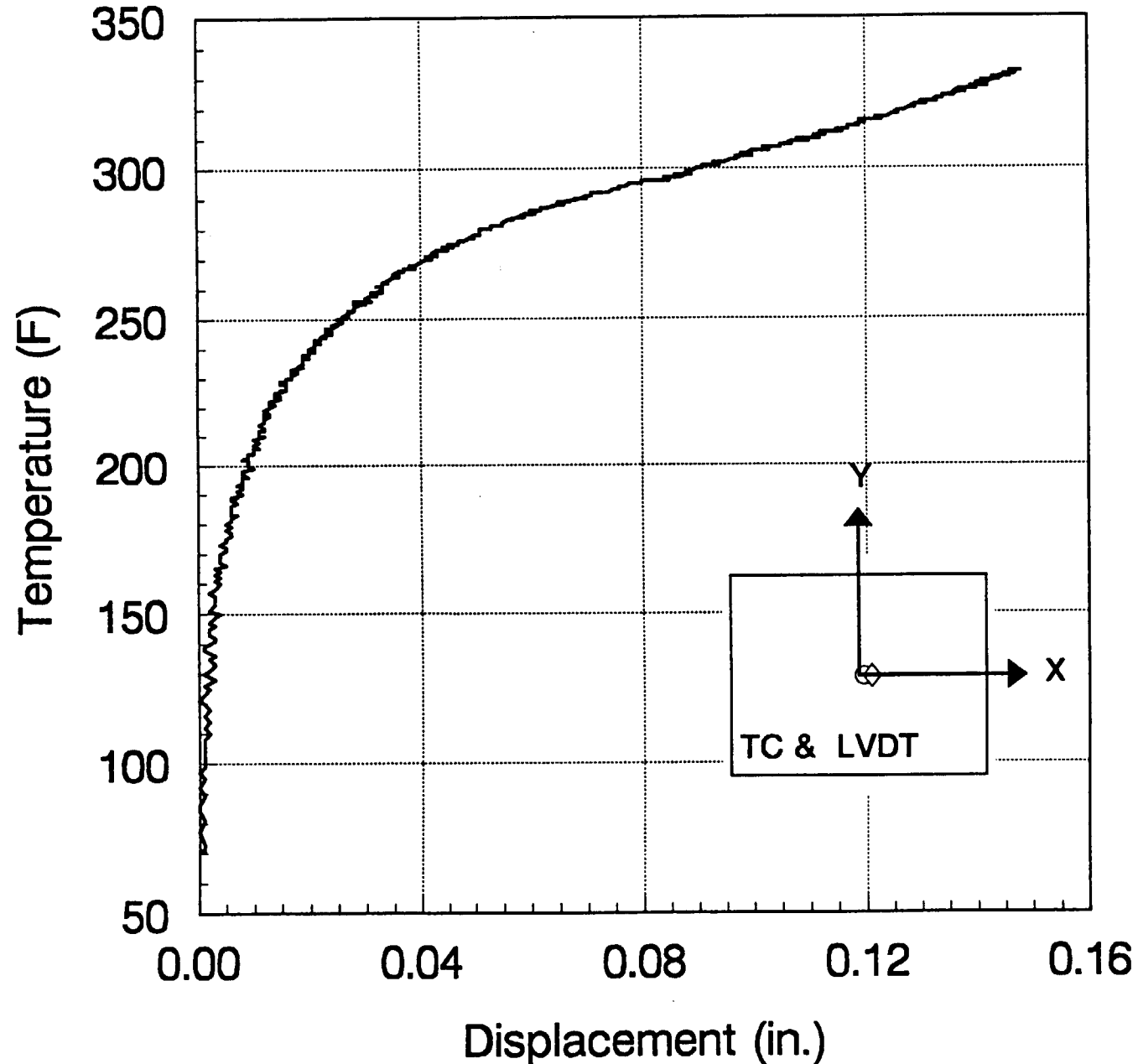


# Panel Strain versus Time Along Y-Axis Test # 2





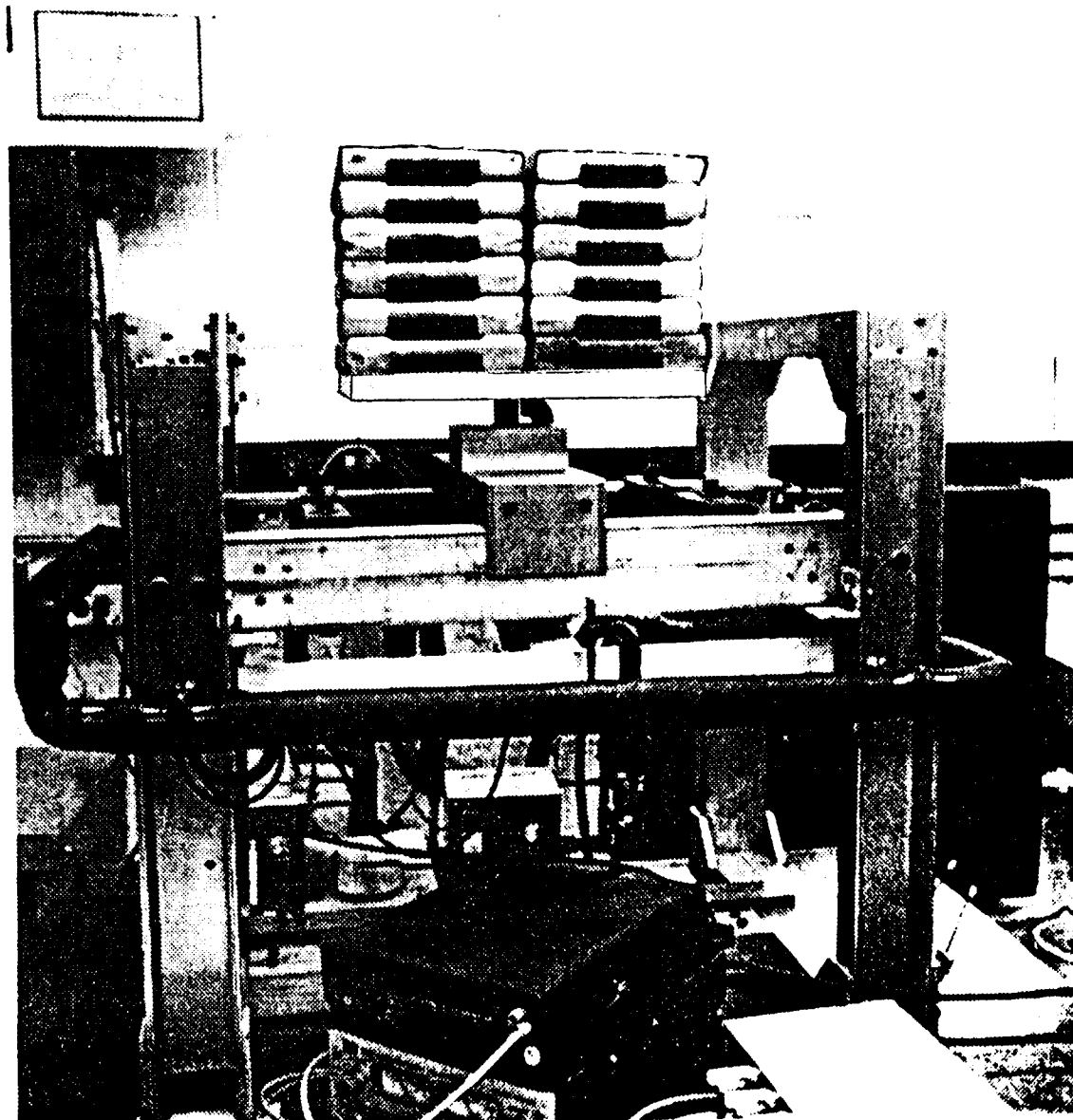
## Panel Temperature versus Displacement Response at the Center Test #2



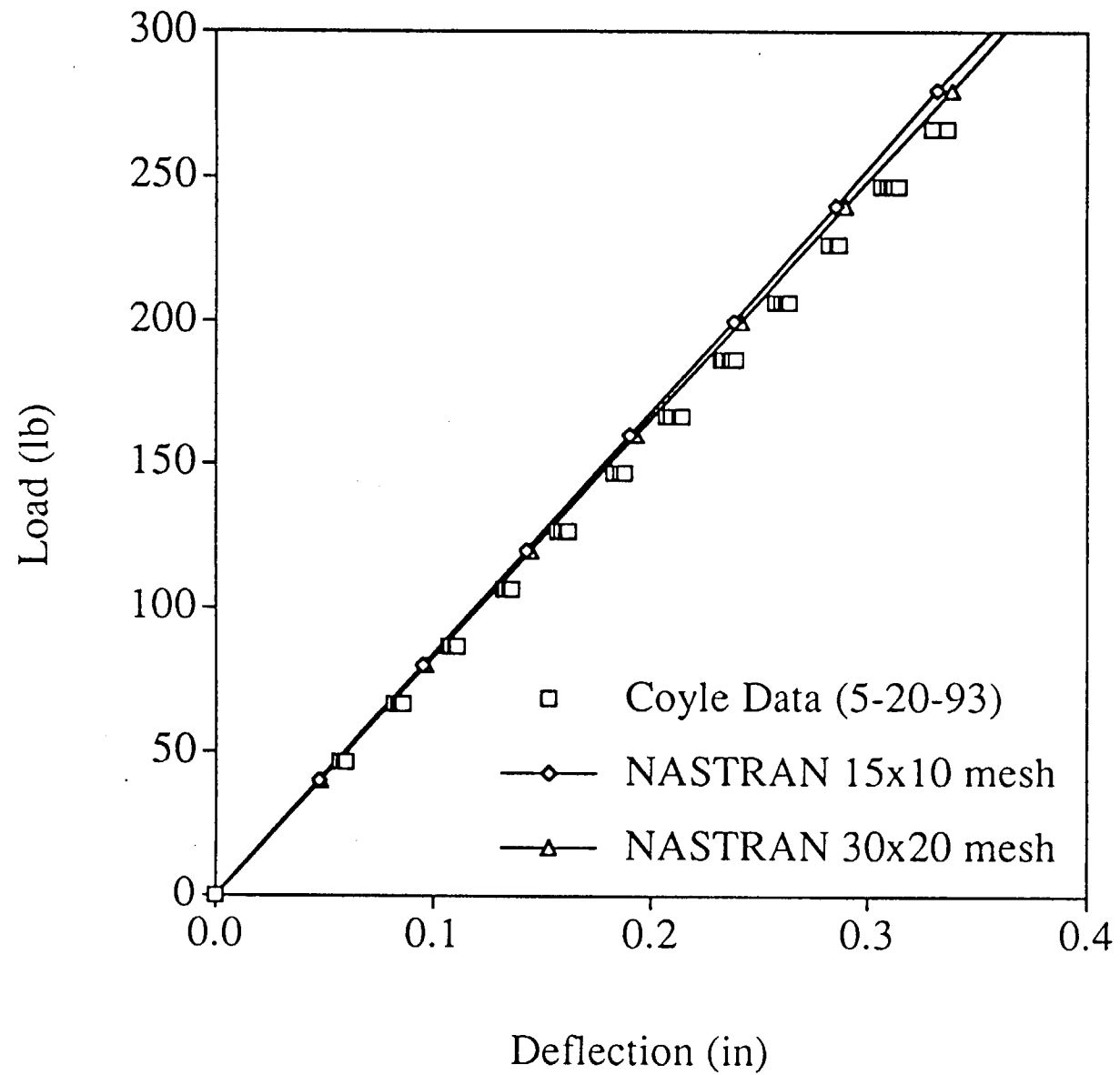
# Boundary Condition Tests

- Insulation Tests (performed earlier)
- Heated Region Width Sensitivity Tests (performed with a FEM)
- Point Support Torque Tests
- The Cooling Plumbing Effects
- LVDT Spring Load Effects

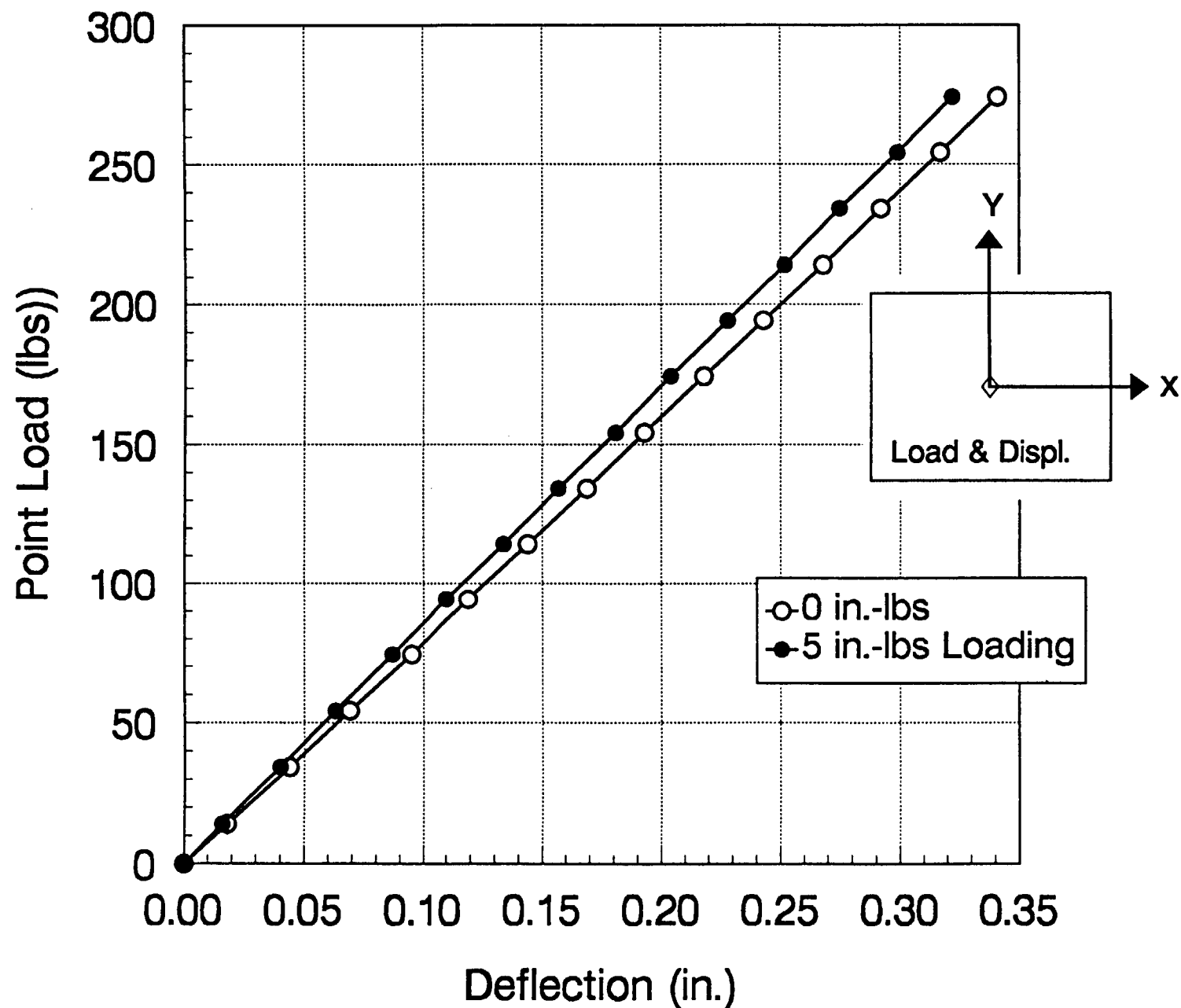
# Point Load Test Setup



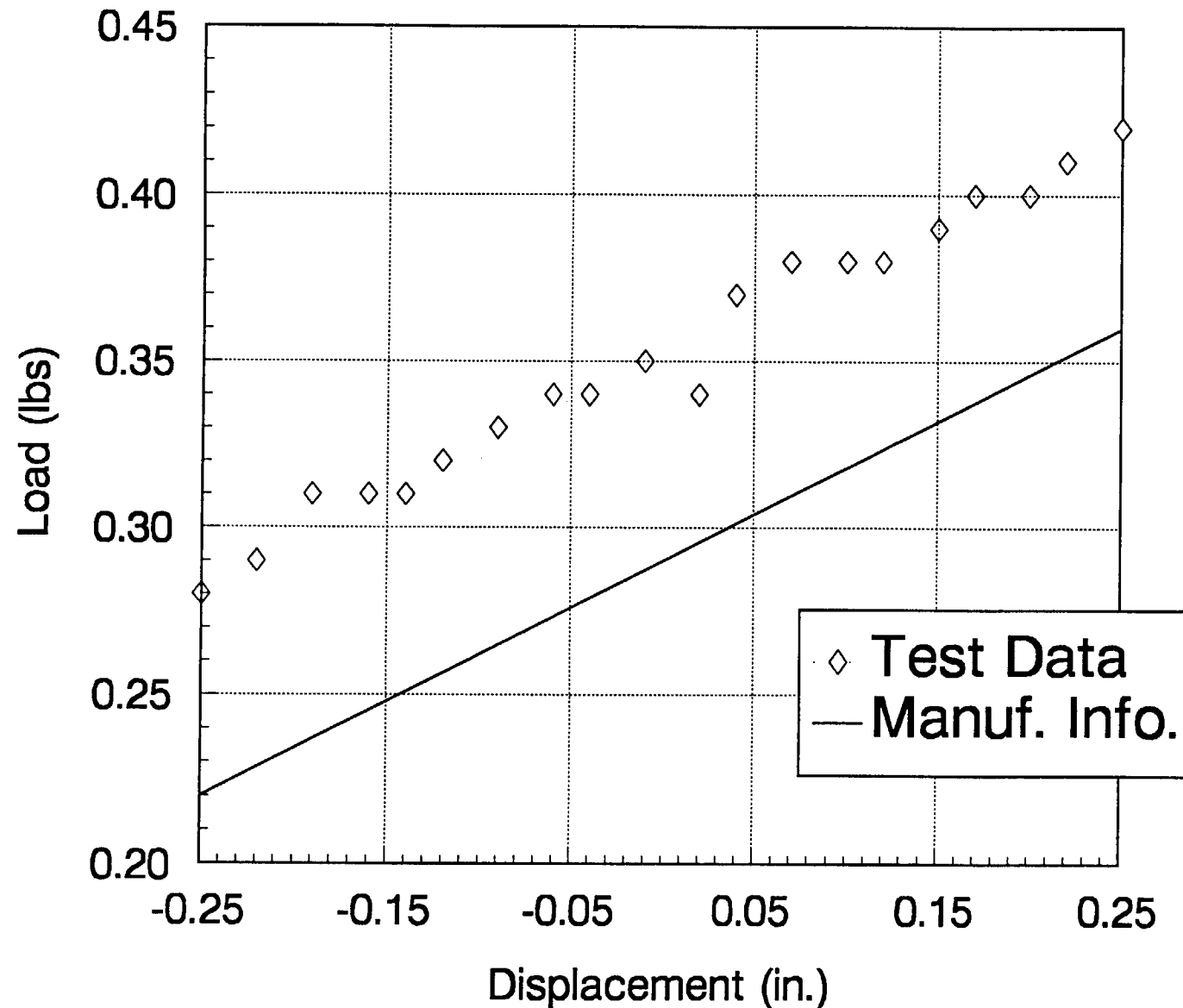
Load-Deflection Curve for Point Load Test



# Point Support Torque Tests For 0 and 5 in.-lbs



# LVDT Spring Load Versus Displacement For A Schaevitz Model GCD-121-250 LVDT



## **Future Research Plans**

- Initiate Thermal Buckling Tests of Stiffened Panels
- Initiate Thermal Buckling Tests of Aluminum Alloy Panels
- Conduct Static Load Yield Tests





APPENDIX I: GRANT PUBLICATIONS (January 1 to June 30, 1993)

1. M. Gambone, D. Gundel and F. Wawner, "The Effect of Isothermal Exposure on SiC Fibers", Proceedings, 17th Annual Conference on Composites, Materials, and Structures, Cocoa Beach Fl, January (1993).
2. D. Gundel, P. Taylor and F. Wawner, "The Fabrication of Thin Oxide Coatings on Ceramic Fibers by a Sol-Gel Technique", Journal of Materials Science, in review (1993).
3. D. Gundel and F. Wawner, "The Influence of Fabrication Quality on the Response of Titanium/SiC Fiber Composites to Thermal Exposure", Composites Engineering, in press (1993).
4. F. Wawner and D. Gundel, "Influence of Thermal and Environmental Exposure on Properties in Ti1100/SCS-6 Composites", Proceedings, 3rd Workshop on Titanium Metal Matrix Composites, La Jolla, CA, June (1993).
5. E.A. Thornton, "Thermal Buckling of Plates and Shells," Applied Mechanics Reviews, in press, (1993).



APPENDIX II: GRANT PRESENTATIONS (January 1 to June 30, 1993)

1. R.P. Gangloff, D.C. Slavik and R.S. Piascik, *Continuum and Micromechanical Modeling of Fatigue Crack Propagation Rate Laws*, SES Eringen Medal Symposium, Charlottesville, VA, June (1993).
2. D.C. Slavik and R.P. Gangloff, *Environmental Fatigue Crack Growth Mechanisms for Al-Li-Cu Alloys*, TMS-AIME Symposium on Fatigue of Advanced Materials, Denver, CO, February (1993).
3. D.C. Slavik and R.P. Gangloff, *Environmental Fatigue Crack Growth Mechanisms for Al-Li-Cu Alloys*, Fatigue 93, March (1993).
4. S.T. Pride, J.L. Hudson and J.R. Scully, *Metastable Pitting of Aluminum and Criteria for the Transition to Stable Pitting*, 1993 Corrosion Research in Progress Symposium, NACE Corrosion 93, March (1993).
5. M. Gambone, D. Gundel and F. Wawner, *The Effect of Isothermal Exposure on SiC Fibers*, 17th Annual Conference on Composites, Materials, and Structures, Cocoa Beach, FL, January (1993).
6. D. Gundel and F. Wawner, *The Influence of Fabrication Quality on the Response of Titanium/SiC Fiber Composites to Thermal Exposure*, 1st SES-ASME-ASCE Joint Meeting, Charlottesville, VA, June (1993).
7. T. McGarry, D. Gundel and F. Wawner, *The Effect of Thermal Exposure on Yttria Coated SCS-6 Fibers*, 1st SES-ASME-ASCE Joint Meeting, Charlottesville, VA, June (1993).
8. F. Wawner and D. Gundel, *Influence of Thermal and Environmental Exposure on Properties in Ti1100/SCS-6 Composites*, 3rd Workshop on Titanium Metal Matrix Composites, La Jolla, CA, June (1993).
9. E.A. Thornton, J.D. Kolenski and R.P. Marino, *Finite Element Study of Plate Buckling Induced by Spatial Temperature Gradients*, AIAA Paper No. 93-1572, AIAA/ASME/ASCE/AHS/ASC 34rd Structures, Structural Dynamics and Materials Conference, LaJolla, CA, April (1993).



APPENDIX III: GRANT PROGRESS REPORTS (January, 1988 to December, 1992)

1. R.P. Gangloff, G.E. Stoner and R.E. Swanson, "Environment Assisted Degradation Mechanisms in Al-Li Alloys", University of Virginia, Report No. UVA/528266/MS88/101, January, 1988.
2. R.P. Gangloff, G.E. Stoner and R.E. Swanson, "Environment Assisted Degradation Mechanisms in Advanced Light Metals", University of Virginia, Report No. UVA/528266/MS88/102, June, 1988.
3. R.P. Gangloff, G.E. Stoner and R.E. Swanson, "Environment Assisted Degradation Mechanisms in Advanced Light Metals", University of Virginia, Report No. UVA/528266/MS89/103, January, 1989.
4. R.P. Gangloff, "NASA-UVa Light Aerospace Alloy and Structures Technology Program", UVa Report No. UVA/528266/MS90/104, August, 1989.
5. R.P. Gangloff, "NASA-UVa Light Aerospace Alloy and Structures Technology Program", UVa Report No. UVA/528266/MS90/105, December, 1989.
6. R.P. Gangloff, "NASA-UVa Light Aerospace Alloy and Structures Technology Program", UVa Report No. UVA/528266/MS90/106, June, 1990.
7. R.P. Gangloff, "NASA-UVa Light Aerospace Alloy and Structures Technology Program", UVa Report No. UVA/528266/MS91/107, January, 1991.
8. R.P. Gangloff, "NASA-UVa Light Aerospace Alloy and Structures Technology Program", UVa Report No. UVA/528266/MS91/108, July, 1991.
9. R.P. Gangloff, "NASA-UVa Light Aerospace Alloy and Structures Technology Program", UVa Report No. UVA/528266/MS92/109, January, 1992.
10. R.P. Gangloff, "NASA-UVa Light Aerospace Alloy and Structures Technology Program", UVa Report No. UVA/528266/MS93/111, July, 1992.
11. R.P. Gangloff, "NASA-UVa Light Aerospace Alloy and Structures Technology Program", UVa Report No. UVA/528266/MSE93/112, March, 1993.



APPENDIX IV: AGENDA OF THE FOURTH ANNUAL NASA-UVA LA<sup>2</sup>ST  
GRANT REVIEW MEETING

AGENDA

FOURTH ANNUAL NASA-UVA LA<sup>2</sup>ST MEETING

Room 256, Building 1205  
Light Alloys Research Laboratory  
NASA-Langley Research Center  
Hampton, Virginia

Day 1: Tuesday, July 20, 1993

- 1:00-1:15 pm Dennis Dicus and Rick Gangloff: Welcome and LA<sup>2</sup>ST Program overview.
- 1:15-1:55 "Effect of Thermal Treatment on the Mechanical Properties of Ti-1100/SCS-6 Composites"; Douglas B. Gundel and F.E. Wawner.
- 1:55-2:25 "Characterization of the Viscoplastic Deformation Response of High Temperature Alloys", Mark A. Rowley and E.A. Thornton.
- 2:25-2:50 "Elevated Temperature Fracture of Advanced IM Aluminum Alloys"; Michael J. Haynes and R.P. Gangloff.
- 2:50-3:10 Break
- 3:10-3:45 "Effect of Specimen Orientation on Microstructural Evolution and Superplastic Properties of Weldalite<sup>TM</sup> Sheet"; Mark T. Lyttle and John A. Wert
- 3:45-4:15 "Effects of Temperature and Microstructure on the Fracture Toughness of AA 2090 and 2090 + In"; John A. Wagner and R.P. Gangloff.
- 4:15-4:50 "Experimental Study of the Nonlinear Viscoplastic Response of High Temperature Structures"; Marshall F. Coyle and E.A. Thornton.
- 6:00 Social (Precise time and place to be announced)

**NOTE:** Twenty-five to 30 minute talks should include 5 minutes of discussion and 35 to 45 minute talks must allot 7 to 10 minutes for discussion, within the scheduled time limit.

Day 2: Wednesday, July 21, 1993

- 8:20-8:55 am "Metastable Pitting in Aluminum Alloys and Criteria for the Transition To Stable Pitting", Sheldon Pride and J.R. Scully.
- 8:55-9:35 "Mechanisms of Localized Corrosion in Alloys 2090 and 2095"; E. Douglas Wall and G.E. Stoner.
- 9:35-10:05 "Environmentally Assisted Cracking of Selected Al-Li-Cu-X Alloys"; Raymond J. Kilmer and G.E. Stoner.
- 10:05-10:20 Break
- 10:20-11:00 "Hydrogen Interactions in Aluminum-Lithium Alloys and Hydrogen Embrittlement of AA2090"; Stephen W. Smith and J.R. Scully.
- 11:00-11:30 "Environmental Fatigue of Alloy 2090 Sheet and Plate"; D.C. Slavik and R.P. Gangloff.
- 11:30-11:55 "Environmental Effects in Fatigue Life Prediction: Dynamic Strain Rate Effects on Cracking in AA7075/NaCl"; Mark E. Mason and R.P. Gangloff.
- 11:55-1:00 pm Lunch
- 1:00-1:30 "Environmental Effects on Fatigue Crack Propagation and Closure in Titanium Alloys"; Sang-Shik Kim and R.P. Gangloff.
- 1:30-2:15 Group discussion between UVa and LaRC participants on the health and direction of the LA<sup>2</sup>ST Grant.
- 2:15 Individual discussions between UVa investigators and LaRC technical contacts on the direction and finances for the 1994 renewal. UVa faculty should schedule as needed.



## DISTRIBUTION LIST

- 1 - 2      Mr. D. L. Dicus  
Contract Monitor  
Metallic Materials Branch, MS 188A  
NASA Langley Research Center  
Hampton, VA 23665
- 3 - 4\*     NASA Scientific and Technical Information Facility  
P. O. Box 8757  
Baltimore/Washington International Airport  
Baltimore, MD 21240
- 5          Mr. Richard J. Siebels  
Grants Officer, M/S 126  
NASA Langley Research Center  
Hampton, VA 23665
- 6          Dr. Darrel R. Tenney  
Materials Division  
NASA Langley Research Center  
Hampton, VA 23665
- 7          Dr. Charles E. Harris  
Mechanics of Materials Branch  
NASA Langley Research Center  
Hampton, VA 23665
- 8          Mr. W. Barry Lisagor  
Metallic Materials Branch  
NASA Langley Research Center  
Hampton, VA 23665
- 9          Mr. T.W. Crooker  
Code RM  
NASA Headquarters  
Washington, DC 20546
- 10         Dr. Robert S. Piascik  
Mechanics of Materials Branch  
NASA Langley Research Center  
Hampton, VA 23665

- 11 Mr. W. Brewer  
Metallic Materials Branch, MS 188A  
NASA Langley Research Center  
Hampton, VA 23665
- 12 Mr. Thomas T. Bales  
Metallic Materials Branch, MS 188A  
NASA Langley Research Center  
Hampton, VA 23665
- 13 Dr. M.J. Shuart  
Aircraft Structures Branch  
NASA Langley Research Center  
Hampton, VA 23665
- 14 Dr. James H. Starnes, Jr.  
Aircraft Structures Branch  
NASA Langley Research Center  
Hampton, VA 23665
- 15 Mr. Dana Ward  
Northrop Corporation  
1 Northrop Avenue  
Mail Zone 3872562  
Hawthorne, CA 90250-3277
- 16 Dr. Santosh K. Das  
Senior Manager  
Metals and Ceramics Laboratory  
Allied-Signal, Inc.  
P. O. Box 1021  
Morristown, NJ 07960
- 17 Mr. E.A. Colvin  
Alcoa Technical Center  
Route 780, 7th Street Road  
Alcoa Center, PA 15069
- 18 Dr. L.M. Angers  
Alcoa Technical Center  
Route 780, 7th Street Road  
Alcoa Center, PA 15069
- 19 Dr. J. Andrew Walker  
Advanced Composite Materials Corporation  
1525 South Buncombe Road  
Greer, SC 29651

- 20 Mr. Fred Casey  
Space Transportation Systems Division  
Rockwell International  
Dept. 289 MC/AC56  
12214 Lakewood Blvd.  
Downey, CA 90241
- 21 E.A. Starke, Jr.; UVA
- 22-24 R.P. Gangloff; MS&E
- 25 G.E. Stoner; MS&E
- 26 J.A. Wert; MS&E
- 27 F.E. Wawner; MS&E
- 28 J.R. Scully; MS&E
- 29 E.A. Thornton; MAE
- 30-31 E.H. Pancake; Clark Hall
- 32 SEAS Preaward Administration Files
- 33 Mr. Gwyn Faile  
Code ED 24  
Marshall Space Flight Center  
Huntsville, AL 35812
- 34 Mr. Brian McPherson  
Code ED 24  
Marshall Space Flight Center  
Huntsville, AL 35812
- 35 Mr. Peter Rimbo  
Boeing Aerospace and Electronics  
Aerospace Group  
Seattle, WA 98124
- 36 Dr. Howard G. Nelson  
NASA-Ames Research Center  
EEM: 213-3  
Moffett Field, CA 94035
- 37 Dr. R.G. Forman  
Mail Code ES-5  
NASA-L.B. Johnson Space Flight Center  
Houston, TX 77058

- 38      Professor A.K. Noor  
         Center for Computational Structures Technology  
         NASA Langley Research Center  
         Hampton, VA 23665
- 39      Prof. A.K. Ghosh  
         Department of Materials Science and Engineering  
         University of Michigan  
         2102 Dow Building  
         Ann Arbor, MI 48109-2136
- 40      Dr. D. Fertton  
         Pechiney Centre de Recherches  
         De Voreppe  
         B.P. 27 -- 38340 Voreppe  
         FRANCE

\*One reproducible copy

Updated July, 1993